remote sensing

Special Issue Reprint

Radar Remote Sensing for Applications in Intelligent Transportation

Edited by
Zhihuo Xu, Jianping Wang and Yongwei Zhang

www.mdpi.com/journal/remotesensing

MDPI

Radar Remote Sensing for Applications in Intelligent Transportation

Radar Remote Sensing for Applications in Intelligent Transportation

Editors

Zhihuo Xu
Jianping Wang
Yongwei Zhang

MDPI • Basel • Beijing • Wuhan • Barcelona • Belgrade • Manchester • Tokyo • Cluj • Tianjin

Editors

Zhihuo Xu
Nantong University
Nantong
China

Jianping Wang
Delft University
of Technology
Delft
The Netherlands

Yongwei Zhang
Nantong University
Nantong
China

Editorial Office
MDPI
St. Alban-Anlage 66
4052 Basel, Switzerland

This is a reprint of articles from the Special Issue published online in the open access journal *Remote Sensing* (ISSN 2072-4292) (available at: https://www.mdpi.com/journal/remotesensing/special_issues/radar_rs_transportation).

For citation purposes, cite each article independently as indicated on the article page online and as indicated below:

LastName, A.A.; LastName, B.B.; LastName, C.C. Article Title. *Journal Name* **Year**, *Volume Number*, Page Range.

ISBN 978-3-0365-7954-2 (Hbk)
ISBN 978-3-0365-7955-9 (PDF)

Cover image courtesy of Zhihuo Xu

Contents

About the Editors . . . . . **vii**

Preface to "Radar Remote Sensing for Applications in Intelligent Transportation" . . . . . **ix**

Zhihuo Xu, Shuaikang Xue and Yuexia Wang
Incoherent Interference Detection and Mitigation for Millimeter-Wave FMCW Radars
Reprinted from: *Remote Sens.* **2022**, *14*, 4817, doi:10.3390/rs14194817 . . . . . **1**

Junhui Qian, Ziyu Liu, Yuanyuan Lu, Le Zheng, Ailing Zhang and Fengxia Han
Radar and Communication Spectral Coexistence on Moving Platform with Interference Suppression
Reprinted from: *Remote Sens.* **2022**, *14*, 5018, doi:10.3390/rs14195018 . . . . . **25**

Haichuan Li, Yongjun Liu, Guisheng Liao and Yufeng Chen
Joint Radar and Communications Waveform Design Based on Complementary Sequence Sets
Reprinted from: *Remote Sens.* **2023**, *15*, 645, doi:10.3390/rs15030645 . . . . . **49**

Bo Yang and Hua Zhang
A CFAR Algorithm Based on Monte Carlo Method for Millimeter-Wave Radar Road Traffic Target Detection
Reprinted from: *Remote Sens.* **2022**, *14*, 1779, doi:10.3390/rs14081779 . . . . . **69**

Can Liang, Yang Li, Xueyao Hu, Yanhua Wang, Liang Zhang, Min Wang and Junliang Guo
Coherent-on-Receive Synthesis Using Dominant Scatterer in Millimeter-Wave Distributed Coherent Aperture Radar
Reprinted from: *Remote Sens.* **2023**, *15*, 1505, doi:10.3390/rs15061505 . . . . . **93**

Qisong Wu, Lingjie Chen, Yanping Li, Zijun Wang, Shuai Yao and Hao Li
Reweighted Robust Particle Filtering Approach for Target Tracking in Automotive Radar Application
Reprinted from: *Remote Sens.* **2022**, *14*, 5477, doi:10.3390/rs14215477 . . . . . **117**

Yong Wang, Di Wang, Yunhai Fu, Dengke Yao, Liangbo Xie and Mu Zhou
Multi-Hand Gesture Recognition Using Automotive FMCW Radar Sensor
Reprinted from: *Remote Sens.* **2022**, *14*, 2374, doi:10.3390/rs14102374 . . . . . **135**

Bin Tan, Zhixiong Ma, Xichan Zhu, Sen Li, Lianqing Zheng, Libo Huang and Jie Bai
Tracking of Multiple Static and Dynamic Targets for 4D Automotive Millimeter-Wave Radar Point Cloud in Urban Environments
Reprinted from: *Remote Sens.* **2023**, *15*, 2923, doi:10.3390/rs15112923 . . . . . **153**

Tianwen Zhang and Xiaoling Zhang
HTC+ for SAR Ship Instance Segmentation
Reprinted from: *Remote Sens.* **2022**, *14*, 2395, doi:10.3390/rs14102395 . . . . . **173**

Qingquan Tan, Kuikui Fan, Wenwen Yang and Guoqing Luo
Low Sidelobe Series-Fed Patch Planar Array with AMC Structure to Suppress Parasitic Radiation
Reprinted from: *Remote Sens.* **2022**, *14*, 3597, doi:10.3390/rs14153597 . . . . . **207**

Zihuan Mao, Shengheng Liu, Si Qin and Yongming Huang
Cramér-Rao Bound of Joint DOA-Range Estimation for Coprime Frequency Diverse Arrays
Reprinted from: *Remote Sens.* **2022**, *14*, 583, doi:10.3390/rs14030583 . . . . . **223**

About the Editors

Zhihuo Xu

Zhihuo Xu received the Ph.D. degree in communication and information system, in 2016, from the University of Chinese Academy of Sciences (UCAS) and the Institute of Electronics of the Chinese Academy of Sciences (IECAS), Beijing, China. He founded Radar Research Group, School of transportation in Nantong University, China, in 2016, where he is currently a Associate Professor. From 2017 to 2018, he was an Academic Visitor with the University of Birmingham, Birmingham, UK. His current research interests include automotive radar system design and signal processing, synthetic aperture radar (SAR), MIMO radar, cognitive radar imaging and radar image processing. He has been a peer reviewer for several international journals, such as the IEEE Transactions on Microwave Theory and Techniques, IEEE Transaction on Vehicular Technology, IEEE Transactions on Geoscience and Remote Sensing, IEEE Transactions on Intelligent Transportation Systems, IEEE Transactions on Industrial Electronics, IEEE Transactions on Electromagnetic Compatibility, IEEE Sensors Journal, IEEE Journal of Selected Topics in Applied Earth Observations and Remote Sensing, IET Radar Sonar and Navigation, IEEE Signal Processing Letter, IEEE Geoscience and Remote Sensing Letters, Signal Processing and Digital Signal Processing.

Jianping Wang

Jianping Wang received the B.Sc. degree from the North China University of Technology, Beijing, China, in 2009, the M.Sc. degree from the Beijing Institute of Technology, Beijing, in 2012, and the Ph.D. degree from the Delft University of Technology, Delft, The Netherlands, in 2018, all in electrical engineering. From August 2012 to April 2013, he worked as a Research Associate at the University of New South Wales (UNSW), Sydney, NSW, Australia, on frequency-modulated continuous-wave (FMCW) synthetic aperture radar (SAR) signal processing for formation flying satellites. He is currently a Post-Doctoral Researcher with the Group of Microwave Sensing, Signals and Systems (MS3), Delft University of Technology. His research interests include microwave imaging, signal processing, and antenna array design. Dr. Wang was a TPC Member of the IET International Radar Conference, Nanjing, China, in 2018. He was a finalist of the Best Student Paper Awards in the International Workshop on Advanced Ground Penetrating Radar (IWAGPR), Edinburgh, U.K., in 2017, and the International Conference on Radar, Brisbane, QLD, Australia, in 2018. He has served as a Reviewer of IEEE Transactions on Geoscience and Remote Sensing (TGRS), IEEE Geoscience and Remote Sensing Letters, IEEE Sensors Journal, IEEE Transactions on Image Processing (TIP), Journal of Applied Geophysics, and so on.

Yongwei Zhang

Yongwei Zhang received the B.S. degree in Communication Engineering from Jilin University in 1996, and the Ph.D. degree from School of Electrical and Electronic Engineering, The University of Manchester, U.K., in 2007. In 1996, he joined Lucent Technologies (AT&T initially), China, where he was an application engineer on 5ESS® system, and later a system engineer and had been worked for Lucent Technologies until 2003. While he had been working for Lucent, in 1998, he was sent as a visitor to the Bell Laboratories, Indian Hill, Naperville, IL, USA, trained in communication system engineering tool development and later certified as an international instructor. In the years working for Lucent Technologies from 1996 to 2003, he had been involved in 5ESS® Switch application engineering and optimization for wireless communication systems. In 2003, he joined The University of Manchester first as a Ph.D. student and later a Research Fellow, then a task leader of the front-end

design work package in Mid-Frequency Aperture Array Consortium for the Square Kilometre Array (SKA). In 2020, he joined Nantong University, his current research interests include array antenna design based on flexible materials, electromagnetics, antenna array calibration, and radio astronomy instrumentation.

Preface to "Radar Remote Sensing for Applications in Intelligent Transportation"

The emergence of self-driving vehicles has sparked curiosity among people, and the technology related to it advances every day. If you were asked to ride in a self-driving vehicle, your first reaction might be: is it safe to ride in a driverless car? Yes, self-driving cars are meant to improve traffic efficiency while ensuring safety. To achieve this goal, the millimeter-wave radar, with its all-weather detection capabilities, has become an important apparatus in the field of self-driving cars. On this crucial turning point, we launched a Special Issue on radar remote sensing in intelligent transportation and received 23 manuscript submissions. After fair and rigorous peer review process, we finally accepted eleven excellent papers covering diverse aspects. Thus, this book reflects the latest research results of radar remote sensing in intelligent transportation to a certain extent.

The automotive millimeter-wave radar has obvious advantages. However, as an active transmission remote sensing technology, the signal transmitted by the radar may become a strong interfering source for neighboring radars. The intensity of this interference signal is usually much higher than that of the target signal, leading to misjudgment by unmanned driving systems and eventually turn into potential traffic accidents. As self-driving technology evolves, the demand for automotive millimeter-wave radar in the market has grown exponentially, and the probability of interference between radars has also increased. The first paper in this book detects interference zone numbers before restoring the echoes in the interference area. Specifically, a sparse-based technique is proposed to suppress non-coherent interference between frequency-modulated continuous wave radars. First, a low-pass filter-based technique is developed to detect the envelope of the interference. Next, the marked areas with interference are treated as missing data. Then, the interference suppression problem is formulated as an echo interpolation recovery problem. Finally, the process of restoring radar echoes is derived based on the alternating direction method. This method has been verified by hardware experiments and has achieved good interference suppression performance.

Sharing radar detection information with neighboring vehicles could better compensate for blind spots in individual vehicle perception and reduce interference. This involves joint communication and radar sensing integration. As a very promising direction in intelligent transportation, this book includes two papers on this topic. The second paper designs a radar spatial-temporal transceiver and communication spatial-temporal codebook in the spectrum coexistence system on moving platforms. The joint radar and communication waveform often have a high range sidelobe, which will degrade the target detection performance of an automotive joint radar and communication system. To solve this problem, the third paper proposes a joint radar and communication complementary waveform group design method by exploiting the philosophy of the complementary sequence.

The constant false alarm rate (CFAR) detector plays a vital role in adaptive target detection of the radar. However, traditional CFAR detection algorithms use a sliding window to find the target limit radar detection speed and efficiency. In such cases, the fourth paper proposes and discusses a CFAR detection method that transforms the Monte Carlo simulation principle into randomly sampling instantaneous Range–Doppler data to improve the radar detection ability for moving targets such as pedestrians and vehicles in traffic environments. The fifth article describes a millimeter-wave distributed coherent aperture radar that can be used to improve the signal-to-noise ratio of the target by coherent-on-receive synthesis. The synchronization errors are calibrated with the estimated coherent parameters of the dominant scatterer, which can be defined as an unknown strong target in radar detection scenarios. Multi-object tracking based on robust detection is an old but new issue for self-driving cars. The sixth paper develops a Reweighted Robust Particle Filtering Approach for

Target Tracking in Automotive Radar Applications.

Fascinatingly, as human–computer interaction continues to evolve, hand gestures are assuming an increasingly vital role in intelligent vehicle control. The seventh paper showcased in this collection introduces a remarkable multi-hand gesture recognition system that leverages automotive frequency-modulated continuous wave (FMCW) radar. Furthermore, the eighth paper focuses on addressing the limitations of traditional radar systems for self-driving. It presents a cutting-edge target tracking algorithm that harnesses the wealth of information provided by 4D millimeter-wave radar point clouds. This novel approach enables more accurate estimation of motion states and target contours, thanks to the higher resolution target point cloud data. It offers a significant advancement in overcoming the challenges faced by traditional radar systems. Beyond land transportation, the exploration of sea transportation also takes center stage in this compilation. In the ninth paper, a groundbreaking hybrid task cascade plus method is proposed, designed to enhance ship instance segmentation in Synthetic Aperture Radar (SAR) images.

The last two papers are related to radar antenna direction. For automobile radar systems, the antenna array requires a low sidelobe level (SLL) to reduce interference. A low-SLL planar array based on linear series-fed patch sub-arrays is presented in the ninth paper. Frequency diverse array (FDA) produces a beampattern with controllable direction and range by slightly shifting the carrier frequencies across the elements, which is attractive in many applications. In the last paper, the analytical expressions of the Cramér-Rao bounds in stochastic signal cases for joint Direction of Arrival-range estimation using coprime FDA are derived.

Finally, we owe a great deal to many people for this book's successful publication. The guest editors would like to express special thanks to the journal editor, Nancy Yang, for her tremendous help. It can be said that without Nancy's long-term vision and pragmatic and meticulous cooperation, this book would not have been published. Nancy's work ability is outstanding, and she is friendly, kind-hearted, beautiful and hardworking. The reason why the remote sensing journal is getting better and better is because of great talents like Nancy. In addition, thanks go to all the paper authors and reviewers. It is your careful and meticulous work that has contributed to our joint efforts in radar remote sensing for intelligent transportation.

Zhihuo Xu, Jianping Wang, and Yongwei Zhang
Editors

remote sensing

MDPI

Article

Incoherent Interference Detection and Mitigation for Millimeter-Wave FMCW Radars

Zhihuo Xu [1,2], Shuaikang Xue [1,2] and Yuexia Wang [1,2,*]

[1] Radar Remote Sensing Group, School of Transportation, Nantong University, Nantong 226019, China
[2] School of Information Science and Technology, Nantong University, Nantong 226019, China
* Correspondence: venus@ntu.edu.cn; Tel.: +86-0513-85962369

Abstract: Current automotive radar technology is almost exclusively implemented using frequency modulated continuous wave (FMCW) radar in the millimeter wave bands. Unfortunately, incoherent interference is becoming a serious problem due to the increasing number of automotive radars in dense traffic situations. To address this issue, this article presents a sparsity-based technique for mitigating the incoherent interference between FMCW radars. First, a low-pass filter-based technique is developed to detect the envelope of the interference. Next, the labeled regions where interference is present are considered as missing data. In this way, the problem of mitigating interference is further formulated as the restoration of the echo using L1 norm-regularized least squares. Finally, the alternating direction method of the multipliers-based technique is applied to restore the radar echoes. Extensive experimental results demonstrate the effective performance of the proposed approach. Compared to state-of-the-art interference mitigation methods, the proposed method remarkably improves the quality of radar targets.

Keywords: millimeter-wave radar; frequency modulated continuous wave (FMCW); incoherent interference; sparse optimization

Citation: Xu, Z.; Xue, S.; Wang, Y. Incoherent Interference Detection and Mitigation for Millimeter-Wave FMCW Radars. *Remote Sens.* **2022**, *14*, 4817. https://doi.org/10.3390/rs14194817

Academic Editor: Piotr Samczynski

Received: 28 June 2022
Accepted: 11 September 2022
Published: 27 September 2022

1. Introduction

Radar is a highly robust and reliable sensor for automotive applications [1]. First, automotive radars measure the relative distance, velocity, and angle of targets through time delay and phase shift of radio signals, and therefore can perform well in adverse weather conditions. Second, automotive radars operate in the millimeter wave band and have a large bandwidth; hence, a high range resolution of 3 cm can be achieved [2]. In addition, the radar system is both simple and effective, using linear frequency-modulated continuous wave (FMCW) technology [3]. Therefore, automotive FMCW radar has the advantageous benefits of small size, light weight, and low power consumption, and is widely used in self-driving vehicle applications [4].

Active signal transmission is one of the advantages of radar; however, it can cause serious interference problems with neighboring radars [5–7]. Similar to non-homogeneous clutter [8,9], radar target detection performance is degraded by incoherent interference. The interference probability can be reduced by alternating the parameters of radar waveforms [10]. Although different FMCW radars use different parameters, incoherent interference can occur when the spectrum of the interfering signal overlaps the transmitted wave of the radar under test. The incoherent interference produces strong noise and even ghost targets. Consequently, suppressing the incoherent interference in radar images is one of the most pressing issues for automotive FMCW radars.

Although the mitigation of incoherent interference remains an open problem, several interference mitigation approaches have been proposed. The first type of approach aims to design radar waveforms to overcome the drawbacks of FMCW radar with a fixed time–frequency relationship. Orthogonal pseudo-random noise waveforms can be designed to reduce the probability of interference [11,12]. Phase-modulated continuous wave

(PMCW) [5] and phase-coded frequency-modulated continuous wave (PC-FMCW) [13] approaches have been successively proposed to avoid interference with FMCW radars. However, mutual interference can nevertheless appear between PMCW and FMCW radars.

In order to be applicable to FMCW radar images, signal post-processing techniques have been used to develop interference suppression methods [14]. Brooker [15] deals with interference by inverse cosine windowing and substituting zeros for the high-amplitude transient. Before removal of transient interference by substituting zeros over the period of interference, accurate interference detection is required in order to determine the location of the interference. Neemat et al. [16] first used image processing techniques to detect interference in the short-time Fourier transform (STFT) domain, then carried out beat signal model parameters estimation analysis using autoregression in the STFT. Finally, they replaced suppressed beat–frequency frames with linear-predicted interpolated ones. Jung et al. [17] applied an order statistics–constant false alarm rate (OS-CFAR) algorithm to identify the interference regions. Then, the Kalman filter was used to estimate the state and predict the signals in the interference region. After filtering of the signal, large peaks in the time domain beat signal were reduced and the target signal was estimated. Wang et al. [18] first cut out the interference-contaminated region of the received signal, then interpolated the signal samples in the cutout segment using the matrix-pencil method.

Unlike the above-mentioned methods of zeroing or reconstructing the signal for interference-contaminated areas, processing of the entire received signal is another technical route to interference suppression. Lee et al. [19] considered the low-intensity target signal as the noise component to be removed and the high-intensity pulse-like interference signal as the signal to be retained. Using a wavelet transform and thresholding the wavelet coefficients of the low-pass filter output, they were able to extract the pulse-like interference signal. Afterwards, the interference signal was subtracted from the original low-pass filter output to generate the desired target signals. The beat frequencies of real targets always present a positive frequency, whereas only the noise and the interference are in the negative half of the frequency spectrum. Thus, Jin and Cao [20] calculated the power of the negative frequency as a reference of interference and fed the positive frequency and negative frequency components into the primary and reference channel, respectively, of an adaptive noise canceler (ANC). Wu et al. [21] proposed an iterative modified threshold method based on empirical mode decomposition (IMT-EMD) for interference suppression in FMCW automotive radars, and applied the consecutive mean square error algorithm to determine the interference-dominated components after decomposing. Specifically, the interference problem can be considered as the sum of two component signals, i.e., the target signal plus the interfering signal. Therefore, interference reduction can be achieved by separating the interfering signal from the received signal. From this perspective, [22] developed an interference mitigation technique to successfully separate the interference from the received signal in the tunable Q-factor wavelet transform domain. Uysal [23] applied morphological component analysis (MCA) [24] theory to decompose the received signal into interference and target signals. Rock et al. [25] evaluated a convolution neural network (CNN)-based method for carrying out interference reduction on real FMCW radar measurements by combining real measurements with simulated interference in order to obtain input–output data suitable for training their CNN model.

In summary, the incoherent interference problem is a pressing problem in automotive FMCW radars that considerably negates the inherent advantages of radar by decreasing the detection probability and reliability of sensors. Although this challenge has been investigated and several aforementioned approaches have been developed in this field, there remains a need for an efficient solution that can help to mitigate the strong interference in radar images. The contributions of this work to this problem can be summarized as follows:

- A simple yet effective interference detection technique using a low-pass filter is presented, and the presence of interference is further determined from the statistics of the output envelope of this filter. In this way, the results of interference detection can indicate the presence or absence of interference. We propose an interference mitigation algorithm that cannot be started in the absence of interference, which significantly increases real-time processing performance.
- A sparsity model is presented to reduce the incoherent interference by considering the interference regions as missing data. Using L1 norm-regularized least squares, an alternating direction method of multipliers (ADMM)-based technique is been derived to restore the radar echoes.
- In several comparison experiments, dynamic incoherent interference is generated; the case of dynamic interference is much closer to the real-world self-driving situation. In experiments with dynamic interference signals, the comparative performance of different algorithms is comprehensively evaluated and the potential use of the algorithms in real roads is further analyzed.
- In addition, both the wavelet-based [19] and the MCA-based [23] methods are improved when using our proposed interference envelop detection approach.
- Our extensive experiments demonstrate that the proposed method significantly outperforms the state-of-the-art methods on both simulated and real radar interference mitigation tasks.

The rest of this paper is outlined as follows. Section 2 introduces the formulations related to the incoherent interference between FMCW radars. Section 3 proposes detection and mitigation of incoherent interference. Section 4 demonstrates the extensive measurements used to compare the proposed techniques with state-of-the-art methods. Section 5 discusses sparsity-based methods, algorithm complexity, and the impact on performance of interference regions that lead to missing data components. Finally, we present our conclusions in Section 6.

2. Incoherent Interference

According to recommendations by the International Telecommunication Union (ITU), most automotive radars currently operate within the 76–81 GHz bandwidth with FMCW signals [26]. The transmitted radar signal $s_{\mathrm{tx}}(t)$ can be written as follows:

$$s_{\mathrm{tx}}(t) = A_{\mathrm{tx}}\cos(2\pi f_c t + \pi k_r t^2), \tag{1}$$

where t is time, A_{tx} is the amplitude of the transmitted signal, f_c is the center frequency of the radar, and k_r is the chirp rate. Suppose a vehicle at a distance R meters from the radar is driving at a speed v m/s; then, the corresponding radar echo is described as

$$s_{\mathrm{rx}}(t) = A_{\mathrm{rx}}\cos[2\pi f_c(t-\Delta t) + \pi k_r(t-\Delta t)^2], \tag{2}$$

where A_{rx} is the amplitude of the echo, the delay time $\Delta t = 2(R+vt)/c$, and c is the velocity of light.

After the dechirp operation, the received signal is expressed as

$$r_t(t) = A_t\cos(2\pi\Delta t k_r t + \phi_r), \tag{3}$$

where A_t is the amplitude of the received signal and ϕ_r is the phase that includes the target Doppler information. The frequency of the target signal with respect to time t is further derived as

$$f_t(t) = \Delta t k_r. \tag{4}$$

If the neighboring radars and the radar under test have the same transmit waveform, then coherent interference may appear; false targets are generated when this type of interference signal enters the radar receiver baseband. Fortunately, this kind of interference is very unlikely to happen because the phase noise between the radar under test and

interfering radars is not correlated. The transmitted signal of a neighboring radar is formulated as

$$s_{\text{txi}}(t) = A_{\text{txi}}\cos[2\pi f_i(t+t_0) + \pi k_i(t+t_0)^2], \tag{5}$$

where t_0 is the time offset with the radar under test as the reference, A_{txi} is the amplitude, f_i is the center frequency, and k_i is the chirp rate for the neighboring radar.

When the transmitted signal of the neighboring radar passes through the receiver of the radar under test, the interfering signal after dechirping is

$$r_i(t) = A_i\cos[2\pi(f_c - f_i)t + \pi(k_r - k_i)t^2 - 2\pi k_i t_0 t + \phi_i], \tag{6}$$

where A_i and ϕ_i are the amplitude and residual phase of the interfering signal, respectively. According to the above equation, the frequency of the interfering signal with respect to time t is

$$f_i(t) = f_c - f_i - k_i t_0 + (k_r - k_i)t. \tag{7}$$

It can be seen that the above interfering signal is a linear FM signal, which is called incoherent interference. The part of the interfering signal with a frequency below half of the radar receiver sampling frequency is fully sampled, and the rest above it is undersampled.

The total received signal can be considered as the sum of the target signal and the interfering signal, that is, $r(t) = r_t(t) + r_i(t)$, as shown in Figure 1. It is worth mentioning that the power of the target signal is proportional to R^{-4} while the amplitude of the interference is proportional to R_i^{-a}, where a is a factor that describes the multi-path transmission of the interfering signal and R_i is the distance between the interfering radar and the radar under test. Low-intensity incoherent interference signals have little effect on radar performance, and only raise the noise floor. In this work, the intensity of the interfering signal is considered to be stronger than that of the target signal, which makes it difficult to suppress the interference. Therefore, $2 \leq a < 4$.

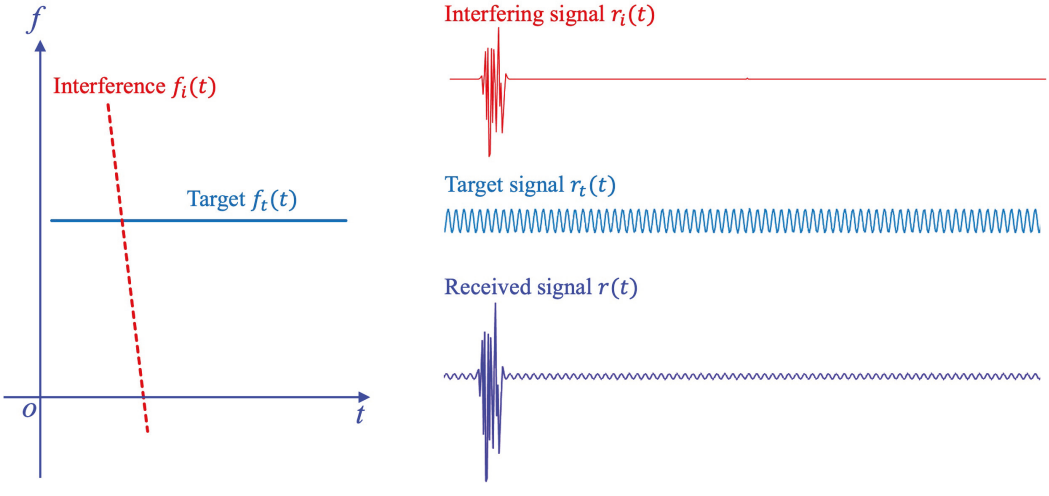

Figure 1. Demonstration of incoherent interference.

3. Proposed Approaches

3.1. Interference Envelope Detection

Interference envelope detection is the first priority in interference mitigation. The precise location of the interference facilitates the reduction of interference with minimal computational complexity. After discrete-time quantization sampling, the received signal

can be described as $r(n)$, where n denotes the nth sample. First, the amplitude information is obtained by taking the modulus of the radar received signal as

$$A_r(n) = |r(n)|. \tag{8}$$

Next, one low-pass finite impulse response filter (LP-FIR) is designed to detect the envelop. The frequency response of the filter is

$$H(\omega) = \sum_{n=0}^{K} h_n e^{-jn\omega}, \tag{9}$$

where K is the order of the filter and h_n is a coefficient of the filter. Thus, the impulse response of the filter can be written as

$$h(n) = \sum_{i=0}^{K} h_i \delta[n-i] = h_n, 0 \le n \le K. \tag{10}$$

There are many methods that can be used to solve the filter coefficients, such as the window function method and the frequency sampling method [27]. Here, a minimum mean square error (MMSE)-based method is applied to design the filter.

To simplify the design, $h(n)$ is expected to be even symmetric and the order K is set as an odd number. Hence, the discrete-time Fourier transform (DTFT) of $h(n)$ can be rewritten as

$$H(\omega) = e^{-j\omega(N+1)/2} \sum_{n=0}^{(K+1)/2} h_n \cos\left(\omega\left(\frac{K+1}{2} - n\right)\right), \tag{11}$$

According to the above equation, the phase response of the filter is $\phi(\omega) = e^{-j\omega(K+1)/2}$. Thus, a desired filter $H_d(\omega)$ can be predefined by combining the phase response $\phi(\omega)$ with a desired amplitude response. The design of the filter can then be further expressed as an MMSE problem:

$$\min_{h(n)}\left(E(\omega) = \int_{-\pi/2}^{\pi/2} \mid H(\omega) - H_d(\omega) \mid^2 d\omega\right). \tag{12}$$

The above problem is minimized by applying the partial derivative of $E(\omega)$ with respect to $h(n)$ to obtain the solution,

$$h(n) = \int_{-\pi/2}^{\pi/2} \cos(n\omega) H_d(\omega) d\omega. \tag{13}$$

Because the frequency of the interference envelope is low, the normalized cutoff frequency of the filter is set to 0.2, the passband normalized frequency is 0.005, the order of the filter is set to 19, and a filter coefficient vector is designed: $h(n) = 0.01 * [0.59, 1.08, 1.91, 2.99, 4.25, 5.61, 6.94, 8.10, 8.97, 9.43, 9.43, 8.97, 8.10, 6.94, 5.61, 4.25, 2.98, 1.91, 1.08, 0.59]$. The amplitude response of the filter is shown in Figure 2.

Applying the designed filter to the amplitude sequence, the envelope $A(n)$ can be obtained:

$$A(n) = \sum_{k=0}^{N-1} h(k) A_r(n-k), \tag{14}$$

where N is the length of the received signal.

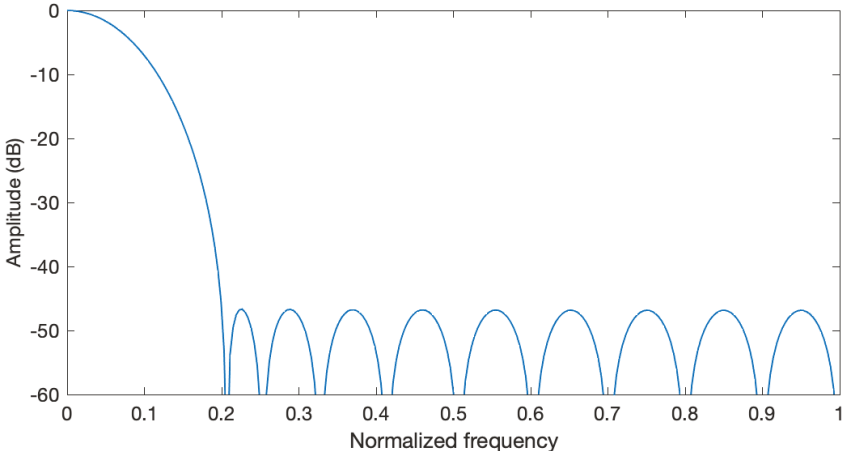

Figure 2. The amplitude response of the designed filter.

3.2. Generating Missing Data for Interference Regions

The method for detecting of the interference envelope described above applies to all the received signals. Next, it is necessary to determine whether there is interference in the received signal. Because the target echo signals are superimposed as complex sine waves, the mean and maximum values of the echo amplitude do not differ very much. However, according to a large number of experiments, the maximum value of the interfering signal amplitude is at least three times larger than the mean value of the echo amplitude; thus, the presence of interference is determined by

$$\text{label}_{\text{inter}} = \begin{cases} 1 & \max(|A(n)|) > 3 * \text{mean}(|A(n)|), \\ 0 & \text{otherwise.} \end{cases} \tag{15}$$

In addition, the $\text{label}_{\text{inter}}$ label indicates whether the proposed data interpolation algorithm is stopped or started, reducing the processing complexity. Then, the nth received signal sample is further determined as either an affected or unaffected sample according to the following equation:

$$z(n) = \begin{cases} 1 & \text{label}_{\text{inter}} \& |A(n)| > \beta * \text{mean}(|A(n)|), \\ 0 & \text{otherwise.} \end{cases} \tag{16}$$

where β is a parameter that depends on the power of the interference.

The interfering areas are then set to be missing data:

$$y^*(n) = \begin{cases} 0 & z(n) = 1, \\ r(n) & z(n) = 0. \end{cases} \tag{17}$$

In keeping with the above equations, Figure 3 presents the detected interference envelope and the received signal with missing data. As can be seen from the plots, the proposed method is able to effectively detect four interference regions and accurately identify the affected samples. As plotted in Figure 4, in the absence of interference the proposed approach accurately sets $\text{label}_{\text{inter}}$ as 0, the received signal is identified as the target signal, and no further interference detection or mitigation is required.

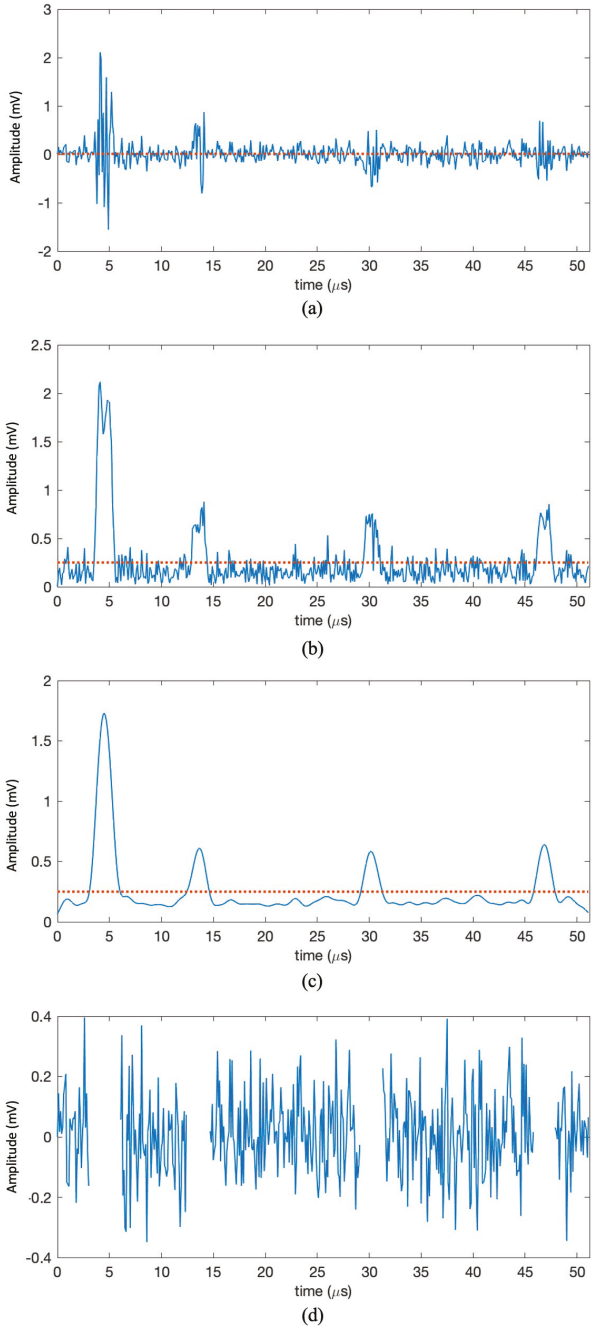

Figure 3. In the presence of interference ($\text{label}_{\text{inter}} = 1$): (**a**) the real part of the received signal; (**b**) the amplitude of the received signal; (**c**) the interference envelope detected by LPF; and (**d**) the received signal containing the affected samples. The dashed line in the subplots indicates the mean value of the corresponding signal.

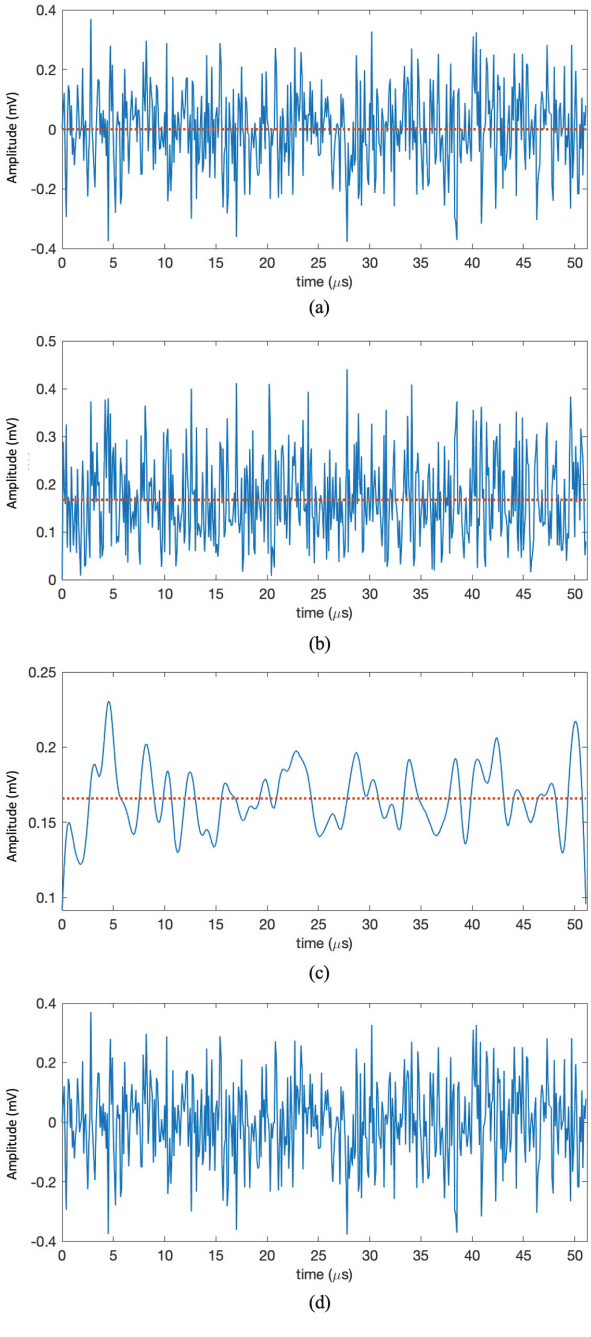

Figure 4. In the absence of interference ($\text{label}_{\text{inter}} = 0$): (**a**) the real part of th received signal; (**b**) the amplitude of the received signal; (**c**) the echo envelope detected by LPF; and (**d**) the received signal that does not contain affected samples. The dashed line in the sub-figures indicates the mean value of the corresponding signal.

3.3. Data Interpolation Using L1 Norm Least Squares Method

Suppose the length of a signal $y(n)$ is N; then, the M-point ($M \geq N$) inverse DFT of the signal $y(n)$ is defined as follows:

$$\mathbf{y} = \mathbf{W}\mathbf{x}, \tag{18}$$

where

$$\mathbf{W} = \frac{1}{M}\begin{bmatrix} 1 & 1 & \cdots & 1 \\ 1 & e^{\frac{j2\pi}{M}} & \cdots & e^{\frac{j(M-1)2\pi}{M}} \\ \vdots & \vdots & & \vdots \\ 1 & e^{\frac{j(N-1)2\pi}{M}} & \cdots & e^{\frac{j(N-1)(M-1)2\pi}{M}} \end{bmatrix},$$

$\mathbf{y} = [y(0), y(1), \cdots, y(N-1)]^{\mathsf{T}}$, and the DFT coefficients $\mathbf{x} = [x(0), x(1), \cdots, x(M-1)]^{\mathsf{T}}$.

Therefore, the DFT coefficient is expressed as

$$\mathbf{x} = \mathbf{W}^{\mathsf{H}}\mathbf{y}, \tag{19}$$

with

$$\mathbf{W}^{\mathsf{H}} = \begin{bmatrix} 1 & 1 & \cdots & 1 \\ 1 & e^{\frac{-j2\pi}{M}} & \cdots & e^{\frac{-j(N-1)2\pi}{M}} \\ \vdots & \vdots & & \vdots \\ 1 & e^{\frac{-j(M-1)2\pi}{M}} & \cdots & e^{\frac{-j(M-1)(N-1)2\pi}{M}} \end{bmatrix},$$

and $\mathbf{W}\mathbf{W}^{\mathsf{H}} = \mathbf{I}$.

In the above discussion the target signal is in the form of a complex sine wave, and is therefore sparse in the DFT domain. Thus, the problem of missing data imputation can be formulated with the L1 norm as

$$\begin{aligned} &\arg\min_{\mathbf{x}} \quad \|\mathbf{x}\|_1, \\ &\text{s.t.} \quad \mathbf{y}^* = \mathbf{z}(\mathbf{W}\mathbf{x}), \end{aligned} \tag{20}$$

where $\mathbf{y}^* = [y^*(0), y^*(1), \cdots, y^*(N-1)]^{\mathsf{T}}$, and $\mathbf{z} = [z(0), z(1), \cdots, z(N-1)]^{\mathsf{T}}$.

The target signal with missing data can be reconstructed by minimizing the objective function:

$$J(\mathbf{x}) = \frac{1}{2}\|\mathbf{y}^* - \mathbf{z}(\mathbf{W}\mathbf{x})\|_2^2 + \lambda\|\mathbf{x}\|_1, \tag{21}$$

where λ is the parameter for the L1 norm term.

The above object function can be further rewritten as

$$\begin{aligned} &\arg\min_{\mathbf{x}} \quad J(\mathbf{x}), \\ &\text{s.t.} \quad \mathbf{x} - \mathbf{v} = 0, \end{aligned} \tag{22}$$

where $\mathbf{v}$ is a new variable vector.

Using the augmented Lagrangian method, the above problem is formulated as

$$L_A(\mathbf{x}, \lambda, \mu) = J(\mathbf{x}) + \lambda(\mathbf{x} - \mathbf{v}) + \frac{\mu}{2}\|\mathbf{x} - \mathbf{v}\|_2^2, \tag{23}$$

where $\mu \geq 0$ is a penalty parameter. ADMM is applied to perform minimization with respect to each of $\mathbf{x}$ and $\mathbf{v}$ to obtain the following iterations:

$$\begin{aligned} \mathbf{x}_k &= \arg\min_{\mathbf{x}} \lambda\|\mathbf{x}\|_1 + \frac{\mu}{2}\|\mathbf{x} - \mathbf{v}_k - \mathbf{d}_k\|_2^2, \\ \mathbf{v}_k &= \arg\min_{\mathbf{v}} \frac{1}{2}\|\mathbf{y}^* - \mathbf{z}(\mathbf{W}\mathbf{x}_k)\|_2^2 + \frac{\mu}{2}\|\mathbf{x}_k - \mathbf{v} - \mathbf{d}_k\|_2^2, \\ \mathbf{d}_{k+1} &= \mathbf{d}_k - (\mathbf{x}_k - \mathbf{v}_k), \end{aligned} \tag{24}$$

where k is the iteration number and $\mathbf{d}_k$ is an intermediate variable vector.

First, minimization with respect to $\mathbf{x}$ is implemented using a soft thresholding:

$$\mathbf{x}_k = \text{soft}\left(\mathbf{v}_k + \mathbf{d}_k, \frac{\lambda}{2\mu}\right), \tag{25}$$

where the soft thresholding operation is defined as

$$\text{soft}(\mathrm{x}, \text{ø}) = \mathrm{x} \cdot \max(1 - \text{ø}/|\mathrm{x}|, 0).$$

Next, minimization with respect to $\mathbf{v}$ is a constrained least squares regularization. Because $\mathbf{W}\mathbf{W}^{\mathsf{H}} = \mathbf{I}$, the solution can be simplified as

$$\mathbf{v}_k = \mathbf{W}^{\mathsf{H}}(\mathbf{y}^* - \mathbf{z}(\mathbf{W}\mathbf{x}_k)). \tag{26}$$

Finally, after convergence of the solution, the estimated received signal is obtained by

$$\widehat{\mathbf{y}} = \mathbf{W}\mathbf{x}_k. \tag{27}$$

3.4. Implementation Details

Figure 5 summarizes the procedures of the proposed techniques. Each echo is processed one by one, then the DFT-based image focusing algorithm is used to focus the radar target, and finally a radar image without interference contamination is obtained. In the radar image focusing algorithm, the data focus is directed to the the ranging and Doppler domains by applying the Fast Fourier Transform (FFT) method. The vectors $\mathbf{v}_k$ and $\mathbf{d}_k$ are set as zero for the first iteration. Because the intensity of radar echoes is small, the parameters in Equation (24) can be set according to the mean value of the radar echoes; specifically, λ can be set to 1 and μ can be set to be proportional to the inverse of the mean intensity of the received signal. Additionally, the iteration number for missing data imputation can be set as 20, which produces satisfactory performance.

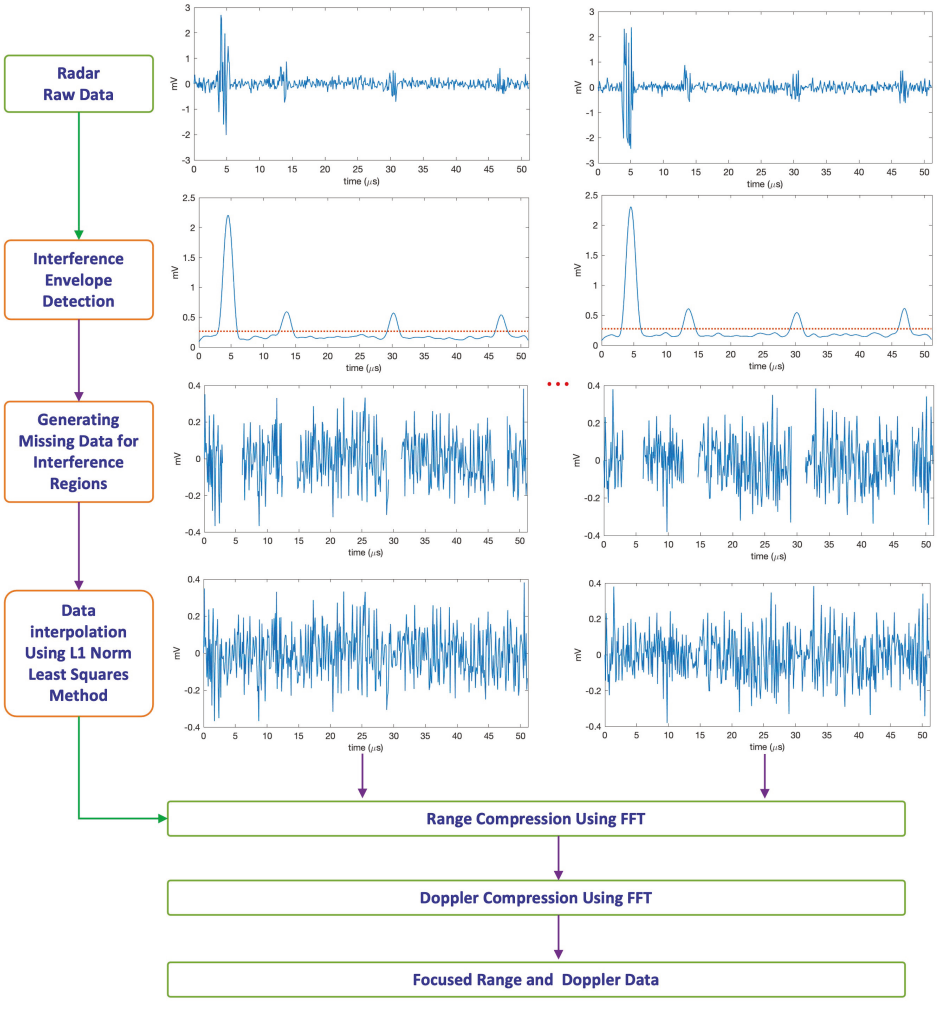

Figure 5. The procedures of the proposed techniques.

4. Validation Experiments

In the following experiments, the proposed technique is compared with three state-of-the-art methods. The first approach is one of the simplest ubiquitous signal processing methods, substituting zeros for the interference regions [15]. The second one represents a more advanced signal processing method using a three-level Haar wavelet with the hard thresholding approach [19]. The final comparison is a sparsity-based MCA method that uses DFT and STFT bases to separate the interfering and target signals, respectively [23]. In the following comparison experiments, the parameters of the wavelet-based and MCA-based methods are set according to references [19] and [23], respectively.

Furthermore, both the wavelet-based [19] and MCA-based [23] methods are improved using the proposed interference envelop detection. Specifically, based on the results of our proposed interference envelope detection method, only the signals in the interference regions are replaced by the outputs of the wavelet and MCA methods.

The comparisons are divided into three groups: stationary interference experiments, dynamic interference experiments, and real radar interference experiments. The first two

types of experiments are implemented by simulations. In the following experiments, both the radar under test and the interfering radar are static and the targets are moving. For the stationary interference experiments, the timing between the victim and interfering radars is synchronized, and the jamming appears in the same area of the received signal. In practice, timing synchronization between radars rarely occurs due to relative motion between the radar under test and the interfering radar, making dynamic interference common. As a result, interference appears in different regions in the received signal of the radar under test. Due to the constraints of the experimental conditions, the radar senors in the described experiments are static; however, the timing between the victim and interfering radars is set asynchronously in order to simulate dynamic interference.

Additionally, thermal noise is added to the simulated signals. The power of the noise was calculated as $\mathrm{P_{nosie}} = \kappa T_e B$, where κ is Boltzman's constant, T_e is the noise temperature, and B is the bandwidth of the radar receiver.

In the case of one-dimensional signals, the signal to interference plus noise ratio (SINR) is used to objectively evaluate the performance of interference suppression. However, for two-dimensional radar images, the radar target is focused through two dimensional range and Doppler domains. Therefore, the peak intensity of the target to interference plus noise ratio (PTINR) is defined here as an objective evaluation index for interference mitigation. Using the peak intensity of the focused target, the PTINR is defined as

$$\mathrm{PTINR} = \frac{\mathrm{P_{target}}}{\mathrm{P_{interference}} + \mathrm{P_{noise}}}, \tag{28}$$

where $\mathrm{P_{target}}$ is the peak intensity (power) of the focused target and $\mathrm{P_{interference}}$ is the power of the interference.

In addition, the subjective evaluation of radar images is mainly based on the quality of the focused target, sidelobes of the focused target, noise floor level, and residual interference distribution as comparative details.

4.1. Simulations

Table 1 provides the simulation parameters for the incoherent interference experiments. Two interfering sources are developed with different start frequencies and chirp rates. The distances of the two interfering sources are 30 m and 50 m from the radar under test, respectively. All the radar sensors are active at the same time. The RCS is 1 $\mathrm{m^2}$ and 3 $\mathrm{m^2}$ for two radar targets at 15 m and 30 m, respectively. The target located at 15 m is moving at 5 m/s, while the other target is static. As shown in Figure 6, there are four interference regions present in the received signal.

Figure 7 illustrates the comparative stationary interference experiments. According to Figure 7a, the stationary interference is distributed on the axis of zero velocity of the focused image, causing the second target to be completely swamped by the large amount of strong noise generated on this axis. Traditional signal processing-based methods such as the ANC and wavelet-based methods are able to suppress the interfering signal to a certain extent. However, the interfering signal is much stronger than the target signal, making it difficult to suppress the interference by traditional signal processing methods, as shown in the plots. Figure 7c illustrates that the wavelet-based approach has difficulty suppressing this strong interference. Using the proposed interference envelope method, the improved wavelet-based method does not perform better; see Figure 7d. This means that the reference regions have not been successfully recovered. Although the MCA method provides slightly better results (Figure 7e), there is a considerable amount of interference energy left in the zero velocity axis, resulting in failure to detect the second radar target. After introducing the proposed interference envelope detection method to improve the MCA method, both targets are successfully recovered and the interference signal energy is more effectively eliminated, as shown in Figure 7f. Figure 7g shows that the simple zero-setting method avoids the interfering signal. However, due to the loss of the target signal in the interfering regions, it leads to strong sidelobes in the focused image. According to Figure 7h, the

proposed method produces a promising focused image that is very close to the ground truth. In many real-world vehicle scenarios, the primary and interfering radars have relative motion, producing dynamic interference. Compared with stationary interference, the interference energy from dynamic interference is distributed in different areas on the focused image; see Figure 8a. As the interference energy is distributed in different regions of the image, the interference intensity is relatively lower, and the different interference suppression algorithms consequently have better performance for dynamic interference suppression, as shown in Figure 8. Similarly, the proposed interference envelope detection approach greatly improves the performance of the MCA method; see Figure 8f. Again, as illustrated in Figure 8h, the proposed approach produces the most focused radar image.

Table 1. Simulation parameters for interference experiments.

Radars	Parameters	Values
Common parameters	Bandwidth	500 MHz
	Sampling rate	10 Msps
	Chirp number	128
Radar under test	Start frequency	77 GHz
	Chirp duration	51.2 µs
	Chirp rate	9.76×10^{12} Hz/s
Interferer 1	Start frequency	77.7 GHz
	Chirp duration	25.6 µs
	Chirp rate	-1.95×10^{13} Hz/s
	Distance	30 m
Interferer 2	Start frequency	76.9 GHz
	Chirp duration	17.07 µs
	Chirp rate	2.93×10^{13} Hz/s
	Distance	50 m

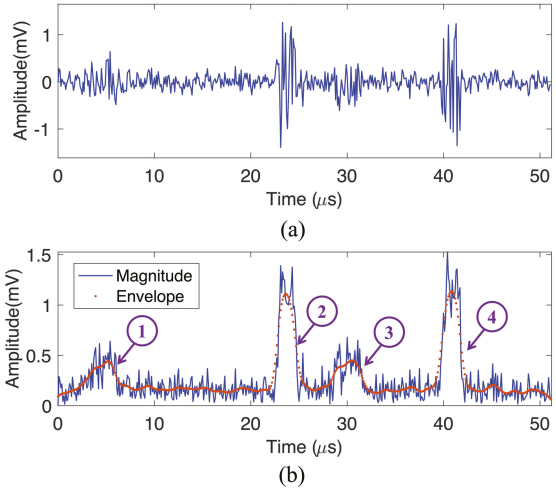

Figure 6. The received signal with interference: (**a**) the real part of the received signal and (**b**) the magnitude of the received signal. The regions marked by circles in (**b**) are the envelopes in which interference appears.

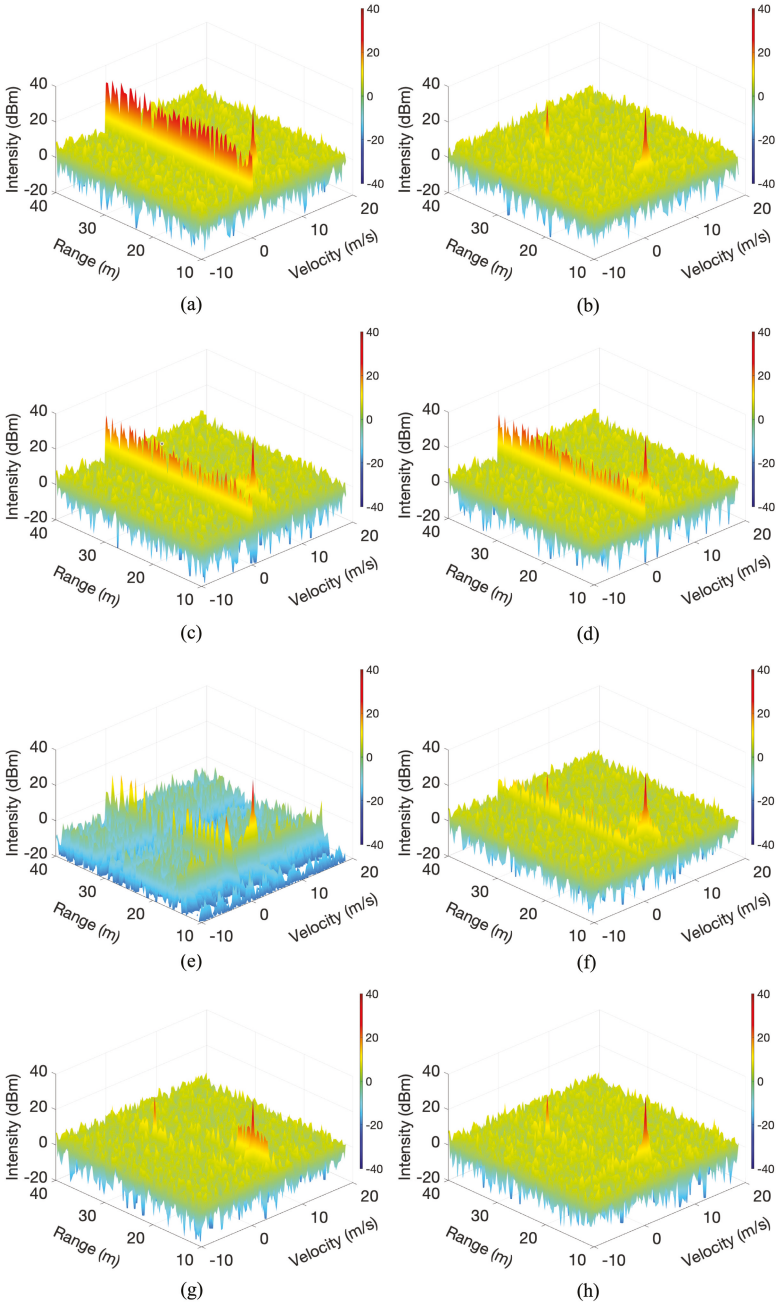

Figure 7. Comparisons on stationary interference simulations. (**a**) Original image; (**b**) Interference-free image; (**c**) Lee et al. [19]; (**d**) Lee et al. [19] + Proposed interference detection; (**e**) Uysal [23]; (**f**) Uysal [23] + Proposed interference detection; (**g**) Brooker [15]; and (**h**) The proposed method.

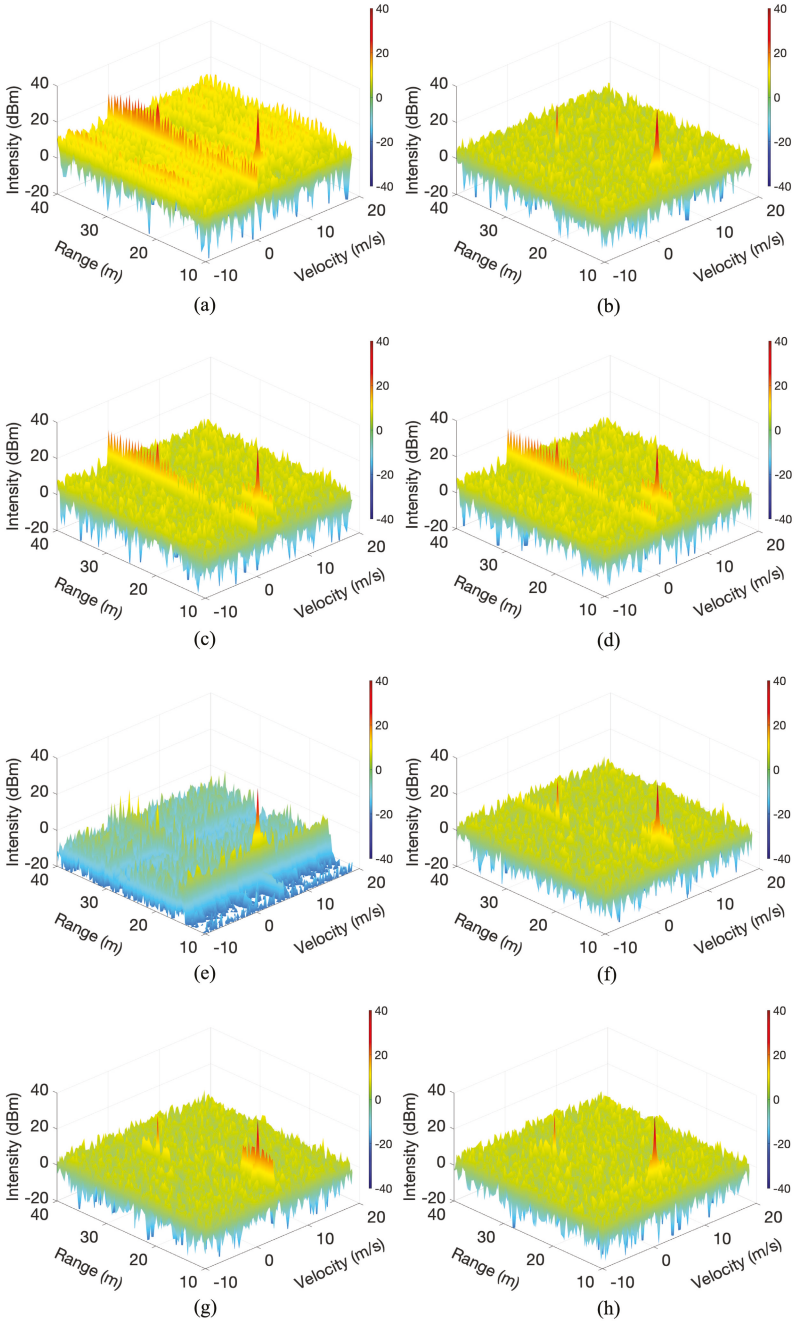

Figure 8. Comparisons on dynamic interference simulations. (**a**) Original image; (**b**) Interference-free image; (**c**) Lee et al. [19]; (**d**) Lee et al. [19] + Proposed interference detection; (**e**) Uysal [23]; (**f**) Uysal [23] + Proposed interference detection; (**g**) Brooker [15]; and (**h**) The proposed method.

Comparisons of object evaluation were conducted as well. The results are reported in Table 2. The larger PTINRs along with the absence of ghost targets indicate the better suppression performance of the associated method. The proposed method has the best performance index in the simulated experiments. Because the static target appears on the zero velocity line axis of the focused image, and is therefore covered by strong interference energy, its PTINR value is −6.1 dB. The wavelet-based method and MCA-based method have limited improvement on this index, while the proposed method can realize an improvement of up to 19.1 dB, a total improvement of 25.2 dB, which is beneficial for subsequent target detection and tracking.

Table 2. Comparisons of PTINRs via simulations. The first number in each term is the result of stationary interference and the second number is the result of dynamic interference.

Methods	Target 1 (dB)	Target 2 (dB)
Original image	25.6, 29.8	−6.1, 6.2
Ground truth without interference	36.8	25.5
Lee et al. [19]	24.9, 30.2	−3.3, 14.9
Lee et al. [19] + the proposed interference detection	26.5, 30.8	−2.7, 20.3
Uysal [23]	26.4, 28.9	3.1, 12.5
Uysal [23] + proposed interference detection	28.6, 35.8	17.7, 23.7
Brooker [15]	19.2, 19.3	15.1, 23.1
The proposed method	31.2 , 36.4	19.1, 24.2

4.2. Real Radar Field Experiments

As shown in Figure 9, real radar interference experiments were conducted using two Texas Instruments AWR1642 mm wave radars and an electric bicycle traveling at approximately 5 m/s forward or backward relative to the radar under test. The distance of the interfering radar was 4 m. The experiment parameters are presented in Table 3.

Figure 10 demonstrates the collected radar data with strong interference. The signal of the sine wave in the plot is the radar target signal, and the signal that changes suddenly and quickly with high intensity is the interfering signal. This coincides with the theoretical derivation in Section 2.

Table 3. Radar parameters used for measurements.

Radars	Parameters	Values
Common parameters	Start frequency	77 GHz
	Bandwidth	547.5 MHz
Radar under test	Chirp number	128
	Sampling rate	10 Msps
	Chirp duration	36.5 µs
	Chirp rate	1.5×10^{13} Hz/s
Interferer	Chirp duration	18.25 µs
	Chirp rate	3.0×10^{13} Hz/s
	Sampling rate	6.25 Msps
	Distance	4 m

Figure 9. Real radar field experiments.

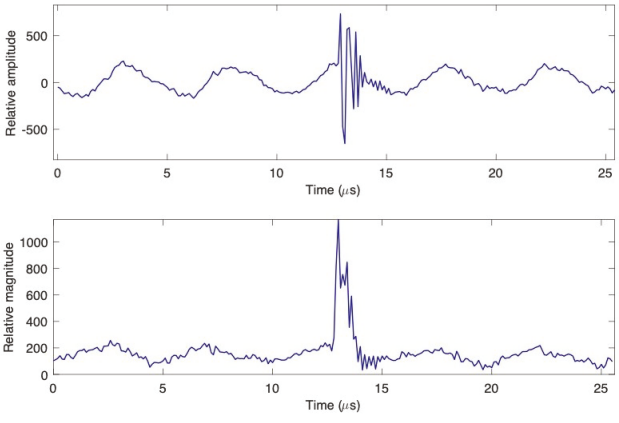

Figure 10. The received signal during the measurement experiments: the plots on the top row is the real part of the signal, and the plots on the bottom row is the magnitude of the received signal.

Figure 11 presents the comparison results of the real radar interference experiments. The stationary targets are distributed on the axis of zero velocity of the focused image, however the moving target is not visible due to strong interference. Compared to the other approaches, the proposed method has the best performance. As shown in Figure 11a, the strong interference energy is distributed over the focused radar image. The main reason for this is that the interfering signal does not repeat at the same location in each received signal with dynamic interference. Compared to the simulated results, the zeroing method produces stronger sidelobes on the focused image, which leads to difficulty in distinguishing between real moving targets; see Figure 11g. The evaluation results reported in Table 4 indicate that the proposed method has the best performance index in the real radar experiments.

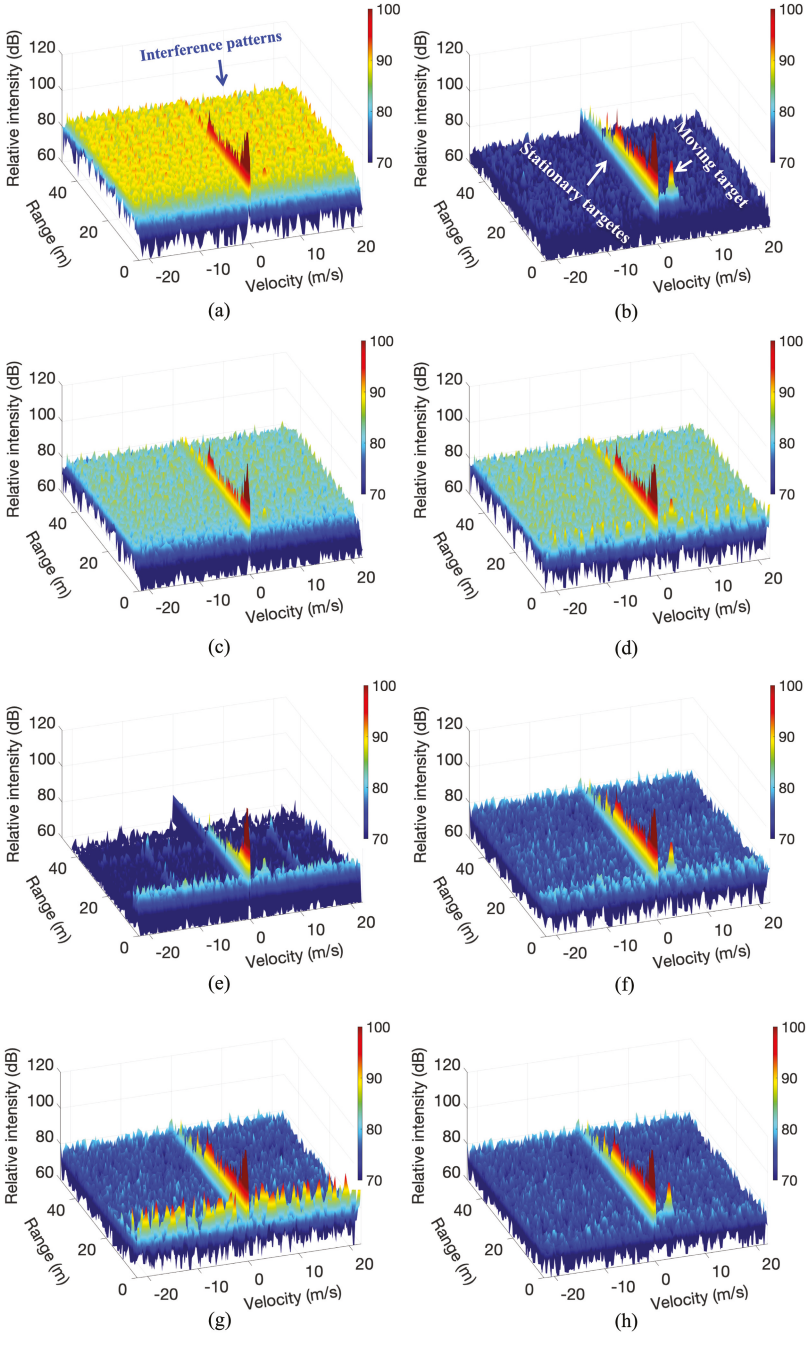

Figure 11. Comparisons using real radar data. (**a**) Original image; (**b**) Interference-free image; (**c**) Lee et al. [19]; (**d**) Lee et al. [19] + Proposed interference detection; (**e**) Uysal [23]; (**f**) Uysal [23] + Proposed interference detection; (**g**) Brooker [15]; and (**h**) The proposed method.

Table 4. Comparisons using measured real radar data.

Methods	PTINRs (dB)	Ghost Targets
Original image	5.1	Yes
Ground truth	24.6	No
Lee et al. [19]	5.9	No
Lee et al. [19] + the proposed interference detection	10.3	Yes
Uysal [23]	3.4	Yes
Uysal [23] + the proposed interference detection	15.7	No
Brooker [15]	15.1	Yes
The proposed method	21.2	No

5. Discussion

5.1. Beyond Sparsity-Based Methods

Certain radar targets have a large radar cross-section (RCS), such as metal buildings on the side of a road, while others have a small RCS, such as pedestrians. All in all, the dynamic range of the received signal is large. Therefore, it is difficult to extract weak targets in an interference environment. Unfortunately, sparsity-based methods have a general drawback in that they tend to remove weak signals as noise. As shown in Figures 7, 8 and 10, the traditional sparsity-based method [23] can only recover strong targets, and loses weak targets. The proposed method, although retaining a sparse framework, proposes an interference detection method that enables signal recovery only for the region where the interference occurs, thus effectively maintaining the signal energy and suppressing the interference signal at the same time.

5.2. Computational Complexity

The complexity of the interference suppression algorithm needs to be as small as possible in order to be suitable for the signal processor of existing automotive millimeter wave radar chips. Therefore, interference-contaminated region detection-based methods have advantages in terms of computing complexity. Zero-based detection methods simply set the interference-contaminated regions to zero, and thus have the least complexity. However, the focused target obtained with such methods loses information and has many sidelobes.

Except for the zeroing method, the wavelet-based method [19], the MCA-based method [23], and the proposed technique are all transform-based approaches, meaning that the computational complexity depends mainly on forward and inverse transformation. In general, the wavelet-based method has the lowest complexity, followed by the proposed method. The MCA method has the highest computational complexity due to the use of both STFT and DFT [23].

5.3. What Is the Percentage of Samples Affected by Interference for Which the Proposed Technique Remains Valid?

In the proposed technique, a greater proportion of interfering samples produce fewer effective received samples, thereby reducing range resolution and signal-to-noise ratio. Therefore, we conducted experiments to investigate the performance of the proposed technique with respect to the differing percentage of interfering samples. According to Figures 12 and 13, when the percentage of interfering samples is below 50%, the performance of the proposed method is satisfactory. The interference signal is generally in the shape of a burst in the time domain, and rarely occupies most of the received signal, allowing the proposed method to cope with the interference in most cases.

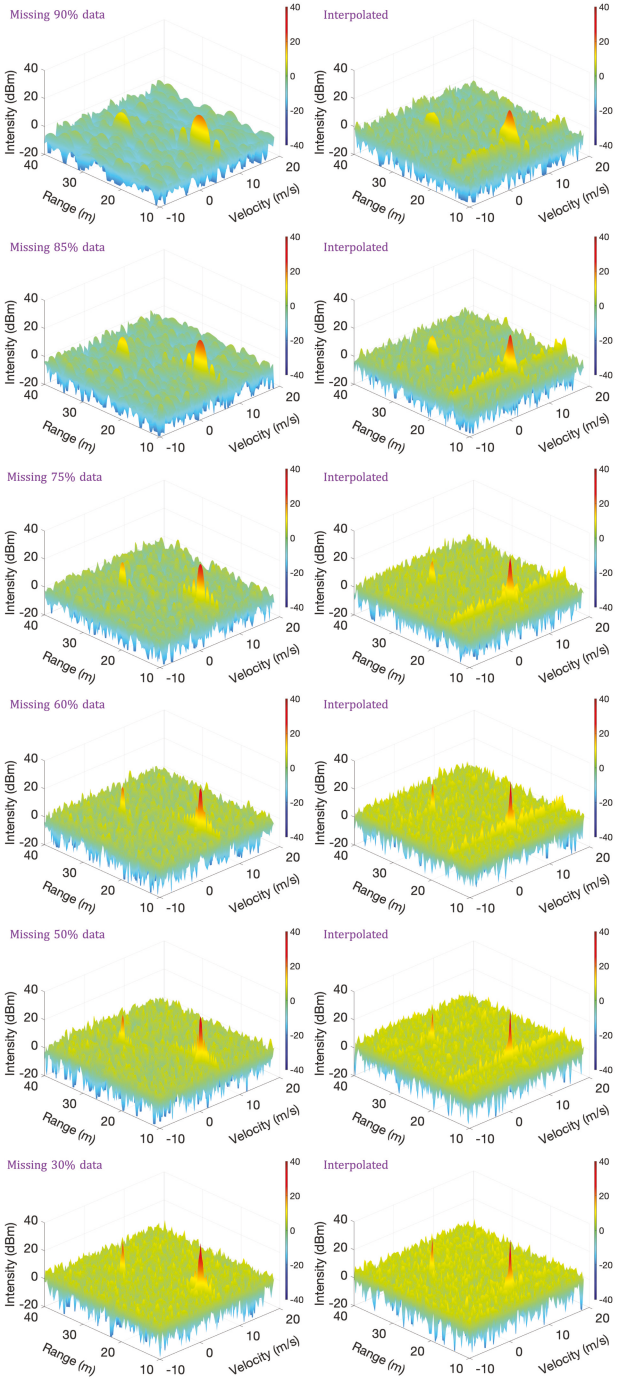

Figure 12. The performance of the proposed technique with respect to different percentages of interfering samples.

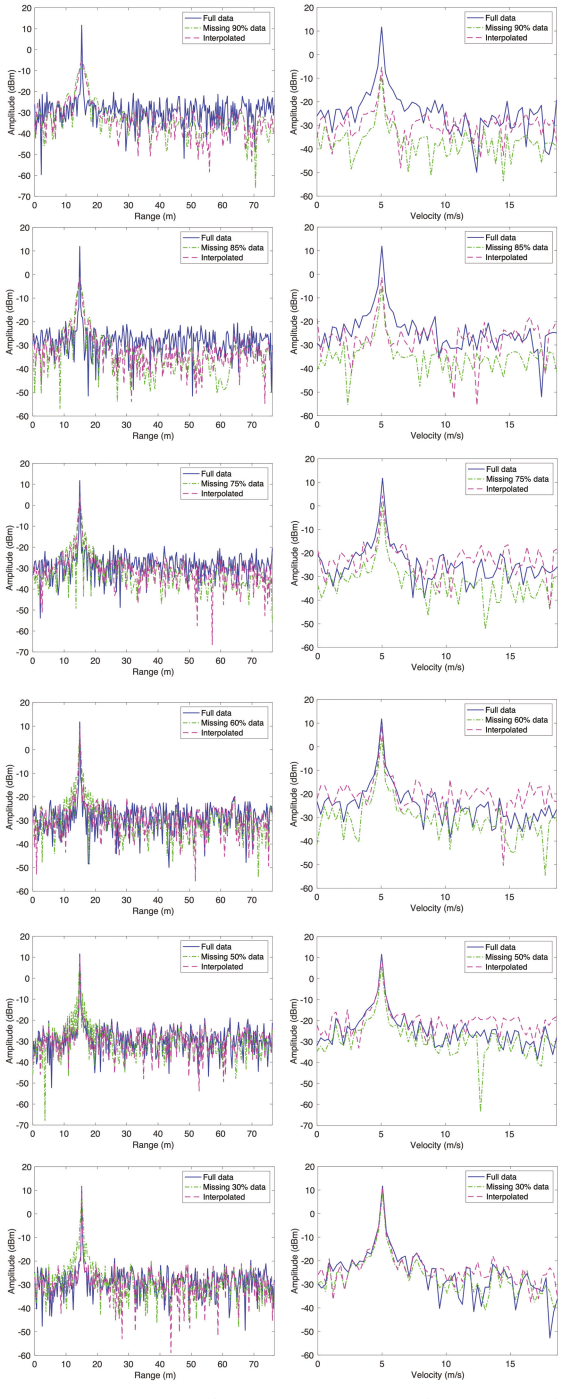

Figure 13. Comparison of range and Doppler profiles in terms of different percentages of interfering samples.

6. Conclusions

In this paper, an effective and feasible interference suppression technique is proposed for the currently important and challenging issue of incoherent interference between automotive FMCW radars. A detailed derivation of the processing of incoherent interference signals is presented. A precise interference envelope detection method is proposed based on a well-designed low-pass filter. This method can avoid interference suppression in cases where the signal is received without interference, thereby reducing the required amount of computation. This work considered the interference problem as a missing radar data problem; the radar target signal is superimposed in complex sinusoidal waves with good sparse characteristics in the DFT domain. Thus, the radar target signal polluted by the incoherent interference can be successfully recovered based on the L1 norm least squares method. Using the proposed method, the radar target can be perfectly focused even in cases of strong interference. Moreover, two current state-of-the-art methods, namely, the wavelet-based and MCA-based methods, are improved when using the proposed interference envelope detection method. Extensive experiments demonstrate the promising performance of the proposed techniques.

This work shows the effectiveness of suppressing interference in the range and Doppler domains. However, this work does have limitations; in particular, it does not investigate interference in spatial multi-channel data. Our future work will focus on interference reduction for spatial multi-channel radar data.

Author Contributions: Conceptualization, Z.X.; methodology, Z.X. and Y.W.; software, Y.W.; validation, S.X. and Y.W.; experimental analysis, S.X.; data collection, Z.X., S.X. and Y.W.; writing—original draft preparation, Y.W.; writing—review and editing, Z.X.; supervision, Z.X. All authors have read and agreed to the published version of the manuscript.

Funding: This work was supported by the National Natural Science Foundation of China (Grant number 42005100) and by the Nantong Science and Technology for Social and Livelihood Key Project (Grant number MS22022016).

Data Availability Statement: Not applicable.

Acknowledgments: Although this work was supported by two projects, the remaining costs of the project did not cover article processing charges for the paper. The editorial team of *Remote Sensing* has been very supportive and helpful. The authors would like to give special thanks to Nancy Yang, Marko Mladenovic, Elenor Wang and the others editors for their generous support, which enabled the paper to be published. Your journal's timely help made us feel sunshine and warmth in the midst of much-needed help, and and we will continue to do meaningful and interesting works and apply for relevant grants in return for our scientific journal and the kind people and well-wishers around the world. In addition, the authors would like to express their sincere gratitude to the editors and reviewers whose insightful comments have further enhanced the quality of the paper.

Conflicts of Interest: The authors declare no conflict of interest.

References

1. Gardill, M.; Schwendner, J.; Fuchs, J. An Approach to Over-the-air Synchronization of Commercial Chirp-Sequence Automotive Radar Sensors. In Proceedings of the 2020 IEEE Topical Conference on Wireless Sensors and Sensor Networks (WiSNeT), San Antonio, TX, USA, 26–29 January 2020; pp. 46–49. [CrossRef]
2. Jasteh, D.; Hoare, E.G.; Cherniakov, M.; Gashinova, M. Experimental Low-Terahertz Radar Image Analysis for Automotive Terrain Sensing. *IEEE Geosci. Remote. Sens. Lett.* **2016**, *13*, 490–494. [CrossRef]
3. Xu, Z.; Baker, C.J.; Pooni, S. Range and Doppler Cell Migration in Wideband Automotive Radar. *IEEE Trans. Veh. Technol.* **2019**, *68*, 5527–5536. [CrossRef]
4. Patole, S.M.; Torlak, M.; Wang, D.; Ali, M. Automotive radars: A review of signal processing techniques. *IEEE Signal Process. Mag.* **2017**, *34*, 22–35. [CrossRef]
5. Alland, S.; Stark, W.; Ali, M.; Hegde, M. Interference in automotive radar systems: Characteristics, mitigation techniques, and current and future research. *IEEE Signal Process. Mag.* **2019**, *36*, 45–59. [CrossRef]
6. Tovar Torres, L.L.; Steiner, M.; Waldschmidt, C. Channel Influence for the Analysis of Interferences Between Automotive Radars. In Proceedings of the 2020 17th European Radar Conference (EuRAD), San Antonio, TX, USA, 26–29 January 2020; pp. 266–269. [CrossRef]

7. Torres, L.L.T.; Roos, F.; Waldschmidt, C. Simulator Design for Interference Analysis in Complex Automotive Multi-User Traffic Scenarios. In Proceedings of the 2020 IEEE Radar Conference (RadarConf20), Florence, Italy, 21–25 September 2020; pp. 1–6. [CrossRef]
8. Hua, X.; Ono, Y.; Peng, L.; Xu, Y. Unsupervised Learning Discriminative MIG Detectors in Nonhomogeneous Clutter. *IEEE Trans. Commun.* **2022**, *70*, 4107–4120. [CrossRef]
9. Rosenberg, L.; Bocquet, S. Non-coherent Radar Detection Performance in Medium Grazing Angle X-Band Sea Clutter. *IEEE Trans. Aerosp. Electron. Syst.* **2017**, *53*, 669–682. [CrossRef]
10. Xu, Z.; Shi, Q.; Shi, J.; Wang, H.; Wei, M.; Gao, R.; Shao, Y.; Tao, H. A novel method of mitigating the mutual interference between multiple LFMCW radars for automotive applications. In Proceedings of the IGARSS 2019–2019 IEEE International Geoscience and Remote Sensing Symposium, Yokohama, Japan, 28 July–2 August 2019; pp. 2178–2181.
11. Xu, Z.; Shi, Q. Interference mitigation for automotive radar using orthogonal noise waveforms. *IEEE Geosci. Remote Sens. Lett.* **2018**, *15*, 137–141. [CrossRef]
12. Xu, Z.; Shi, Q.; Sun, L. Novel Orthogonal Random Phase-Coded Pulsed Radar for Automotive Application. *J. Radars* **2018**, *7*, 364–375. [CrossRef]
13. Uysal, F. Phase-coded FMCW Automotive Radar: System Design and Interference Mitigation. *IEEE Trans. Veh. Technol.* **2019**, *69*, 270–281. [CrossRef]
14. Yuan, M.; Xu, Z.; Shi, Q. Wiener filter based automotive millimeter wave radar interference adaptive reduction. *J. Electron. Meas. Instrum.* **2021**, *35*, 194–201. [CrossRef]
15. Brooker, G.M. Mutual Interference of Millimeter-Wave Radar Systems. *IEEE Trans. Electromagn. Compat.* **2007**, *49*, 170–181. [CrossRef]
16. Neemat, S.; Krasnov, O.; Yarovoy, A. An interference mitigation technique for FMCW radar using beat-frequencies interpolation in the STFT domain. *IEEE Trans. Microw. Theory Techn.* **2019**, *67*, 1207–1220. [CrossRef]
17. Jung, J.; Lim, S.; Kim, J.; Kim, S.C.; Lee, S. Interference Suppression and Signal Restoration Using Kalman Filter in Automotive Radar Systems. In Proceedings of the 2020 IEEE International Radar Conference (RADAR), Washington, DC, USA, 28–30 April 2020; pp. 726–731.
18. Wang, J.; Ding, M.; Yarovoy, A. Matrix-Pencil Approach-Based Interference Mitigation for FMCW Radar Systems. *IEEE Trans. Microw. Theory Techn.* **2021**, *69*, 5099–5115. [CrossRef]
19. Lee, S.; Lee, J.Y.; Kim, S.C. Mutual Interference Suppression Using Wavelet Denoising in Automotive FMCW Radar Systems. *IEEE Trans. Intell. Transp. Syst.* **2021**, *22*, 887–897. [CrossRef]
20. Jin, F.; Cao, S. Automotive Radar Interference Mitigation using Adaptive Noise Canceller. *IEEE Trans. Veh. Technol.* **2019**, *68*, 3747–3754. [CrossRef]
21. Wu, J.; Yang, S.; Lu, W.; Liu, Z. Iterative modified threshold method based on EMD for interference suppression in FMCW radars. *IET Radar Sonar Navig.* **2020**, *14*, 1219–1228. [CrossRef]
22. Xu, Z.; Yuan, M. An Interference Mitigation Technique for Automotive Millimeter Wave Radars in the Tunable Q-Factor Wavelet Transform Domain. *IEEE Trans. Microw. Theory Techn.* **2021**, *69*, 5270–5283. [CrossRef]
23. Uysal, F. Synchronous and asynchronous radar interference mitigation. *IEEE Access* **2018**, *7*, 5846–5852. [CrossRef]
24. Afonso, M.V.; Bioucas-Dias, J.M.; Figueiredo, M.A. Fast image recovery using variable splitting and constrained optimization. *IEEE Trans. Image Process.* **2010**, *19*, 2345–2356. [CrossRef]
25. Rock, J.; Roth, W.; Toth, M.; Meissner, P.; Pernkopf, F. Resource-Efficient Deep Neural Networks for Automotive Radar Interference Mitigation. *IEEE J. Sel. Top. Signal Process.* **2021**, *15*, 927–940. [CrossRef]
26. International Telecommunication Union. *Systems Characteristics of Automotive Radars Operating in the Frequency Band 76–81 GHz for Intelligent Transport Systems Applications*; Mobile, Radiodetermination, Amateur and Related Satellite Service; International Telecommunication Union: Geneva, Switzerland, 2018.
27. Kidambi, S. Design of Noise Transfer Functions for Delta–Sigma Modulators Using the Least-pth Norm. *IEEE Trans. Circuits Syst. II Express Briefs* **2019**, *66*, 707–711. [CrossRef]

remote sensing

MDPI

Article

Radar and Communication Spectral Coexistence on Moving Platform with Interference Suppression

Junhui Qian [1,†], Ziyu Liu [1,†], Yuanyuan Lu [1,†], Le Zheng [2,3,*], Ailing Zhang [1] and Fengxia Han [4]

[1] School of Microelectronic and Communication Engineering, Chongqing University, Chongqing 400044, China
[2] School of Information and Electronics, Beijing Institute of Technology, Beijing 100081, China
[3] Beijing Institute of Technology Chongqing Innovation Center, Chongqing 401120, China
[4] School of Software Engineering, Tongji University, Shanghai 201804, China
* Correspondence: le.zheng.cn@gmail.com; Tel.: +86-151-3067-5311
† These authors contributed equally to this work.

Abstract: With the development of intelligent transportation, radar and communication on moving platforms are competing for the spectrum. In this paper, we propose and demonstrate a new algorithmic framework for radar-communication spectral coexistence system on moving platform with mutual interference suppression, in which communication rate and the radar signal-to-interference-plus-noise ratio (SINR) are simultaneously optimized, under the energy constraints for the two systems and the radar constant modulus constraint. The radar spatial-temporal filter at the receiver and transmitting waveform are optimized, while the codebook matrix is optimized for the communication system. To cope with the established non-convex problem with triplet variables, we decouple the original problem into multiple subproblems, for which an alternating algorithm based on iterative procedures is derived with lower computational complexity. Specifically, the subproblems of communication codebook and radar filter design are convex and the closed-form solutions can be easily obtained, while the radar waveform optimization is non-convex. Then we propose a novel scheme by exploiting the alternating direction method of multipliers (ADMM) based on minorization-maximization (MM) framework. Finally, to reveal the effectiveness of the proposed algorithm in different scenarios, numerical results are provided.

Keywords: spectrum sharing; non-convex optimization; alternating iteration; ADMM

Citation: Qian, J.; Liu, Z.; Lu, Y.; Zheng, L.; Zhang, A.; Han, F. Radar and Communication Spectral Coexistence on Moving Platform with Interference Suppression. *Remote Sens.* **2022**, *14*, 5018. https://doi.org/10.3390/rs14195018

Academic Editors: Zhihuo Xu, Jianping Wang and Yongwei Zhang

Received: 12 August 2022
Accepted: 28 September 2022
Published: 9 October 2022

1. Introduction

With the explosive growth of the wireless information transformation industry [1], the usage of radar is important in numerous civilian applications, including remote sensing, collision avoidance, and vehicles intelligent cruise control. Meanwhile, a large amount of spectrum resources are also occupied by the wireless communication for traffic control, autonomous driving, and information services [2,3]. For example, the high UHF radars overlap with GSM communication systems, and the S-band radar systems partially overlap with Long Term Evolution and WiMax systems [4,5]. Hence, the available spectrum is becoming more and more cramped. To deal with such issue, spectrum sharing between radar and wireless communication, as an emerging topic, has attracted considerable attentions and yielded several literatures recently [6–10]. In general, there are two main research directions. The first research direction refers to the Dual-functional Radar-Communication Systems, for which a unique platform integrating radar with communication functions is developed. This joint radar communication (JRC) model enhances information sharing and has the advantages of low cost, small size, low power consumption, spectrum sharing, performance improvement and security [5]. Another research direction concentrates on the radar-communication coexistence systems that operate at the same frequency band, which results in the joint design of spectrally overlaid systems. In this case, the mutual

interference between different systems will lead to great challenge to the required Quality of Service (QoS) even with low-level cross interfering signals [11].

In spectrally overlaid systems, different subsystems have conflicting objective performances [12], which will lead to the mutual interference between the subsystems. Therefore, mutual interference suppression is needed to enable the spectrum sharing and guarantee the required QoS. Early studies were mainly based on transmitter design and evaluated the performance of coexistence systems via controlling the mutual interference produced by competing subsystems, e.g., the radar waveform design addressed a non-convex optimization in a spectrally crowded environment [13]; the codebook design improved the communication rate in the presence of strong radar interference [14]. These literatures on spectrum sharing address interference management for single-antenna radar or communication systems. To further realize the interference management in multi-antenna systems, the radar-communication coexistence system using MIMO structure were introduced in [15,16], which both MIMO radar and MIMO communication system use single antenna transmitter and receiver with long separation. The cooperation between the two systems means that the antenna positions between the two systems are shared in terms of knowledge sharing [17]. In addition, thanks to the recent developments of cognitive wireless networks, intellisense provides the possibility for the coexistence of radar system and existing communication system. Radar and communication systems could be conscious of each other's existence by sharing messages, thus facilitating the joint design between radar and communication systems [18–20]. The spectrum sharing co-design of radar and communication systems using MIMO technology was introduced in [21,22], whereby the design degrees of freedom (DoFs) under control was adopted at all transmitters in the coexistence systems. Since, such co-design requires information sharing between subsystems, the payback would be less mutual interference and better figure of merit for the coexistence system. Since spatial-temporal processing has potential advantages in spectrum sharing, there have been growing interests in the usage of spatial-temporal processing architecture in the co-design of subsystems. Compared with the conventional spectrum sharing designs, the spatial-temporal processing architecture collects signals from numerous pulses and antennas, and accommodatively adjusts the radar spatial-temporal filter, which increases Doppler resolution and suppresses the clutter and mutual interference simultaneously. On the algorithmic side, the convex optimization technique, e.g., semidefinite relaxation technique, is usually developed for the joint design. However, such method suffered from high computational complexity [12,21].

In general, different critical issues for radar and communication system spectral coexistence are developed based on different figures of merits [23]. However, it is worth noting that few studies have addressed the issue of spectral coexistence on moving platforms, which exacerbates the location-induced interference and makes the co-design problem more challenging [24]. For example, as an emerging remote sensing medium, the rise of autonomous driving leads to increased highway capacity and passenger comfort, which requires reliable communications to transfer the state information of each platform [25]. In order to reduce the mutual interference between automotive radars using millimeter wave frequency modulated continuous wave radars under dense traffic conditions, several methods to reduce mutual interference have been proposed [26]. For example, [27] introduces the tunable Q-factor wavelet transform domain and applies it to separate the interference from target signals. In this spectrum sharing situation, the range-Doppler processing, detection, and dynamic range enhancement strategies for the radar in autonomous driving are involved [28,29]. Thus, major challenges in the application of autonomous driving are the vibration and motion of the platform. The interference mitigation of the autonomous driving also needs to be considered, including not only the self-interference, but also the cross interference from the communication system in spectrum sharing scenarios [30]. In addition, most of the existing designs focus on the optimization with single radar target. However, in real scenarios, the radar sometimes has to detect multiple targets, e.g., in multi-target tracking scenarios, in which the adaptive resource management for radar is

necessary [31,32]. Moreover, the increasing number of constraints would exacerbate the computational burden.

Against the aforementioned background, a new algorithmic framework is proposed for the radar-communication spectrum coexistence system on moving platform. We presume the coexistence system is equipped with MIMO antennas and its spatial-temporal probing signal can be used as an additional DoFs. To cope with multiple targets, this paper will investigate the problem of spectrum sharing with a set of separated SINRs for radar. The DoFs under control consists of the spatial-temporal transmit waveform, the filter of receiver for the radar, and the spatial-temporal codebook matrix for the communication system. Then, under multiple constraints, the SINR of radar and communication rate are formulated for simultaneous optimization. Towards this end, an alternate iteration algorithm for multiple subproblems is contrived for solving the designed non-convex triplet variables problem. After a series of manipulations, two convex subproblems are formulated for communication codebook design and radar filter optimization respectively, and a non-convex architecture is derived for radar waveform. The convex subproblems could be solved easily in closed-form, while the non-convex subproblem can be solved by exploiting the alternating direction method of multipliers (ADMM) based on minorization-maximization (MM) framework [33]. Finally, a comprehensive performance assessment is provided.

Notations: $\mathcal{CN}(\mathbf{c},\mathbf{C})$ denotes the complex Gaussian distribution with mean $\mathbf{c}$ and variance $\mathbf{C}$. $(\cdot)^T$, $(\cdot)^H$ and $(\cdot)^*$ represent the transpose, Hermitian and conjugate operators, respectively. vec($\mathbf{C}$) and det($\mathbf{C}$) denote the vectorization and determinant of the matrix $\mathbf{C}$. $\odot$ and $\otimes$ denote the Hadamard operator and Kronecker operator respectively. diag$(\cdot)$ and Tr$(\cdot)$ denote the diagonal operator and trace operator, respectively. As to a complex-valued vector $\mathbf{c}$, its real-valued forms is defined as $\mathbf{c}_r=\left[\Re(\mathbf{c})^{\mathrm{T}},\Im(\mathbf{c})^{\mathrm{T}}\right]^{\mathrm{T}}$. For a complex-valued matrix $\mathbf{C}$, the real-valued forms is given by $\mathbf{C}_r=\begin{bmatrix}\Re(\mathbf{C}),-\Im(\mathbf{C})\\ \Im(\mathbf{C}),\Re(\mathbf{C})\end{bmatrix}$. $(\mathbf{c})^+=\max(0,\mathbf{c})$ represents the positive part of $\mathbf{c}$.

2. Signal Model

As shown in Figure 1, assume two moving narrow band systems using the same frequency, where a communication system based on MIMO structure is equipped with $M_{C,t}$ transmit and $M_{C,r}$ receive elements, and a monostatic radar system with MIMO structure is equipped with $M_{R,t}$ transmit and $M_{R,r}$ receive elements [34]. We consider the cooperation is coordinated by the control center, which collects information from the two subsystems, computes jointly optimal designed parameters and sends each scheme back to the corresponding system. In this work, we address spectrum sharing during the phase that the receive antennas obtain measurements of the target returns. The information transformation between the receive antennas and control center, can be viewed as the interference between two communication systems and is out the scope of the paper [35]. During a Pulse Repetition Time, each transmit antenna of the radar transmits L pulses, denoted by vector $\mathbf{s}=\mathrm{vec}\left[\mathbf{s}(1)^T,\mathbf{s}(2)^T\ldots,\mathbf{s}(L)^T\right]^T\in\mathbb{C}^{M_{R,t}L\times 1}$, where $\mathbf{s}(l)\in\mathbb{C}^{M_{R,t}\times 1}$ is the radar transmit vector of the l-th epoch. Assume that the M radar far-field moving targets located at the range gate l_m and azimuth θ_m, an observation signal for M radar targets at epoch l is modeled as [36–38]

$$\mathbf{y}_R(l)=\sum_{m=1}^{M}\alpha_m e^{j2\pi(l-1)f_{d,m}}\mathbf{a}_r^*(\theta_m)\mathbf{a}_t^H(\theta_m)\mathbf{s}(l-l_m)+\mathbf{y}_i(l)+\mathbf{y}_c(l)+\mathbf{y}_n(l), \tag{1}$$

where α_m is the path loss of the m-th target, and $\mathbb{E}\left[|\alpha_m|^2\right]=\sigma_0^2$, l_m is the range cell index of the m-th radar target related to the range cell of interest. $\mathbf{y}_i(l)$ and $\mathbf{y}_c(l)$ represent the communication interference and clutter respectively. $\mathbf{y}_n(l)\sim\mathcal{CN}\left(\mathbf{0},\sigma_R^2\mathbf{I}_{M_{R,r}}\right)$ is the additive white Gaussian noise. For notational simplicity, we introduce $\mathbf{A}(\theta)=\mathbf{a}_r^*(\theta)\,\mathbf{a}_t^H(\theta)$ with

$\mathbf{a}_t(\cdot)$ and $\mathbf{a}_r(\cdot)$ denoting the transmit and receive steering vectors, respectively. By defining $\mathbf{y}_R \triangleq \left[\mathbf{y}_R(1)^T, \ldots, \mathbf{y}_R(L)^T\right]^T$, $\mathbf{y}_i \triangleq \left[\mathbf{y}_i(1)^T, \ldots, \mathbf{y}_i(L)^T\right]^T$, $\mathbf{y}_c \triangleq \left[\mathbf{y}_c(1)^T, \ldots, \mathbf{y}_c(L)^T\right]^T$, and $\mathbf{y}_n \triangleq \left[\mathbf{y}_n(1)^T, \ldots, \mathbf{y}_n(L)^T\right]^T$, we can have the whole observation vector with a compact form as

$$\mathbf{y}_R = \sum_{m=1}^{M} \alpha_m \left(\mathbf{J}_L(l_m) \otimes \mathbf{I}_{M_{R,r}}\right) \mathbf{A}(f_{d,m}, \theta_m)\mathbf{s} + \mathbf{y}_i + \mathbf{y}_c + \mathbf{y}_n, \tag{2}$$

where

$$\mathbf{A}(f_{d,m}, \theta_m) = \mathrm{diag}(\mathbf{p}(f_{d,m})) \otimes \mathbf{A}(\theta_m), \tag{3}$$

let $\mathbf{p}(f_{d,m}) = \left[1, e^{j2\pi f_{d,m}}, \ldots, e^{j2\pi f_{d,m}(L-1)}\right]^T$ represent the temporal steering vector with $f_{d,m}$ representing the m-th radar target Doppler frequency. $\mathbf{J}_L(d) = (\mathbf{J}_L(-d))^T$ is a $L \times L$ transform matrix, and its (l_1, l_2)-th element is given by

$$\left[\mathbf{J}_L(d)\right]_{l_1,l_2} = \begin{cases} 1, & d \in \{-(L-1), \ldots, L-1\} \\ & \text{and } l_1 - l_2 = d, \\ 0, & \text{otherwise.} \end{cases} \tag{4}$$

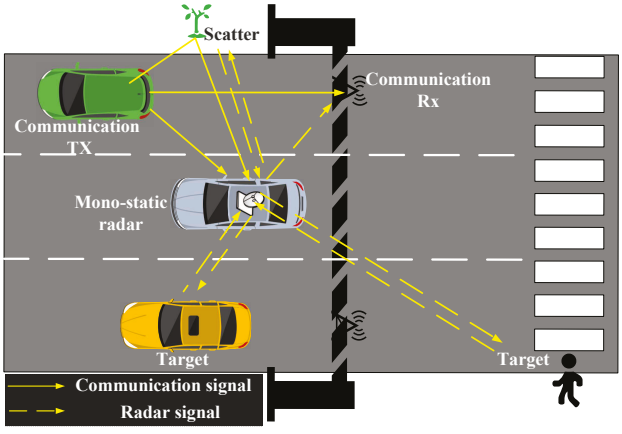

Figure 1. A Photo illustration of Radar and Communication Spectral Coexistence on Vehicle Platform.

Moreover, assume the j-th clutter or the c-th interference from communication system is distributed in the range-azimuth bin $\left(r_{\{j,c\}}, k\right), r_{\{j,c\}} \in \{0, \ldots, \tilde{L}-1\}, k \in \{0, \ldots, K-1\}$. $\tilde{L} \leq L$ represents the number of range rings, and K denotes the number of discrete azimuth segments, then the clutter obeys the model

$$\mathbf{y}_i(l) = \sum_{j=1}^{J} \alpha_j \, e^{j2\pi f_{d,j}(l-1)} \, \mathbf{A}(\theta_j) \, \mathbf{s}(l - r_j), 0 \leq r_j \leq l-1, \tag{5}$$

where α_j denotes the complex amplitude with $\mathbb{E}\left[|\alpha_j|^2\right] = \sigma_j^2$, $f_{d,j}$ and θ_j denote the normalized Doppler frequency and azimuth of the j-th clutter, respectively.

Suppose the normalized Doppler frequency $f_{d,j} \sim U\left(\bar{f}_{d,j} - \frac{\varepsilon_j}{2}, \bar{f}_{d,j} + \frac{\varepsilon_j}{2}\right), j \in 1, 2, \ldots, J$ with mean $\bar{f}_{d,j}$, where ε_j denotes the uncertainty of $\bar{f}_{d,j}$. Then the covariance matrix of clutter is given by

$$\mathbb{E}\left[\mathbf{y}_i(l_1)\mathbf{y}_i^H(l_2)\right] = \sum_{j=1}^{J} \sigma_j^2 \mathbf{A}(\theta_j)\mathbf{s}(l_1 - r_j)\mathbf{s}^H(l_2 - r_j)\mathbf{A}^H(\theta_j) e^{j2\pi \bar{f}_{d,j}(l_1 - l_2)} \frac{\sin\left[\pi\varepsilon_j(l_1 - l_2)\right]}{\pi\varepsilon_j(l_1 - l_2)}. \tag{6}$$

As to the m-th radar target at the range gate l_m, the clutter covariance matrix with a compact form can be expressed as

$$\begin{aligned}\boldsymbol{\Sigma}_{\mathbf{y}_i}(\mathbf{s}, l_m) &= \mathbb{E}\left[\mathbf{y}_i \mathbf{y}_i^H\right] \\ &= \sum_{j=1}^{J} \left(\mathbf{J}_L(r_j - l_m) \otimes \mathbf{A}(\theta_j)\right)\left[\left(\mathbf{s}\mathbf{s}^H\right) \odot \boldsymbol{\Xi}_j\right]\left(\mathbf{J}_L(r_j - l_m) \otimes \mathbf{A}(\theta_j)\right)^H,\end{aligned} \tag{7}$$

where

$$\boldsymbol{\Xi}_j = \sigma_j^2 \boldsymbol{\Phi}_{\varepsilon_j}^{\tilde{f}_{d,j}} \otimes \mathbf{Y}_{M_{R,t}}, \tag{8}$$

$$\boldsymbol{\Phi}_{\varepsilon_j}^{\tilde{f}_{d,j}}(l_1, l_2) = e^{j2\pi \tilde{f}_{d,j}(l_1 - l_2)} \frac{\sin\left[\pi \varepsilon_j (l_1 - l_2)\right]}{\pi \varepsilon_j (l_1 - l_2)}, \forall (l_1, l_2) \in \{1, 2, \ldots, L\}^2, \tag{9}$$

with $\mathbf{1}_{M_{R,t}} = [1, 1, \ldots, 1]^T$, $\mathbf{Y}_{M_{R,t}} = \mathbf{1}_{M_{R,t}} \mathbf{1}_{M_{R,t}}^T$, and σ_j^2 denoting the corresponding power of the j-th clutter.

In narrow band communication systems where the maximum excessive delay of P interference signals is much smaller than the sampling interval T_s, i.e., $\max_{p \neq p'} \left| r_p - r_{p'} \right| \ll T_s$ [39], we get $r_p \approx r_c, \forall p$, which means that P communication interferences fall in the same range ring r_c to the radar receiver. In this case, we consider P channels for communication interference: the p-th path with angle of departure φ_p, angle of arrival θ_p and fading coefficient $\eta_1(p)$, the expression is written as

$$\mathbf{B}_1 = \sum_{p=1}^{P} \eta_1(p)\, \mathbf{a}_r^*(\theta_p)\, \mathbf{b}_t^H(\varphi_p) = \sum_{p=1}^{P} \eta_1(p) \mathbf{B}_{1,p}, \tag{10}$$

where $\eta_1(p)$ represents the fading coefficient of the p-th propagation path, and $\mathbf{b}_t(\varphi_p)$ is the p-th transmit steering vector from the communication systems. We thus define:

$$\boldsymbol{\Xi}_C \triangleq \boldsymbol{\Psi}^{f'_{d,p}} \otimes \mathbf{Y}_{M_{C,t}}, \tag{11}$$

in which

$$\boldsymbol{\Psi}^{f'_{d,p}}(l_1, l_2) = e^{j2\pi f'_{d,p}(l_1 - l_2)}, \forall (l_1, l_2) \in \{1, 2, \ldots, L\}^2, \tag{12}$$

and $\mathbf{Y}_{M_{C,t}} = \mathbf{1}_{M_{C,t}} \mathbf{1}_{M_{C,t}}^T$, where $f'_{d,p}$ denotes the Doppler shift of the p-th communication signal. Then, the covariance matrix of communication interference will have a similar form as the clutter component (7), i.e.,

$$\begin{aligned}&\boldsymbol{\Sigma}_{\mathbf{y}_c}(\mathbf{X}, l_m) = \mathbb{E}\left[\mathbf{x}_C \mathbf{x}_C^H\right] \\ &= \sum_{p=1}^{P} \left(\mathbf{J}_L(r_p - l_m) \otimes \mathbf{B}_{1,p}\right)\left[\mathbb{E}\left[\mathbf{x}\mathbf{x}^H\right] \odot \boldsymbol{\Xi}_C\right]\left(\mathbf{J}_L(r_p - l_m) \otimes \mathbf{B}_{1,p}\right)^H \\ &= \sum_{p=1}^{P} \left(\mathbf{J}_L(r_p - l_m) \otimes \mathbf{B}_{1,p}\right)\left[\mathbf{X} \odot \boldsymbol{\Xi}_C\right]\left(\mathbf{J}_L(r_p - l_m) \otimes \mathbf{B}_{1,p}\right)^H,\end{aligned} \tag{13}$$

where the communication codewords are denoted by $\mathbf{x} = \left(\left[\mathbf{x}(1)^T, \ldots, \mathbf{x}(L)^T\right]\right)^T$ with $\mathbf{x} \sim \mathcal{CN}(\mathbf{0}, \mathbf{X})$ [40]. In order to reduce the complexity of design, we only optimize the space-time covariance matrix $\mathbf{X}$.

Concerning the communication system, the received signal can be expressed as

$$\mathbf{z}_C = \hat{\mathbf{H}}\mathbf{x} + \sum_{q=1}^{Q} \hat{\mathbf{B}}_2\left(f_{d,q}, q\right)\mathbf{s} + \mathbf{n}_C, \tag{14}$$

where $\hat{\mathbf{H}} = (\mathbf{I}_L \otimes \mathbf{H})$, $\mathbf{H}$ is channel matrix. $\hat{\mathbf{B}}_2\left(f_{d,q}, q\right) = \mathrm{diag}\left(\mathbf{p}\left(f_{d,q}\right)\right) \otimes \mathbf{B}_{2,q}$, $\mathbf{B}_{2,q} = \mathbf{b}_r^*(\varphi_q)\,\mathbf{a}_t^H(\theta_q)$, where $\mathbf{b}_r(\varphi_q)$ represents the receive steering vector of the q-th path. Similar to the definition of (10), we set

$$\mathbf{B}_2 = \sum_{q=1}^{Q} \eta_2(q)\mathbf{B}_{2,q}, \tag{15}$$

where $\eta_2(q)$ represents the fading coefficient of the q-th propagation path at the communication receiver, Q is the number of paths impacting on the communication receiver, and $\mathbf{n}_C \sim \mathcal{CN}\left(\mathbf{0}, \sigma_C^2\mathbf{I}_{M_{C,r}L}\right)$ denotes the additive white Gaussian noise. It is supposed that the channel matrices $\mathbf{H}$, $\mathbf{B}_1$ and $\mathbf{B}_2$ are fully known at the spectral coexistence system. Practically, the information can be periodically communicated by a pilot channel [41,42]. However, the exact direction information may not be obtained because of the possible mismatches. Therefore, we assume that $\{\theta\}$ and $\{\varphi\}$ are independent random variables and can be expressed as

$$\begin{array}{l} \tilde{\theta}_m \sim U[\theta_m - \varpi_m, \theta_m + \varpi_m], m = 0, \cdots, M \\ \tilde{\theta}_j \sim U\left[\theta_j - \varpi_j, \theta_j + \varpi_j\right], j = 0, \cdots, J \\ \tilde{\theta}_p \sim U\left[\theta_p - \varpi_p, \theta_p + \varpi_p\right], p = 0, \cdots, P \\ \tilde{\varphi}_p \sim U\left[\varphi_p - \varpi_p, \varphi_p + \varpi_p\right], p = 1, \cdots, P \\ \tilde{\theta}_q \sim U\left[\theta_q - \varpi_q, \theta_q + \varpi_q\right], q = 0, \cdots, Q \\ \tilde{\varphi}_q \sim U\left[\varphi_q - \varpi_q, \varphi_q + \varpi_q\right], q = 1, \cdots, Q, \end{array} \tag{16}$$

where ϖ_m, ϖ_j, ϖ_p, ϖ_q are the uncertainties on the corresponding direction information.

3. Problem Formulation

Since improving the accuracy of parameter estimation and signal detection in presence of interference can be achieved by a higher SINR level, we take maximizing the output SINR as a criterion for radar transceiver design. Specifically, by assuming $\mathbf{w}_m \neq \mathbf{0}$, the $\mathrm{SINR}_m(\mathbf{X}, \mathbf{s}, \mathbf{w}_m)$ for the m-th target can be written as

$$\mathrm{SINR}_m(\mathbf{X}, \mathbf{s}, \mathbf{w}_m) = \frac{\sigma_0^2\left|\mathbf{w}_m^H\left(\mathbf{J}_L(l_m - l_m) \otimes \mathbf{I}_{M_{R,r}}\right)\mathbf{A}\left(f_{d,m}, \theta_m\right)\mathbf{s}\right|^2}{\mathbf{w}_m^H\left(\mathbf{\Sigma}_{\mathbf{y}_s}(\mathbf{s}, l_m) + \mathbf{\Sigma}_{\mathbf{y}_i}(\mathbf{s}, l_m) + \mathbf{\Sigma}_{\mathbf{y}_c}(\mathbf{X}, l_m) + \sigma_R^2\mathbf{I}\right)\mathbf{w}_m}, \tag{17}$$

where

$$\begin{aligned} \mathbf{\Sigma}_{\mathbf{y}_s}(\mathbf{s}, l_m) &= \mathbb{E}\left[\mathbf{y}_s\mathbf{y}_s^H\right] \\ &= \sum_{i=1, i\neq m}^{M} \sigma_0^2\left(\mathbf{J}_L(l_i - l_m) \otimes \mathbf{I}_{M_{R,r}}\right)\mathbf{A}(f_{d,m}, \theta_m)\mathbf{s}\mathbf{s}^H\left(\left(\mathbf{J}_L(l_i - l_m) \otimes \mathbf{I}_{M_{R,r}}\right)\mathbf{A}(f_{d,m}, \theta_m)\right)^H, \end{aligned} \tag{18}$$

with

$$\mathbf{y}_s = \sum_{i=1, i\neq m}^{M} \alpha_i\left(\mathbf{J}_L(l_i - l_m) \otimes \mathbf{I}_{M_{R,r}}\right)\mathbf{A}(f_{d,m}, \theta_m)\mathbf{s} \tag{19}$$

denoting the interference term produced by the other $M - 1$ radar targets.

For the radar, the SINR in (17) given the scope of inspection can be regarded as a relevant figure of merit. For this purpose, assuming $\left|\mathbf{w}_m^H\mathbf{A}(f_{d,m}, \theta_m)\mathbf{s}\right| \neq 0$, the figure of merit is given by

$$\mathrm{SINR}(\mathbf{X}, \mathbf{s}, \mathbf{w}_m) = \left(\sum_{m=1}^{M} \frac{\zeta_m}{\mathrm{SINR}_m(\mathbf{X}, \mathbf{s}, \mathbf{w}_m)}\right)^{-1}, \tag{20}$$

where $\{\zeta_m\}$ is a positive weight. For simple numerical description, we define $\mathbf{\Sigma}_{in}(\mathbf{X}, \mathbf{s}, l_m) \triangleq \mathbf{\Sigma}_{\mathbf{y}_s}(\mathbf{s}, l_m) + \mathbf{\Sigma}_{\mathbf{y}_i}(\mathbf{s}, l_m) + \mathbf{\Sigma}_{\mathbf{y}_c}(\mathbf{X}, l_m) + \sigma_R^2\mathbf{I}_{M_{R,t}L}$. Based on the above guidelines, for the communication system, the covariance matrix of the interference-plus-noise can be formulated as

$$\mathbf{R}_{Cin} = \sum_{q=1}^{Q} \hat{\mathbf{B}}_2\left(f_{d,q}, q\right)\left(\mathbf{s}\mathbf{s}^H\right)\hat{\mathbf{B}}_2^H\left(f_{d,q}, q\right) + \sigma_C^2 \mathbf{I}_{M_{C,r}L}. \tag{21}$$

In order to match $\mathbf{R}_{Cin}$, we define the "communication rate" of the space-time communication channel as

$$C(\mathbf{X}, \mathbf{s}) \triangleq \frac{1}{M_{C,t}M_{C,r}} \log_2 \det\left(\mathbf{I}_{M_{C,r}L} + \mathbf{R}_{Cin}^{-1}\hat{\mathbf{H}}\mathbf{X}\hat{\mathbf{H}}^H\right). \tag{22}$$

Our goal is to optimize the communication system rate and radar output SINR simultaneously. Due to the fact that the energy of the transmitter is limited in most cases and to obtain desirable properties according to envelope constancy and sidelobe levels with a reference signal $\mathbf{s}_0$, we require the shape of radar waveform with normalized transmitted energy $\|\mathbf{s}\|^2 = 1$ satisfying [43]

$$\|\mathbf{s} - \mathbf{s}_0\|_\infty \leq \gamma, \tag{23}$$

where γ rules the degree of the similarity. The above constraint can be equivalently converted to

$$(\mathbf{s} - \mathbf{s}_0)^H \mathbf{B}_i (\mathbf{s} - \mathbf{s}_0) \leq \gamma, i = 1, \cdots, M_{R,t}L, \tag{24}$$

where $\mathbf{B}_i \in \mathbb{C}^{M_{R,t}L \times M_{R,t}L}$ represents a square matrix where all elements except (i, i)-th element equal to 1 are 0. Regarding to the communication system, we put an energy constraint on the transmitter, namely

$$\mathbb{E}\left[\mathrm{Tr}\left(\mathbf{x}\mathbf{x}^H\right)\right] = \mathrm{Tr}(\mathbf{X}) \leq E_C. \tag{25}$$

According to [44], the classic SINR maximization problem of radar can be solved via the MVDR criterion. Without loss of generality, by setting $\mathbf{w}_m^H\left(\mathbf{I}_L \otimes \mathbf{I}_{M_{R,r}}\right)\mathbf{A}(f_{d,m}, \theta_m)\mathbf{s} = \mathbf{w}_m^H\mathbf{A}(f_{d,m}, \theta_m)\mathbf{s} = \epsilon$ for $\forall m$ with the constant $\epsilon = 1$, we reformulate the radar SINR as

$$\mathrm{SINR}(\mathbf{X}, \mathbf{s}, \mathbf{w}_m) = \left(\sum_{m=1}^{M} \zeta_m \mathbf{w}_m^H \mathbf{\Sigma}_{in}(\mathbf{X}, \mathbf{s}, l_m)\mathbf{w}_m\right)^{-1}. \tag{26}$$

Finally, we recommend minimizing an appropriate weighted radar residual interference power and communication rate, i.e.,

$$\begin{aligned} \min_{\mathbf{X},\mathbf{s},\mathbf{w}_m} \quad & \omega_1 \frac{\sum_{m=1}^{M} \zeta_m \mathbf{w}_m^H \mathbf{\Sigma}_{in}(\mathbf{X},\mathbf{s},l_m)\mathbf{w}_m}{|F_1^\star|} - \omega_2 \frac{C(\mathbf{X},\mathbf{s})}{|F_2^\star|}, \\ \text{s.t.} \quad & \mathbf{w}_m^H \mathbf{A}(f_{d,m}, \theta_m)\mathbf{s} = \epsilon, m = 1, \cdots, M, \\ & (\mathbf{s} - \mathbf{s}_0)^H \mathbf{B}_i (\mathbf{s} - \mathbf{s}_0) \leq \gamma, i = 1, \cdots, M_{R,t}L, \\ & \mathrm{Tr}(\mathbf{X}) \leq E_C, \\ & \|\mathbf{s}\|^2 = 1, \end{aligned} \tag{27}$$

where $F_1 = \sum_{m=1}^{M} \zeta_m \mathbf{w}_m^H \mathbf{\Sigma}_{in}(\mathbf{X}, \mathbf{s}, l_m)\mathbf{w}_m$ represents the interference-plus-noise power, and $F_2 = -C(\mathbf{X}, \mathbf{s})$ is given by (22). Assuming that $F_1^\star$ and $F_2^\star$ are the corresponding achievable optima values. $0 \leq \omega_1 \leq 1$ and $0 \leq \omega_2 \leq 1$ are weighted parameters. Typically, $\omega_1 + \omega_2 = 1$, which reflects the degree of importance of the two conflicting objectives in the coexistence system. In the following section, we will derive the solutions to problem (27) through the proposed algorithm framework.

4. The Designed Alternating Procedure

Problem (27) is non-convex relating to the triplet parameters ($\mathbf{X}$, $\mathbf{s}$, $\mathbf{w}_m$), and finding the solutions would cause a daunting complexity. We develop an alternating algorithm on the basis of the following iterative procedure.

4.1. Communication Transmit Codebook Optimization

Firstly, we optimize $\mathbf{X}$ while $\mathbf{s}$ and $\mathbf{w}_m$ are fixed:

$$\begin{aligned} \min_{\mathbf{X}} \quad & \omega_1 \frac{\sum_{m=1}^{M} \zeta_m \mathbf{w}_m^H \boldsymbol{\Sigma}_{in}(\mathbf{X},\mathbf{s},l_m)\mathbf{w}_m}{|F_1^\star|} - \omega_2 \frac{C(\mathbf{X},\mathbf{s})}{|F_2^\star|}, \\ \text{s.t.} \quad & \mathrm{Tr}(\mathbf{X}) \le E_C. \end{aligned} \tag{28}$$

Theorem 1. *Let* $\mathbf{W_m} = \mathbf{w_m}\mathbf{w_m^H}$*, then the residual interference-plus-noise of is given by*

$$\sum_{m=1}^{M} \zeta_m \mathbf{w}_m^H \boldsymbol{\Sigma}_{in}(\mathbf{X},\mathbf{s},l_m)\mathbf{w}_m = \mathrm{Tr}\big(\bar{\boldsymbol{\Sigma}}_{\mathbf{y}_c}(\mathbf{W}_m)\mathbf{X}\big) + \kappa_1, \tag{29}$$

where κ_1 *is a positive item independent of* $\mathbf{X}$*.* $\bar{\boldsymbol{\Sigma}}_{\mathbf{y}_c}(\mathbf{W}_m) = \sum_{m=1}^{M} \zeta_m \bar{\boldsymbol{\Sigma}}_{\mathbf{y}_c}(\mathbf{W}_m, l_m)$*, and*

$$\bar{\boldsymbol{\Sigma}}_{\mathbf{y}_c}(\mathbf{W}_m, l_m) = \sum_{p=1}^{P} \big(\mathbf{J}_L(r_p - l_m) \otimes \mathbf{B}_{1,p}\big)^H [\mathbf{W}_m \odot \bar{\boldsymbol{\Xi}}_C] \big(\mathbf{J}_L(r_p - l_m) \otimes \mathbf{B}_{1,p}\big). \tag{30}$$

Proof of Theorem 1. It can be shown that the communication interference onto the radar can be expressed as

$$\begin{aligned} & \mathbf{w}_m^H \boldsymbol{\Sigma}_{\mathbf{y}_c}(\mathbf{X}, l_m)\mathbf{w}_m \\ &= \sum_{p=1}^{P} \mathbb{E}\Big[\mathbf{x}^H \big(\mathbf{J}_L(r_p - l_m) \otimes \mathbf{B}_{1,p}\big)^H [\mathbf{W_m} \odot \bar{\boldsymbol{\Xi}}_C] \big(\mathbf{J}_L(r_p - l_m) \otimes \mathbf{B}_{1,p}\big)\mathbf{x}\Big] \\ &= \mathrm{Tr}\left(\sum_{p=1}^{P} \big(\mathbf{J}_L(r_p - l_m) \otimes \mathbf{B}_{1,p}\big)^H [\mathbf{W}_m \odot \bar{\boldsymbol{\Xi}}_C] \big(\mathbf{J}_L(r_p - l_m) \otimes \mathbf{B}_{1,p}\big)\mathbf{X}\right) \\ &= \mathrm{Tr}\big(\bar{\boldsymbol{\Sigma}}_{\mathbf{y}_c}(\mathbf{W}_m, l_m)\mathbf{X}\big), \end{aligned} \tag{31}$$

where

$$\bar{\boldsymbol{\Xi}}_C = \Big(\boldsymbol{\Psi}^{f'_{d,p}}(l_1, l_2)\Big)^* \otimes \mathbf{Y}_{M_{R,r}}. \tag{32}$$

Based on (31), we have

$$\begin{aligned} & \sum_{m=1}^{M} \zeta_m \mathbf{w}_m^H \boldsymbol{\Sigma}_{in}(\mathbf{X},\mathbf{s},l_m)\mathbf{w}_m = \sum_{m=1}^{M} \zeta_m \mathrm{Tr}\big(\bar{\boldsymbol{\Sigma}}_{\mathbf{y}_c}(\mathbf{W}_m, l_m)\mathbf{X}\big) + \\ & \underbrace{\sum_{m=1}^{M} \zeta_m \mathbf{w}_m^H \Big(\boldsymbol{\Sigma}_{\mathbf{y}_s}(\mathbf{s}, l_m) + \boldsymbol{\Sigma}_{\mathbf{y}_i}(\mathbf{s}, l_m) + \sigma_R^2 \mathbf{I}\Big)\mathbf{w}_m}_{\kappa_1}, \end{aligned} \tag{33}$$

which completes the proof. □

By exploiting Theorem 1, the subproblem (28) can be transformed as

$$\begin{aligned} \min_{\mathbf{X}} \quad & \omega_1 \frac{\mathrm{Tr}\big(\bar{\boldsymbol{\Sigma}}_{\mathbf{y}_c}(\mathbf{W}_m)\mathbf{X}\big)}{|F_1^\star|} - \omega_2 \frac{C(\mathbf{X},\mathbf{s})}{|F_2^\star|}, \\ \text{s.t.} \quad & \mathrm{Tr}(\mathbf{X}) \le E_C, \end{aligned} \tag{34}$$

which is a convex problem involving multiple matrix variables. Therefore, by using standard convex optimization techniques, the above problem can be solved with the complexity of $O\left(\left((LM_{C,t})^2\right)^{3.5}\right)$. The Lagrange dual method is used for the problem (34) and thus a low-cost closed-form solution can be obtained. Ignoring the items that do not rely on $\mathbf{X}$, the Lagrangian of (34) can be expressed as

$$\begin{aligned}\mathcal{L}(\mathbf{X},\mu_0) = \mu_0(\mathrm{Tr}(\mathbf{X}) - E_C) + \tfrac{w_1}{|F_1^\star|}\mathrm{Tr}\big(\bar{\mathbf{\Sigma}}_{\mathbf{y}_c}(\mathbf{W}_m)\mathbf{X}\big) \\ - \tfrac{w_2}{|F_2^\star|M_{C,t}M_{C,r}}\log_2\det\Big(\mathbf{I}_{M_{C,r}L} + \mathbf{R}_{Cin}^{-1}\hat{\mathbf{H}}\mathbf{X}\hat{\mathbf{H}}^H\Big),\end{aligned} \tag{35}$$

where $\mu_0 \geq 0$ is the dual variable. Then, the dual problem be formulated as

$$\max_{\mu_0\geq 0}\inf_{\mathbf{X}\succeq\mathbf{0}} \mathcal{L}(\mathbf{X},\mu_0) \triangleq \max_{\mu_0\geq 0} g(\mu_0), \tag{36}$$

where $g(\mu_0)$ denotes the duality function. In addition, since (34) is convex satisfying Slater's condition and strong duality [45], i.e., the dual gap is set to zero. By using the "water-filling (WF)", the optimal solution can be indicated as

$$\mathbf{X}^\star(\mu_0) = \left(\tfrac{w_1\bar{\mathbf{\Sigma}}_{\mathbf{y}_c}(\mathbf{W}_m)}{|F_1^\star|} + \mu_0\mathbf{I}_{M_{C,t}L}\right)^{-1/2}\tilde{\mathbf{U}}\tilde{\mathbf{\Sigma}}\tilde{\mathbf{U}}^H\left(\tfrac{w_1\bar{\mathbf{\Sigma}}_{\mathbf{y}_c}(\mathbf{W}_m)}{|F_1^\star|} + \mu_0\mathbf{I}_{M_{C,t}L}\right)^{-1/2}, \tag{37}$$

where $\mathbf{X}^\star(\mu_0)$ denotes the optimal $\mathbf{X}$ for a given μ_0, and $\tilde{\mathbf{U}}$ denotes the right singularity matrix of $\tilde{\mathbf{H}}$, the expression is given as

$$\tilde{\mathbf{H}} = \mathbf{R}_{Cin}^{-1/2}\hat{\mathbf{H}}\left(\frac{w_1\bar{\mathbf{\Sigma}}_{\mathbf{y}_c}(\mathbf{W}_m)}{|F_1^\star|} + \mu_0\mathbf{I}_{M_{C,t}L}\right)^{-1/2}, \tag{38}$$

$\tilde{\mathbf{\Sigma}} = \mathrm{diag}(\tilde{\gamma}_1,\ldots,\tilde{\gamma}_r)$, $\tilde{\gamma}_i = \left(\frac{w_2}{|F_2^\star|M_{C,t}M_{C,r}} - 1/\tilde{\sigma}_i^2\right)^+, i = 1,\ldots,r$. r represents the rank of $\tilde{\mathbf{H}}$, $\tilde{\sigma}_i$ denotes the i-th positive singular value of the matrix $\tilde{\mathbf{H}}$, and $\sum_{i=1}^{M_{min}}\tilde{\gamma}_i = E_C$, where $M_{min} \triangleq \min(M_{C,t}L, M_{C,r}L)$. μ_0 can be obtained via the bisection method fulfilling the power constraint.

4.2. Radar Receive Filter Optimization

For the second step, given $\mathbf{s}$ and $\mathbf{X}$, the optimization of the receive filter is solved by the MVDR criterion:

$$\mathbf{w}_m = \frac{\mathbf{\Sigma}_{in}(\mathbf{X},\mathbf{s},l_m)^{-1}\mathbf{A}(f_{d,m},\theta_m)\mathbf{s}}{\mathbf{A}(f_{d,m},\theta_m)\mathbf{s}^H\mathbf{\Sigma}_{in}(\mathbf{X},\mathbf{s},l_m)^{-1}\mathbf{A}(f_{d,m},\theta_m)\mathbf{s}}, l = 1,\ldots,M. \tag{39}$$

Thus the filter for each radar target can be computed.

4.3. Radar Transmit Waveform Optimization

In the third step, we consider to optimize $\mathbf{s}$ with fixed $\mathbf{w}_m$ and $\mathbf{X}$, for which the subproblem can be converted to

$$\begin{aligned}\min_{\mathbf{s}}\quad & \omega_1\frac{\sum_{m=1}^{M}\zeta_m\mathbf{w}_m^H\mathbf{\Sigma}_{in}(\mathbf{X},\mathbf{s},l_m)\mathbf{w}_m}{|F_1^\star|} - \omega_2\frac{C(\mathbf{X},\mathbf{s})}{|F_2^\star|}, \\ \text{s.t.}\quad & \mathbf{w}_m^H\mathbf{A}(f_{d,m},\theta_m)\mathbf{s} = 1, m = 1,\cdots,M, \\ & (\mathbf{s}-\mathbf{s}_0)^H\mathbf{B}_i(\mathbf{s}-\mathbf{s}_0) \leq \gamma, i = 1,\cdots,M_{R,t}L, \\ & \|\mathbf{s}\|^2 = 1,\end{aligned} \tag{40}$$

which is non-convex because of the right side of the cost function and the quadratic equation constraints. Generally, it is difficult to straightforwardly tackle such a non-convex problem and there is no closed-form solution. Therefore, we first derive a minorizing function for the communication rate (right-hand side) of the objective function, i.e., $C(\mathbf{X},\mathbf{s})$, and then an iteration procedure with lower computational complexity based on MM-ADMM is developed.

4.3.1. Minorizing Function Construction

We first simplify the radar interference term of the original problem before building the minorizing function for the transmission rate. The energy at the output of the radar filter can be rewritten as follows by ignoring the parts that don't depend on $\mathbf{s}$ in the first portion of the objective function in (40).

$$\begin{aligned}
&\mathbf{w}_m^H \boldsymbol{\Sigma}_{\mathbf{y}_s}(\mathbf{s}, l_m)\mathbf{w}_m^H \\
&= \mathbf{w}_m^H \sum_{i=1, i\neq m}^{M} \sigma_0^2 \left(\mathbf{J}_L(l_i - l_m) \otimes \mathbf{I}_{M_{R,r}}\right)\mathbf{A}(f_{d,m}, \theta_m)\mathbf{s}\mathbf{s}^H \\
&\quad \left(\left(\mathbf{J}_L(l_i - l_m) \otimes \mathbf{I}_{M_{R,r}}\right)\mathbf{A}(f_{d,m}, \theta_m)\right)^H \mathbf{w}_m \\
&= \mathbf{s}^H \Bigg(\sum_{i=1, i\neq m}^{M} \left(\left(\mathbf{J}_L(l_i - l_m) \otimes \mathbf{I}_{M_{R,r}}\right)\mathbf{A}(f_{d,m}, \theta_m)\right)^H \mathbf{w}_m \mathbf{w}_m^H \\
&\qquad \underbrace{\sigma_0^2 \left(\mathbf{J}_L(l_i - l_m) \otimes \mathbf{I}_{M_{R,r}}\right)\mathbf{A}(f_{d,m}, \theta_m)}_{\bar{\boldsymbol{\Sigma}}_{\mathbf{y}_s}(\mathbf{s}, l_m)} \Bigg) \mathbf{s}.
\end{aligned} \tag{41}$$

Following the same line of derivation, the filtered radar clutter power can be expressed as

$$\begin{aligned}
&\mathbf{w}_m^H \boldsymbol{\Sigma}_{\mathbf{y}_i}(\mathbf{s}, l_m)\mathbf{w}_m \\
&= \mathbf{s}^H \left\{ \sum_{j=1}^{J} \left(\mathbf{J}_L(r_j - l_m) \otimes \mathbf{A}(\theta_j)\right)^H \left[\mathrm{diag}(\mathbf{w}_m)\bar{\boldsymbol{\Xi}}_j \mathrm{diag}(\mathbf{w}_m)^H\right] \left(\mathbf{J}_L(r_j - l_m) \otimes \mathbf{A}(\theta_j)\right) \right\} \mathbf{s} \\
&= \mathbf{s}^H \underbrace{\left\{ \sum_{j=1}^{J} \left(\mathbf{J}_L(r_j - l_m) \otimes \mathbf{A}(\theta_j)\right)^H \left[\mathbf{W}_m \odot \bar{\boldsymbol{\Xi}}_j\right] \left(\mathbf{J}_L(r_j - l_m) \otimes \mathbf{A}(\theta_j)\right) \right\}}_{\bar{\boldsymbol{\Sigma}}_{\mathbf{y}_i}(\mathbf{W}_m, l_m)} \mathbf{s} \\
&= \mathbf{s}^H \bar{\boldsymbol{\Sigma}}_{\mathbf{y}_i}(\mathbf{W}_m, l_m)\mathbf{s},
\end{aligned} \tag{42}$$

with

$$\bar{\boldsymbol{\Xi}}_j = \sigma_j^2 \left(\boldsymbol{\Phi}_{\varepsilon_j}^{\bar{f}_{d,j}}(l_1, l_2)\right)^* \otimes \mathbf{Y}_{M_{R,r}}, \ \forall (l_1, l_2) \in \{1, \ldots, L\}^2. \tag{43}$$

For ease of notation, we set $\bar{\boldsymbol{\Sigma}}_{\mathbf{s}}(\mathbf{W}_m) = \sum_{m=1}^{M} \zeta_m \left(\bar{\boldsymbol{\Sigma}}_{\mathbf{y}_s}(\mathbf{s}, l_m) + \bar{\boldsymbol{\Sigma}}_{\mathbf{y}_i}(\mathbf{W}_m, l_m)\right)$. The communication rate is convex in respect of $\mathbf{s}$, to tackle the maximizing problem, the rate is rewritten as

$$C(\mathbf{X}, \mathbf{s}) = \underbrace{\frac{1}{M_{C,t}M_{C,r}} \log_2 \det\left(\mathbf{R}_{Cin} + \hat{\mathbf{H}}\mathbf{X}\hat{\mathbf{H}}^H\right)}_{f_1(\mathbf{s})} \underbrace{- \frac{1}{M_{C,t}M_{C,r}} \log_2 \det(\mathbf{R}_{Cin})}_{f_2(\mathbf{s})}. \tag{44}$$

Next, we construct two functions that minorize $f_1(\mathbf{s})$ and $f_2(\mathbf{s})$ in (44), as a result of which the MM algorithm can be used to solve the problem (40).

Theorem 2. *Define* $\mathbf{F} = \mathbf{s}\mathbf{s}^H$ *and* $\mathbf{F}^{(k_0)} = \mathbf{s}^{(k_0)}\left(\mathbf{s}^{(k_0)}\right)^H$, *assume* $\mathcal{S}$ *is the feasible set for* $\mathbf{F}$. *As to any* $\mathbf{F}, \mathbf{F}^{(k_0)} \in \mathcal{S}$, *a valid surrogate function,* $\tilde{C}\left(\mathbf{F}, \mathbf{F}^{(k_0)}\right)$ *at the* k_0*-th iteration, can be formulated as*

$$\tilde{C}\left(\mathbf{F}, \mathbf{F}^{(k_0)}\right) = \mathrm{Tr}\left(\mathbf{Y}^{(k_0)}\boldsymbol{\Gamma}_1(\mathbf{F})\right) + \mathrm{Tr}\left(\boldsymbol{\Gamma}_2\left(\mathbf{F}^{(k_0)}\right)\mathbf{F}\right) + \kappa_u, \tag{45}$$

where κ_u *is a term independent of* $\mathbf{F}$,

$$\boldsymbol{\Gamma}_1(\mathbf{F}) = \begin{bmatrix} \tilde{\mathbf{R}}^{-1} & \tilde{\mathbf{R}}^{-1} \sum\limits_{q=1}^{Q} \hat{\mathbf{B}}_2\left(f_{d,q}, q\right) \mathbf{F} \hat{\mathbf{B}}_2^H\left(f_{d,q}, q\right) \\ \tilde{\mathbf{R}}^{-1} & \mathbf{I}_{M_{C,r}L} + \tilde{\mathbf{R}}^{-1} \sum\limits_{q=1}^{Q} \hat{\mathbf{B}}_2\left(f_{d,q}, q\right) \mathbf{F} \hat{\mathbf{B}}_2^H\left(f_{d,q}, q\right) \end{bmatrix}, \tag{46}$$

$$\begin{aligned} &\boldsymbol{\Gamma}_2\left(\mathbf{F}^{(k_0)}\right) \triangleq -\left(\frac{\partial f_2(\mathbf{F})}{\partial \mathbf{F}}\right)^T_{\mathbf{F}=\mathbf{F}^{(k_0)}} \\ &= -\sum_{q=1}^{Q} \left(\hat{\mathbf{B}}_2\left(f_{d,q}, q\right)\right)^H \left(\sum_{q=1}^{Q} \hat{\mathbf{B}}_2\left(f_{d,q}, q\right) \mathbf{F}^{(k_0)} \left(\hat{\mathbf{B}}_2\left(f_{d,q}, q\right)\right)^H + \sigma_C^2 \mathbf{I}_{M_{C,r}L}\right)^{-1} \hat{\mathbf{B}}_2\left(f_{d,q}, q\right), \end{aligned} \tag{47}$$

$$\mathbf{Y}^{(k_0)} = -\boldsymbol{\Gamma}_1\left(\mathbf{F}^{(k_0)}\right)^{-1} \mathbf{E}^H \left(\mathbf{E}^H \boldsymbol{\Gamma}_1\left(\mathbf{F}^{(k_0)}\right) \mathbf{E}\right)^{-1} \mathbf{E} \boldsymbol{\Gamma}_1\left(\mathbf{F}^{(k_0)}\right)^{-1}. \tag{48}$$

with $\tilde{\mathbf{R}} = \sigma_C^2 \mathbf{I}_{M_{C,r}L} + \hat{\mathbf{H}} \mathbf{X} \hat{\mathbf{H}}^H$ *and* $\mathbf{E} = \left[\mathbf{I}_{M_{C,r}L}\, \mathbf{0}_{M_{C,r}L \times M_{C,r}L}\right]$.

Proof of Theorem 2. As to the function f_1, by exploiting the property of matrix determinant, we have:

$$\begin{aligned} &\log_2 \det\left(\mathbf{R}_{Cin} + \hat{\mathbf{H}} \mathbf{X} \hat{\mathbf{H}}^H\right) \\ &= -\log_2 \det\left(\sum_{q=1}^{Q} \hat{\mathbf{B}}_2\left(f_{d,q}, q\right) \left(\mathbf{s}\mathbf{s}^H\right) \hat{\mathbf{B}}_2^H\left(f_{d,q}, q\right) + \tilde{\mathbf{R}}\right). \end{aligned} \tag{49}$$

Based on the Woodbury matrix identity, for given matrices $\mathbf{A}, \mathbf{B}, \mathbf{U}, \mathbf{V}$, we have

$$\left(\mathbf{A} + \mathbf{U}\mathbf{B}\mathbf{V}\right)^{-1} = \mathbf{A}^{-1} + \mathbf{A}^{-1}\mathbf{U}\mathbf{B}\mathbf{V}\mathbf{A}^{-1}\left(\mathbf{I} + \mathbf{U}\mathbf{B}\mathbf{V}\mathbf{A}^{-1}\right)^{-1}. \tag{50}$$

Then, the inverse of the matrix in (49) becomes to

$$\begin{aligned} &\left(\tilde{\mathbf{R}} + \sum_{q=1}^{Q} \hat{\mathbf{B}}_2\left(f_{d,q}, q\right) \left(\mathbf{s}\mathbf{s}^H\right) \hat{\mathbf{B}}_2^H\left(f_{d,q}, q\right)\right)^{-1} \\ &= \tilde{\mathbf{R}}^{-1} + \tilde{\mathbf{R}}^{-1} \sum_{q=1}^{Q} \hat{\mathbf{B}}_2\left(f_{d,q}, q\right) \left(\mathbf{s}\mathbf{s}^H\right) \hat{\mathbf{B}}_2^H\left(f_{d,q}, q\right) \\ &\left(\mathbf{I}_{M_{C,r}L} + \tilde{\mathbf{R}}^{-1} \sum_{q=1}^{Q} \hat{\mathbf{B}}_2\left(f_{d,q}, q\right) \left(\mathbf{s}\mathbf{s}^H\right) \hat{\mathbf{B}}_2^H\left(f_{d,q}, q\right)\right)^{-1} \tilde{\mathbf{R}}^{-1}. \end{aligned} \tag{51}$$

By exploiting the block matrix inversion property, the right-hand side of (51) can be transformed to $\mathbf{E}^H \boldsymbol{\Gamma}_1^{-1}(\mathbf{F}) \mathbf{E}$. Note that $\log\det\left(\mathbf{E}^H \boldsymbol{\Gamma}_1^{-1}(\mathbf{F}) \mathbf{E}\right)$ is convex with respect to $\boldsymbol{\Gamma}_1(\mathbf{F})$. The convex function can be minorized by its supporting hyperplanes, i.e.,

$$\begin{aligned} \log\det\left(\mathbf{E}^H \boldsymbol{\Gamma}_1^{-1}(\mathbf{F}) \mathbf{E}\right) &\geq f_1\left(\mathbf{s}, \mathbf{s}^{(k_0)}\right) \\ &= \log\det\left(\mathbf{E}^H \boldsymbol{\Gamma}_1^{-1}\left(\mathbf{F}^{(k_0)}\right) \mathbf{E}\right) \\ &\quad + \mathrm{Tr}\left(\mathbf{Y}^{(k_0)}\left(\boldsymbol{\Gamma}_1(\mathbf{F}) - \boldsymbol{\Gamma}_1\left(\mathbf{F}^{(k_0)}\right)\right)\right), \end{aligned} \tag{52}$$

where $\mathbf{Y}^{(k_0)}$ denotes the gradient of $\log\det\left(\mathbf{E}^H \boldsymbol{\Gamma}_1(\mathbf{F}) \mathbf{E}\right)$ at $\boldsymbol{\Gamma}_1\left(\mathbf{F}^{(k_0)}\right)$. Concerning the second term of (44), it is simple to demonstrate that function $f_2(\mathbf{s})$ is a convex function with respect to $\mathbf{F} = \mathbf{s}\mathbf{s}^H$ and we have

$$\begin{aligned} &-\log_2 \det\left(\sum_{q=1}^{Q} \hat{\mathbf{B}}_2\left(f_{d,q}, q\right) (\mathbf{F}) \hat{\mathbf{B}}_2^H\left(f_{d,q}, q\right) + \sigma_C^2 \mathbf{I}_{M_{C,r}L}\right) \\ &\geq -\log_2 \det\left(\sum_{q=1}^{Q} \hat{\mathbf{B}}_2\left(f_{d,q}, q\right) \left(\mathbf{F}^{(k_0)}\right) \hat{\mathbf{B}}_2^H\left(f_{d,q}, q\right) + \sigma_C^2 \mathbf{I}_{M_{C,r}L}\right) + \mathrm{Tr}\left(\boldsymbol{\Gamma}_2\left(\mathbf{F}^{(k_0)}\right)\left(\mathbf{F} - \mathbf{F}^{(k_0)}\right)\right), \end{aligned} \tag{53}$$

where $\mathbf{\Gamma}_2\left(\mathbf{F}^{(k_0)}\right)$ denotes the gradient of $f_2(\mathbf{F})$ at $\mathbf{F}^{(k_0)}$. Ignoring the terms that do not depend on $\mathbf{F}$, (45) can be derived from (52) and (47).

To make the formulation of the minorizer (52) simpler, $\mathbf{Y}^{(k_0)}$ can be partitioned as

$$\mathbf{Y}^{(k_0)} = \begin{bmatrix} \mathbf{Y}_{11}^{(k_0)} & \mathbf{Y}_{12}^{(k_0)} \\ \left(\mathbf{Y}_{12}^{(k_0)}\right)^H & \mathbf{Y}_{22}^{(k_0)} \end{bmatrix}. \tag{54}$$

Then the expression of $\mathrm{Tr}\left(\mathbf{Y}^{(k_0)}\mathbf{\Gamma}_1(\mathbf{F})\right)$ in (45) can be transformed as

$$\begin{aligned} &\mathrm{Tr}\left(\begin{array}{c} \left(\mathbf{Y}_{11}^{(k_0)}+\mathbf{Y}_{12}^{(k_0)}\right)\tilde{\mathbf{R}}^{-1}+\left(\mathbf{Y}_{12}^{(k_0)}\right)^H\tilde{\mathbf{R}}^{-1} \\ \sum_{q=1}^{Q}\hat{\mathbf{B}}_2\left(f_{d,q},q\right)\mathbf{F}\hat{\mathbf{B}}_2^H\left(f_{d,q},q\right)+\mathbf{Y}_{22}^{(k_0)} \\ \left(\mathbf{I}_{M_{C,r}L}+\tilde{\mathbf{R}}^{-1}\sum_{q=1}^{Q}\hat{\mathbf{B}}_2\left(f_{d,q},q\right)\mathbf{F}\hat{\mathbf{B}}_2^H\left(f_{d,q},q\right)\right) \end{array}\right) \\ &= \mathrm{Tr}\left(\underbrace{\left(\begin{array}{c} \sum_{q=1}^{Q}\hat{\mathbf{B}}_2^H\left(f_{d,q},q\right)\left(\mathbf{Y}_{12}^{(k_0)}\right)^H\tilde{\mathbf{R}}^{-1} \\ \hat{\mathbf{B}}_2\left(f_{d,q},q\right)+\sum_{q=1}^{Q}\hat{\mathbf{B}}_2^H\left(f_{d,q},q\right) \\ \mathbf{Y}_{22}^{(k_0)}\tilde{\mathbf{R}}^{-1}\hat{\mathbf{B}}_2\left(f_{d,q},q\right) \end{array}\right)}_{\mathbf{\Gamma}_{12}}\mathbf{F}\right)+\kappa_u, \end{aligned} \tag{55}$$

which completes the proof. □

According to $\mathrm{Tr}(\mathbf{DS}) = \mathrm{Tr}\left(\mathbf{Dss}^H\right) = \mathbf{s}^H\mathbf{Ds}$ and omitting the constant terms, the problem (40) can be turned into:

$$\begin{aligned} \min_{\mathbf{s}} \quad & \mathbf{s}^H\mathbf{\Gamma}^{(k_0)}\mathbf{s}, \\ \text{s.t.} \quad & \mathbf{w}_m^H\mathbf{A}(f_{d,m},\theta_m)\mathbf{s}=1, m=1,\cdots,M, \\ & (\mathbf{s}-\mathbf{s}_0)^H\mathbf{B}_i(\mathbf{s}-\mathbf{s}_0)\le\gamma, i=1,\cdots,M_{R,t}L, \\ & \|\mathbf{s}\|^2=1. \end{aligned} \tag{56}$$

where $\mathbf{\Gamma}^{(k_0)} = \frac{w_1}{|F_1^\star|}\bar{\mathbf{\Sigma}}_{\mathbf{s}}(\mathbf{W}_m)+\frac{w_2}{|F_2^\star|}\mathbf{\Gamma}_{12}$. Problem (56) is non-convex quadratically-constrained quadratic program (QCQP), which is difficult to solve. However, such a problem can be addressed using CVX tools with $\mathcal{O}(M_{R,t}L)^{4.5}$ (see [46] for details). In the following, an iteration procedure with lower computational complexity based on MM-ADMM is developed.

4.3.2. Radar Transmit Waveform Optimization Based on ADMM

To overcome the problem(56), we exploit the ADMM algorithm. It can be shown that problem (56)'s first restriction can be equivalently rewritten as

$$\mathbf{s}^H(\mathbf{A}(f_{d,m},\theta_m))^H\mathbf{W}_m(\mathbf{A}(f_{d,m},\theta_m))\mathbf{s}=1, m=1,\cdots,M. \tag{57}$$

Take note that the following decomposition is always valid

$$\mathbf{A}(f_{d,m},\theta_m)^H\mathbf{W}_m\mathbf{A}(f_{d,m},\theta_m)=\mathbf{T}_m^H\mathbf{T}_m, m=1,\cdots,M, \tag{58}$$

where $\mathbf{T}_m\in\mathbb{C}^{M_RL\times M_RL}$ is rank-one Hermitian matrix. Problem (56) is equivalent to

$$\begin{aligned} \min_{\mathbf{s}} \quad & \mathbf{s}^H\mathbf{\Gamma}^{(k_0)}\mathbf{s}, \\ \text{s.t.} \quad & \mathbf{s}^H\mathbf{T}_m^H\mathbf{T}_m\mathbf{s}=1, m=1,\cdots,M, \\ & (\mathbf{s}-\mathbf{s}_0)^H\mathbf{B}_i(\mathbf{s}-\mathbf{s}_0)\le\gamma, i=1,\cdots,M_{R,t}L, \\ & \|\mathbf{s}\|^2=1. \end{aligned} \tag{59}$$

We assume that the real-valued forms of $\mathbf{s}$, $\mathbf{s}_0$, $\mathbf{\Gamma}^{(k_0)}$, $\mathbf{T}_m$, and $\mathbf{B}_i$ are denoted by $\mathbf{s}_r$ $\mathbf{s}_{r,0}$, $\mathbf{\Gamma}_r$, $\mathbf{T}_{r,m}$, and $\mathbf{B}_{r,i}$, respectively. Problem (59) can be recast into the following real-valued form by inserting the variables $\mathbf{f}$, $\mathbf{g}_i$ and $\mathbf{h}$

$$\begin{aligned}
\min_{\mathbf{s}_r,\,\mathbf{f},\,\{\mathbf{g}_i\}} \quad & \mathbf{s}_r^T\mathbf{\Gamma}_r\mathbf{s}_r, && \text{(60a)}\\
\text{s.t.} \quad & \mathbf{f}_m = \mathbf{T}_{r,m}\mathbf{s}_r, m = 1,\cdots,M, && \text{(60b)}\\
& \mathbf{g}_i = \mathbf{B}_{r,i}(\mathbf{s}_r - \mathbf{s}_{r,0}), i = 1,\cdots,M_{R,t}L, && \text{(60c)}\\
& \mathbf{h} = \mathbf{s}_r, && \text{(60d)}\\
& \|\mathbf{f}_m\|^2 = 1, m = 1,\cdots,M, && \text{(60e)}\\
& \|\mathbf{g}_i\|^2 \le \gamma, i = 1,\cdots,M_{R,t}L. && \text{(60f)}\\
& \|\mathbf{h}\|^2 = 1. && \text{(60g)}
\end{aligned}$$

The Lagrangian of (60) is

$$\begin{aligned}
&\mathcal{L}(\mathbf{s}_r,\{\mathbf{f}_m\},\{\mathbf{g}_i\},\mathbf{h},\{\boldsymbol{o}_m\},\{\boldsymbol{\varsigma}_i\},\boldsymbol{\pi}) =\\
&\mathbf{s}_r{}^T\mathbf{\Gamma}_r\mathbf{s}_r + \sum_{m=1}^{M}\left(\boldsymbol{o}_m^T(\mathbf{T}_{r,m}\mathbf{s}_r - \mathbf{f}_m) + \tfrac{\rho_1}{2}\|\mathbf{T}_{r,m}\mathbf{s}_r - \mathbf{f}_m\|^2\right) +\\
&\sum_{i=1}^{M_{R,t}L}\left(\boldsymbol{\varsigma}_i^T(\mathbf{B}_{r,i}(\mathbf{s}_r - \mathbf{s}_{r,0}) - \mathbf{g}_i) + \tfrac{\rho_2}{2}\|\mathbf{B}_{r,i}(\mathbf{s}_r - \mathbf{s}_{r,0}) - \mathbf{g}_i\|^2\right)\\
&+\left(\boldsymbol{\pi}^T(\mathbf{s}_r - \mathbf{h}) + \tfrac{\rho_3}{2}\|\mathbf{s}_r - \mathbf{h}\|^2\right),
\end{aligned} \tag{61}$$

the Lagrange multipliers $\{\boldsymbol{o}_m\}_1^M$, $\{\boldsymbol{\varsigma}_i\}_1^{M_{R,t}L}$ and $\boldsymbol{\pi}$ correspond to the (60b), (60c) and (60d) respectively; and the positive parameters ρ_1, ρ_2 and ρ_3 are corresponding penalties. The penalties are chosen based on the eigenvalues of $\mathbf{\Gamma}_r$ [47] (Theorem 4). The procedure of ADMM method is given as:

$$\mathbf{s}_r^{(k_1+1)} = \arg\min_{\mathbf{s}_r} \mathcal{L}\left(\mathbf{s}_r, \mathbf{f}_m^{(k_1)}, \ldots, \boldsymbol{\varsigma}_i^{(k_1)}\right), \tag{62a}$$

$$\mathbf{f}_m^{(k_1+1)} = \arg\min_{\mathbf{f}_m} \mathcal{L}\left(\mathbf{s}_r^{(k_1+1)}, \mathbf{f}_m, \mathbf{g}_i^{(k_1)}, \ldots, \boldsymbol{\varsigma}_i^{(k_1)}\right), \tag{62b}$$

$$\mathbf{g}_i^{(k_1+1)} = \arg\min_{\mathbf{g}_i} \mathcal{L}\left(\mathbf{s}_r^{(k_1+1)}, \mathbf{f}_m^{(k_1+1)}, \mathbf{g}_i, \boldsymbol{o}^{(k_1)}, \ldots, \boldsymbol{\varsigma}_i^{(k_1)}\right), \tag{62c}$$

$$\mathbf{h}_i^{(k_1+1)} = \arg\min_{\mathbf{h}} \mathcal{L}\left(\mathbf{s}_r^{(k_1+1)}, \ldots, \mathbf{h}_i, \boldsymbol{o}^{(k_1)}, \boldsymbol{\pi}_i^{(k_1)}, \boldsymbol{\varsigma}_i^{(k_1)}\right), \tag{62d}$$

$$\boldsymbol{o}_m^{(k_1+1)} = \boldsymbol{o}_m^{(k_1)} + \rho_1\left(\mathbf{T}_{r,m}\mathbf{s}_r^{(k_1+1)} - \mathbf{f}_m^{(k_1+1)}\right), \tag{62e}$$

$$\boldsymbol{\varsigma}_i^{(k_1+1)} = \boldsymbol{\varsigma}_i^{(k_1)} + \rho_2\left(\mathbf{B}_{r,i}\left(\mathbf{s}_r^{(k_1+1)} - \mathbf{s}_{r,0}\right) - \mathbf{g}_i^{(k_1+1)}\right). \tag{62f}$$

$$\boldsymbol{\pi}^{(k_1+1)} = \boldsymbol{\pi}^{(k_1)} + \rho_3\left(\mathbf{s}_r^{(k_1+1)} - \mathbf{g}^{(k_1+1)}\right). \tag{62g}$$

4.3.3. Update of $\mathbf{s}_r$

The optimization of (62a) can be rewritten as

$$\begin{aligned}
\mathbf{s}_r^{(k_1+1)} = \arg\min_{\mathbf{s}_r} & \mathbf{s}_r^T\mathbf{\Gamma}_r\mathbf{s}_r + \sum_{m=1}^{M}\left(\left(\boldsymbol{o}^{(k_1)}\right)^T\mathbf{T}_{r,m}\mathbf{s}_r + \right.\\
& \left.\tfrac{\rho_1}{2}\left\|\mathbf{T}_{r,m}\mathbf{s}_r - \mathbf{f}_m^{(k_1)}\right\|^2\right) + \sum_{i=1}^{M_{R,t}L}\left(\left(\boldsymbol{\varsigma}_i^{(k_1)}\right)^T\left(\mathbf{B}_{r,i}(\mathbf{s}_r - \mathbf{s}_{r,0})\right.\right.\\
& \left.\left.-\mathbf{g}_i\right) + \tfrac{\rho_2}{2}\|\mathbf{B}_{r,i}(\mathbf{s}_r - \mathbf{s}_{r,0}) - \mathbf{g}_i\|^2\right) + \left(\left(\boldsymbol{\pi}^{(k_1)}\right)^T\mathbf{s}_r\right.\\
& \left.+\tfrac{\rho_3}{2}\left\|\mathbf{s}_r - \mathbf{h}^{(k_1)}\right\|^2\right).
\end{aligned} \tag{63}$$

The first order optimality conditions for (63) are

$$\begin{aligned}\mathbf{0}_{M_{R,t}L} =& 2\boldsymbol{\Gamma}_r\mathbf{s}_r + \sum_{m=1}^{M}\left(\mathbf{T}_{r,m}^T\mathbf{o}_m^{(k_1)} + \rho_1\mathbf{T}_{r,m}^T\left(\mathbf{T}_{r,m}\mathbf{s}_r - \mathbf{f}^{(k_1)}\right)\right)\\ &+ \sum_{i=1}^{M_{R,t}L}\left(\mathbf{B}_{r,i}^T\boldsymbol{\varsigma}_i^{(k_1)} + \rho_2\mathbf{B}_{r,i}^T((\mathbf{B}_{r,i}\mathbf{s}_r - \mathbf{s}_{r,0}) - \mathbf{g}_i)\right)\\ &+ \left(\boldsymbol{\pi}^{(k_1)} + \rho_3\left(\mathbf{s}_r - \mathbf{h}^{(k_1)}\right)\right),\end{aligned} \tag{64}$$

where $\mathbf{0}_a$ signifies a column vector of a-dimensional with all-zero entries, leading to

$$\begin{aligned}\mathbf{s}_r^{(k_1+1)} =& \left(2\boldsymbol{\Gamma}_r + \rho_1\sum_{m=1}^{M}\mathbf{T}_{r,m}^T\mathbf{T}_{r,m} + \rho_2\sum_{i=1}^{M_{R,t}L}\mathbf{B}_{r,i}^T\mathbf{B}_{r,i} + \rho_3\mathbf{I}\right)^{-1}\\ &\left(\rho_1\sum_{m=1}^{M}\mathbf{T}_{r,m}^T\mathbf{f}_m^{(k_1)} + \rho_2\sum_{i=1}^{M_{R,t}L}\mathbf{B}_{r,i}^T\left(\mathbf{s}_{r,0} + \mathbf{g}_i^{(k_1)}\right) + \rho_3\mathbf{h}^{(k_1)}\right.\\ &\left. - \sum_{m=1}^{M}\mathbf{T}_{r,m}^T\mathbf{o}_m^{(k_1)} - \sum_{i=1}^{M_{R,t}L}\mathbf{B}_{r,i}^T\boldsymbol{\varsigma}_i^{(k_1)} - \boldsymbol{\pi}^{(k_1)}\right).\end{aligned} \tag{65}$$

4.3.4. Update of $\mathbf{f}_m$

The optimization of (62b) can be rewritten as

$$\begin{aligned}\min_{\{\mathbf{f}_m\}}\quad & -\left(\mathbf{o}_m^{(k_1)}\right)^T\mathbf{f}_m + \tfrac{\rho_1}{2}\|\mathbf{T}_{r,m}\mathbf{s}_r - \mathbf{f}_m\|^2\\ \text{s.t.}\quad & \|\mathbf{f}_m\|^2 = 1, m = 1, \cdots, M,\end{aligned} \tag{66}$$

whose closed-form solution is

$$\mathbf{f}_m^{(k_1+1)} = \frac{\tilde{\mathbf{f}}_m^{(k_1+1)}}{\left\|\tilde{\mathbf{f}}_m^{(k_1+1)}\right\|}, \tag{67}$$

with $\tilde{\mathbf{f}}_m^{(k_1+1)} = \mathbf{T}_{r,m}\mathbf{s}_r^{(k_1+1)} + \boldsymbol{o}_m^{(k_1)}/\rho_1$.

4.3.5. Update of $\mathbf{g}_i$

Problem (62d) can be rewritten as

$$\begin{aligned}\arg\min_{\{\mathbf{g}_i\}}\quad & -\left(\boldsymbol{\varsigma}^{(k_1)}\right)^T\mathbf{g}_i + \tfrac{\rho_3}{2}\left\|\mathbf{B}_{r,i}\left(\mathbf{s}_r^{(k_1+1)} - \mathbf{s}_{r,0}\right) - \mathbf{g}_\mathbf{i}^{(\mathbf{k_1+1})}\right\|^2\\ \text{s.t.}\quad & \|\mathbf{g}_i\|^2 \le \gamma.\end{aligned} \tag{68}$$

The solution can be achieved via proximal algorithm, i.e.,

$$\mathbf{g}_i^{(k_1+1)} = \begin{cases}\tilde{\mathbf{g}}_i^{(l_2+1)}, & \text{if } \left\|\tilde{\mathbf{g}}_i^{(k_1+1)}\right\| \le \sqrt{\gamma}\\ \frac{\sqrt{\gamma}}{\left\|\tilde{\mathbf{g}}_i^{(k_1+1)}\right\|}\tilde{\mathbf{g}}_i^{(k_1+1)}, & \text{otherwise,}\end{cases} \tag{69}$$

with $\tilde{\mathbf{g}}_i^{(k_1+1)} = \mathbf{B}_{r,i}\left(\mathbf{s}_r^{(k_1+1)} - \mathbf{s}_{r,0}\right) + \boldsymbol{\varsigma}^{(k_1)}\Big/\rho_3$.

4.3.6. Update of $\mathbf{h}$

The optimization of (62c) can be rewritten as

$$\begin{aligned}\arg\min_{\mathbf{h}}\quad & -\left(\boldsymbol{\pi}^{(k_1)}\right)^T\mathbf{h} + \tfrac{\rho_3}{2}\left\|\mathbf{s}_r^{(k_1+1)} - \mathbf{h}\right\|^2\\ \text{s.t.}\quad & \|\mathbf{h}\|^2 = 1,\end{aligned} \tag{70}$$

the solution is given as

$$\mathbf{h}^{(k_1+1)} = \frac{\tilde{\mathbf{h}}^{(k_1+1)}}{\left\|\tilde{\mathbf{h}}^{(k_1+1)}\right\|}, \tag{71}$$

with $\tilde{\mathbf{h}}^{(k_1+1)} = \mathbf{s}_r^{(k_1+1)} + \boldsymbol{\pi}^{(k_1)}/\rho_3$.

As to the computational complexity for the developed formulation, the $\mathbf{X}$ can be optimized by using WF with $\mathcal{O}(M_{C,t}L)^3$. The optimized $\mathbf{w}_m$ can be obtained based on (39) with complexity $\mathcal{O}\left((M_{R,r}L)^3\right)$. The complexity of $\mathbf{s}_r$ is $\mathcal{O}\Big((M_{R,t}L)^3\Big)$ at each iteration due to the matrix inverse; the other variables requires the computational complexity linearly with $M_{R,t}L$ [48]. Finally, Algorithm 1 summarizes the overall technique of the alternating approach. Notice that the above ADMM method which directly handles the transformed non-convex problem may not always ensure the convergence theoretically. Suitable initializations and penalty parameters are necessary to ensure convergence. Hence, the penalties are chosen based on the eigenvalues of $\boldsymbol{\Gamma}_r$ in (60) and the initialization of $\mathbf{s}$ is set to be $\mathbf{s}_0$ [47] (Theorem 4).

In such monostatic radar and communication spectral coexistence system on moving platform, the cooperation is coordinated by the control center. The information from radar and communication systems is collected by the control center. However, such information will be aging or not usable due to time lag between the channel estimation phase / optimization phase and deployment phase. In order to improve the real-time performance, we will try to improve the hardware of each subsystem to enhance its own computing power, and cancel the control center in the future work. That is, the radar and communication systems calculate their own optimal signaling scheme through the collected information [49].

Algorithm 1 Procedure for $\mathbf{X}$, $\mathbf{w}_m$ and $\mathbf{s}$ Optimization

Input: $\mathbf{w}_0 = \frac{1}{\sqrt{L}}\mathbf{I}_L \otimes \mathbf{a}_r^*(\theta_0)$, $\mathbf{s}_0 = \frac{1}{\sqrt{L}}\mathbf{I}_L \otimes \mathbf{a}_t^*(\theta_0)$, w_1, $\mathbf{H}$, $\mathbf{B}_1$, $\mathbf{B}_2$.
Initialize: Let $k_1 = k_2 = 0$, $\mathbf{w}^{(k_2)} = \mathbf{w}_0$, $\mathbf{s}^{(k_2)} = \mathbf{s}_0$, $\lambda_1 \geq 0$, $\lambda_2 \geq 0$;
Output: $\mathbf{X}^{(k_2+1)}$, $\mathbf{w}^{(k_2+1)}$, $\mathbf{s}^{(k_2+1)}$.

Repeat
  Set $k_2 \leftarrow k_2 + 1$;
  Compute $\mathbf{X}^{(k_2)}$ via (37), with $\mathbf{w} = \mathbf{w}^{(k_2-1)}$ and $\mathbf{s} = \mathbf{s}^{(k_2-1)}$ respectively;
  Compute $\mathbf{w}^{(k_2)}$ via (39) with $\mathbf{X} = \mathbf{X}^{(k_2)}$ and $\mathbf{s} = \mathbf{s}^{(k_2)}$, respectively;
  Set $k_0 = 1$;
  Compute $\boldsymbol{\Gamma}^{(k_0)} = \frac{w_1}{|F_1^*|}\bar{\boldsymbol{\Sigma}}_{\mathbf{s}}(\mathbf{W}_m) + \frac{w_2}{|F_2^*|}\boldsymbol{\Gamma}_{12}$ in (56);
While $\left|\mathbf{s}^H\boldsymbol{\Gamma}^{(k_0+1)}\mathbf{s} - \mathbf{s}^H\boldsymbol{\Gamma}^{(k_0)}\mathbf{s}\right|$ is small than a threshold **do**
Repeat
  Set $k_1 \leftarrow k_1 + 1$;
  Calculate $\mathbf{s}_r^{(k_1+1)}$ by (65);
  Calculate $\mathbf{f}^{(k_1+1)}$ by (69);
  Calculate $\mathbf{g}_i^{(k_1+1)}$ by (71), for all $i = 1, \cdots M_{R,t}L$;
  Calculate $\boldsymbol{o}^{(k_1+1)}$ and $\boldsymbol{\pi}_i^{(k_1+1)}$, for all $i = 1, \cdots M_{R,t}L$, using (62e) and (62g), respectively;
Until the convergence of ADMM is reached;
  $\mathbf{s}^{(k_0)} \leftarrow \mathbf{s}^{(k_1+1)}$;
  Set $k_0 \leftarrow k_0 + 1$;
end
  $\mathbf{s}^{(k_2)} \leftarrow \mathbf{s}^{(k_0+1)}$;
Until the change of the objective function in (27) is small than a threshold.

5. Results and Discussion

In simulations, the radar has $M_{R,t} = 6$ transmit antennas and $M_{R,r} = 6$ receive antennas, and the communication has $M_{C,t} = 3$ transmit antennas and $M_{C,r} = 3$ receiver antennas. We set $\tilde{L} = 6$ as the code length. The noise variance of coexistence system is $\sigma_R^2 = \sigma_C^2 = 0.001$. We set $E_C = 1$ for energy constraint of communication system. And with zero mean and unit variance, $\mathbf{H}$ uses the Rayleigh fading channel.

As to the considered coexistence system, e.g., as shown in Figure 1, the vehicles in an intelligent transportation system that needs to share information in a rapidly changing environment, and the radar requires a wide Doppler range to detect fast vehicles and slow pedestrians. Thus, some other parameters can be given as follows. For the radar, the directions of two targets are located at -10° and 10°, respectively, with normalized Doppler frequencies 0.2 and -0.3, respectively. The clutters are evenly distributed in $\left[-\frac{\pi}{2}, \frac{\pi}{2}\right]$ with a discrete azimuth of 90 in each ring. Similarly, for all clutters, we consider $r_j = 0$ and $\varepsilon_j = 0.04$. For the mutual interference $P = Q = 10$ between two systems. We assumed that the azimuth of $\mathbf{B}_1$ is distributed in $[-40^\circ, -20^\circ]$, $\{f_{d,q}\} \in [0.2, 0.35]$, $\{r_c' = 0\}$ and $\mathrm{INR_R} = 15\mathrm{dB}$. As to $\mathbf{B}_2$, we assume that angle parameters are randomly distributed in $[20^\circ, 30^\circ]$ with the associated Doppler shift of $\{f_{d,p}\} \in [-0.35, -0.2]$ and $\mathrm{INR_C} = 25\mathrm{dB}$. Except where otherwise noted, the uncertainties on the direction information are set as $\varpi_m = \varpi_j = \varpi_p = \varpi_q = 3^\circ$. The similarity parameter is set as $\gamma = 0.1$. The radar reference waveform $\mathbf{s}_0$ is exploited with Linear Frequency Modulation. The penalty parameters are set as $\rho_1 = \rho_2 = \rho_3 = 1$. We set $\omega_1 = \omega_2 = 0.5$.

Firstly, we evaluate the convergence behavior of the proposed design versus γ. In Figure 2, the objective value under different outer iteration numbers is investigated. It can be shown that the proposed design converges for all values of the similarity parameter γ that are taken into consideration, and $\gamma = 1.8$ provides the best performance, which is reasonable because the larger similarity parameter γ could provide additional DoFs in procedure.

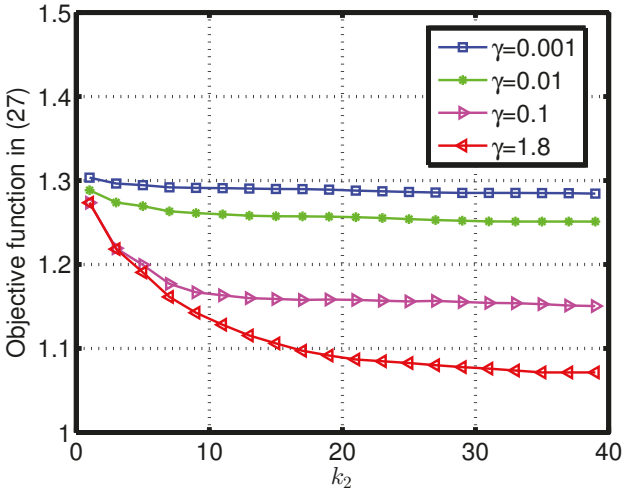

Figure 2. The objective value with outer iteration number under different similarity parameter γ.

In Figure 3, the constraint convergence in $\mathbf{s}$ optimization is examined. The residuals for auxiliary variables are defined as follows in the ADMM procedure:

$$
\begin{aligned}
d_{f_{max}} &= \max_{m=1,\cdots,M} \left\| \mathbf{T}_{r,m}\mathbf{s}_r^{(k_1)} - \mathbf{f}^{(k_1)} \right\|, \\
d_{g_{max}} &= \max_{i=1,\cdots,M_{R,t}L} \left\| \mathbf{B}_{r,i}\mathbf{s}_\mathbf{r}^{(\mathbf{k_1})} - \mathbf{s}_{\mathbf{r,0}} - \mathbf{g}_\mathbf{i}^{(\mathbf{k_1})} \right\|, \\
d_h &= \left\| \mathbf{s}_r^{(k_1)} - \mathbf{h}^{(k_1)} \right\|.
\end{aligned} \tag{72}
$$

As to better illustrate the constraint convergence in $\mathbf{s}$ optimization, we set the termination tolerances in (72) as 10^{-5} [50]. Figure 3 reports the residuals of the constraints from (60b) to (60d) versus k_1 of ADMM. It can be shown that the stopping criterion is satisfied for all considered constraints.

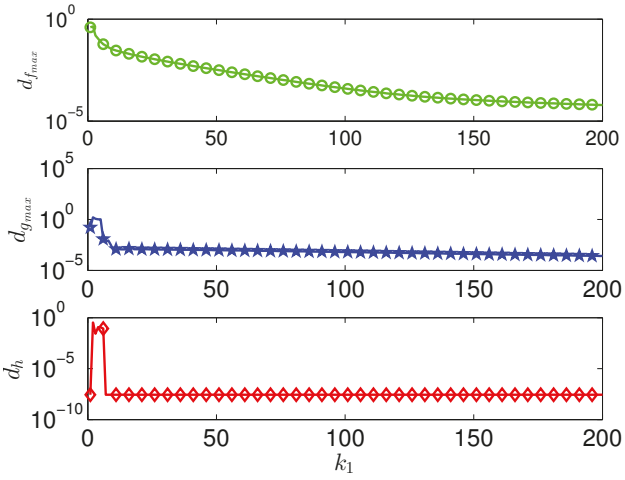

Figure 3. The residuals of (60b) to (60d) vs the k_1 of Algorithm 1.

Figure 4 shows the radar cross-ambiguity function's (CAF) [46] about the radar target response for outer iteration number $k_0 = \{10, 40\}$. It can be observed that the main lobes are at the target location, null is at the communication interference location, and the clutter ridge is dispersed diagonally. Furthermore, it can be demonstrated that the value drops as the number of iterations increases in the interference region including clutter and the interference from communication system. This trend highlights that Algorithm 1 is able to suitably shape the CAF for interference suppression within small iterations, i.e., the proposed design provides fast convergence properties.

The performance of the developed design is next examined in relation to various mutual interference strengths with $\mathrm{INR}_R = \mathrm{INR}_C$. As a benchmark, we also consider the objective values obtained by exploiting different algorithms: the Semi-Definite Programming (SDP) and randomization procedure (labeled as "Joint Design with SDP-R") for $\mathbf{s}$ optimization [51], the transmit design for $\mathbf{X}$ and $\mathbf{s}$ optimization (labeled as "Transmit Optimized"), as well as the disjoint design, namely, no mutual interference management (labeled as "Uncooperative Optimized"). Figure 5 expresses the objective value in terms of $\mathrm{INR}_R = \mathrm{INR}_C$ for various levels of mutual interference channel. We can see that the objective value grows as the INR increases; the proposed joint design provides the best performance. The primary reason is that more DoFs can be achieved in the coexistence system, which also implies the necessity of the joint design for spectrum sharing system in practical applications. Correspondingly, Figures 6 and 7 express the radar SINR and communication rate in terms of $\mathrm{INR}_R = \mathrm{INR}_C$ for various levels of mutual interference channel. It can be shown that the two system performance degrade with the mutual increasing. It is interesting to notice that, for the uncooperative optimized design, the communication rate is better than the joint solution, the main reason is that the weighted design can adjust

the priority of the two systems, and in this scenario, the better radar performance can be achieved as shown in Figure 6.

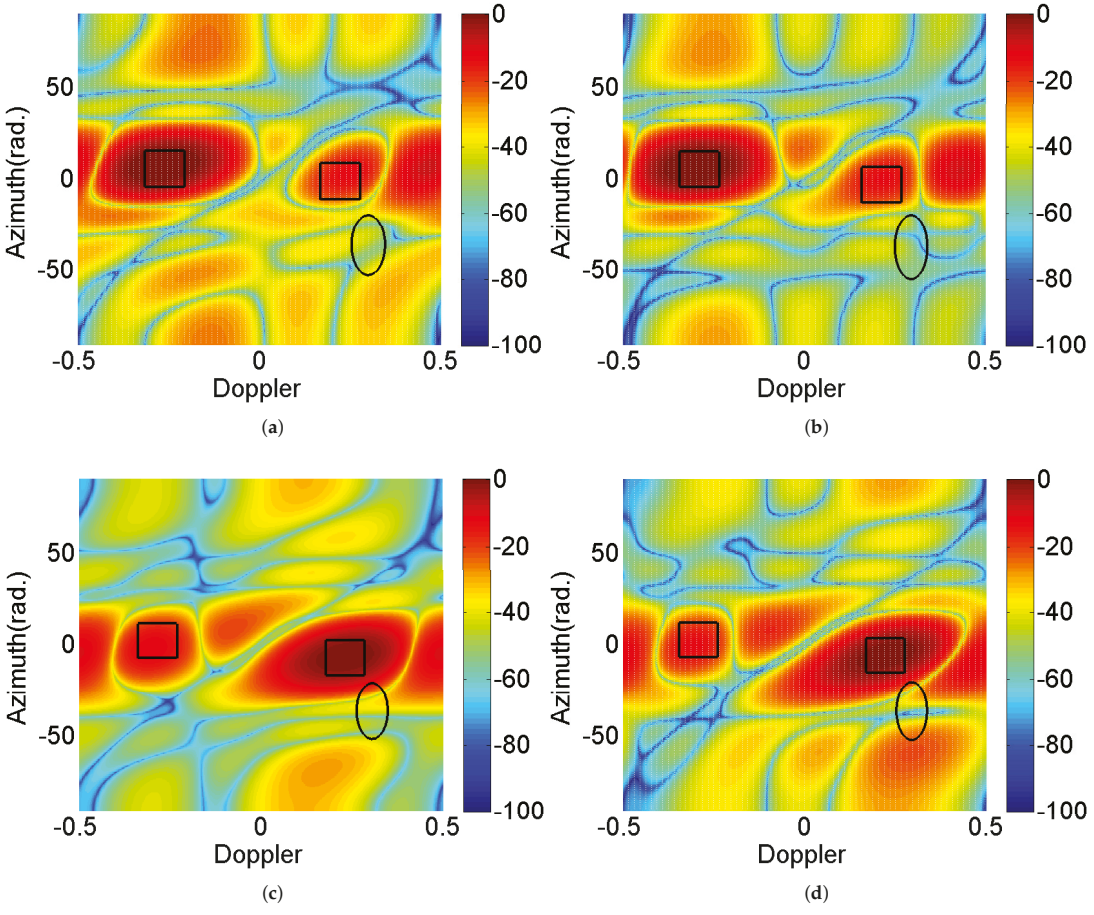

Figure 4. Doppler-azimuth plane of CAF of radar multi-targets for outer iteration number $k_2 = \{10, 40\}$: **(a)** $\mathbf{w}_1^*$ and $\mathbf{s}^*$, $k_2 = 10$, **(b)** $\mathbf{w}_1^*$ and $\mathbf{s}^*$, $k_2 = 40$, **(c)** $\mathbf{w}_2^*$ and $\mathbf{s}^*$, $k_2 = 10$, **(d)** $\mathbf{w}_2^*$ and $\mathbf{s}^*$, $k_2 = 40$ (solid line rectangles and ellipse respectively denote the locations of the radar targets, the interference sources from communication system).

Moreover, Figure 8 depicts the Doppler-azimuth plane of radar CAF. In the scenario, the number of radar target is set as one and the target is located at 10° with $f_{d,m} = -0.3$, the other parameters remain the same as Figure 4. For comparison, the concept of radar SINR optimization with communication rate constraint is used (see e.g., [46,52]). The communication rate is required to be greater than 4. It can be demonstrated that both systems have strong convergence qualities. Additionally, it can be noticed that the proposed design has more prominent peak values for the radar target and lower values at the clutter ridge and communication interference ranges, implying that the proposed formulation performs better. In effect, the formulation of radar optimization with communication constraint would lead to performance degradation due to the shrinkage operation for the set of lower bound of communication rate.

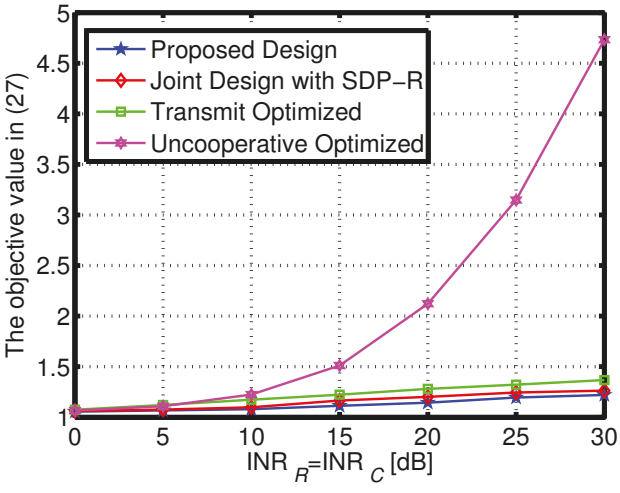

Figure 5. The objective value under different $\mathrm{INR}_R = \mathrm{INR}_C$ of mutual interference.

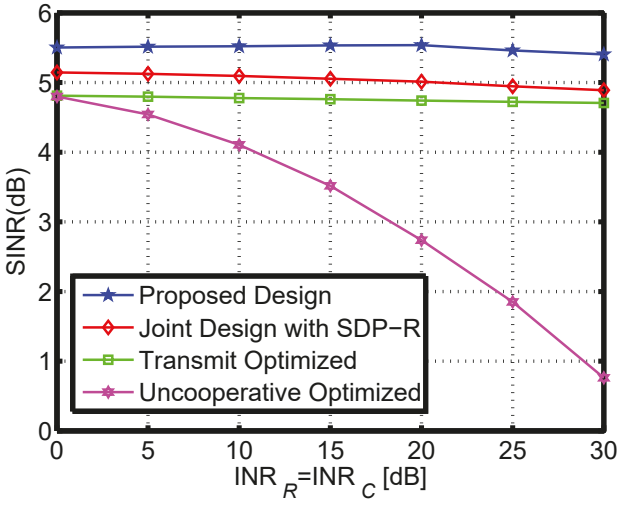

Figure 6. The radar SINR under different $\mathrm{INR}_R = \mathrm{INR}_C$ of mutual interference.

To further investigate the system performance in the environment of dynamic variation, the sensitiveness of the previous strategies is examined. In particular, assume that the estimated channel matrices are $\hat{\mathbf{B}}_1 = \mathbf{B}_1 + \Delta\mathbf{B}_1$ and $\hat{\mathbf{B}}_2 = \mathbf{B}_2 + \Delta\mathbf{B}_2$, where $\Delta\mathbf{B}_1 = e_1^2 \parallel \mathbf{B}_1 \parallel_F^2$ and $\Delta\mathbf{B}_2 = e_1^2 \parallel \mathbf{B}_2 \parallel_F^2$ denote the channel estimation error matrices. In this exemplification study, e_1^2 is set to be 0.1. The other parameters remain unchanged. Figure 9 shows the objective value under different $\mathrm{INR}_R = \mathrm{INR}_C$ of mutual interference for channel mismatch. Combing the results in Figure 5, some degradations are observed, but the proposed design still effectively mitigates both the clutter and the mutual interference.

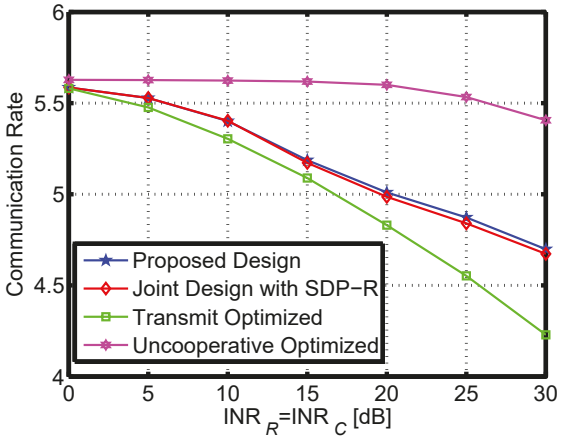

Figure 7. The communication rate under different $\mathrm{INR}_R = \mathrm{INR}_C$ of mutual interference.

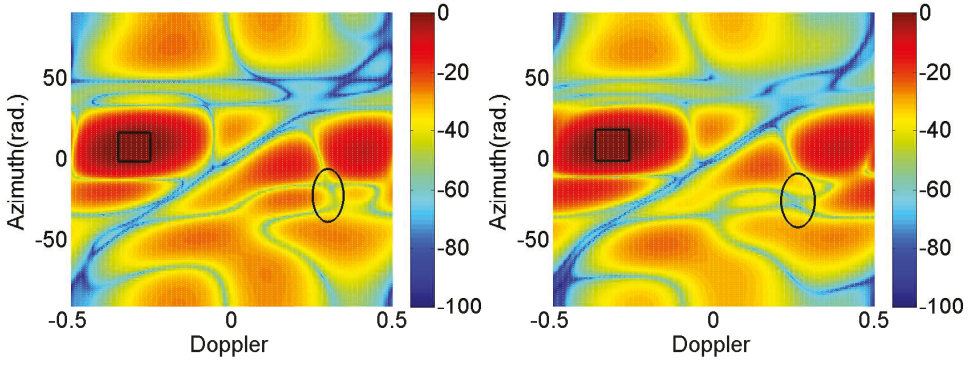

(**a**) (**b**)

Figure 8. Doppler-azimuth plane of CAF for iteration number $k_2 = \{10, 50\}$ for different formulations.

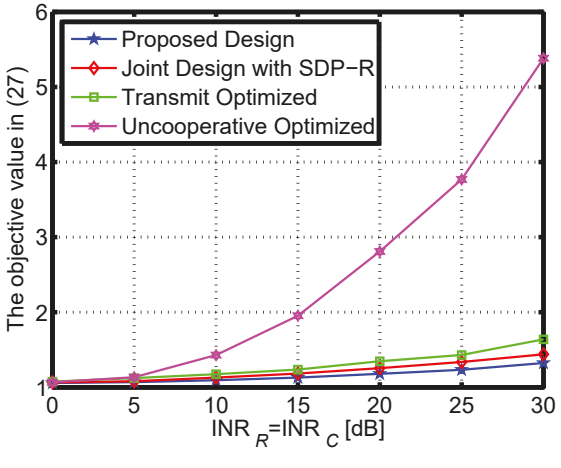

Figure 9. The objective value under different $\mathrm{INR}_R = \mathrm{INR}_C$ of mutual interference for channel mismatch.

6. Conclusions

In this paper, we aim to jointly design the radar spatial-temporal transceiver and the communication spatial-temporal codebook in the spectrum coexistence system on moving platforms. Owing to the non-convexity of the original formulated problem, an alternate scheme is developed to optimize the designed DoFs based on the dual algorithm, the MVDR method and MM-ADMM. Analytical proofs have been provided for the algorithms' convergences. Finally, the simulation results are shown to verify the performance of the proposed algorithm.

Author Contributions: Conceptualization, J.Q. and Z.L.; methodology, J.Q. and L.Z.; writing—original draft and formal analysis, Y.L., A.Z. and F.H.; writing—review and editing, Z.L. and Y.L. All authors have read and agreed to the published version of the manuscript.

Funding: This work was supported in part by the National Key R&D Program of China (Grant No. 2018YFE0202101, 2018YFE0202103), in part by the National Natural Science Foundation of China under Grants 62001064 and 62201388, and in part by the Chongqing Science and Technology Commission under Grant cstc2020jcyjmsxmX0705.

Data Availability Statement: Not applicable.

Acknowledgments: The authors would like to thank the reviewers and editor for their valuable comments and suggestions.

Conflicts of Interest: The authors declare no conflict of interest.

References

1. De Matthaeis, P.; Oliva, R.; Soldo, Y.; Cruz-Pol, S. Spectrum Management and Its Importance for Microwave Remote Sensing [Technical Committees]. *IEEE Geosci. Remote Sens. Mag.* **2018**, *6*, 17–25. [CrossRef]
2. Zheng, L.; Lops, M.; Eldar, Y.C.; Wang, X. Radar and communication coexistence: An overview: A review of recent methods. *IEEE Signal Process. Mag.* **2019**, *36*, 85–99. [CrossRef]
3. Yang, J.; Aubry, A.; Maio, A.D.; Yu, X.; Cui, G. Design of Constant Modulus Discrete Phase Radar Waveforms Subject to Multi-Spectral Constraints. *IEEE Signal Process. Lett.* **2020**, *27*, 875–879. [CrossRef]
4. Hassanien, A.; Amin, M.G.; Aboutanios, E.; Himed, B. Dual-function radar communication systems: A solution to the spectrum congestion problem. *IEEE Signal Process. Mag.* **2019**, *36*, 115–126. [CrossRef]
5. Mishra, K.V.; Shankar, M.B.; Koivunen, V.; Ottersten, B.; Vorobyov, S.A. Toward millimeter-wave joint radar communications: A signal processing perspective. *IEEE Signal Process. Mag.* **2019**, *36*, 100–114. [CrossRef]
6. Qian, J.; Venturino, L.; Lops, M.; Wang, X. Radar and Communication Spectral Coexistence in Range-Dependent Interference. *IEEE Trans. Signal Process.* **2021**, *69*, 5891–5906. [CrossRef]
7. Wu, W.; Han, G.; Cao, Y.; Huang, Y.; Yeo, T.S. MIMO Waveform Design for Dual Functions of Radar and Communication With Space-Time Coding. *IEEE J. Sel. Areas Commun.* **2022**, *40*, 1906–1917. [CrossRef]
8. Kafafy, M.; Ibrahim, A.S.; Ismail, M.H. Optimal Placement of Reconfigurable Intelligent Surfaces for Spectrum Coexistence With Radars. *IEEE Trans. Veh. Technol.* **2022**, *71*, 6574–6585. [CrossRef]
9. Fang, Z.; Wang, W.; Wang, J.; Liu, B.; Tang, K.; Lou, L.; Heng, C.H.; Wang, C.; Zheng, Y. Integrated Wideband Chip-Scale RF Transceivers for Radar Sensing and UWB Communications: A Survey. *IEEE Circuits Syst. Mag.* **2022**, *22*, 40–76. [CrossRef]
10. Hassanien, A.; Amin, M.G.; Aboutanios, E.; Himed, B. Cognitive radar waveform design and prototype for coexistence with communications. *IEEE Sens. J.* **2022**, *22*, 9787–9802.
11. Cohen, D.; Mishra, K.V.; Eldar, Y.C. Spectrum Sharing Radar: Coexistence via Xampling. *IEEE Trans. Aerosp. Electron. Syst.* **2018**, *54*, 1279–1296. [CrossRef]
12. Qian, J.; Wang, S.; Chen, Z.; Qian, G.; Fu, N. Robust Design for Spectral Sharing System Based on MI Maximization Under Direction Mismatch. *IEEE Trans. Veh. Technol.* **2022**, *71*, 6831–6836. [CrossRef]
13. Marler, R.T.; Arora, J.S. The weighted sum method for multi-objective optimization: New insights. *Struct. Multidiscipl. Optim.* **2010**, *41*, 853–862. [CrossRef]
14. Hao, Y.; Ni, Q.; Li, H.; Hou, S. On the energy and spectral efficiency tradeoff in massive MIMO-enabled HetNets with capacity-constrained backhaul links. *IEEE Trans. Commun.* **2017**, *65*, 4720–4733. [CrossRef]
15. Cheng, Z.; Han, C.; Liao, B.; He, Z.; Li, J. Communication-aware waveform design for mimo radar with good transmit beampattern. *IEEE Trans. Signal Process.* **2018**, *66*, 5549–5562. [CrossRef]
16. Chen, N.; Wei, P.; Gao, L.; Zhang, H. Beampattern synthesis and spectral compatibility based mimo radar waveform design. *Digit. Signal Process.* **2021**, *118*, 103211. [CrossRef]
17. He, Q.; Wang, Z.; Hu, J.; Blum, R.S. Performance Gains From Cooperative MIMO Radar and MIMO Communication Systems. *IEEE Signal Process. Lett.* **2019**, *26*, 194–198. [CrossRef]

18. Li, Z.; Shi, J.; Liu, W.; Pan, J.; Li, B. Robust Joint Design of Transmit Waveform and Receive Filter for MIMO-STAP Radar Under Target and Clutter Uncertainties. *IEEE Trans. Veh. Technol.* **2022**, *71*, 1156–1171. [CrossRef]
19. Khawar, A.; Abdel-Hadi, A.; Clancy, T.C. Spectrum sharing between S-band radar and LTE cellular system: A spatial approach. In Proceedings of the 2014 IEEE International Symposium on Dynamic Spectrum Access Networks (DYSPAN), McLean, VA, USA, 1–4 April 2014; pp. 7–14.
20. Shahriar, C.; Abdelhadi, A.; Clancy, T.C. Overlapped-MIMO radar waveform design for coexistence with communication systems. In Proceedings of the 2015 IEEE Wireless Communications and Networking Conference (WCNC), New Orleans, LA, USA, 9–12 March 2015; pp. 223–228.
21. Bo, L.; Petropulu, A.P.; Trappe, W. Optimum Co-Design for Spectrum Sharing between Matrix Completion Based MIMO Radars and a MIMO Communication System. *IEEE Trans. Signal Process.* **2016**, *64*, 4562–4575.
22. Qian, J.; Liu, Z.; Wang, K.; Fu, N.; Wang, J. Transmission Design for Radar and Communication Spectrum Sharing Enhancement. *IEEE Trans. Veh. Technol.* **2022**. [CrossRef]
23. Qian, J.; He, Z.; Huang, N.; Li, B. Transmit Designs for Spectral Coexistence of MIMO Radar and MIMO Communication System. *IEEE Trans. Circuits Syst. II Express Briefs* **2018**, *65*, 2072–2076. [CrossRef]
24. Chen, P.; Zheng, L.; Wang, X.; Li, H.; Wu, L. Moving Target Detection Using Colocated MIMO Radar on Multiple Distributed Moving Platforms. *IEEE Trans. Signal Process.* **2017**, *65*, 4670–4683. [CrossRef]
25. Bilik, I.; Longman, O.; Villeval, S.; Tabrikian, J. The Rise of Radar for Autonomous Vehicles: Signal Processing Solutions and Future Research Directions. *IEEE Signal Process. Mag.* **2019**, *36*, 20–31. [CrossRef]
26. Wang, J. CFAR-Based Interference Mitigation for FMCW Automotive Radar Systems. *IEEE Trans. Intell. Transp. Syst.* **2022**, *23*, 12229–12238. [CrossRef]
27. Xu, Z.; Yuan, M. An Interference Mitigation Technique for Automotive Millimeter Wave Radars in the Tunable Q-Factor Wavelet Transform Domain. *IEEE Trans. Microw. Theory Tech.* **2021**, *69*, 5270–5283. [CrossRef]
28. Brooker.; G., M. Mutual Interference of Millimeter-Wave Radar Systems. *IEEE Trans. Electromagn. Compat.* **2007**, *49*, 170–181. [CrossRef]
29. Goppelt, M.; BlöCher, H.L.; Menzel, W. Automotive radar-investigation of mutual interference mechanisms. *Adv. Radio Sci.* **2010**, *8*, 55–60. [CrossRef]
30. Liu, F.; Cui, Y.; Masouros, C.; Xu, J.; Han, T.X.; Eldar, Y.C.; Buzzi, S. Integrated Sensing and Communications: Toward Dual-Functional Wireless Networks for 6G and Beyond. *IEEE J. Sel. Areas Commun.* **2022**, *40*, 1728–1767. [CrossRef]
31. Garcia, N.; Haimovich, A.M.; Lops, M.; Lops, M. Resource Allocation in MIMO Radar With Multiple Targets for Non-Coherent Localization. *IEEE Trans. Signal Process.* **2014**, *62*, 2656–2666. [CrossRef]
32. Yu, X.; Alhujaili, K.; Cui, G.; Monga, V. MIMO Radar Waveform Design in the Presence of Multiple Targets and Practical Constraints. *IEEE Trans. Signal Process.* **2020**, *68*, 1974–1989. [CrossRef]
33. Xu, Z.; Xue, S.; Wang, Y. Incoherent Interference Detection and Mitigation for Millimeter-Wave FMCW Radars. *Remote Sens.* **2022**, *14*, 4817. [CrossRef]
34. Wang, J.; Aubry, P.; Yarovoy, A. 3-D Short-Range Imaging With Irregular MIMO Arrays Using NUFFT-Based Range Migration Algorithm. *IEEE Trans. Geosci. Remote Sens.* **2020**, *58*, 4730–4742. [CrossRef]
35. Zhang, R.; Liang, Y.C.; Cui, S. Dynamic resource allocation in cognitive radio networks. *IEEE Signal Process. Mag.* **2010**, *27*, 102–114. [CrossRef]
36. Karbasi, S.M.; Aubry, A.; Carotenuto, V.; Naghsh, M.M.; Bastani, M.H. Knowledge-based design of space-time transmit code and receive filter for a multiple-input-multiple-output radar in signal-dependent interference. *IET Radar Sonar Navig.* **2015**, *9*, 1124–1135. [CrossRef]
37. Aubry, A.; DeMaio, A.; Farina, A.; Wicks, M. Knowledge-Aided (Potentially Cognitive) Transmit Signal and Receive Filter Design in Signal-Dependent Clutter. *IEEE Trans. Aerosp. Electron. Syst.* **2013**, *49*, 93–117. [CrossRef]
38. Gini, F.; Maio, A.D.; Patton, L. *Waveform Design and Diversity for Advanced Radar Systems*; The Institution of Engineering and Technology: London, UK, 2012.
39. Zeng, Y.; Zhang, R. Millimeter Wave MIMO With Lens Antenna Array: A New Path Division Multiplexing Paradigm. *IEEE Trans. Commun.* **2015**, *64*, 1557–1571. [CrossRef]
40. Zhang, X.; Li, H.; Liu, J.; Himed, B. Joint delay and doppler estimation for passive sensing with direct-path interference. *IEEE Trans. Signal Process.* **2016**, *64*, 630–640. [CrossRef]
41. Filo, M.; Hossain, A.; Biswas, A.R.; Piesiewicz, R. Cognitive pilot channel: Enabler for radio systems coexistence. In Proceedings of the 2009 Second International Workshop on Cognitive Radio and Advanced Spectrum Management, Aalborg, Denmark, 18–20 May 2009, pp. 17–23.
42. Gottumukkala, V.K.V.; Minn, H. Capacity Analysis and Pilot-Data Power Allocation for MIMO-OFDM With Transmitter and Receiver IQ Imbalances and Residual Carrier Frequency Offset. *IEEE Trans. Veh. Technol.* **2012**, *61*, 553–565. [CrossRef]
43. Maio, A.D.; Nicola, S.D.; Huang, Y.; Luo, Z.Q. Design of Phase Codes for Radar Performance Optimization With a Similarity Constraint. *IEEE Trans. Signal Process.* **2009**, *57*, 610–621. [CrossRef]
44. Trees, H.L.V. *Optimum Array Processing, Part IV of Detection, Estimation, and Modulation Theory*; Wiley: Hoboken, NJ, USA, 2002.
45. Boyd, S.; Vandenberghe, L. *Convex Optimization*; Cambridge University Press: Cambridge, UK, 2004.

46. Qian, J.; Lops, M.; Zheng, L.; Wang, X.; He, Z. Joint System Design for Co-existence of MIMO Radar and MIMO Communication. *IEEE Trans. Signal Process.* **2018**, *66*, 3504–3519. [CrossRef]
47. Ghadimi, E.; Teixeira, A.; Shames, I.; Johansson, M. Optimal Parameter Selection for the Alternating Direction Method of Multipliers (ADMM): Quadratic Problems. *IEEE Trans. Autom. Control* **2015**, *60*, 644–658. [CrossRef]
48. Yeh, J. *Real Analysis: Theory of Measure and Integration*; World Scientific: Singapore, 2006.
49. Lu, J.; Liu, F.; Sun, J.; Liu, Q.; Miao, Y. Joint Estimation of Target Parameters and System Deviations in MIMO Radar With Widely Separated Antennas on Moving Platforms. *IEEE Trans. Aerosp. Electron. Syst.* **2021**, *57*, 3015–3028. [CrossRef]
50. Boyd, S.; Parikh, N.; Chu, E.; Peleato, B.; Eckstein, J. Distributed optimization and statistical learning via the alternating direction method of multipliers. *Found. Trends® Mach. Learn.* **2011**, *3*, 1–122.
51. Cui, G.; Li, H.; Rangaswamy, M. MIMO Radar Waveform Design With Constant Modulus and Similarity Constraints. *IEEE Trans. Signal Process.* **2014**, *62*, 343–353. [CrossRef]
52. Qian, J.; Lu, M.; Huang, N. Radar and Communication Co-Existence Design Based on Mutual Information Optimization. *IEEE Trans. Circuits Syst. II Express Briefs* **2020**, *67*, 3577–3581. [CrossRef]

remote sensing

MDPI

Article

Joint Radar and Communications Waveform Design Based on Complementary Sequence Sets

Haichuan Li [1], Yongjun Liu [1,*], Guisheng Liao [1] and Yufeng Chen [2]

[1] National Laboratory of Radar Signal Processing, Xidian University, Xi'an 710071, China
[2] Hangzhou Institute of Technology, Xidian University, Hangzhou 311200, China
* Correspondence: yjliu@xidian.edu.cn

Abstract: The joint radar and communications (JRC) waveform often has a high range sidelobe, which will degrade the target detection performance of an automotive JRC system. To solve this problem, a joint radar and communications complementary waveform group (JRC-CWG) design method is proposed in this paper by exploiting the philosophy of the complementary sequence. In the JRC-CWG, the traditional unimodular communications waveforms, such as the binary phase shift keying (BPSK) waveform, are used to perform the communications function. The sum of the autocorrelation function (SACF) of JRC-CWG is optimized to minimize the sidelobe level. Furthermore, considering that the JRC-CWG has poor Doppler resilience, a Doppler-resilient joint radar and communications complementary waveform (DR-JRC-CWG) design method is proposed to improve the Doppler resilience. Finally, the simulation results show that the proposed JRC-CWG and DR-JRC-CWG have superior radar performances without the degradation in communications performance in terms of the bit error rate (BER).

Keywords: joint radar and communications; complementary sequence; joint radar and communications complementary waveform group; Doppler resilience

Citation: Li, H.; Liu, Y.; Liao, G.; Chen, Y. Joint Radar and Communications Waveform Design Based on Complementary Sequence Sets. *Remote Sens.* **2023**, *15*, 645. https://doi.org/10.3390/rs15030645

Academic Editors: Zhihuo Xu, Jianping Wang and Yongwei Zhang

Received: 24 December 2022
Revised: 18 January 2023
Accepted: 19 January 2023
Published: 21 January 2023

1. Introduction

In recent years, with the development of automotive radar and communications technologies, more and more radar and communications systems have been deployed in vehicles [1,2]. For example, in an intelligent transportation system (ITS), both radar and communications devices are integrated in a vehicle [3]. In an ITS, the vehicle needs to convey information to other cars or communications base stations via a communications device and detects targets including other vehicles, pedestrians, and roadblocks via a radar device. However, with the development of the fifth-generation (5G) communications technology and the millimeter-wave radar technology, radar and communications systems tend to use the same frequency bands, which will result in mutual interference between these two systems [4]. Since the space in a vehicle is limited, radar and communications devices have to be deployed close together, which aggravates the interference between radar and communications systems in vehicles [5]. Moreover, with the increasing demand for spectral resources for both radar and communications systems, the shortage of spectral resources becomes more and more serious [6]. To solve these problems, joint radar and communications (JRC) systems are proposed, which can alleviate the interference between radar and communications and improve the efficiency of spectral resources [7].

Usually, JRC systems can be divided into two types [8]. One type is called the co-existence JRC system, wherein radar and communications are regarded as two individuals. The co-existence JRC system aims at minimizing the mutual interference between radar and communications subsystems [9]. The other type is termed the co-use JRC system, in which the transmit waveforms are optimized to simultaneously carry out both radar and communications functions [10] to avoid mutual interference between radar and communications.

In the co-existence JRC system, radar and communications occupy different resources in some domains, such as the time domain, frequency domain [11], spatial domain [12], and so on [5]. For example, in the co-existence JRC system, radar and communications can work in different time slots [13]. The main defect of this approach is that radar and communications cannot operate at the same time. In [14,15], a spectral notching JRC system is proposed with the assumption that the bandwidth of radar is much greater than that of communications. In this system, radar and communications operate in different frequencies, although they can work at the same time. In [16], a JRC system that performs radar and communications functions in different directions is investigated. In this system, the transmit waveforms of each element of the array are optimized to synthesize specific radar or communications waveforms in the desired radar and communications directions.

To design a co-use JRC system, the main challenge is how to make an optimal trade-off between radar and communications functions [13,17,18]. In order to perform the radar function in the mainlobe of the array and convey the communications information in the sidelobe simultaneously, various methods are proposed in [19,20]. In [19], the sidelobe of the transmit beam is devised to transmit communications information at different pulse repetition intervals (PRIs), and the mainlobe of the transmit beam is designed to remain unchanged to guarantee radar performance. As an extension, the method in [19] is used for multi-user scenarios in [20]. The main shortcoming of this kind of JRC system is the low communications rate since only one communication symbol is conveyed in each PRI [19,20].

To increase the communications rate, the traditional communications waveforms are modified to perform both radar and communications functions in [21]. The key to this type of method is to modify the traditional communications waveforms to satisfy radar demands [22]. One typical example is the JRC waveform based on the orthogonal frequency division multiplexing (OFDM) waveform [23–25], which has a considerably high communications rate [26]. However, the OFDM waveform has a nonconstant modulus. In order to detect targets as far as possible, the amplifier of the radar transmitter usually operates in the nonlinear region [27]. However, this will cause serious distortion when the transmit waveform has a nonconstant modulus, and the radar and communications performance will be degraded [28]. In view of this, a JRC waveforms design method based on unimodular waveforms has been studied [29].

Nevertheless, the JRC waveforms proposed in [23–25,29] have high autocorrelation sidelobe levels. In an automotive radar, if the autocorrelation sidelobe level of the transmit waveform is high, the returns from targets with small radar cross sections (RCSs) may be submerged by the sidelobes of targets with large RCSs at receivers [30]. In view of this, to ensure the radar performance of JRC systems, transmit waveforms with low autocorrelation sidelobe levels are required in JRC systems. To design unimodular JRC waveforms with low sidelobe levels, a JRC waveform combining the linear frequency modulation (LFM) waveform and the binary phase-shift keying (BPSK) waveform is proposed in [31,32]. The JRC waveform is obtained by directly multiplying the BSPK waveform with the LFM waveform. For the BPSK in this method, the angular separation between the modulated bits "1" and "0" is set to be $\phi_\delta(\phi_\delta < \pi)$ rather than π as with the traditional BPSK waveforms. Using this method, the designed JRC waveform in [31,32] can achieve a better autocorrelation performance with the degradation in the bit error rate (BER). In [13], based on the traditional unimodular communications waveform, the author designs a JRC waveform by optimizing the phase perturbation in each chip, which is named the optimized phase perturbation (OPP) waveform. To keep the JRC waveform with a low BER, the phase perturbation of each chip of the JRC waveform is constrained by an upper bound.

The aforementioned co-use JRC waveforms are all obtained by using single waveforms. However, the autocorrelation sidelobe of a single waveform cannot be decreased to as low as possible [33]. To further decrease the autocorrelation sidelobe level of JRC waveforms, a feasible way is to exploit the philosophy of the complementary sequence set (CSS) to design co-use JRC waveforms. A CSS contains multiple subsequences. The sum of the autocorrelation function (SACF) of subsequences in the CSS is the Kronecker delta function,

i.e., all sidelobes of the SACF of subsequences are zero [34]. This property makes CSS a promising sequence to be used to design waveforms with low range sidelobe levels, which has been shown in radar applications [35,36]. In our work, the philosophy of the CSS is exploited to design the JRC waveforms.

In this paper, based on CSSs, two co-use JRC waveforms design methods are proposed. At first, unimodular JRC waveforms with low sidelobe levels are devised, which are called the JRC complementary waveform group (JRC-CWG). The devised JRC-CWG has a considerably low sidelobe level as well as good communications performance. Each JRC-CWG contains two kinds of unimodular waveforms. One kind of waveform carry out both radar and communications functions, and are termed waveforms with communications information (WCI). The traditional communications waveforms, such as the BPSK waveforms, are employed as the WCIs. The other kind of waveform in the JRC-CWG are called the waveforms to be optimized (WTO), which are optimized to suppress the sidelobe level of the JRC-CWG. Furthermore, considering that the Doppler resilience of the designed JRC-CWG is poor [37–39], a Doppler-resilient JRC complementary waveform (DR-JRC-CWG) design method is proposed. To design the DR-JRC-CWG, the Doppler sensitivity of the designed JRC-CWG is analyzed first. Specifically, the Taylor expansion terms of the ambiguity function (AF) of the JRC-CWG near the region of zero Doppler shift are derived, and this shows that the nonzero-order Taylor expansion terms will impact the Doppler resilience of JRC-CWG. Hence, the coefficients of the low-order Taylor expansion terms are utilized in the formulated optimization problem to design the DR-JRC-CWG. To solve these optimization problems, an iterative algorithm is proposed based on the framework of the Fletcher–Reeves conjugate gradient (FR-CG) algorithm and the FFT algorithm.

The contributions of our work are summarized as follows:

(1) A new co-use JRC waveform is devised by exploiting the philosophy of the complementary sequence and is called the JRC-CWG.
(2) Compared with the JRC waveforms proposed in [31] and [13], the designed JRC-CWG has a much lower sidelobe level and better communications performance in terms of BER.
(3) A new Doppler resilient waveform design method is proposed to design the DR-JRC-CWG that is not sensitive to Doppler shift caused by the relative radial velocity between the vehicle and target.
(4) An algorithm based on the framework of the FR-CG algorithm and the FFT algorithm is proposed to design the DR-JRC-CWG.

The rest of this paper is organized as follows. In Section 2, the model of JRC-CWG and the signal processing procedure at radar and communications receivers are introduced. In Section 3, the optimization problems for the JRC-CWG and DR-JRC-CWG design are developed and the optimal JRC-CWG and DR-JRC-CWG are devised. In Section 4, several simulation results are presented. Discussions are drawn in Section 5. Finally, a conclusion is made in Section 6.

Notations: Non-bold letters and bold lower-case letters represent scalars and vectors, respectively. Bold capital letters represent matrices. The n-th element of vector $\mathbf{s}$ is represented as $s(n)$, and the k-th row and n-th column entry of matrix $\mathbf{F}$ is represented as $\mathbf{F}(k,n)$. $\mathbf{0}_{K\times N}$ denotes the $K \times N$ matrix of zeros. The N-order identity matrix is denoted by $\mathbf{I}_N$. $(\cdot)^*$, $(\cdot)^T$, and $(\cdot)^H$ stand for conjugate, transpose, and conjugate transpose, respectively. $\|\cdot\|_F$ denotes the Frobenius norm. $\odot$ represents the Hadamard product operator. $|\cdot|$ takes the absolute value of each element of a vector or matrix. $\mathrm{Re}\{\cdot\}$ denotes the real part of a complex value. $\mathbb{C}$ denotes the complex space.

2. JRC-CWG Model

2.1. Transmit JRC-CWG Model

In this paper, we consider an ITS as shown in Figure 1. In Figure 1, the yellow car that is equipped with an automotive JRC system transmits the JRC waveforms to detect the white bus and simultaneously sends communications information to it.

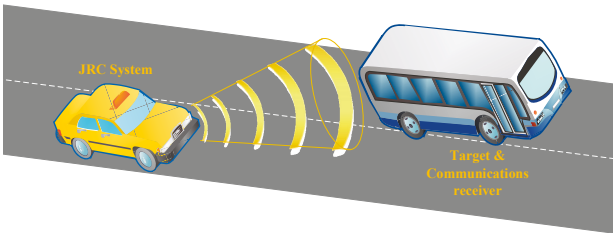

Figure 1. Intelligent transportation system.

In this paper, we consider that the transmit JRC waveform is the JRC-CWG, as shown in Figure 2. There are G groups of JRC-CWGs transmitted in each coherent processing interval (CPI) to perform radar and communications jointly. Each JRC-CWG contains M waveforms, and, hence, there are GM waveforms that will successively be transmitted with a fixed PRI, denoted as T in Figure 2. Let $\mathbf{S}_g = \left[\mathbf{s}_{g,1}, \mathbf{s}_{g,2}, \ldots, \mathbf{s}_{g,M}\right] \in \mathbb{C}^{N\times M}$ be the matrix formed by the waveforms of the g-th JRC-CWG. $\mathbf{s}_{g,m}$ is the m-th transmit waveform in the g-th JRC-CWG, which is denoted as

$$\mathbf{s}_{g,m} = \left[s_{g,m}(1), s_{g,m}(2), \ldots, s_{g,m}(N)\right]^T \tag{1}$$

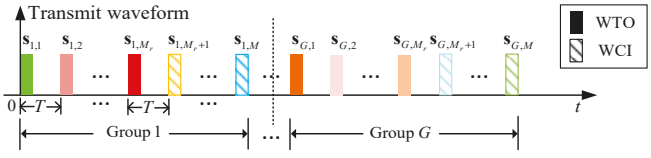

Figure 2. The transmit waveform model of the JRC-CWGs.

In (1), $s_{g,m}(n) = \frac{1}{\sqrt{N}} e^{j\theta_{g,m}(n)}$ denotes the n-th entry of $\mathbf{s}_{g,m}$; $\theta_{g,m}(n)$ represents the phase of $s_{g,m}(n)$; and N is the length of $\mathbf{s}_{g,m}$.

In each transmit JRC-CWG, the first M_r transmit waveforms are WTOs, which are represented by solid bars, and the last M_c transmit waveforms are WCIs, which are represented by shadowed bars in Figure 2. Clearly, it can be seen that $M = M_r + M_c$. That is to say, the whole JRC-CWG consists of WTOs and WCIs. In order to perform the communications function, the traditional unimodular communications waveforms, such as BPSK waveforms, will be employed as the WCIs. The WCIs are determined by the transmitted communications information. In order to improve the radar performance, the WTOs are optimized to suppress the sidelobe level of the whole JRC-CWG.

In this paper, we consider a radar and communication system with a single transmit antenna. It is worth noting that the proposed JRC-CWG is also applicable for multiple transmit antennas and receive antennas. This will be discussed in our future work.

2.2. Receive Signal Model at the Radar Receiver

The receive signal model at the radar receiver is shown in Figure 3a. For the sake of simplicity, we only consider returns from one point target in this paper. It can be easily extended to more general scenarios. Furthermore, it is reasonable to assume that the velocity of the vehicles is low. Hence, the Doppler shift of the returns in one PRI can be regarded as a constant value. Thus, the sampled return from a point target at the radar receiver of the JRC system can be represented as

$$\mathbf{s}^r_{g,m} = \delta_g \rho e^{j2\pi f_d T(m-1)} \mathbf{s}_{g,m} + \mathbf{n}_{g,m} \tag{2}$$

where δ_g is the complex scattering coefficient including the path loss and RCS of the target. According to [40,41], the RCS of a target can be described using the Swerling I model, i.e., the RCS of the target does not fluctuate in each CPI, and it will only fluctuate during different CPIs. Further to this, the path loss can be regarded as a constant value in each CPI. Thus, we assume that δ_g is a constant value in the g-th CPI. $\rho = e^{j2\pi f_d T[(g-1)M]}$, and $f_d = 2v/\lambda$ denotes the Doppler frequency, where v is the relative radial velocity between the JRC system and the target, and λ is the wavelength of the transmit waveforms. $\mathbf{n}_{g,m} \in \mathbb{C}^{N\times 1}$ is the vector of complex Gaussian white noise.

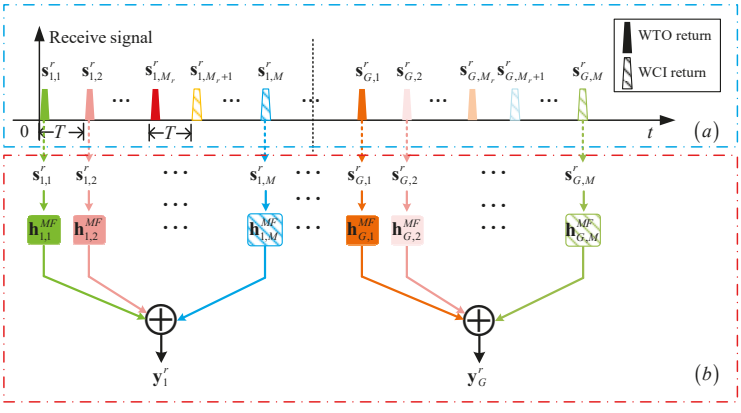

Figure 3. (**a**) Receive signal at the radar receiver. (**b**) Signal processing procedure.

The signal processing procedure at the radar receiver is shown in Figure 3b. $\mathbf{h}_{g,m}^{MF}$ denotes the matched filter of $\mathbf{s}_{g,m}$. As depicted in Figure 3b, the matched filter output of the g-th JRC-CWG returns are coherently accumulated, which can be denoted as

$$\mathbf{y}_g^r = \delta_g \rho \sum_{m=1}^{M} e^{j2\pi f_d T(m-1)} \mathbf{r}_{g,m} + \sum_{m=1}^{M} \mathbf{n}'_{g,m} \tag{3}$$

where $\mathbf{n}'_{g,m} \in \mathbb{C}^{K\times 1}$ $(K = 2N-1)$ is the matched filter output of $\mathbf{n}_{g,m}$, which is still a Gaussian white noise vector. $\mathbf{r}_{g,m} = \left[r_{g,m}(1-N), \ldots, r_{g,m}(-1), r_{g,m}(0), r_{g,m}(1), \ldots, r_{g,m}(N-1)\right]^T$ denotes the auto correlation function of $\mathbf{s}_{g,m}$, where

$$r_{g,m}(n) = \mathbf{s}_{g,m}^H \mathbf{U}_n \mathbf{s}_{g,m}, \quad \text{for } n = 0, 1, \ldots, N-1 \tag{4}$$

and $r_{g,m}(n) = r_{g,m}^*(-n)$, for $n = 1-N, 2-N, \ldots, -1$. $\mathbf{U}_n$ is expressed as

$$\mathbf{U}_n = \begin{bmatrix} \mathbf{0}_{n\times(N-n)} & \mathbf{I}_{N-n} \\ \mathbf{0}_{(N-n)\times(N-n)} & \mathbf{0}_{(N-n)\times n} \end{bmatrix}, \quad n = 0, 1, \ldots, N-1 \tag{5}$$

2.3. Receive Signal Model at the Communications User

The signal received by the communications user is denoted as $\mathbf{s}_{g,m}^c$ in Figure 4, where [42]

$$\mathbf{s}_{g,m}^c = \delta_h \mathbf{s}_{g,m} + \mathbf{n}_{g,m}^c \tag{6}$$

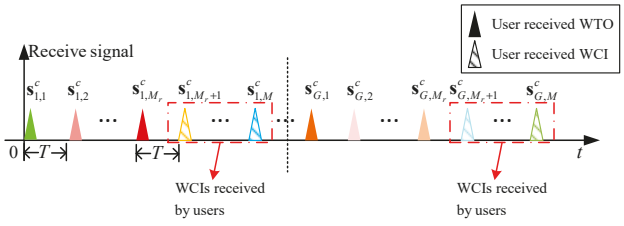

Figure 4. Receive signal at the communications user.

δ_{lh} is the communications channel coefficient [42,43], and $\mathbf{n}^c_{g,m}$ is the vector of complex Gaussian white noise at the communications receiver.

Note that all the signals transmitted by the JRC systems, including the WTOs and the WCIs are received by the communications user. Only the WCIs need to be decoded by the user. It is assumed that the user knows the number of the WTOs M_r, and the number of WCIs M_c in each JRC-CWG. In view of this, WCIs can be extracted, and the communications messages can be decoded according to the modulation scheme of the WCIs.

The communications rate and BER are usually utilized to measure the performance of communications. The communications rate of the JRC-CWG can be represented as

$$R_b = \frac{M_c}{M \cdot T} N B_0 \text{ bit/s} \tag{7}$$

where M_c is the number of WCIs in each JRC-CWG; M is the number of waveforms in each JRC-CWG; T is the PRI; N is the length of each WCI; and B_0 is the number of bits carried by each symbol of the WCI. For instance, if the BPSK waveforms are employed as the WCI, $B_0 = 1$. If the 16-PSK waveforms are employed as the WCI, $B_0 = 4$.

Since the traditional unimodular communications waveforms are employed as the WCIs, the BER of the JRC-CWG is the same as that of the traditional constant modulus communications waveform under the same condition.

3. JRC-CWG and DR-JRC-CWG Design

3.1. JRC-CWG Design with Low Sidelobe Level

In the ITS, when the relative radial velocity between the JRC system and the target is small or can be obtained, the effect of Doppler shift on the matched filter output can be ignored. For this case, the JRC-CWG design method is proposed without considering the Doppler shift in this section.

3.1.1. Problem Formulation

When the relative radial velocity v is 0, (3) can be rewritten as

$$\mathbf{y}^r_g = \delta_g \mathbf{f}_g + \sum_{m=1}^{M} \mathbf{n}'_{g,m} \tag{8}$$

where $\mathbf{f}_g = \sum_{m=1}^{M} \mathbf{r}_{g,m}$ is defined as the SACF of the g-th JRC-CWG. To suppress the sidelobe level of $\mathbf{f}_g$ while designing the unimodular JRC-CWG, the optimization problem can be formulated as [39]

$$\begin{aligned} &\min_{\mathbf{S}^R_g} \ \tfrac{1}{M}\mathbf{f}^H_g \mathbf{f}_g - 1 \\ &s.t. \ \ \left|s_{g,m}(n)\right| = \tfrac{1}{\sqrt{N}} \ \ m = 1,2,\ldots,M, \ \ n = 1,2,\ldots,N \end{aligned} \tag{9}$$

where $\mathbf{S}^R_g = \left[\mathbf{s}_{g,1},\ldots,\mathbf{s}_{g,M_r}\right] \in \mathbb{C}^{N\times M_r}$ is the matrix formed by all WTOs of the g-th JRC-CWG. The g-th optimal JRC-CWG can be obtained by solving the optimization problem

in (9). To obtain G optimal JRC-CWGs, G optimization problems similar to (9) should be solved in parallel. The proposed optimization problem is a fourth-order polynomial minimization problem with nonlinear constraints, which is hard to be solved. Note that the objective function can be transformed into a frequency domain using the Wiener–Khinchin theorem, which can be performed by applying the FFT algorithm to reduce the computational complexity. Moreover, by only optimizing the phase of WTOs, the constraints in (9) can be cancelled. Hence, (9) can be transformed to be

$$\min_{\mathbf{\Theta}_g} \left[\sum_{m=1}^{M} \mathbf{x}_{g,m} \odot \mathbf{x}_{g,m}^*\right]^H \left[\sum_{m=1}^{M} \mathbf{x}_{g,m} \odot \mathbf{x}_{g,m}^*\right] \tag{10}$$

where $\mathbf{\Theta}_g = \left[\theta_{g,1}, \ldots, \theta_{g,M_r}\right] \in \mathbb{C}^{N \times M_r}$ is the phase of WTOs in $\mathbf{S}_g^R$. $\mathbf{x}_{g,m} = \tilde{\mathbf{F}}_K \tilde{\mathbf{s}}_{g,m}$, where $\tilde{\mathbf{s}}_{g,m} = \begin{bmatrix} \mathbf{s}_{g,m}^T & \mathbf{0}_{(N-1)\times 1}^T \end{bmatrix}^T$, and $\tilde{\mathbf{F}}_K$ is the $K(K = 2N - 1)$ point discrete Fourier transform (DFT) matrix.

3.1.2. JRC-CWG Design Algorithm

In this section, an algorithm based on the framework of the FR-CG algorithm and the FFT algorithm is applied to solve (10).

Define

$$D\left(\mathbf{\Theta}_g\right) = \left[\sum_{m=1}^{M} \mathbf{x}_{g,m} \odot \mathbf{x}_{g,m}^*\right]^H \left[\sum_{m=1}^{M} \mathbf{x}_{g,m} \odot \mathbf{x}_{g,m}^*\right] \tag{11}$$

To solve (10), the gradient of $D\left(\mathbf{\Theta}_g\right)$ with respect to $\mathbf{\Theta}_g$ is required to be derived. To achieve this, the gradient of $D\left(\mathbf{\Theta}_g\right)$ with respect to $\theta_{g,m}(n)$ $(m \leq M_r)$ is derived first. According to the definition of the gradient of the real-valued function with respect to complex variables in [44], the gradient of $D\left(\mathbf{\Theta}_g\right)$ with respect to $\theta_{g,m}(n)$ is represented as

$$\begin{aligned} \frac{\partial D\left(\mathbf{\Theta}_g\right)}{\partial \theta_{g,m}(n)} &= \frac{\partial D\left(\mathbf{\Theta}_g\right)}{\partial s_{g,m}(n)} \cdot \frac{\partial s_{g,m}(n)}{\partial \theta_{g,m}(n)} + \frac{\partial D\left(\mathbf{\Theta}_g\right)}{\partial s_{g,m}^*(n)} \cdot \frac{\partial s_{g,m}^*(n)}{\partial \theta_{g,m}(n)} \\ &= j\frac{\partial D\left(\mathbf{\Theta}_g\right)}{\partial s_{g,m}(n)} \cdot s_{g,m}(n) - j\frac{\partial D\left(\mathbf{\Theta}_g\right)}{\partial s_{g,m}^*(n)} \cdot s_{g,m}^*(n) \end{aligned} \tag{12}$$

In (12), j represents the imaginary unit. According to the chain rule, we can determine that

$$\begin{aligned} \frac{\partial D\left(\mathbf{\Theta}_g\right)}{\partial s_{g,m}(n)} &= \sum_{k=1}^{K} \frac{\partial D\left(\mathbf{\Theta}_g\right)}{\partial \gamma_g(k)} \frac{\partial \gamma_g(k)}{\partial x_{g,m}(k)} \frac{\partial x_{g,m}(k)}{\partial s_{g,m}(n)} \\ &= \sum_{k=1}^{K} \gamma_g^*(k) x_{g,m}^*(k) \tilde{\mathbf{F}}_K(k,n) \end{aligned} \tag{13}$$

and

$$\begin{aligned} \frac{\partial D\left(\mathbf{\Theta}_g\right)}{\partial s_{g,m}^*(n)} &= \sum_{k=1}^{K} \frac{\partial D\left(\mathbf{\Theta}_g\right)}{\partial \gamma_g^*(k)} \frac{\partial \gamma_g^*(k)}{\partial x_{g,m}^*(k)} \frac{\partial x_{g,m}^*(k)}{\partial s_{g,m}^*(n)} \\ &= \sum_{k=1}^{K} \gamma_g(k) x_{g,m}(k) \tilde{\mathbf{F}}_K^*(k,n) \end{aligned} \tag{14}$$

In (13) and (14), $\gamma_g(k)$ is the k-th element of $\boldsymbol{\gamma}_g$, and $\boldsymbol{\gamma}_g = \sum_{m=1}^{M} \mathbf{x}_{g,m} \odot \mathbf{x}_{g,m}^*$. From (13) and (14), we can determine that

$$\frac{\partial D\left(\mathbf{\Theta}_g\right)}{\partial s_{g,m}(n)} = \left[\frac{\partial D\left(\mathbf{\Theta}_g\right)}{\partial s_{g,m}^*(n)}\right]^* \tag{15}$$

From (12) to (15), the gradient of $D\left(\boldsymbol{\Theta}_g\right)$ with respect to $\theta_{g,m}$ can be represented as

$$\begin{aligned}\frac{\partial D\left(\boldsymbol{\Theta}_g\right)}{\partial \theta_{g,m}} &= \left\{\mathbf{V}\left[\tilde{\mathbf{F}}_K\left(2\boldsymbol{\gamma}_g \odot \mathbf{x}_{g,m}^*\right)\right]\right\} \odot \left(j\mathbf{s}_{g,m}\right) \\ &+\left\{\mathbf{V}\left[\tilde{\mathbf{F}}_K^H\left(2\boldsymbol{\gamma}_g \odot \mathbf{x}_{g,m}\right)\right]\right\} \odot \left(-j\mathbf{s}_{g,m}^*\right) \\ &= 2\mathrm{Re}\left\{\left\{\mathbf{V}\left[\tilde{\mathbf{F}}_K\left(2\boldsymbol{\gamma}_g \odot \mathbf{x}_{g,m}^*\right)\right]\right\} \odot \left(j\mathbf{s}_{g,m}\right)\right\}\end{aligned} \tag{16}$$

where $\mathbf{V} = \left[\mathbf{I}_N, \mathbf{0}_{N\times(N-1)}\right]$. Using (16), the gradient of $D\left(\boldsymbol{\Theta}_g\right)$ with respect to $\boldsymbol{\Theta}_g$ can be calculated, and the FR-CG algorithm can be applied to solve (10). Note that (10) and (16) can be calculated with the FFT algorithm to reduce computational complicity. The detailed algorithm for designing the g-th JRC-CWG is summarized in Algorithm 1.

Algorithm 1: The JRC-CWG design algorithm.

Input: G, M_c, M_r, N, the threshold ε, and WCIs.
Step 1: Initialize $\boldsymbol{\Theta}_g^{(0)} = \left[\theta_{g,1}^{(0)}, \ldots, \theta_{g,M_r}^{(0)}\right]$, let $k_0 = 0$, $\alpha_0 = 0$, and the search direction $\tilde{\mathbf{V}}_d^{(0)} = \mathbf{0}_{N\times M_r}$.
Step 2: Calculate the gradient matrix $\tilde{\mathbf{G}}_g^{(k_0)} = \left[\tilde{\mathbf{g}}_{g,1}^{(k_0)}, \tilde{\mathbf{g}}_{g,2}^{(k_0)}, \ldots \tilde{\mathbf{g}}_{g,M_r}^{(k_0)}\right]$ using (16), where $\tilde{\mathbf{g}}_{g,m}^{(k_0)} = \partial D\left[\boldsymbol{\Theta}_g^{(k_0)}\right] / \partial \theta_{g,m}^{(k_0)}$.
Step 3: Calculate the search direction $\tilde{\mathbf{V}}_d^{(k_0+1)} = -\tilde{\mathbf{G}}_g^{(k_0)} + \alpha_{k_0}\tilde{\mathbf{V}}_d^{(k_0)}$.
Step 4: Compute $\boldsymbol{\Theta}_g^{(k_0+1)} = \boldsymbol{\Theta}_g^{(k_0)} + \lambda_{k_0}\tilde{\mathbf{V}}_d^{(k_0+1)}$, where λ_{k_0} is the optimal solution that minimizes $D\left[\boldsymbol{\Theta}_g^{(k_0+1)}\right]$, which is obtained with the line search method [45].
Step 5: If $\left|D\left[\boldsymbol{\Theta}_g^{(k_0+1)}\right] - D\left[\boldsymbol{\Theta}_g^{(k_0)}\right]\right| \le \varepsilon$, go to **Output**,
else (1) Let $k_0 = k_0 + 1$;
(2) Calculate the gradient matrix $\tilde{\mathbf{G}}_g^{(k_0)} = \left[\tilde{\mathbf{g}}_{g,1}^{(k_0)}, \tilde{\mathbf{g}}_{g,2}^{(k_0)}, \ldots \tilde{\mathbf{g}}_{g,M_r}^{(k_0)}\right]$ using (16), where $\tilde{\mathbf{g}}_{g,m}^{(k_0)} = \partial D\left[\boldsymbol{\Theta}_g^{(k_0)}\right] / \partial \theta_{g,m}^{(k_0)}$;
(3) Calculate $\alpha_{k_0} = \left\|\tilde{\mathbf{G}}_g^{(k_0)}\right\|_F^2 / \left\|\tilde{\mathbf{G}}_g^{(k_0-1)}\right\|_F^2$;
(4) Turn to **Step 3.**
Output: The phase of WTOs $\boldsymbol{\Theta}_g^{(k_0+1)}$.

3.1.3. Computational Complexity Analysis

For the proposed algorithm to design the JRC-CWG in Algorithm 1, the computational complexity of step 2 is $O(M_r(M+1)K\log_2(K))$. The computational cost of step 3 is $O(NM_r)$. In step 4, the computational complexity is $O(\tilde{N}MK\log_2(K))$, where $\tilde{N}$ is the search time to obtain λ_{k_0} with the line search method. In step 5 (2), the computational complexity is $O(M_r(M+1)K\log_2(K))$, and the computational cost of step 5 (3) is $O(NM_r)$. The total computational complexity of each iteration of the JRC-CWG design algorithm is approximately $O\left(M_r(M+1)K\log_2(K) + \tilde{N}MK\log_2(K) + 2NM_r\right)$. Hence, the computational complexity of the JRC-CWG design algorithm in Algorithm 1 is approximately $O\left(\tilde{L}M_r(M+1)K\log_2(K) + \tilde{L}\tilde{N}MK\log_2(K) + 2\tilde{L}NM_r\right)$, where $\tilde{L}$ is the number of iterations.

3.2. DR-JRC-CWG Design

In Section 3, we have designed the JRC-CWG under the assumption that the relative radial velocity v between the JRC system and the target is known or can be ignored. However, the accurate v is hard to be obtained, or v cannot be ignored in practice. The range sidelobe level of the received JRC-CWG will increase if v cannot be compensated at the radar receiver. To decrease the range sidelobe level of the received JRC-CWG with Doppler shift, a Doppler-resilient JRC-CWG, i.e., the DR-JRC-CWG is devised in this section.

3.2.1. Doppler Sensitivity Analysis

According to (3), the sum of matched filter outputs of the g-th JRC-CWG with Doppler shift f_d is

$$y_g^r(n, f_d) = \delta_g \rho \sum_{m=1}^{M} e^{j2\pi(m-1)f_d T} \mathbf{s}_{g,m}^H \mathbf{U}_n \mathbf{s}_{g,m} + \sum_{m=1}^{M} \mathbf{n}'_{g,m} \tag{17}$$

As shown in (17), the Doppler frequency f_d will affect the range sidelobe level of the JRC-CWG. It is necessary to design the DR-JRC-CWG when f_d cannot be accurately acquired.

According to (17), the AF of the g-th JRC-CWG is defined as

$$\begin{gathered} y_g(n, \varphi_d) = \sum_{m=1}^{M} e^{j2\pi(m-1)\varphi_d} \mathbf{s}_{g,m}^H \mathbf{U}_n \mathbf{s}_{g,m}, \\ \text{for } n = 0, 1, \ldots, N-1 \end{gathered} \tag{18}$$

and $y_g(n, \varphi_d) = y_g^*(-n, \varphi_d)$, for $n = 1-N, 2-N, \ldots, -1$, where $\varphi_d = f_d T$ is the normalized Doppler frequency.

Next, the AF of the g-th JRC-CWG is analyzed using the Taylor formula, and we will show how the nonzero-order Taylor expansion terms affect the Doppler resilience of the JRC-CWG. The Taylor expansion of the AF of the g-th JRC-CWG around $\varphi_d = 0$ can be represented as

$$y_g(n, \varphi_d) = \sum_{q=0}^{\infty} \frac{\sum_{m=1}^{M} (m-1)^q \mathbf{s}_{g,m}^H \mathbf{U}_n \mathbf{s}_{g,m}}{q!} (j2\pi\varphi_d)^q \tag{19}$$

Introduce $\boldsymbol{\beta}_{g,q} = \left[\beta_{g,q}(1-N), \ldots, \beta_{g,q}(0), \ldots \beta_{g,q}(N-1)\right]^T$, where

$$\begin{gathered} \beta_{g,q}(n) = \frac{1}{q!} \sum_{m=1}^{M} (m-1)^q \mathbf{s}_{g,m}^H \mathbf{U}_n \mathbf{s}_{g,m} \\ \text{for } \; n = 0, 1, \ldots, N-1 \end{gathered} \tag{20}$$

and $\beta_{g,q}(n) = \beta_{g,q}^*(-n)$, for $n = 1-N, 2-N, \ldots, -1$, and then, (19) can be rewritten as

$$y_g(n, \varphi_d) = \sum_{q=0}^{\infty} \beta_{g,q}(n) (j2\pi\varphi_d)^q \tag{21}$$

Let

$$P_{g,q}(n, \varphi_d) = \beta_{g,q}(n) (j2\pi\varphi_d)^q \tag{22}$$

Then, (21) can be rewritten as

$$y_g(n, \varphi_d) = \sum_{q=0}^{\infty} P_{g,q}(n, \varphi_d). \tag{23}$$

In (23), $y_g(n, \varphi_d)$ can be regarded as the summation of $P_{g,q}(n, \varphi_d)$ for different q. When $q = 0$, we will obtain

$$P_{g,0}(n, \varphi_d) = \sum_{m=1}^{M} \mathbf{s}_{g,m}^H \mathbf{U}_n \mathbf{s}_{g,m} \tag{24}$$

In (24), it can be seen that $P_{g,0}(n, \varphi_d)$ is the SACF of the g-th JRC-CWG. This indicates that only the zero-order Taylor expansion term is considered in the optimization problem (10). However, according to (23), if only the zero-order Taylor expansion term $P_{g,0}(n, \varphi_d)$ is considered in the JRC-CWG design, the nonzero-order Taylor expansion terms of y_g will deteriorate the Doppler resilience of the JRC-CWGs. Hence, to suppress the sidelobe level of the JRC-CWG around $\varphi_d = 0$, more Taylor expansion terms of y_g, i.e., $P_{g,q}$, should be

optimized. Moreover, according to (20) and (22), as q increases, the value of $P_{g,q}(n,\varphi_d)$ decreases because of the term $1/q!$. This means that some lower order of $P_{g,q}$ has the major effect on the Doppler resilience of the JRC-CWG. Furthermore, according to (22), when optimizing $P_{g,q}$, the term $(j2\pi\varphi_d)^q$ can be regarded as a constant. Hence, it is reasonable to optimize $P_{g,q}$ by optimizing $\boldsymbol{\beta}_{g,q}$. In summary, to design the DR-JRC-CWG, $\boldsymbol{\beta}_{g,q}$ for $q=0,1,\ldots,Q$, should be jointly optimized.

3.2.2. Problem Formulation

From the discussion above, the optimization problem to design the g-th DR-JRC-CWG can be represented as

$$\begin{aligned} &\min_{\mathbf{s}_g^R} \sum_{q=0}^{Q} \tilde{w}_q \left(\tfrac{1}{\tilde{E}(q)} \boldsymbol{\beta}_{g,q}^H \boldsymbol{\beta}_{g,q} - 1 \right) \\ &s.t. \quad \left| s_{g,m}(n) \right| = \tfrac{1}{\sqrt{N}} \quad m=1,2,\ldots,M, \quad n=1,2,\ldots,N \end{aligned} \tag{25}$$

where $\tilde{E}(q) = \frac{1}{q!} \cdot \sum_{m=1}^{M} (m-1)^q$, and $\tilde{w}_q$ is the weight satisfying $\sum_{q=0}^{Q} \tilde{w}_q = 1$. Similar to (10), to obtain G optimal DR-JRC-CWGs, G optimization problems similar to (25) should be solved in parallel. It can be seen that when $Q=0$, the optimization problem in (25) will be the optimization problem in (9). Similar to (10), the optimization problem (25) can be transformed into

$$\min_{\boldsymbol{\Theta}_g} \sum_{q=0}^{Q} \tilde{w}_q \left[\sum_{m=1}^{M} (m-1)^q \mathbf{x}_{g,m} \odot \mathbf{x}_{g,m}^* \right]^H \left[\sum_{m=1}^{M} (m-1)^q \mathbf{x}_{g,m} \odot \mathbf{x}_{g,m}^* \right] \tag{26}$$

3.2.3. DR-JRC-CWG Design Algorithm

For simplicity, let

$$D_{dop}(\boldsymbol{\Theta}_g) = \sum_{q=0}^{Q} \tilde{w}_q h_{g,q}(\boldsymbol{\Theta}_g) \tag{27}$$

where $h_{g,q}(\boldsymbol{\Theta}_g) = \left[\sum_{m=1}^{M} (m-1)^q \mathbf{x}_{g,m} \odot \mathbf{x}_{g,m}^* \right]^H \left[\sum_{m=1}^{M} (m-1)^q \mathbf{x}_{g,m} \odot \mathbf{x}_{g,m}^* \right]$. The gradient of $D_{dop}(\boldsymbol{\Theta}_g)$ with respect to $\boldsymbol{\Theta}_g$ can be represented as

$$\frac{\partial D_{dop}(\boldsymbol{\Theta}_g)}{\partial \boldsymbol{\Theta}_g} = \sum_{q=0}^{Q} \tilde{w}_q \frac{\partial h_{g,q}(\boldsymbol{\Theta}_g)}{\partial \boldsymbol{\Theta}_g} \tag{28}$$

The gradient of $h_{g,q}(\boldsymbol{\Theta}_g)$ with respect to $\boldsymbol{\theta}_{g,m}$ $(m \le M_r)$ is

$$\frac{\partial h_{g,q}(\boldsymbol{\Theta}_g)}{\partial \boldsymbol{\theta}_{g,m}} = 2\mathrm{Re}\left\{ (m-1)^q \left\{ \mathbf{V}\left[\tilde{\mathbf{F}}_K \left(2\boldsymbol{\gamma}_{g,q} \odot \mathbf{x}_{g,m}^* \right) \right] \right\} \odot \left(j\mathbf{s}_{g,m} \right) \right\} \tag{29}$$

where $\boldsymbol{\gamma}_{g,q} = \sum_{m=1}^{M} \left[(m-1)^q \mathbf{x}_{g,m} \odot \mathbf{x}_{g,m}^* \right]$. The derivation of (29) is similar to that in (16). In addition, (27) and (29) can be computed using the FFT algorithm to reduce the computational complexity. The DR-JRC-CWG design algorithm is summarized in Algorithm 2.

Algorithm 2: The DR-JRC-CWG design algorithm

Input: G, M_c, M_r, N, $\bar{w}_q$, the threshold ε, Q, and WCIs.
Step 1: Initialize $\mathbf{\Theta}_g^{(0)} = \left[\theta_{g,1}^{(0)}, \ldots, \theta_{g,M_r}^{(0)}\right]$, and let $k_0 = 0$, $\alpha_0 = 0$, and $\tilde{\mathbf{V}}_d^{(0)} = \mathbf{0}_{N\times M_r}$.
Step 2: Calculate the gradient matrix $\tilde{\mathbf{G}}_g^{(k_0)} = \left[\tilde{\mathbf{g}}_{g,1}^{(k_0)}, \tilde{\mathbf{g}}_{g,2}^{(k_0)}, \ldots \tilde{\mathbf{g}}_{g,M_r}^{(k_0)}\right]$ using (28) and (29), where $\tilde{\mathbf{g}}_{g,m}^{(k_0)} = \partial D\left[\mathbf{\Theta}_g^{(k_0)}\right]/\partial\theta_{g,m}^{(k_0)}$.
Step 3: Calculate the search direction $\tilde{\mathbf{V}}_d^{(k_0+1)} = -\tilde{\mathbf{G}}_g^{(k_0)} + \alpha_{k_0}\tilde{\mathbf{V}}_d^{(k_0)}$.
Step 4: Compute $\mathbf{\Theta}_g^{(k_0+1)} = \mathbf{\Theta}_g^{(k_0)} + \lambda_{k_0}\tilde{\mathbf{V}}_d^{(k_0+1)}$, where λ_{k_0} is the optimal solution that minimizes $D_{dop}\left[\mathbf{\Theta}_g^{(k_0+1)}\right]$, which is obtained with the line search method.
Step 5: If $\left|D_{dop}\left[\mathbf{\Theta}_g^{(k_0+1)}\right] - D_{dop}\left[\mathbf{\Theta}_g^{(k_0)}\right]\right| \le \varepsilon$, go to **Output**,
else (1) Let $k_0 = k_0 + 1$;
(2) Calculate the gradient matrix $\tilde{\mathbf{G}}_g^{(k_0)} = \left[\tilde{\mathbf{g}}_{g,1}^{(k_0)}, \tilde{\mathbf{g}}_{g,2}^{(k_0)}, \ldots \tilde{\mathbf{g}}_{g,M_r}^{(k_0)}\right]$ using (28) and (29), where $\tilde{\mathbf{g}}_{g,m}^{(k_0)} = \partial D\left[\mathbf{\Theta}_g^{(k_0)}\right]/\partial\theta_{g,m}^{(k_0)}$;
(3) Calculate $\alpha_{k_0} = \|\tilde{\mathbf{G}}_g^{(k_0)}\|_F^2 / \|\tilde{\mathbf{G}}_g^{(k_0-1)}\|_F^2$;
(4) Turn to **Step 3.**
Output: The phase of WTOs $\mathbf{\Theta}_g^{(k_0+1)}$.

3.2.4. Computational Complexity Analysis

For the DR-JRC-CWG design algorithm in Algorithm 2, the computational complexity of step 2 is $O((Q+1)M_r(M+1)K\log_2(K))$. The computational cost of step 3 is $O(NM_r)$. The computational complexity of step 4 is $O\big((Q+1)\tilde{N}MK\log_2(K)\big)$, where $\tilde{N}$ is the search time to obtain λ_{k_0} with the line search method. Moreover, in step 5 (2), the computational complexity is $O((Q+1)M_r(M+1)K\log_2(K))$, and the computational cost of step 5 (3) is $O(NM_r)$. Then, the total computational complexity of each iteration of the DR-JRC-CWG design algorithm is approximately $O\big((Q+1)\big(M_r(M+1)+\tilde{N}M\big)K\log_2(K)+2NM_r\big)$. Hence, the computational complexity of the DR-JRC-CWG design algorithm in Algorithm 2 is approximately $O\big(\tilde{L}(Q+1)\big(M_r(M+1)+\tilde{N}M\big)K\log_2(K)+2\tilde{L}NM_r\big)$, where $\tilde{L}$ is the number of iterations.

4. Results

In this section, several simulation results are given to evaluate the performances of the designed JRC-CWG and the DR-JRC-CWG. In the following, unless otherwise mentioned, the number of groups G of the JRC-CWG or the DR-JRC-CWG is set to be 1. The peak-to-sidelobe ratio (PSLR) of SACF of the JRC-CWG and the DR-JRC-CWG is utilized to measure their sidelobe performance. The BPSK and the 16-PSK waveforms are employed as the WCIs for the designed JRC-CWG and DR-JRC-CWG. For the WCIs with BPSK modulation, the JRC-CWG is denoted as the JRC-CWG-BPSK, and the DR-JRC-CWG is denoted as DR-JRC-CWG-BPSK in the following. For the WCIs with 16-PSK modulation, the JRC-CWG and the DR-JRC-CWG are denoted as the JRC-CWG-16-PSK and the DR-JRC-CWG-16-PSK, respectively.

4.1. Performance of the JRC-CWG

Let the number of WCIs M_c in each JRC-CWG be fixed to 1, and the sidelobe performance of the JRC-CWG with different numbers of waveforms M used in each JRC-CWG is shown in Figure 5. The sidelobe performances of the two other JRC waveforms, i.e., the LFM-BPSK waveform in [31] and the OPP waveform in [13], are also shown in Figure 5. In Figure 5, the OPP-BPSK denotes the OPP waveforms modulated by the BPSK waveforms. The length of each JRC waveform in Figure 5 is N = 64. To measure the sidelobe performance of the LFM-BPSK waveforms and the OPP-BPSK waveforms, the PSLR of SACF of M different LFM-BPSK waveforms and M different OPP-BPSK waveforms are calculated, respectively.

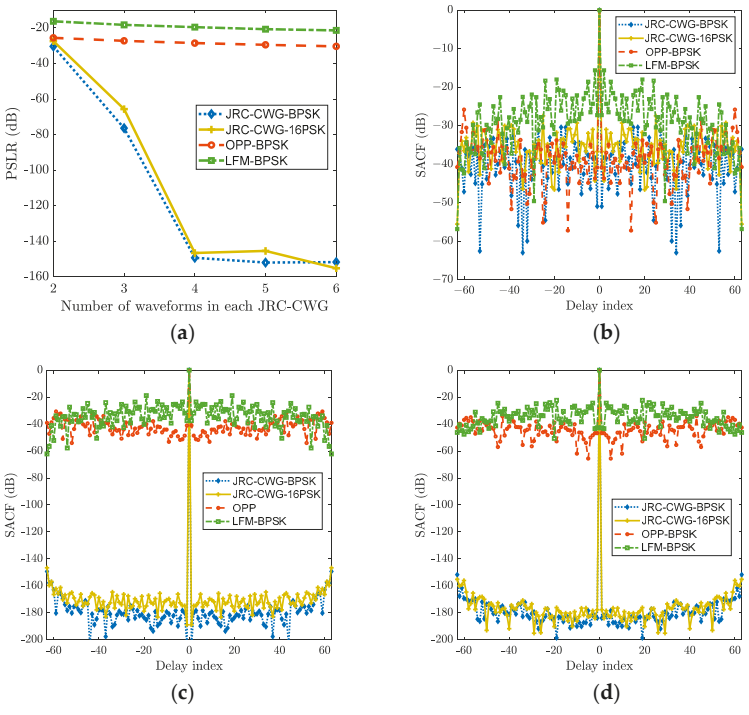

Figure 5. (**a**) PSLRs of the JRC waveforms with different number of waveforms M in each JRC-CWG. (**b**) SACF with $M = 2$. (**c**) SACF with $M = 4$. (**d**) SACF with $M = 6$.

In Figure 5a, the PSLRs of the JRC waveforms versus M are given. Moreover, the SACFs of the JRC waveforms with the number of waveforms M =2,4,6 are shown, respectively, in Figure 5b–d. In Figure 5a, when M increases, the PSLR of all JRC waveforms decreases, and the PSLRs of the designed JRC-CWG-BPSK and the JRC-CWG-16-PSK decrease faster than those of the other two JRC waveforms. Specifically, when $M = 2$, the PSLR of the JRC-CWG-BPSK is 4.8 dB lower than that of the OPP-BPSK waveform, and 14.1 dB lower than that of the LFM-BPSK waveform. When $M = 2$, the PSLR of the designed JRC-CWG-16-PSK is 3.9 dB lower than that of the OPP-BPSK waveform and 13.2 dB lower than that of the LFM-BPSK waveform. When $M = 4$, the PSLRs of the designed JRC-CWG-BPSK and JRC-CWG-16-PSK are at least 120 dB lower than those of the OPP-BPSK waveform and the LFM-BPSK waveform. As depicted in Section 2, $M = M_r + M_c$, where M_r is the number of WTOs employed in each JRC-CWG. Thus, M_r will increase with the increasing M when M_c is fixed. With the increase in M_r, more degrees of freedom will be employed to suppress the sidelobe of the JRC-CWG SACF according to (9), which will lead to a lower PSLR than other JRC waveforms. Due to the limitation of the computation accuracy of the used computer, the PSLR of the designed JRC-CWG is approximately -150 dB and will not decrease anymore when $M \geq 4$. Furthermore, it can be seen in Figure 5 that the sidelobe performance of the designed JRC-CWG-BPSK is close to that of the designed JRC-CWG-16-PSK with different M. That is to say, the modulation approach has little influence on the sidelobe performance of the designed JRC-CWG.

From Figure 5, we can see that with a sufficiently large M, the sidelobe level of the designed JRC-CWG can be sufficiently suppressed. However, in practice, a large M is usually not recommended. With a large M, it will take a longer time to transmit one JRC-CWG, and the coefficient δ_g in (2) may be changed. In practice, the M should make sure that the coefficient δ_g does not change during the CPI.

4.2. Performance of the DR-JRC-CWG

In this subsection, the performance of DR-JRC-CWG will be shown. The AF defined in (18) and Delay-Doppler maps of the designed JRC-CWG-BPSK are shown in Figure 6(a1,a2). Let $\mathbf{w} = \left[\tilde{w}_0, \tilde{w}_1, \ldots, \tilde{w}_Q\right]^T$ collect the weights in (26), and the AFs and Delay-Doppler maps of the designed DR-JRC-CWG-BPSK and DR-JRC-CWG-16-PSK with different weights $\mathbf{w}$ are shown in Figure 6(b1–d2). Furthermore, the AFs and Delay-Doppler maps of the LFM-BPSK waveform and OPP-BPSK waveform are shown in Figure 6(e1–f2). The simulation parameters used in Figure 6 are listed in Table 1.

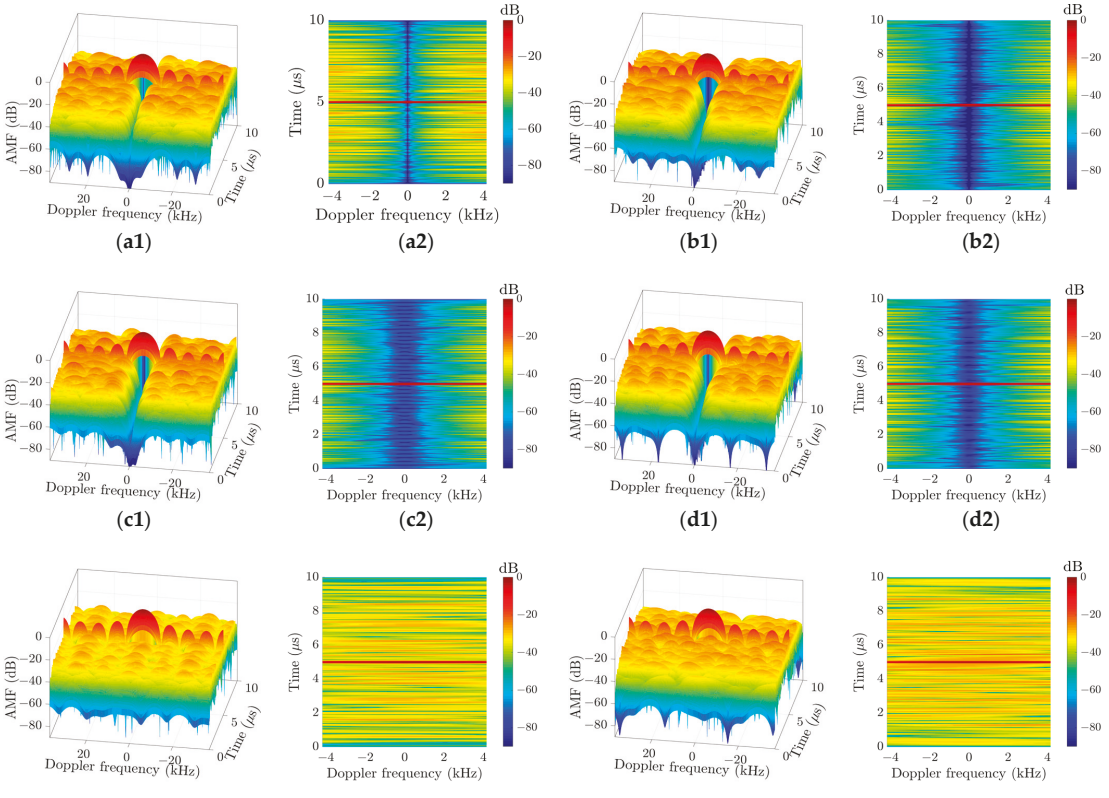

Figure 6. AFs and Delay-Doppler maps of the JRC waveforms. (**a1**) AF of the JRC-CWG-BPSK; (**a2**) Delay-Doppler map of the JRC-CWG-BPSK; (**b1**) AF of the DR-JRC-CWG-BPSK with $\mathbf{w} = \mathbf{w}_1$; (**b2**) Delay-Doppler map of the DR-JRC-CWG-BPSK with $\mathbf{w} = \mathbf{w}_1$; (**c1**) AF of the DR-JRC-CWG-BPSK with $\mathbf{w} = \mathbf{w}_2$; (**c2**) Delay-Doppler map of the DR-JRC-CWG-BPSK with $\mathbf{w} = \mathbf{w}_2$; (**d1**) AF of the DR-JRC-CWG-16-PSK with $\mathbf{w} = \mathbf{w}_2$; (**d2**) Delay-Doppler map of the DR-JRC-CWG-16-PSK with $\mathbf{w} = \mathbf{w}_2$; (**e1**) AF of the OPP-BPSK waveform; (**e2**) Delay-Doppler map of the OPP-BPSK waveform; (**f1**) AF of the LFM-BPSK waveform; and (**f2**) Delay-Doppler map of the LFM-BPSK waveform.

Table 1. Parameters used in Figure 6.

Figure	JRC Waveform	Q	w	M_c	M	T_p	PRI	N
Figure 6(a1,a2)	JRC-CWG-BPSK	0	-	1	6	5 µs	20 µs	64
Figure 6(b1,b2)	DR-JRC-CWG-BPSK	1	$\mathbf{w}_1 = [0.95, 0.05]^T$	1	6	5 µs	20 µs	64
Figure 6(c1,c2)	DR-JRC-CWG-BPSK	1	$\mathbf{w}_2 = [0.9, 0.1]^T$	1	6	5 µs	20 µs	64
Figure 6(e1,e2)	DR-JRC-CWG-16-PSK	1	$\mathbf{w}_2 = [0.9, 0.1]^T$	1	6	5 µs	20 µs	64
Figure 6(e1,e2)	OPP-BPSK	-	-	-	6	5 µs	20 µs	64
Figure 6(f1,f2)	LFM-BPSK	-	-	-	6	5 µs	20 µs	64

From Figure 6, we can see that all the AFs have a 'thumbtack' shape. It can be seen that there is a valley in the AFs of the designed JRC-CWG-BPSK, DR-JRC-CWG-BPSK, and DR-JRC-CWG-16-PSK around $f_d = 0$, while there is no valley in the AFs of the LFM-BPSK waveform and the OPP-BPSK waveform. This means that the designed JRC-CWG-BPSK, DR-JRC-CWG-BPSK, and DR-JRC-CWG-16-PSK have better PSLR performances around $f_d = 0$ than the other two JRC waveforms. Moreover, the valley indicates that the PSLRs of the JRC-CWG-BPSK, DR-JRC-CWG-BPSK, and DR-JRC-CWG-16-PSK increase as f_d increases, which is consistent with the analysis of (17). Compared with Figure 6(a2), the valley in Figure 6(b2,c2,d2) is much wider. The wider the valley is, the more slowly the PSLR will increase with the increase in f_d. Therefore, compared with the designed JRC-CWG-BPSK, the devised DR-JRC-CWG-BPSK and DR-JRC-CWG-16-PSK have better Doppler resilience. Furthermore, compared with Figure 6(b2), the valley in Figure 6(c2) is wider, which indicates that the Doppler resilience of the designed DR-JRC-CWG-BPSK will be improved when the weight $\tilde{w}_1$ in $\mathbf{w}$ is increased. From Figure 6, we can see that compared with the LFM-BPSK waveform, OPP-BPSK waveform, and the JRC-CWG, the proposed DR-JRC-CWG has the best Doppler resilience. This indicates that the designed DR-JRC-CWG is more suitable to be employed by automotive JRC systems than other JRC waveforms when f_d cannot be obtained or ignored.

In Figure 7, the relationship between the PSLR and Doppler frequency is shown. The simulation parameters in Figure 7 are the same as those in Figure 6. In accordance with the IEEE 802.11p standard, we assume that the carrier frequency of the JRC waveforms in Figure 7 is 5.9 GHz [46], i.e., the wavelength λ is 0.051 m. In Figure 7, the horizontal line for -35 dB is plotted. To make sure the PSLRs of the JRC waveforms are lower than -35 dB, the maximum Doppler frequencies and the corresponding radial velocities of the target in Figure 7 are listed in Table 2.

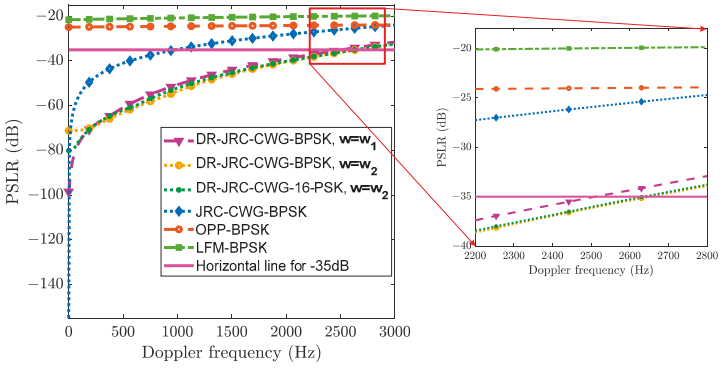

Figure 7. Relation curves between PSLR and Doppler frequency.

Table 2. PSLRs of the JRC waveforms and the corresponding velocities.

JRC Waveform	w	PSLR (dB)	f_d (Hz)	Velocity (m/s)
JRC-CWG-BPSK	-	-35	986.3	25.1
DR-JRC-CWG-BPSK	$\mathbf{w}_1 = [0.95, 0.05]^T$	-35	2513.0	63.9
DR-JRC-CWG-BPSK	$\mathbf{w}_2 = [0.9, 0.1]^T$	-35	2654.0	67.5
DR-JRC-CWG-16-PSK	$\mathbf{w}_2 = [0.9, 0.1]^T$	-35	2631.4	66.9
OPP-BPSK	-	-35	NA	NA
LFM-BPSK	-	-35	NA	NA

In Table 2, the NA stands for not-applicable. It can be determined that if the PSLR of the JRC waveform is required to be lower than -35 dB, the OPP-BPSK waveform and the LFM-BPSK waveform will not be applicable. To make sure the PSLR is lower than -35 dB, the radial velocity v between the JRC platform and the target should satisfy that $v < 25.1$ m/s for JRC-CWG-BPSK, $v < 63.9$ m/s for DR-JRC-CWG-BPSK with $\mathbf{w} = \mathbf{w}_1$, $v < 67.5$ m/s for the DR-JRC-CWG-BPSK with $\mathbf{w} = \mathbf{w}_2$, and $v < 66.9$ m/s for the DR-JRC-CWG-16-PSK with $\mathbf{w} = \mathbf{w}_2$, respectively. Hence, the designed DR-JRC-CWGs have better Doppler resilience than the designed JRC-CWGs. Compared with the DR-JRC-CWG-BPSK with $\mathbf{w} = \mathbf{w}_1$, i.e., $\tilde{w}_1 = 0.05$, and $\mathbf{w} = \mathbf{w}_2$, i.e., $\tilde{w}_1 = 0.1$, it can be observed that the Doppler resilience of the designed DR-JRC-CWG-BPSK will be improved when the weight $\tilde{w}_1$ in $\mathbf{w}$ is increased. Moreover, the designed DR-JRC-CWG-BPSK with $\mathbf{w} = \mathbf{w}_2$ has a similar performance to the designed DR-JRC-CWG-16-PSK with $\mathbf{w} = \mathbf{w}_2$. From Figure 7, we can see that the designed DR-JRC-CWG has better Doppler resilience than the OPP-BPSK waveform, the LFM-BPSK waveform, and the JRC-CWG. Moreover, the Doppler resilience of the designed DR-JRC-CWG satisfies the demand of automotive JRC systems, while that of other JRC waveforms does not.

In Figure 7, compared with the designed JRC-CWG-BPSK, the PSLR of the designed DR-JRC-CWG-BPSK at $f_d = 0$ is larger. Moreover, the larger the weight $\tilde{w}_1$ in $\mathbf{w}$ is, the larger the PSLR of the designed DR-JRC-CWG-BPSK at $f_d = 0$ is. Specifically, the PSLR of the designed JRC-CWG-BPSK at $f_d = 0$ is -151.9 dB. For the designed DR-JRC-CWG-BPSK with $\mathbf{w} = \mathbf{w}_1$, and the DR-JRC-CWG-BPSK with $\mathbf{w} = \mathbf{w}_2$, the PSLR at $f_d = 0$ is -98.5 dB and -71.2 dB, respectively. Note that in the multi-objective optimization problem (25), the Doppler resilience and the sidelobe level of SACF of the DR-JRC-CWG are jointly optimized, whereas in the optimization problem (9) only the sidelobe level of the SACF of the JRC-CWG is optimized. Hence, the PSLR of the DR-JRC-CWG may be higher than that of the JRC-CWG. Moreover, the larger the weight $\tilde{w}_1$ in $\mathbf{w}$ is, the higher the PSLR will be.

From Figure 7, it can be seen that the DR-JRC-CWG has a worse sidelobe performance than the JRC-CWG at $f_d = 0$. In practice, the user can employ the DR-JRC-CWG at first to estimate the velocity of the target. Then, the JRC-CWG can be employed, since the Doppler shift can be compensated at the radar receiver by using the estimated velocity.

Generally, an ITS often suffers serious clutter. In this scenario, the estimated target output signal-to-noise ratios (SNRs) of the JRC waveforms with different Doppler frequencies are illustrated in Figure 8. The simulation parameters of the JRC waveforms in Figure 8 are the same as those in Figure 7. The SNR is estimated by using the SNR estimation method in [47]. The input SNR of the JRC system is 0 dB in Figure 8. It can be seen that as the Doppler frequency increases, the output SNR of all the JRC waveforms decreases. However, the output SNR of the designed DR-JRC-CWG decreases slower than that of the other JRC waveforms. Furthermore, the output SNRs of the designed JRC-CWG and the DR-JRC-CWG are higher than those of the OPP-BPSK and the LFM-BPSK waveforms when $f_d = 0$. Hence, the DR-JRC-CWG has the best performance in terms of the output SNR.

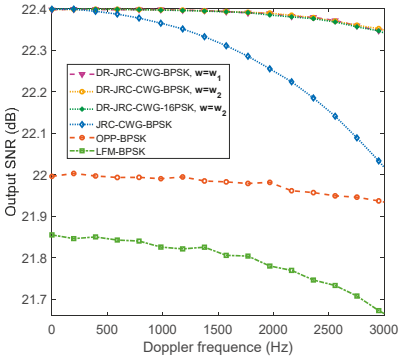

Figure 8. Output SNRs of the JRC waveforms at the radar receiver with different Doppler frequencies.

4.3. Communications Performance

In this subsection, the BER and communications rate are applied to evaluate the communications performance of the JRC waveforms.

The variations in the BER with the bit energy-to-noise power spectral density ratios (which is denoted as E_b/N_0 in Figure 9) of the JRC waveforms with the BPSK and 16-PSK modulation schemes are shown in Figure 9a,b, respectively. Moreover, the BERs of the traditional BPSK waveform and the traditional 16-PSK waveform are also illustrated in Figure 9. The OPP-16-PSK in Figure 9b denotes the OPP waveforms with 16-PSK modulation. In Figure 9a, we can see that both the designed JRC-CWG-BPSK and DR-JRC-CWG-BPSK have the same BER as the traditional BPSK waveforms. To make sure the BER is lower than 10^{-5}, the E_b/N_0 should be greater than 9.6 dB for the JRC-CWG-BPSK and DR-JRC-CWG-BPSK, greater than 11.1 dB for the OPP-BPSK waveform, and greater than 12.4 dB for the LFM-BPSK waveform. For the JRC waveforms with 16-PSK modulation in Figure 9b, the designed JRC-CWG-16-PSK and DR-JRC-CWG-16-PSK have the same BER performance as the traditional 16-PSK waveforms. To ensure that the BER is lower than 10^{-5}, the E_b/N_0 should be greater than 17.5 dB for the designed JRC-CWG-16PSK and DR-JRC-CWG-16PSK, and greater than 23.4 dB for the OPP-16-PSK. Obviously, compared with the other two JRC waveforms, the designed JRC-CWG and DR-JRC-CWG have the best communications performances in terms of BER for the same modulation scheme.

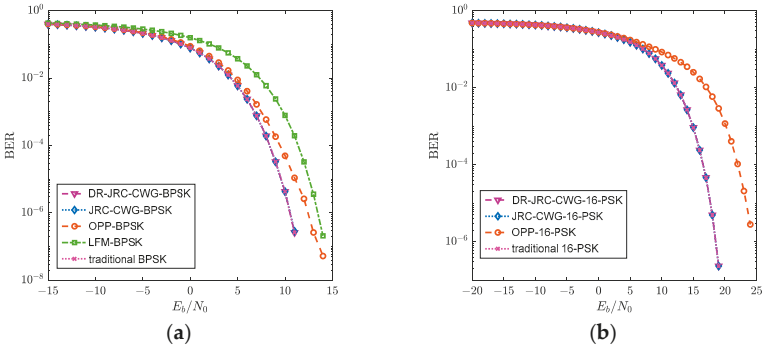

(**a**) (**b**)

Figure 9. (**a**) BERs of the JRC waveforms with BPSK modulation; (**b**) BERs of the JRC waveforms with 16-PSK modulation.

The communications rates of the JRC-CWG and the DR-JRC-CWG are given in (7). It can be seen from (7) that the communications rate of the JRC-CWG or the DR-JRC-CWG will be increased when the number of WCIs in each JRC-CWG or DR-JRC-CWG M_c is

increased. Let M be a fixed value of 16, the PRI T be 25 μs, and the length of each waveform N be 64; the relationship between the communications rate and the PSLR of the designed JRC-CWG-16-PSK and the DR-JRC-CWG-16-PSK is shown in Figure 10. According to (7), the communications rate of the designed JRC-CWG-16-PSK and DR-JRC-CWG-16-PSK is $R_b = 0.64M_c$ Mbps. It can be seen that for the designed JRC-CWG-16-PSK and DR-JRC-CWG-16-PSK, the PSLR increases as the communications rate or M_c increases. Specifically, when the communications rate is 0.64 Mbps, i.e., $M_c = 1$, the PSLRs of the designed JRC-CWG-16-PSK and the DR-JRC-CWG-16-PSK are -165.3 dB and -118.8 dB, respectively. When the communications rate is increased to 9.6 Mbps, i.e., $M_c = 15$, the PSLRs of the designed JRC-CWG-16-PSK and the DR-JRC-CWG-16-PSK are increased to -33.0 dB and -30.7 dB, respectively. Since $M = M_r + M_c$, the number of WTOs M_r in each JRC-CWG or DR-JRC-CWG will decrease when M_c increases with M being fixed. Since only the WTOs are optimized to improve the sidelobe performance of the designed JRC waveforms in the optimization problems (9) and (25), the degrees of freedom of the optimization problems will decrease when M_r decreases, which will lead to a worse PSLR performance. It can be observed that there is a trade-off between the communications rate and the PSLR of the designed JRC-CWG-16-PSK and DR-JRC-CWG-16-PSK. In practice, when designing the JRC-CWG or the DR-JRC-CWG, the trade-off curve in Figure 10 can be used to satisfy the requirements of the PSLR and the communications rate.

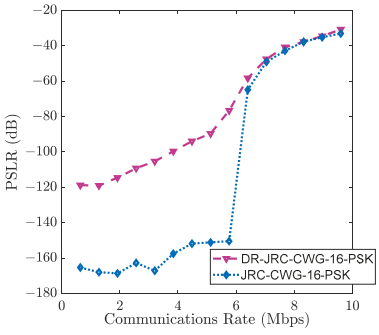

Figure 10. PSLRs of the designed JRC-CWG-16-PSK and DR-JRC-CWG-16-PSK versus communications rates.

The maximum communications rates and the corresponding PSLRs of the JRC waveforms are listed in Table 3. The simulation parameters used in Table 3 are the same as those in Figure 10. Although the OPP-16-PSK has a slightly higher communications rate than the designed JRC-CWG-16-PSK and DR-JRC-CWG-16-PSK, it has much worse performance in terms of PSLR and BER according to Figure 9b.

Table 3. Maximum communications rates and the corresponding PSLRs of the JRC waveforms.

JRC Waveform	Communications Rate (Mbps)	PSLR (dB)
DR-JRC-CWG-16-PSK	9.6	−30.72
JRC-CWG-16-PSK	9.6	−33.01
OPP-16-PSK	10.24	−17.33
LFM-BPSK	2.56	−19.27

5. Discussion

In this paper, the JRC-CWG and the DR-JRC-CWG design methods were proposed, which have low sidelobe levels and good communications performances. The designed JRC-CWG and the DR-JRC-CWG can be used for automotive JRC systems. However, the proposed methods have to make a trade-off between the radar and communications perfor-

mance. In our future work, we will try to avoid this compromise. Moreover, polarization is an important characteristic that can be considered in waveform design to improve the performance of JRC waveforms [38]. The multiple-input multiple-output (MIMO) technique is not only used in radar but also in communications, and can also be employed in JRC-CWG design in our future work.

6. Conclusions

In this paper, we designed a JRC waveform group based on CSSs called the JRC-CWG. In order to achieve better radar performance, the JRC-CWG was optimized to obtain the SACF with a low sidelobe level. However, it has poor Doppler resilience. To improve the Doppler resilience of the JRC-CWG, the DR-JRC-CWG design method was proposed. To devise the JRC-CWG and DR-JRC-CWG, the algorithm based on the framework of the FR-CG algorithm and the FFT algorithm was employed, which can be implemented using FFT to decrease the calculation complexity. Compared with the OPP waveform and LFM-BPSK waveform, the designed JRC-CWG and DR-JRC-CWG have favorable radar and communications performances.

Author Contributions: Conceptualization, H.L., Y.L. and G.L.; writing—original draft preparation, H.L.; writing—review and editing, Y.L. and Y.C.; supervision, G.L.; funding acquisition, Y.L. and G.L.; All authors have read and agreed to the published version of the manuscript.

Funding: This work was supported by the National Natural Science Foundation of China (NSFC) under Grants 62001352 and 61931016, by the Fundamental Research Funds for the Central Universities under grant no. XJS220207, and by the Foundation for Innovative Research Groups of the National Natural Science Foundation of China under grant no. 61621005.

Data Availability Statement: The data presented in this study are available on request from the corresponding author.

Conflicts of Interest: The authors declare no conflict of interest.

References

1. Dokhanchi, S.H.; Shankar, M.R.B.; Stifter, T.; Ottersten, B. OFDM-based automotive joint radar-communication system. In Proceedings of the 2018 IEEE Radar Conference, Oklahoma City, OK, USA, 23–27 April 2018.
2. Ma, Z.; Huo, Q.; Yang, X.; Zhao, X. Safety cruise control of connected vehicles using radar and vehicle-to-vehicle communi-cation. *IEEE Syst. J.* **2020**, *14*, 4602–4613. [CrossRef]
3. Dokhanchi, S.H.; Mysore, B.S.; Mishra, K.V.; Ottersten, B. A mmWave automotive joint radar-communications system. *IEEE Trans. Aerosp. Electron. Syst.* **2019**, *55*, 1241–1260. [CrossRef]
4. Kumari, P.; Gonzalez-Prelcic, N.; Heath, R.W. Investigating the IEEE 802.11ad standard for millimeter wave automotive radar. In Proceedings of the 2015 IEEE 82nd Vehicular Technology Conference, Boston, MA, USA, 6–9 September 2015.
5. Dokhanchi, S.H.; Shankar, M.R.B.; Alaee-Kerahroodi, M.; Stifter, T.; Ottersten, B. Adaptive waveform design for automotive joint radar-communications systems. In Proceedings of the 2019 IEEE International Conference on Acoustics, Speech and Signal Processing, Brighton, UK, 12–17 May 2019.
6. Paul, B.; Chiriyath, A.R.; Bliss, D.W. Survey of RF communications and sensing convergence research. *IEEE Access* **2017**, *5*, 252–270. [CrossRef]
7. Luong, N.C.; Lu, X.; Hoang, D.T.; Niyato, D.; Kim, D.I. Radio resource management in joint radar and communication: A comprehensive survey. *IEEE Commun. Surv. Tutor.* **2021**, *23*, 780–814. [CrossRef]
8. Cheng, Z.; He, Z.; Liao, B. Hybrid beamforming for multi-carrier dual-function radar-communication system. *IEEE Trans. Cogn. Commun. Netw.* **2021**, *7*, 1002–1015. [CrossRef]
9. Liu, F.; Masouros, C.; Petropulu, A.P.; Griffiths, H.; Hanzo, L. Joint radar and communication design: Applications, state-of-the-art, and the road ahead. *IEEE Trans. Commun.* **2020**, *68*, 3834–3862. [CrossRef]
10. Zhang, Q.Y.; Zhou, Y.; Zhang, L.R.; Gu, Y.B.; Zhang, J. Waveform design for a dual-function radar-communication system based on CE-OFDM-PM signal. *IET Radar Sonar Navig.* **2019**, *13*, 566–572. [CrossRef]
11. Qian, J.; Tian, F.; Huang, N.; Liu, T. Multiobjective optimization for spectral coexistence of radar and communication system. In Proceedings of the 2019 IEEE Radar Conference, Boston, MA, USA, 22–26 April 2019.
12. Ahmed, A.; Zhang, Y.D.; Gu, Y. Dual-function radar-communications using QAM-based sidelobe modulation. *Dig. Signal Process.* **2018**, *82*, 166–174. [CrossRef]
13. Zhou, S.; Liang, X.; Yu, Y.; Liu, H. Joint radar-communications co-use waveform design using optimized phase perturbation. *IEEE Trans. Aerosp. Electron. Syst.* **2019**, *55*, 1227–1240. [CrossRef]

14. Aubry, A.; De Maio, A.; Govoni, M.A.; Martino, L. On the design of multi-spectrally constrained constant modulus radar signals. *IEEE Trans. Signal Process.* **2020**, *68*, 2231–2243. [CrossRef]
15. Fan, W.; Liang, J.; So, H.C.; Lu, G. Min-max metric for spectrally compatible waveform design via log-exponential smoothing. *IEEE Trans. Signal Process.* **2020**, *68*, 1075–1090. [CrossRef]
16. Jiang, M.; Liao, G.; Yang, Z.; Liu, Y.; Chen, Y. Integrated radar and communication waveform design based on a shared array. *Signal Process.* **2021**, *182*, 107956. [CrossRef]
17. Liu, Y.; Liao, G.; Xu, J.; Yang, Z.; Zhang, Y. Adaptive OFDM integrated radar and communications waveform design based on information theory. *IEEE Commun. Lett.* **2017**, *21*, 2174–2177. [CrossRef]
18. Ciuonzo, D.; De Maio, A.; Foglia, G.; Piezzo, M. Intrapulse radar-embedded communications via multiobjective optimization. *IEEE Trans. Aerosp. Electron. Syst.* **2015**, *51*, 2960–2974. [CrossRef]
19. Hassanien, A.; Amin, M.G.; Zhang, Y.D.; Ahmad, F. Dual-function radar-communications: Information embedding using sidelobe control and waveform diversity. *IEEE Trans. Signal Process.* **2016**, *64*, 2168–2181. [CrossRef]
20. Ahmed, A.; Zhang, Y.M.D.; Himed, B. Multi-user dual-function radar-communications exploiting sidelobe control and waveform diversity. In Proceedings of the 2018 IEEE Radar Conference, Oklahoma City, OK, USA, 23–27 April 2018.
21. Jiang, Z.M.; Rihan, M.; Zhang, P.; Huang, L.; Deng, Q.; Zhang, J.; Mohamed, E.M. Intelligent reflecting surface aided du-al-function radar and communication system. *IEEE Syst. J.* **2021**, *16*, 475–486. [CrossRef]
22. Yang, J.; Cui, G.; Yu, X.; Kong, L. Dual-use signal design for radar and communication via ambiguity function sidelobe control. *IEEE Trans. Veh. Technol.* **2020**, *69*, 9781–9794. [CrossRef]
23. Liu, Y.; Liao, G.; Xu, J.; Yang, Z.; Huang, L.; Zhang, Y. Transmit power adaptation for orthogonal frequency division multi-plexing integrated radar and communication systems. *J. Appl. Remote Sens.* **2017**, *11*, 035017. [CrossRef]
24. Sit, Y.L.; Nuss, B.; Zwick, T. On mutual interference cancellation in a MIMO OFDM multiuser radar-communication network. *IEEE Trans. Veh. Technol.* **2018**, *67*, 3339–3348. [CrossRef]
25. Liu, Y.; Liao, G.; Yang, Z. Robust OFDM integrated radar and communications waveform design based on information theory. *Signal Process.* **2019**, *162*, 317–329. [CrossRef]
26. Liu, Y.; Liao, G.; Yang, Z.; Xu, J. Joint range and angle estimation for an integrated system combining MIMO radar with OFDM communication. *Multidimens. Syst. Signal Process.* **2019**, *30*, 661–687. [CrossRef]
27. Chiriyath, A.R.; Ragi, S.; Mittelmann, H.D.; Bliss, D.W. Novel radar waveform optimization for a cooperative ra-dar-communications system. *IEEE Trans. Aerosp. Electron. Syst.* **2019**, *55*, 1160–1173. [CrossRef]
28. Jiang, M.; Liao, G.; Yang, Z.; Liu, Y.; Chen, Y. Tunable filter design for integrated radar and communication waveforms. *IEEE Commun. Lett.* **2021**, *25*, 570–573. [CrossRef]
29. Zeng, Y.; Ma, Y.; Sun, S. Joint radar-communication with cyclic prefixed single carrier waveforms. *IEEE Trans. Veh. Technol.* **2020**, *69*, 4069–4079. [CrossRef]
30. Sun, S.; Xu, L.; Jeong, N. Sparse step-frequency MIMO radar design for autonomous driving. In Proceedings of the 2021 IEEE Radar Conference, Atlanta, GA, USA, 8–14 May 2021.
31. Nowak, M.J.; Zhang, Z.; Qu, Y.; Dessources, D.A.; Wicks, M.; Wu, Z. Co-designed radar-communication using linear frequency modulation waveform. *IEEE Aerosp. Electron. Syst. Mag.* **2016**, *31*, 918–923. [CrossRef]
32. Nowak, M.J.; Zhang, Z.; LoMonte, L.; Wicks, M.; Wu, Z. Mixed-modulated linear frequency modulated radar-communications. *IET Radar Sonar Navig.* **2017**, *11*, 313–320. [CrossRef]
33. Sarwate, D.V.; Pursley, M.B. Crosscorrelation properties of pseudorandom and related sequences. *Proc. IEEE* **1980**, *68*, 593–619. [CrossRef]
34. Golay, M.J.E. Complementary series. *IRE Trans. Inf. Theory* **1961**, *7*, 82–87. [CrossRef]
35. Kishigami, T.; Morita, T.; Yomo, H.; Yasugi, M.; Nakagawa, Y. Advanced wide field of view millimeter-wave radar using orthogonal complementary codes. In Proceedings of the 2014 IEEE Radar Conference, Cincinnati, OH, USA, 19–23 May 2014.
36. Akita, M.; Watanabe, M.; Inaba, T. Development of millimeter wave radar using stepped multiple frequency complementary phase code and concept of MIMO configuration. In Proceedings of the 2017 IEEE Radar Conference, Seattle, WA, USA, 8–12 May 2017.
37. Overdevest, J.; Jansen, F.; Uysal, F.; Yarovoy, A. Doppler influence on waveform orthogonality in 79 GHz MIMO phase-coded automotive radar. *IEEE Trans. Veh. Technol.* **2019**, *69*, 16–25. [CrossRef]
38. Pezeshki, A.; Calderbank, A.R.; Moran, W.; Howard, S.D. Doppler resilient Golay complementary waveforms. *IEEE Trans. Inf. Theory* **2008**, *54*, 4254–4266. [CrossRef]
39. Wang, F.; Pang, C.; Wu, H.; Li, Y.; Wang, X. Designing constant modulus complete complementary sequence with high Doppler tolerance for simultaneous polarimetric radar. *IEEE Signal Process. Lett.* **2019**, *26*, 1837–1841. [CrossRef]
40. Swerling, P. Probability of detection for fluctuating targets, IRE Trans. *Inf. Theory.* **1960**, *6*, 269–308. [CrossRef]
41. Zheng, L.; Lops, M.; Eldar, Y.C.; Wang, X.D. Radar and Communication Coexistence: An Overview. *IEEE Signal Process. Mag.* **2019**, *36*, 85–99. [CrossRef]
42. Liu, F.; Yuan, W.; Masouros, C.; Yuan, J. Radar-assisted predictive beamforming for vehicle-to-infrastructure links. In Proceedings of the 2020 IEEE International Conference on Communications Workshops, Dublin, Ireland, 7–11 June 2020.
43. Liu, F.; Cui, Y.; Masouros, C.; Xu, J.; Han, T.X.; Eldar, Y.C.; Buzzi, S. Integrated sensing and communications: Towards du-al-functional wireless networks for 6G and beyond. *IEEE J. Sel. Areas Commun.* **2022**, *40*, 1728–1767. [CrossRef]

44. Delgado, K.K. The complex gradient operator and the CR-calculus. *arXiv* **2009**, arXiv:0906.4835.
45. Nocedal, J.; Wright, S.J. *Numerical Optimization*; Springer: Berlin/Heidelberg, Germany, 2006; pp. 34–63.
46. Kumari, P.; Choi, J.; Gonzalez-Prelcic, N.; Heath, R.W. IEEE 802.11ad-based radar: An approach to joint vehicular commu-nication-radar system. *IEEE Trans. Veh. Technol.* **2018**, *67*, 3012–3027. [CrossRef]
47. Rice, M. Data-aided and non-data-aided maximum likelihood SNR estimators for CPM. *IEEE Trans. Commun.* **2015**, *63*, 4244–4253. [CrossRef]

remote sensing

MDPI

Article

A CFAR Algorithm Based on Monte Carlo Method for Millimeter-Wave Radar Road Traffic Target Detection

Bo Yang and Hua Zhang *

School of Aerospace Science and Technology, Xidian University, Xi'an 710071, China; byang_18@stu.xidian.edu.cn
* Correspondence: zhanghua@mail.xidian.edu.cn

Abstract: The development of Intelligent Transportation Systems (ITS) puts forward higher requirements for millimeter-wave radar surveillance in the traffic environment, such as lower time delay, higher sensitivity, and better multi-target detection capability. The Constant False Alarm Rate (CFAR) detector plays a vital role in the adaptive target detection of the radar. Still, traditional CFAR detection algorithms use a sliding window to find the target limit radar detection speed and efficiency. In such cases, we propose and discuss a CFAR detection method, which transforms the Monte Carlo simulation principle into randomly sampling instantaneous Range–Doppler Matrix (RDM) data, to improve the detection ability of radar for moving targets such as pedestrians and vehicles in the traffic environment. Compared with conventional methods, simulation and real experiments show that the method breaks through the reference window limitation and has higher detection sensitivity, higher detection accuracy, and lower detection delay. We hope to promote the detection application of millimeter-wave radar in road traffic scenes.

Keywords: millimeter-wave radar traffic surveillance; constant false alarm algorithm; moving target detection; Monte Carlo simulation; random sampling

Citation: Yang, B.; Zhang, H. A CFAR Algorithm Based on Monte Carlo Method for Millimeter-Wave Radar Road Traffic Target Detection. *Remote Sens.* **2022**, *14*, 17794. https://doi.org/10.3390/rs14081779

Academic Editors: Zhihuo Xu, Jianping Wang and Yongwei Zhang

Received: 19 February 2022
Accepted: 5 April 2022
Published: 7 April 2022

Publisher's Note: MDPI stays neutral with regard to jurisdictional claims in published maps and institutional affiliations.

1. Introduction

Using millimeter-wave radar as a monitoring system has recently raised increased in various fields attributed to its high detection accuracy and weather resistance. In road traffic applications, accurate acquisition of moving target information such as pedestrians and vehicles on the road is one of traffic radar's most basic and essential tasks. However, with the development of intelligent transportation systems, the timely reflection of road conditions and realization of traffic accident warnings become necessary, which puts higher requirements on the low processing delay of radar systems. Therefore, we start from the radar target detection method to reduce the system processing delay and improve the system's real-time while ensuring high monitoring performance.

Generally, a number of approaches have been proposed to improve radar performance in traffic scenes, which can be mainly classified into two categories: (1) Around the signal processing direction, reduce or eliminate the interference signal as much as possible to ensure the purity of the target signal. (2) Design better detectors.

In the field of suppressing interference signals, cutting the interference-contaminated samples out of the signal is the most direct interference suppression method. Still, it also suppresses part of the valid signal of targets, resulting in less accurate reconstruction of the cutout samples of useful signals. To alleviate this effect, an iterative matrix-pencil (MP) method-based extrapolation for interference mitigation is proposed [1], but the accuracy of the reconstructed signal will decrease with the increase of the proportion of the contaminated samples. To improve signal reconstruction accuracy, an approach based on the sparse and low-rank decomposition of the Hankel matrix is proposed [2], however, iteration and best quality selection increase the complexity of the algorithm. For dealing with inter-radar interference, some new methods are proposed, such as designing a new orthogonal noise

waveform [3] or presenting an interference mitigation technique in the tunable Q-factor wavelet transform (TQWT) domain [4]. In addition, some researchers have started from range and Doppler cell migration calibration to reduce signal distortion [5].

Designing better detectors is another direction to improve the application ability of radar. Compared with signal interference suppression, although the improvement of radar detection performance is weak, the design of the detector is more straightforward. In particular, in most cases, it will not add additional links and computational complexity, which is more suitable for low-cost radar systems with low-performance processors. So this paper studies from the perspective of detector design. In the actual application of radar, the target always appears before the complex and changeable noise background, which is subject to changes in time and location, so the fixed threshold detection method cannot effectively distinguish the target from the background noise [6]. Radar Constant False Alarm Rate(CFAR) detection, which adaptively sets the detection threshold by evaluating current clutter environments [7,8], is a crucial technology for separating targets and background. Thus, an appropriate CFAR detection algorithm can improve radar detection performance and provide accurate target information for radar data processing. It also emerged as a key research aspect in radar detection.

The earliest proposed CFAR detection algorithm is the Cell Average CFAR (CA-CFAR) [9], which is based on the average local noise power level to detect targets. Design a reference window, take the window's center unit as the candidate target, and use the amplitude accumulation value of other units in the window as the estimated value of background noise power. Whether the target exists is determined by judging the power value of the candidate target and the estimated noise power value. The CA-CFAR has poor detection performance under non-uniform noise and multi-target environments since interference signals or other targets within the reference window lead to background noise estimation error. Aiming at the problem of CA-CFAR detection performance degradation under multi-target or non-uniform noise, the maximum selection detection (GO-CFAR) [10] and the minimum selection detection (SO-CFAR) [11] are proposed. The GO-CFAR can maintain good false alarm control performance in a clutter edge environment, but "target masking" in a multi-target environment will appear. The SO-CFAR has a good multi-target resolution ability, but its false alarm control ability is weak. Ordered Statistical CFAR (OS-CFAR) [12] is another typical CFAR detection method derived from the median filter concept in digital image processing. It arranges the sample units in the reference window according to the power value and selects one of the sample power values as the decision threshold. Compared with the detection performance of CA-CFAR, OS-CFAR has strong robustness to multi-target detection, but it has a high resulting CFAR loss. Some new methods combining OS and CA are proposed. Take the trimmed-mean detector (TM-CFAR) [13] algorithm as an example. The sample points in the reference window are sorted by amplitude value like OS-CFAR. Then remove part of the sample points with the largest and smallest amplitudes. Finally, the remaining sample points are averaged as the estimated value of background noise.

Now, new CFAR detection algorithms have been proposed based on traditional methods for different application requirements. Some scholars are dedicated to studying the multi-target detection capabilities of the detector. For example, the OSCA-CFAR algorithm is proposed, which combines the CA-CFAR algorithm and the OS-CFAR algorithm, to improve the multi-target detection capability of millimeter-wave radars, and gives algorithm performance simulation under an ideal noise environment [14]. Some researchers focus on improving the detection performance of the detector in a complex cluster environment. A Comp-CFAR method is proposed according to the central limit theorem and the logarithmic compression principle of the signal for targets detection in the clutter with long smearing effect characteristics [15]. A CFAR detector based on zlog(z) is used to reduce the false alarm rate in Weibull clutter [16]. Some other scholars have proposed a new method combined with machine learning [17]. Train a feedforward artificial neural network (ANN)

on the data set containing the input and output of the CFAR sliding window to improve the efficiency of CFAR detection. However, this way increases the complexity of the algorithm.

Table 1 briefly summarizes the CFAR detection algorithms mentioned above. All current CFAR algorithms achieve target detection by designing a reference window and processing the data in the window. The design of the reference window can effectively reduce the level of clutter interference, but there are two drawbacks. One is that sliding the window reduces the efficiency of detecting objects. Especially in Linear Frequency Modulated Continuous Wave (LFMCW) radar systems, the input to the CFAR detector is a two-dimensional Range–Doppler Matrix (RDM). Although the principle of the CFAR algorithm has not changed, the sliding of the reference window has changed from a one-dimensional sliding search to a two-dimensional sliding search, which dramatically reduces the real-time performance of radar target detection. The other drawback is that the window limits the sample points for background noise estimation. Theoretically, the more sample points are used, the more accurate the estimated noise power value and the higher the CFAR detection accuracy. The design and sliding of the reference window limit the efficiency of radar target detection.

Table 1. A brief summary of the characteristics of CFAR algorithms.

CFAR Algorithms	Advantages	Disadvantages	Reference Window
CA-CFAR	High detection SNR in uniform noise	Low multi-target detection capability, High detection performance in non-uniform noise	YES
GO-CFAR	Good false alarm control in clutter edge	Low multi-target detection capability	YES
SO-CFAR	High multi-target detection capability	Low false alarm control ability	YES
OS-CFAR	Strong robustness to multi-target detection	High resulting CFAR loss	YES
OSCA-CFAR	High robust in multi-target situations, Low resulting CFAR loss	Performance degradation in non-pure noise situations	YES
Comp-CFAR	Suppression of clutter interference with long smearing effect characteristics	High algorithm complexity	YES
zlog(z)-CFAR	Reduce the false alarm rate in Weibull clutter	High algorithm complexity	YES
Machine learning	High detection accuracy	Low timeliness	YES

Fortunately, compared with the complex background environment such as the sea surface, the background noise in the traffic road is relatively simple. Especially when radar monitors moving targets, the effect of background noise data on detection can be eliminated using the de-zeroing Doppler method. Combining the non-ideal target motion (vehicle turning, braking and lane changing), the irregularity of the target reflection area, and the independence of the frame data, we consider that the moving target echoes in the traffic road obey the ideal Swerling II model. Based on the above analysis, a reference window designed for complex noise and interference reduction may not be necessary for road traffic monitoring applications where the background noise is relatively clean. Instead, the sliding window increases the algorithm's time complexity and reduces the efficiency of radar monitoring. To meet the requirement of low processing latency for traffic monitoring radar systems, we propose a CFAR algorithm based on the Monte Carlo to improve radar detection efficiency and sensitivity to moving targets in the traffic environment. Compared with the traditional algorithm, the algorithm has higher detection sensitivity and, more importantly, does not require the design and sliding of the reference window, which dramatically reduces the algorithm time complexity and improves the

detection speed and efficiency. The contributions of this paper are summarized as follows: First, in the proposed CFAR detection algorithm, the entire RDM matrix area is randomly sampled to obtain the sample points of the background noise power estimation at the current moment. The principle is converting the Monte Carlo simulation principle, which gets properties of unknown quantities by independently repeating experiments, into a random sampling of the RDM matrix domain. This way breaks through the limitation of the reference window and can increase a large number of sample points for background noise estimation. Second, an interference point filtering method improves the accuracy of background noise estimation. Sort and filter the sample points according to the amplitude value of the sample points to remove possible target points or interference points. Then, the background noise estimated power value is obtained by the mean method. Finally, the target points in the RDM matrix are extracted by the background noise estimate. In addition, the parameter setting method of the algorithm is given, i.e., according to the current physical platform and application environment, algorithm parameter values are obtained through repeated statistics. The configuration parameter process only needs to be executed once when the radar system environment is unchanged. Compared with the conventional method, simulations and practical experiments show that the method has higher detection sensitivity, higher detection accuracy, and lower detection latency, which improve radar detection efficiency in traffic surveillance.

The structure of this paper is organized as follows: The Section 2 introduces the characteristics of traffic scenes, the principle of radar detection targets, and the characteristics of radar background noise in traffic scenes. Then, in Section 3, we give the principle and model of the new CFAR detection algorithm and give the process of obtaining relevant parameters. In Section 4, we analyze the performance of the new CFAR detection algorithm through simulation and real experiments. Finally, Section 5 summarizes the conclusions of this paper.

2. Traffic Scene Overview, Radar CFAR Detection Principle, and Background Noise Analysis

2.1. Traffic Scene Overview

Usually, traffic sensors are installed on both sides of the road or on a fixed bracket extending to the center of the road (as shown in Figure 1), and they are required to have the following essential functions:

- High detection sensitivity. All targets in the field of view can be completely detected, including partial occlusion of the target;
- Low information delay capability. It can reflect road conditions in real-time, i.e., the delay between data acquisition and road conditions output is required to be as short as possible (ideally, the delay should not exceed 100 ms);
- Weather resistance. The sensor shall minimize the impact caused by night, fog, and other weather.

Millimeter-wave radar is considered to have the potential to be used in urban traffic monitoring since not affected by the environment, has high range resolution, and has low application cost. The CFAR detector as a vital part of radar target extraction has been extensively studied. By studying the traditional CFAR algorithm and analyzing the characteristics of the traffic environment, we give a new CFAR detection algorithm to improve the sensitivity of radar to target detection, multi-target detection ability, and reduce delay. We hope it provides a unique reference for enhancing the adaptability of the radar in urban traffic monitoring.

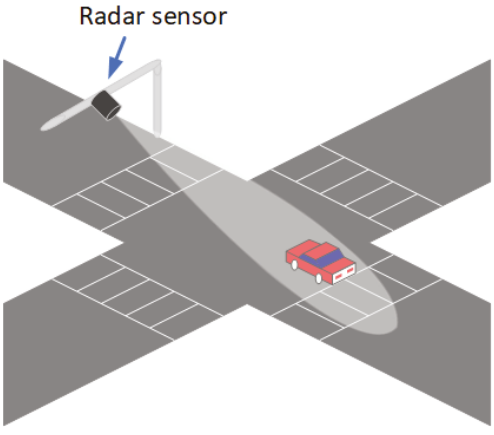

Figure 1. Traffic road scene.

2.2. Conventional Adaptive CFAR Detection Based on RDM

The FMCW millimeter-wave radar system is composed of an antenna array, a mixer, an Analog-to-Digital Converter (ADC), and digital signal processing [18]. The radar receives and processes target electromagnetic echo signals to acquire target information. The radar antenna receives the target echo information. It mixes echo information with the current transmitted signal in the mixer. The intermediate frequency signal from the mixer is converted into a digital signal by the ADC unit for signal processing. In the data processing system, the chirps signal group is processed by the Fast Fourier Transform (FFT) of the distance dimension and the velocity dimension in turn. Finally, a two-dimensional RDM containing the target position and velocity information is obtained by a single pulse linear detection [19]. The RDM data will be sent to the detection unit to achieve target extraction, usually for the constant false alarm detector. The radar signal processing flow is shown in Figure 2.

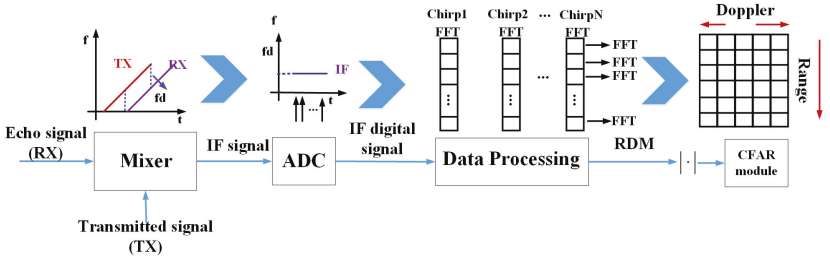

Figure 2. Radar signal processing.

The radar target detector performs a test procedure on each cell inside the RDM to distinguish between the target signal and noise based on the threshold T, where the threshold T is composed of the threshold factor α and the average noise power μ, i.e., $T = \alpha \cdot \mu$. The average noise power measures the current radar noise floor, but it will change due to temperature changes or other physical effects. Therefore, the fixed noise power estimate value will cause the detector to produce false alarms. Let H_0 means there is no target in the signal, H_1 means there is a target in the signal, and Y represents a detection cell in the RDM. According to the Neyman-Pearson criterion, the false alarm probability P_{fa} is:

$$P_{fa} = P(H_1|H_0) = P(Y > T) = \int_T^{+\infty} f(y)dy, \quad (1)$$

where $f(y)$ represents probability density function, when target radar cross-sectional area is the Swerling II model, $f(y)$ is the exponential distribution (square law detection), or Rayleigh distribution (linear detection).

The average noise power needs to be adaptively estimated to maintain a constant false alarm rate. So a CFAR detection technology based on variables in a two-dimensional RDM to estimate the average noise power adaptively is proposed. Here we introduce several typical CFAR algorithms.

Assume that the size of an RDM matrix is $M \times L$, and a reference window with a size of $n \times l$ is designed, as shown in Figure 3. The blue cell represents the detection cell ($X_{m,n}$), where m represents the position index of the detection cell X in the RDM matrix, and n represents the velocity index. The red area represents the reference window, and the CFAR detection algorithm evaluates the local average noise power based on the variables in the reference window.

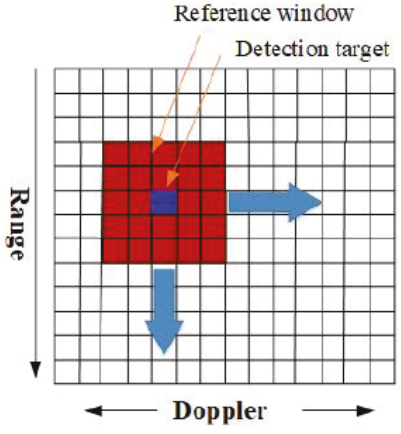

Figure 3. RDM detection matrix.

In the two-dimensional CA-CFAR algorithm [20], the unknown local noise expectation value is estimated based on the average of all variables' power in the two-dimensional reference window:

$$\mu_{CA} = \frac{1}{n \times l} \sum_{i=1}^{n} \sum_{j=1}^{l} X_{i,j}, \tag{2}$$

where μ_{CA} represents the background noise estimate value of the CA-CFAR algorithm. Then the adaptive detection threshold $T_{CA} = \mu_{CA} \cdot \alpha$ can be obtained.

The two-dimensional OS-CFAR algorithm [21] also evaluates the local noise power through the variables in the reference window. Unlike the CA-CFAR, the OS-CFAR algorithm takes out all variables in the reference window and sorts them according to their magnitude:

$$X^1 \leq X^2 \leq X^3 \leq \cdots \leq X^K \leq \cdots \leq X^{N \times M}, \tag{3}$$

The Kth value is selected as the average noise power. Then the adaptive detection threshold $T_{OS} = \mu_{OS} \cdot \alpha = X^K \cdot \alpha$ can be obtained.

The OSCA-CFAR [22] is a detection algorithm combining the CA-CFAR algorithm with the OS-CFAR algorithm. Firstly, it uses the one-dimensional OS-CFAR to sort each N Doppler unit according to the magnitude in the distance direction, as shown in Figure 4.

Then, the Kth row is selected in the Doppler direction. Finally, a CA-CFAR procedure is applied to obtain the average noise power:

$$\mu_{OSCA} = \frac{1}{l}\sum_{j=1}^{l} X_K^j, \tag{4}$$

where μ_{OSCA} represents the background noise estimate value of the OSCA-CFAR algorithm. Then the adaptive detection threshold $T_{OSCA} = \mu_{OSCA} \cdot \alpha$ can be obtained.

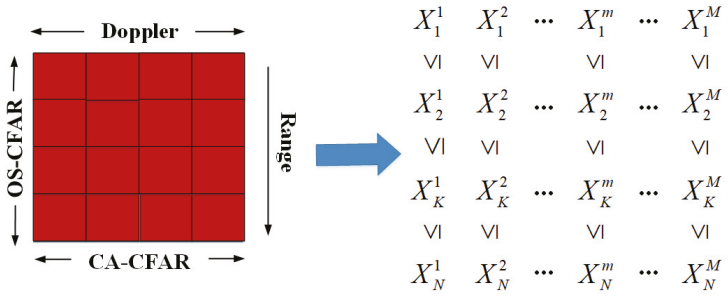

Figure 4. OSCA-CFAR detection.

The amplitude of the detection cell $(X_{m,n})$ is compared with the threshold T. If $X_{m,n} > T$, the detection cell is considered the target. Otherwise, it is noise. Then, move the reference window and perform the detection on the new cell. The reference window performs two-dimensional sliding in the RDM matrix to realize the detection of all cells. In addition, designing appropriate reference windows according to different scenarios can reduce interference and improve detection accuracy. Some typical reference windows are shown in Figure 5.

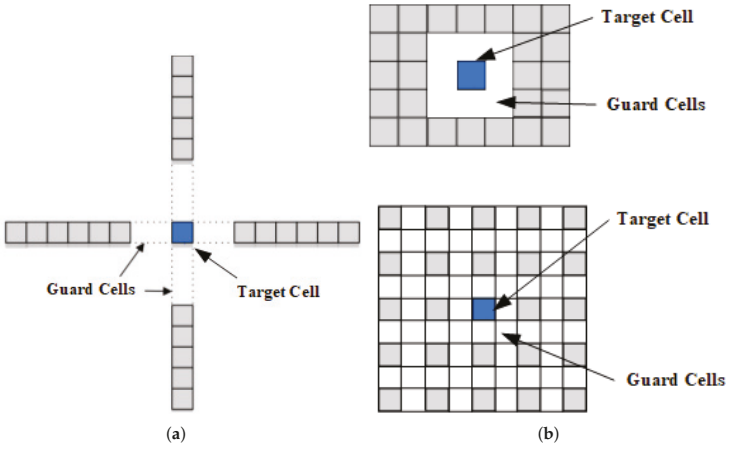

Figure 5. Typical reference window model. (**a**) Cross window. (**b**) Rectangular window.

Theoretically, the more sample points used to estimate the background noise power, the more accurate the background noise estimation will be. The design and application of the reference window prevent the introduction of interference points which is beneficial for complex environments. However, it limits the optional number of background noise sample points and increases the retrieval process. When the target and the background

environment are easily separated, or the background environment is relatively simple in some scenes, applying the reference window is not necessary.

2.3. Radar Background Noise Analysis in Traffic Scenea

To analyze the background noise characteristics of traffic roads, we collect data through a self-designed millimeter-wave radar system whose parameters are shown in Table 2. The radar chip (CAL77S244) based Radio Frequency(RF) front-end with three transmitting and four receiving antennas is used to transmit millimeter-wave and receive target echo signals. Additionally, a four-channel high-speed ADC is used for data acquisition. Finally, digital processing algorithms and extraction of target information are implemented on a back-end baseband processing system based on FPGA and ARM architecture. The data acquisition scene and radar system are shown in Figure 6.

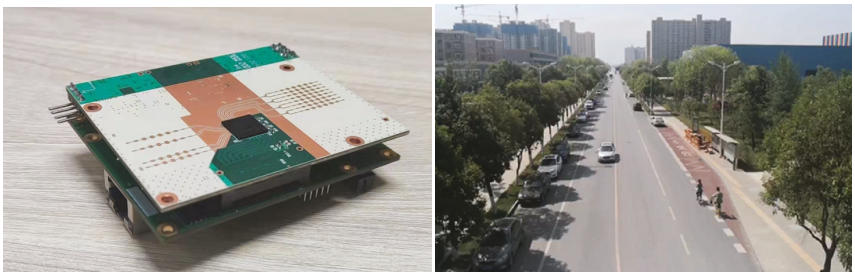

(**a**) (**b**)

Figure 6. (**a**) Radar system. (**b**) Data collection scenario.

Table 2. Radar system parameters.

Item	Parameters	Item	Parameters
Chirp number	256	Range FFT points	512
B	160 MHz	F_s	20 MHz
R_{max}	200 m	$R_{resolution}$	0.732 m
V_{max}	31.847 m/s	$V_{resolution}$	0.249 m/s

Figure 7 illustrates background noise data collection and display. Figure 7a is a flow chart of constant false alarm detection data acquisition. In this radar system, four receiving channels receive the radar's electromagnetic echoes in the background environment and obtain the RDM matrix through incoherent accumulation. Figure 7b shows the distribution of the power amplitude of the RDM under the condition with no moving targets. The power amplitude value is abrupt and uneven in the zero-Doppler region (stationary objects region), which is caused by a combination of factors such as the number of objects at different distances and the size of the object's reflection area. Preliminary observation shows that the noise power is distributed evenly in the non-zero Doppler domain (moving targets region), and there is no apparent abrupt change. In addition, the power of stationary objects does not significantly extend to the area where the moving targets are located.

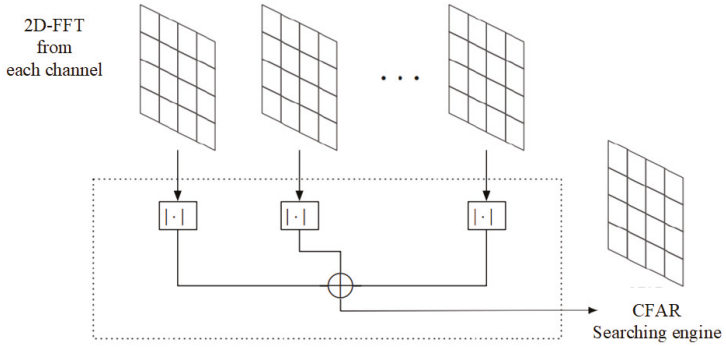

(**a**)

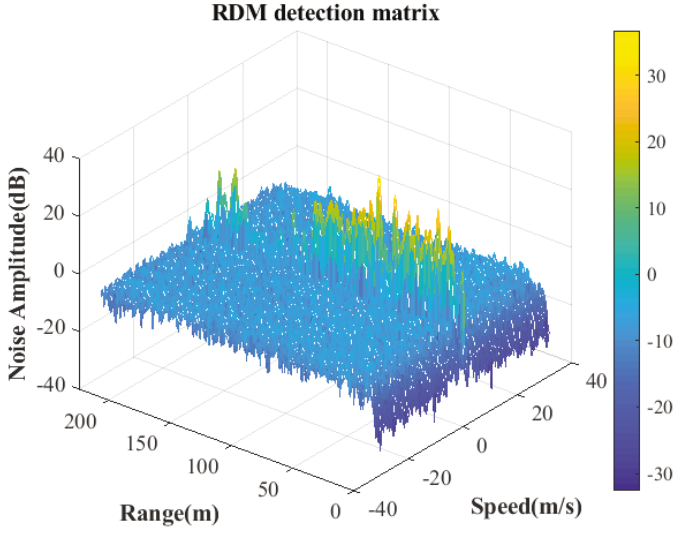

(**b**)

Figure 7. (**a**) RDM data acquisition process. (**b**) Data collection scenario.

We use distance dimension and velocity dimension data variance, an effective method to measure the degree of data dispersion, to evaluate the distribution of noise power amplitudes in the moving target area in the RDM matrix. We count the variance of each row (velocity dimension) or column (distance dimension) of the dataset in RDM as shown in Figure 8 (average of multiple statistics). It is worth noting that before calculating the variance, taking the average speed of pedestrians as a reference (0.5 m/s), we eliminated the cells where the static object is located in the RDM matrix, i.e., cells with speed below 0.5 m/s. Both the variance of the velocity dimension and the variance of the distance dimension are less than 0.018. We can think that the background noise power amplitude is relatively uniform in the non-zero Doppler domain.

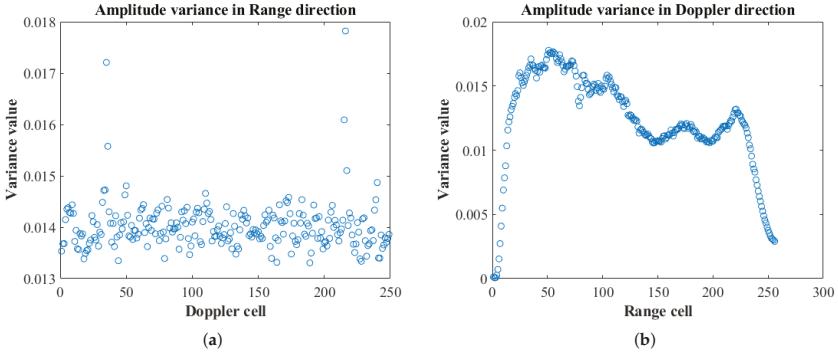

(**a**) (**b**)

Figure 8. Background noise amplitude dispersion in RDM matrix (**a**) Noise amplitude variance in range direction. (**b**) Noise amplitude variance in Doppler direction.

The power density distribution is given as another characteristic of background noise. Previously, we assumed that the radar noise distribution satisfies the Rayleigh distribution:

$$y = f(x|\sigma) = \frac{x}{\sigma^2} e^{\left(\frac{-x^2}{2\sigma^2}\right)}, \tag{5}$$

where σ is the Rayleigh distribution parameter. The non-zero Doppler cells in RDM are sampled and processed by MATLAB Distribution Fitter Toolbox, and then the distribution of data (purple) and the fitting curve of Rayleigh distribution (red) are shown in Figure 9a. Figure 9b shows the matching degree between data probability distribution and Rayleigh distribution, i.e., the closer the data is to a curve line, the more consistent it is with Rayleigh distribution.

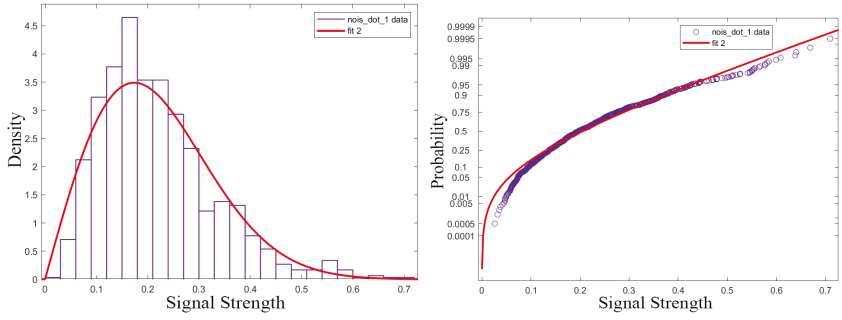

(**a**) (**b**)

Figure 9. Simulation and fitting experiment example of RDM matrix noise density function (**a**) Noise distribution curve. (**b**) Matching degree of Rayleigh distribution.

Through the analysis, we can get the following two conclusions:

- In the static target region of the RDM matrix, the variation amplitude of noise power fluctuates greatly. However, in the moving target area of the RDM matrix, the amplitude distribution of background noise power is uniform, the dispersion is small, and there is no edge effect;
- In the moving target area in the RDM matrix, the noise amplitude of each unit is independent of each other and meets the probability density distribution (Rayleigh distribution) with similar parameters.

In this scenario, we propose a Monte Carlo-based CFAR detection algorithm to improve radar monitoring efficiency by processing the entire RDM area instead of local reference window data and window sliding.

3. A CFAR Algorithm Based on Monte Carlo Sampling

3.1. Expectation Calculation Principle Based on Monte Carlo Sampling

Assuming that n samples are drawn from a population with a total number of N elements without replacement, each sample has the same probability of being sampled each time. This sampling method is called random sampling, and the sample drawn is called random sample. When each sampling process is independent of the other, the process is called Monte Carlo sampling. Monte Carlo sampling can be used to obtain the expectation of random variables.

For example, we can use Monte Carlo sampling to find the expectation of function $f(x)$ [23]. Let X denote a random variable and the probability distribution $p(x)$. To calculate the expectation of $f(x)$, we only need to continuously sample from $p(x)$:

$$E_N(f) = \frac{1}{N}\sum_{i=1}^{N} f(X_i), \tag{6}$$

where N represents the number of sample points, X_i represents the value of the ith sample point. When the sample N is large enough, the mean A is equivalent to the expectation of $f(x)$, i.e., $A = E_N(f)$. Further, we know that the Monte Carlo sampling principle obtains the statistical characteristics of parameters through many random independent experiments and uses the statistical value to replace the real result [24]. In addition, in probability theory and statistics, the expectation is related to probability distribution parameters that reflect the sample population amplitude characteristics. Therefore, obtaining unknown quantities by Monte Carlo sampling provides a new idea for calculating the average noise power in the RDM matrix.

Through the previous analysis, we approximately believe that the noise power of each detection cell in the RDM dataset follows the same probability distribution (Rayleigh distribution) with roughly the same parameters, which is also the premise of using the Monte Carlo principle. However, unlike the Monte Carlo sampling principle, we transform the independent random sampling in the time dimension into the random sampling on the RDM dataset at the current moment. For each detection unit in the RDM matrix as a random variable X, the unknown average noise power μ is considered the expected value of the function $f(x)$. The detection unit in the RDM matrix performs random sampling to obtain the estimated value of the background noise power in the moving target area at the current moment. We name this method MC-CFAR.

3.2. MC-CFAR Algorithm Model

A complete MC-CFAR processing model mainly includes background noise sample extraction part, interference point removal part, average noise estimation part, and threshold output part (as shown in Figure 10). Moreover, the processing flow of using the MC-CFAR algorithm to detect moving targets is as follows:

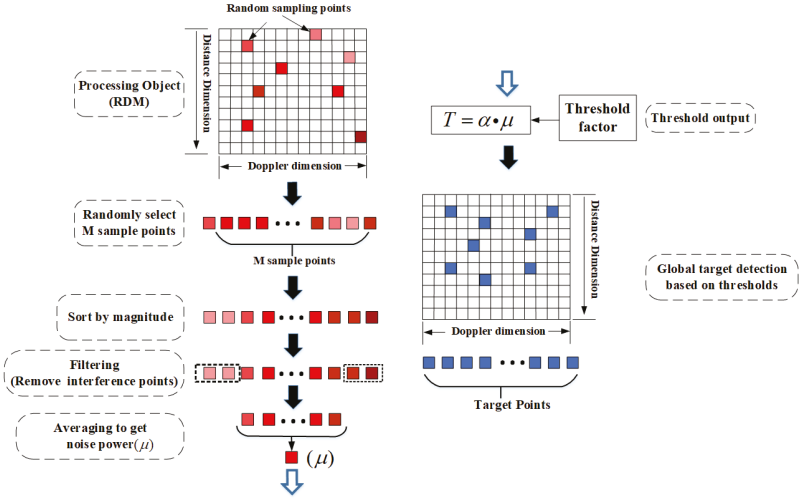

Figure 10. MC-CFAR processing model.

Step 1: Background noise sample point extraction. In the MC-CFAR algorithm, all detection units in the RDM matrix are regarded as the total sample size. Additionally, each detection cell is viewed as an individual sample to be sampled. Considering the RDM matrix as a two-dimensional coordinate system, once the scale of the RDM matrix is determined ($S_{RDM} = R \times D$), the coordinates of all detection units are also determined. Any cell can be represented as $X_{r,d}$, where r represents the distance index, $r = 1, 2, \ldots R$; d represents the speed index, $d = 1, 2, \ldots D$. Samples are drawn from the population without repetition according to specific rules, and this process is systematic random sampling. Then, M background noise sample points are obtained.

Step 2: Interference point removal. The sample points obtained in step 1 cannot be directly used to evaluate the background noise power value because the target points or abnormal points may be extracted, which will cause the background noise estimation error. Similar to the data processing method in the TM-CFAR algorithm, the sample points are first sorted according to the power amplitude:

$$X^1 \leq X^2 \leq \cdots \leq X^q \leq \cdots \leq X^{M-k} \leq \cdots \leq X_M, \tag{7}$$

Then, k maximum points and q minimum points are removed, and it is considered that the remaining $M - k - q$ sample points only contain background noise power points.

Step 3: Noise average power estimation. Average the remaining $M - q - k$ sample points, and the average value will be used as the estimated value of the current background average noise power in the RDM matrix.

$$\mu_{mc} = \frac{1}{M-k-q} \sum_{i=k}^{M-k-q} X^i, \tag{8}$$

Step 4: Threshold output. The threshold factor α_{mc} is multiplied by the average noise power estimate to get the decision threshold T:

$$T = \alpha_{mc} \cdot \mu_{mc}, \tag{9}$$

Step 5: Target detection. Each detection cell in the RDM matrix is sequentially compared with the threshold value T. If $X > T$, the target exists, otherwise, the target does not exist.

3.3. MC-CFAR Algorithm Parameter Settings

3.3.1. Random Sampling Strategy

The interference point removal link can eliminate the interference caused by abnormal points or target points to a certain extent, but it cannot completely eliminate it. A good sampling strategy can reduce the probability of the existence of interference points, reduce the burden of interference point removal, and make the estimated value of background noise more accurate.

Figure 11 shows three simple sampling strategies. When the radar monitors the slow-moving road section (urban intersections), sampling points distribution can be consciously expanded to the high-speed area (the left side of Figure 11). Similarly, when the radar monitors the high-moving road section(highway) or variable-speed road section (Mixed vehicles and pedestrians), the sampling strategy in the middle or the right side of Figure 11 can be selected, respectively.

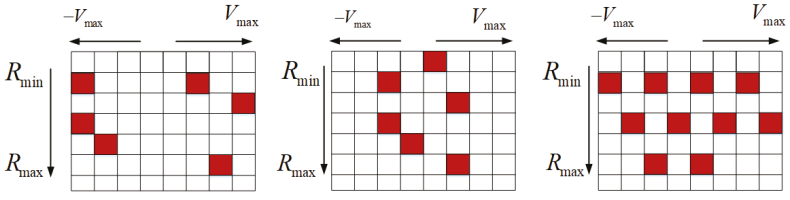

Figure 11. Three simple sampling strategies.

3.3.2. Sampling Points Number M and Threshold Factor α

The number of sampling points M and the threshold factor α_{mc} are two essential parameters in the MC-CFAR algorithm, which need to be determined before the algorithm is executed. In the MC-CFAR algorithm, the higher the number of sample points, the closer the background noise estimate is to the actual value, and the size of the threshold factor also affects the probability of the target being detected, both of which will affect the false alarm probability (P_{fa}) of the detector. Thus we determine the values of M and α_{mc} according to different P_{fa} requirements.

Different from traditional CFAR algorithms, it isn't easy to give a definite curve formula between parameters and P_{fa} in the MC-CFAR algorithm. So, we use Monte Carlo experiments to obtain approximate relationships, i.e., get the probability of false alarms under different parameters through independently repeated experiments. Figure 12 shows the relationship between the MC-CFAR algorithm parameters and P_{fa}. Moreover, the following conditions have been used for the simulation: RDM size is 256×256 with Rayleigh distribution noise; $k = \frac{1}{32}M$; Monte Carlo experiments number is 10^5 for each group parameters.

In Figure 12, when the number of sample points is small, the number of sample points is the main factor. Under the same threshold factor, the less the number of sample points, the higher the false alarm rate of the algorithm. With the increase of sample points, the false alarm rate decreases. When the number of sample points reaches a certain order of magnitude, the impact of the rise of sample points on the false alarm rate becomes smaller, and the threshold factor becomes the main factor. Then, determine MC-CFAR algorithm parameters according to different constant false alarm probabilities.

Considering the difference between the simulation experiment and the actual application, in actual application, before the radar detects the road vehicle, the Monte Carlo experiment is performed on the road environment to obtain the best MC-CFAR algorithm parameters under the radar platform. When the detection environment and platform remain unchanged, this step only needs to be performed once.

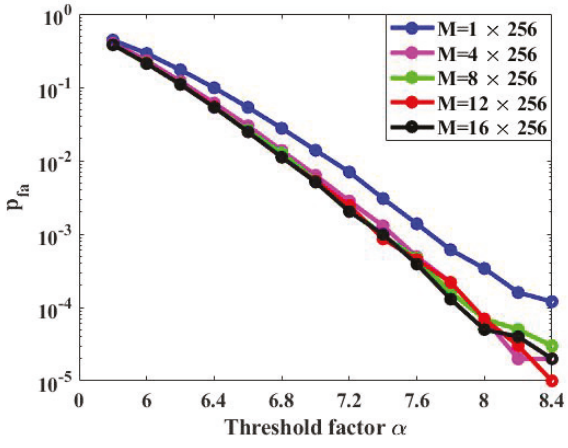

Figure 12. Relationship between threshold factor and false alarm rate in MC-CFAR.

4. Numerical Simulations and Real Experiments

This chapter presents the simulation test and actual experimental results of the algorithm. Furthermore, a comparison with the conventional CFAR algorithm is carried out in the same test environment.

4.1. Performance Simulation of MC-CFAR

According to the characteristics of the traffic scene and the requirements for the monitoring system in the application of road vehicle monitoring, we choose the algorithm detection sensitivity, algorithm multi-target detection ability, and algorithm time complexity as the key research objects. The detection performance of the MC-CFAR algorithm is evaluated by simulation and compared with the conventional algorithms (e.g., CA-CFAR, OS-CFAR, OSCA-CFAR).

4.1.1. Algorithm Detection Sensitivity

The detection sensitivity of the radar constant false alarm algorithm reflects the radar's ability to detect weak signals. The higher the detection sensitivity, the stronger the radar's ability to detect weak signals. The relationship between the detection probability P_d of the algorithm and the Signal-to-Noise Ratio (SNR) of the target echo is used to measure the detection sensitivity of the constant false alarm detection algorithm.

We use the radar system to obtain a large amount of snapshot data of traffic scenes (the radar system and traffic scene are shown in Figure 6), and these snapshot data do not contain any moving targets. The background noise data of the moving target area is obtained by summing, averaging, and de-zeroing Doppler, which will be used for simulation. Randomly insert target points with different SNR into the background noise data, and then evaluate the detection sensitivity of the algorithm by counting the number of successful detections of the algorithm. For fairness, the P_{fa} of all algorithms is unified to 10^{-4}. The number of repetitions for each SNR experiment is 10^8.

Figure 13 shows the detection probability of different algorithms for different SNR signals. In the overall trend of change, the algorithm detection probability has the same changing trend: as the target SNR increases, the detection target probability increases. In the low SNR part, the detection probability of the algorithm is generally low. Still, the detection probability of MC-CFAR is the highest, and the detection probability of MC-CFAR rises the fastest. Moreover, as the signal SNR increases, the gap between detection probabilities keeps increasing. With the further improvement of SNR, the detection probability gap between the algorithms approaches gradually. When the target SNR reaches a particular

strength, the detection probability of all algorithms reaches 100%. The MC-CFAR algorithm has the highest detection sensitivity through simulation analysis compared with other detection algorithms, primarily due to the more accurate background noise estimation and the ability to obtain more sample points. Under the same false alarm rate, MC-CFAR can detect weak SNR targets.

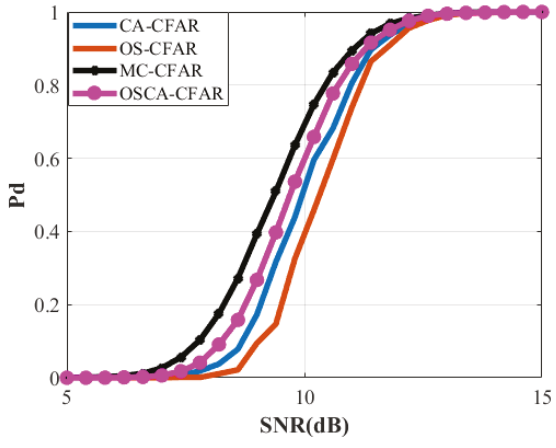

Figure 13. The relationship between detection probability and SNR.

4.1.2. Multi-target Detection Performance

The masking effect means that the distance between the targets is so close that the detection algorithm cannot detect all the targets simultaneously, making the radar detection have a high false dismissal probability in a multi-target environment.

In the simulation experiment of the multi-target detection ability of the algorithm, the SNR of each target should be as high as possible to eliminate the missed detection of the algorithm caused by low SNR. In the clutter background with a length of 200, four targets are added at 46, 48, 50, and 52 with two as the distance difference between targets; Taking 20 as the distance between the targets, add targets at 90 and 110, respectively; finally, add independent targets at 145. Under the same false alarm rate $P_{fa} = 10^{-4}$, the decision threshold of each algorithm at different positions can be obtained, as shown in the blue waveform in Figure 14.

The purpose of detecting the independent point 145 is to eliminate the interference of the target SNR on the algorithm multi-target detection performance judgment. When the distance between targets keeps shrinking, the target masking effect of CA-CFAR gradually manifests, and for targets at points 46, 48, 50, and 52, only points 46 and 52 can be detected. However, the MC-CFAR, the OS-CFAR, and the OSCA-CFAR algorithms still accurately detect four targets. In 1D distance dimension detection, the OSCA-CFAR algorithm is the same as the OS-CFAR algorithm due to the absence of the Doppler dimension, which does not affect the determination of multi-target detection capability. Through simulation analysis, the MC-CFAR has good multi-target detection capabilities.

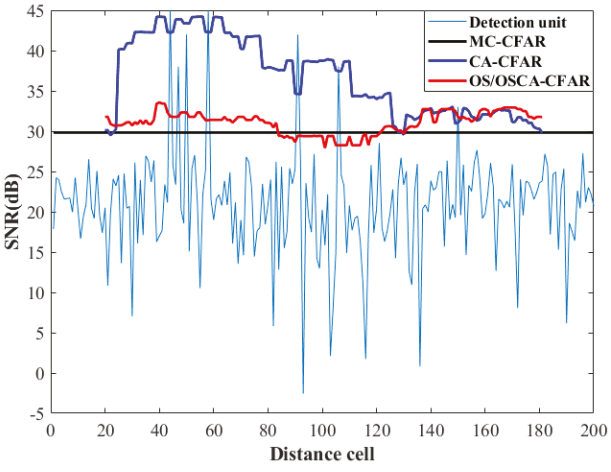

Figure 14. Multi-target detection simulation of MC-CFAR algorithm.

4.1.3. Algorithm Time Complexity

The quality of an algorithm is often measured by two aspects Two aspects often measure the quality of an algorithm: on the one hand, each input of the algorithm can output the correct result and stop; on the other hand, the efficiency of the algorithm is considered, including the time complexity [25] and space complexity of the algorithm. Suppose the size of the RDM domain is $N \times N$; For the convenience of calculation, the number of sampling points in the MC-CFAR algorithm is set to $M = \frac{1}{L}(N \times N)$, where L is an integer greater than 1. For the conventional CFAR algorithm, set the size of the sliding window to $n \times n$, where n is an integer greater than 1. The time complexity of the algorithm is shown in formula (9).

$$O(CFAR) = \begin{cases} O(N^2 n^2), & CA \\ O(N^2(n^2 \log_2 n^2)), & OS \\ O(N^2 \log_2 n + \frac{N^2}{n}), & OSCA' \\ O(\frac{N^2}{L} \log_2 \frac{N^2}{L}) + O(\frac{N^2}{L}), & MC \end{cases} \tag{10}$$

To show the low time complexity of the MC-CFRA algorithm, we set $L = 2$ in the simulation, i.e., extract half of the points of the RDM matrix. The selection of sampling points in real-time applications is much smaller than this value (refer to Figure 11). The reference window length (n) of the conventional CFAR algorithm takes a range of 12 to 18, here we let $n = 16$. The time complexity of each algorithm versus the size of the RDM matrix as shown in Figure 15. The time complexity of the OS-CFAR algorithm increases sharply with the increase of the area of the RDM detection matrix. When the number of detection units is small, the time complexity difference among MC-CFAR, CA-CFRA, and OSCA-CFAR algorithms is not apparent. However, with the increase of detection matrix area, the low time complexity of the MC-CFAR algorithm becomes more and more prominent. Compared with other algorithms, the MC-CFAR algorithm has the lowest time complexity, which reduces the time delay of the radar in traffic surveillance.

In this chapter, the performance of the MC-CFAR algorithm is simulated and analyzed from three aspects of algorithm sensitivity, multi-target detection performance, and algorithm complexity. Additionally, compared with CA-CFAR, OS-CFAR, and OSCA-CFAR algorithms, it can better meet the needs of radar applications in traffic scenarios.

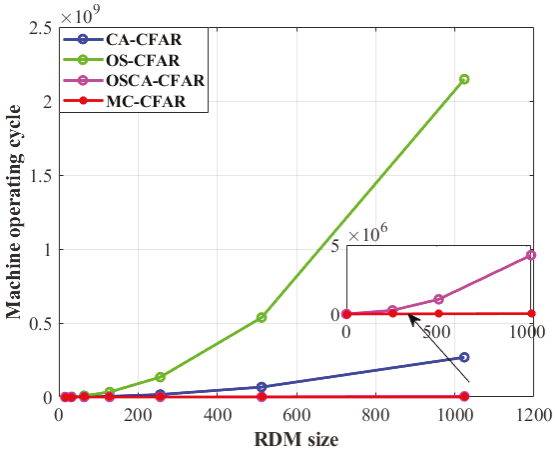

Figure 15. The relationship between the time complexity of the algorithm and the size of the detection matrix.

4.2. Real Experiments

In this chapter, we port the algorithm to the radar system platform and show the application effect of the algorithm in real traffic scenarios.

4.2.1. Define an Evaluation Method and Add a New Scenario

To better describe the algorithm's performance and evaluate the advantages and disadvantages between the algorithms, we have defined an evaluation method that is easy to statistics and operates before testing. Figure 16 shows the detection process of the CFAR detector. An RDM matrix containing two targets is sent to the CFAR detector. The coordinates (x, y, z) of the two targets are (−1.4928, 48.3398, 6.9442) and (−2.7369, 40.4297, 16.5703) respectively, where x is the target speed, y is the target distance, and z is the target power, as shown in Figure 16a. After passing through the CFAR detector (If the detection cell is the target, it is marked as 1. Otherwise, it is marked as 0), as shown in Figure 16b, the detection results are presented in two target area blocks, and there are errors between the coordinates of some points and the real target points. For example, the distance and speed of the detection points are (−1.4928, 48.3398) and (−2.2393, 39.5508), respectively. The reason for this phenomenon is that in the actual radar detection process, the energy of the target will expand to adjacent cells since the target is not an ideal pulse, which makes the detection result of the constant false alarm detector appear blocky instead of dotted.

Therefore, the 8-domain connectivity method is used for point aggregation to count the number of targets detected by the detector. Moreover, at the same time, allow the actual target coordinate value and the detection result coordinate value to have an error within 3σ, where σ is the range resolution or the radar speed resolution. Given the above description, when analyzing the detection results of each frame, this paper defines the data frame with the target number of the detection result consistent with the real number and the coordinate error within the range as a "good frame". Additionally, in the experiment, the probability of a "good frame" is used as an index to evaluate algorithm detection performance.

In addition, we add a new scenario (see Figure 17) for testing only pedestrian detection because pedestrian trajectories are random and difficult to control. The results are used to supplement and contrast the road vehicle detection experiments.

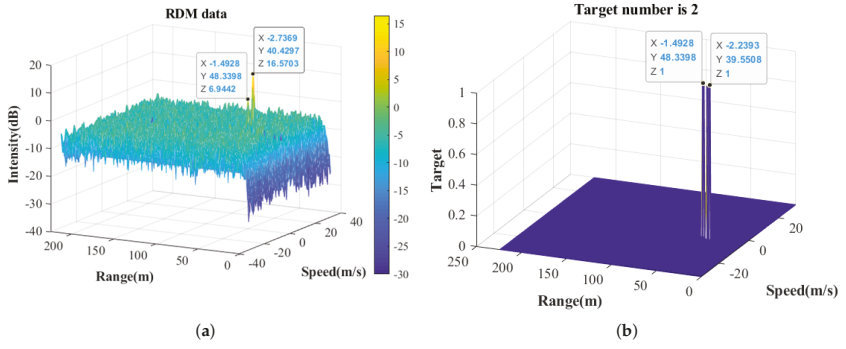

Figure 16. CFAR detection example. (**a**) RDM data. (**b**) CFAR result.

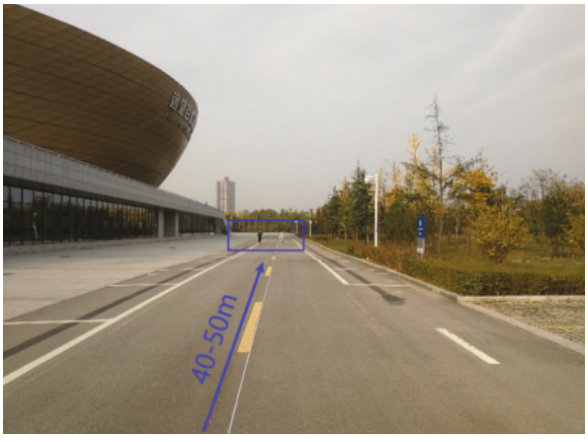

Figure 17. Additional experiments for pedestrian detection.

4.2.2. Algorithm Testing at an "Ideal Distance"

We first conduct multi-object detection experiments for each algorithm at ideal distances. Due to the difference between simulation and actual measurement, the algorithm detection performance with the same configuration parameters will fluctuate due to changes in radar system platforms or application scenarios. In order to have a fair comparison of all the methods, we need to modify the configuration parameters of each algorithm to achieve the best detection performance in the current scene and radar system. We choose the median of the maximum distances the radar platform can detect as the "ideal distance" to adjust the algorithm parameters. This scenario can minimize external factors, especially the target SNR. The radar platform parameters are shown in Table 2, and the maximum detection range of the radar system to pedestrians is 90–100 m, and the maximum detection range of the radar platform to vehicles is 180–200 m. The median detection distance is selected as the best detection distance of the radar platform for experiments. i.e., 40–50 m is considered the "ideal detection environment" for pedestrian detection, and 90–100 m is regarded as the "ideal distance" for vehicle detection.

Different algorithms are tested in the "ideal detection environment", and the detection performance of the algorithms is evaluated by "good frame" rate. Each algorithm is tested on the radar platform, and the "good frame" rate of the algorithm under different parameter configurations is shown in Figure 18. For CA-CFAR, OS-CFAR, and OSCA-CFAR, the detection effect is mainly affected by the reference window and threshold factor. Different

threshold factors and reference window sizes yield different "good frame" rates, and with this parameter configuration, the higher the good frame rate, the better the radar detection performance, as shown in Figure 18a–c. Figure 18d shows the relationship between the MC-CFAR good frame rate and the number of sampling points, and the threshold factor. For MC-CFAR, when the number of sampling points reaches a certain number, the detection performance of the algorithm is mainly affected by the threshold factor.

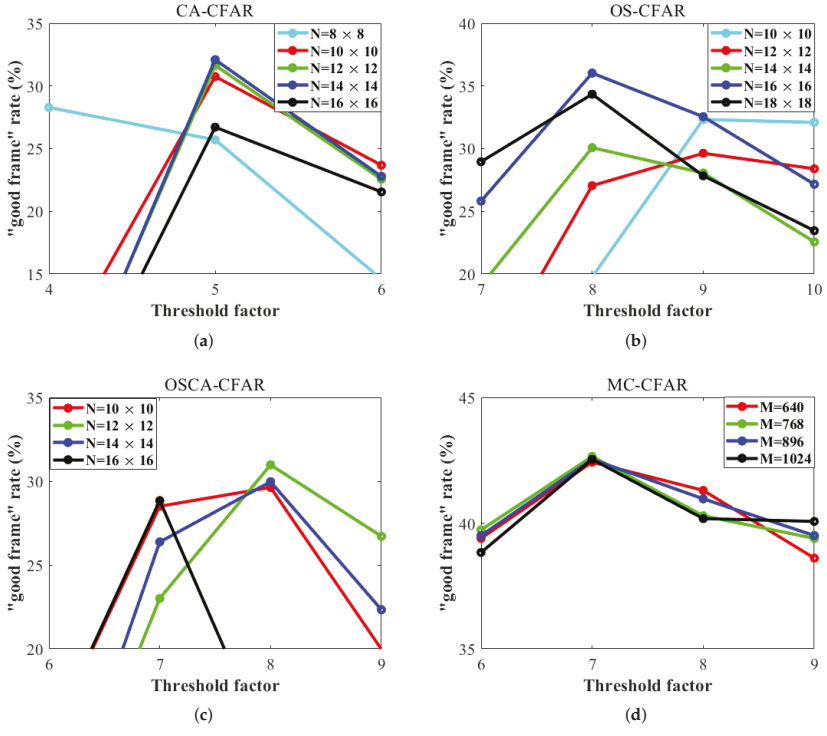

Figure 18. The relationship between algorithm performance and different parameter configurations at "ideal distance ". (**a**) CA-CFAR test results. (**b**) OS-CFAR test results. (**c**) OSCA-CFAR test results. (**d**) MC-CFAR test results.

After many experiments and statistics, the optimal parameter configuration and detection effect of different algorithms on this radar platform can be obtained, as shown in Table 3. The MC-CFAR has the best detection performance at "ideal distances" through experiments.

Table 3. Radar system parameters.

Algorithm	Window Length/Samples Number	Threshold Factor	Good Frame Rate (%)
CA-CFAR	10–14	5–6	30–33
OS-CFAR	10–16	8–10	30–33
OSCA-CFAR	10–14	7–9	28–31
MC-CFAR	384–896	6–8	40–43

4.2.3. Algorithm Detection Probability at Different Distances

This section explores how the algorithm detects objects at different distances. For fairness, we configure the optimal parameters for each detection algorithm, which are the configuration parameters when the "good frame" rate is the highest in "ideal distance" detection. The parameter selection is shown in Table 4.

Table 4. Parameter selection.

Algorithm	Window Length/Samples Number	Threshold Factor
CA-CFAR	14	5
OS-CFAR	16	8
OSCA-CFAR	12	8
MC-CFAR	768	7

In the same environment, algorithm detection experiments are carried out at different distances. The experimental results are shown in Figure 19.

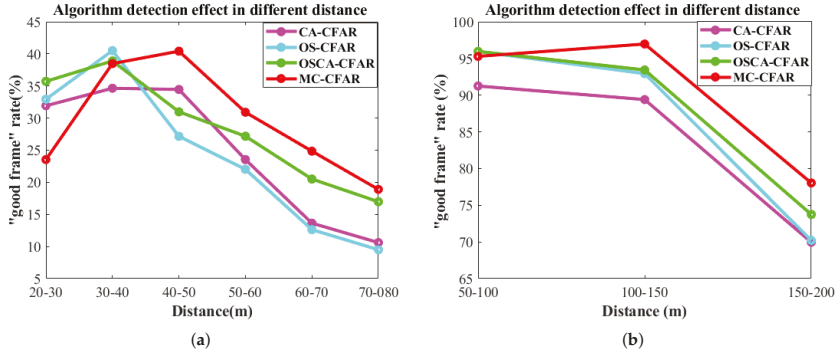

Figure 19. Algorithm testing at different distances. (**a**) Pedestrian detection results. (**b**) Vehicle detection results.

Figure 19 shows the trend of the "good frame" rate of different algorithms at different distances. Figure 19a shows the detection result of the algorithm on pedestrians. When the target is close, the OS-CFAR algorithm has the best detection performance, and the MC-CFAR detection algorithm has the worst effect. However, as the distance increases, the detection performance of the MC-CFAR algorithm gradually exceeds other algorithms and becomes the best. When the distance increases, the detection performance of all algorithms begins to decline, but MC-CFAR still maintains the best detection effect. Figure 19b shows the detection results of different algorithms on the vehicle at different distances. Consistent with the former phenomenon: when the target is close to the radar, the detection effect of MC-CFAR is poor. As the distance increases, the detection effect of MC-CFAR gradually rises and becomes the best among the algorithms.

Through the analysis of close-range target data, we preliminarily give the reasons for the decline in detection accuracy of the MC-CFAR algorithm. On the one hand, with the decrease in the distance between the target and the radar, the power of the target echo becomes stronger, which leads to a larger diffusion range of the sidelobe energy around. On the other hand, when the target is in close range, the shape of the target can not be ignored, that is, the target changes from point target to block target in the detector. Due to the different reflected energy intensity in different areas, the probability of isolated clutter points around the target will be increased. Compared with vehicles, pedestrians have more irregular shapes and generate more clutter points. The power of these clutter points

is higher than the background noise power and lower than the target main lobe energy, they are easier to be detected by MC-CFAR with the highest detection sensitivity. So the "good frame" rate of the MC-CFAR algorithm is reduced at a close distance, especially for pedestrian detection.

The experimental results show that compared with other CFAR algorithms, the MC-CFAR algorithm has higher detection sensitivity, especially for medium and long-range targets. However, the accuracy of the MC-CFAR algorithm in the detection of close-range targets is reduced, especially for the detection of irregular moving targets. Fortunately, although the false alarm rate has increased, the target information is not lost. In addition, it is worth noting that the MC-CFAR has the lowest algorithm complexity in the actual test process, as shown in Table 5.

Table 5. Algorithm running clock cycles (time complexity).

Algorithm	Clock Cycle
CA-CFAR	11,478,544
OS-CFAR	524,288
OSCA-CFAR	234,837
MC-CFAR	8448

In this chapter, the multi-target detection experiments of pedestrians and vehicles are carried out on the CFAR detection algorithm through the real radar platform. Compared with the traditional algorithm, the MC-CFAR algorithm has higher detection sensitivity and accuracy and better adapts to the traffic environment.

5. Conclusions

In this work, a CFAR algorithm based on the Monte Carlo principle is proposed for millimeter-wave radar moving targets detection in the road traffic environment. Numerical simulations and real experiments are also provided and analyzed. The algorithm has the following characteristics and advantages: (i) Random sampling of the entire RDM matrix area instead of conventional reference window design and sliding is the most significant feature of the MC-CFAR algorithm. (ii) In the road traffic environment, compared with the conventional CFAR algorithm, MC-CFAR has higher detection sensitivity because it can obtain more background noise sample points, which is attributed to the overall sampling of RDM. (iii) In particular, the MC-CFAR algorithm greatly reduces the time complexity of detection, which is of great help to improve the timeliness of radar traffic applications.

In future work, on the one hand, we study about algorithm performance improvement: (1) further analyze the reasons for the degradation of the algorithm in close-range target detection performance, reduce the false alarm rate of the algorithm close view detection, and improve the algorithm full section detection performance. (2) optimize the sample point extraction strategy and interference point suppression method to improve the algorithm robustness. On the other hand, extending the application area of the algorithm: due to the high sensitivity and low CFAR loss characteristics of the MC-CFAR algorithm, more target details can be retained when applied to target-background separation, which makes it possible to apply the algorithm to the field of radar imaging. We hope the work can provide a new idea for radar CFAR research.

Author Contributions: Conceptualization, B.Y. and H.Z.; investigation, H.Z.; writing—original draft preparation, B.Y. and H.Z.; writing—review and editing, B.Y. All authors have read and agreed to the published version of the manuscript.

Funding: This work was supported partially by the National Natural Science Foundation of China, Constellation cooperative autonomous navigation using time-varying astronomical signals in relativistic space-time (No. 61771371). And Civil aerospace technology advanced research project (No. D020403). The authors greatly appreciate the above financial support.

Data Availability Statement: Not applicable.

Conflicts of Interest: This manuscript has not been published or presented elsewhere in part or in its entirety, and is not under consideration by another journal. There are no conflicts of interest to declare.

Abbreviations

The following abbreviations are used in this manuscript:

ITS	Intelligent Transportation Systems
CFAR	Constant False Alarm Detection
RDM	Range–Doppler Matrix
ADC	Analog-to-Digital Converter
FFT	the Fast Fourier Transform
RF	Radio Frequency
SNR	Signal-to-Noise Ratio
P_{fa}	False Alarm Probability
P_{fd}	Detection Probability
CA-CFAR	Cell Average Constant False Alarm Detection
OS-CFAR	Ordered Statistical Constant False Alarm Detection
OSCA-CFAR	An algorithm to combine the CA-CFAR algorithm and the OS-CFAR algorithm
MC-CFAR	The algorithm proposed in this paper

References

1. Wang, J.; Ding, M.; Yarovoy, A. Matrix-Pencil Approach-Based Interference Mitigation for FMCW Radar Systems. *IEEE Trans. Microw. Theory Tech.* **2021**, *69*, 5099–5115. [CrossRef]
2. Wang, J.; Ding, M.; Yarovoy, A. Interference Mitigation for FMCW Radar With Sparse and Low-Rank Hankel Matrix Decomposition. *IEEE Trans. Signal Process.* **2022**, *70*, 822–834. [CrossRef]
3. Xu, Z.; Shi, Q. Interference Mitigation for Automotive Radar Using Orthogonal Noise Waveforms. *IEEE Geosci. Remote Sens. Lett.* **2018**, *15*, 137–141. [CrossRef]
4. Xu, Z.; Yuan, M. An Interference Mitigation Technique for Automotive Millimeter Wave Radars in the Tunable Q-Factor Wavelet Transform Domain. *IEEE Trans. Microw. Theory Tech.* **2021**, *69*, 5270–5283. [CrossRef]
5. Xu, Z.; Baker, C.J.; Pooni, S. Range and Doppler Cell Migration in Wideband Automotive Radar. *IEEE Trans. Veh. Technol.* **2019**, *68*, 5527–5536. [CrossRef]
6. Moustafa, A.; Ahmed, F.M.; Moustafa, K.H.; Halwagy, Y. A new CFAR processor based on guard cells information. In Proceedings of the 2012 IEEE Radar Conference, Atlanta, GA, USA, 7–11 May 2012 ; pp. 133–137.
7. Farina, A.; Studer, F.A. A review of CFAR detection techniques in radar systems. *Microw. J.* **1986**, *29*, 115.
8. Gandhi, P.; Kassam, S. Analysis of CFAR processors in nonhomogeneous background. *IEEE Trans. Aerosp. Electron. Syst.* **1988**, *24*, 427–445. [CrossRef]
9. Finn, H.M. Adaptive detection mode with threshold control as a function of spatially sampled-clutter-level estimates. *RCA Rev.* **1968**, *29*, 414–465.
10. Trunk, G. Range Resolution of Targets Using Automatic Detectors. *IEEE Trans. Aerosp. Electron. Syst.* **1978**, *AES-14*, 750–755. [CrossRef]
11. Pace, P.; Taylor, L. False alarm analysis of the envelope detection GO-CFAR processor. *IEEE Trans. Aerosp. Electron. Syst.* **1994**, *30*, 848–864. [CrossRef]
12. Rohling, H. Radar CFAR Thresholding in Clutter and Multiple Target Situations. *IEEE Trans. Aerosp. Electron. Syst.* **1983**, *AES-19*, 608–621. [CrossRef]
13. Blake, S. OS-CFAR theory for multiple targets and nonuniform clutter. *IEEE Trans. Aerosp. Electron. Syst.* **1988**, *24*, 785–790. [CrossRef]
14. Yan, J.; Li, X.; Shao, Z. Intelligent and fast two-dimensional CFAR procedure. In Proceedings of the 2015 IEEE International Conference on Communication Problem-Solving (ICCP), Guilin, China, 16–18 October 2015; pp. 461–463. [CrossRef]
15. Liu, Y.; Zhang, S.; Suo, J.; Zhang, J.; Yao, T. Research on a New Comprehensive CFAR (Comp-CFAR) Processing Method. *IEEE Access* **2019**, *7*, 19401–19413. [CrossRef]
16. Gouri, A.; Mezache, A.; Oudira, H. Radar CFAR detection in Weibull clutter based on zlog(z) estimator. *Remote Sens. Lett.* **2020**, *11*, 581–589. [CrossRef]
17. Carretero, M.V.i.; Harmanny, R.I.A.; Trommel, R.P. Smart-CFAR, a machine learning approach to floating level detection in radar. In Proceedings of the 2019 16th European Radar Conference (EuRAD), Paris, France, 2–4 October 2019; pp. 161–164.
18. Lin, J.J.; Li, Y.P.; Hsu, W.C.; Lee, T.S. Design of an FMCW radar baseband signal processing system for automotive application. *Springerplus* **2016**, *5*, 42. [CrossRef] [PubMed]

19. Liao, H.E.; Lin, G.Y.; Sheu, M.H.; Siao, S.M.; Wan, S.S. A Computation Efficiency AND-CFAR for FMCW Radar Receiver. In Proceedings of the 2013 Ninth International Conference on Intelligent Informatio Hiding and Multimedia Signal Processing, Beijing, China, 16–18 October 2013; pp. 108–112. [CrossRef]
20. Acosta, G.G.; Villar, S.A. Accumulated CA–CFAR Process in 2-D for Online Object Detection From Sidescan Sonar Data. *IEEE J. Ocean. Eng.* **2015**, *40*, 558–569. [CrossRef]
21. Villar, S.A.; Acosta, G.G.; Solari, F.J. OS-CFAR process in 2-D for object segmentation from Sidescan Sonar data. In Proceedings of the 2015 XVI Workshop on Information Processing and Control (RPIC), Cordoba, Argentina, 6–9 October 2015; pp. 1–6. [CrossRef]
22. Kronauge, M.; Rohling, H. Fast Two-Dimensional CFAR Procedure. *IEEE Trans. Aerosp. Electron. Syst.* **2013**, *49*, 1817–1823. [CrossRef]
23. Ma, H.; Liu, Y. Research Based on the Monte-Carlo Method to Calculate the Definite Integral. In Proceedings of the 2011 Third Pacific-Asia Conference on Circuits, Communications and System (PACCS), Wuhan, China, 17–18 July 2011; pp. 1–3.
24. Djurić, P.M. Monte Carlo methods for signal processing: Recent advances. In Proceedings of the 2004 12th European Signal Processing Conference, Vienna, Austria, 6–10 September 2004; pp. 853–860.
25. Xiang, W. Analysis of the Time Complexity of Quick Sort Algorithm. In Proceedings of the 2011 International Conference on Information Management, Innovation Management and Industrial Engineering, Shenzhen, China, 26–27 November 2011; Volume 1, pp. 408–410.

remote sensing

MDPI

Article

Coherent-on-Receive Synthesis Using Dominant Scatterer in Millimeter-Wave Distributed Coherent Aperture Radar

Can Liang [1,2,3], Yang Li [1,2,3,4], Xueyao Hu [1,2,3,4], Yanhua Wang [1,2,3,4,5,*], Liang Zhang [1,2,3], Min Wang [4] and Junliang Guo [4]

[1] Radar Research Laboratory, School of Information and Electronics, Beijing Institute of Technology, Beijing 100081, China
[2] Electromagnetic Sensing Research Center of CEMEE State Key Laboratory, Beijing Institute of Technology, Beijing 100081, China
[3] Beijing Key Laboratory of Embedded Real-Time Information Processing Technology, Beijing 100081, China
[4] Beijing Institute of Technology Chongqing Innovation Center, Chongqing 401120, China
[5] Advanced Technology Research Institute, Beijing Institute of Technology, Jinan 250300, China
* Correspondence: wyhlucky@bit.edu.cn

Abstract: The target signal-to-noise ratio (SNR) can be notably improved by coherent-on-receive synthesis (CoRS) in distributed coherent aperture radar (DCAR). A core challenge of CoRS is to estimate the coherent parameters (CPs), including time, frequency, and phase, in order to cohere the multi-radar within DCAR. Conventional methods usually rely on the target's own information to estimate the CPs, which is not available in highly dynamic environments. Additionally, the CPs of different targets, especially the phase, are unequal in high-frequency systems. This means that we cannot directly use the CPs of one target to compensate for others. To address these issues, an adaptive CoRS method using the dominant scatterer is proposed for millimeter-wave (MMW) DCAR in this paper. The basic idea is to correct the CPs of the dominant scatterer to compensate for other targets. The novelty lies in the adaptive phase compensation based on the estimated CPs. This phase compensation depends on a series of discrete phase values, which are derived from the limit of synthesis loss within a given configuration. Hence, this method avoids the requirement of prior information or massive searches for the possible locations of other targets. Moreover, the dominant scatterer in this work is an unknown target with strong scattering points in radar detection scenarios, and we focus on analyzing its selection criteria. To validate the proposed method, a prototype system has been fabricated and evaluated through experiments. It is demonstrated that the multi-target can realize CoRS effectively, thus enhancing the target SNR.

Keywords: coherent-on-receive synthesis; distributed coherent aperture radar; coherent parameters; dominant scatterer

Citation: Liang, C.; Li, Y.; Hu, X.; Wang, Y.; Zhang, L.; Wang, M.; Guo, J. Coherent-on-Receive Synthesis Using Dominant Scatterer in Millimeter-Wave Distributed Coherent Aperture Radar. *Remote Sens.* **2023**, *15*, 1505. https://doi.org/10.3390/rs15061505

Academic Editors: Zhihuo Xu, Jianping Wang and Yongwei Zhang

Received: 19 January 2023
Revised: 26 February 2023
Accepted: 6 March 2023
Published: 8 March 2023

1. Introduction

Distributed coherent aperture radar (DCAR), which is composed of several independent unit radars, has potential for radar detection, tracking, and recognition [1–3]. These unit radars can be placed in different positions and used together in a coherent and cooperative way to enhance the target energy significantly.

A typical mode of DCAR is coherent-on-receive synthesis (CoRS) [4–6]. With this mode, DCAR could promote the target signal-to-noise ratio (SNR) by M^2 times, where M is the number of unit radars. In CoRS, the multiple-unit radars rely on hardware for synchronization and transmit orthogonal signals [7–9]. This hardware allows the target echoes to be separated at each receiver. By analyzing these echoes, we can estimate the coherent parameters (CPs) between different unit radars, including transmission time, frequency, and phase [10,11]. The estimated CPs can then be used to carefully adjust the echoes so that the echoes can be added together at the same time and phase. The synthesis performance

of DCAR depends on high-accuracy CP estimations. Moreover, the demands for estimation accuracy also increase with the radar carrier frequency and bandwidth. Therefore, the majority of the research on CoRS is focused on the low-frequency system [12–14].

To align the time and phase between unit radars, hardware-based methods have been investigated in the literature [15–18]. They utilize wired or wireless connections to obtain high-precision synchronization. However, these methods commonly require highly complex hardware. Additionally, even with almost ideal synchronization, real-time monitoring and calibration are still required in practical applications because of hardware instability.

Estimating the CPs based on observed target echoes is an effective way to solve the above problems. Existing estimation methods can be roughly divided into two categories. One is detecting the target's own peak in returns for estimations [19,20], and the other is utilizing a cooperative target with prior information, called the dominant scatterer [21,22]. However, these methods are quite limited in highly dynamic scenarios. The former will fail when all scattering points of the target are undetectable, and the premise of the latter, requiring prior information, is hardly valid in many applications. Furthermore, using the estimated CPs of one target, the phases of other targets may still not be aligned in multiple-unit radars. This is caused by the spatial phase between different targets, which can be neglected in previous low-frequency systems. In high-frequency systems, such as millimeter-wave (MMW), the spatial phase may vary significantly, so we cannot directly use the estimated CPs of one target to compensate for the others.

In this paper, a novel CoRS method is proposed to solve the above issues for MMW DCAR. The basic idea is to correct the CPs of the dominant scatterer to compensate for other targets. Unlike the previous works that use a pre-positioned corner reflector or active backscatter transponder as the dominant scatterer, the proposed method employs an unknown target with strong scattering points to estimate the CPs in radar detection scenarios. For the dominant scatterer, we focused on analyzing its selection criteria and procedure. Furthermore, an adaptive phase compensation approach was explored to correct the estimated CPs of the dominant scatterer. This approach can compensate for the phases of different targets using a series of discrete phase values. Different from the general approaches that compensate the phases by searching for the possible positions of other targets point-by-point, the determination of discrete phase values in this approach is derived by the limit of synthesis loss within a given MMW DCAR configuration. This approach can simultaneously align the phase of targets located in a certain region based on the phase relationship between multiple unit radars. Hence, it can significantly reduce the number of phase compensations searches and remove the need for the spatial position of other targets. Finally, a prototype system composed of three MMW radars with a common trigger was fabricated, and the proposed concepts were confirmed via measurements with this prototype system. The main contributions in this work can be summarized as follows:

1. We first introduce the coherent-on-receive synthesis into the millimeter-wave distributed coherent aperture radar. This method can be widely used in millimeter-wave radar applications, such as autonomous driving and precision guidance;
2. An adaptive compensation approach is proposed to correct the estimated CPs of the dominant scatterer. On the one hand, prior information about the dominant scatterer is not required, and we can choose an unknown target with strong scattering points to estimate the CPs in radar detection scenarios. On the other hand, there is also no need for the spatial position of other targets as prior information;
3. The proposed MMW DCAR can be adaptively cohered based on observed target echoes, thus reducing the hardware demands for high-accuracy synchronization.

The remainder of this paper is organized as follows. In Section 2, we introduce the workflow and signal model of CoRS in DCAR. In Section 3, the proposed method is described and derived in detail. Moreover, its constraints are also analyzed to present the selection criteria of the dominant scatterer. In Section 4, the proposed method's evaluation via simulations is reported. Section 5 illustrates the real-data results with a prototype

system to verify the feasibility of the proposed method. Finally, we conclude this paper with a summary of the main outcomes in Section 6.

2. Background

2.1. Workflow of CoRS in DCAR

The distributed coherent aperture radar (DCAR) is composed of M unit radars. An M^2 SNR gain could be obtained over a unit radar when coherence-on-receive synthesis (CoRS) is realized, which makes it capable of attaining the equivalent performance compared with a large aperture radar.

There are three steps, including system hardware synchronization, coherent parameters estimation, and cohere-on-receive synthesis, in the operation procedure of CoRS, as displayed in Figure 1. The workflow can be illustrated as follows:

1. The multiple-unit radars within DCAR rely on wired or wireless connections to ensure that they can operate at the same time.
2. Due to the imperfect synchronization and the unequal range between different unit radars and targets, there are multidimensional differences between any two radars, called coherent parameters (CPs). To solve this problem, the multiple unit radars transmit the orthogonal waveforms with the same time base, which allows the target echoes to be separated at each receiver's matched filter output. By detecting the target peaks in different echoes, the CPs can be estimated.
3. The estimated CPs are used to adjust the echoes of multiple unit radars, and then the adjusted echoes are added together with the same time and phase to obtain the SNR gain.

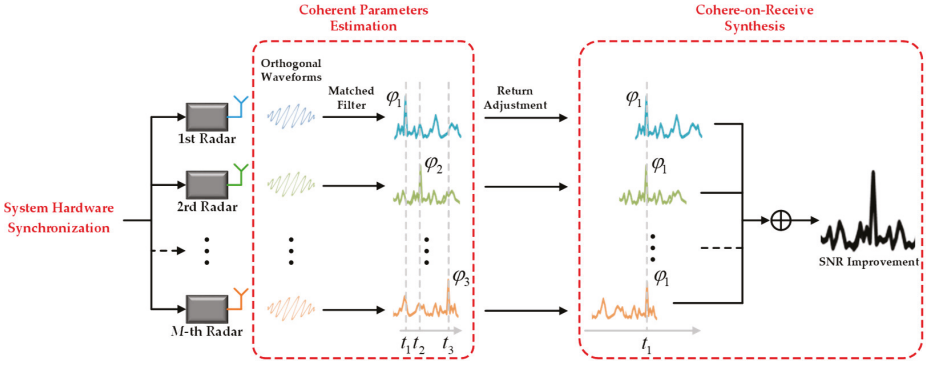

Figure 1. The workflow diagram of CoRS in DCAR.

2.2. Signal Model

Multiple-unit radars transmit the orthogonal waveforms to guarantee that mixed echoes can be separated at the receivers. The basis waveform in this work is the fast chirp sequence [23–27], where a series of chirp signals is successively transmitted in one coherent processing interval (CPI). With the basis waveform, various orthogonal techniques have been reviewed in [28], such as time division, frequency division, and code division.

The frequency-division method limits the available bandwidth for each transmitter as well as the range resolution [29,30]. Moreover, its intermediate frequency (IF) should have a large bandwidth to hold the mixer output, resulting in high hardware costs. The code-division method modulates different phase sequences on the transmission pulses [31–33]. Due to its imperfect orthogonality, this waveform will have relatively high sidelobes in the spectrum. The high sidelobes may reduce the estimation accuracy of coherent parameters, resulting in an overall loss of synthesis.

Considering the above issues, we recommend using the time-division method. This method is simple, but the unambiguous Doppler range will be reduced. To solve this problem, staggered PRT or multiple PRT approaches can be used to estimate the ambiguity number [34,35]. These approaches have a good performance in resolving velocity ambiguity, yet have a relatively low data rate. Additionally, the time-division method will also receive interference signals from other radars in many applications, such as traffic scenarios. Although the parameters of the signals may be different, they may produce non-phase-referenced interference, which will limit the performance of CoRS. In this regard, interference mitigation approaches [36–39] can be employed to solve this issue. Based on these approaches, we can first estimate the interfering signal. Then, after removing the estimated interference, the radar echoes can be restored with sparsity-based techniques.

Utilizing the time-division method, as shown in Figure 2, in a single chirp duration, only one unit radar transmits a linear chirp of the form:

$$s(t) = exp\left[j2\pi\left(f_0 t + \frac{1}{2}kt^2\right)\right], \tag{1}$$

with carrier frequency f_0, frequency slope $k = B/T$, where B is the sweep bandwidth and T represents pulse repetition time (PRT).

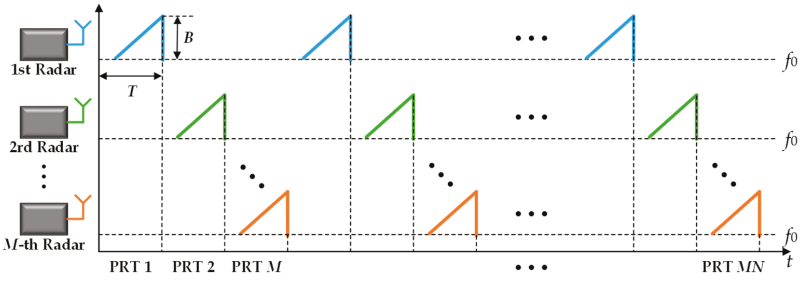

Figure 2. The fast chirp sequence waveform used in the MMW DCAR with time-division method.

Since the proposed MMW DCAR only relies on a common trigger for synchronization, it leads to multidimensional synchronization errors between any two unit radars. Assuming that the synchronization errors of the m-th radar, compared with the reference radar (the first radar), include time synchronization error ΔT_m, frequency synchronization error Δf_m, and phase synchronization error $\Delta\varphi_m$, the echo of the m-th transmitting radar and the n-th receiving radar can be expressed as

$$s_{mn}(t) = \exp\left[j2\pi\left((f_0 + \Delta f_{mn})(t - \tau_{mn}) + \frac{1}{2}k(t - \tau_{mn})^2\right) + j\Delta\varphi_{mn}\right], \tag{2}$$

with

$$\tau_{mn} = \frac{R_{mn} + v_{mn}t}{c} + \Delta T_{mn} \tag{3}$$

$$\Delta T_{mn} = \Delta T_m - \Delta T_n \tag{4}$$

$$\Delta f_{mn} = \Delta f_m - \Delta f_n \tag{5}$$

$$\Delta\varphi_{mn} = \Delta\varphi_m - \Delta\varphi_n \tag{6}$$

where R_{mn} and v_{mn} represent the sum of the propagation distance and radial velocity of the target, and c is the speed of light.

Further, the beat signal can be obtained with de-chirp processing as

$$s_{beat,mn}(t) = exp\left[j2\pi\left((f_0 + \Delta f_{mn})\tau_{mn} + k\tau_{mn}t - \frac{1}{2}k(\tau_{mn})^2\right) + j\Delta\varphi_{mn}\right]. \tag{7}$$

Supposing $t = t_s + t_p$, where t_s is the sampling time in PRT and $t_p = p \times$ PRT denotes the velocity dimension sampling time, the beat signal can be modified as

$$s_{beat,mn}(t_s,t_p) = exp\left\{ j2\pi \left[\begin{array}{l} \left(\frac{kR_{mn}+f_0v_{mn}+\Delta f_{mn}v_{mn}-kv_{mn}\Delta T_{mn}+kv_{mn}t_s}{c} + k\Delta T_{mn} - \Delta f_{mn}\right)t_s \\ +\left(\frac{f_0v_{mn}+\Delta f_{mn}v_{mn}-kv_{mn}\Delta T_{mn}+kv_{mn}t_s}{c}\right)t_p \\ +\left(\frac{(f_0+\Delta f_{mn}+k\Delta T_{mn})R_{mn}}{c} + (f_0+\Delta f_{mn})\Delta T_{mn} - \frac{k\Delta T_{mn}^2}{2}\right) - \frac{k}{2}\left(\frac{R_{mn}+v_{mn}t_s+v_{mn}t_p}{c}\right)^2 \end{array} \right] + j\Delta\varphi_{mn} \right\}. \quad (8)$$

Note that the quadratic phase terms within the beat signal have been neglected because their contribution to the phase change is small, referring to [22]. Further, the beat signal can be simplified as

$$s_{beat,mn}(t_s,t_p) = exp\left[j2\pi\left(\Phi_s t_s + \Phi_p t_p + \Phi_C\right)\right] \cdot exp[j\Delta\varphi_{mn}], \quad (9)$$

where

$$\Phi_s = k\Delta T_{mn} - \Delta f_{mn} + \frac{kR_{mn} + f_0 v_{mn}}{c} \quad (10)$$

$$\Phi_p = \frac{f_0 v_{mn} + \Delta f_{mn} v_{mn} - k v_{mn}\Delta T_{mn}}{c} \quad (11)$$

$$\Phi_C = \frac{f_0 R_{mn} + \Delta f_{mn} R_{mn} - k R_{mn}\Delta T_{mn}}{c} + (f_0 + \Delta f_{mn})\Delta T_{mn}. \quad (12)$$

The classical signal model with the time-division method was derived. Usually, the sampled data are stacked together in a cube according to the fast time and slow time. Hence, the range and velocity of the targets are separately extracted with a two-dimensional fast Fourier transform (2D-FFT) from this data cube, which can be expressed as

$$\begin{aligned} S_{mn}(f_r,f_v) &= \mathcal{F}\left[s_{beat,mn}(t_s,t_p)\right] \\ &= sinc(f_r - \Phi_s)\cdot sinc(f_v - \Phi_p)\cdot exp[j2\pi(\Phi_C)]\cdot exp[j\Delta\varphi_{mn}], \end{aligned} \quad (13)$$

where $\mathcal{F}[\cdot]$ represents the 2D-FFT processing.

Clearly, the target can be focused on the range–Doppler spectrum; however, there is an uncertain deviation caused by the synchronization errors. To estimate the deviations in range or the Doppler spectrum, we can detect the target peak in different echoes. However, the phase deviation, as in Equation (12), which is proportional to the radar carrier frequency, is related to the target's spatial position and the synchronization errors. Therefore, it may vary significantly for different targets in high-frequency systems. This means that the available region for estimating CPs of phases is quite limited. When we compensate the phases using the CPs of one target, the phases of other targets cannot be aligned, leading to a great CoRS loss.

3. Proposed Method

To solve the above problem, a novel coherent-on-receive synthesis method using the dominant scatterer is proposed, and its processing flow is presented in Figure 3.

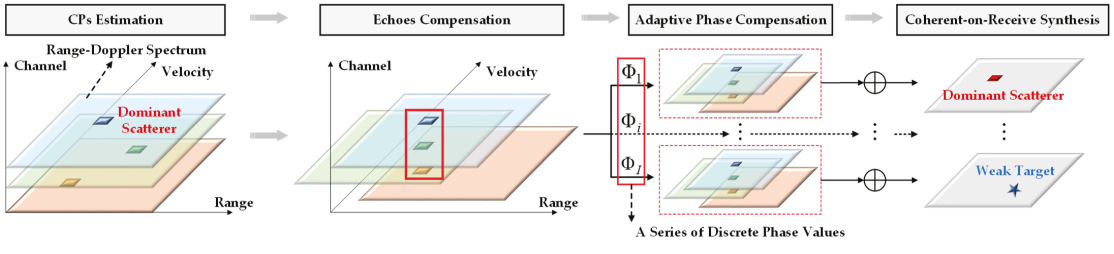

Figure 3. The processing flow of the proposed method using the dominant scatterer.

First, the proposed method uses the dominant scatterer to estimate CPs, in which the dominant scatterer is realized as an unknown strong target in radar detection scenarios.

Second, the echoes of multiple unit radars can be compensated with the estimated CPs of the dominant scatterer. In this way, the range and velocity of different targets in multiple unit radars can be aligned, but the phase requires further adjustment.

Third, an adaptive compensation approach was explored to align the phases of various targets in multiple unit radars. The phases of different targets are compensated with discrete phase values. Unlike the general approaches that compensate the phases by searching for the possible positions of other targets point-by-point, the determination of discrete phase values in this work is derived by the limit of synthesis loss within a given MMW DCAR configuration. This approach can simultaneously align the phase of targets located in a certain region based on the phase relationship between multiple unit radars. Hence, it can significantly reduce the number of phase compensation searches, and there is no need for the spatial position of other targets.

Furthermore, we derived the constraints of the proposed method and focused on analyzing the selection criteria and procedure of the dominant scatterer. The theoretical CoRS gain is also deduced to evaluate the performance of the proposed method in practice.

3.1. CP Estimation Using Dominant Scatterer

According to the focusing positions, we can estimate the CPs using the dominant scatterer. In previous works, the dominant scatterer was realized as a pre-positioned corner reflector or active backscatter transponder, which is hardly valid in high-dynamic scenarios. Instead, the dominant scatterer in this work is defined as an unknown target with strong scattering points in radar detection scenarios, such as vehicles, signs, etc.

The specific estimation method is similar to conventional methods. Assuming that channel 1T1R is the reference channel, which consists of the first transmitting and receiving radar, according to Equation (9), the beat signal in channel 1T1R without synchronization errors can be derived and simplified as

$$s_{beat,11}(t_s, t_p) = exp\left\{ j2\pi \left[\left(\frac{f_0 v_{11}}{c} + \frac{kR_{11}}{c} \right) t_s + \frac{f_0 v_{11}}{c} t_p + \frac{f_0 R_{11}}{c} \right] \right\}. \tag{14}$$

Correspondingly, the estimated CPs for time can be obtained as

$$\Delta \hat{T}_{mn} = \Delta T_{mn} - \frac{\Delta f_{mn}}{k} + \frac{R_{mn} - R_{11}}{c} + \frac{f_0 (v_{mn} - v_{11})}{ck}. \tag{15}$$

Similarly, the estimated CPs for velocity can be calculated as

$$\Delta \hat{V}_{mn} = \frac{v_{mn} - v_{11}}{2} + \frac{\Delta f_{mn} v_{mn}}{2f_0} - \frac{k v_{mn}}{2f_0} \Delta T_{mn}. \tag{16}$$

Moreover, the CPs for phase can also be estimated as

$$\Delta \hat{\varphi}_{mn} = 2\pi \left[(f_0 + \Delta f_{mn}) \Delta T_{mn} + \frac{f_0 (R_{mn} - R_{11})}{c} + \frac{(\Delta f_{mn} - k \Delta T_{mn}) R_{mn}}{c} \right] + \Delta \varphi_{mn}. \tag{17}$$

3.2. Echoes Compensation and Analysis

Using the estimated CPs, as in Equations (15) to (17), the beat signal can be compensated as

$$s'_{beat,mn}(t_s, t_p) = s_{beat,mn}(t_s, t_p) \cdot exp(-j2\pi k \Delta \hat{T}_{mn} \cdot t_s) \cdot exp(-j2\pi k f_0 \Delta \hat{V}_{mn} \cdot t_p) \cdot exp(-j\Delta \hat{\varphi}_{mn}). \tag{18}$$

After compensation, the multidimensional parameters can be aligned with the reference channel. This means that the echoes can be added together to enhance the SNR of the dominant scatterer. However, due to the spatial difference, the compensated signal of other weak targets may have deviations. These deviations may lead to a great synthesis loss of

weak targets. Therefore, we carefully derive the deviations and present an analysis thereof in the following.

Assuming that the CPs of a weak target can be estimated, the ideal compensated signal can be aligned to the reference channel and is expressed as

$$s'_{beat,mn}(t_s,t_p)|_{DS\to WT} = exp\left[j2\pi\left(\left(\frac{f_0 v_{11}|_{WT}}{c}+\frac{kR_{11}|_{WT}}{c}\right)t_s+\frac{f_0 v_{11}|_{WT}}{c}t_p+\frac{f_0 R_{11}|_{WT}}{c}\right)\right], \tag{19}$$

where $R_{11}|_{WT}$ and $v_{11}|_{WT}$ denote the range and velocity of the weak target in reference channel.

Due to the lack of the estimated CPs of the weak target, we can only utilize the CPs of the dominant scatterer to compensate for the beat signal. In this way, the compensated signal can be derived as

$$\begin{aligned} s'_{beat,mn}(t_s,t_p)|_{DS\to WT} &= s_{beat,mn}(t_s,t_p)|_{WT}\cdot exp(-j2\pi k\Delta\hat{T}_{mn}\cdot t_s)\cdot exp(-j2\pi k f_0\Delta\hat{V}_{mn}\cdot t_p)\cdot exp(-j\Delta\hat{\varphi}_{mn}) \\ &= exp\left\{ j2\pi\left[\begin{array}{l}\left(\frac{k(R_{mn}|_{WT}-R_{mn}|_{DS}+R_{11}|_{DS})}{c}+\frac{f_0(v_{mn}|_{WT}-v_{mn}|_{DS}+v_{11}|_{DS})}{c}-\frac{k(v_{mn}|_{WT}-v_{mn}|_{DS})\Delta T_{mn}}{c}\right)t_s \\ +\left(\frac{f_0(v_{mn}|_{WT}-v_{mn}|_{DS}+v_{11}|_{DS})}{c}+\frac{(\Delta f_{mn}-k\Delta T_{mn})(v_{mn}|_{WT}-v_{mn}|_{DS})}{c}\right)t_p \\ \frac{f_0(R_{mn}|_{WT}-R_{mn}|_{DS}+R_{11}|_{DS})}{c}+\frac{(\Delta f_{mn}-k\Delta T_{mn})(R_{mn}|_{WT}-R_{mn}|_{DS})}{c}\end{array}\right]\right\}. \end{aligned} \tag{20}$$

Comparing Equations (19) and (20), it is apparent that the results including range, velocity, and phase are shifted. Specifically, the deviations can be calculated as

$$\Delta R_{mn}|_{DS\to WT} \approx \frac{R_{mn}|_{WT}-R_{mn}|_{DS}+R_{11}|_{DS}-R_{11}|_{WT}}{2}, \tag{21}$$

$$\Delta V_{mn}|_{DS\to WT} \approx \frac{v_{mn}|_{WT}-v_{mn}|_{DS}+v_{11}|_{DS}-v_{11}|_{WT}}{2}, \tag{22}$$

$$\Delta\varphi_{mn}|_{DS\to WT} = 2\pi\left(\frac{f_0(R_{mn}|_{WT}-R_{mn}|_{DS}+R_{11}|_{DS}-R_{11}|_{WT})}{c}+\frac{(\Delta f_{mn}-k\Delta T_{mn})(R_{mn}|_{WT}-R_{mn}|_{DS})}{c}\right). \tag{23}$$

Herein, the range and velocity deviations are simplified because the neglected terms are much smaller than the reserved ones, which can be expressed as follows.

$$\frac{f_0(v_{mn}|_{WT}-v_{mn}|_{DS}+v_{11}|_{DS}-v_{11}|_{WT})}{c}-\frac{k(v_{mn}|_{WT}-v_{mn}|_{DS})\Delta T_{mn}}{c} \ll \frac{k(R_{mn}|_{WT}-R_{mn}|_{DS}+R_{11}|_{DS}-R_{11}|_{WT})}{c}, \tag{24}$$

$$\frac{k(v_{mn}|_{WT}-v_{mn}|_{DS})\Delta T_{mn}}{c} \ll \frac{f_0(v_{mn}|_{WT}-v_{mn}|_{DS}+v_{11}|_{DS}-v_{11}|_{WT})}{c}. \tag{25}$$

Obviously, the deviations in range and velocity are caused by the geometry of the target relative to multiple unit radars. It is difficult to further compensate them due to the lack of a weak target position. In this regard, we define the constraints for dominant scatterer compensation so that these two deviations cannot exceed half a resolution cell after compensation. The specific derivation and analysis are presented in Section 3.4.

The phase deviation, as in Equation (23), is composed of two terms. The former is only determined by multi-target spatial positions, and the latter is a coupling term with the spatial positions and the synchronization errors. Similarly, it is difficult to accurately compensate for the phases due to the lack of weak target information. Moreover, the phase deviation is proportional to the radar carrier frequency. It will vary significantly for different targets in the MMW system, and hence is required to be adjusted for effective CoRS.

3.3. Adaptive Compensation for Phases

To align the phases of different targets in multi-channels, an adaptive compensation method is proposed. Considering that the phase deviation is composed of two terms, we performed two-step compensations to align the phases in multi-channels.

First, we utilized the information and CPs of the dominant scatterer to compensate for the coupling term, which is composed of the spatial positions and the synchronization errors. Thereafter, due to the lack of weak target information, we propose to compensate the

phase adaptively with discrete phase values. The determination of discrete phase values is derived from the limit of synthesis loss within a given MMW DCAR configuration. Hence, this approach can simultaneously align the phase of targets located in a certain region based on the phase relationship between multiple unit radars. It can significantly reduce the compensation number and remove the need of the spatial position of weak targets.

3.3.1. Compensation for Coupling Term

To eliminate the coupling term of phase deviation, the signal of each channel can be compensated with the CPs of the dominant scatterer and can be expressed as

$$S_{corr}(f_r, f_v) = \mathcal{F}\left[s'_{beat,mn}(t_s, t_p)\big|_{DS\to WT}\right] \cdot exp\left(-j2\pi\left(\frac{k(\mathbf{R}_{unit} - R_{mn}|_{DS})\Delta\hat{T}_{mn}}{c}\right)\right). \quad (26)$$

where $\mathbf{R}_{unit} = [R_1,\ R_2, \cdots,\ R_{\max}]$ represents the cells in range spectrum.

After compensating for the coupling term, the phase deviation of the weak target can be derived as

$$\begin{aligned} \Delta\varphi'_{mn}|_{DS\to WT} &= \Delta\varphi_{mn}|_{DS\to WT} - 2\pi\left[\frac{k(R_{mn}|_{WT} - R_{mn}|_{DS})\Delta\hat{T}_{mn}}{c}\right] \\ &= 2\pi\left[\begin{array}{l}\frac{f_0(R_{mn}|_{WT} - R_{mn}|_{DS} + R_{11}|_{DS} - R_{11}|_{WT})}{c} \\ + \frac{k(R_{mn}|_{WT} - R_{mn}|_{DS})^2}{c^2} + \frac{f_0(R_{mn}|_{WT} - R_{mn}|_{DS})(v_{mn}|_{WT} - v_{mn}|_{DS})}{c^2}\end{array}\right] \\ &\approx 2\pi\left[\frac{f_0(R_{mn}|_{WT} - R_{mn}|_{DS} + R_{11}|_{DS} - R_{11}|_{WT})}{c}\right]. \end{aligned} \quad (27)$$

Herein, it is apparent that the compensated phase deviation only relies on the multi-target spatial positions.

3.3.2. Compensation for Spatial Phase

Although the compensated phase deviation is only related to the multi-target positions, aligning the phases of weak targets is a challenging task. On the one hand, we cannot obtain prior information on weak targets to compensate the phase directly. On the other hand, compensating via searching for the possible positions of the weak targets leads to a large number of compensations. To this end, we propose to compensate the phase adaptively with discrete phase values, which are derived by the limit of synthesis loss within a given MMW DCAR configuration.

First, in a given configuration, the relative relationships of the compensated phase deviations of the weak targets within multi-channel are derived. Second, we define the acceptable synthetic gain loss and construct an inequality equation from this loss. Finally, the phase tolerance is deduced by solving the inequality equation. The phase tolerance is a discrete phase value, which can be defined as the maximum acceptable phase difference between any two channels. According to this tolerance, we can adjust the phases of multi-channel adaptively with the relative relationship. The specific derivation of this approach is described as follows.

The compensated phase deviation in channel mTnR in Equation (27) can be rewritten as

$$\Delta\varphi'_{mn}|_{DS\to WT} = 2\pi\left(\frac{f_0(R_m|_{WT} + R_n|_{WT} - R_m|_{DS} - R_n|_{DS} + 2R_1|_{DS} - 2R_1|_{WT})}{c}\right), \quad (28)$$

where $R_i|_{DS}$ and $R_i|_{WT}$ represent the one-way propagation range from dominant scatterer and weak target to i-th radar.

In a given MMW DCAR configuration, the relative relationship of the compensated phase deviations can be derived as

$$\begin{cases} \Delta\varphi'_{1n}|_{DS\to WT} = \Delta\varphi'_{n1}|_{DS\to WT} \\ \Delta\varphi'_{mn}|_{DS\to WT} = \Delta\varphi'_{1m}|_{DS\to WT} + \Delta\varphi'_{1n}|_{DS\to WT} \\ \Delta\varphi'_{nn}|_{DS\to WT} = 2\times\Delta\varphi'_{1n}|_{DS\to WT}. \end{cases} \tag{29}$$

Thereafter, we analyzed and derived the signal power after CoRS. Herein, it is assumed that multi-channel signals after compensation have the same amplitude and only the phase deviations. For the MMW DCAR composed of N unit radars, the signal power of N^2 channels after CoRS can be expressed as

$$\begin{aligned} P_{CoRS} &= [exp(j\Delta\varphi'_{11}|_{DS\to WT}) + \cdots + exp(j\Delta\varphi'_{mn}|_{DS\to WT}) + \cdots + exp(j\Delta\varphi'_{NN}|_{DS\to WT})]^2 \\ &= \left[\sum_{m=1}^{N}\sum_{n=1}^{N} exp(j\Delta\varphi'_{mn}|_{DS\to WT})\right]^2 \\ &= \left|\left[\sum_{m=1}^{N} exp(j\Delta\varphi'_{1m}|_{DS\to WT})\right]\times\left[\sum_{n=1}^{N} exp(j\Delta\varphi'_{1n}|_{DS\to WT})\right]\right|^2 \\ &= \left[\sum_{m=1}^{N} exp(j\Delta\varphi'_{1m}|_{DS\to WT})\right]^4. \end{aligned} \tag{30}$$

Correspondingly, the theoretical signal power after synthesis, in which each channel is aligned to the reference channel, can be denoted as

$$P_{Opt} = \left[\sum_{m=1}^{N}\sum_{n=1}^{N}[exp(j\Delta\varphi'_{11}|_{DS\to WT})]\right]^2 = N^4. \tag{31}$$

Due to the phase deviations, there is a certain gain loss. We define the acceptable synthetic gain loss as P_{GL}, which can be expressed as

$$\begin{aligned} & P_{CoRS} \geq P_{Opt} - P_{GL} \\ \Leftrightarrow\ & \left[\sum_{m=1}^{N} exp(j\Delta\varphi'_{1m}|_{DS\to WT})\right]^4 \geq \left(10^{-P_{GL}/10}\right)\times N^4 \\ \Leftrightarrow\ & \left[\sum_{m=1}^{N} exp(j\Delta\varphi'_{1m}|_{DS\to WT})\right]^2 \geq \left(10^{-P_{GL}/20}\right)\times N^2. \end{aligned} \tag{32}$$

According to the Euler formula, it can be rewritten as

$$\begin{aligned} & \left[\sum_{m=1}^{N} exp(j\Delta\varphi'_{1m}|_{DS\to WT})\right]^2 \geq \left(10^{-P_{GL}/20}\right)\times N^2 \\ \Leftrightarrow\ & \left[\left(\sum_{m=1}^{N} cos(\Delta\varphi'_{1m}|_{DS\to WT})\right) + j\left(\sum_{m=1}^{N} sin(\Delta\varphi'_{1m}|_{DS\to WT})\right)\right]^2 \geq \left(10^{-P_{GL}/20}\right)\times N^2 \\ \Leftrightarrow\ & N + \sum_{m=1}^{N}\sum_{n\neq m}^{N} cos(\Delta\varphi'_{1m}|_{DS\to WT} - \Delta\varphi'_{1n}|_{DS\to WT}) \geq \left(10^{-P_{GL}/20}\right)\times N^2. \end{aligned} \tag{33}$$

By solving the inequality equation, Equation (33), we can obtain a certain phase tolerance. This tolerance is defined as the maximum acceptable phase difference between any two channels and can be derived as

$$\begin{aligned} & \forall m,n,\left(N^2-N\right)cos(\Delta\varphi'_{1m}|_{DS\to WT} - \Delta\varphi'_{1n}|_{DS\to WT}) \geq \left(10^{-P_{GL}/20}\right)\times N^2 - N \\ \Rightarrow\ & \forall m,n,|\Delta\varphi'_{1m}|_{DS\to WT} - \Delta\varphi'_{1n}|_{DS\to WT}| \leq arccos\left(\frac{\left(10^{-P_{GL}/20}\right)\times N-1}{N-1}\right) = \varphi_{Tole}. \end{aligned} \tag{34}$$

This phase tolerance is a discrete phase value, that is used to guide the compensation of each channel. For an arbitrary channel, we can cyclically compensate a phase value to satisfy

the derived tolerance. Within the phase region $[-\pi, \pi]$, the number of compensations can be denoted as

$$Num_{correct} = \lceil \pi / \varphi_{Tole} \rceil, \tag{35}$$

and the value for each compensation can be expressed as

$$\varphi_{correct} = \frac{2k_{\varphi}\pi}{\lceil \pi / \varphi_{Tole} \rceil}, k_{\varphi} = 0, 1, \cdots, \lceil \pi / \varphi_{Tole} \rceil - 1. \tag{36}$$

It should be noted that only the channels from 1T2R to 1T*N*R are required to be compensated. Owing to the relationship, as in Equation (29), the remaining channels can be compensated adaptively. Therefore, the total number of compensations for N unit radars can be deduced as

$$Num_{All} = (Num_{correct})^{N-1} = (\lceil \pi / \varphi_{Tole} \rceil)^{N-1}. \tag{37}$$

Utilizing the proposed method, the phases of the weak target can be aligned in one of the sets of compensations. This method can simultaneously align the phase of targets located in a certain region based on the phase relationship between multiple unit radars. Hence, it can significantly reduce the number of compensations, and there is no need for the spatial position of other targets.

3.4. Selection of Dominant Scatterer

The dominant scatterer in this work is defined as an unknown target with strong scattering points in radar detection scenarios, such as vehicles, signs, etc. Its selection may directly affect the synthetic performance of other targets. Therefore, we focused on analyzing the selection criteria and procedure of the dominant scatterer.

The constraints of the proposed method will vary with the positions of the dominant scatterer, and the synthetic gain of weak targets also relies on the dominant scatterer's SNR. In this regard, we defined the constraints using the dominant scatterer and performed the simulations on the influence of the dominant scatterer position and SNR. The selection criteria and procedure can be obtained from the results.

3.4.1. Analysis of Constraints

In Section 3.2, we derived and analyzed the deviations in range and velocity after compensation using the dominant scatterer. These two deviations may lead to the failure of the proposed method. This means that the compensations using the dominant scatterer are valid for a certain region, as depicted in Figure 4. Specifically, we defined the constraint that the deviations could not exceed half of a resolution cell after compensation.

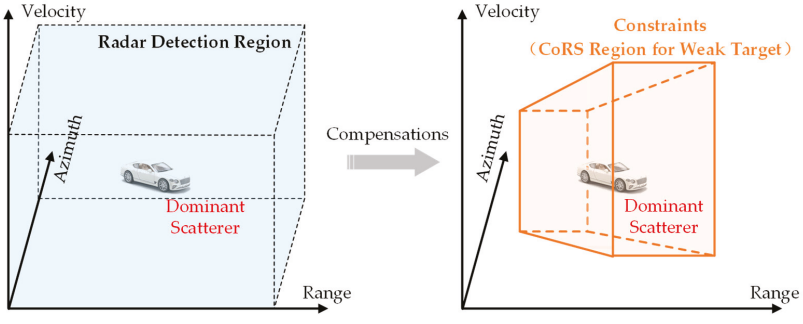

Figure 4. Conceptual diagram of constraints for the compensation using the dominant scatterer.

For the purpose of simplification, the MMW DCAR used in this work was considered a rigid system. Namely, the relative motion states of multi-unit radars can be considered

constant. On this basis, a typical scenario composed of the MMW DCAR and two targets is displayed in Figure 5. The specific constraints in this scenario are derived as follows.

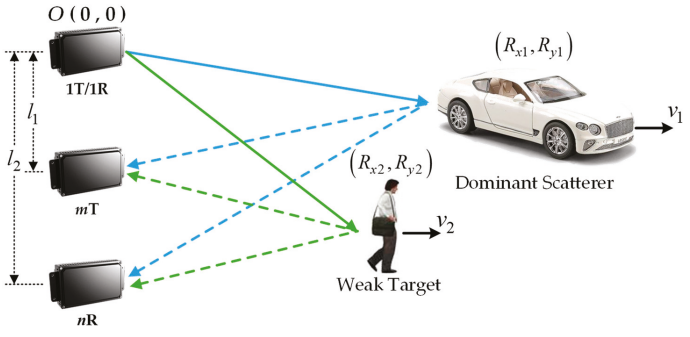

Figure 5. Geometric diagram of the DCAR and multi-target.

The compensated signals of the weak target should be focused on the same range cell in each channel, which can be expressed as

$$\Delta R_{mn}\Big|_{DS\to WT} = \left|\frac{R_{mn}|_{WT} - R_{mn}|_{DS} + R_{11}|_{DS} - R_{11}|_{WT}}{2}\right| \le \frac{R_{res}}{2}, \tag{38}$$

where R_{res} represents the range resolution. As shown in Figure 5, the coordinates of the weak target are required to meet the first constraint, which can be further deduced as

$$\left|\begin{array}{c}\sqrt{(R_{x2}-l_1)^2+R_{y2}^2}+\sqrt{(R_{x2}-l_2)^2+R_{y2}^2}-2\sqrt{R_{x2}^2+R_{y2}^2}\\ -\sqrt{(R_{x1}-l_1)^2+R_{y1}^2}-\sqrt{(R_{x1}-l_2)^2+R_{y1}^2}+2\sqrt{R_{x1}^2+R_{y1}^2}\end{array}\right| \le R_{res}. \tag{39}$$

Similarly, the compensated signal must be focused on the same velocity cell, which can be denoted as

$$\Delta V_{mn}|_{DS\to WT} = \left|\frac{v_{mn}|_{WT} - v_{mn}|_{DS} + v_{11}|_{DS} - v_{11}|_{WT}}{2}\right| \le \frac{V_{res}}{2}, \tag{40}$$

where V_{res} represents the velocity resolution. Then, we can derive the second constraint for the weak target as

$$\left|\begin{array}{c}\left(\frac{R_{y2}}{\sqrt{(R_{x2}-l_1)^2+R_{y2}^2}}+\frac{R_{y2}}{\sqrt{(R_{x2}-l_2)^2+R_{y2}^2}}-\frac{2R_{y2}}{\sqrt{R_{x2}^2+R_{y2}^2}}\right)v_2\\ -\left(\frac{R_{y1}}{\sqrt{(R_{x1}-l_1)^2+R_{y1}^2}}+\frac{R_{y1}}{\sqrt{(R_{x1}-l_2)^2+R_{y1}^2}}-\frac{2R_{y1}}{\sqrt{R_{x1}^2+R_{y1}^2}}\right)v_1\end{array}\right| \le V_{res}. \tag{41}$$

Furthermore, due to the shift of the range spectrum caused by the synchronization errors, the proposed method requires that the multi-target in all channels must be within the observation region after translation, which can be denoted as

$$\forall m, n, 0 < \hat{R}_{mn} < R_{max}, \tag{42}$$

where R_{max} is the maximum observation in the range spectrum. Hence, the third constraint can be derived as

$$\forall m, n, \begin{cases} R - \left|\frac{c\Delta T_{mn}}{2} - \frac{c\Delta f_{mn}}{2k}\right| > 0 \\ R + \left|\frac{c\Delta T_{mn}}{2} - \frac{c\Delta f_{mn}}{2k}\right| < R_{max} \end{cases} \Leftrightarrow \left|\frac{c\Delta T_{mn}}{2} - \frac{c\Delta f_{mn}}{2k}\right| < R < R_{max} - \left|\frac{c\Delta T_{mn}}{2} - \frac{c\Delta f_{mn}}{2k}\right|. \tag{43}$$

In summary, the compensations for weak targets are valid for a certain region that relies on the position and velocity of the dominant scatterer. We performed the simulations on this in the next subsection to analyze the selection criteria for the dominant scatterer.

3.4.2. Selection Criteria

We performed the simulations to determine the influence of the dominant scatterer position and SNR. The selection criteria and procedure can be obtained from the results.

The comparison tests are composed of four scenarios in which the dominant scatterer is located in different positions, as given in Table 1. Moreover, the parameters of the MMW DCAR configuration and the weak target traversal region are presented in Table 2.

Table 1. Parameters of the dominant scatterer position.

Parameters	Test 1	Test 2	Test 3	Test 4
Cross range	0 m	−10 m	0 m	0 m
Radial range	60 m	60 m	150 m	60 m
Velocity	20 m/s	20 m/s	20 m/s	−5 m/s

Table 2. Parameters of the MMW DCAR configuration and weak target.

	Parameter	Value
MMW DCAR	Carrier frequency	77 GHz
	Range resolution	0.5 m
	Velocity resolution	0.3 m/s
	Number of radars	3
	Radar spacing	0.3 m/0.2 m
Weak Target	Traversal region in cross range	[−15 m 15 m]
	Traversal region in radial range	[10 m 210 m]
	Traversal region in velocity	[−10 m/s 10 m/s]
	Traversal interval in cross range	0.15 m
	Traversal interval in radial range	1 m
	Traversal interval in velocity	0.2 m/s

According to Equations (21) and (22), the deviations in range and velocity are calculated and depicted in Figures 6–9. The effective regions, satisfying the constraint that the deviations cannot exceed half of a resolution cell after compensation, are also presented. The part marked in red corresponds to the effective region, which covers the majority of radar detection scenarios. This means that the proposed method can be effectively adapted to many applications.

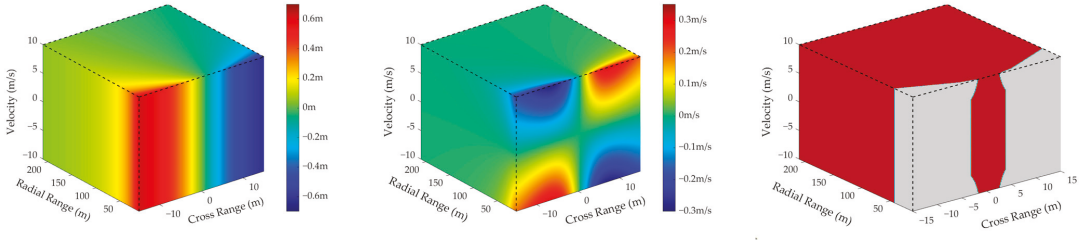

(**a**) (**b**) (**c**)

Figure 6. The simulation results of Test 1. (**a**,**b**) display the range and velocity deviations. (**c**) represents radar detection scenario, including effective region (red) and ineffective region (gray).

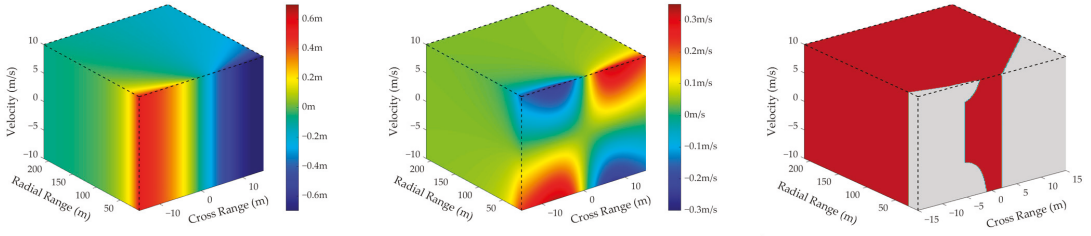

(**a**) (**b**) (**c**)

Figure 7. The simulation results of Test 2. (**a**,**b**) display the range and velocity deviations. (**c**) represents radar detection scenario, including effective region (red) and ineffective region (gray).

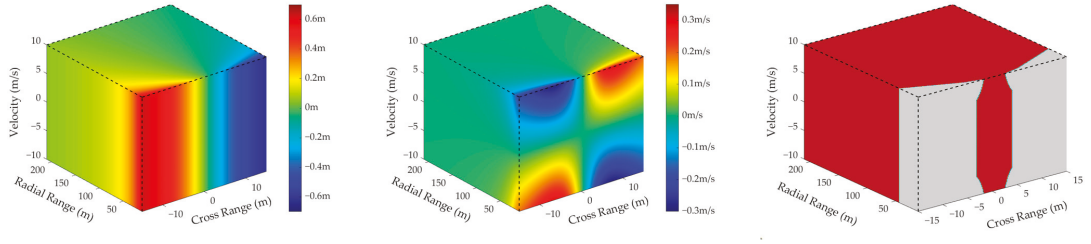

(**a**) (**b**) (**c**)

Figure 8. The simulation results of Test 3. (**a**,**b**) display the range and velocity deviations. (**c**) represents radar detection scenario, including effective region (red) and ineffective region (gray).

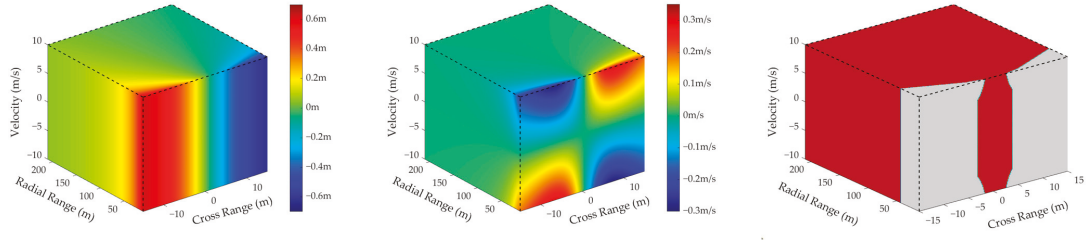

(**a**) (**b**) (**c**)

Figure 9. The simulation results of Test 4. (**a**,**b**) display the range and velocity deviations. (**c**) represents radar detection scenario, including effective region (red) and ineffective region (gray).

As shown in Figures 6–9, it is apparent that the radial range and velocity of the dominant scatterer have a negligible impact on the effective region. On the contrary, the deviations will increase with the cross range, and the corresponding effective region will reduce significantly, as shown in Table 3. Therefore, the first criterion is that the dominant scatterer should be close to the normal direction of MMW DCAR, i.e., its azimuth should be relatively small.

Table 3. The proportion satisfying the constraints.

	Test 1	**Test 2**	**Test 3**	**Test 4**
Proportion	93.58%	89.84%	93.57%	93.58%

The dominant scatterer in this work is a non-cooperative target, which may have multiple scattering points at a short range [40]. The CP estimations require scattering point matching; the multiple scattering points can lead to mismatching and a negative estimation. Thus, we recommend choosing a target with a medium- or long-range as the dominant scatterer, which is the second selection criterion.

Furthermore, the dominant scatterer's SNR determines the accuracy of the CP estimations, which potentially has an essential impact on the synthetic performance of weak targets. In this regard, we performed the simulations on the synthetic gain loss of the weak target with respect to the dominant scatterer's SNR. The dominant scatterer SNR was set from 10 dB to 25 dB with a 1 dB interval, and 1000 Monte Carlo simulations were performed for each SNR.

The simulation results are displayed in Figure 10. As the dominant scatterer's SNR increases, the synthetic performance of the weak target is enhanced. In particular, the synthetic performance tends to be stable with an SNR higher than 13 dB. Hence, the third criterion is to choose one of the targets with a higher SNR as the dominant scatterer. For a scenario containing multiple high SNR targets, these targets can all be used as the dominant scatterer, and can then be further refined using the above two criteria.

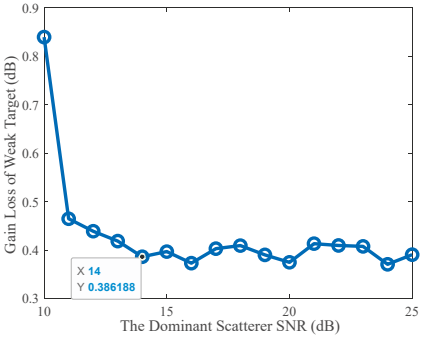

Figure 10. The synthetic SNR gain loss of the weak target versus the dominant scatterer's SNR.

In summary, the dominant scatterer in the paper can be defined as a medium- or long-range target that is close to the radar's normal direction. Moreover, its SNR should be as higher than 13 dB as possible. According to these selection criteria, the selection procedure of the dominant scatterer in practice is illustrated in Figure 11.

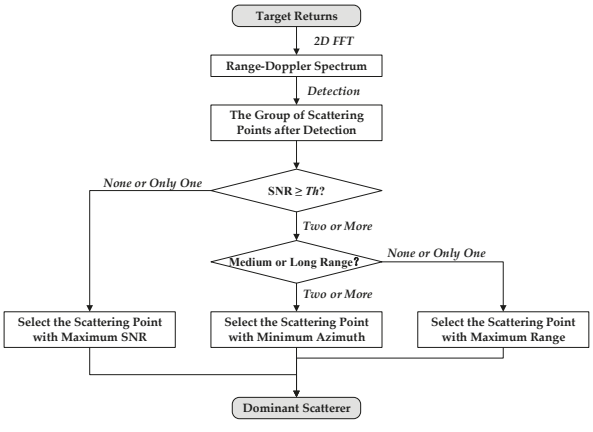

Figure 11. The selection procedure of the dominant scatterer, where ***Th*** is set to 13 dB in this paper.

3.5. Derivation of Theoretical Synthetic SNR

SNRs in multiple unit radars may be different due to the influence of noise. Hence, to evaluate the proposed method, the theoretical synthetic SNR is required to be derived as follows.

Assuming that the signal amplitude and noise power in channel mTnR are K_{mn} and P_{mn}, the target SNR can be expressed as

$$SNR_{mn} = K_{mn}^2 / P_{mn}. \tag{44}$$

Thereafter, the theoretical signal amplitude after CoRS is the sum of the signal amplitude in each channel, which is expressed as

$$A_{sig} = \sum_{m=1}^{N} \sum_{n=1}^{N} K_{mn} \tag{45}$$

Similarly, the accumulated noise power after CoRS can be denoted as

$$P_{Noise} = \sum_{m=1}^{N} \sum_{n=1}^{N} P_{mn}. \tag{46}$$

Therefore, the theoretical SNR can be obtained as

$$SNR_{theory} = A_{sig}^2 / P_{Noise} = \left(\sum_{m=1}^{N} \sum_{n=1}^{N} K_{mn} \right)^2 / \sum_{m=1}^{N} \sum_{n=1}^{N} P_{mn}. \tag{47}$$

Let $\gamma_{mn} = P_{mn} / P_{11}$, which indicates the noise power ratio of the channel mTnR to the reference channel. Thereby, we can rewrite Equation (47) as

$$\begin{aligned} SNR_{Theory} &= \frac{1}{\sum_{m=1}^{N} \sum_{n=1}^{N} \gamma_{mn}} \times \frac{1}{P_{mn}} \times \left(\sum_{m=1}^{N} \sum_{n=1}^{N} K_{mn} \right)^2 \\ &= \frac{1}{\sum_{m=1}^{N} \sum_{n=1}^{N} \gamma_{mn}} \times \left(\sum_{m=1}^{N} \sum_{n=1}^{N} \sqrt{\gamma_{mn}} \times \sqrt{SNR_{mn}} \right)^2. \end{aligned} \tag{48}$$

4. Simulations

We assessed the proposed method via simulations and present an analysis thereof. A typical scenario composed of one dominant scatterer and two weak targets was set up. The synthetic performance of all targets in continuous CPIs is presented, and the specific results are discussed within a single CPI. Moreover, the proposed method is also compared with the noncoherent integration method in terms of detection improvement.

4.1. CoRS for Multiple Targets

The simulation scenario is composed of three targets, the parameters of which are given in Table 4. The used MMW DCAR consists of three unit radars. It is important to note that the acceptable synthetic gain loss is defined as 3 dB in simulation. Therefore, the phase tolerance can be calculated as 27.9° according to Equation (34). Additionally, the compensation number for each channel and the MMW DCAR can be deduced as 7 times and 49 times, respectively.

4.1.1. Synthetic Results in Continuous CPIs

Utilizing the proposed method, the synthetic results of different targets in continuous CPIs are illustrated in Figure 12. Herein, the theoretical SNR, as in Equation (48), was used as a guideline for evaluation.

Since the multidimensional parameters of the dominant scatterer can be aligned with its own estimated CPs, the synthetic results in Figure 12a are consistent whether adaptive phase compensation is employed or not. However, due to the phase deviation, the synthetic performance of weak targets will decline significantly when using the dominant scatterer compensation only, as illustrated in Figure 12b,c. Instead, the synthetic results of weak targets can be effectively improved with the proposed method. Particularly, the maximum gain loss of these targets is 1.9 dB, which satisfies the definition.

Table 4. Parameters of multiple targets.

Target Classification	Parameters	Value
Dominant Scatterer	Cross range	−3 m
	Radial range	45 m
	Radial velocity	−9 m/s
	SNR	15 dB
First Weak Target	Cross range	0 m
	Radial range	30 m
	Radial velocity	3 m/s
	SNR	4 dB
Second Weak Target	Cross range	3 m
	Radial range	55 m
	Radial velocity	−2 m/s
	SNR	3 dB

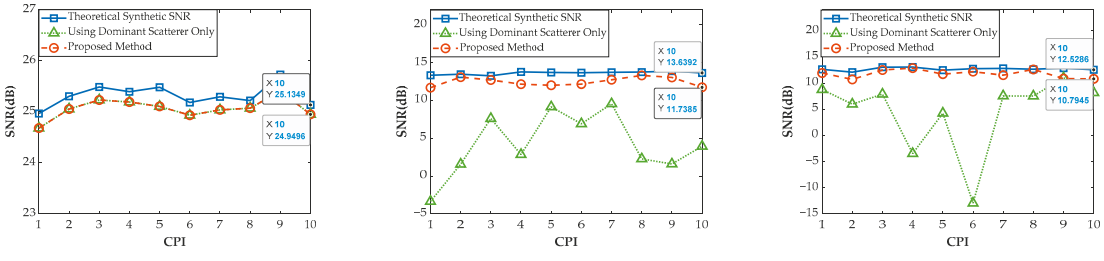

(**a**) (**b**) (**c**)

Figure 12. Multi-target coherent-on-receive synthesis results in consecutive CPIs. (**a**) Results of the dominant scatterer. (**b**) Results of the first weak target. (**c**) Results of the second weak target.

4.1.2. Synthetic Results within a Single CPI

To demonstrate the synthetic performance, the simulation results of the 10th CPI are presented in Figures 13–15. Due to the synchronization errors, these targets focused on different range cells in multi-channel, as illustrated in Figure 13. The echoes can be calibrated with the estimated CPs of the dominant scatterer. Figure 14 shows that the deviations caused by the synchronization errors were eliminated, and thereby the multi-target was aligned in the range spectrum. From Figure 15a, the dominant scatterer can be synthesized effectively, while the weak targets suffer a great loss due to the phase deviation. Utilizing the proposed method, the weak targets can achieve CoRS with adaptive phase compensation, as shown in Figure 15b,c.

To specifically verify the effectiveness of the proposed method, Table 5 gives the numerical comparison results. Since the signal discreteness in FFT processing causes a fence effect, the targets' SNRs have a slight variation after compensation using estimated CPs. It is verified that the targets' SNRs in multi-channels do not change significantly, and thus their impact can be neglected in the actual processing.

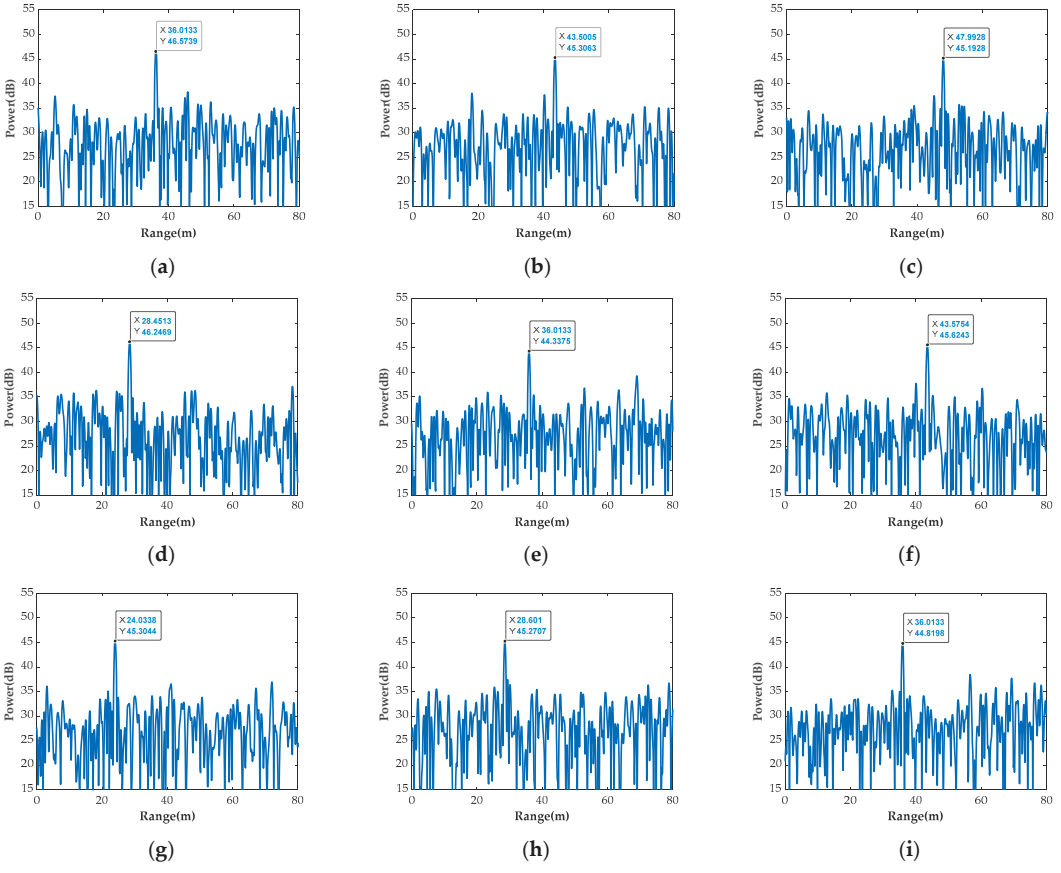

Figure 13. The range spectra of the original beat signal in multi-channel. (**a**–**i**) are the channels 1T1R to 3T3R, respectively.

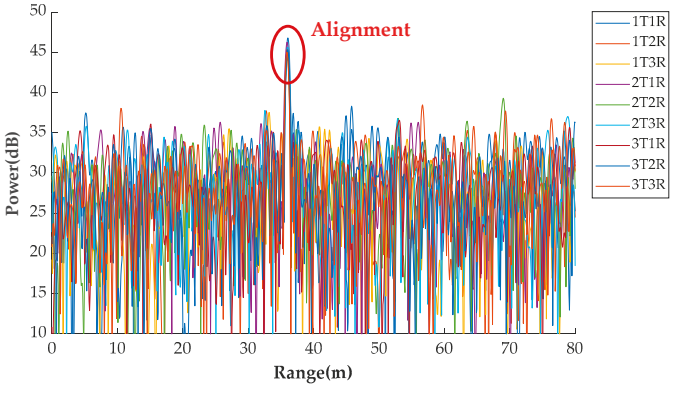

Figure 14. The range spectra after dominant scatterer compensation.

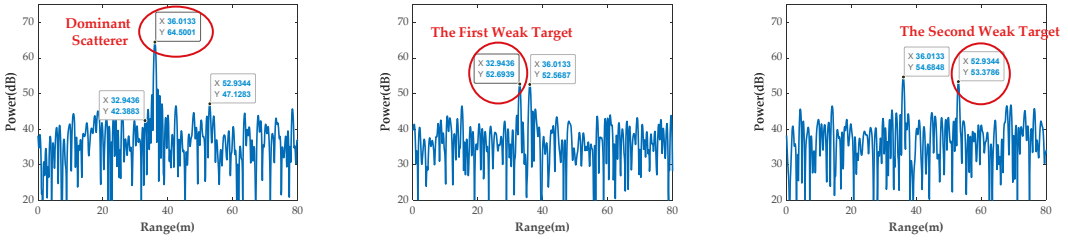

Figure 15. Multi-target CoRS results via the proposed method. (**a**) Results of the dominant scatterer. (**b**) Results of the first weak target. (**c**) Results of the second weak target.

Table 5. The numerical comparison results (dB) of simulations.

	Parameters	Channels								
		1T1R	1T2R	1T3R	2T1R	2T2R	2T3R	3T1R	3T2R	3T3R
Original signal	Noise power	30.2	29.1	30.0	29.9	30.0	30.0	30.1	29.1	29.9
	Dominant scatterer SNR	16.4	16.2	15.1	16.3	14.3	15.7	15.2	16.1	14.9
	First weak target SNR	2.9	5.3	4.1	4.0	3.7	3.8	3.2	5.7	4.2
	Second weak target SNR	2.4	3.0	1.8	4.3	3.5	2.7	2.2	4.8	2.0
Compensated signal	Noise power	30.2	29.4	30.0	29.5	30.0	29.6	29.8	29.1	29.9
	Dominant scatterer SNR	16.4	15.9	15.1	16.7	14.3	16.1	15.5	16.1	14.9
	First weak target SNR	2.9	5.0	4.1	4.4	3.7	4.2	3.5	5.7	4.2
	Second weak target SNR	2.4	2.7	1.8	4.7	3.5	3.1	2.5	4.8	2.0
Theoretical SNR	Dominant scatterer	25.1								
	First weak target	13.6								
	Second weak target	12.5								
Proposed method	Dominant scatterer	24.9 (Gain loss: 0.2 dB)								
	First weak target	11.7 (Gain loss: 1.9 dB)								
	Second weak target	10.8 (Gain loss: 1.7 dB)								

For the dominant scatterer, its synthetic SNR is 24.9 dB, with a gain loss of 0.2 dB compared to the theoretical result. Additionally, with the proposed method, the SNR gain losses of two weak targets are 1.9 dB and 1.7 dB, respectively. In summary, it is demonstrated that these targets can match the defined acceptable synthetic gain loss well. Namely, multi-target can be effectively synthesized, thus improving the target SNR and enhancing the radar detection performance significantly.

4.2. Detection Performance Comparison

The feasibility of the proposed method was further evaluated with the constant false alarm detection (CFAR) algorithm [41–43]. We compared it with the noncoherent integration method based on the square law detector [44,45]. Herein, the dominant scatterer with SNR = 20 dB was fixed, and a weak target was randomly generated in the radar detection region that satisfies the constraints, with the weak target's SNR in a single channel set from 0 dB to 20 dB. We performed the Monte Carlo simulations 1000 times via different methods, which are demonstrated in Figure 16.

Compared with using a single channel, using two types of synthesis methods can improve the detection performance. However, the noncoherent integration method suffers a great loss in the case of a low SNR. As the SNR increases, this method can enhance target detection, with a maximum gain of approximately 3.5 dB. On the contrary, the proposed method is stable at both high and low SNR conditions. With an equivalent detection probability, the proposed method improves by approximately 9 dB.

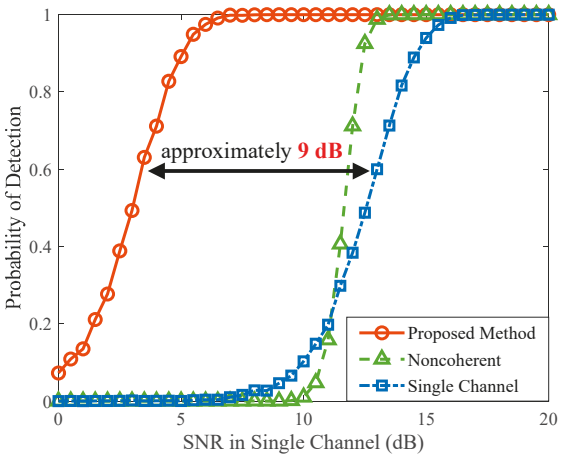

Figure 16. Detection performance utilizing CFAR algorithm with 1000 Monte Carlo simulations.

5. Experiments

The proposed CoRS method using the dominant scatterer was verified by measurements in a typical urban environment. The prototype system was fabricated, and the hardware components of the MMW DCAR are presented.

The prototype system in this work is composed of three radars with an operating frequency range of 76.0 GHz to 81.0 GHz. It employs a wired trigger, which is generated by a separate signal source and provides a trigger pulse to the radars with cables of equal length. An overview of the basic parameters of these radars is given in Table 6.

Table 6. Parameters of the test radars.

Parameter	Value
Center frequency	77.0 GHz
Bandwidth	200 MHz
Chirp duration	40 µs
Pulse repetition time	48 µs
IF bandwidth	12.5 MHz
Clock frequency	80 MHz

In the prototype system, a certain timing difference between the high levels of the trigger pulse at the radars is unavoidable because of the imperfect electrical length of the lines. Since each radar is independent, there may be an uncertain timing difference when their internal clocks detect the trigger pulse. The combined timing difference is the main factor that contributes to the arbitrary initial time delay. Furthermore, these independent unit radars are also subject to random deviations in carrier frequency and phase.

The prototype system, which contains three MMW radars and a wired trigger, is displayed in Figure 17. The test scenario consisted of a vehicle as the dominant scatterer and a pedestrian as the weak target.

With the time-division method, the multi-channel signals can be separated at each receiver. The range–Doppler spectra are presented in Figure 18. Clearly, due to the system synchronization errors, the focus positions are offset, which can be calibrated with the dominant scatterer.

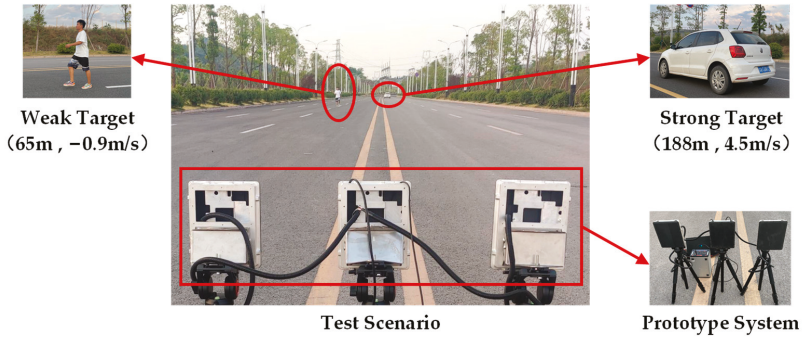

Figure 17. The prototype system and the test scenario consisting of a vehicle and a pedestrian.

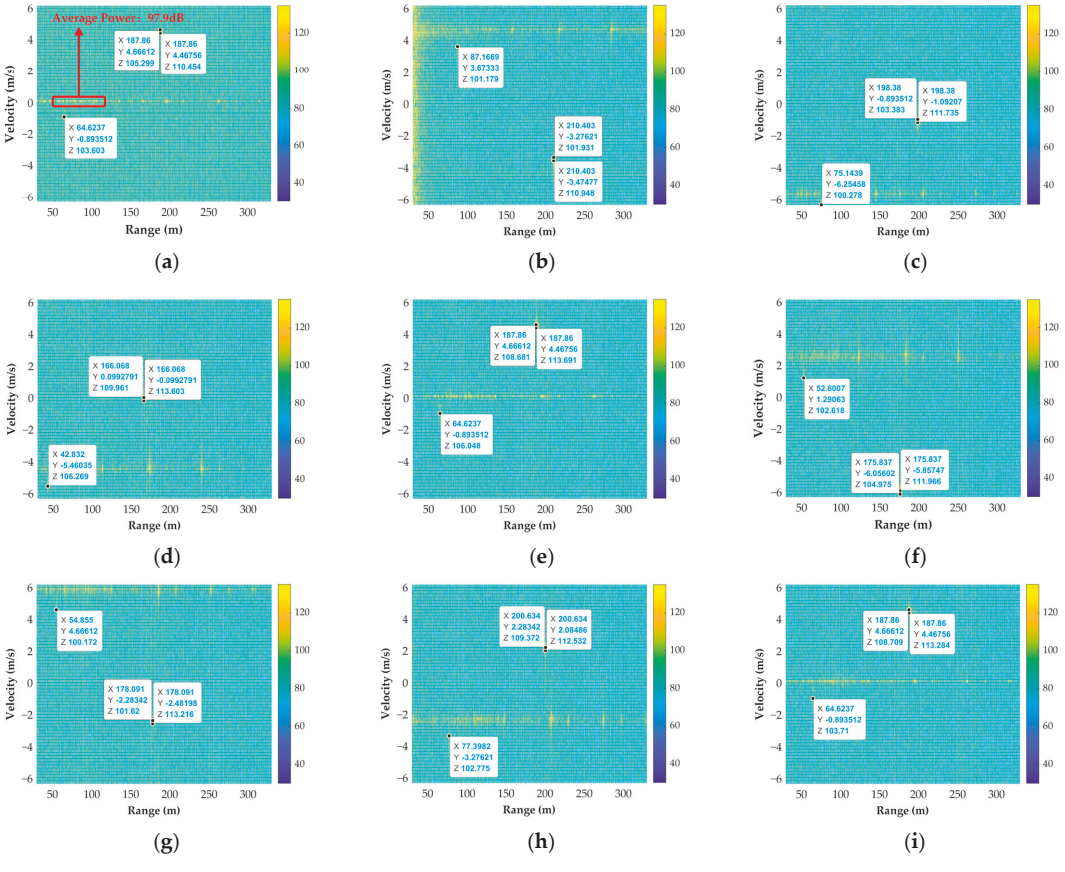

Figure 18. The range–Doppler spectra of multi-channel with real data. (**a**–**i**) are the channels 1T1R to 3T3R, respectively.

In the real-data experiment, the vehicle had two strong scattering points. We chose the stronger scattering point as the dominant scatterer of the proposed method. The optimal synthetic results for the vehicle and the pedestrian are demonstrated in Figure 19a,b, respectively.

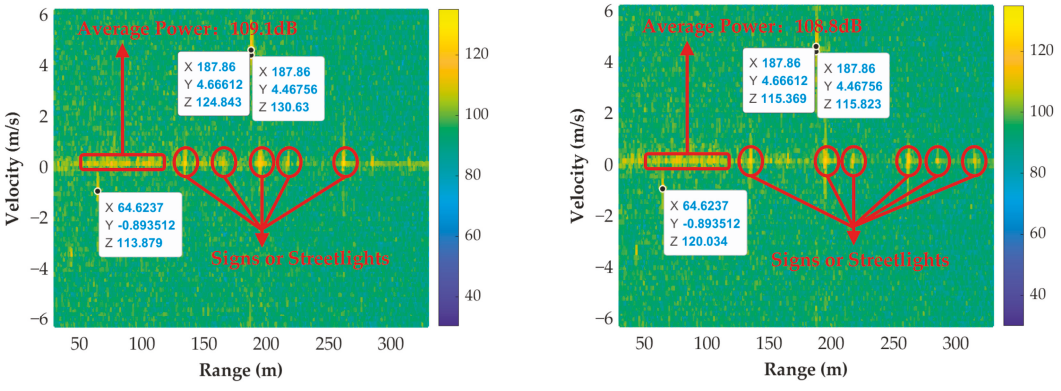

(**a**) (**b**)

Figure 19. The optimal CoRS results in multiple-phase compensation groups. (**a**) Results of the vehicle. (**b**) Results of the pedestrian.

The numerical comparison results from the real-data experiment are given in Table 7. The theoretical SNR of the stronger scattering point after synthesis is calculated at 33.2 dB, while the actual SNR can be improved to 32.0 dB. For weak scattering points, the CoRS can be realized by using the estimated CPs only. Its theoretical and actual SNR after synthesis are 27.2 dB and 26.2 dB, respectively. The pedestrian is also synthesized with the proposed method, and its theoretical and actual SNR after synthesis can be calculated as 23.8 dB and 21.6 dB. Additionally, it should be noted that several stationary targets including signs and streetlights can also be effectively synthesized, as shown in Figure 19. To sum up, the proposed method satisfies the defined acceptable synthetic gain loss (3 dB) for each target, which can enhance the target SNR effectively.

Table 7. The numerical comparison results (dB) with real data.

	Parameters	Channels								
		1T1R	1T2R	1T3R	2T1R	2T2R	2T3R	3T1R	3T2R	3T3R
Original signal	Noise power	89.2	88.6	87.8	89.8	89.4	88.5	88.8	89.0	87.9
	Vehicle Point 1 SNR	21.3	22.3	23.9	23.8	24.3	23.5	24.4	23.5	25.4
	Vehicle Point 2 SNR	16.1	13.3	15.6	19.8	19.3	16.5	12.8	20.4	20.8
	Pedestrian SNR	14.4	12.6	12.5	16.5	16.6	14.1	11.6	13.8	14.8
Theoretical SNR	Vehicle Point 1					33.2				
	Vehicle Point 2					27.2				
	Pedestrian					23.8				
Proposed method	Vehicle Point 1					32.0 (Gain loss: 1.2 dB)				
	Vehicle Point 2					26.2 (Gain loss: 1.0 dB)				
	Pedestrian					21.6 (Gain loss: 2.2 dB)				

Furthermore, the power near the zero frequency in the Doppler spectrum is higher than that at other frequencies. This is caused by the ground clutter and some stationary targets (e.g., trees, curbs, etc.) in the urban environment. As illustrated in Figures 18a and 19a, the signal power in this part is 97.9 dB and 109.1 dB, with 11.2 dB of gain. It is well known that the ideal synthetic gain for targets is approximately 19.0 dB, while the gain for noise is 9.5 dB. Consequently, the gain of clutter is intermediate between the noise and the target, which may have a negative impact on the improvement of the proposed method for stationary targets.

6. Conclusions

This paper describes a millimeter-wave distributed coherent aperture radar that can be used to improve the target SNR by coherent-on-receive synthesis. The synchronization errors are calibrated with the estimated coherent parameters of the dominant scatterer, which can be defined as an unknown strong target in radar detection scenarios. We focused on the selection criteria of the dominant scatterer by analyzing the constraints of the proposed method. Furthermore, an adaptive compensation approach was further explored to expand the available region for the estimated CPs of the dominant scatterer. This approach can compensate for the phases of different targets within multiple-unit radars using discrete phase values. The determination of discrete phase values is derived from the limit of synthesis loss within a given MMW DCAR configuration. Hence, this approach avoids massive searches for possible locations of other targets and the requirement of prior information.

The presented theory and the corresponding method were evaluated via extensive simulations and experiments. The constraints and limitations of the system were verified to meet the application requirements. Utilizing the proposed method, multi-target can achieve the desired synthetic results in sequential CPIs. Compared with the noncoherent integration method, the proposed method is stable at both high and low SNR conditions, yet with a higher SNR gain. Furthermore, a prototype system was fabricated and used to verify the proposed method. The experiment results match well with the simulations, showing the efficacy of the proposed method.

Author Contributions: Conceptualization, C.L. and Y.L.; methodology, C.L. and Y.W.; validation, C.L., M.W. and J.G.; formal analysis, X.H. and L.Z.; writing—original draft preparation, C.L. and Y.W.; writing—review and editing, Y.W., X.H. and L.Z.; supervision, Y.L. All authors have read and agreed to the published version of the manuscript.

Funding: This research was funded by the National Key R&D Program of China (Grant No. 2018YFE0202101, 2018YFE0202103), Natural Science Foundation of Chongqing, China (Grant No. cstc2020jcyj-msxmX0812) and project ZR2021MF134 supported by Shandong Provincial Natural Science Foundation.

Data Availability Statement: Not applicable.

Conflicts of Interest: The authors declare no conflict of interest.

References

1. Coutts, S.; Cuomo, K.; McHarg, J.; Robey, F.; Weikle, D. Distributed Coherent Aperture Measurements for Next Generation BMD Radar. In Proceedings of the IEEE Workshop on Sensor Array and Multichannel Processing, Waltham, MA, USA, 12–14 July 2006.
2. Godrich, H.; Haimovich, A.M.; Blum, R.S. Target Localization Accuracy Gain in MIMO Radar-Based Systems. *IEEE Trans. Inf. Theory* **2010**, *56*, 2783–2802. [CrossRef]
3. Dai, F.; Li, Y.; Wang, Y.; Chen, H. Efficient Implementation for SBL-Based Coherent Distributed mmWave Radar Imaging. *Remote Sens.* **2023**, *15*, 1054. [CrossRef]
4. Cuomo, K.M.; Coutts, S.D.; McHarg, J.C.; Pulsone, N.B.; Robey, F.C. *Wideband Aperture Coherence Processing for Next Generation Radar (NexGen)*; MIT Lincoln Laboratory: Lexington, MA, USA, 2004.
5. Long, T.; Zhang, H.; Zeng, T.; Liu, Q.; Chen, X.; Zheng, L. High Accuracy Unambiguous Angle Estimation Using Multi-Scale Combination in Distributed Coherent Aperture Radar. *IET Radar Sonar Nav.* **2017**, *11*, 1090–1098. [CrossRef]
6. Liang, C.; Wang, Y.; Yang, Z.; Hu, X.; Pei, Q.; Gu, W.; Zhang, L. Cooperative Automotive Radars with Multi-Aperture Multiplexing MIMO Sparse Array Design. *Electronics* **2022**, *11*, 1198. [CrossRef]
7. Fletcher, A.S.; Robey, F.C. Performance Bounds for Adaptive Coherence of Sparse Array Radar. In Proceedings of the 11th Conference Adaptive Sensors Array Processing, Lexington, MA, USA, 11–13 March 2003.
8. Li, J.; Stoica, P. MIMO Radar with Colocated Antennas. *IEEE Signal Process. Mag.* **2007**, *24*, 106–114. [CrossRef]
9. Gottinger, M.; Hoffmann, M.; Christmann, M.; Schütz, M.; Kirsch, F.; Gulden, P.; Vossiek, M. Coherent Automotive Radar Networks: The Next Generation of Radar-Based Imaging and Mapping. *IEEE J. Microw.* **2021**, *1*, 149–163. [CrossRef]
10. Sun, P.; Tang, J.; He, Q.; Tang, B.; Tang, X. Cramer-Rao bound of parameters estimation and coherence performance for next generation radar. *IET Radar Sonar Nav.* **2013**, *7*, 553–567. [CrossRef]
11. Tang, X.; Tang, J.; He, Q.; Wan, S.; Tang, B.; Sun, P.; Zhang, N. Cramer-Rao Bounds and Coherence Performance Analysis for Next Generation Radar with Pulse Trains. *Sensors* **2013**, *13*, 5347–5367. [CrossRef]

12. Brookner, E. Phased-Array and Radar Breakthroughs. In Proceedings of the IEEE Radar Conference, Boston, MA, USA, 17–20 April 2007.
13. Kuschel, H.; O'Hagan, D. Passive Radar from History to Future. In Proceedings of the 11-th International Radar Symposium, Vilnius, Lithuania, 16–18 June 2010.
14. Kuschel, H. Approaching 80 Years of Passive Radar. In Proceedings of the 2013 International Conference on Radar, Adelaide, SA, Australia, 9–12 September 2013.
15. Stelzer, A.; Jahn, M.; Scheiblhofer, S. Precise Distance Measurement with Cooperative FMCW Radar Units. In Proceedings of the 2008 IEEE Radio and Wireless Symposium, Orlando, FL, USA, 22–24 January 2008.
16. Feger, R.; Pfeffer, C.; Schmid, C.M.; Lang, M.J.; Tong, Z.; Stelzer, A. A 77-GHz FMCW MIMO Radar Based on Loosely Coupled Stations. In Proceedings of the 7th German Microwave Conference, Ilmenau, Germany, 12–14 March 2012.
17. Butt, F.A.; Aslam, M.A.; Zafar, M.T.; Naqvi, I.H.; Riaz, U. Synchronization of Long-Range, Widely-Separated MIMO Radar Network using GSM Protocol. In Proceedings of the 19th International Radar Symposium, Bonn, Germany, 20–22 June 2018.
18. Steiner, M.; Keller, M.; Geiß, J.; Vossiek, M.; Waldschmidt, C. Synchronization of Radar Sensors in a Network Based on Inter-Sensor Interference. In Proceedings of the 2019 16th European Radar Conference (EuRAD), Paris, France, 2–4 October 2019.
19. Zhang, H.; Lei, Z.; Song, Y. Coherent Parameters Estimation Method Based on MUSIC and KF in Wideband DCAR. In Proceedings of the IET International Radar Conference, Hangzhou, China, 14–16 October 2015.
20. Zeng, T.; Yin, P.; Liu, Q. Wideband Distributed Coherent Aperture Radar Based on Stepped Frequency Signal: Theory and Experimental Results. *IET Radar Sonar Nav.* **2016**, *10*, 672–688. [CrossRef]
21. Edstaller, S.; Mueller, D. Vector Velocity and Position Measurement Using a 77-GHz Cooperative Radar System. In Proceedings of the 2019 IEEE MTT-S International Microwave Symposium (IMS), Boston, MA, USA, 2–7 June 2019.
22. Edstaller, S.; Mueller, D. A Cooperative Radar System with Active Reference Target Synchronization for Kinematic Target Analysis. *IEEE Trans. Microw. Theory Tech.* **2021**, *69*, 4118–4131. [CrossRef]
23. Rabideau, D.J. MIMO Radar Waveforms and Cancellation Ratio. *IEEE Trans. Aerosp. Electron. Syst.* **2012**, *48*, 1167–1178. [CrossRef]
24. Kronauge, M.; Rohling, H. New Chirp Sequence Radar Waveform. *IEEE Trans. Aerosp. Electron. Syst.* **2014**, *50*, 2870–2877. [CrossRef]
25. Hu, X.; Lu, M.; Li, Y.; Wang, Y. Motion Compensation for TDM MIMO Radar by Sparse Reconstruction. *Electron. Lett.* **2017**, *53*, 1604–1606. [CrossRef]
26. Patole, S.M.; Torlak, M.; Wang, D.; Ali, M. Automotive Radars: A Review of Signal Processing Techniques. *IEEE Signal Process. Mag.* **2017**, *34*, 22–35. [CrossRef]
27. Hu, X.; Li, Y.; Lu, M.; Wang, Y.; Yang, X. A Multi-Carrier-Frequency Random-Transmission Chirp Sequence for TDM MIMO Automotive Radar. *IEEE Trans. Veh. Technol.* **2019**, *68*, 3672–3685. [CrossRef]
28. Sun, S.; Petropulu, A.P.; Poor, H.V. MIMO Radar for Advanced Driver-Assistance Systems and Autonomous Driving: Advantages and Challenges. *IEEE Signal Process. Mag.* **2020**, *37*, 98–117. [CrossRef]
29. Feger, R.; Pfeffer, C.; Stelzer, A. A Frequency-Division MIMO FMCW Radar System Based on Delta–Sigma Modulated Transmitters. *IEEE Trans. Microw. Theory Tech.* **2014**, *62*, 3572–3581. [CrossRef]
30. Kim, E.H.; Kim, K.H. Random Phase Code for Automotive MIMO Radars Using Combined Frequency Shift Keying-Linear FMCW Waveform. *IET Radar Sonar Nav.* **2018**, *12*, 1090–1095. [CrossRef]
31. Benedetto, J.J.; Konstantinidis, I.; Rangaswamy, M. Phase-Coded Waveforms and Their Design. *IEEE Signal Process. Mag.* **2009**, *26*, 22–31. [CrossRef]
32. Uysal, F. Phase-Coded FMCW Automotive Radar: System Design and Interference Mitigation. *IEEE Trans. Veh. Technol.* **2020**, *69*, 270–281. [CrossRef]
33. Overdevest, J.; Jansen, F.; Uysal, F.; Yarovoy, A. Doppler Influence on Waveform Orthogonality in 79 GHz MIMO Phase-Coded Automotive Radar. *IEEE Trans. Veh. Technol.* **2020**, *69*, 16–25. [CrossRef]
34. Ferrari, A.; Berenguer, C.; Alengrin, G. Doppler Ambiguity Resolution Using Multiple PRF. *IEEE Trans. Aerosp. Electron. Syst.* **1997**, *33*, 738–751. [CrossRef]
35. Rossum, W.; van Anitori, L. Simultaneous Resolution of Range-Doppler Ambiguities using Agile Pulse Intervals with Sparse Signal Processing. In Proceedings of the 2020 IEEE Radar Conference, Florence, Italy, 21–25 September 2020.
36. Wang, J. CFAR-Based Interference Mitigation for FMCW Automotive Radar Systems. *IEEE Trans. Intell. Transp. Syst.* **2021**, *23*, 12229–12238. [CrossRef]
37. Xu, Z.; Yuan, M. An Interference Mitigation Technique for Automotive Millimeter Wave Radars in the Tunable Q-Factor Wavelet Transform Domain. *IEEE Trans. Microw. Theory Tech.* **2021**, *69*, 5270–5283. [CrossRef]
38. Xu, Z.; Xue, S.; Wang, Y. Incoherent Interference Detection and Mitigation for Millimeter-Wave FMCW Radars. *Remote Sens.* **2022**, *14*, 4817. [CrossRef]
39. Xu, Z. Bi-Level *l*1 Optimization-Based Interference Reduction for Millimeter Wave Radars. *IEEE Trans. Intell. Transp. Syst.* **2023**, *24*, 728–738. [CrossRef]
40. Sun, L.; Yu, H.; Lan, J.; Fu, Z.; He, Z.; Pu, J. Tracking of Multiple Maneuvering Random Hypersurface Extended Objects Using High Resolution Sensors. *Remote Sens.* **2021**, *13*, 2963. [CrossRef]
41. Smith, M.E.; Varshney, P.K. Intelligent CFAR Processor Based on Data Variability. *IEEE Trans. Aerosp. Electron. Syst.* **2000**, *36*, 837–847. [CrossRef]

42. Tao, D.; Anfinsen, S.N.; Brekke, C. Robust CFAR Detector Based on Truncated Statistics in Multiple-Target Situations. *IEEE Trans. Geosci. Remote Sens.* **2016**, *54*, 117–134. [CrossRef]
43. Cao, Z.; Li, J.; Song, C.; Xu, Z.; Wang, X. Compressed Sensing-Based Multitarget CFAR Detection Algorithm for FMCW Radar. *IEEE Trans. Geosci. Remote Sens.* **2021**, *59*, 9160–9172. [CrossRef]
44. Bird, J.S. Calculating the Performance of Linear and Square-Law Detectors. *IEEE Trans. Aerosp. Electron. Syst.* **1995**, *31*, 39–51. [CrossRef]
45. Morgan, D.R.; Madsen, C.K. Wide-Band System Identification Using Multiple Tones with Allpass Filters and Square-Law Detectors. *IEEE Trans. Circuits–I* **2006**, *53*, 1151–1165. [CrossRef]

remote sensing

MDPI

Article

Reweighted Robust Particle Filtering Approach for Target Tracking in Automotive Radar Application

Qisong Wu [1,2,*], Lingjie Chen [1], Yanping Li [1], Zijun Wang [1], Shuai Yao [1] and Hao Li [3]

[1] Key Laboratory of Underwater Acoustic Signal Processing, Ministry of Education, Southeast University, Nanjing 210096, China
[2] Purple Mountain Laboratories, Nanjing 211111, China
[3] Science and Technology on Near-Surface Detection Laboratory, Wuxi 214035, China
* Correspondence: qisong.wu@seu.edu.cn

Abstract: In view of the decline of filtering accuracy caused by measured outliers in target tracking application, a novel reweighted robust particle filter is proposed to acquire accurate state estimates in an automotive radar system. To infer the importance of each entry in the multidimensional contaminated measurement vector, we employ a weight vector, which follows a Gamma distribution, to model the measured noise and carry out accurate state estimates. Additionally, the particle filter method is employed to perform approximate posterior inference of state estimates in the nonlinear model. The Cramer–Rao lower bound is provided for the performance evaluation of the proposed method. Both simulation and experimental results demonstrate the superiorities of the proposed algorithm over other robust solutions.

Keywords: outlier-robust; particle filter; tracking; automotive radar

Citation: Wu, Q.; Chen, L.; Li, Y.; Wang, Z.; Yao, S.; Li, H. Reweighted Robust Particle Filtering Approach for Target Tracking in Automotive Radar Application. *Remote Sens.* **2022**, *14*, 5477. https://doi.org/10.3390/rs14215477

Academic Editors: Zhihuo Xu, Jianping Wang and Yongwei Zhang

Received: 7 September 2022
Accepted: 20 October 2022
Published: 31 October 2022

Publisher's Note: MDPI stays neutral with regard to jurisdictional claims in published maps and institutional affiliations.

1. Introduction

In the field of autonomous driving, automotive radars have become the core sensors due to their all-time and all-weather environmental perception capabilities. Effective target tracking is essential for the autonomous driving systems to formulate correct and timely driving strategies. By clustering the point cloud data of Millimeter Waveform (MMW) radar, the target can be detected and located in the automotive application scenario. However, the occurrence of measurement abnormalities in real-world applications is a common phenomenon that may arise due to reasons such as unexpected disturbances, temporary sensor failures, and calibration errors [1]. A typical example is to track a walking pedestrian on the road through an MMW radar sensor in action. The occlusion of roadside obstacles, such as parked cars, walls, and so on, can corrupt the range measurement, and glint, speckle, and phase noise can contaminate radar data [2–4]. The input of most tracking algorithms is the result of target detection. If the target is suddenly lost or temporarily occluded, the target trajectory will be interrupted [5]. Moreover, the clutter cannot be completely filtered out of radar measurements can lead to false detections and causes measurement abnormalities [6]. In addition, the non-line-of-sight (NLOS) multipath propagation of the transmitted electromagnetic wave is also one of a source of measurement abnormalities [7]. The Kalman filter (KF) offers an optimal estimation method for the linear dynamic model with a Gaussian state and measurement noise [8]. However, owing to the complex electromagnetic propagation and changeable environment, the measurement noise is a typical non-Gaussian in the MMW radar sensor and would result in measurement abnormalities, also named outliers. The presence of these outliers may degrade the performance of standard KF, thus yielding poor estimates of the state of interest [9].

A number of efforts have been devoted to addressing the issue. Outliers rejection methods are used in robust state estimation and object tracking [10]. A robust filter approach in [11] has been developed by viewing measurements as clearly distinguished outliers from

normal values using Projection Statistics (PS). In [12–14], classical recursive approaches are converted into batch-mode regression form and iteratively reweighted least squares algorithms are used to estimate the states. A measurement-weighting-based whitening procedure is designed to distinguish outliers from normal measurements to improve the state estimation accuracy [15]. Another class of approaches is based on the heavy-tailed noise model, such as Student's t distributions and Laplace distributions [16–19]. A scalar weight, which follows a Gamma distribution, is introduced for each observed sample such that the variance matrices of measurement noise can be reassessed in the state estimation [20,21]. Filtering and smoothing algorithms, which are much more robust yet only slightly more involved than the standard inference algorithm, are derived by assigning Wishart distribution to the noise covariance matrix [22]. By choosing the inverse Wishart priors, the measurement noise covariance matrices can be inferred based on the variational Bayes (VB) approach [23].

In this paper, a reweighted robust particle filter is proposed to acquire more accurate state estimation with robustness to outliers in the nonlinear model. Motivated by the aforementioned methods in [20,21], we generalize models to the more comprehensive case of multidimensional outlier measurements. Specifically, a weight vector, which follows conditional independent Gamma distribution, is employed to reassess the contribution of each entry in the multidimensional outlier measurement. The proposed method can be regarded as a reweighted robust filter. The particle filter (PF) method is utilized to perform the approximate posterior inference of state estimates. The Cramer–Rao bound of the proposed method is also provided for performance analysis. Both simulations and experiments demonstrate the effectiveness of the proposed method.

Notations: We use lower-case (upper-case) bold characters to denote vectors (matrices). $(\cdot)^T$ denotes the transpose of a matrix or vector. $\mathrm{diag}(\mathbf{x})$ represents a diagonal matrix that uses the elements of $\mathbf{x}$ as its diagonal elements. $p(\cdot)$ denotes the probability density function (pdf). $x \sim \mathcal{N}(a, b)$ denotes that random variable x follows a Gaussian distribution with mean a and variance b. $\mathbf{x} \in \mathcal{R}^N$ denotes a real-value vector $\mathbf{x}$ with the dimension of N and $\mathbf{x} \in \mathcal{R}^{N \times M}$ denotes a real-value matrix $\mathbf{x}$ with the dimension of $N \times M$.

2. Proposed Model

2.1. Problem Formulation

A typical nonlinear discrete-time state-space model can be expressed as

$$\begin{aligned} \boldsymbol{\theta}_k &= f(\boldsymbol{\theta}_{k-1}) + \mathbf{u}_k \\ \mathbf{z}_k &= h(\boldsymbol{\theta}_k) + \mathbf{n}_k \end{aligned} \tag{1}$$

where $\boldsymbol{\theta}_k \in \mathcal{R}^N$ and $\mathbf{z}_k \in \mathcal{R}^M$ represent the state vector and measurement vector at time step k, $f(\cdot)$ and $h(\cdot)$ denote nonlinear state and measurement functions, respectively, $\mathbf{u}_k \in \mathcal{R}^N$ and $\mathbf{n}_k \in \mathcal{R}^M$ are the zero-mean Gaussian white process noises satisfying $\mathbf{u}_k \sim \mathcal{N}(\mathbf{0}, \mathbf{Q})$ and $\mathbf{n}_k \sim \mathcal{N}(\mathbf{0}, \mathbf{R})$, and $\mathbf{Q}$ and $\mathbf{R}$ are the process noise covariance matrix and measurement noise covariance matrix, respectively. The model in Equation (1) is just regarded to be a typical nonlinear system model, and the system state can be estimated by a nonlinear Kalman filter [24].

In real automotive radar applications, typical representative scenarios are often encountered in which the target of interest may be obscured by other interferences or clutters, and the acquired measurement vector, such as range, velocity, and azimuth, in the automotive radar system would fall outside a valid range and become outliers, since the acquired measurement samples at this time directly come from interferences. The weighted robust Kalman filter method has been developed by introducing a scalar w_k into the measurement noise covariance matrix $\mathbf{R}$ for the improved estimates of the updated $\boldsymbol{\theta}_k$ [21]. However, the main limitation of this work is that even if it allows the treatment of multidimensional measurement, a scalar weight is considered for the entire observation vector, thus equally treating all the entries regardless of which entry is corrupted. On the one hand, the entries

in the measurement vector represent diverse physical quantities respectively in the real radar system and have diverse signal-to-noise ratios. On the other hand, the variance of each entry is often influenced by the automotive radar system, such as the wider bandwidth radar system, resulting in a smaller range variance and smaller number of receiver channels, leading to a poorer azimuth measurement. Therefore, introducing a scaler in the measurement vector may be not an optimal way to treat them equally.

2.2. Generative Model

To address this issue, we introduce a novel Bayesian algorithm that treats the weights associated with each entry in the measurement vector data probabilistically. In particular, we introduce a weight vector $\mathbf{w}_k$ to learn the dynamical noise covariance matrix, and a reweighted robust particle filter method is proposed to acquire improved state-space estimates in a nonlinear model in the presence of contaminated measurements. We modify the measurement noise equation as follows by introducing a weight vector $\mathbf{w}_k$,

$$\mathbf{n}_k \sim \mathcal{N}\left(\mathbf{0}, \mathbf{W}_k^{-1}\mathbf{R}\right), \tag{2}$$

where $\mathbf{W}_k \in \mathcal{R}^{M\times M}$ is a diagonal matrix with the weight vector $\mathbf{w}_k = [w_{k,1}, \cdots, w_{k,M}]^T \in \mathcal{R}^M$ on its diagonal at time step k, and $\mathbf{W}_k^{-1}$ is the inverse of the matrix $\mathbf{W}_k$. The Gamma prior distribution is introduced for the elements of $\mathbf{w}_k$ to ensure that they remain positive and is written by

$$\begin{aligned} \mathbf{z}_k|\boldsymbol{\theta}_k, \mathbf{W}_k &\sim \mathcal{N}\left(h(\boldsymbol{\theta}_k), \mathbf{W}_k^{-1}\mathbf{R}\right) \\ \boldsymbol{\theta}_k|\boldsymbol{\theta}_{k-1} &\sim \mathcal{N}(f(\boldsymbol{\theta}_{k-1}), \mathbf{Q}) \\ w_{k,m} &\sim \text{Gamma}(w_{k,m}|v_m/2, v_m/2), \end{aligned} \tag{3}$$

where $m = 1, \cdots, M$, v_m is the mth hyperparameter in the vector $\mathbf{v}$ for the Gamma distribution. According to Equation (3), the modified model has the capability of dynamically learning the measurement noise covariance and adjusting the weights of each entry in the measurement vector for improved estimates of the state vector with effectively alleviating outliers.

2.3. Reweighted Robust Particle Filter

In this subsection, we develop a reweighted robust particle filter using statistical inference over the aforementioned model. The particle filter, utilizing the Monte Carlo method, is selected to provide approximate posterior estimation in the nonlinear model [25]. The state estimation generally focuses on the expectation calculation of posterior distribution,

$$\mathbf{E}[g(\boldsymbol{\theta})|\mathbf{z}_{1:k}] = \int g(\boldsymbol{\theta})p(\boldsymbol{\theta}|\mathbf{z}_{1:k})d\boldsymbol{\theta} \tag{4}$$

where $g(\boldsymbol{\theta})$ is the function of the variable $\boldsymbol{\theta}$, and $p(\boldsymbol{\theta}|\mathbf{z}_{1:k})$ represents the posterior probability density function for $\boldsymbol{\theta}$ given the measurement vector data $\mathbf{z}_{1:k}$. However, the posterior distribution $p(\boldsymbol{\theta}|\mathbf{z}_{1:k})$ is often difficult to analytically acquire due to the manipulation of the multiple integration. The importance sampling (IS) is often used to perform the posterior distribution by introducing a nominal distribution $\pi(\boldsymbol{\theta}|\mathbf{z}_{1:k})$ that often utilizes a Gaussian distribution,

$$\begin{aligned}\mathbf{E}[g(\boldsymbol{\theta})|\mathbf{z}_{1:k}] &= \int g(\boldsymbol{\theta})\frac{p(\boldsymbol{\theta}|\mathbf{z}_{1:k})}{\pi(\boldsymbol{\theta}|\mathbf{z}_{1:k})}\pi(\boldsymbol{\theta}|\mathbf{z}_{1:k})d\boldsymbol{\theta} \\ &= \int g(\boldsymbol{\theta})\frac{p(\mathbf{z}_{1:k}|\boldsymbol{\theta})p(\boldsymbol{\theta})}{p(\mathbf{z}_{1:k})\pi(\boldsymbol{\theta}|\mathbf{z}_{1:k})}\pi(\boldsymbol{\theta}|\mathbf{z}_{1:k})d\boldsymbol{\theta} \\ &= \frac{\int g(\boldsymbol{\theta})\frac{p(\mathbf{z}_{1:k}|\boldsymbol{\theta})p(\boldsymbol{\theta})}{\pi(\boldsymbol{\theta}|\mathbf{z}_{1:k})}\pi(\boldsymbol{\theta}|\mathbf{z}_{1:k})d\boldsymbol{\theta}}{\int \frac{p(\mathbf{z}_{1:k}|\boldsymbol{\theta})p(\boldsymbol{\theta})}{\pi(\boldsymbol{\theta}|\mathbf{z}_{1:k})}\pi(\boldsymbol{\theta}|\mathbf{z}_{1:k})d\boldsymbol{\theta}}.\end{aligned} \tag{5}$$

The particle weight $\omega(\boldsymbol{\theta})$ is defined as

$$\omega(\boldsymbol{\theta}) = \frac{p(\mathbf{z}_{1:k}|\boldsymbol{\theta})p(\boldsymbol{\theta})}{\pi(\boldsymbol{\theta}|\mathbf{z}_{1:k})}. \tag{6}$$

The Equation (5) can be rewritten by introducing the $\omega(\boldsymbol{\theta})$:

$$\begin{aligned}\mathbf{E}[g(\boldsymbol{\theta})|\mathbf{z}_{1:k}] &= \frac{\int g(\boldsymbol{\theta})\omega(\boldsymbol{\theta})\pi(\boldsymbol{\theta}|\mathbf{z}_{1:k})d\boldsymbol{\theta}}{\int \omega(\boldsymbol{\theta})\pi(\boldsymbol{\theta}|\mathbf{z}_{1:k})d\boldsymbol{\theta}} \\ &\approx \frac{\sum_{s=1}^{S} g\left(\boldsymbol{\theta}^{(s)}\right)\omega(\boldsymbol{\theta}^{(s)})}{\sum_{s=1}^{S}\omega(\boldsymbol{\theta}^{(s)})}\end{aligned} \tag{7}$$

where $s = 1, \ldots, S$, and S is the total number of sampling particles. According to the Markov properties of the model, the particle weights $\omega_k^{(s)}$ can be deduced in the recursion form

$$\omega_k^{(s)} \propto \frac{p\left(\mathbf{z}_k|\boldsymbol{\theta}_k^{(s)}\right)p\left(\boldsymbol{\theta}_k^{(s)}|\boldsymbol{\theta}_{k-1}^{(s)}\right)}{\pi\left(\boldsymbol{\theta}_k^{(s)}|\boldsymbol{\theta}_{0:k-1}^{(s)}, \mathbf{z}_{1:k}\right)}\omega_{k-1}^{(s)}. \tag{8}$$

Generally, $\pi(\boldsymbol{\theta}_k|\boldsymbol{\theta}_{0:k-1}, \mathbf{z}_{1:k}) = p(\boldsymbol{\theta}_k|\boldsymbol{\theta}_{k-1})$ is often used in the importance sampling, and thus the recursion in Equation (8) can be reduced into

$$\omega_k^{(s)} \propto p\left(\mathbf{z}_k|\boldsymbol{\theta}_k^{(s)}\right)\omega_{k-1}^{(s)}. \tag{9}$$

According to Equation (9), it is obvious that the problem eventually converts to computation of $p(\mathbf{z}_k|\boldsymbol{\theta}_k)$, which can be achieved from the marginal likelihood utilizing Bayesian inference. Considering the fact that $\mathbf{W}_k$ is independent of $\boldsymbol{\theta}_k$, we have

$$\begin{aligned}&p(\mathbf{z}_k|\boldsymbol{\theta}_k) \\ &= \int p(\mathbf{z}_k|\boldsymbol{\theta}_k, \mathbf{W}_k)p(\mathbf{W}_k|\boldsymbol{\theta}_k)d\mathbf{W}_k \\ &= \prod_{m=1}^{M}\int p(z_{k,m}|\boldsymbol{\theta}_k, w_{k,m})p(w_{k,m})dw_{k,m} \\ &= \prod_{m=1}^{M}\int_0^{\infty}\mathcal{N}\left(z_{k,m} \mid \mu_{k,m}, \frac{r_{m,m}}{w_{k,m}}\right)\mathrm{Gam}\left(w_{k,m} \mid \frac{v_m}{2}, \frac{v_m}{2}\right)dw_{k,m} \\ &= \prod_{m=1}^{M}\frac{\Gamma\left(\frac{v_m}{2}+\frac{1}{2}\right)}{\Gamma\left(\frac{v_m}{2}\right)}\left(\frac{\lambda_m}{\pi v_m}\right)^{\frac{1}{2}}\left[1+\frac{\lambda_m(z_{k,m}-\mu_{k,m})^2}{v_m}\right]^{-\frac{v_m}{2}-\frac{1}{2}}.\end{aligned} \tag{10}$$

where $\mu_{k,m}$ is the mth element of the vector $h(\boldsymbol{\theta}_k)$; $\lambda_m = r_{m,m}^{-1}$ is the mth element on the diagonal of matrix $\mathbf{R}^{-1}$. The entire reweighted robust particle filter (RR-PF) method is summarized as Algorithm 1.

Algorithm 1 Reweighted Robust Particle Filter

Input: $\{\boldsymbol{\theta}_{k-1}^{(s)} : s = 1, \ldots, S\}$

Output: $\langle \boldsymbol{\theta}_k \rangle$, $\{\boldsymbol{\theta}_k^{(s)} : s = 1, \ldots, S\}$

1: Draw new samples: $\tilde{\boldsymbol{\theta}}_k^{(s)} \sim p\left(\boldsymbol{\theta}_k | \boldsymbol{\theta}_{k-1}^{(s)}\right), s = 1, \ldots, S$

2: Calculate particles weights: $\tilde{\omega}_k^{(s)}$ in Equations (9) and (10)

3: Perform resampling with $\tilde{\boldsymbol{\theta}}_k^{(s)}$ and $\tilde{\omega}_k^{(s)}$ to acquire $\boldsymbol{\theta}_k^{(s)}$ in Equation (7)

4: Estimate system state $\langle \boldsymbol{\theta}_k \rangle = \sum_{s=1}^{S} \boldsymbol{\theta}_k^{(s)} / S$

5: **return** $\langle \boldsymbol{\theta}_k \rangle$, $\{\boldsymbol{\theta}_k^{(s)} : s = 1, \ldots, S\}$

2.4. Algorithm Analysis

In this subsection, detailed analysis is provided to illustrate the reason why the proposed method is more robust to the outlier compared with the conventional heavy-tail multivariate Student's *t*-distributed (CMSt) [26,27]. For comparison, we provide the probability density function (pdf) of the CMSt as

$$p(\mathbf{z}_k|\boldsymbol{\theta}_k) \propto \frac{\Gamma\left(\frac{v}{2} + \frac{M}{2}\right)}{\Gamma\left(\frac{v}{2}\right)} \left[1 + \frac{(\mathbf{z}_k - \boldsymbol{\mu})^T \mathbf{R}^{-1} (\mathbf{z}_k - \boldsymbol{\mu})}{v}\right]^{-\frac{M}{2} - \frac{v}{2}}. \tag{11}$$

We take 2D pdfs with $M = 2$ as an example to illustrate the roles of the robustness to outliers. In this example, $\mathbf{z}_k = [x_k, y_k]^T$, $\boldsymbol{\mu} = [0, 0]^T$, $\mathbf{R}^{-1} = \mathrm{diag}([1, 1])$, and $\mathbf{v} = [v, v]^T = [0.5, 0.5]^T$ are shown in Figure 1. It is observed that both pdfs exhibit heavy-tailed properties, which indicates their robustness to outliers. The differences lie in that there exist quite prominent ridges along the *x*-axis and *y*-axis in the proposed pdf, which makes the model more adapted to the changes in the independent variable in the direction perpendicular to the ridges than CMSt.

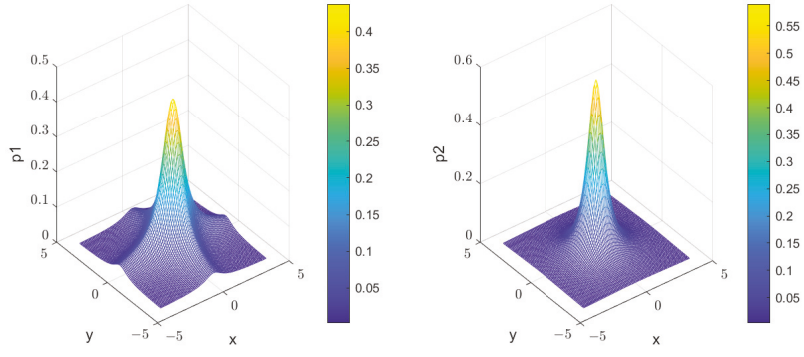

(**a**) (**b**)

Figure 1. Pdfs of the proposed model and CMSt in the 2D example. (**a**) Pdf plot of the proposed model. (**b**) Pdf plot of the CMSt.

In order to intuitively show the role of the proposed pdf in the particle filter, we illustrate the evolution of particle weights. In the particle filter, at $(k-1)$th time step, the particles are acquired with an identical weight to estimate $\langle \boldsymbol{\theta}_{k-1} \rangle$ based on the resampling technique, shown in Figure 2a. It is observed that these particle balls have the same sizes, and thus have identical weights, although the particle unreliability is different, as shown in the middle surface in Figure 2a. It is also found that the blue particle ball with a small value in the color bar denotes that this particle is highly reliable, however, the yellow ball with a large value suggests an unreliable particle. At the *k*th time step, when the new

measurement vector data z_k are provided, particle weights in the kth time step will evolve according to Equation (9). The evolved result of particle weights in Equation (10) is shown on the top surface, and the result in Equation (11) is provided in the bottom surface.

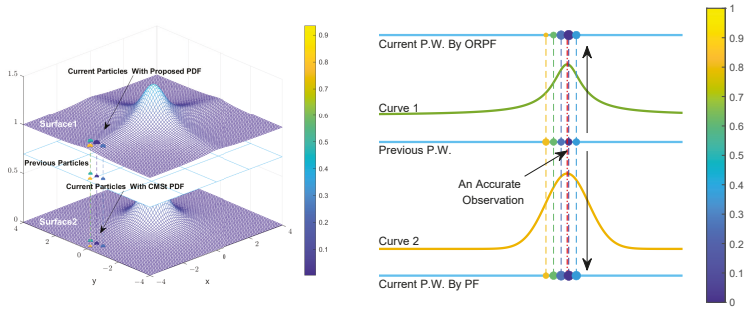

(**a**) (**b**)

Figure 2. The evolution of particle weights. (**a**) 3D plots of evolution of particle weights. (**b**) slice plots of evolution of particle weights. (Particle weights are denoted by the sizes of their corresponding particle balls, and the particle unreliability is depicted and illustrated by the colors.)

To clearly illustrate the roles of the pdfs in Equation (10) compared with that in Equation (11), we provide slice plots of the pdfs the along y-axis. It is observed that the plot of the sharper pdf in the proposed method would encourage the contributions from the reliable particle, and it would weaken the particle weight concerning these unreliable particles, shown in the top plot in Figure 2b. It is found that the blue particle ball has a higher weight due to its high reliability in the current time step, whereas the yellow one has a lower weight in the proposed model compared with those in the bottom pdf of the CMSt. In conclusion, the proposed method encourages the contributions from the particle weights of reliable particles and weakens the contributions from the unreliable particles by discriminatively treating the observed vector data. This could be the reason why the proposed method is more robust to outliers and acquires improved state estimates compared with the CMSt method.

2.5. Cramer–Rao Bound for the Model

To further explore the performance bound of the proposed method, CRLB analysis is provided in this section. We first define a latent parameter set concerning the random parameter set p($\boldsymbol{\Theta}$); the mean-square error matrix is generally served as a measure of error and is given by

$$\boldsymbol{\Sigma}_\epsilon = \mathrm{MSE}(\hat{\boldsymbol{\Theta}}) \triangleq \mathbf{E}\Big[\big(\hat{\boldsymbol{\Theta}} - \boldsymbol{\Theta}\big)\big(\hat{\boldsymbol{\Theta}} - \boldsymbol{\Theta}\big)^T\Big], \tag{12}$$

where $\boldsymbol{\Theta}$ are the latent variable parameter collection, $\hat{\boldsymbol{\Theta}}$ denote estimates of the corresponding variables, and $\mathbf{E}(x)$ denotes the expectation operator for the variable x.

The Bayesian Information Matrix (BIM), which is commonly employed in time-invariant statistical models, is often used for CRLB analysis and can be written by

$$\mathbf{J} = -\mathbf{E}\Big\{\bigtriangledown_{\boldsymbol{\Theta}}[\bigtriangledown_{\boldsymbol{\Theta}} \ln p(\boldsymbol{\Theta}, \mathbf{Z})]^T\Big\} \triangleq \mathbf{E}\Big\{[\bigtriangledown_{\boldsymbol{\Theta}} \ln p(\boldsymbol{\Theta}, \mathbf{Z})][\bigtriangledown_{\boldsymbol{\Theta}} \ln p(\boldsymbol{\Theta}, \mathbf{Z})]^T\Big\}, \tag{13}$$

where $p(\boldsymbol{\Theta}, \mathbf{Z})$ is the joint probability distribution, and $\bigtriangledown_{\boldsymbol{\Theta}}$ denotes the first-order partial derivative operator concerning the variable vector $\boldsymbol{\Theta}$, which can be expressed by

$$\nabla_{\mathbf{\Theta}} = \left[\frac{\partial}{\partial \mathbf{\Theta}_1}, \frac{\partial}{\partial \mathbf{\Theta}_2}, \cdots\right]^T \tag{14}$$

According to the Bayesian CRLB analysis, we have

$$\mathbf{\Sigma}_\epsilon \geqslant \mathbf{J}^{-1}. \tag{15}$$

The inequality suggests that the matrix on the left is non-negative.

According to posterior Cramer–Rao bounds analysis, we have the recursive sequence $\mathbf{J}_k$ of posterior information submatrices for estimating the state vector $\boldsymbol{\theta}_k$ at the kth time step [28]

$$\mathbf{J}_k = \mathbf{D}_k^{22} - \mathbf{D}_k^{21}\left(\mathbf{J}_{k-1} + \mathbf{D}_k^{11}\right)^{-1}\mathbf{D}_k^{12}, \tag{16}$$

where

$$\mathbf{D}_k^{11} = \mathbf{E}\Big[-\nabla_{\boldsymbol{\theta}_{k-1}} \nabla_{\boldsymbol{\theta}_{k-1}}^T \ln p(\boldsymbol{\theta}_k|\boldsymbol{\theta}_{k-1})\Big], \tag{17}$$

$$\mathbf{D}_k^{12} = \mathbf{E}\Big[-\nabla_{\boldsymbol{\theta}_{k-1}} \nabla_{\boldsymbol{\theta}_k}^T \ln p(\boldsymbol{\theta}_k|\boldsymbol{\theta}_{k-1})\Big], \tag{18}$$

$$\mathbf{D}_k^{21} = \mathbf{E}\Big[-\nabla_{\boldsymbol{\theta}_k} \nabla_{\boldsymbol{\theta}_{k-1}}^T \ln p(\boldsymbol{\theta}_k|\boldsymbol{\theta}_{k-1})\Big] = (\mathbf{D}_k^{12})^T. \tag{19}$$

$\mathbf{D}_k^{22}$ can be decomposed into

$$\mathbf{D}_k^{22} = \mathbf{D}_k^{22,a} + \mathbf{D}_k^{22,b}, \tag{20}$$

where

$$\mathbf{D}_k^{22,a} = \mathbf{E}\Big[-\nabla_{\boldsymbol{\theta}_k} \nabla_{\boldsymbol{\theta}_k}^T \ln p(\boldsymbol{\theta}_k|\boldsymbol{\theta}_{k-1})\Big], \tag{21}$$

$$\mathbf{D}_k^{22,b} = \mathbf{E}\Big[-\nabla_{\boldsymbol{\theta}_k} \nabla_{\boldsymbol{\theta}_k}^T \ln p(\mathbf{z}_k|\boldsymbol{\theta}_k)\Big], \tag{22}$$

The initial information submatrix can be obtained from the prior probability distribution $p(\boldsymbol{\theta}_0)$

$$\mathbf{J}_0 = \mathbf{E}\Big[-\nabla_{\boldsymbol{\theta}_0} \nabla_{\boldsymbol{\theta}_0}^T \ln p(\boldsymbol{\theta}_0)\Big], \tag{23}$$

where $p(\boldsymbol{\theta}_0)$ denotes the initial prior distribution of the variable vector $\boldsymbol{\theta}_0$.

Using the nonlinear discrete-time state-space model in Equations (1) and (10), we have

$$-\ln p(\boldsymbol{\theta}_k|\boldsymbol{\theta}_{k-1}) = \frac{1}{2}\Big\{[\boldsymbol{\theta}_k - f(\boldsymbol{\theta}_{k-1})]^T \mathbf{Q}^{-1}[\boldsymbol{\theta}_k - f(\boldsymbol{\theta}_{k-1})]\Big\} + \text{const}, \tag{24}$$

$$-\ln p(\mathbf{z}_k|\boldsymbol{\theta}_k) = \sum_{m=1}^{M}\left(\frac{v_m}{2} + \frac{1}{2}\right)\ln\left\{1 + \frac{\lambda_m[\mathbf{z}_{k,m} - h(\boldsymbol{\theta}_k)_m]^2}{v_m}\right\} + \text{const}. \tag{25}$$

Then,

$$\mathbf{D}_k^{11} = \mathbf{E}_{\boldsymbol{\theta}_{k-1}}\left\{\left[\nabla_{\boldsymbol{\theta}_{k-1}} f^T(\boldsymbol{\theta}_{k-1})\right]\mathbf{Q}^{-1}\left[\nabla_{\boldsymbol{\theta}_{k-1}} f^T(\boldsymbol{\theta}_{k-1})\right]^T\right\}, \tag{26}$$

$$\mathbf{D}_k^{12} = -\mathbf{E}_{\boldsymbol{\theta}_{k-1}}\left\{\left[\nabla_{\boldsymbol{\theta}_{k-1}} f^T(\boldsymbol{\theta}_{k-1})\right]\right\}\mathbf{Q}^{-1}, \tag{27}$$

$$\mathbf{D}_k^{21} = \left[\mathbf{D}_k^{12}\right]^T, \tag{28}$$

$$\mathbf{D}_k^{22} = \mathbf{Q}^{-1} + \mathbf{E}_{\boldsymbol{\theta}_k}\Big[\nabla_{\boldsymbol{\theta}_k} \nabla_{\boldsymbol{\theta}_k}^T \ln p(\mathbf{z}_k|\boldsymbol{\theta}_k)\Big]. \tag{29}$$

It is observed that it is difficult to carry out these integrals, the sequential Monte Carlo method is used to perform the approximations, and we define the variables $\mathbf{\Lambda}^{11}$, $\mathbf{\Lambda}^{12}$, and $\mathbf{\Lambda}^{22}$ as

$$\mathbf{\Lambda}^{11}(\boldsymbol{\theta}_{k-1}) = \left[\bigtriangledown_{\boldsymbol{\theta}_{k-1}} f^T(\boldsymbol{\theta}_{k-1})\right] \mathbf{Q}^{-1} \left[\bigtriangledown_{\boldsymbol{\theta}_{k-1}} f^T(\boldsymbol{\theta}_{k-1})\right]^T, \tag{30}$$

$$\mathbf{\Lambda}^{12}(\boldsymbol{\theta}_{k-1}) = -\bigtriangledown_{\boldsymbol{\theta}_{k-1}} f^T(\boldsymbol{\theta}_{k-1}), \tag{31}$$

$$\mathbf{\Lambda}^{22}(\boldsymbol{\theta}_k) = \bigtriangledown_{\boldsymbol{\theta}_k} \bigtriangledown_{\boldsymbol{\theta}_k}^T \ln p(\mathbf{z}_k|\boldsymbol{\theta}_k). \tag{32}$$

Therefore, we can rewrite Equations (26)–(29) as follows:

$$\begin{aligned} \mathbf{D}_k^{11} &= \int \mathbf{\Lambda}^{11}(\boldsymbol{\theta}_{k-1}) p(\boldsymbol{\theta}_{k-1}) d\boldsymbol{\theta}_{k-1} \\ &= \int p(\mathbf{z}_{k-1}) \left\{ \int \mathbf{\Lambda}^{11}(\boldsymbol{\theta}_{k-1}) p(\boldsymbol{\theta}_{k-1}|\mathbf{z}_{k-1}) d\boldsymbol{\theta}_{k-1} \right\} d\mathbf{z}_{k-1}, \end{aligned} \tag{33}$$

$$\begin{aligned} \mathbf{D}_k^{12} &= \int \mathbf{\Lambda}^{12}(\boldsymbol{\theta}_{k-1}) p(\boldsymbol{\theta}_{k-1}) d\boldsymbol{\theta}_{k-1} \\ &= \int p(\mathbf{z}_{k-1}) \left\{ \int \mathbf{\Lambda}^{12}(\boldsymbol{\theta}_{k-1}) p(\boldsymbol{\theta}_{k-1}|\mathbf{z}_{k-1}) d\boldsymbol{\theta}_{k-1} \right\} d\mathbf{z}_{k-1}, \end{aligned} \tag{34}$$

$$\begin{aligned} \mathbf{D}_k^{22} &= \mathbf{Q}^{-1} + \int \mathbf{\Lambda}^{22}(\boldsymbol{\theta}_k) p(\boldsymbol{\theta}_k) d\boldsymbol{\theta}_k \\ &= \mathbf{Q}^{-1} + \int p(\mathbf{z}_k) \left\{ \int \mathbf{\Lambda}^{22}(\boldsymbol{\theta}_k) p(\boldsymbol{\theta}_k|\mathbf{z}_k) d\boldsymbol{\theta}_k \right\} d\mathbf{z}_k. \end{aligned} \tag{35}$$

These integrals can be approximated by the mean of samples after having a series of samples corresponding to the density. We perform T Monte Carlo samples with the time steps of K for the calculation of the expectation instead of the integral operator over $\mathbf{z}_k$ and obtain the measurement sample matrix $\mathbf{Z}_{1:T,1:K}$. $\mathbf{z}_{t,k-1}$ denotes the tth measurement sample at the $(k-1)$th time step. Consequently, Equations (33)–(35) can be calculated by

$$\mathbf{D}_k^{11} \approx \frac{1}{T} \sum_{t=1}^{T} \left\{ \int \Lambda^{11}(\boldsymbol{\theta}_{k-1}) p(\boldsymbol{\theta}_{k-1}|\mathbf{z}_{t,k-1}) d\boldsymbol{\theta}_{k-1} \right\} \tag{36}$$

$$\mathbf{D}_k^{12} \approx \frac{1}{T} \sum_{t=1}^{T} \left\{ \int \Lambda^{12}(\boldsymbol{\theta}_{k-1}) p(\boldsymbol{\theta}_{k-1}|\mathbf{z}_{t,k-1}) d\boldsymbol{\theta}_{k-1} \right\} \tag{37}$$

$$\mathbf{D}_k^{22} \approx \mathbf{Q}^{-1} + \frac{1}{T} \sum_{t=1}^{T} \left\{ \int \Lambda^{22}(\boldsymbol{\theta}_k, \mathbf{z}_k) p(\boldsymbol{\theta}_k|\mathbf{z}_{t,k}) d\boldsymbol{\theta}_k \right\} \tag{38}$$

We further perform Monte Carlo samples over the variable $\boldsymbol{\theta}_k$ instead of an integral operator over $\boldsymbol{\theta}_k$ at the tth sample, and formulas inside the braces in Equations (36)–(38) can be expressed as

$$\mathbf{D}_{t,k}^{11} \approx \frac{1}{L} \sum_{l=1}^{L} \Lambda^{11}(\boldsymbol{\theta}_{t,k-1}^{(l)}) \tag{39}$$

$$\mathbf{D}_{t,k}^{12} = \left(\mathbf{D}_{t,k}^{21}\right)^T \cong \frac{1}{L} \sum_{l=1}^{L} \Lambda^{12}(\boldsymbol{\theta}_{t,k-1}^{(l)}) \tag{40}$$

$$\mathbf{D}_{t,k}^{22} \approx \frac{1}{L} \sum_{l=1}^{L} \Lambda^{22}(\boldsymbol{\theta}_{t,k}^{(l)}, \mathbf{z}_{t,k}) \tag{41}$$

where $\boldsymbol{\theta}_{t,k-1}^{(l)}$ and $\boldsymbol{\theta}_{t,k}^{(l)}$ are, respectively, samples drawn from the posterior distributions of $p(\boldsymbol{\theta}_{t,k-1}|\boldsymbol{z}_{t,k-1})$ and $p(\boldsymbol{\theta}_{t,k}|\boldsymbol{z}_{t,k})$, and L is the number of samples. According to the approximate inference method, the Markov Chain Monte Carlo (MCMC) method is utilized to estimate $\boldsymbol{\theta}_{t,k}$ with the state transition probability $p(\boldsymbol{\theta}_k|\boldsymbol{\theta}_{k-1})$ in Equation (24) and the likelihood function $p(\mathbf{z}_k|\boldsymbol{\theta}_k)$ in Equation (25). The following Equations (33)–(35) and (39)–(41), can be rewritten by

$$\mathbf{D}_k^{11} \approx \frac{1}{T}\sum_{t=1}^{T}\left\{\frac{1}{L}\sum_{l=1}^{L}\Lambda^{11}(\boldsymbol{\theta}_{t,k-1}^{(l)})\right\} \tag{42}$$

$$\mathbf{D}_k^{12} \approx \left(\mathbf{D}_k^{21}\right)^T \cong \frac{1}{T}\sum_{t=1}^{T}\left\{\frac{1}{L}\sum_{l=1}^{L}\Lambda^{12}(\boldsymbol{\theta}_{t,k-1}^{(l)})\right\} \tag{43}$$

$$\mathbf{D}_k^{22} \approx \mathbf{Q}^{-1} + \frac{1}{T}\sum_{t=1}^{T}\left\{\frac{1}{L}\sum_{l=1}^{L}\Lambda^{22}(\boldsymbol{\theta}_{t,k}^{(l)}, \mathbf{z}_{t,k})\right\} \tag{44}$$

When the number of samples L is large enough, the estimated results would converge to true values. Finally, we arrive at the resulting Monte-Carlo-based posterior Cramer–Rao bound (MC-PCRB).

3. Simulations and Experiments

In this simulation, we take target tracking in the automotive radar system as an example. The state process model with the constant velocity, which is a typically linear equation, can be expressed by

$$\boldsymbol{\theta}_k = f(\boldsymbol{\theta}_{k-1}) + \mathbf{u}_k = \mathbf{A}\boldsymbol{\theta}_{k-1} + \mathbf{u}_k \tag{45}$$

where $\boldsymbol{\theta}_k = [x_k, y_k, \dot{x}_k, \dot{y}_k]$, containing the two-dimensional location (x_k, y_k) and the corresponding velocities $(\dot{x}_k, \dot{y}_k)$ of the vehicle. The state transition matrix $\mathbf{A}$ can be written by

$$\mathbf{A} = \begin{bmatrix} 1 & 0 & \Delta T & 0 \\ 0 & 1 & 0 & \Delta T \\ 0 & 0 & 1 & 0 \\ 0 & 0 & 0 & 1 \end{bmatrix} \tag{46}$$

where ΔT denotes the sampling interval of the radar. The nonlinear measurement model in the automotive radar system can be denoted by,

$$\begin{bmatrix} R_k \\ \phi_k \\ V_k \end{bmatrix} = h\left(\begin{bmatrix} x_k \\ y_k \\ \dot{x}_k \\ \dot{y}_k \end{bmatrix}\right) = \begin{bmatrix} \sqrt{x_k^2 + y_k^2} \\ \arctan\left(\frac{x_k}{y_k}\right) \\ \frac{x_k\dot{x}_k + y_k\dot{y}_k}{\sqrt{x_k^2+y_k^2}} \end{bmatrix}. \tag{47}$$

where R_k denotes the measured range of the target at the time step k, ϕ_k represents the measured spatial information, and V_k is its measured radial velocity.

3.1. Performance Testing on Simulated Data

In this simulation, a spiral trajectory is considered, and the spiral trajectory can be generated by a radius reduction circular motion. Assume that the radar continuously acquires the observed measurement vector, and the measurements containing outliers are generated according to the mixture model

$$\mathbf{z}_k|\boldsymbol{\theta}_k, c_{k,m} \sim \begin{cases} \mathrm{U}(\mathbf{z}_k|a_m, b_m), & \text{if } c_{k,m} = 0 \\ \mathcal{N}(\mathbf{z}_k|h(\boldsymbol{\theta}_k), \mathbf{R}), & \text{if } c_{k,m} = 1 \end{cases} \tag{48}$$

where $c_{k,m} = 0$ indicates a normal measurement from the mth dimension at the kth time step clutter and $U(\cdot)$ is a uniform distribution, while $c_{k,m} = 1$ indicates the measurement vector is a normal one, and noises follow Gaussian distribution with the measurement noise covariance matrix $\mathbf{R} = \mathrm{diag}([4, 0.01, 1])$. The processed noise covariance matrix is assumed to be $\mathbf{Q} = \mathrm{diag}([0.1, 0.1, 0.01, 0.01])$. Multidimensional outliers caused by interferences or clutters are assumed to be drawn from the uniform distribution with the following parameters: $[a_1, b_1] = [10, 90]$ in the range entry in the measurement vector,

$[a_2, b_2] = [-\pi/2, \pi/2]$ in the azimuth entry, and $[a_3, b_3] = [-10, 10]$ in the velocity entry. The probability of outliers is assumed to be constant over time, that is, $c_{k,m}$ is a Bernoulli random variable with the probability of $p(c_{k,m} = 0) = 0.2$. In the particle filter method, the number of particles S is 500, and hyperparameters $\mathbf{v}$ are set to be $[10, 10, 10]^T$. The total step number K is 1000 with the sampling interval ΔT of 0.01 s. All the results are implemented on the PC with CPU (Intel Core i7-10700K) using Matlab R2020a.

For the performance evaluation of estimated target location, the root of mean square error (RMSE) and normalized mean square error (NMSE) are defined as performance indexes

$$\mathrm{RMSE}_k = \sqrt{\left(\langle x_k \rangle - x_k^{\mathrm{TRUE}}\right)^2 + \left(\langle y_k \rangle - y_k^{\mathrm{TRUE}}\right)^2} \tag{49}$$

$$\mathrm{NMSE} = \frac{1}{K} \sum_{k=1}^{K} \frac{\mathrm{RMSE}_k}{\sqrt{\left(x_k^{\mathrm{TRUE}}\right)^2 + \left(y_k^{\mathrm{TRUE}}\right)^2}} \tag{50}$$

where $\langle \boldsymbol{\theta}_k \rangle = [\langle x_k \rangle, \langle y_k \rangle, \langle \dot{x}_k \rangle, \langle \dot{y}_k \rangle]^T$ denotes the estimated state vector at the step time k. The performance comparisons of tracking results with the conventional particle filter (PF) and other robust solutions, including the weighted robust PF (WR-PF) and the outlier robust extended KF (OR-EKF), are provided in Figure 3. It is observed that the estimated trajectory is the closest to the truth one compared with the WR-PF and OR-EKF methods, and thus the proposed method has the smallest NMSE. Note that the results in the PF method are not provided due to quite a sensitivity to outliers, yielding significantly poor performances.

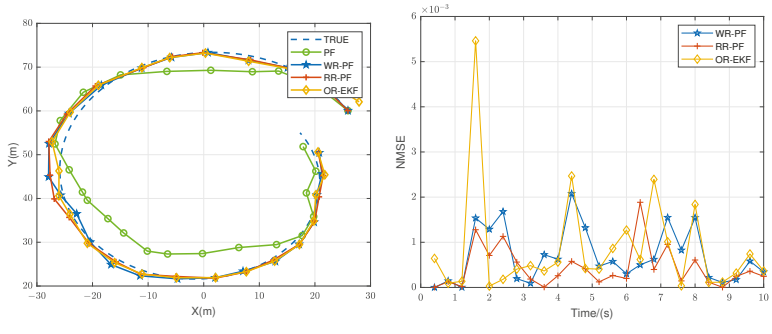

(**a**) (**b**)

Figure 3. Performance comparisons on simulated data. (**a**) Estimated target locations. (**b**) Estimated RMSE.

The performances versus outlier ratios with $p(c_{k,m} = 0)$ are also examined. The outlier ratio varies from 0% to 50%, and all other parameters are kept in this simulation. It is reasonable that the NMSEs generally decreases with decreases in the outlier ratios. It is observed that the proposed method has the lowest NMSE across all ratios compared with other methods, as shown in Figure 4.

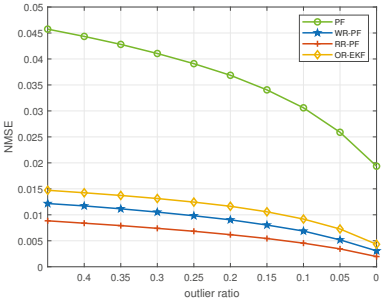

Figure 4. Estimated NMSE versus outlier ratios.

In addition, we also introduce average Mahalanobis distance as the performance index to evaluate the performance of the entire estimated state-space vector and defined it as

$$\mathrm{D_M} = \frac{1}{K}\sum_{k=1}^{K}\sqrt{\left(\langle\boldsymbol{\theta}_k\rangle - \boldsymbol{\theta}_k^{\mathrm{TRUE}}\right)\mathbf{Q}^{-1}\left(\langle\boldsymbol{\theta}_k\rangle - \boldsymbol{\theta}_k^{\mathrm{TRUE}}\right)} \tag{51}$$

where $\boldsymbol{\theta}_k = [x_k, y_k, \dot{x}_k, \dot{y}_k]$ is the true state vector containing the two-dimensional location (x_k, y_k) and the corresponding velocities $(\dot{x}_k, \dot{y}_k)$ of the vehicle. $\langle\boldsymbol{\theta}_k\rangle$ denotes the estimated vector of $\boldsymbol{\theta}_k$, and $\mathbf{Q}$ is the process noise covariance matrix provided in the simulations.

The performance results versus outlier ratios are also examined in Figure 5, the proposed method has the lowest Mahalanobis distance across all ratios, and thus has better performance than those in the WR-PF and OR-EKF methods. Note that the results in the PF method are not provided due to quite a sensitivity to outliers, yielding significantly poor performances.

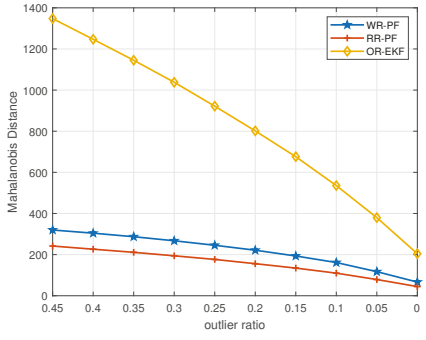

Figure 5. Estimated Mahalanobis distance versus outlier ratios.

In the following simulations, diverse types of outliers in the multidimensional measurements are considered to examine the performances of the proposed method. First, we consider only range outliers in the multidimensional measurements, that is to say, the azimuth and velocity entries are abnormal values with $p(c_{k,2}) = p(c_{k,3}) = 0$. It is found that both PF-based methods have better performances than that in the KF-based method, shown in Figure 6. The main reason may be the nonlinear approximation in the measurement function in the EKF method. These two PF-based outlier-robust methods can effectively address the range outlier issue and acquire comparable NMSEs, even though the NMSEs in the WR-PF method are a little bit smaller than those in the proposed method in the target location estimation, shown in Figure 6a. The possible reason could be that the entry of range is much larger than the other two entries in the multidimensional measurements, and thus the scalar weight in the WR-PF method is learned and estimated to accurately

model the measurement noise variances, particularly in the noise variance of the range entry in the multidimensional measurements, such that the lower NMSEs in the target locations can be obtained. However, to evaluate the performance of the entire estimated state-space vector in the filtering methods, the proposed method has the lowest average Mahalanobis distance across outlier ratios, shown in Figure 6b. Therefore, it suggests that the proposed method has better estimation performances in the entire state-space vector estimation by treating the weights associated with each entry in the measurement vector data probabilistically.

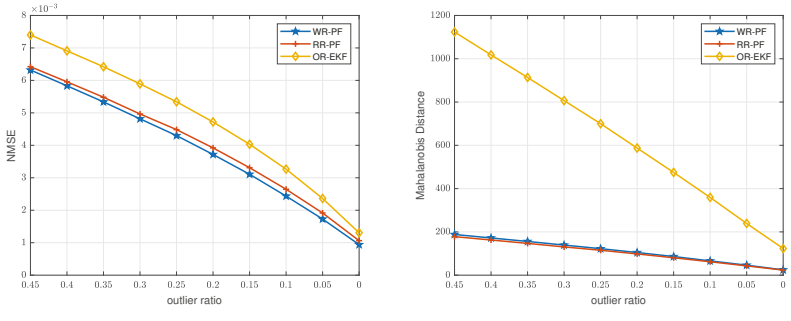

(**a**) (**b**)

Figure 6. Estimated errors versus only range outliers in multidimensional measurements. (**a**) NMSE comparisons. (**b**) Mahalanobis distance comparisons.

Then, we consider only azimuth outliers in the multidimensional measurements, and the other two entries are normal values. The proposed method has the lowest estimated NMSE in both average Mahalanobis distance and NMSE compared with those in the OR-EKF and WR-PF methods, shown in Figure 7. Finally, Figure 8 shows the performance comparisons between the proposed method and the other two robust solutions in the only velocity outliers case, and it is observed that the proposed method has clear performance improvements and has the lowest NMSE and average Mahalanobis distance across normal measurement ratios.

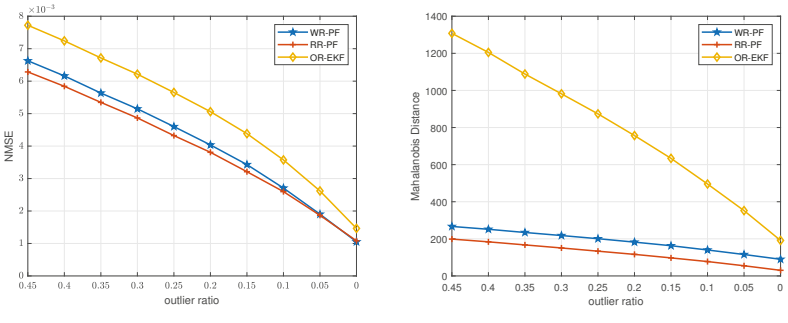

(**a**) (**b**)

Figure 7. Estimated errors versus only azimuth outliers in multidimensional measurements. (**a**) NMSE comparisons. (**b**) Mahalanobis distance comparisons.

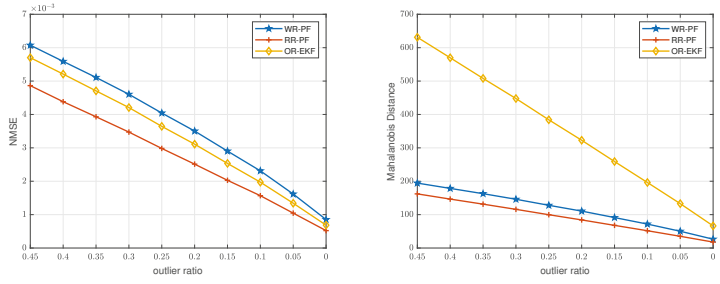

(**a**) (**b**)

Figure 8. Estimated errors versus only radial velocity outliers in multidimensional measurements. (**a**) NMSE comparisons. (**b**) Mahalanobis distance comparisons.

Table 1 shows the average executive comparisons of these robust solutions. It is observed that the executive time of the proposed method is comparable to these PF-based methods, whereas the proposed method has the best performance among them. It is reasonable that the OR-EKF method has the smallest executive time among all these methods owing to its analytical formulation, whereas it generally has slightly poorer performance than the PF-based robust solutions such as the WR-PF and RR-PF methods.

Table 1. Executive time comparisons.

Method	PF	OR-EKF	WR-PF	RR-PF
Average executive time	0.0269 s	0.0096 s	0.0317 s	0.0367 s

3.2. Cramer–Rao Bound Analysis of the Proposed Algorithm

To further illustrate the estimation performance of the algorithm, we provide the Cramer–Rao Bound for the nonlinear system to serve as the reference for the estimation error. We present the universal MC-PCRB method above for discrete-time state-space models to solve the iterative Cramer–Rao bound at each step in Equation (16). Figure 9 shows the comparison results among these methods. The outlier ratios are assigned to be $p(c_{k,1}) = p(c_{k,2}) = p(c_{k,3}) = 0.2$. It is observed that the RMSEs in the outlier robust methods generally decrease with the increases in the time step, except in the conventional PF method. The proposed method is generally close to the PCRLB, and thus has the lowest RMSE. The proposed method has higher RMSEs than the WR-PF method in the early stage because of more parameters to learn. In theory, the proposed method would approach the PCRLB, as long as the number of particles approaches infinity while tracking under a stable state.

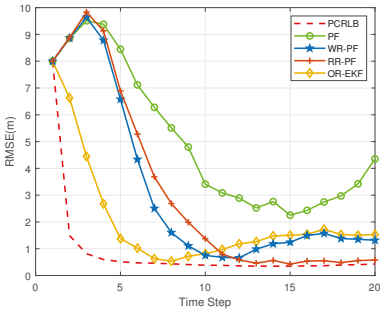

Figure 9. Bounds comparisons of estimated errors.

3.3. Experimental Results Based on Real Data

In this subsection, real data collected by the automotive millimeter wave (MMW) radar with linear modulated continuous waveform (LFMCW) are used to verify the algorithm's effectiveness. In the automotive radar application, pedestrian tracking based on the MMW radar is often an issue of great importance. Therefore, we consider pedestrian tracking in these experiments. A 77 GHz millimeter wave radar, whose parameters are shown in Table 2, is used to carry out experiments. An LFMCW waveform with a bandwidth of 4 GHz is used for the high range resolution of 0.0375 m, and the sampling rate of 6.25 MHz is used to acquire raw data. Two-dimensional (2D) Fourier Transform (FT) is firstly implemented on the raw data, and thus the constant false alarm ratio (CFAR) technique is used to acquire the estimates of the range and velocity of the walking pedestrian. Finally, the digital beamforming technique is utilized to obtain the azimuth of the pedestrian. To this end, the measurement vector is acquired for further target tracking. During the data collection of the pedestrian, several artificial blocks are place along the tracking path, and then some outlier measurements occur in the acquired measurement vector.

Table 2. Parameters for the LFMCW Radar System.

Parameters	Definition	Values
f_c	Carrier frequency	77 GHz
B	Bandwidth	4 GHz
F_s	Sampling rate	6.25 MHz
T	Pulse duration	50 μs
FFT_r	Range FFT points	128

In the first experiment trial, the pedestrian walked from the location (1.5, 2.5) to the location (−1.5, 2.1) along a straight line. There is an artificial blocker from the location (−0.3, 1.5) to the location (0.3, 1.5). The sketch map is shown in Figure 10. The measurement vector data have some outliers from the 30th to the 37th time step because of crossing the blocker. The acquired measurement vector data are given in Figure 11. It is observed that the measurement vectors involve several obvious outliers at several time steps due to the artificial occlusion or clutters reflected from the complex environment. The tracking results and the corresponding RMSEs are, respectively, shown in Figure 12a,b. It demonstrates that the estimated trajectory in the proposed method is much closer to the true one, and thus it has the lowest RMSE compared with other methods. It is found that there exist a few fluctuations in the interval from the 20th time step and the 35th time step; a possible reason may result from the measurement precision issue of pedestrian walking trajectory in the real experiment, and the true trajectory of the walking pedestrian may be around the preassigned straight line, with some inevitable fluctuations when the pedestrian walked along the straight line in the natural walking state. Although a few fluctuations appear, the RMSEs of the proposed method reach a pretty small level, and they are almost the lowest across time steps compared with other robust solutions.

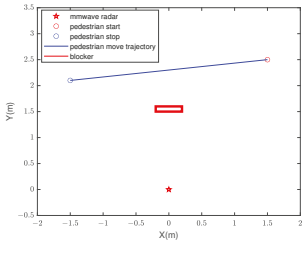

Figure 10. Experiment environment sketch map.

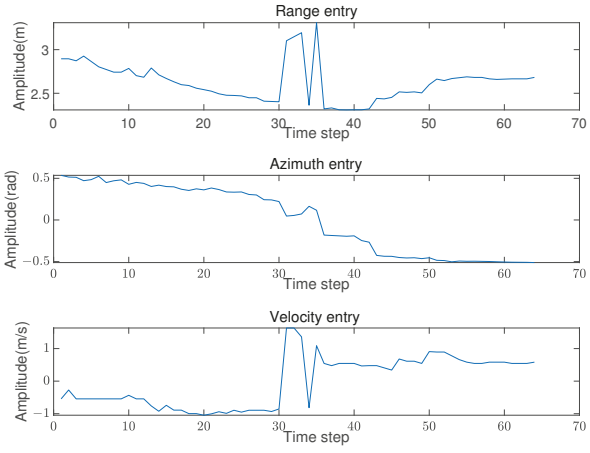

Figure 11. Raw data plots in three-dimensional entries in the measurement vector.

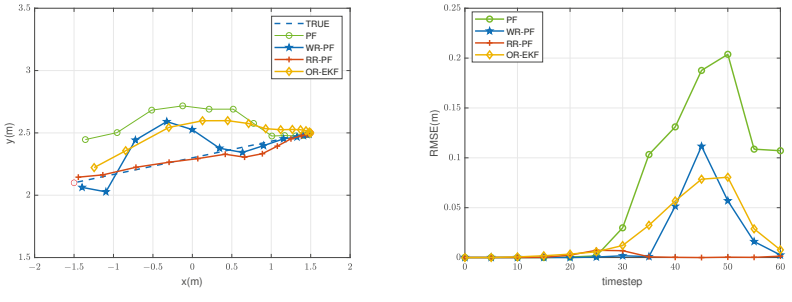

(**a**) (**b**)

Figure 12. Performance comparisons of tracking results in the real data. (**a**) Tracking results based on real data. (**b**) RMSE comparisons.

In the second experiment trial, the slightly complex trajectory, which involves curvilinear motion, turning around, and sharp turning, is considered to verify the effectiveness of the proposed method. The acquired measurement vector data are provided in Figure 13, and it is observed that the measurement vectors have obvious outliers at a few time steps due to the clutters reflected from the complex electromagnetic environment. The tracking results and the corresponding RMSEs are, respectively, shown in Figure 14a,b. They demonstrate that the estimated trajectory in the proposed method is much closer to the true one and almost has the lowest RMSE compared with other robust methods.

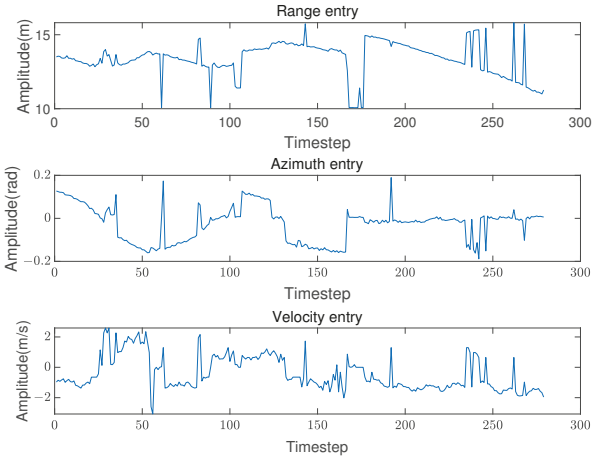

Figure 13. Raw data plots in three-dimensional entries in the measurement vector.

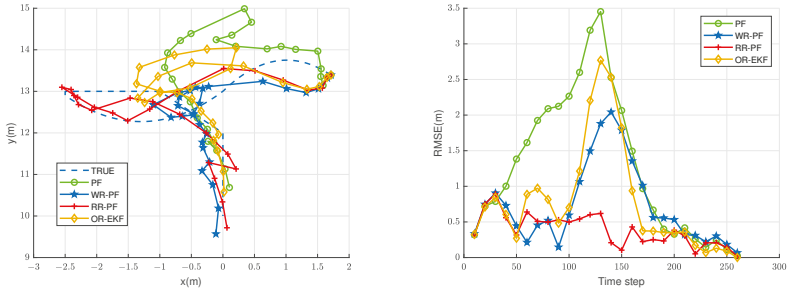

(**a**) (**b**)

Figure 14. Performance comparisons of tracking results in the real data. (**a**) Tracking results based on real data. (**b**) RMSE comparisons.

4. Conclusions

In this paper, we consider the nonlinear filtering problem in the presence of contaminated measurements. A novel reweighted robust particle filter method was proposed for accurate target tracking in the automotive radar system. We generalized nonlinear filtering to the more comprehensive case of multidimensional outlier measurements and enhanced state vector estimates by probabilistically learning a weight vector for each entry in the multidimension measurement vector. The particle filter technique was adopted to make an approximate posterior in this nonlinear system. We also illustrated the reason that the proposed method is more robust to outliers. Finally, the Cramer–Rao lower bound of the proposed method was also provided. Both simulations and experiments verified the superiority of the proposed method over other robust solutions.

Author Contributions: Conceptualization, Q.W.; methodology, Q.W., L.C., Y.L. and S.Y.; softwarep, L.C.; validation,; formal analysis, Q.W.; investigation, Q.W., Z.W. and H.L.; writing—original draft preparation, Q.W., L.C. and Y.L.; writing—Q.W. and L.C.; supervision, S.Y. and H.L.; funding acquisition, Q.W. All authors have read and agreed to the published version of the manuscript.

Funding: The work was supported in part in part by Key Laboratory of Underwater Acoustic Countermeasure Technology under Grant No. 2022JCJQLB03305, National Natural Science Foundation under Grants No. 91938203, in part by Fundamental Research Funds for the Central University under Grant No. 2242022k30016, in part by National Defense Basis Scientific Research program of China under Grant No. JCKY2019110C143, and in part by Science and Technology on Near-Surface Detection Laboratory Pre-research Fund under Grant No. 6142414200505.

Data Availability Statement: Not applicable.

Conflicts of Interest: The authors declare no conflict of interest.

References

1. Lewis, T. *Outliers in Statistical Data*, 3rd ed.; John Wiley & Sons: Hoboken, NJ, USA, 1994; p. 608.
2. Du, H.; Wang, W.; Bai, L. Observation noise modeling based particle filter: An efficient algorithm for target tracking in glint noise environment. *Neurocomputing* **2015**, *158*, 155–166. [CrossRef]
3. Nigam, N.; Saxena, T.; Richhariya, V. Global high dimension outlier algorithm for efficient clustering outlier detection. In Proceedings of the 2016 Symposium on Colossal Data Analysis and Networking (CDAN), Indore, India, 18–19 March 2016.
4. Zhu, J.; Kia, S. Bias compensation for UWB ranging for pedestrian geolocation applications. *IEEE Sens. Lett.* **2019**, *3*, 1–4. [CrossRef]
5. Bai, J.; Li, S.; Huang, L.; Chen, H. Robust detection and tracking method for moving object based on radar and camera data fusion. *IEEE Sens. J.* **2021**, *21*, 10761–10774. [CrossRef]
6. Zhou, T.; Yang, M.; Jiang, K.; Wong, H.; Yang, D. MMW radar-based technologies in autonomous driving: A review. *Sensors* **2020**, *20*, 7283. [CrossRef] [PubMed]
7. Wu, Q.; Lai, Z.; Amin, M.G.Through-the-wall radar imaging based on Bayesian compressive sensing exploiting multipath and target structure. *IEEE Trans. Comput. Imag.* **2021**, *7*, 422–435. [CrossRef]
8. Kalman, R.E. A new appraoch to linear filtering and prediction problems. *J. Basic Eng.* **1960**, *82*, 35–45. [CrossRef]
9. Zhai, G.; Wu, C.; Wang, Y. Millimeter wave radar target tracking based on adaptive kalman filter. In Proceedings of the 2018 IEEE Intelligent Vehicles Symposium (IV), Changshu, China, 26–30 June 2018; pp. 453–458.
10. Fang, H.; Haile, M.A.; Wang, Y. Robust extended kalman filtering for systems with measurement outliers. *IEEE Trans. Control Syst. Technol.* **2022**, *30*, 795–802. [CrossRef]
11. Mili, L.; Cheniae, M.G.; Vichare, N.S.; Rousseeuw, P.J. Robust state estimation based on projection statistics of power systems. *IEEE Trans. Power Syst.* **1996**, *11*, 1118–1127. [CrossRef]
12. Thomas, L.; Mili, L. A robust GM-estimator for the automated detection of external defects on barked hardwood logs and stems. *IEEE Trans. Signal Proc.* **2007**, *55*, 3568–3576. [CrossRef]
13. Gandhi, M.A; Mili, L. Robust kalman filter based on a generalized maximum-likelihood-type estimator. *IEEE Trans. Signal Proc.* **2010**, *58*, 2509–2520. [CrossRef]
14. Zhao, J.; Netto, M.; Mili, L. A robust iterated extended kalman filter for power system dynamic state estimation. *IEEE Trans. Power Syst.* **2017**, *32*, 3205–3216. [CrossRef]
15. De Palma, D.; Indiveri, G. Output outlier robust state estimation. *Int. J. Adapt. Control Signal Proc.* **2017**, *31*, 581–607. [CrossRef]
16. Pich, R.; Sárkká, S.; Hartikainen, J. Recursive weighted robust filtering and smoothing for nonlinear systems using the multivariate student-t distribution. In Proceedings of the IEEE International Workshop on Machine Learning for Signal Processing, Santander, Spain, 23–26 September 2012; pp. 1–6.
17. Tapia, E. Gaussian and student-t filtering using implicit measurements via variational bayes. In Proceedings of the IEEE International Workshop on Machine Learning for Signal Processing (MLSP), Reims, France, 21–24 September 2014; pp. 1–6.
18. Wang, H.; Li, H.; Zhang, W.; Wang, H. Laplace l_1 robust Kalman filter based on majorization minimization. In Proceedings of the 20th International Conference on Information Fusion (Fusion), Xi'an, China, 10–13 July 2017; pp. 1–5.
19. Wang, G.; Yang, C.; Ma, X. A novel robust nonlinear Kalman filter based on multivariate laplace distribution. *IEEE Trans. Circ. Syst. Exp. Brief.* **2021**, *68*, 2705–2709. [CrossRef]
20. Ting, J.-A.; Theodorou, E.; Schaal, S. Learning a weighted robust Kalman filter. In Proceedings of the Machine Learning: ECML 2007, Warsaw, Poland, 17–21 September 2007; pp. 748–756.
21. Ting, J.-A.; Theodorou, E.; Schaal, S. A Kalman filter for robust outlier detection. In Proceedings of the 2007 IEEE/RSJ International Conference on Intelligent Robots and Systems, San Diego, CA, USA, 29 October–2 November 2007; pp. 1514–1519.
22. Agamennoni, G.; Nieto, J.I.; Nebot, E.M. An outlier-robust Kalman filter. In Proceedings of the 2011 IEEE International Conference on Robotics and Automation, Shanghai, China, 9–13 May 2011; pp. 1551–1558.
23. Huang, Y.; Zhang, Y.; Wu, Z.; Li, N.; Chambers, J. A novel adaptive kalman filter with inaccurate process and measurement noise covariance matrices. *IEEE Trans. Autom. Control* **2018**, *63*, 594–601. [CrossRef]
24. Julier, S.J.; Uhlmann, J.K.; Durrant-Whyte, H. A new approach for filtering nonlinear systems. In Proceedings of the 1995 American Control Conference—ACC'95, Seattle, WA, USA, 21–23 June 1995; pp. 1628–1632.
25. Arulampalam, M.S.; Maskell, S.; Gordon, N.; Clapp, T. A tutorial on particle filters for online nonlinear/non-Gaussian Bayesian tracking. *IEEE Trans. Signal Proc.* **2002**, *50*, 174–188. [CrossRef]

26. Huang, Y.; Zhang, Y.; Li, N.; Chambers, J. A robust gaussian approximate filter for nonlinear systems with heavy tailed measurement noises. In Proceedings of the IEEE International Conference on Acoustics, Speech and Signal Processing (ICASSP), Shanghai, China, 20–25 March 2016; pp. 4209–4213.
27. Xu, D.; Shen, C.; Shen, F. A robust particle filtering algorithm with non-gaussian measurement noise using student-t distribution. *IEEE Signal Proc. Lett.* **2014**, *21*, 30–34. [CrossRef]
28. Tichavsky, P.; Muravchik, C.H.; Nehorai, A. Posterior Cramer-Rao bounds for discrete-time nonlinear filtering. *IEEE Trans. Signal Proc.* **1998**, *46*, 1386–1396. [CrossRef]

remote sensing

MDPI

Article

Multi-Hand Gesture Recognition Using Automotive FMCW Radar Sensor

Yong Wang [1,*], Di Wang [1], Yunhai Fu [2], Dengke Yao [1], Liangbo Xie [1] and Mu Zhou [1]

[1] School of Communication and Information Engineering, Chongqing University of Posts and Telecommunications, Chongqing 400065, China; S210101128@stu.cqupt.edu.cn (D.W.); S190131007@stu.cqupt.edu.cn (D.Y.); xielb@cqupt.edu.cn (L.X.); zhoumu@cqupt.edu.cn (M.Z.)
[2] Wuhan Martime Communication Research Institute, Wuhan 430025, China; fucloudsea@gmail.com
* Correspondence: yongwang@cqupt.edu.cn

Abstract: With the development of human–computer interaction(s) (HCI), hand gestures are playing increasingly important roles in our daily lives. With hand gesture recognition (HGR), users can play virtual games together, control the smart equipment, etc. As a result, this paper presents a multi-hand gesture recognition system using automotive frequency modulated continuous wave (FMCW) radar. Specifically, we first constructed the range-Doppler map (RDM) and range-angle map (RAM), and then suppressed the spectral leakage, and dynamic and static interferences. Since the received echo signals with multi-hand gestures are mixed together, we propose a spatiotemporal path selection algorithm to separate the mixed multi-hand gestures. A dual 3D convolutional neural network-based feature fusion network is proposed for feature extraction and classification. We developed the FMCW radar-based platform to evaluate the performance of the proposed multi-hand gesture recognition method; the experimental results show that the proposed method can achieve an average recognition accuracy of 93.12% when eight gestures with two hands are performed simultaneously.

Keywords: frequency modulated continuous wave radar; gesture recognition; multi-hand; deep learning

Citation: Wang, Y.; Wang, D.; Fu, Y.; Yao, D.; Xie, L.; Zhou, M. Multi-Hand Gesture Recognition Using Automotive FMCW Radar Sensor. *Remote Sens.* **2022**, *14*, 2374. https://doi.org/10.3390/rs14102374

Academic Editors: Zhihuo Xu, Jianping Wang and Yongwei Zhang

Received: 20 April 2022
Accepted: 13 May 2022
Published: 14 May 2022

1. Introduction

With the development of wireless sensing [1], human–computer interaction (HCI) [2] has widely been applied in daily life. The hand gesture recognition (HGR) technique, an important 'way' of HCI, is used in smart homes, robot control, virtual games, etc. For example, with HGR, users can control smart devices and play interactive virtual games. More importantly, with the development of intelligent vehicles, the application of gesture recognition in intelligent-assisted driving is particularly important. The driver can control various functions inside the car through gestures, such as adjusting the in car entertainment system or switching on or off the air conditioner, to help drivers concentrate and improve the driving safety. As a result, HGR is receiving a lot of attention; this paper focuses on HGR.

According to the acquisition method of hand gesture data, HGR can be divided into three types: (i) wearable sensor-based HGR [3], (ii) vision-based HGR [4], and radar-based HGR [5,6]. Based on the wearable sensors, the wearable-based HGR in [3] can acquire the motion information of hand gestures and achieve recognition accuracy as high as 99.3%. Since this method involves wearing sensors, wearable sensors usually bring uncomfortable and inconvenient experiences to users. On the other hand, vision-based HGR [4] applies cameras to capture RGB or depth images of hand gestures, in combination with image processing or computer vision for gesture recognition. Although the recognition accuracy is relatively high, vision-based HGR is usually invalid in case of poor lighting conditions and non-line-of-sight. Radar-based HGR applies the radar sensor to collect the hand gesture

motion in a device-free manner. It has a non-contact advantage, is not affect by light, and has attracted much attention in both academic and the industry [7,8].

In general, radar-based HGR mainly contains two stages: (i) signal preprocessing and (ii) gesture feature extraction and classification. In the first stage, the raw radar signal is collected and processed to obtain the motion parameters (such as range or Doppler) of hand gestures. In References [7,8], the authors used two-dimensional fast Fourier transform (2D-FFT) to estimate the range and Doppler map (RDM) of hand gestures. To improve the quality of RDM, Wang et al. in [9] adopted the gradient threshold to filter out the step peak in RDM, and then used the wavelet transform to further enhance RDM. To reduce the interferences, the authors in [10] adopted the neighbor threshold detection method instead of the constant false alarm rate (CFAR) [11] to filter out the interference targets and detect the hand gesture targets. After suppressing the interference signal by the first-order recursive filter, the authors in [12] used the lognormal CFAR to detect the hand gestures. Although there were some works focusing on interference suppression and hand gesture detection, they only considered the range and Doppler information of hand gestures. In fact, the angle information of hand gestures provided an additional dimension to describe the hand gesture motion. As a result, the motion parameters (range, Doppler, and angle) in combination with interference suppression should be fully utilized to explore the performance of HGR. In the stage of feature extraction and classification of HGR, a deep learning method, such as the convolutional neural network (CNN) [13,14] was proven to be an effective mean for HGR. The deep convolutional neural network (DCNN) was applied to extract the gesture features of micro-Doppler and achieve gesture recognition with 14 types of hand gestures [15]. However, the time features of the hand gesture motion were ignored, restricting the recognition accuracy of HGR. In References [16,17], 3D convolutional neural networks (3D-CNN) were presented to extract the motion features of continuous gestures. However, this 3D-CNN only focused on the local time features of hand gestures, and ignored the global time features of hand gestures. Zhang et al. [18] applied the long short term memory (LSTM) network [19] to learn the global time features. In [12], Yang et al. proposed a reused LSTM network to extract the trajectory features of the range, angle, and Doppler of hand gestures.

The aforementioned researchers conducted a lot of work and promoted the development of HGR. However, all of them focused on HGR with a single hand gesture. In many applications, such as virtual games and collaborative control, multi-hand gestures should be recognized simultaneously. When there are multiple dynamic hand gestures in front of the radar, the echo signals of multiple gestures mix together, and the multi-hand gesture recognition becomes more difficulty. Peng et al. [20] explored the multi-hand gesture recognition using the different ranges that corresponded to different hand gestures. Unfortunately, this method is not applicable when the multi-hand gestures have the same range. By using the range and angle information of multi-hand gestures with the beamforming technique, Wang et al. [21] extracted each gesture signal successively and then carried out a 2D-FFT operation to obtain the Doppler spectrum of each hand gesture. Although range and angle parameters are used for multi-hand gesture recognition, the Doppler information is missing. More importantly, when the multi-hand gestures have the same range and different hand gestures have similar Doppler characteristics, the recognition accuracies of the above two multi-hand gesture recognition methods are pessimistic. Therefore, this paper applies the automotive frequency modulated continuous wave (FMCW) radar, and tries to design a multi-hand gesture recognition system by making full use of the three-dimensional parameters of range, Doppler, and angle, and designing a novel deep learning network. The main contributions of this paper are summarized as follows.

Firstly, we applied 3D-FFT on the fast-time domain, slow-time domain, and antenna domain to estimate the range, Doppler, and angle parameters. Specifically, the 2D-FFT was applied to construct the RDM, and the angle FFT was applied on the results of range FFT among multiple antennas to construct the range-angle map (RAM). We applied the Hanning window to suppress the spectral leakage, two-dimensional CA-CFAR (2D-CA-CFAR) to

suppress the dynamic interference, and the average power of several continuous frames in feature maps to suppress the static interference in RDMs and RAMs of multi-hand gestures.

Secondly, we propose a spatiotemporal path selection algorithm to separate the multi-hand gestures in RDMs and RAMs. We designed a dual 3D-CNN-based feature fusion network (D-3D-CNN-FN) for feature extraction and classification of the separated hand gestures. Specifically, the dual 3D-CNN network was presented to extract the features of RDMs and RAMs, and the extracted features from multiple frames were then fused and input into LSTM. The output feature sequence is classified by softmax.

Finally, we designed a platform and used eight types of multi-hand gestures to validate the effectiveness of the proposed multi-hand gesture recognition system; the experimental results verify the superiority of the proposed method.

The rest of this paper is organized as follows. Section 2, introduces signal processing of FMCW radar. Section 3 details the proposed multi-hand gesture recognition system, including interference suppression, multi-hand gestures separation, and hand gesture recognition. Experiments are carried out in Section 4 and followed by a conclusion in Section 5.

2. Radar Signal Processing

In this section, we analyze the working principle of the automotive FMCW radar and construct the RDM and RAM maps of multi-hand gesture parameters in details.

2.1. IF Signal of FMCW Radar

The FMCW radar generates a linear frequency modulation continuous signal through a waveform generator and transmits it by the transmitters. The transmitted signal is reflected by multi-hand gestures, and is then received by the receiving antennas. The intermediate frequency (IF) signal is obtained (shown in Figure 1) by mixing the transmitted and received signals, filtering out the high frequency part.

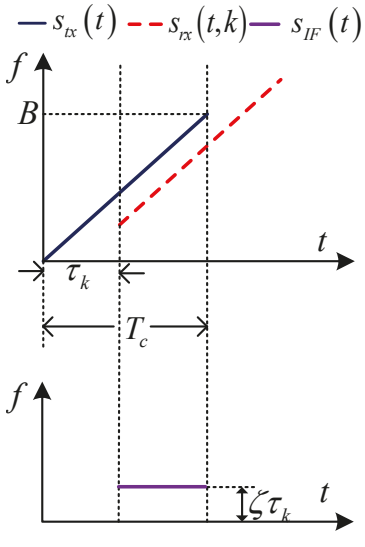

Figure 1. IF signal extraction.

The transmitted signals of the FMCW radar is

$$s_{tx}(t) = A_{tx}\cos(2\pi(f_0 t + St^2/2 + \phi_0(t))), \quad (1)$$

where A_{tx} is the amplitude, f_0 is the initial frequency, and $S = B/T_c$ is the slope of transmitted signal. B is the bandwidth of the radar, T_c is the sweep period, and $\phi_0(t)$ is the initial phase of the transmitted signal.

The received signal reflected by the k-th target (hand) can be expressed as

$$s_{rx}(t,k) = A_{rx}\cos(2\pi(f_0(t-\tau_k) + \zeta(t-\tau_k)^2/2 + \phi_0(t-\tau_k))), \tag{2}$$

where A_{rx} and $\tau_k = 2R_k/c$, respectively, represent the amplitude and flight time of the received echo signal, R_k is the range from the k-th target (hand) to the radar, and $\phi_0(t-\tau_k)$ is the phase of the received signal.

The received signal and the transmitted signal are sent to the mixer and passed through a low power filter (LPF) to obtain an IF signal. The IF signal is expressed as

$$s_{IF}(t) = \sum_{k=1}^{K} A_k \cos(2\pi(S_t\tau_k + f_0\tau_k)) + N(t), \tag{3}$$

where K is the number of hand gesture targets, A_k is the amplitude of the IF signal of the hand gesture target, and $N(t)$ is the white Gaussian noise.

2.2. Theory of Parameters Estimation

To achieve multi-hand gesture recognition, in this paper, the range, Doppler, and angle parameters of the FMCW radar are applied. In this subsection, we analyze the estimation theories of these three parameters.

2.2.1. Range Estimation

If we obtain the delayed time of the echo signal, the range between the radar and hand gesture target is calculated, i.e., $R_k = \tau_k c/2$. In fact, the delayed time cannot be obtained directly. Fortunately, according to the principle of the IF signal extraction in Figure 1, we find that the delayed time determines the frequency of the IF signal, and the relationship is as follows.

$$f_{IF} = S \cdot \tau_k = \frac{B}{T_c} \cdot \tau_k. \tag{4}$$

Therefore, the delayed time is expressed as

$$\tau_k = \frac{T_c}{B} f_{IF}. \tag{5}$$

Then, the range can be computed

$$R(f_{IF}) = \frac{cT_c}{2B} f_{IF}. \tag{6}$$

Since the radar configuration parameters are predefined, the bandwidth B and the sweep period T_c are fixed. Then, different hand gesture targets in front of the radar result in different IF frequencies, and different ranges can be obtained. According to [22], the range resolution of the FMCW radar is $d_{res} = \frac{c}{2B}$. The maximum detection range of the FMCW radar

$$R_{max} = d_{res} T_c f_s. \tag{7}$$

The range resolution is determined by the bandwidth, and the maximum detection range is affected by bandwidth, sweep period, as well as the sampling frequency. Therefore, to maintain the requirement with different ranges, these three parameters should be carefully designed.

2.2.2. Doppler Estimation

To measure the Doppler of a moving hand gesture target, at least two chirps are required. Specifically, the phase difference of two continuous chirp signals is first calculated [23]

$$\Delta\phi = \phi_2 - \phi_1 = \frac{4\pi v T_c}{\lambda}. \tag{8}$$

where ϕ_1 and ϕ_2 are the phases of the two chirp signals, λ is the wavelength, and v is the Doppler of the moving target; it is expressed as $v = \frac{\lambda}{4\pi v T_c}$.

The Doppler resolution is $v_{res} = \frac{\lambda}{2M_n T_c}$, where M_n is the chirp number in a frame. The maximum detected Doppler is $v_{max} = \frac{\lambda}{4T_c}$. The Doppler resolution is decided by the chirp number and sweep period, and the maximum detection Doppler is only determined by the sweep period.

2.2.3. Angle Estimation

Since the FMCW radar has multiple transmitting and receiving antennas, we can estimate the angle of the hand gesture target using the phase differences of multiple receiving antennas. The multiple receiving antennas cause path differences of the echo signal from the same target, resulting in the phase difference. The phase difference between two adjacent receiving antennas is

$$\Delta\varphi = 2\pi\Delta d/\lambda, \tag{9}$$

where $\Delta d = l\sin\theta$ is the path difference, l is the range between the two continuous receiving antennas, and θ is the arrival angle of the signal.

Then, the arrival angle can be expressed as

$$\theta = \sin^{-1}\left(\frac{\lambda\Delta\varphi}{2\pi l}\right). \tag{10}$$

Then, we can estimate the arrival angle by searching the spectral peak.

2.3. 3D-FFT-Based RDM and RAM Construction

Based on the range, Doppler, and angle estimation analysis, this subsection gives the RDM and RAM construction process in detail. Assume that M frames are transmitted, and each frame contains N chirps and the number sampling points of each chirp is N_{adc}. Since the three parameters can be estimated by 3D-FFT [24], we performed 3D-FFT to construct the RDM and RAM. The process of 3D-FFT for range, Doppler, and angle estimation is shown in Figure 2.

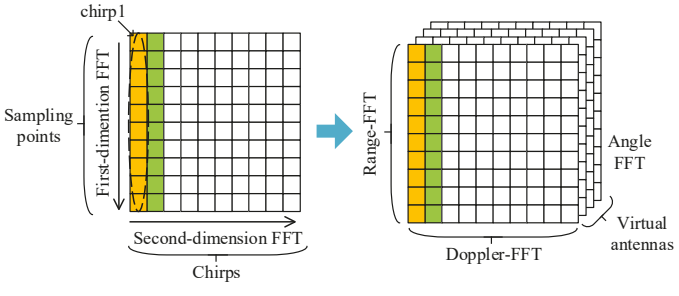

Figure 2. 3D-FFT process.

To obtain the three parameters, FFT was firstly carried out on the sampling points of each chirp (such an operation is called range-FFT) to obtain the range of the multi-hand gestures. Based on the results of the first FFT, the FFT was further carried out over N chirps

of a frame to obtain the Doppler frequency (called Doppler-FFT). By performing the 2D-FFT on different frames, we obtained the RDMs of a complete multi-hand gesture. RDMs can be obtained using a single transmitting and a single receiving antenna. With multiple transmitting and receiving antennas, the results of 2D-FFT (RDM) from different antennas were summed, resulting in less clutter and a higher SNR [25]. On the other hand, with multiple transmitting and receiving antennas, we can estimate the angle of the multi-hand gestures-based on the results of RDM. Generally, the third FFT is carried out on the results of RDM over different antennas. Then, we searched the spectral peak on the results of the third FFT to obtain the range-angle maps of multi-hand gestures.

3. Proposed Multi-Hand Gesture Recognition System

In this section, the proposed multi-hand gesture recognition system is presented, shown in Figure 3. Since there are a lot of interferences in the parameter maps (i.e., RDM and RAM), to achieve a satisfactory recognition accuracy, we have to suppress the interferences. The multi-hand gesture is then separated by the proposed spatiotemporal path selection algorithm. Finally, the separated hand gestures are trained and tested by the designed deep learning network.

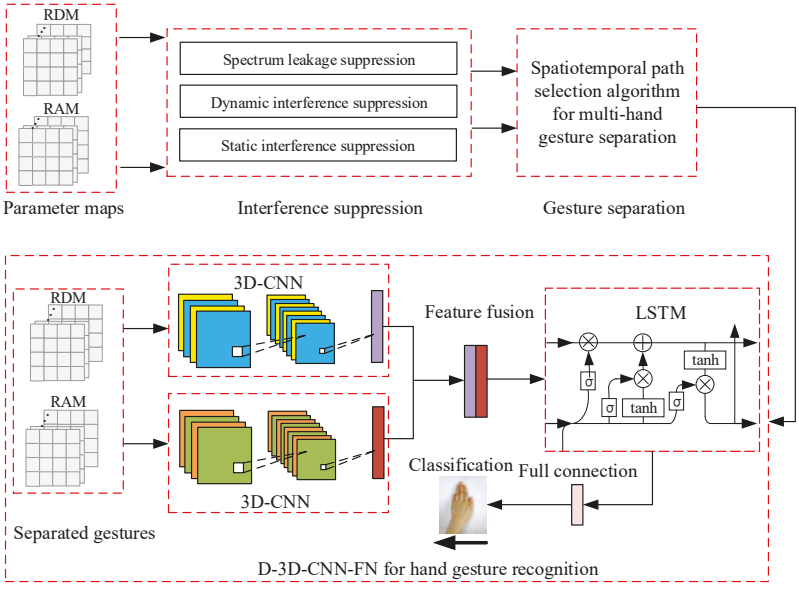

Figure 3. Proposed multi-hand gesture recognition flowchart.

3.1. Interference Suppression

There are many interferences in the IF signal. To suppress the interference from the interfering radars, the authors in [26] designed novel orthogonal noise waveforms; the key idea is that the signal in the current transmission pulse is orthogonal to the next transmission signal. In [27], the authors proposed a tunable Q-factor wavelet transform to suppress the mutual interference between automotive FMCW radars. In [28], Wang utilized a one-dimensional CFAR to detect interferences and the detection map was dilated to generate a mask for interference suppression. In case of radar self-motion, the authors in [29] investigated a range alignment processing approach for breathing estimation considering the radar self-motion and target motion. This work can be applied in the field of assistive devices for the disabled. In [30], Haggag et al. introduced a reliable and robust probabilistic method to estimate the radar self-motion. Different from the above cases, in our considered scenario, the interfering radar was not considered and the interferences in the IF signal

mainly came from the static and moving objectives in the test environment. In this paper, the interferences mainly came from the thermal noise inside the radar system, moving targets (such as torso and arms), and static targets (wall or static objects), etc. These interferences in RDMs and RAMs have significant impacts on the separation of multi-hand gestures and the recognition accuracy of hand gestures. Towards this end, we suppressed the interferences in RDMs and RAMs from the following three aspects.

3.1.1. Spectral Leakage Cancellation

The spectral leakage mainly comes from the system noise and the aperiodicity of signal truncation of the ADC sampling. The system noise causes ghost targets near the radar, while aperiodicity of signal truncation spectrum tailing in the whole frequency band, resulting in pseudo peaks around the target. Therefore, we added the Hanning window [31] to the 'three-dimensional' of the data cube. Specifically, the Hanning window was added to the sampling points of each chirp, the same sampling points of multiple chirps and the sampling points from different antennas. The results in the next section show that such an operation reduces the spectral leakage.

3.1.2. Dynamic Interference Suppression

Moving targets, such as the arms and torso, cause dynamic interferences in RDMs and RAMs. Therefore, we applied the 2D-CA-CFAR algorithm [32] to suppress these dynamic interferences in RDMs and RAMs. The 2D-CA-CFAR algorithm computes the average interference power in the referenced window in RDM (or RAM), and obtains an adaptive power threshold. The power in RDM (or RAM), higher than the threshold, is marked as hand gesture, otherwise it is marked as interference. Finally, we moved the referenced window along the range and Doppler domain (or range and angle domain) in turn to suppress the dynamic interference of RDM and extract the multi-hand target.

3.1.3. Static Interference Suppression

Although the 2D-CA-CFAR algorithm suppresses the dynamic interferences from the torso or arms, there still exists static interferences caused by the wall or static objects. Obviously, the Doppler of the static target in RDM is zero, and the range and angle of static targets in RAM keep stable. Therefore, we computed the average power of RDMs (or RAMs) over several continuous frames and subtracted the average power from RDMs (or RAMs) obtained after dynamic interference suppression. In the experiments, the averaged power was computed using five continuous frames. The authors in [33] proposed a range and Doppler cell migration correction (RDCMC) algorithm to solve the range and Doppler cell migration problem. In the future, we will apply this algorithm in combination with our interference suppression scheme on RDM and RAM to obtain better feature maps of multi-hand gestures.

3.2. Spatiotemporal Path Selection Algorithm

The parameter maps of multi-hand gestures were obtained after map construction and interference suppression. Since one frame constructs one RDM and one RAM, we collected M frames to ensure that the RDMs and RAMs contained complete multi-hand gestures. Due to the different range, the Doppler, and angle of the multi-hand gesture, different hand gesture targets show different highlights in RDM and RAM. The same hand gesture needs to be matched in RDM and RAM over different frames. However, since the range, Doppler, and angle of the multi-hand gesture are changing, the strengths of the same hand gestures in RDM and RAM on different frames are different. As a result, we cannot simply apply the strength to match the same hand gesture over different frames. Thus, based on the continuous variation characteristics in space and time, we propose a spatiotemporal path selection algorithm to separate the multi-hand gesture.

To show the separation procedure, we took RDM as an example (RAM follows the same procedure). Firstly, we found the hand gesture target that had the maximum am-

plitude in the first frame of RDM. We denoted by $Y_1(r^1, d^1)$ the maximum amplitude of the first hand gesture, and (r^1, d^1) the corresponding coordinate. Then, we calculated the cost function from (r^1, d^1) in the first frame to all the points in the second frame. The cost function is defined as

$$c_{ij}^1 = -|Y_1(r^1, d^1)| - |Y_2(r_{ij}^2, d_{ij}^2)| + \omega_{ij}^1, \tag{11}$$

where $Y_2(r_{ij}^2, d_{ij}^2)$ is the amplitude of the hand gestures in the second frame, $i = 1, \cdots, N_{adc}$ and $j = 1, \cdots, N$, r_{ij}^2 and d_{ij}^2 are, respectively, the coordinates of the range and Doppler at the second frame, ω_{ij} is the weight function between (r^1, d^1) and (r_{ij}^2, d_{ij}^2) . The weight function is defined as

$$\omega_{ij}^1 = \alpha_i^1 \|r^1 - r_{ij}^2\|_2 + \alpha_j^1 \|d^1 - d_{ij}^2\|_2, \tag{12}$$

where α_i^1 and α_j^1 are the weight factors of the range and Doppler domain, respectively, and $\|\cdot\|_2$ is the Euclidean norm.

We found the minimum value of the cost function by searching all of the computed cost values. Following the search procedure, we can obtain the coordinates of the first hand gesture target in all the M RDMs. Since the hand gesture target occupied several consecutive coordinates, we used a rectangular window to select the hand gesture target based on the obtained coordinates. To extract the rest of the hand gesture targets, we subtracted the obtained hand gesture targets from RDMs until all the hand gestures were separated. The detailed separation process is concluded in Algorithm 1.

Algorithm 1 Spatiotemporal path selection algorithm for multi-hand gesture separation.

1: Compute the hand gesture number in each RDM, denoted by N_n.
2: **for** $N_n > 1$ do
3: Initialize the frame $f = 1$.
4: **for** $f < M$ do
5: Compute the maximum amplitude $Y_f(r^f, d^f)$ and the corresponding coordinate at the f-th frame (r^f, d^f), and record the cost function C.
6: **for** each coordinate $(r_{ij}^{f+1}, d_{ij}^{f+1})$ in RDM at $f+1$-th frame do
7: Record the amplitude $Y_{f+1}(r_{ij}^{f+1}, d_{ij}^{f+1})$.
8: Compute the weight $\omega_{ij}^f = \alpha_i^f \|r^f - r_{ij}^{f+1}\|_2 + \alpha_j^f \|d^f - d_{ij}^{f+1}\|_2$
9: Compute the cost function $c_{ij}^f = -|Y_f(r^f, d^f)| - |Y_{f+1}(r_{ij}^{f+1}, d_{ij}^{f+1})| + \omega_{ij}^f$, and add c_{ij}^f into C.
10: **end for**
11: Compute the corresponding coordinate $(r^{f+1}, d^{f+1}) = \text{argmin}_{r_{ij}^{f+1}, d_{ij}^{f+1}} c_{ij}^f$ of $Y_f(r^f, d^f)$ at the $f+1$-th frame.
12: Construct a window centered on (r^{f+1}, d^{f+1}) , and obtain the RDM of the N_n-th hand gesture at the $f+1$-th frame.
13: Update $f = f + 1$.
14: **end for**
15: Subtract the RDM of the N_n-th hand gesture target from the RDM of multi-hand gesture, and update $N_n = N_n - 1$.
16: **end for**

The input of Algorithm 1 is the M RDMs of multi-hand gestures and the output is the separated M RDMs of the N_n single hand gestures. The hand gesture target in the first RDM was selected randomly, and the selected hand gesture was then subtracted. Then, by applying Algorithm 1, we obtained the M RDMs of each hand gesture. Similarly, the RAMs of each hand gesture can be obtained.

3.3. D-3D-CNN-FN for HGR

After the multi-hand gestures were separated by the proposed spatiotemporal path selection algorithm, we input the separated hand gesture dataset of RDMs and RAMs into the designed deep learning network for HGR. A total of 32 frames contained a single complete multi-hand gesture motion. To realize real-time applications, we had to segment the continuous data flow into a single complete gesture motion by finding the start and end times of the continuous multi-hand gesture motion. Since the motion features of each hand gesture are described by multiple continuous RDMs and RAMs, the features and continuity of each hand gesture should be carefully considered. Therefore, we propose a dual 3D-CNN-based feature fusion network for HGR, shown in Figure 3. The dual 3D-CNN is applied to extract the features of RDMs and RAMs, and the LSTM network is further applied to extract the continuous features of the gesture motion. The detailed procedure is described as follows.

3.3.1. 3D-CNN-Based Feature Extraction

Since each hand gesture has M RDMs and M RAMs, we applied two 3D-CNNs to respectively extract the feature of RDMs and RAMs. Then, the extracted feature sequences of range-Doppler and range-angle were fused. The detailed architecture of the dual 3D-CNN is shown in Figure 4.

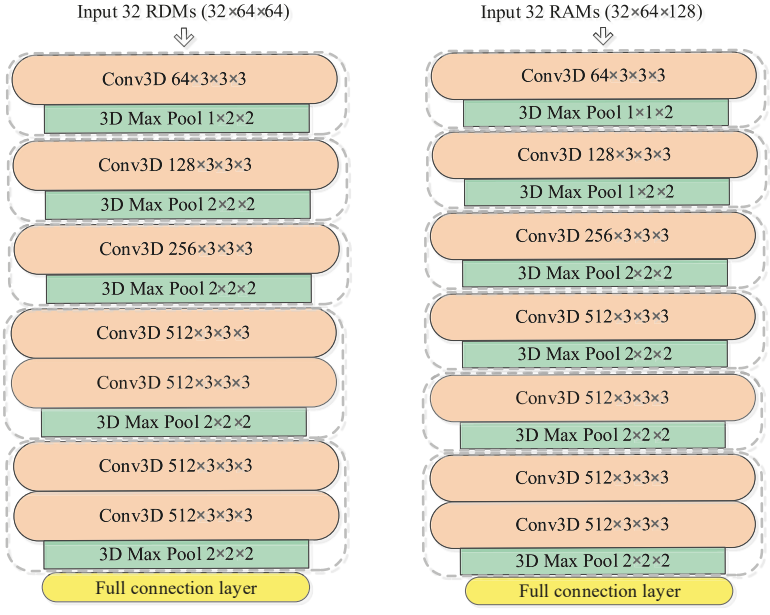

Figure 4. Architecture of dual 3D-CNN.

The sizes of RDM and RAM were 64 × 64 and 64 × 128, respectively, and the sizes were determined by the sampling points of each chirp and the chirp number in each frame. To extract the features of 32 RDMs, the designed network contained five 3D convolution and pooling layers, and one full connection layer. We carried out one 3D convolution and one maximum pooling operation in each layer of the first three 3D convolution and pooling layers. In the fourth and fifth layers, we carried out two 3D convolutions and one maximum pooling operation. To reduce the network parameters and improve the generalization ability of the network, all the convolution operations adopted a 3 × 3 × 3 convolution kernel, followed by the linear activation function of ReLu to reduce the interdependence

between parameters and alleviate the overfitting phenomenon of the network. To fulfill the characteristics of RAMs, the 3D-CNN for feature extraction of RAMs contained six 3D convolution and pooling layers; each layer applied maximum pooling. Since the size of RAM is 64 × 128, we used 1 × 1 × 2 and 1 × 2 × 2 in the first two pooling layers to maintain the size of RDM. To extract subtle local features of hand gestures, we carried out two 3D convolution operations in the final 3D convolution layer.

3.3.2. LSTM-Based Time Sequential Feature Extraction

The dual 3D-CNN extracts the dynamic hand gesture features of RDMs and RAMs over M frames, and obtains range-Doppler and range–angle features with two 1 × 1024 feature sequences. To obtain the time sequential features of the complete dynamic hand gesture, the LSTM network was applied. Since the two time sequential features were fused sequentially to obtain the feature sequence with 2 × 1024, the step of the applied LSTM network is 2. Then, the feature with size 2 × 1 is sent to each LSTM, and the time sequential feature with 1 × 1024 is the output. The LSTM for the time sequential feature extraction is shown in Figure 5. In Figure 5, f_t the forgetting gate, i_t is the input gate, c_t is the storage unit, and h_t is the hidden layer state. At each time step, i_t, f_t, c_t, o_t, and h_t are expressed as

$$\begin{cases} i_t &= \sigma(W_{mi} \cdot \mathrm{TF}_t + W_{hi} \cdot h_{t-1} + W_{ci} c_{t-1} + b_i) \\ f_t &= \sigma\Big(W_{mf} \cdot \mathrm{TF}_t + W_{hf} \cdot h_{t-1} + W_{cf} c_{t-1} + b_f\Big) \\ \tilde{c}_t &= \sigma f_t \odot + i_t \odot \tanh(W_{mc} \cdot \mathrm{TF}_t + W_{hc} \cdot h_{t-1} + b_c) \\ c_t &= f_t \cdot \tilde{c}_{t-1} + i_t \cdot \tilde{c}_t \\ o_t &= \tanh(W_{mo} \cdot \mathrm{TF}_t + W_{ho} \cdot h_{t-1} + W_{co} c_{t-1} + b_o) \\ h_t &= \tilde{o}_t \cdot \tanh(c_t) \end{cases}, \tag{13}$$

where $\sigma(\cdot)$ is the sigmoid function, $\tanh(\cdot)$ is the tanh function, $\sigma(x) = \frac{1}{1+e^{-x}}$, W_{mi}, W_{hi}, W_{ci}, W_{mf}, W_{hf}, W_{cf}, W_{mc}, W_{hc}, W_{hc}, W_{mo}, W_{ho}, and W_{co} are the weights in the LSTM unit, and b_f, b_i, and b_c are the corresponding biases.

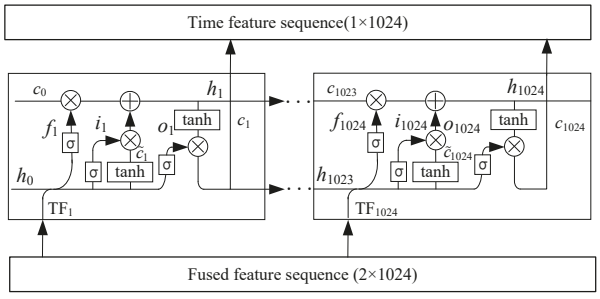

Figure 5. LSTM network-based time series feature extraction.

3.3.3. Gesture Classification

The output of the LSTM network is the time sequential feature of the hand gesture with 1 × 1024. To classify the hand gesture using the time sequential features, we first normalized the sequences and input them into the full connection layer. The feature sequences were then input into the following normalized exponential function

$$softmax_{v_i} = \frac{\exp(w_i^T v_i)}{\sum_{j=1}^{k} \exp(w_j^T v_j)}, \tag{14}$$

where i is the i-th hand gesture, v_i is the i-th element of the feature sequence, w_i is the weight corresponding to v_i, and k is the types of hand gestures.

4. Experiments and Analysis

4.1. Experimental Setup

In this paper, we designed and built a multi-hand gesture recognition platform using the automotive FMCW radar and data collection card provided by Texas Instruments (TI). The FMCW radar sensor is AWR1642 [34], and the data collection card is DCA1000 [35], shown in Figure 6. The collected data were processed by a personal computer (PC); the recognition results were displayed with the graphical user interface (GUI). The radar had two transmitting and four receiving antennas; the start frequency was 77 GHz and the bandwidth was 4 GHz. We collected 32 frames to acquire the complete multi-hand gestures; the detailed radar parameters are configured in Table 1. In the experiment, the Intel-6700K processor and NVIDIA-GTX1080 graphics card were used.

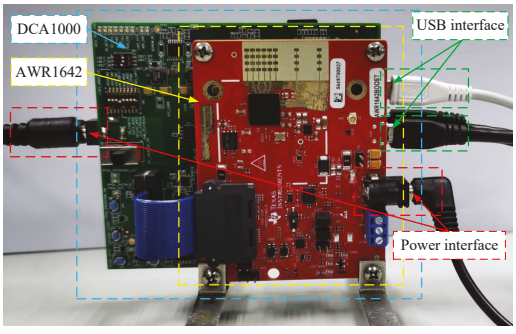

Figure 6. The adopted radar sensor and data collection card.

Table 1. Radar configuration parameters.

Parameters	Values	Parameters	Values
f_c	77 GHz	K_s	105.202 MHz/µs
B	3.997 GHz	λ	3.9 mm
N_{adc}	64	N_c	128
r_{res}	0.0446 m	T_c	38 µs
r_{max}	2.8531 m	v_{res}	0.4006 m/s
F_s	2 MHz	v_{max}	25.6366 m/s

We designed eight types of multi-hand gestures with two-hands (the method presented in this paper is also feasible to the case of multiple hands (more than two); we will leave the test for future work. Since the FMCW radar can distinguish the two hands from the range and angle, the presented method can be applied to recognize the gestures of the driver and passenger in the front row of the car), shown in Figure 7a. The arrows indicate the movement directions of the hand gestures. Although there were eight types of multi-hand gestures, each hand performed four types of hand gestures. After multi-hand gesture separation, there were eight hand gestures in total, namely left hand slides to left (LSL), left hand slides to right (LSR), left hand slides to up (LSU), left hand slides to down (LSD), and right hand slides to left (RSL), right hand slides to right (RSR), right hand slides to up (RSU), right hand slides to down (RSD), shown in Figure 7a. Since the left hand and right hand perform similar actions, these similar features increased the recognition difficulty. To improve the robustness of the design deep learning network, we collected multi-hand gestures of three men and two women, and each person collected 100 multi-hand gesture data. As a result, each multi-hand gesture had 500 data; there were 4000 data for the eight types of multi-hand gestures in total.

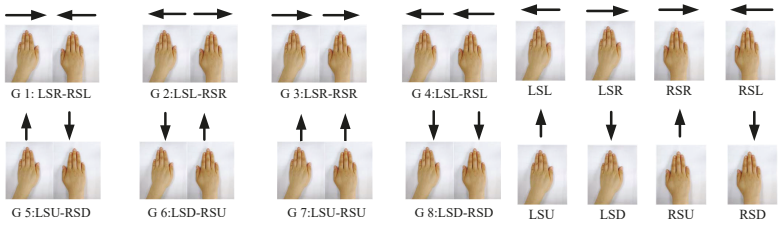

(**a**) Multi-hand gestures (**b**) Separated hand gestures

Figure 7. Hand gesture types.

4.2. Results and Analysis

4.2.1. Effect of Interference Suppression

To show the effect of interference suppression, we used the RDM of the multi-hand gesture G1 in Figure 7 at the 10-th frame, and the results are shown in Figure 8a–d. It can be seen from Figure 8 that the spectral leakage in the original RDM was suppressed. Moreover, the dynamic interferences (caused by the torso and arms as well as micro-motion in the environment) in Figure 8b labeled by black boxes were suppressed. The static interferences caused by the wall or static objects were also suppressed in Figure 8d.

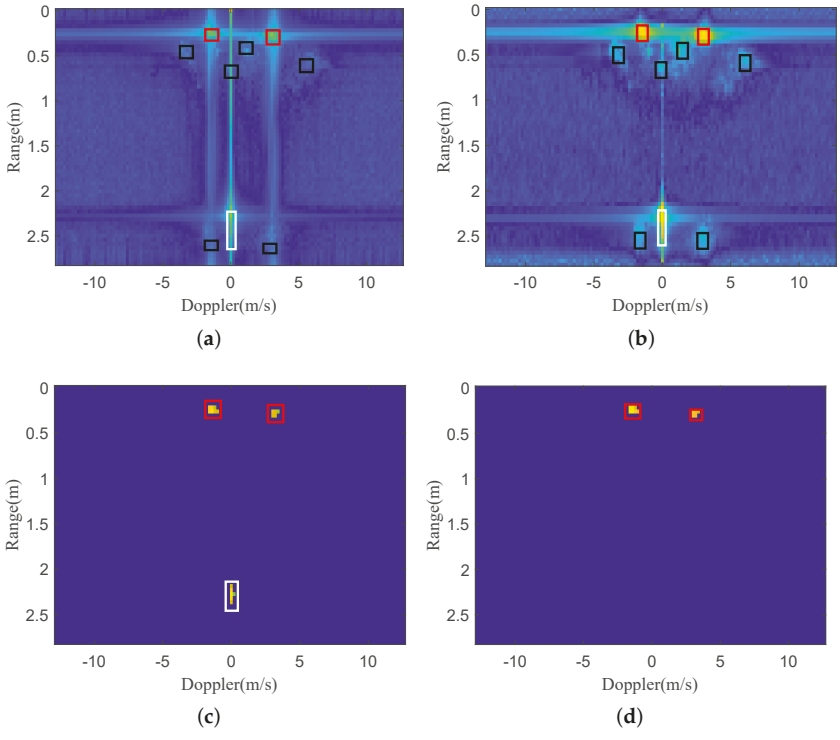

Figure 8. Effect of interference suppression for RDM. (**a**) Original. (**b**) With the added Hanning Window. (**c**) Dynamic interference suppression. (**d**) Static interference suppression.

We also used the RAM of the same hand gesture, as in Figure 8a–d to show the effect of interference suppression, shown in Figure 9a,b. We can see from Figure 9a that the two hand gesture targets are located at -30° and 40°. Due to the spectral leakage and interferences,

there were interference targets in the original RAM, marked by black and white boxes. Figure 9b shows that the two hand gesture targets are clearly after interference suppression.

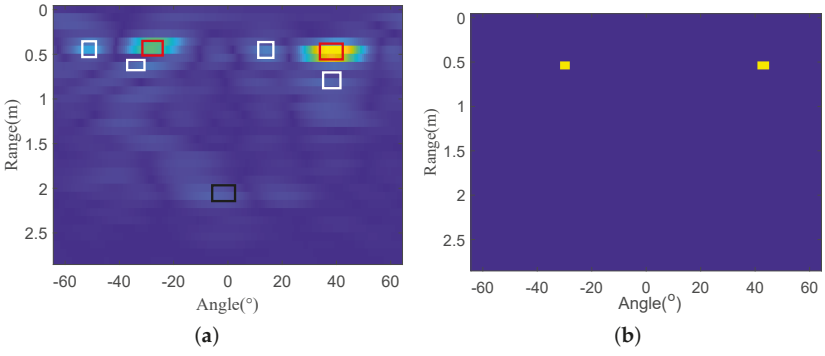

Figure 9. Effect of interference suppression for RAM. (**a**) Original. (**b**) After interference suppression.

4.2.2. Impact of Training Dataset Size

In this HGR experiment, we first analyzed the influence of the ratios of the training to the testing dataset of 2:8, 5:5, 7:3 and 8:2 on the results, shown in Figure 10. It can be seen that when the ratio is 2:8, the generalization ability and recognition result of the D-3D-CNN-FN network is very poor, which is mainly because of the poor fitting ability of the small training dataset. By increasing the ratio, there are more experimental samples in the training set, which makes the recognition accuracy of the proposed network higher. When the ratio is 7:3, the D-3D-CNN-FN network has the best performance, and a ratio of 7:3 in the following experiments.

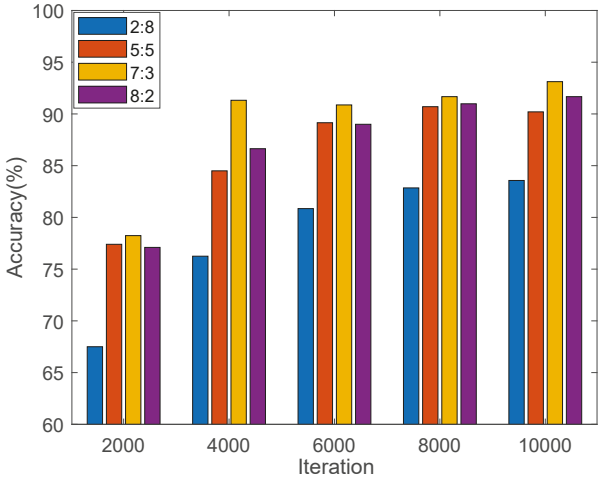

Figure 10. Accuracy under different dataset ratios.

4.2.3. Impact of Learning Rate

Since the learning rate adjusts the weight during network training using the loss function, Figure 11 compares the recognition performance of the network under different learning rates. It can be seen that with a large learning rate, such as 0.001 and 0.005, the D-3D-CNN-FN network fails to converge or falls into a local optimum. If the weight is too

small (such as 0.00001), the D-3D-CNN-FN network will converge very slowly. As a result, we set the learning rate to 0.00008 in the following experiments.

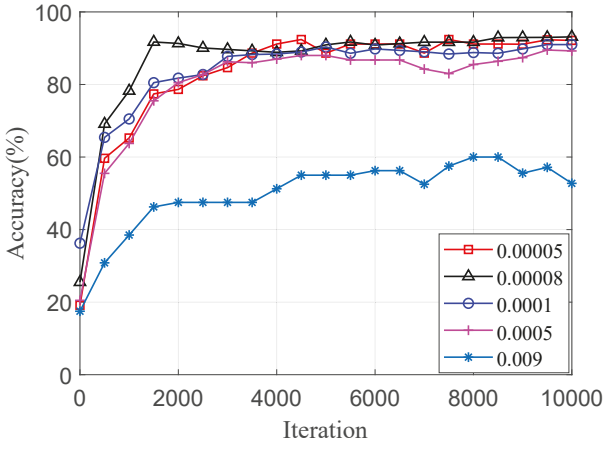

Figure 11. Accuracy under different learning rates.

4.2.4. Recognition Accuracy Comparison

To verify the effectiveness of the D-3D-CNN-FN, we took 3D-CNN [17] with RDMs or RAMs and dual 3D-CNN with RDMs and RAMs for comparison. The comparison methods are marked by 3D-CNN+RDM, 3D-CNN+RAM and D-3D-CNN+RDM and RAM, respectively. The dual 3D-CNN (D-3D-CNN) applied two 3D-CNN networks to extract features of RDMs and RAMs, directly followed by the softmax classifier. The ratio of the training dataset to the test data set was 7:3, the initial learning rate was set to 0.0008, and the iteration number used for training was 10,000.

The training accuracy comparison on the test dataset is shown in Figure 12. Since the proposed D-3D-CNN-FN applied dual 3D-CNN for local feature extraction of both RDMs and RAMs and used LSTM for global time feature extraction, the proposed D-3D-CNN-FN has higher recognition accuracy than D-3D-CNN. Moreover, 3D-CNN with RDMs or RAMs have poor recognition accuracy mainly because of the limited motion parameters.

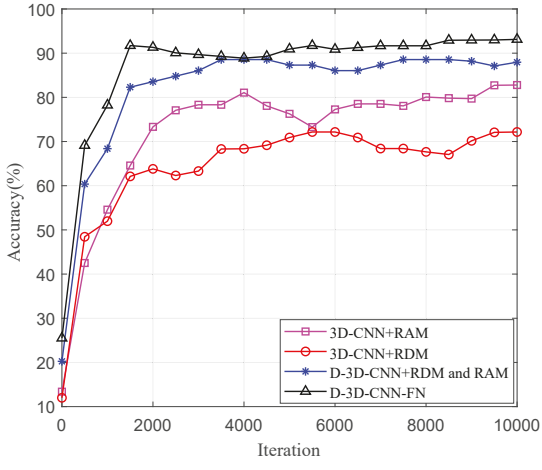

Figure 12. Training process comparison of each network.

The recognition accuracies of each type of gesture are summarized in Table 2. We used 'Ave'. to represent the average recognition accuracy in Table 2. Compared to 3D-CNN with only RDM or RAM, D-3D-CNN uses two network branches to respectively learn the local features of RDM and RAM, and then fuses the features and input into a full connection layer for classification. As a result, the average recognition accuracy (86.95%) of dual 3D-CNN is improved by 4.2 compared to the single branch 3D-CNN. With fused feature input into the LSTM for global feature extraction, the average recognition accuracy of the proposed D-3D-CNN-FN is about 6.2 higher than that of the D-3D-CNN network.

Table 2. Recognition accuracy comparison (%).

Parameter	**3D-CNN**	**3D-CNN**	**D-3D-CNN**	**D-3D-CNN-FN**
Dataset	**RDM**	**RAM**	**RDM+RAM**	**RDM+RAM**
LSL	73.33	86.67	89.67	**94.33**
LSR	71.67	83.33	87.67	**96.67**
LSU	69.00	81.67	86.33	**90.67**
LSD	74.67	82.00	83.00	**91.33**
RSL	72.33	79.67	90.00	**95.00**
RSR	75.00	83.33	86.67	**93.33**
RSU	70.00	86.67	84.33	**91.67**
RSD	71.33	86.67	88.00	**92.00**
Ave.	72.16	82.79	86.95	**93.12**

5. Conclusions

In this paper, we proposed a multi-hand gesture recognition method using an automotive FMCW radar sensor. The 3D-FFT was applied to construct the maps of RDM and RAM. Then, the interference was suppressed and the multi-hand gestures were separated by the proposed spatiotemporal path selection algorithm. The dual 3D-CNNs were proposed to extract the features of RDM and RAM, and the fused features were input into the LSTM network. The performance of the presented system was validated on the self-built dataset. The results showed that the averaged recognition accuracy of the proposed method was 93.12%, which was improved by 6.2 compared with the state-of-the-art. In the future, we will design an efficient and robust interference suppression scheme, as well as a deep learning network with the consideration of radar self-motion. Moreover, we will carry out real-time tests with more hands and more multi-hand gesture types. The multi-hand gesture recognition system applies the radar to recognize the multi-hand gestures in a device-free manner. It has potential application in intelligent driving, industry 4.0, HVAC systems, etc.

Author Contributions: Y.W. conceived the original idea and wrote the paper; D.W. and D.Y. collected and tested the multi-hand gesture recognition system; Y.F., L.X. and M.Z. analyzed the data and revised the paper. All authors have read and agreed to the published version of the manuscript.

Funding: This work was supported in part by the National Natural Science Foundation of China under grant 61901076; in part by the National Science Foundation of Chongqing under grant cstc2020jcyj-msxmX0865; in part by the China Postdoctoral Science Foundation under grant 2021M693773; and in part by the Science and Technology Research Program of Chongqing Education Commission, under grant KJQN201900603.

Data Availability Statement: Not applicable.

Acknowledgments: The authors would like to thank the reviewers and editor for their valuable comments and suggestions.

Conflicts of Interest: The authors declare no conflict of interest.

References

1. Chen, X.; Chen, L.; Chao, F.; Fang, D. Sensing our world using wireless signals. *IEEE Internet Comput.* **2019**, *23*, 38–45. [CrossRef]
2. Ye, Y.; He, C.; Liao, B.; Qian, G. Capacitive proximity sensor array with a simple high sensitivity capacitance measuring circuit for human-computer interaction. *IEEE Sens. J.* **2018**, *8*, 5906–5914. [CrossRef]
3. Simao, M.; Gibaru, O.; Neto, P. Online recognition of incomplete gesture data to interface collaborative robots. *IEEE Trans. Ind. Electron.* **2019**, *66*, 9372–9382. [CrossRef]
4. Zhang, W.; Wang, J.; Lan, F. Dynamic Hand Gesture Recognition Based on Short-Term Sampling Neural Networks. *IEEE/CAA J. Autom. Sin.* **2021**, *8*, 110–120. [CrossRef]
5. Wang, Y.; Shu, Y.; Jia, X.; Xie, L.; Zhou, M. Multi-feature fusion-based hand gesture sensing and recognition system. *IEEE Geosci. Remote Sens. Lett.* **2022**, *19*, 1–5.
6. Sakamoto, T.; Gao, X.; Yavari, E.; Rahman, A.; Boric-Lubecke, O.; Lubecke, V.M. Radar-based hand gesture recognition using I-Q echo plot and convolutional neural network. In Proceedings of the IEEE Conference on Antenna Measurements and Applications (CAMA), Tsukuba, Japan, 4–6 December 2017; pp. 393–395.
7. Hazra, S.; Santra, A. Short-range radar-based gesture recognition system using 3D CNN with triplet loss. *IEEE Access* **2019**, *7*, 125623–125633. [CrossRef]
8. Molchanov, P.; Gupta, S.; Kim, K.; Pulli, K. Short-range FMCW monopulse radar for hand-gesture sensing. In Proceedings of the IEEE Radar Conference (RadarConf), Arlington, VA, USA, 10–15 May 2015; pp. 1491–1496.
9. Wang, Y.; Wang, S.; Zhou, M.; Jiang, Q.; Tian, Z. TS-I3D based hand gesture recognition method with radar sensor. *IEEE Access* **2019**, *7*, 22902–22913. [CrossRef]
10. Xia, Z.; Luomei, Y.; Zhou, C.; Xu, F. Multidimensional feature representation and learning for robust hand-gesture recognition on commercial millimeter-wave radar. *IEEE Trans. Geosci. Remote Sens.* **2020**, *59*, 4749–4764. [CrossRef]
11. Howard, S.; Weinberg, G. Optimal predictive inference and noncoherent CFAR detectors. *IEEE Trans. Aerosp. Electron. Syst.* **2019**, *56*, 2603–2615. [CrossRef]
12. Yang, Z.; Zheng, X. Hand gesture recognition based on trajectories features and computation-efficient reused LSTM network. *IEEE Sens. J.* **2021**, *21*, 16945–16960. [CrossRef]
13. Chung, H.; Chung, Y.; Tsai, W. An efficient hand gesture recognition system based on deep CNN. In Proceedings of the IEEE International Conference on Industrial Technology (ICIT), Melbourne, Australia, 13–15 February 2019; pp. 853–858.
14. Wang, S.; Song, J.; Lien, J.; Poupyrev, I.; Hilliges, O. Interacting with soli: Exploring fine-grained dynamic gesture recognition. In Proceedings of the Radio-frequency Spectrum Symposium on User Interface Software and Technology, Tokyo, Japan, 16–19 October 2016; pp. 851–860.
15. Skaria, S.; Al-Hourani, A.; Lech, M.; Evans, R. Hand-gesture recognition using two-antenna doppler radar with deep convolutional neural networks. *IEEE Sens. J.* **2021**, *19*, 3041–3048. [CrossRef]
16. Molchanov, P.; Gupta, S.; Kim, K.; Kautz, J. Hand gesture recognition with 3D convolutional neural networks. In Proceedings of the IEEE Conference on Computer Vision and Pattern Recognition Workshops (CVPRW), Boston, MA, USA, 7–12 June 2015; pp. 1–7.
17. Zhang, W.; Wang, J. Dynamic hand gesture recognition based on 3D convolutional neural network models. In Proceedings of the IEEE 16th International Conference on Networking, Sensing and Control (ICNSC), Banff, AB, Canada, 9–11 May 2019; pp. 224–229.
18. Zhang, Z.; Tian, Z.; Zhou, M. Latern: Dynamic continuous hand gesture recognition using FMCW radar sensor. *IEEE Sens. J.* **2018**, *18*, 3278–3289. [CrossRef]
19. Kumar, S.; Subha, D. Prediction of depression from EEG signal using long short term memory (LSTM). In Proceedings of the 2019 3rd International Conference on Trends in Electronics and Informatics ICOEI, Tirunelveli, India, 23–25 April 2019; pp. 1248–1253.
20. Peng, Z.; Li, C.; Munoz-Ferreras, J.; Gomez-Garcia, R. An FMCW radar sensor for human gesture recognition in the presence of multiple targets. In Proceedings of the IEEE MTT-S International Microwave Bio Conference (IMBIOC), Gothenburg, Sweden, 15–17 May 2017; pp. 1–3.
21. Wang, J.; Ran, Z.; Gao, Q.; Ma, X.; Pan, M.; Xue, K. Multi-person device-free gesture recognition using mmWave signals. *China Commun.* **2021**, *18*, 186–199. [CrossRef]
22. Zhang, D.; Hu, Y.; Chen, Y. Mtrack: Tracking multiperson moving trajectories and vital signs with radio signals. *IEEE Internet Things J.* **2021**, *8*, 3904–3914. [CrossRef]
23. Donoho, D. De-noising by soft-thresholding. *IEEE Trans. Inf. Theory* **2002**, *41*, 613–627. [CrossRef]
24. He, W.; Wang, Y.; Zhou, M.; Wang, B. A novel parameters correction and multivariable decision tree method for edge computing enabled HGR system. *Neurocomputing* **2022**, *487*, 203–213. [CrossRef]
25. Tu, J.; Lin, J. Fast acquisition of heart rate in noncontact vital sign radar measurement using time-window-variation technique. *IEEE Trans. Instrum. Meas.* **2015**, *65*, 112–122. [CrossRef]
26. Xu, Z.; Yuan, M. An interference mitigation technique for automotive millimeter wave radars in the tunable Q-factor wavelet transform domain. *IEEE Trans. Microw. Theory Tech.* **2021**, *69*, 5270–5283. [CrossRef]
27. Xu, Z.; Shi, Q. Interference mitigation for automotive radar using orthogonal noise waveforms. *IEEE Geosci. Remote Sens. Lett.* **2017**, *15*, 137–141. [CrossRef]
28. Wang, J. CFAR-based interference mitigation for FMCW automotive radar systems. *IEEE Trans. Intell. Transp. Syst.* **2021**. [CrossRef]

29. Cardillo, E.; Li, C.; Caddemi, A. Millimeter-wave radar cane: A blind people aid with moving human recognition capabilities. *IEEE J. Electromagn. Microwaves Med. Biol.* **2021**. [CrossRef]
30. Haggag, K.; Lange, S.; Pfeifer, T.; Protzel, P. A credible and robust approach to ego-motion estimation using an automotive radar. *IEEE Robot. Autom. Lett.* **2022**, *7*, 6020–6027. [CrossRef]
31. Chintakindi, S.; Varaprasad, O.; Siva Sarma, D. Improved Hanning window based interpolated FFT for power harmonic analysis. In Proceedings of the TENCON 2015—2015 IEEE Region 10 Conference, Macao, China, 1–4 November 2015; pp. 1–5.
32. Yang, J.; Lu, C.; Li, L. Target detection in passive millimeter wave image based on two-dimensional cell-weighted average CFAR. In Proceedings of the IEEE 11th International Conference on Signal Processing, Beijing, China, 21–25 October 2012; pp. 917–921.
33. Xu, Z.; Baker, C.J.; Pooni, S. Range and Doppler cell migration in wideband automotive radar. *IEEE Trans. Veh. Technol.* **2019**, *68*, 5527–5536. [CrossRef]
34. Single-Chip 76-GHz to 81-GHz Automotive Radar Sensor Integrating DSP and MCU. Available online: https://www.ti.com/product/AWR1642 (accessed on 19 April 2022).
35. Real-Time Data-Capture Adapter for Radar Sensing Evaluation Module. Available online: https://www.ti.com/tool/DCA1000EVM (accessed on 19 April 2022).

remote sensing

MDPI

Article

Tracking of Multiple Static and Dynamic Targets for 4D Automotive Millimeter-Wave Radar Point Cloud in Urban Environments

Bin Tan [1], Zhixiong Ma [1,*], Xichan Zhu [1], Sen Li [1], Lianqing Zheng [1], Libo Huang [2] and Jie Bai [2]

[1] The School of Automotive Studies, Tongji University, Shanghai 201804, China
[2] The School of Information and Electricity, Zhejiang University City College, Hangzhou 310015, China
* Correspondence: mzx1978@tongji.edu.cn

Abstract: This paper presents a target tracking algorithm based on 4D millimeter-wave radar point cloud information for autonomous driving applications, which addresses the limitations of traditional 2 + 1D radar systems by using higher resolution target point cloud information that enables more accurate motion state estimation and target contour information. The proposed algorithm includes several steps, starting with the estimation of the ego vehicle's velocity information using the radial velocity information of the millimeter-wave radar point cloud. Different clustering suggestions are then obtained using a density-based clustering method, and correlation regions of the targets are obtained based on these clustering suggestions. The binary Bayesian filtering method is then used to determine whether the targets are dynamic or static targets based on their distribution characteristics. For dynamic targets, Kalman filtering is used to estimate and update the state of the target using trajectory and velocity information, while for static targets, the rolling ball method is used to estimate and update the shape contour boundary of the target. Unassociated measurements are estimated for the contour and initialized for the trajectory, and unassociated trajectory targets are selectively retained and deleted. The effectiveness of the proposed method is verified using real data. Overall, the proposed target tracking algorithm based on 4D millimeter-wave radar point cloud information has the potential to improve the accuracy and reliability of target tracking in autonomous driving applications, providing more comprehensive motion state and target contour information for better decision making.

Keywords: target tracking; 4D millimeter-wave radar; motion state estimation; autonomous driving

Citation: Tan, B.; Ma, Z.; Zhu, X.; Li, S.; Zheng, L.; Huang, L.; Bai, J. Tracking of Multiple Static and Dynamic Targets for 4D Automotive Millimeter-Wave Radar Point Cloud in Urban Environments. *Remote Sens.* **2023**, *15*, 2923. https://doi.org/10.3390/rs15112923

Academic Editors: Francesco Nex and Mohammad Awrangjeb

Received: 23 April 2023
Revised: 17 May 2023
Accepted: 31 May 2023
Published: 3 June 2023

1. Introduction

For autonomous driving systems, accurately sensing the surrounding environment is crucial. Among the various vehicle sensing sensors, millimeter-wave radar is capable of obtaining position and speed information of targets, and can operate in complex weather conditions such as rain, fog, and bright sunlight exposure [1].

Conventional 2 + 1D (x, y, v) millimeter-wave radar is effective in measuring the radial distance, radial velocity, and horizontal angular information of a target. However, when compared to cameras and LIDAR, which are the other major sensors used in autonomous driving, traditional millimeter-wave radar has a lower angular resolution and cannot provide height angle information of the target. In autonomous driving scenarios, where vehicle or pedestrian targets are common, the small number of points and low angular resolution of individual targets in the scene can result in large errors in size and location estimation. To address this issue, high-resolution 4D (x, y, z, v) millimeter-wave radar has been developed, which can provide height angle information of targets with higher angular resolution. This enables more accurate edge information of targets and more precise estimation of a target's size and position.

Radar target tracking plays a critical role in millimeter-wave radar sensing. By providing a continuous position and velocity profile of a target, radar target tracking offers higher accuracy and reliability compared to a single measurement from the radar. Furthermore, it can effectively eliminate false detections.

Most conventional millimeter-wave radar tracking methods focus on point targets, which provide target ID, position, and velocity information. However, 4D millimeter-wave radar can measure multiple scattering centers per target, making direct application of point cloud tracking methods unsuitable. In addition, contour information, such as target size and orientation, is critical in autonomous driving environments. Therefore, accurate estimation of target ID, position, size, direction, and velocity information is necessary for 4D millimeter-wave radar target tracking. Despite considerable research on point target tracking using millimeter-wave radar, there is limited research on 4D millimeter-wave radar-based target tracking methods. Dynamic target tracking using 4D millimeter-wave radar presents several challenges, including variation in target size and multiple individual target measurement points. Furthermore, 4D millimeter-wave radar can measure static targets in the scene, while conventional millimeter-wave radar usually filters out static targets due to the absence of altitude angle information, which can result in false positives. Therefore, 4D millimeter-wave radar target tracking can also estimate the contour shape information of static targets. This paper focuses on developing tracking methods for multiple dynamic and static targets throughout a scene using 4D millimeter-wave radar.

The most commonly used multi-target tracking methods for millimeter-wave radar based on point targets include nearest neighbor data association (NN) [2,3], global nearest neighbor association (GNN) [4,5], multiple hypothesis tracking (MHT) [6,7], joint probabilistic data association (JPDA) [8,9], and the random finite set method (RFS) [10–12]. The nearest neighbor association algorithm selects the observation point that falls within the association gate and is closest to the tracking target as the association point. The global nearest neighbor algorithm minimizes the total distance or association cost. The joint probabilistic data association algorithm combines data association probabilities. The multi-hypothesis tracking algorithm calculates the probability and likelihood for each track. The RFS approach models objects and measurements as random finite sets.

In high-resolution millimeter-wave radar or 4D millimeter-wave automotive radar, a road target often spans multiple sensor resolution units, which poses challenges for tracking. In the extended target tracking problem for millimeter-wave radar, the position of the target measurement point on the object is represented as a probability distribution that changes with the sensor measurement angle, and the measurement point may appear or disappear. Therefore, tracking extended targets using millimeter-wave radar presents a significant challenge.

One approach to address the extended target tracking problem is to include a clustering process that reduces multiple measurements to a single measurement, which can then be tracked using a point target tracking method. In extended target tracking, clustering can be used to partition the point cloud. In automotive millimeter-wave radar target tracking, the size and shape of the clustering clusters vary due to the different size and reflection properties of the targets. Therefore, density-based spatial clustering of applications with noise (DBSCAN) [13] is commonly used to cluster radar points. However, density-based clustering methods rely on fixed parameter values and may perform poorly with targets of different densities. As a result, several methods that allow for different clustering parameters have been proposed, such as ordering points to identify the clustering structure (OPTICS) [14], hierarchical DBSCAN (HSBSCAN) [15], and tracking-assisted multi-hypothesis clustering [16].

Other approaches to extended target tracking involve designing object measurement models. Some examples include the elliptic random matrix model [17], the random hypersurface model [18], and the Gaussian process model [19]. In millimeter-wave radar vehicle target tracking, various vehicle target models have been proposed, such as a direct

scattering model [20], a variational radar model [21], a B-spline chained ellipses model [22], and the data-region association model [23].

Although several methods exist for extended target tracking using millimeter-wave radar, many of them rely on simulation data for extended target tracking theory. In practical scenarios, challenges such as varied point cloud probability distributions of different extended targets, and diverse position relationships when different targets are associated require further investigation on certain tracking algorithms. Moreover, some algorithms focus on tracking vehicle targets, and thus it is essential to explore ways to adapt tracking algorithms to different types of targets with varying sizes. Additionally, there have been limited studies on 4D millimeter-wave radar target tracking, and, therefore, the effectiveness of such methods on 4D millimeter-wave radar needs to be explored. This paper presents an effective 4D millimeter-wave radar target tracking method with the following contributions.

1. This paper proposes a 4D millimeter-wave radar point cloud-based multi-target tracking algorithm for estimating the ID, position, velocity, and shape information of targets in continuous time.
2. The proposed target tracking solution includes point cloud velocity compensation, clustering, dynamic and static attribute update, dynamic target 3D border generation, static target contour update, and target trajectory management processes.
3. To address the issue of the varying size and shape of dynamic and static targets, a binary Bayesian filtering method [24] is utilized to extract static and dynamic targets during the tracking process.
4. Kalman filtering is used for dynamic targets such as vehicles, pedestrians, bicycles, and other targets, combined with the target's track information and radial velocity information to estimate the target's 3D border information.
5. For static targets such as road edges, green belts, buildings, and other non-regular shaped targets, the rolling ball method is employed to estimate and update the shape contour boundaries of the targets.

The structure of this paper is organized as follows. Section 2 describes the tracking problem. Section 3 presents the proposed solution to the tracking problem, which includes compensating for target velocity, clustering point clouds, determining target associations, identifying dynamic and static targets, updating contour shape states, and creating, retaining, and deleting trajectories. Section 4 presents the experimental setup and results. Finally, Section 5 summarizes the research.

2. Materials and Methods

The objective of this paper is to derive state estimates for both dynamic and static targets within the field of view of 4D millimeter-wave radar, using the point cloud measurement volume of the radar. This includes obtaining 3D edge information of dynamic targets and contour shape information of static targets.

2.1. Measurement Modeling

4D millimeter-wave radar point cloud measurement includes information on the position along the x, y, and z-axes as well as the radial velocity v^r and intensity I. The radial velocity information is obtained through direct measurement as the target point's relative radial velocity. Each measurement point can be expressed as:

$$z_j = \begin{bmatrix} x_j & y_j & z_j & v_j^r & I_j \end{bmatrix} \tag{1}$$

where z_j represents the measurement, j represents the j-th point, and v_j^r represents the relative radial velocity of the j-th point.

As shown in Figure 1, 4D millimeter-wave radar point clouds are utilized to measure targets at three distinct time steps, revealing that the detected target points are dynamic and can vary over time, possibly appearing or disappearing at different locations. This poses a

significant challenge in accurately estimating the target's location and shape. To account for sensor noise and the inherent uncertainty in the measurement model, a probabilistic model is often employed to describe the measurement process.

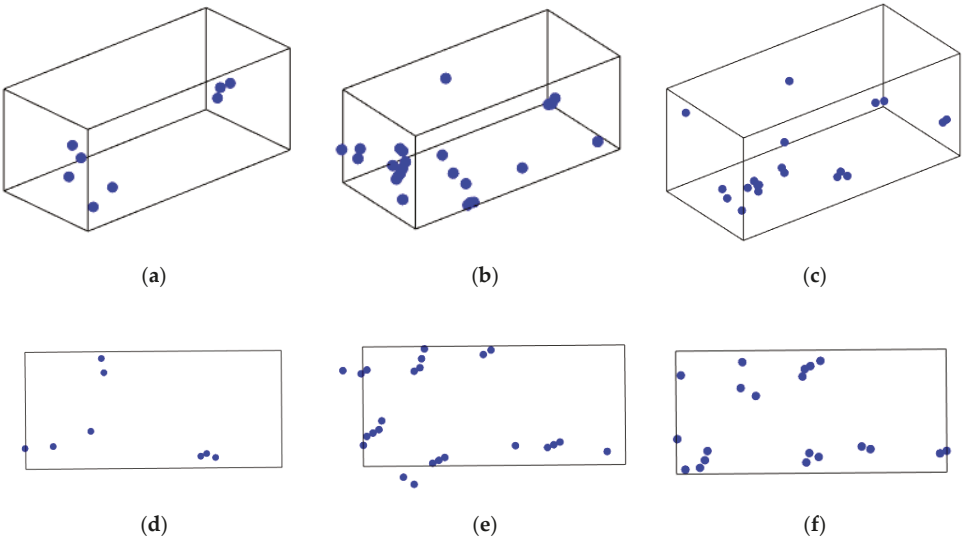

Figure 1. Measurements of the same target at adjacent moments. (**a**) 3D view of the target point cloud at moment $t-2$. (**b**) 3D view of the target point cloud at moment $t-1$. (**c**) 3D view of the target point cloud at moment t. (**d**) Top view of the target point cloud at moment $t-2$. (**e**) Top view of the target point cloud at moment $t-1$. (**f**) Top view of the target point cloud at moment t.

For multiple measurements of the expansion target, this can be expressed as:

$$Z = \left\{ z^j \right\}_{j=1}^{n} \tag{2}$$

where Z is the set of measurement quantities, z^j is a single measurement quantity, j is the number of measurements, and n is the total number of measurements.

The probability distribution of the measurements obtained from the target state can be expressed as:

$$p(Z_k|X_k) \tag{3}$$

where Z_k is the measurement at moment k for a target with target state X_k.

2.2. Target State Modeling

The aim of this paper is to estimate the states of both dynamic and static targets in the 4D millimeter-wave radar field of view using point cloud measurements. For the dynamic targets, their states can be described as follows:

- Position state: The target's position in three-dimensional space (x y z).
- Motion state: Since the target's position in the z-axis direction remains relatively stable in autonomous driving scenarios, the motion state can be simplified to the target's velocity in the x-axis and y-axis directions on the vehicle motion plane (v_x v_y).
- Profile shape state: This describes the shape and size of the target. For a 3D dynamic target in a road environment, it can be modeled as a 3D cube (l w h θ) since its shape and size states do not change substantially. Its extended state contains the size and rotation direction of the target.

Therefore, the state estimation of a 3D dynamic target in a road environment at time k can be represented as X_k, which consists of the position state (x y z), the motion state (v_x v_y), and the profile shape state (l w h θ).

$$X_k^d = [x_k \; y_k \; z_k \; v_{xk} \; v_{yk} \; l_k \; w_k \; h_k \; \theta_k] \tag{4}$$

The states of the static targets in this paper can be described as follows:

- Position state: The position of the target in the z-axis direction in space (z position).
- Motion state: For static targets, the absolute velocity is zero, and the relative velocity can be estimated as the negative of the velocity of the ego vehicle's motion (v_{xk} v_{yk}).
- The profile shape state of the target: For a 3D static target in a road environment, it can be modeled as a target surrounded by an edge box, which is represented as a set of n 2D enclosing points and their heights (h $\{x_j \quad y_j\}_{j=1}^{n}$).

The state estimation of a 3D static target in a road environment can be expressed as:

$$X_d^s = [\{x_j \quad y_j\}_{j=1}^{n} \; v_{xk} \; v_{yk} \; h_k \; z_k] \tag{5}$$

2.3. Method

The proposed solution in this paper is illustrated in Figures 2 and 3:

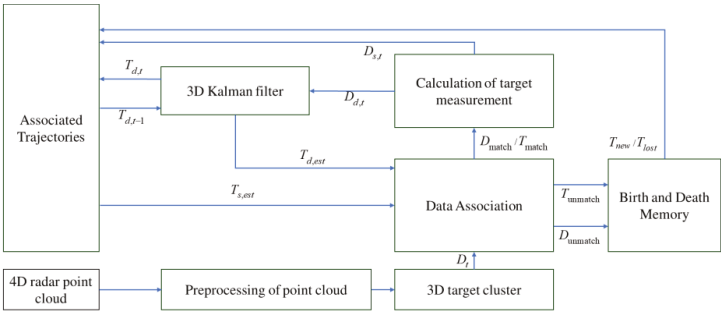

Figure 2. 4D millimeter-wave radar point cloud tracking framework.

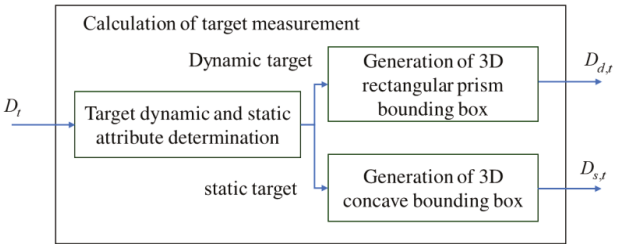

Figure 3. Module of calculation of target measurement.

In Figures 2 and 3, time is represented by t, the detection value is represented by D, the trajectory is represented by T, the dynamic target is represented by d, and the static target is represented by s.

The 4D radar data is input to generate point cloud data of the scene. The point cloud is preprocessed to compensate for the velocity information and convert relative radial velocity to absolute radial velocity. The static scene from the previous frame is matched with the current frame to aid in associating static and dynamic targets. A clustering module is used to classify the points into different target proposals. Data association is performed using an optimal matching algorithm. For the clustered targets that are successfully associated,

their dynamic and static attributes are updated using a binary Bayesian filtering algorithm. For dynamic targets, the target state is updated using a Kalman filtering method to obtain the 3D bounding box of the target. For static targets, the bounding box state is updated using the rolling ball method. For unassociated clustered targets, trajectory initialization is performed, historical trajectories that are not associated are retained or deleted, and trajectories in overlapping regions are merged.

2.3.1. Point Cloud Preprocessing

Before feeding the millimeter-wave radar point cloud into the tracking framework, several preprocessing steps are performed. Firstly, the relative radial velocity information of the point cloud is compensated for absolute radial velocity, allowing for the extraction of dynamic and static targets in the scene and the updating of their states based on radial velocity information. Additionally, due to the motion of the radar, the world coordinate systems of the front and back point clouds are different, and multi-frame point clouds are matched to facilitate the association of dynamic and static targets. Further details on these steps can be found in previous work [25].

After obtaining the ego vehicle's speed v_s, the compensation amount, $\hat{v}_c^r$, for the radial velocity of the target can be calculated. Then, the absolute velocity of each target point, v_a^r, can be calculated as follows:

$$v_a^r = v_d^r - \hat{v}_c^r \tag{6}$$

The radar point cloud conversion relationship can be expressed as:

$$H = [R, t] \tag{7}$$

$$Y_{n-1}^n = H_{n-1} P_{n-1} \tag{8}$$

Y_{n-1}^n is the point set after the point cloud of the $(n-1)$-th frame is registered to the point cloud of the n-th frame. P_{n-1} is the information of the n-th point.

2.3.2. Clustering and Data Association

- Radar Point Cloud Clustering

After preprocessing the point cloud data, the large number of points are grouped into different targets using clustering techniques based on their position and velocity characteristics. One commonly used clustering algorithm for radar point clouds is density-based spatial clustering of applications with noise (DBSCAN) [13], which can automatically detect clustering structures of arbitrary shapes without requiring any prior knowledge. DBSCAN determines clusters by calculating the density around sample points, grouping points with higher density together to form a cluster, and determining the boundary between different clusters by the change in density. The DBSCAN algorithm takes spatial coordinates (x, y, z) and radial distance (v_a^r) of the data points as input. Specifically, the DBSCAN algorithm can be executed in the following steps:

- Calculation of the number of data points $N(p)$ in the neighborhood of a data point p:

$$N(p) = \{q \in Z : dist(p, q) \leq \varepsilon\} \tag{9}$$

Here, Z is the dataset, $dist(p, q)$ is the Euclidean distance between the data points p and q, and ε is the radius of the neighborhood.

- Determination of whether a data point p is a core point: If $N(p) \geq MinPts$, then p is a core point.
- Expanding the cluster: Starting from any unvisited core point, find all data points that are density-reachable from the core point, and mark them as belonging to the same cluster.

- Determination of whether a data point is density-reachable: A data point p is density-reachable from a data point q if there exists a core point c such that both c and p are in the neighborhood of q and the distance between c and p is less than ε.
- Marking noise points: Any unassigned data points are marked as noise points.

By executing the above steps, the DBSCAN algorithm can complete the clustering process and assign the data points to different clusters and noise points.

After clustering the k targets, the features of the j-th target are represented as:

$$f_j = \left\{ \overline{x}_j \quad \overline{y}_j \quad \overline{z}_j \quad \overline{v}_j^r \quad \overline{I}_j \right\} \tag{10}$$

where ($\overline{x}_j \quad \overline{y}_j \quad \overline{z}_j \quad \overline{v}_j^r \quad \overline{I}_j$) are calculated as the averages of the point cloud features within each target. The features of all clustering targets can be expressed as:

$$F = \left\{ f_j \right\}_{j=1}^{n} \tag{11}$$

- Data Association

  For the j-th trajectory, its features are denoted as:

$$g_j = \left\{ \widetilde{x}_j \quad \widetilde{y}_j \quad \widetilde{z}_j \quad \widetilde{v}_j \quad \widetilde{I}_j \right\} \tag{12}$$

  The features of all trajectories can be expressed as:

$$G = \left\{ g_j \right\}_{j=1}^{n} \tag{13}$$

The purpose of data correlation is to select which measurements are used to update the state estimate of the real target and to determine which measurements come from the target and which come from clutter. In this paper, it is necessary to correlate all clustered targets F and all trajectories G. One of the most widely used algorithms for target association is the Hungarian algorithm, which is a classical graph theoretic algorithm that can be used to maximize the matching of bipartite graphs. It can be used in a variety of target association algorithms for radar or images, and in target tracking it can be used to match point clouds in target clusters at different time steps to achieve target association. Assuming that there are radar historical trajectories and clustered targets, where the clustered targets contain m targets and the radar trajectories contain n targets, a cost matrix can be defined where $\mathrm{Cost}(i, j)$ denotes the cost between the i-th point in the trajectory and the j-th point in the clustered targets. Depending on the needs of the target tracking, the cost function can be calculated from factors such as target clustering centroids, average velocity, and intensity characteristics. The Hungarian algorithm finds the optimal matching solution with the minimum cost by converting the bipartite graph into a directed complete graph with weights and by finding the augmented paths in the graph.

The substitution matrix is calculated using the cost function, which is a combination of the position cost and the velocity/intensity cost. The cost function is defined as:

$$\mathrm{Cost}(i, j) = \alpha_1 \times PositionCost(i, j) + \alpha_2 \times VelocityIntensityCost(i, j)) \tag{14}$$

where α_1 is the weight of the position cost and α_2 is the weight of the velocity/intensity cost. The position cost can be calculated based on the distance between the target centroid and the trajectory prediction at the current time step, while the velocity/intensity cost can be calculated based on the difference in velocity and intensity between the target and the trajectory prediction.

Once the cost function has been calculated, the Hungarian algorithm can be used to find the optimal matching solution with the minimum cost. The resulting substitution matrix C is a binary matrix, where $C(i, j) = 1$ if target i is matched to the trajectory j, and $C(i, j) = 0$ otherwise.

2.3.3. Target Status Update

- Target Dynamic Static Property Update

By integrating the absolute velocity information of a target with a binary Bayesian filter, its static and dynamic attributes can be updated. To estimate the target's dynamic probability at a given moment, the ratio of points with a speed greater than a given value to the total number of points in the target's point cloud is calculated. Bayes' theorem is used in the binary Bayesian filter to update the state of the target, which can be either static or dynamic, represented by a binary value of 0 or 1, respectively, at time t.

Applying Bayes' theorem:

$$p(x|z_{1:t}) = \frac{p(z_t|x, z_{1:t-1})p(x|z_{1:t-1})}{p(z_t|z_{1:t-1})} = \frac{p(z_t|x)p(x|z_{1:t-1})}{p(z_t|z_{1:t-1})} \tag{15}$$

The Bayes' rule is applied to the measurement mode $p(z_t|x)$:

$$p(z_t|x) = \frac{p(x|z_t)p(z_t)}{p(x)} \tag{16}$$

Then,

$$p(x|z_{1:t}) = \frac{p(x|z_t)p(z_t)p(x|z_{1:t-1})}{p(x)p(z_t|z_{1:t-1})} \tag{17}$$

For the opposite event $\neg x$,

$$p(\neg x|z_{1:t}) = \frac{p(\neg x|z_t)p(z_t)p(\neg x|z_{1:t-1})}{p(\neg x)p(z_t|z_{1:t-1})} \tag{18}$$

Then,

$$\frac{p(x|z_{1:t})}{p(\neg x|z_{1:t})} = \frac{p(x|z_t)p(x|z_{1:t-1})p(\neg x)}{p(\neg x|z_t)p(\neg x|z_{1:t-1})p(x)} = \frac{p(x|z_t)}{1-p(x|z_t)} \frac{p(x|z_{1:t-1})}{1-p(x|z_{1:t-1})} \frac{1-p(x)}{p(x)} \tag{19}$$

The log odds belief at time t is:

$$l_t(x) = \log \frac{p(x|z_t)}{1-p(x|z_t)} - \log \frac{p(x)}{1-p(x)} + l_{t-1}(x) \tag{20}$$

And,

$$l_0(x) = \log \frac{p(x)}{1-p(x)} \tag{21}$$

Then,

$$l_t(x) = l_{t-1}(x) + \log \frac{p(x|z_t)}{1-p(x|z_t)} - l_0 \tag{22}$$

In dynamic and static attribute updates, $p(x|z_t)$ is calculated as the ratio of the number of points with a velocity greater than a given value v_d to the total number of points in the target point cloud.

- Dynamic Target State Update

The state estimation of a 3D dynamic target in a road environment at time k can be represented as X_k^d by Equation (4), which consists of the position state (x y z), the motion state (v_x v_y), and the profile shape state (l w h θ).

To update the state of a target, it is necessary to perform additional calculations on the existing clustered targets to obtain measurements of its current state. These calculations may involve analyzing the shape and center position of the target, as well as estimating its velocity. Once these calculations are completed, the status of the target can be updated based on the latest information available, allowing for more accurate tracking and prediction of the target's movement.

When computing measurements of clustered targets for dynamic targets, it is necessary to obtain the rectangular box enclosing the target. The height of the rectangular box can be calculated from the maximum and minimum height of the point cloud, while the other parameters of the rectangular box can be obtained from the enclosing rectangular box in the x and y planes.

However, calculating the rotation angle of the rectangular box is the most challenging part of target shape estimation, especially in imaging millimeter-wave radar, where the number of point clouds is limited and the contours of the point clouds are not well-defined. To address this issue, this paper proposes a method for calculating the rotation angle based on the combination of point cloud position and velocity information and trajectory angle. This approach provides a more accurate and robust estimate of the rotation angle, leading to improved target tracking and prediction.

The rectangular box of the point cloud is fitted using the L shape fitting method [26]. When working with points on a 2D plane, the least squares method is a common approach to finding the best-fitting rectangle for these points.

$$\begin{aligned} &\underset{P,\theta,c_1,c_2}{\text{minimize}} \sum_{i\in P} \left(x_i \cos\theta + y_i \sin\theta - c_1\right)^2 + \sum_{i\in Q} \left(-x_i \sin\theta + y_i \cos\theta - c_2\right)^2 \\ &\text{subject to } P \cup Q = \{1, 2, \ldots, m\}\ c_1, c_2 \in R\ \ 0^\circ \le \theta \le 90^\circ \end{aligned} \tag{23}$$

The above optimization problem can be approximated by using a search-based algorithm to find the best-fitting rectangle. The basic idea is to iterate through all possible directions of the rectangle. At each iteration, a rectangle is found that points in that direction and contains all scanned points. The distances from all points to the four edges of the rectangle are then obtained, based on which the points can be divided into two sets, p and q, and the corresponding squared errors are calculated as the objective function in the above equation. After iterating through all directions and obtaining all corresponding squared errors, the squared errors can be plotted as a function of the angle variation trend. Algorithm 1 is as follows.

Algorithm 1

- **Input**: data points $X = (x, y)$
- **Output**: criterion Q_p

For $\theta = 0$ **to** $\pi/2 - \delta$ step δ do
    $\hat{e}_1 = (\cos\theta, \sin\theta)$
    $\hat{e}_2 = (-\sin\theta, \cos\theta)$
    $C_1 = X \cdot \hat{e}_1^T$
    $C_2 = X \cdot \hat{e}_2^T$
    $q =$ CalculatecriterionX(C_1, C_2)
    $Q_p(\theta) = q$
end for

The algorithm for defining the calculate criterion, CalculatecriterionX(C_1, C_2), using the minimum rectangular area method as described in this paper, is as follows:

$$c_1^{\max} = \max\{C_1\},\ c_1^{\min} = \min\{C_1\} \tag{24}$$

$$c_2^{\max} = \max\{C_1\},\ c_1^{\min} = \min\{C_2\} \tag{25}$$

$$\alpha = -(c_1^{\max} - c_1^{\min})(c_2^{\max} - c_2^{\min}) \tag{26}$$

After calculating to obtain $Q_p(\theta)$, the probability $P_p(\theta)$ is calculated as:

$$P_p(\theta) = \frac{\max(Q(\theta)) - Q_p(\theta) + \min(Q_p(\theta))}{\sum_{\theta} Q_p(\theta)} \tag{27}$$

For a target on a two-dimensional plane, if the velocities of the point clouds on the target are assumed to be approximately equal, the orientation of the velocities can be estimated. Since millimeter-wave radar has different radial velocities at different points, this estimated velocity orientation can be used as an approximation for the rotation angle of the estimated rectangle for the calculation of the rotation angle, as follows.

The radial velocity measured by millimeter-wave radar can be expressed as

$$v_d^r = v_{d,x}\frac{x}{R} + v_{d,y}\frac{y}{R} \tag{28}$$

$$v_d^r = v_{d,x}(\frac{x}{R} + \tan\theta\frac{y}{R}) \tag{29}$$

Similar can be achieved by using a search-based algorithm to find the right angle, where the criterion is calculated as the variance. Algorithm 2 is as follows.

Algorithm 2

- **Input**: $X = (\frac{x}{Rv_d^r}, \frac{y}{Rv_d^r})$
- **Output**: criterion Q_v

1. **For** $\theta = 0$ **to** $2 * \pi - \delta$ step δ do
2. $\hat{e} = (1, \tan\theta)$
3. $C = X \cdot \hat{e}^T$
4. $q = \text{variance}\{C\}$
5. $Q_v(\theta) = q$
6. **end for**

After calculating to obtain $Q_v(\theta)$, the probability $P_v(\theta)$ is calculated as:

$$P_v(\theta) = \frac{\max(Q_v(\theta)) - Q_v(\theta) + \min(Q_v(\theta))}{\sum_{\theta} Q_v(\theta)} \tag{30}$$

Calculating the historical trajectory angle as θ_l and the probability as a Gaussian distribution with center at θ_l and variance at δ_l:

$$P_t(\theta) = N(\theta, \sigma^2) + P_t \tag{31}$$

$$P_h(\theta) = \frac{P_t(\theta)}{\sum_{\theta} P_t(\theta)} \tag{32}$$

Angular probabilities estimated from the point cloud position and velocity information and trajectory angles are fused using a weighted average.

$$P(\theta) = \alpha_1 P_p(\theta) + \alpha_2 P_v(\theta) + \alpha_1 P_h(\theta) \tag{33}$$

The theta value that maximizes $P(\theta)$ is chosen as the measured value, and the rectangular boundary $\{a_i x + b_i y = c_i | i = 1, 2, 3, 4\}$ is calculated as:

$$C_1^* = X \cdot (\cos\theta^*, \sin\theta^*)^T, C_2^* = X \cdot (-\sin\theta^*, \cos\theta^*)^T \tag{34}$$

$$a_1 = \cos\theta^*, b_1 = \sin\theta^*, c_1 = \min\{C_1^*\} \tag{35}$$

$$a_2 = -\sin\theta^*, b_2 = \cos\theta^*, c_2 = \min\{C_2^*\} \tag{36}$$

$$a_3 = \cos\theta^*, b_3 = \sin\theta^*, c_3 = \max\{C_1^*\} \tag{37}$$

$$a_4 = -\sin\theta^*, b_4 = \cos\theta^*, c_4 = \max\{C_2^*\} \tag{38}$$

From the process described above, the following parameters of the clustered target can be calculated: the centroid coordinates in three-dimensional space (x, y, z), the length, width, and height of the rectangular box enclosing the target, and the rotation angle (θ) of the rectangular box.

The velocity information of the target can be calculated by Equation (32).

Then, the measurement can be expressed as:

$$Z_{t,k} = [x_k \quad y_k \quad z_k \quad v_{xk} \quad v_{yk} \quad l_k \quad w_k \quad h_k \quad \theta_k] \tag{39}$$

The state transfer model of the target motion can be modeled as:

$$X_t = FX_{t-1} + \xi_t \tag{40}$$

where ξ_t is the system white Gaussian noise with covariance $\eta(\xi; 0, R)$.

The sensor's observation model is described as:

$$z_t = Hx_{t-1} + \zeta_t \tag{41}$$

where ζ_t is the measurement white Gaussian noise with covariance $\eta(\zeta; 0, Q)$.

Based on Equations (40) and (41), since the state and measurement equations of the target can be expressed in linear forms, the state can be updated by the Kalman filter.

- Static Target State Update

The state estimation of a 3D static target in a road environment can be expressed as Equation (5)

When calculating measurements for clustered target detection in static scenarios, obtaining the enclosing box of the target is necessary. The height of the enclosing box can be determined by computing the maximum and minimum heights of the point cloud, while the other parameters of the enclosing box can be obtained from the enclosing concave hull in the x and y planes.

The specific steps of the algorithm are as follows:

1. For any point p and rolling ball radius a, search for all points within a distance of $2a$ from p in the point cloud, denoted as the set Q.
2. Select any point $p_1(x, y)$ from Q and calculate the coordinates of the center of the circle passing through p and p_1 with a radius of alpha. There are two possible center coordinates, denoted as p_2 and p_3.
3. Remove p_1 from the set Q and calculate the distances between the remaining points and the points p_2 and p_3. If all distances are greater than a, the point p is considered a boundary point.
4. If all distances are not greater than a, iterate over all points in Q as the new p and repeat steps (2) and (3). If a point is found that satisfies the conditions in steps (2) and (3), it is considered a boundary point and the algorithm moves on to the next point. If no such point is found among the neighbors of p, then p is considered a non-boundary point.

Through Formula (7) of the radar point cloud velocity compensation part, v_{xk} and v_{yk} of the static target can be calculated, and the vehicle speed can be updated through the Kalman filter.

2.3.4. Track Management

In multi-object tracking, the number of targets is typically unknown and can vary as targets and clutter appear and disappear from the scene. Therefore, effective management of target trajectories is essential. For associated detections and trajectories, their states are preserved and updated over time. In cases where detections cannot be associated with any existing trajectory, new trajectories are generated and released as visible trajectories if their lifespan exceeds a predefined threshold T_r. For unassociated trajectories, their states are also preserved and updated. However, if their unassociated time exceeds a second threshold T_u, the trajectories are deleted to avoid unnecessary computational load.

3. Results

3.1. Experiment Setup

To verify the proposed algorithm, data from a 4D radar in road conditions were acquired using a data acquisition platform. The platform includes a 4D radar, LIDAR, and camera sensors, as shown in Figure 4. The 4D radar is installed in the middle of the front ventilation grille, and the LIDAR collects 360° of environmental information. The camera and 4D radar capture information within the field of view. The true value frame of the tracking target was labeled using the LIDAR and camera sensors. The performance parameters of the 4D radar sensor are shown in Table 1. The TJ4DRadSet [27] dataset was collected and is used for the algorithm analysis. As shown in Figure 4, the collection platforms of the dataset are displayed.

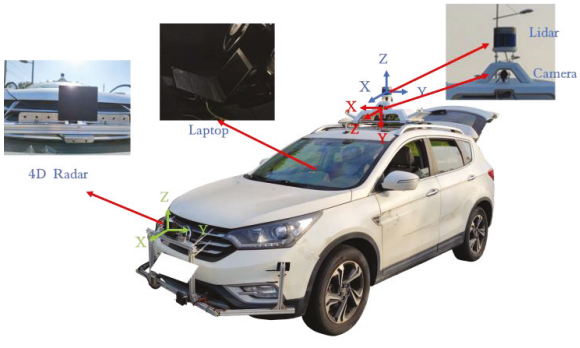

Figure 4. Data acquisition platform, including 4D radar, lidar, and camera sensor.

Table 1. Performance parameters of millimeter-wave radar in experimental data acquisition.

Sensors	Resolution			FOV		
	Range	Azimuth	Elevation	Range	Azimuth	Elevation
4D radar	0.86 m	<1°	<1°	400 m	113°	45°

3.2. Results and Evaluation

In order to investigate the impact of velocity errors on the angle estimation under different distances and angles, the graphs shown in Figures 5–10 were plotted.

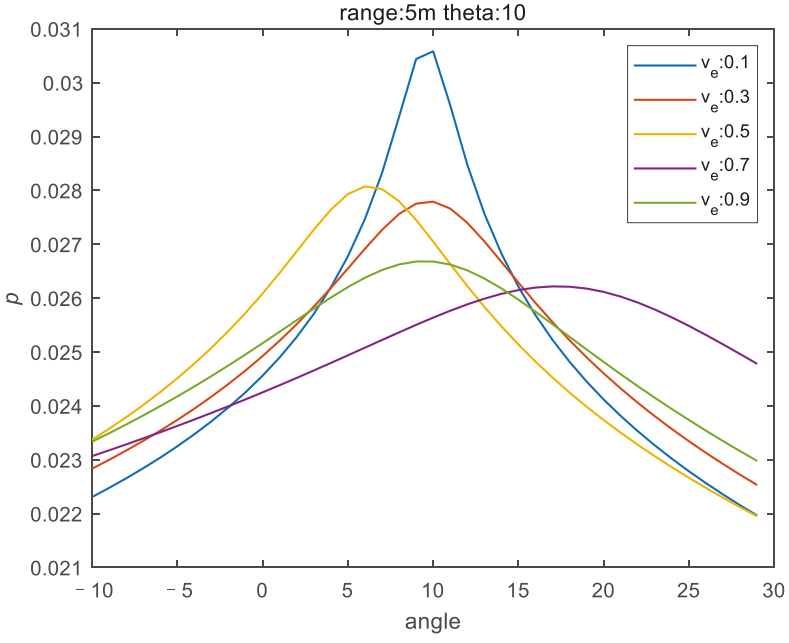

Figure 5. The relationship between velocity estimation and angle under a distance of 5 m and an object rotation angle of 10 degrees, considering different radial velocity measurement errors.

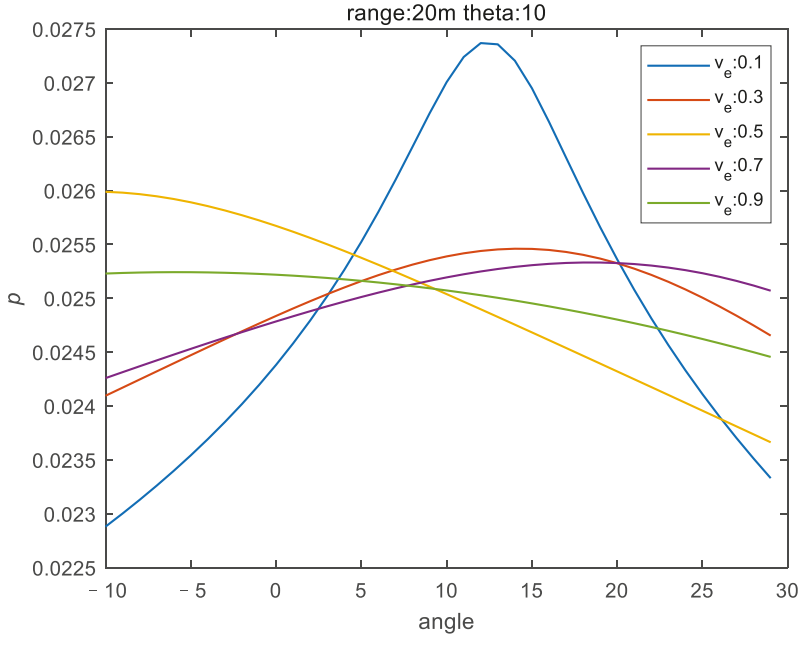

Figure 6. The relationship between velocity estimation and angle under a distance of 20 m and an object rotation angle of 10 degrees, considering different radial velocity measurement errors.

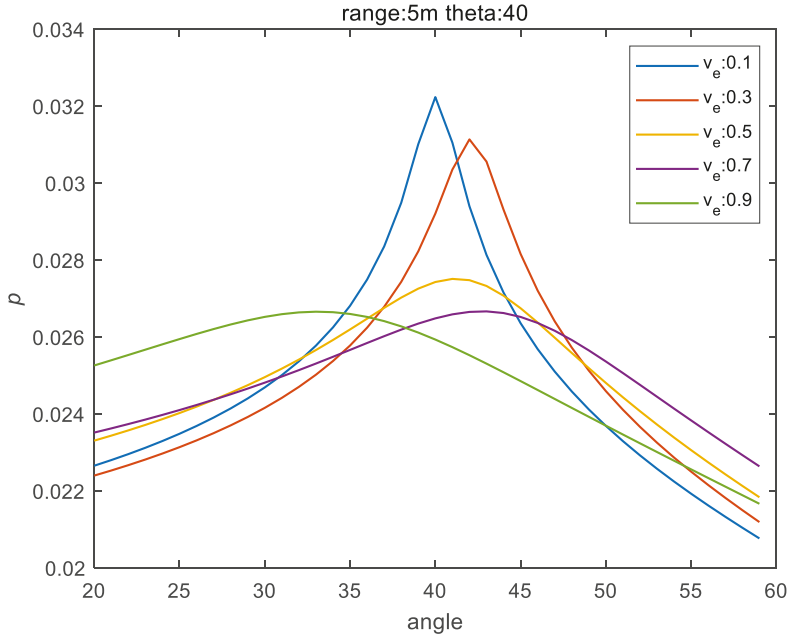

Figure 7. The relationship between velocity estimation and angle under a distance of 5 m and an object rotation angle of 40 degrees, considering different radial velocity measurement errors.

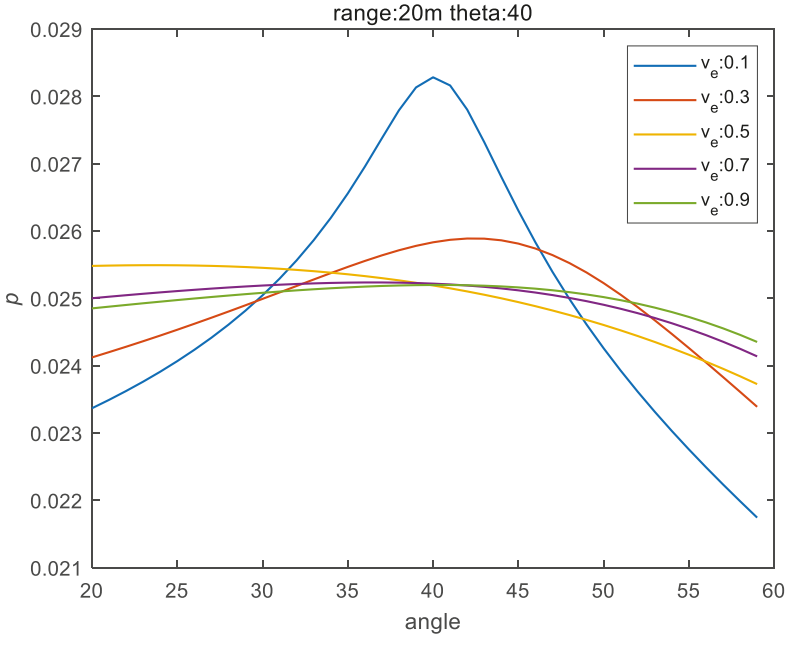

Figure 8. The relationship between velocity estimation and angle under a distance of 20 m and an object rotation angle of 40 degrees, considering different radial velocity measurement errors.

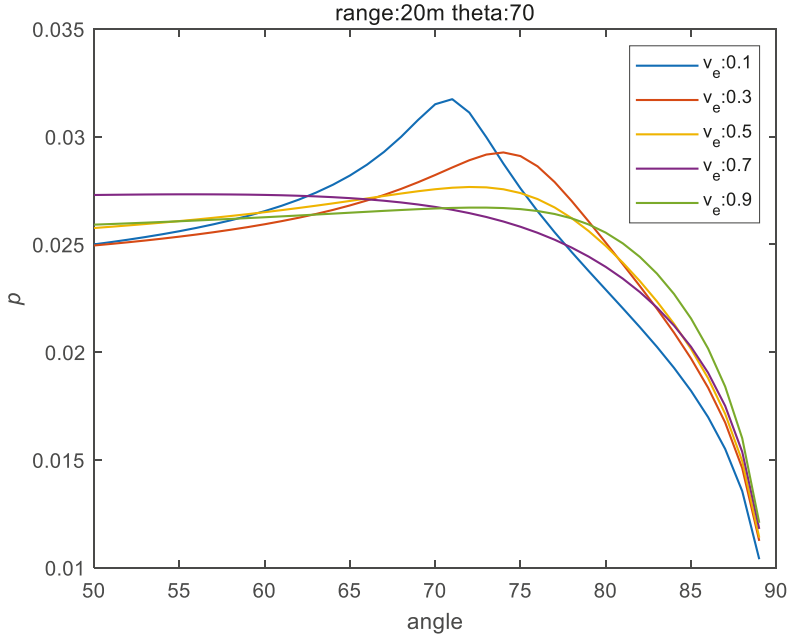

Figure 9. The relationship between velocity estimation and angle under a distance of 20 m and an object rotation angle of 70 degrees, considering different radial velocity measurement errors.

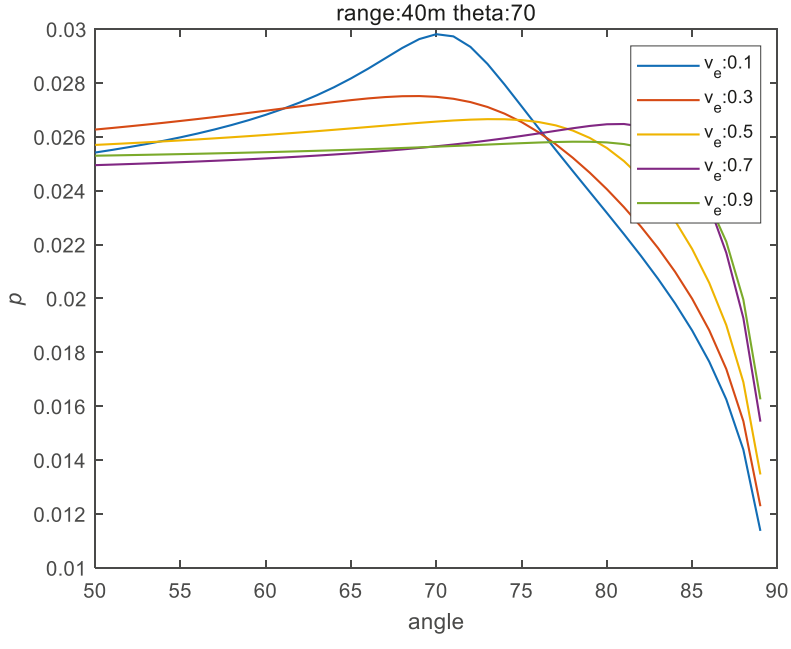

Figure 10. The relationship between velocity estimation and angle under a distance of 40 m and an object rotation angle of 70 degrees, considering different radial velocity measurement errors.

From Figures 5–10, it can be observed that when the radial velocity error is small, the estimation of the rotation angle can be made using velocity measurements from multiple points, and a shorter distance is more favorable for estimating the rotation angle based on the velocity.

Due to the limited number of millimeter-wave radar points, the rotation angle estimation of the dynamic target is fused by different methods. As shown in Figures 11 and 12, the rotation angle of the dynamic target can be better estimated.

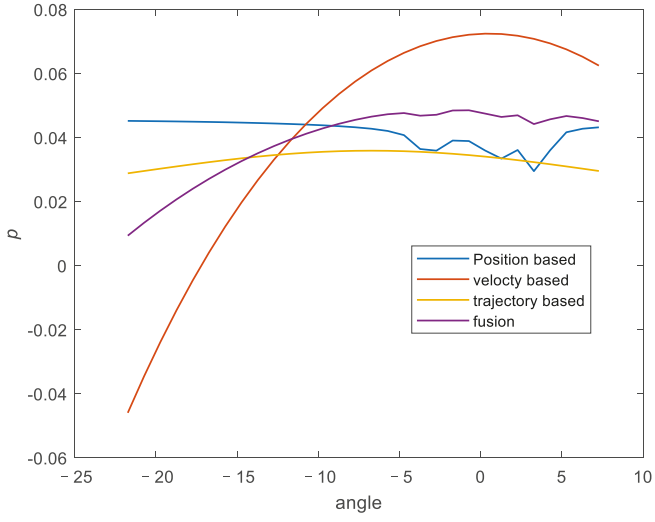

Figure 11. Method for estimating dynamic targets at different angles, and the relationship between probability and angle changes.

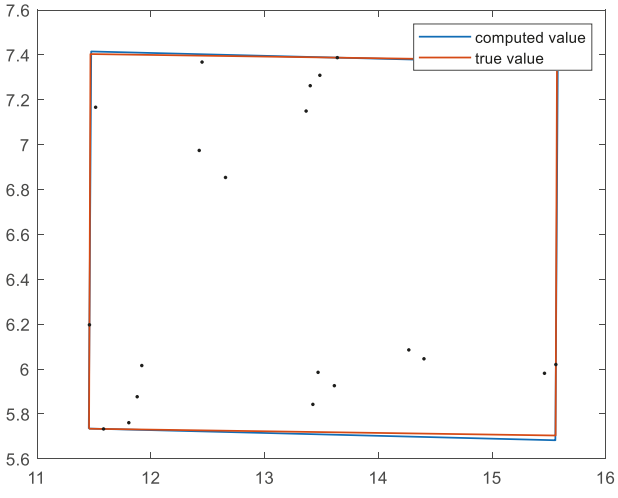

Figure 12. Rectangle formed by the estimated rotation angle and the true rotation angle.

Figures 13–15 show the state estimation of dynamic targets and static targets in a 4D millimeter-wave radar scenario. Different estimated dynamic targets, static targets, and true bounding boxes of dynamic targets have been labeled.

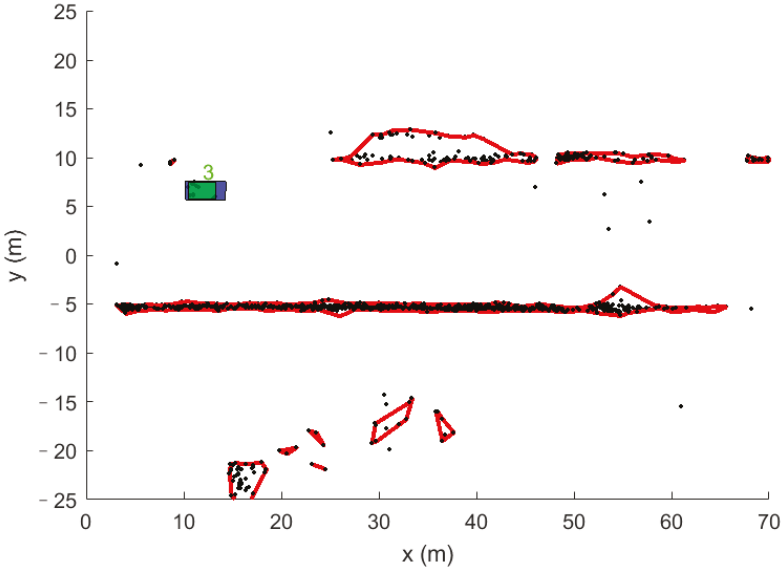

Figure 13. Results of 4D millimeter-wave radar point cloud and target tracking for a single vehicle, where the green box represents a dynamic target, the red box represents a static target, and the blue box represents the true box of a dynamic target.

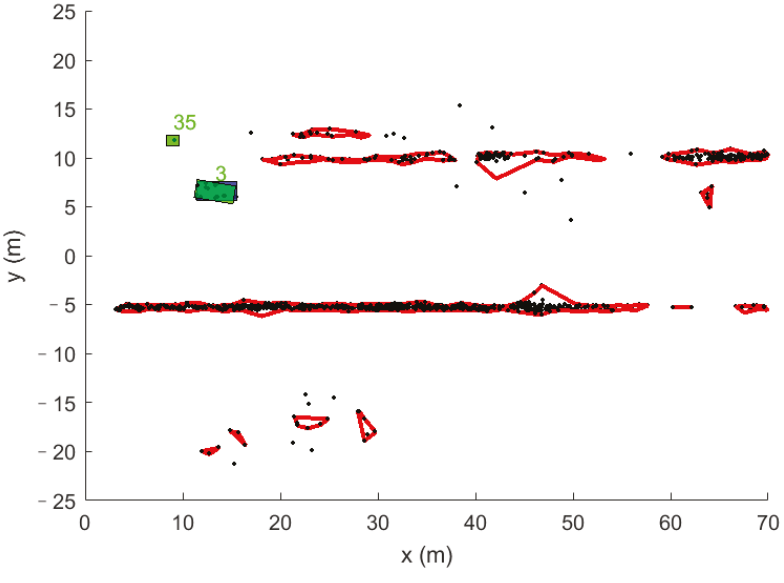

Figure 14. Results of 4D millimeter-wave radar point cloud and target tracking for a single vehicle, including an incorrect dynamic detection, where the green box represents a dynamic target, the red box represents a static target, and the blue box represents the true box of a dynamic target.

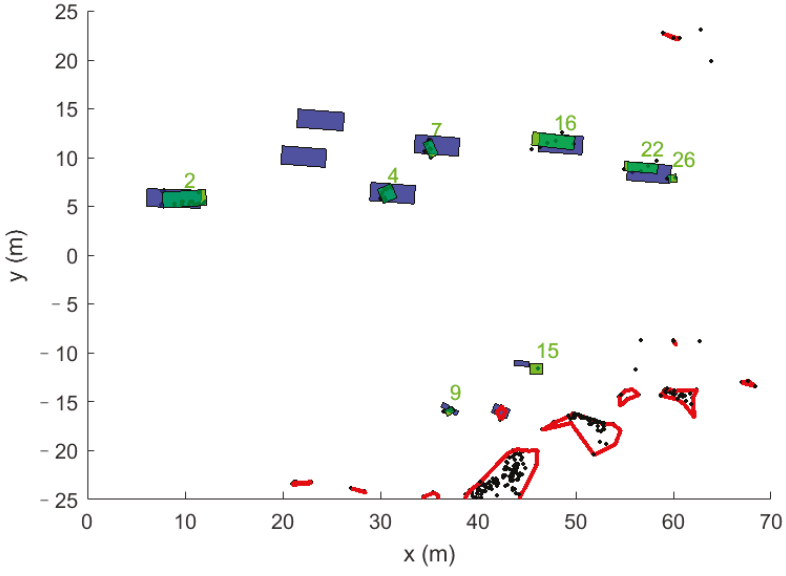

Figure 15. Results of 4D millimeter-wave radar point cloud and target tracking for multiple objects, where the green box represents a dynamic target, the red box represents a static target, and the blue box represents the true box of a dynamic target.

Figure 16 shows the effects of different performance parameters in the target tracking scene.

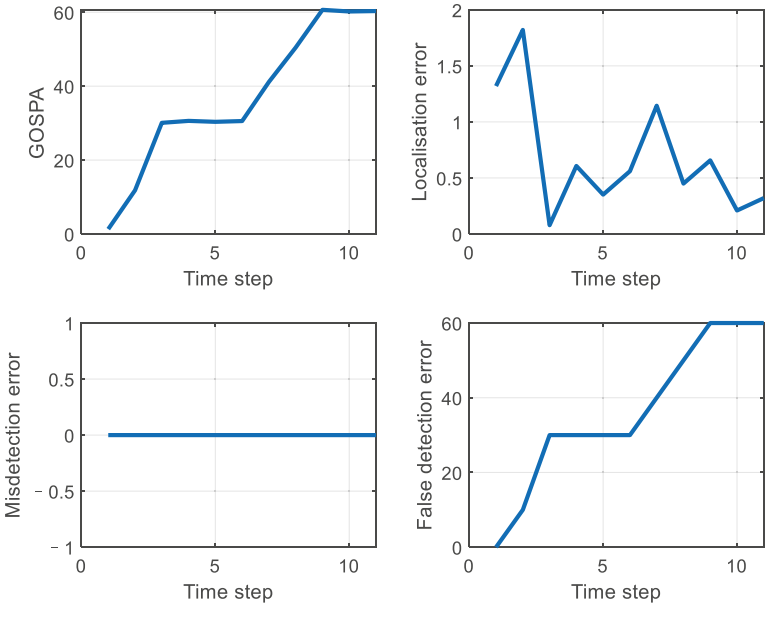

Figure 16. Performance curves of different indicators for dynamic targets in a tracking scenario.

4. Discussion

The proposed 4D radar object tracking method based on radar point clouds can effectively estimate the position and state information of radar targets. This provides more accurate information for perception and planning in autonomous driving. By utilizing radar point clouds, the method improves the tracking and prediction of surrounding objects, enabling autonomous vehicles to make informed decisions in real time. Precise localization and tracking of radar targets enhance situational awareness, allowing autonomous vehicles to navigate complex environments with greater reliability and safety. Overall, this method significantly enhances the perception and planning capabilities of autonomous driving systems, contributing to the development of safer and more efficient autonomous vehicles.

5. Conclusions

In summary, this paper presents a 4D radar-based target tracking algorithm framework that utilizes 4D millimeter-wave radar point cloud information for autonomous driving awareness applications. The algorithm overcomes the limitations of conventional 2 + 1D radar systems and utilizes higher resolution target point cloud information to achieve more accurate motion state estimation and target profile information. The proposed algorithm includes several steps, such as ego vehicle speed estimation, density-based clustering, and binary Bayesian filtering to identify dynamic and static targets, as well as state updates of dynamic and static targets. Experiments are conducted using measurements from 4D millimeter-wave radar in a real-world in-vehicle environment, and the algorithm's performance is validated by actual measurement data. The algorithm can improve the accuracy and reliability of target tracking in autonomous driving applications. This method focuses on the tracking framework for 4D radar. However, further research is needed to investigate the details of certain aspects such as motion models, filters, and ego-vehicle pose estimation.

Author Contributions: Conceptualization, B.T., Z.M. and X.Z.; methodology, B.T., Z.M. and X.Z.; software, B.T.; validation, B.T., S.L. and L.Z.; formal analysis, L.Z.; investigation, S.L.; resources, L.H.; data curation, B.T. and L.Z.; writing—original draft preparation, Z.M.; writing—review and editing, B.T. and Z.M.; visualization, L.Z.; supervision, X.Z. and L.H.; project administration, X.Z. and J.B.; funding acquisition, X.Z. and J.B. All authors have read and agreed to the published version of the manuscript.

Funding: This research was funded by the National Key R&D Program of China (2022YFB2503404).

Data Availability Statement: Not applicable.

Conflicts of Interest: The authors declare no conflict of interest.

References

1. Chen, Q.; Xie, Y.; Guo, S.; Bai, J.; Shu, Q. Sensing System of Environmental Perception Technologies for Driverless Vehicle: A Review of State of the Art and Challenges. *Sens. Actuators A Phys.* **2021**, *319*, 112566. [CrossRef]
2. Ester Bar-Shalom, Y.; Fortmann, T.E.; Cable, P.G. Tracking and Data Association. *J. Acoust. Soc. Am.* **1990**, *87*, 918–919. [CrossRef]
3. Han, Z.; Wang, F.; Li, Z. Research on Nearest Neighbor Data Association Algorithm Based on Target "dynamic" Monitoring Model. In Proceedings of the 2020 IEEE 4th Information Technology, Networking, Electronic and Automation Control Conference (ITNEC), Chongqing, China, 12–14 June 2020; IEEE: New York, NY, USA, 2020.
4. Konstantinova, P.; Udvarev, A.; Semerdjiev, T. A Study of a Target Tracking Algorithm Using Global Nearest Neighbor Approach. In Proceedings of the 4th International Conference on Computer Systems and Technologies E-Learning—CompSysTech'03, Rousse, Bulgaria, 19–20 June 2003; ACM Press: New York, NY, USA, 2003.
5. Sinha, A.; Ding, Z.; Kirubarajan, T.; Farooq, M. Track Quality Based Multitarget Tracking Approach for Global Nearest-Neighbor Association. *IEEE Trans. Aerosp. Electron. Syst.* **2012**, *48*, 1179–1191. [CrossRef]
6. Blackman, S.S. Multiple Hypothesis Tracking for Multiple Target Tracking. *IEEE Aerosp. Electron. Syst. Mag.* **2004**, *19*, 5–18. [CrossRef]
7. Kim, C.; Li, F.; Ciptadi, A.; Rehg, J.M. Multiple Hypothesis Tracking Revisited. In Proceedings of the 2015 IEEE International Conference on Computer Vision (ICCV), Santiago, Chile, 7–13 December 2015; IEEE: New York, NY, USA, 2015.

8. Rezatofighi, S.H.; Milan, A.; Zhang, Z.; Shi, Q.; Dick, A.; Reid, I. Joint Probabilistic Data Association Revisited. In Proceedings of the 2015 IEEE International Conference on Computer Vision (ICCV), Santiago, Chile, 7–13 December 2015; IEEE: New York, NY, USA, 2015.
9. Habtemariam, B.; Tharmarasa, R.; Thayaparan, T.; Mallick, M.; Kirubarajan, T. A Multiple-Detection Joint Probabilistic Data Association Filter. *IEEE J. Sel. Top. Signal Process.* **2013**, *7*, 461–471. [CrossRef]
10. Ristic, B.; Beard, M.; Fantacci, C. An Overview of Particle Methods for Random Finite Set Models. *Inf. Fusion* **2016**, *31*, 110–126. [CrossRef]
11. Vo, B.-T.; Vo, B.-N.; Cantoni, A. Bayesian Filtering with Random Finite Set Observations. *IEEE Trans. Signal Process.* **2008**, *56*, 1313–1326. [CrossRef]
12. Beard, M.; Reuter, S.; Granstrom, K.; Vo, B.-T.; Vo, B.-N.; Scheel, A. Multiple Extended Target Tracking with Labeled Random Finite Sets. *IEEE Trans. Signal Process.* **2016**, *64*, 1638–1653. [CrossRef]
13. Ester, M.; Kriegel, H.-P.; Sander, J.; Xu, X. A Density-Based Algorithm for Discovering Clusters in Large Spatial Databases with Noise. In Proceedings of the Second International Conference on Knowledge Discovery and Data Mining, Portland, Oregon, 2–4 August 1996; Volume 96, pp. 226–231.
14. Ankerst, M.; Breunig, M.M.; Kriegel, H.-P.; Sander, J. OPTICS: Ordering Points to Identify the Clustering Structure. *ACM Sigmod Record* **2008**, *99*.
15. Campello, R.J.; Moulavi, D.; Sander, J. Density-Based Clustering Based on Hierarchical Density Estimates. In *Advances in Knowledge Discovery and Data Mining, Proceedings of the 17th Pacific-Asia Conference, PAKDD 2013, Gold Coast, Australia, 14–17 April 2013*; Proceedings, Part II 17; Springer: Berlin/Heidelberg, Germany, 2013; pp. 160–172.
16. Koch, J.W. Bayesian Approach to Extended Object and Cluster Tracking Using Random Matrices. *IEEE Trans. Aerosp. Electron. Syst.* **2008**, *44*, 1042–1059. [CrossRef]
17. Haag, S.; Duraisamy, B.; Govaers, F.; Fritzsche, M.; Dickmann, J.; Koch, W. Extended Object Tracking Assisted Adaptive Multi-Hypothesis Clustering for Radar in Autonomous Driving Domain. In Proceedings of the 2021 21st International Radar Symposium (IRS), Berlin, Germany, 21–22 June 2021; IEEE: New York, NY, USA, 2021.
18. Baum, M.; Hanebeck, U.D. Extended Object Tracking with Random Hypersurface Models. *IEEE Trans. Aerosp. Electron. Syst.* **2014**, *50*, 149–159. [CrossRef]
19. Wahlstrom, N.; Ozkan, E. Extended Target Tracking Using Gaussian Processes. *IEEE Trans. Signal Process.* **2015**, *63*, 4165–4178. [CrossRef]
20. Knill, C.; Scheel, A.; Dietmayer, K. A Direct Scattering Model for Tracking Vehicles with High-Resolution Radars. In Proceedings of the 2016 IEEE Intelligent Vehicles Symposium (IV), Gothenburg, Sweden, 19–22 June 2016; IEEE: New York, NY, USA, 2016.
21. Scheel, A.; Dietmayer, K. Tracking Multiple Vehicles Using a Variational Radar Model. *IEEE Trans. Intell. Transp. Syst.* **2019**, *20*, 3721–3736. [CrossRef]
22. Cao, X.; Lan, J.; Li, X.R.; Liu, Y. Automotive Radar-Based Vehicle Tracking Using Data-Region Association. *IEEE Trans. Intell. Transp. Syst.* **2022**, *23*, 8997–9010. [CrossRef]
23. Yao, G.; Wang, P.; Berntorp, K.; Mansour, H.; Boufounos, P.; Orlik, P.V. Extended Object Tracking with Automotive Radar Using B-Spline Chained Ellipses Model. In Proceedings of the ICASSP 2021–2021 IEEE International Conference on Acoustics, Speech and Signal Processing (ICASSP), Toronto, ON, Canada, 6–11 June 2021; IEEE: New York, NY, USA, 2021.
24. Thrun, S. Probabilistic Robotics. *Commun. ACM* **2002**, *45*, 52–57. [CrossRef]
25. Tan, B.; Ma, Z.; Zhu, X.; Li, S.; Zheng, L.; Chen, S.; Huang, L.; Bai, J. 3D Object Detection for Multi-Frame 4D Automotive Millimeter-Wave Radar Point Cloud. *IEEE Sens. J.* **2022**, *23*, 1125–11138.
26. Zhang, X.; Xu, W.; Dong, C.; Dolan, J.M. Efficient L-Shape Fitting for Vehicle Detection Using Laser Scanners. In Proceedings of the 2017 IEEE Intelligent Vehicles Symposium (IV), Los Angeles, CA, USA, 11–14 June 2017; IEEE: New York, NY, USA, 2017.
27. Zheng, L.; Ma, Z.; Zhu, X.; Tan, B.; Li, S.; Long, K.; Sun, W.; Chen, S.; Zhang, L.; Wan, M.; et al. TJ4DRadSet: A 4D Radar Dataset for Autonomous Driving. In Proceedings of the 2022 IEEE 25th International Conference on Intelligent Transportation Systems (ITSC), Macau, China, 8–12 October 2022; IEEE: New York, NY, USA, 2022; pp. 493–498.

remote sensing

MDPI

Article

HTC+ for SAR Ship Instance Segmentation

Tianwen Zhang and Xiaoling Zhang *

School of Information and Communication Engineering, University of Electronic Science and Technology of China, Chengdu 611731, China; twzhang@std.uestc.edu.cn
* Correspondence: xlzhang@uestc.edu.cn

Abstract: Existing instance segmentation models mostly pay less attention to the targeted characteristics of ships in synthetic aperture radar (SAR) images, which hinders further accuracy improvements, leading to poor segmentation performance in more complex SAR image scenes. To solve this problem, we propose a hybrid task cascade plus (HTC+) for better SAR ship instance segmentation. Aiming at the specific SAR ship task, seven techniques are proposed to ensure the excellent performance of HTC+ in more complex SAR image scenes, i.e., a multi-resolution feature extraction network (MRFEN), an enhanced feature pyramid net-work (EFPN), a semantic-guided anchor adaptive learning network (SGAALN), a context ROI extractor (CROIE), an enhanced mask interaction network (EMIN), a post-processing technique (PPT), and a hard sample mining training strategy (HSMTS). Results show that each of them offers an observable accuracy gain, and the instance segmentation performance in more complex SAR image scenes becomes better. On two public datasets SSDD and HRSID, HTC+ surpasses the other nine competitive models. It achieves 6.7% higher box AP and 5.0% higher mask AP than HTC on SSDD. These are 4.9% and 3.9% on HRSID.

Keywords: synthetic aperture radar; ship instance segmentation; HTC+; deep learning; convolutional neural network

Citation: Zhang, T.; Zhang, X. HTC+ for SAR Ship Instance Segmentation. *Remote Sens.* **2022**, *14*, 2395. https://doi.org/10.3390/rs14102395

Academic Editors: Zhihuo Xu, Jianping Wang and Yongwei Zhang

Received: 10 April 2022
Accepted: 13 May 2022
Published: 17 May 2022

1. Introduction

Ship surveillance has received widespread attention [1–4]. Synthetic aperture radar (SAR) is an active microwave sensor [5–7]. It works regardless of weather and light conditions, and is more suitable for ship monitoring than optical sensors [8]. Traditional methods [9,10] rely overly on hand-picked features, reducing model flexibility and migration. Now, more efforts are devoted to deep learning-based methods [11].

Most scholars use boxes to detect ships in the SAR community [12], but the instance segmentation at both box- and pixel-level has received less attention [13]. Moreover, Xu et al. [14] studied the dynamic detection of offshore wind turbines by spatial machine learning in SAR images, but offshore facilities and ships have different radar scattering characteristics. Some works [15–22] have studied SAR ship instance segmentation, but they mostly used models for generic objects directly, without considering the targeted characteristics of SAR ship objects, hindering further accuracy improvements and leading to poor segmentation performance in more complex SAR image scenes [23].

Thus, we propose HTC+ to explore better SAR ship instance segmentation. HTC is selected because it may be the best model [24]. For SAR ship mission, we enhance HTC using seven techniques for incremental performance to form HTC+. It is similar to the update from YOLOv3 [25] to YOLOv4 [26]. (1) A multi-resolution feature extraction network (MRFEN) is used to boost multi-scale feature description. (2) An enhanced feature pyramid network (EFPN) is designed to enhance better small ship search ability. (3) A semantic-guided anchor adaptive learning network (SGAALN) is proposed to optimize anchors. (4) A context ROI extractor (CROIE) is designed to boost background discrimination. (5) An enhanced mask interaction network (EMIN) is designed to boost multi-stage mask feature fusion. (6) A post-processing technique (PPT) using NMS [27] and Soft-NMS [28]

is used to reduce missed detections of densely moored ships. (7) A hard sample mining training strategy (HSMTS) [29] is used to deal with complex scenes and cases. Experiments are performed on two public datasets SSDD [13] and HRSID [15]. Results show that seven novelties contribute to improving accuracy; HTC+ offers the best accuracy over the other nine competitive models. The instance segmentation performance in more complex SAR image scenes becomes better. HTC+ offers 6.7% box AP and 5.0% mask AP increments on the vanilla HTC on SSDD; they are 4.9% and 3.9% on HRSID.

The contributions of our work are summarized as follows:

1. The vanilla HTC is designed for generic objects, with limited performance for SAR ships. Thus, we improve it to form its updated version HTC+ to achieve better SAR ship instance segmentation performance.
2. Aimed at the specific SAR ship task, we propose seven techniques (MRFEN, EFPN, SGAALN, CROIE, EMIN, PPT and HSMTS) to enable the excellent performance of HTC+. Here, the motivation and implementation of each technique are both related to the mission characteristics of SAR ships.
3. HTC+ offers a huge increase in accuracy building on HTC, which also surpasses the other nine competitive models.

The rest of this paper is arranged as follows. Section 2 reviews some related works. Section 3 introduces the methodology. Experiments are described in Section 4. Results are shown in Section 5. Ablation studies are made in Section 6. More discussions are introduced in Section 7. Finally, a summary of this paper is made in Section 8.

2. Related Works

In this section, we will review some commonly-used generic instance segmentation models in the computer vision community in Section 2.1. Afterwards, some existing SAR ship instance segmentation models will be introduced in Section 2.2.

2.1. Instance Segmentation

Mask R-CNN [30] is the most classic instance segmentation model, which designed a mask prediction branch on the basis of Faster R-CNN [31]. To measure mask quality, Mask Scoring R-CNN [32] added a scoring network to provide confidences of mask prediction. Cascade Mask R-CNN [33] designed a multi-stage detection and mask head with increasing intersection over union (IOU) thresholds to improve hypotheses quality and ease overfitting. PANet [34] added a bottom-top path aggregation to boost FPN's representation. To make full use of multi-scale features, Rossi et al. [35] proposed a novel region of interest (ROI) extraction layer (GROIE) for instance segmentation. YOLACT [36] is a real-time one-stage instance segmentation model, but its accuracy is poorer than two-stage ones. Furthermore, HTC [24] combined Cascade R-CNN and Mask R-CNN to leverage relationships between detection and segmentation, offering the state-of-the-art performance [37,38]. Therefore, we select it as our experimental baseline.

2.2. SAR Ship Instance Segmentation

Recently, many scholars in the SAR community have started to study SAR ship instance segmentation. Since the first public dataset called HRSID was released by Wei et al. [15] in 2020, various methods have emerged. Su et al. [16] proposed a high-quality network named HQ-ISNet for remote sensing object instance segmentation. They measured the model performance on SAR images; the results indicated the effectiveness of the proposed model. Yet, their model was just a mechanical borrowing from the computer vision community, without thought of appropriateness, hampering further performance improvements. Zhao et al. [17] proposed SA R-CNN which added attention mechanisms to boost accuracy, but the performance among complex scenes was still limited. Gao et al. [18] proposed an anchor-free model called CenterMask and a centroid-distance based loss to enhance benefits of ship feature learning, but such anchor-free models still cannot handle complex scenes

and cases [29]. HTC was applied to SAR ship instance segmentation by Zhang et al. [19], but such direct use led to limited accuracy for SAR ships.

In 2022, Fan et al. [20] designed an efficient instance segmentation paradigm (EISP) for interpreting SAR and optical images, which adopted transformers to extract features. Yet, this paradigm did not consider the targeted characteristics of SAR ships, with limited performance. Zhang et al. [21] designed a full-level context squeeze-and-excitation ROI extractor for SAR ship instance segmentation, but their method only considered extracting the optimized feature subset, and ignored improvements in other parts of the network, leading to limited ship segmentation performance in more complex SAR image scenes. Ke et al. [22] proposed a global context boundary-aware network to improve the positioning performance of the bounding box so as to achieve better segmentation effects, but they did not consider differences between segmentation tasks and detection tasks. Zhang et al. [23] improved Mask R-CNN further by using context information, and squeeze-and-excitation mechanism, but their network did not have adequate mask information interaction, leading to poor segmentation performance in more complex scenes.

In short, the above existing methods mostly used models for generic objects in the computer vision community directly. In other words, they did not consider the targeted characteristics of SAR ship objects, which hinders further accuracy improvements. Thus, we will research useful techniques in this paper to boost instance segmentation especially for SAR ships.

3. Methodology

Aiming at the specific SAR ship task, we explore ways to enhance each component's performance on the basis of the vanilla HTC [24] to achieve the progressive improvements to the overall performance, resulting in the evolution from HTC to HTC+. Our research thinking is similar to the evolution from YOLOv3 [25] to YOLOv4 [26] where YOLOv4 proposed five key techniques and adopted some useful tricks to enhance YOLOv3 further.

Figure 1 depicts HTC+ architecture. MRFEN is a backbone network to extract multi-resolution ship features. EFPN is to improve multi-scale feature representation. SGAALN is to learn anchor location and shape used in the region proposal network (RPN) [31] that is responsible for producing proposals. Classifier (CLS) is used to identify foreground and background. Regressor (REG) predicts proposal positions. CROIE is to map proposals from RPN into MRFEN's feature maps to extract feature subsets [21] for the box-mask prediction head. EMIN predicts box and mask. PPT post-processes outputs. HSMTS works only in training selected hard samples to handle complex scenes and cases.

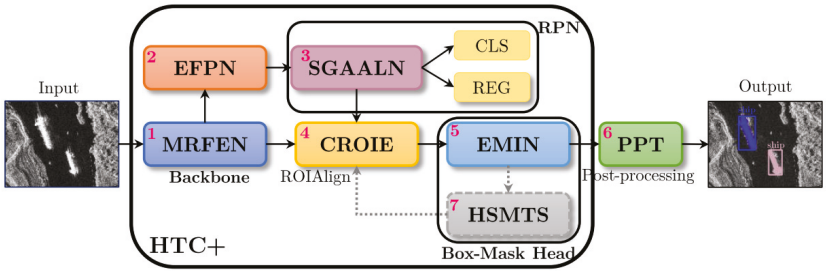

Figure 1. HTC+ architecture. (1) MRFEN denotes the multi-resolution feature extraction network; (2) EFPN denotes the enhanced feature pyramid network; (3) GAALN denotes the semantic-guided anchor adaptive learning network; (4) CROIE denotes the context regions of interest extractor; (5) EMIN denotes the enhanced mask interaction network; (6) PPT denotes the post-processing technique; (7) HSMTS denotes the hard sample mining training strategy. Seven novelties are marked by red numbers 1–7. The first five belong to the network architecture's improvements. The remaining two constitute extra tricks to boost performance further. Moreover, here, RPN denotes the region proposal network, CLS denotes classification, and REG denotes regression.

Moreover, for ease of reading, we summarize the following materials in Table 1. Next, we will introduce the seven components for incremental accuracy in detail in the following sub-sections Sections 3.1–3.7.

Table 1. Materials arrangement of the methodology.

Section ID	Sub-Section ID
Section 3.1. Multi-Resolution Feature Extraction Network (MRFEN)	Section 3.1.1. Multi-Resolution Feature Extraction (MRFF) Section 3.1.2. Multi-Scale Attention-Based Feature Fusion (MSAFF) Section 3.1.3. Atrous Spatial Pyramid Pooling (ASPP)
Section 3.2. Enhanced Feature Pyramid Network (EFPN)	Section 3.2.1. Content-Aware ReAssembly of Features (CARAFE) Section 3.2.2. Feature Balance (FB) Section 3.2.3. Feature Refinement (FR) Section 3.2.4. Feature Enhancement (FE)
Section 3.3. Semantic-Guided Anchor Adaptive Learning Network (SGAALN)	Section 3.3.1. Anchor Location Prediction (ALP) Section 3.3.2. Anchor Shape Prediction (ASP) Section 3.3.3. Feature Adaption (FA)
Section 3.4. Context Regions of Interest Extractor (CROIE)	Section 3.4.1. Concatenation Section 3.4.2. Channel Shuffle Section 3.4.3. Dimension Reduction Squeeze-and Excitation (DRSE)
Section 3.5. Enhanced Mask Interaction Network (EMIN)	Section 3.5.1. Global Feature Self-Attention (GFSA) Section 3.5.2. Adaptive Mask Feature Fusion (AMFF)
Section 3.6. Post-Processing Technique (PPT)	–
Section 3.7. Hard Sample Mining Training Strategy (HSMTS)	–

3.1. Multi-Resolution Feature Extraction Network (MRFEN)

Existing approach. The raw HTC adopted the high-to-low resolution paradigm as the network deepens to extract features, as shown in Figure 2a, e.g., ResNet [39] and ResNeXt [40], i.e., the network depth is inversely proportional to the resolution. Still, this paradigm is not well-suited to SAR ship tasks, considering the two aspects below.

On the one hand, four stages in Figure 2a extract multi-scale features equally, i.e., the same number of conv blocks [e.g., 4 in Figure 2a]. Yet, the ship size distribution of existing datasets is uneven as in Figure 3a,b, i.e., small ships are far more than large ones. The main reason for this phenomenon is that SAR is a "bird-eye" remote sensing earth observation tool that is different from "person-eye" natural scene cameras. Thus, one should treat them differently. Otherwise, a huge performance imbalance between small ships and large ships will occur. We think that one should arrange heavy networks for small ship detection because they are more difficult to detect for fewer feature pixels; for contrast, one should use light networks for large ship detection because they are easier to detect due to their clearer features.

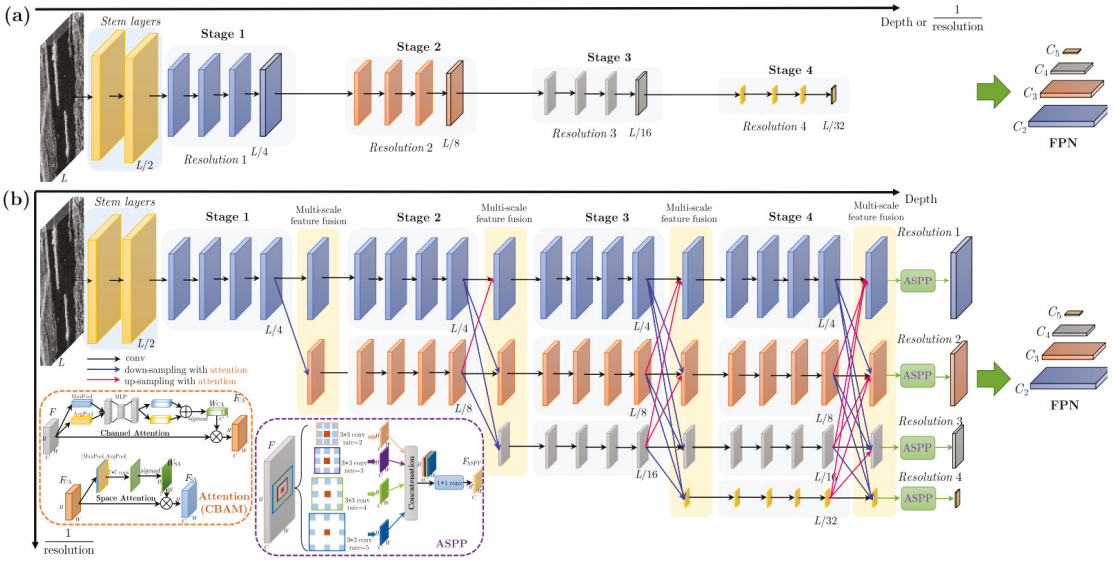

Figure 2. Different backbone networks for feature extraction. (**a**) Existing approach: the backbone network of HTC. (**b**) Proposed approach: the backbone network of HTC+ (MRFEN).

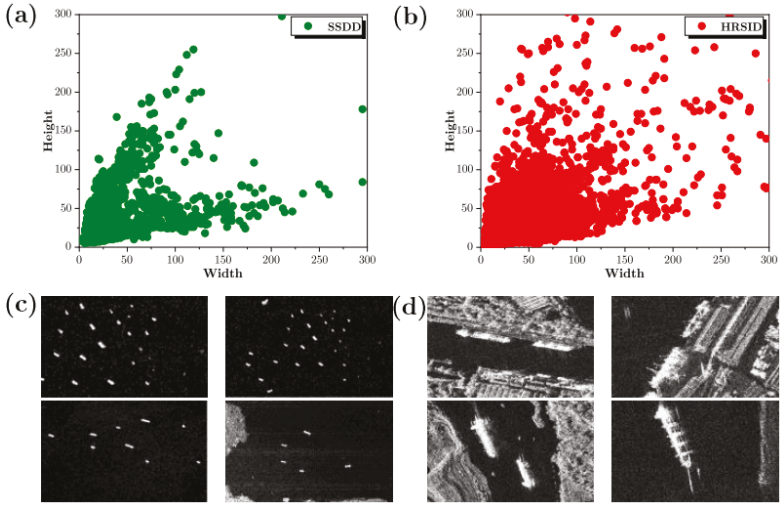

Figure 3. Multi-scale SAR ships. (**a**) Ship size uneven distribution in SSDD. (**b**) Ship size uneven distribution in HRSID. (**c**) Small ships. (**d**) Large ships.

On the other hand, the network backend in Figure 2a is lacking in rich high-resolution representations, i.e., the spatial position information is lost to some degree. This is not conducive to handling position-sensitive vision problems [37], e.g., SAR ship instance segmentation. Thus, one should maintain high-resolution position representations totally across the whole conv process. Moreover, we think that the strong coupling between the depth and resolution directions potentially limits feature description capacity. Signs [41,42] have indicated that decoupling them would help to improve the performance of pixel-sensitive tasks.

Proposed approach. Given the above, we designed MRFEN to extract more precise position representations and richer semantic representations. Moreover, although the multi-resolution approach offers limited accuracy gains for small ships, it can improve the instance segmentation performance of very large ships when the high-resolution mode is used. Figure 2b shows its architecture. MRFEN has three design concepts, i.e., (1) multi-resolution feature extraction (MRFF) in Section 3.1.1, (2) multi-scale attention-based feature fusion (MSAFF) in Section 3.1.2, and (3) atrous spatial pyramid pooling (ASPP) in Section 3.1.3.

3.1.1. Multi-Resolution Feature Extraction (MRFF)

We retain high-resolution representations across the entire system, including, the uppermost resolution-1 branch. This can boost instance segmentation of small ships due to more position information and heavier network parameters. The resolution-2 branch starts from the stage-2; the resolution-3 branch starts from the stage-3; the resolution-3 branch starts from the stage-4. This leverages lighter networks for larger ships so as to adapt to their easier detection. Consequently, the network depth and resolution are decoupled smoothly, which can enable networks to optimize their parameters among a larger search space so as to further enhance fitting or learning capacity. Briefly, the above can be described by

$$\begin{aligned} \mathcal{N}_{11} \rightarrow \mathcal{N}_{21} \rightarrow \mathcal{N}_{31} \rightarrow \mathcal{N}_{41} \\ \searrow \mathcal{N}_{22} \rightarrow \mathcal{N}_{32} \rightarrow \mathcal{N}_{42} \\ \searrow \mathcal{N}_{33} \rightarrow \mathcal{N}_{43} \\ \searrow \mathcal{N}_{44} \end{aligned} \tag{1}$$

where $\mathcal{N}_{sr}$ denotes the sub-network of the s-th stage and the r-th resolution, $\rightarrow$ denotes the conv process, and $\searrow$ denotes the down-sampling process. Different from image pyramid in [43], the low-resolution in MRFEN comes from the previous high-resolution down-sampling, rather than the down-sampling on the input image. This is because feature maps from the front-end high-resolution sub-network are more representative.

3.1.2. Multi-Scale Attention-Based Feature Fusion (MSAFF)

There are no direct interactions between different resolution branches after the network depth and resolution are decoupled. This hampers network information flow, possibly increasing the risk of overfitting of their separate local optimization. Moreover, training within their own closed cyberspace may also slow down the training convergence speed, declining performance. Therefore, it is essential to perform multi-scale feature fusion. (In this paper, the resolution and the scale share the same meaning.) Integrating features with different scales, the down-sampling and up-sampling were widely adopted [37,44,45]. Still, different from these authors, we suggest to first use an attention module for a feature refinement, and then execute the down-sampling and up-sampling. This can enable more valuable features to be transmitted to another branch so as to avoid possible negative interferences. Taking $\mathcal{N}_{42}$ in Equation (1) as an example, we get its feature maps $\mathcal{F}_{42}$ by

$$\mathcal{F}_{42} = \mathcal{F}_{32} + DownSamp^{2\times}(f_{attention}(\mathcal{F}_{31})) + UpSamp^{2\times}(f_{attention}(\mathcal{F}_{33})) \tag{2}$$

where $\mathcal{F}_{sr}$ denotes the feature maps of $\mathcal{N}_{sr}$, $DownSamp^{n\times}$ denotes the n times down-sampling, $UpSamp^{n\times}$ denotes the n times up-sampling, and $f_{attention}$ denotes the refinement operation using an attention module. We implement $f_{attention}$ by a convolutional block attention module (CBAM) [46] with channel attention and space channel attention. One can also use other advanced attention modules [47] for better performance. In this work, we select CBAM, because it is the most famous and has been used by many scholars in the SAR community [17].

The network architecture of CBAM is shown in the orange dashed box in Figure 2b. Let its input be $F \in \mathbb{R}^{H\times W\times C}$ where H and W are the height and width of feature maps and C is the channel number. Then the channel attention is responsible for generating a channel-dimension weight matrix $W_{CA} \in \mathbb{R}^{1\times 1\times C}$ to measure the important levels of C

channels; the space attention is responsible for generating a space-dimension weight matrix $W_{SA} \in \mathbb{R}^{H\times W\times 1}$ to measure the important levels of space-elements across the entire $H \times W$ space. They range from 0 to 1 by a sigmoid activation. The result of the channel attention is denoted by $F_{CA} = F \cdot W_{CA}$. The result of the space attention is denoted by $F_{SA} = F_{CA} \cdot W_{SA}$. See [46] for CBAM's details.

3.1.3. Atrous Spatial Pyramid Pooling (ASPP)

Although the multi-scale attention-based feature fusion offers some other resolution responses from other branches, these kinds of responses are still limited among the total responses. Thence, we adopt the atrous spatial pyramid pooling (ASPP) [48] to deal with this problem. Its network architecture is depicted in the purple dashed box in Figure 2b. ASPP utilizes atrous convs [49,50] with different dilated rates to achieve multi-resolution feature responses in the single-resolution branch. It is described by

$$F_{\text{ASPP}} = f_{1\times 1}\left(\left[f^2_{3\times 3}(F), f^3_{3\times 3}(F), f^4_{3\times 3}(F), f^5_{3\times 3}(F)\right]\right) \tag{3}$$

where F denotes the input, F_{ASPP} denotes the output, $f^r_{3\times 3}$ denotes a 3×3 conv with a dilated rate of r, and $f_{1\times 1}$ denotes a 1×1 conv for channel reduction, i.e., from four atrous convs concatenation $4C$ to the raw C of F. In this way, different dilated rates will enable different resolution responses, as well yielding different scope contexts. We set four dilated rates for the accuracy-speed trade-off. More might offer better performance but must sacrifice speed. Different from [48], four dilated rates are set to 2, 3, 4 and 5 because of the small size of the low-solution branch ($L/32 \times L/32$). Especially, ASPP can also allow our MRFEN to enlarge receptive fields so as to receive more ship surrounding context information. This is conducive to alleviating background interferences, e.g., blur edges, sidelobes, ship wakes, speckle noise (SAR imaging mechanisms), tower crane [8], and inshore facilities, as in Figure 4.

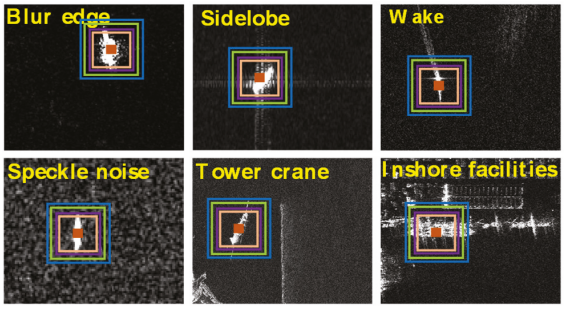

Figure 4. SAR ships and ships' surrounding contexts. Boxes with different colors and sizes denotes the atrous convs with different dilated rates.

Finally, the outputs of ASPP with different resolution levels will constitute the inputs of FPN (C_2, C_3, C_4 and C_5). It is also different from the previous network in Figure 2a that makes the last layers of all stages constitute the inputs of FPN. Figure 2b performs better than Figure 2a because the former offers richer high-resolution position representation and richer low-resolution semantic representation at the same time among each stage.

3.2. Enhanced Feature Pyramid Network (EFPN)

Existing approach. The vanilla HTC followed the standard FPN paradigm [51] to ensure multi-scale performance as shown in Figure 5a. In Figure 5, C_2, C_3, C_4 and C_5 are the inputs of FPN which are from the backbone network as shown in Figure 2. However, this standard FPN offers limited performance for SAR ship instance segmentation from the following three aspects.

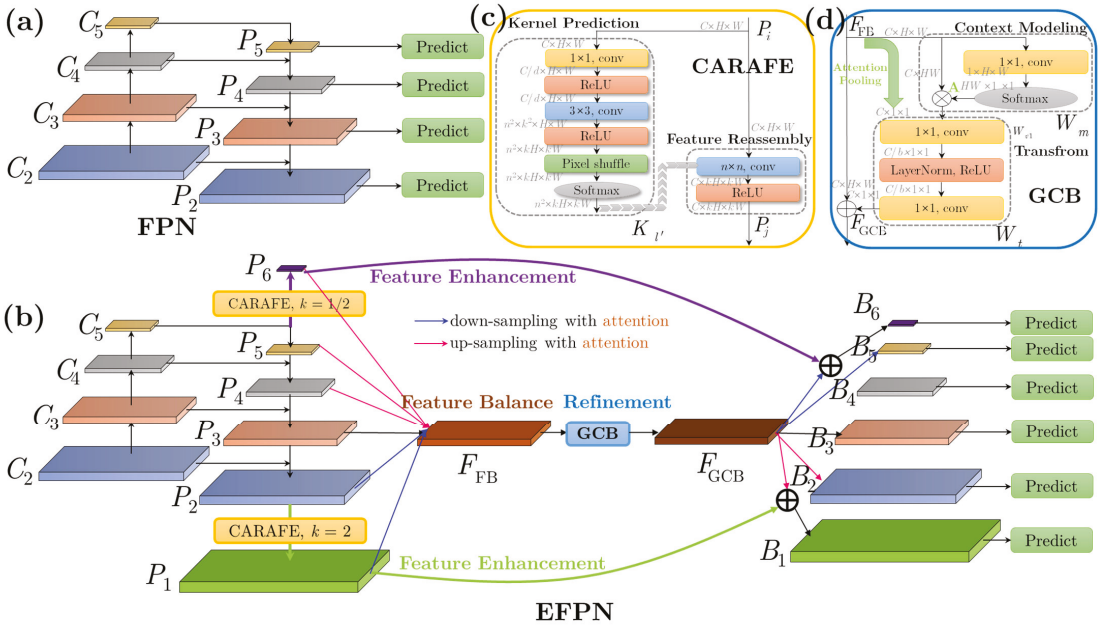

Figure 5. Feature pyramid networks. (**a**) Existing approach: FPN of HTC. (**b**) Proposed approach: EFPN of HTC+. (**c**) CARAFE implementation. (**d**) GCB implementation.

Firstly, on account of the huge resolution difference, e.g., 1 m resolution for TerraSAR-X and 20 m resolution for Sentinel-1, ships in SAR images present a huge scale difference as shown in Figure 6a,b. This situation is called the cross-scale effect [52], e.g., the extremely small ships in Figure 6c vs. the extremely large ships in Figure 6d. The standard FPN was designed for the natural object detection, e.g., COCO [53] and PASCAL [54] datasets. These datasets are with a relatively small scale difference. Thus, the raw FPN has some challenges to handle such cross-scale problems due to its limited FPN levels. From the clustering results of *K*-means, the raw four levels P_2, P_3, P_4 and P_5 are inferior to six levels in terms of the network multi-scale feature learning ability. The mean IOU of the former is 0.5913, lower than that of the latter 0.6490. Thus, we use more levels to deal with this special SAR ship cross-scale instance segmentation.

Secondly, small ships always constitute the majority among existing datasets for the characteristics of the "bird-eye" view of SAR. The raw bottom-level P_2 is with limited searching ability for small ships in Figure 6c, because small ships are diluted after multiple down-sampling operations (from L to $L/4$) due to their faint spatial features. As a result, a large number of small ships will be missed, reducing HTC's overall performance. Thus, we suggest to generate a lower level P_1 to handle this problem, because lower levels offer richer spatial position information, which is beneficial for small ship instance segmentation.

Thirdly, although the original top-level P_5 may detect the extremely large ships in Figure 6d successfully by using a rectangle bounding box, it is still with limited pixel-segmentation performance. Different parts of the ship hull have different materials, resulting in differential radar electromagnetic scatterings. This makes the pixel brightness distribution of the ship in a SAR image extremely uneven. This will bring huge difficulties to classifiers for their effective pixel-level discrimination. Therefore, we suggest to generate a higher level P_6 to handle this problem, because high levels can offer more semantic information by shrinking large ships to reach the purpose of removing the ship hull's internal "black" pixels; then in the mask recovery process, the nearest neighbor interpolation can fill

those internal "black" pixels using correct predicted ship "white" pixels, so as to achieve better segmentation performance, as shown in Figure 6d.

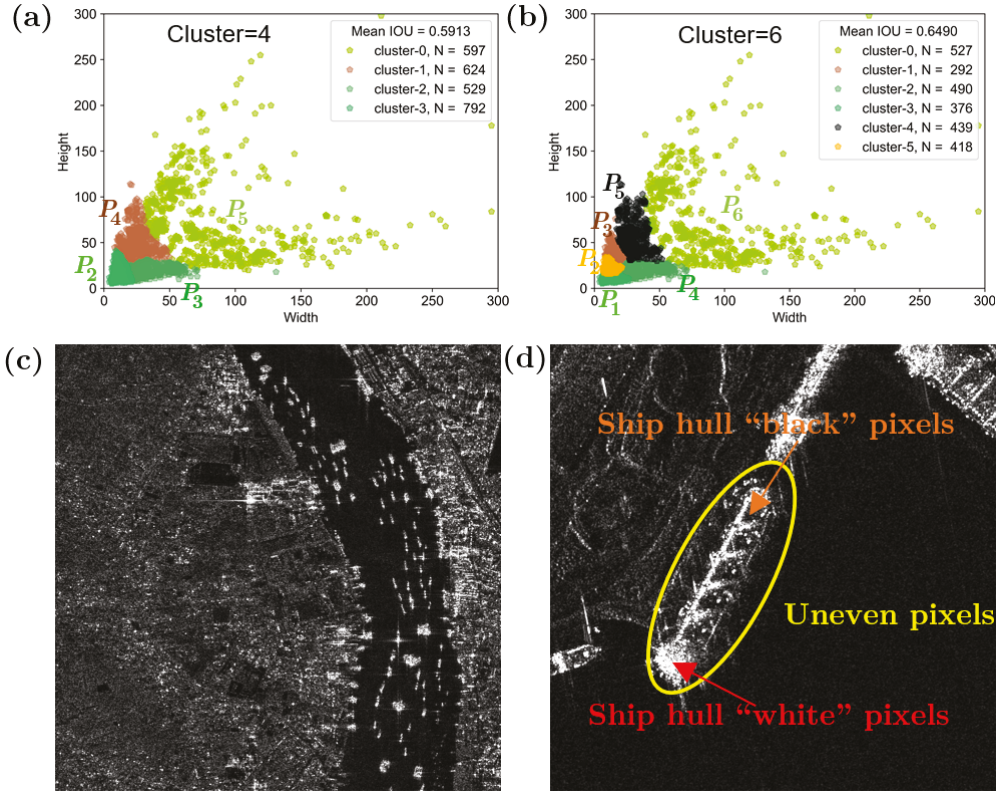

Figure 6. (**a**) Cluster results of four levels of HTC. (**b**) Cluster results of six levels of HTC+. Here, K-means is used for more intuitive presentation. (**c**) An SAR image with extremely small ships. (**d**) An SAR image with extremely large ships. Here, (**c**,**d**) have a huge scale difference due to different resolutions, i.e., cross-scale.

Proposed approach. Given the above, we propose an enhanced feature pyramid network (EFPN) to enhance multi-scale instance segmentation. Figure 5b shows its architecture. EFPN has four design concepts, i.e., (1) content-aware reassembly of features (CARAFE) in Section 3.2.1, (2) feature balance (FB) in Section 3.2.2, (3) feature refinement (FR) in Section 3.2.3, and (4) feature enhancement (FE) in Section 3.2.4.

3.2.1. Content-Aware ReAssembly of Features (CARAFE)

We draw lessons from the advanced Content-Aware ReAssembly of Features (CARAFE) [55] to generate an extra higher top-level P_6 and an extra lower bottom-level P_1. Note that the raw CARAFE did not offer a down-sampling operation; here, we expand it by adding an extra hyper-parameter k. $k = 2$ denotes the up-sampling. $k = 1/2$ denotes the down-sampling. (i) *Generate* P_1. Wang et al. [55] have confirmed that CARAFE was superior to the nearest neighbor and the bilinear interpolation which both focus on the subpixel neighborhoods, failing to capture the richer semantic information required by dense prediction tasks, and it was also superior to the adaptive *deconv* [56] which uses a fixed kernel for all samples, resulting in limited receptive fields. CARAFE can enable instance-specific

content-aware handling, offering a large field of view, which can generate adaptive kernels on-the-fly. It can also aggregate global contextual information, enabling preferable performance for object detection [55]. Thence, it is adopted to generate P_1. (ii) *Generate* P_6. Shelhamer et al. [57] pointed out that the simple max-pooling would increase the risk of feature loss. Thus, to leverage CARAFE's advantage, we extend it for more effective feature down-sampling. The above is described by

$$\begin{aligned} P_1 &= \text{CARAFE}^{\times 2}(P_2) \\ P_6 &= \text{CARAFE}^{\times \frac{1}{2}}(P_5) \end{aligned} \tag{4}$$

Here, CARAFE$^{\times k}$ denotes the k times down/up-sampling using CARAFE. It needs to be noted that one can follow the above operation to generate more levels, e.g., P_0, P_7, but the trade-off between speed and accuracy should be carefully considered.

Figure 5c shows the implementation of CARAFE. It contains a kernel prediction process and a feature reassembly one. (i) The former is to predict an adaptive k times down/up-sampling kernel $K_{l'}$ corresponding to the l' location of feature maps from the original l location. The kernel size is $n \times n$ which means $n \times n$ neighbors of the location l. Here, n is set to 5 empirically, the same as the raw report [55]. In other words, CARAFE considers the surrounding 5 pixels for down/up-sampling interpolation ($5 \times 5 = 25$ pixels). Moreover, the contribution weights of these 25 pixels are obtained by the adaptive learning. During the kernel prediction process, a 1×1 conv is to compress channel to refine salient features, where the compression ratio d is set to 4, i.e., the raw 256 channels are compressed to 64 ones. This can not only reduce the calculation burden, but also ensure the benefits of predicted kernels [58]. One 3×3 conv is to encode contents whose channel number is $n^2 \times k^2$ where k denotes the down/up-sampling ratio (i.e., from $H \times W$ to $kH \times kW$). The dimension transformation is completed using a pixel shuffle operation. Each reassembly kernel is normalized by a softmax function spatially so as to reflect the weight of each sub-content. Finally, the learned kernel $K_{l'}$ will serve as the kernel for the subsequent feature reassembly process. (ii) The latter is a simple $n \times n$ conv, but its conv kernel parameters are determined by $K_{l'}$. In the above way, the resulting down/up-sampling feature maps have the ability of content perception, yielding the better feature representation. More details can be found in [55].

3.2.2. Feature Balance (FB)

Cross-scale ships predicted in different FPN levels have a huge feature imbalance [59] especially with the increase of levels. This imbalance also potentially leads to unstable training coming from the huge number gap between small ships and large ships. Thence, we follow the practice from [59] to balance ship features with huge differences, i.e.,

$$\begin{aligned} F_{\text{FB}} = \tfrac{1}{6}\{ & UpSamp^{8\times}(f_{attention}(P_6)) + UpSamp^{4\times}(f_{attention}(P_5)) + UpSamp^{2\times}(f_{attention}(P_4)) \\ & + P_3 + DownSamp^{2\times}(f_{attention}(P_2)) + DownSamp^{4\times}(f_{attention}(P_1))\} \end{aligned} \tag{5}$$

Here, to fully leverage the advantage of the attention in Equation (2), before up/down-sampling, each level is also processed by CBAM to further increase representation power. Moreover, we rescale all levels into the P_3 level empirically, because it is located at the middle of the pyramid, provided with both richer position information and semantic information. It can consider both lower levels P_1, P_2 and higher levels P_4, P_5, P_6. P_4 is also a middle level of the pyramid; still it is not used as the rescaled level, because we hold the view that the network should better contain more space position features for better small ship instance segmentation. Once all levels are rescaled to the same level, an average operation is performed for their balanced feature fusion. In this way, the resulting condensed multi-scale features contain balanced semantic features and position features from various resolutions. Finally, large ship features and small ones can complement

each other to facilitate the information flow, alleviating feature imbalance and promoting network smooth training.

3.2.3. Feature Refinement (FR)

To recover a more robust FPN, we also adopt a global context block (GCB) [60] to refine the condensed multi-scale features F_{FB} further. Such practice is in fact motivated by Libra R-CNN [59]. However, their used non-local block [61] only can capture spatial dependence, but the channel dependence is neglected. Therefore, we adopt the more advanced GCB to reach this aim, achieving global feature self-attention and meeting channel squeeze-and-excitation (SE) [62] simultaneously. Figure 5d shows its architecture. GCB contains a context modeling module and a transform module. (i) The former first uses 1×1 conv W_k and a *softmax* activation to generate the attention weights A; then, conducts a global attention pooling to achieve the global context features, i.e., from $C \times H \times W$ to $C \times 1 \times 1$. It is equivalent to the global average pooling in SE [62], but the average operation is replaced with the adaptive operation here. (ii) The latter is similar to SE, but before the rectified linear unit (ReLU) activation, the output of the 1×1 squeeze conv W_{v1} is first normalized to ensure better generalization, equivalent to the regularization of batch normalization (BN) [63]. Here, to refine more salient features of six FPN levels, the squeeze ratio r is set to 6. The last 1×1 conv W_{v2} is used to transform bottlenecks to capture channel-wise dependencies. Finally, an element-wise matrix addition is used for feature fusion. More details can be found in [60].

3.2.4. Feature Enhancement (FE)

To reduce the risk of feature loss from the boundary levels P_1 and P_6 due to their relatively large up/down-sampling ratios, we also add extra two skip connections for their feature enhancement while recovering them, i.e.,

$$\begin{aligned} B_1 &= P_1 + UpSamp^{4\times}(f_{attention}(F_{\mathrm{FB}})) \\ B_6 &= P_6 + DownSamp^{8\times}(f_{attention}(F_{\mathrm{FB}})) \end{aligned} \tag{6}$$

where B_j denotes the i-th level of the recovered FPN. Here, we obtain the other remaining levels using the reverse operation of Equation (5). Finally, the recovered FPN B_i will be able to predict cross-scale SAR ships in a more elegant and stable paradigm.

3.3. Semantic-Guided Anchor Adaptive Learning Network (SGAALN)

Existing approach. The raw HTC used the classic anchor generation scheme [31] as in Figure 7a. This scheme uniformly arranges dense anchors with fixed shapes to every location among an image. However, it is not suitable for SAR ship instance segmentation.

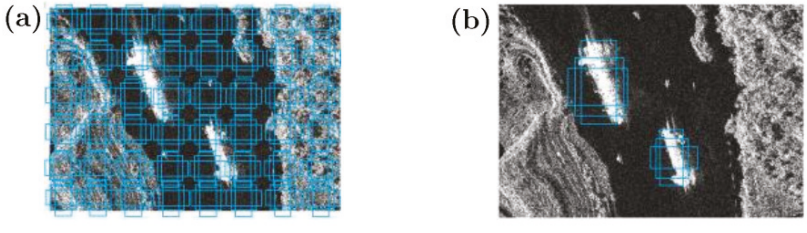

Figure 7. Different anchor generation schemes. (**a**) Existing approach: dense and shape-fixed anchors of HTC. (**b**) Proposed approach: Sparse and shape-adaptive anchors of HTC+. Blue boxes denote anchor boxes.

On the one hand, ships in SAR images exhibit a sparse distribution due to the characteristic of SAR "bird-eye" remote sensing view, e.g., there are only 2.12 ships on average among one image in the SSDD dataset. The uniform and dense anchor allocation to everywhere in a SAR image will potentially increase false alarms; additionally, numerous anchors are redundant, causing a heavier computational burden. Thus, one should better first adaptively predict possible positions where ships are more likely to occur; then arrange anchors on these possible positions to handle the above problem. On the other hand, the raw anchors with fixed shapes (width, height and aspect ratio) are not conducive to multi-scale prediction, with slower training speed. The hand-crafted preset anchors with fixed shapes are not in line with real ships with changeable shapes, reducing multi-scale performance. Although one can draw support from the *K*-means clustering on the specific dataset for better initial anchors [25], it is troublesome when this practice is applied to more datasets. Moreover, the initial anchors are still with fixed shapes, not resolving substantive issues. Thus, we should adaptively predict anchor shapes to handle the above problem.

Proposed approach. Given the above, we establish a semantic-guided anchor adaptive learning network (SGAALN) to achieve the adaptive anchor location prediction and the adaptive anchor shape prediction. The execution visual effect of SGAALN is shown in Figure 7b. Here, we leverage high-level semantic features to reach this aim, because they enable higher anchor quality than low-level ones [29]. SGAAL has three design concepts, i.e., (1) anchor location prediction (ALP) in Section 3.3.1, (2) anchor shape prediction (ASP) in Section 3.3.2, and (3) feature adaption (FA) in Section 3.3.3.

3.3.1. Anchor Location Prediction (ALP)

We use a 1×1 conv W_L whose channel number is set to 1 for the adaptive anchor location prediction, as shown in Figure 8a. This conv works on the inputted semantic features denoted by Q. The resulting feature maps are with a $H \times W \times 1$ dimension. $H \times W$ is the whole 2D space. This feature map is then activated by a *sigmoid* function to achieve the probability of ship occurrence $P_{ship} \in [0,\ 1]$ at the (x, y) position cross the whole $H \times W$ 2D space. When P_{ship} is bigger than the preset threshold ϵ_t, this (x, y) position will generate anchors; otherwise, this position will be removed where no anchors are generated. Here, ϵ_t is set to 0.01 empirically according to the experimental results in Section 6.3.

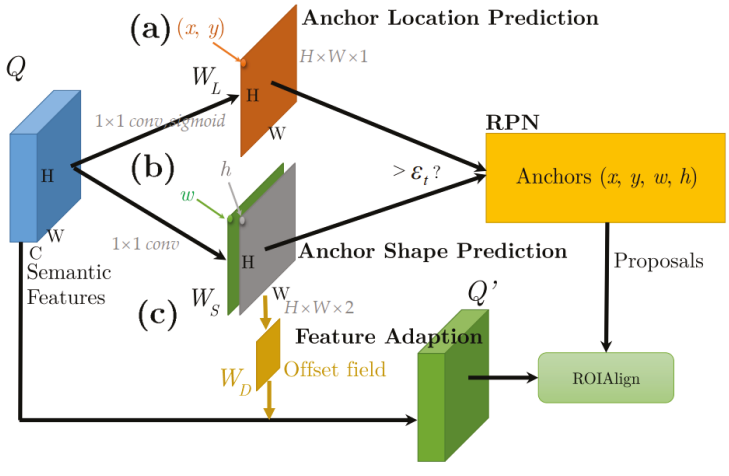

Figure 8. SGAALN architecture. (**a**) Anchor location prediction. (**b**) Anchor shape prediction. (**c**) Feature adaption.

3.3.2. Anchor Shape Prediction (ASP)

We arrange another one 1×1 conv W_S whose channel number is set to 2 for the adaptive anchor shape prediction, as shown in Figure 8b. This conv works on the input semantic features denoted by Q as well. The resulting feature maps are with a $H \times W \times 2$ dimension. This is because we need to estimate two parameters, i.e., the anchor width w and height h. Note that the anchor shape prediction works on all positions of the whole $H \times W$ 2D space in consideration of an easy network implementation. Finally, according to the previously obtained anchor prediction locations, the redundant shape predictions are filtered. As a result, the adaptive anchor parameter (x, y, w, h) is achieved which will be inputted to RPN for classification and regression.

3.3.3. Feature Adaption (FA)

Due to the cross-scale effect of SAR ships, the adaptively predicted anchors will also exhibit a huge shape difference. Yet, this will bring about a huge encoded content difference on the inputted semantic features when they are pooled for the subsequent box and mask prediction. Thus, large anchors should encode content in a large region, while small anchors should have a small region, accordingly. However, the raw semantic features Q do not meet this point because it is designed for fixed-shape anchors. Coincidentally, the existing deformable convs [64] can offer an effective solution for this issue, where the previously learned anchor shape (w, h) exactly corresponds to deformable conv kernel's bias (i.e., the offset field). Thence, we use a deformable convs W_D to process the inputted semantic features Q for such feature adaption, i.e.,

$$q_i^{'} = W_D(q_i, w_i, h_i) \tag{7}$$

where w_i and h_i are the i-th position anchors' width and height $i \in \mathbb{R}^{H \times W}$, $q_i \in Q$, and $q_i^{'} \in Q'$. Q' denotes the output of feature adaption. The optimized anchors enable better proposals to extract ROI feature subsets using ROIAlign.

3.4. Context Regions of Interest Extractor (CROIE)

Existing approach. The raw HTC followed the standard two-stage ROI extractor (ROIE) of Mask R-CNN [30] to extract feature subsets of ROIs for the subsequent mask prediction, as shown in Figure 9a. That is, the bounding box prediction is first conducted, and then, the mask prediction is performed in the resulting $h \times w$ box. However, this practice is still with limited SAR ship mask prediction performance. On the one hand, the mask prediction relies heavily on the box prediction. If the offered boxes are not accurate, the mask prediction must become poor. From Figure 9a, the features for mask prediction exist in the corresponding box with limited receptive fields, reducing the global field of vision. This will decline segmentation performance improvements. One the other hand, as in Figure 4, due to the special SAR imaging mechanism, SAR ships have many complex surroundings outside the compact box, e.g., blur edges, sidelobes, ship wakes, speckle noise, tower crane, and inshore facilities. They will bring some non-negligible effects for mask prediction. Thus, the compact box makes it impossible for mask prediction to observe more ship backgrounds, e.g., ship-like pixel noise and ship wakes. Although the box can eliminate the cross-sidelobe deviating from the ship center too far, a few sidelobe and noise pixels in the box can make it difficult to ensure segmentation learning benefits. Thus, it is necessary to expand the receptive field to explicitly find out the clear boundary between ship and its context surrounding.

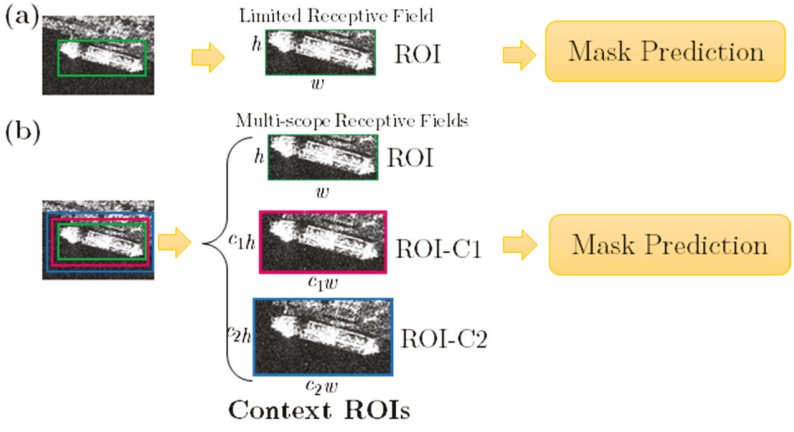

Figure 9. Different ROI extractors (ROIEs). (**a**) Existing approach: ROIE of HTC. (**b**) Proposed approach: CROIE of HTC+.

Proposed approach. Given the above, we design a context ROI extractor (CROIE) to add multi-scope contexts to the box for better mask prediction, as shown in Figure 9b. We arrange two different scope contexts denoted by ROI-C1 with a size of $c_1w \times c_1h$ and ROI-C2 with a size of $c_2w \times c_2h$. Here, c_1 and c_2 ($c_2 > c_1 > 1$) are two amplification factors which are set to 1.5 and 2.0, respectively, according to experiments in Section 6.4. This idea is motivated by Kang et al. [65]; however, differently, we consider multi-scope contexts. Moreover, we do not use more context ROIs, e.g., ROI-C3, considering the trade-off of speed and accuracy. Figure 10 shows CROIE's implementation. CROIE has three design concepts, i.e., (1) concatenation in Section 3.4.1, (2) channel shuffle in Section 3.4.2, and (3) dimension reduction squeeze-and excitation (DRSE) in Section 3.4.3.

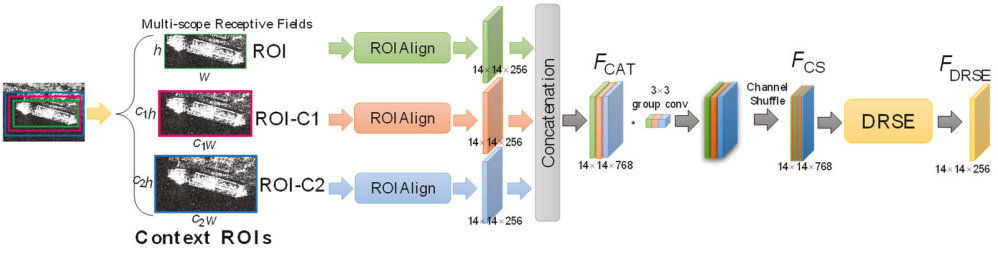

Figure 10. Implementation of CROIE.

3.4.1. Concatenation

We concatenate three feature subsets after ROIAlign. We find that the feature concatenation performs better than the feature adding, because the former achieves feature reuse for better deep supervision. Then, we use a 3×3 group conv to refine them for subsequent operations where the group division factor g is set to 3. The above is described by

$$F_{\mathrm{CAT}} = f_{3\times3,3}([\mathrm{ROIAlign}(\mathrm{ROI}), \mathrm{ROIAlign}(\mathrm{ROI}-\mathrm{C1}), \mathrm{ROIAlign}(\mathrm{ROI}-\mathrm{C2})]) \quad (8)$$

where $f_{3\times3,3}$ denotes the 3×3 group conv whose group division factor is 3, and F_{CAT} denotes the output of concatenation.

3.4.2. Channel Shuffle

To reduce the effect of feature collaboration consistency in the single ROI, we also shuffle the resulting features F_{CAT} along the channel dimension to enable more powerful representation. The result is denoted by F_{CS}.

3.4.3. Dimension Reduction Squeeze-and-Excitation (DRSE)

To balance allocation contributions of different ROIs with different context scopes, we also design a dimension reduction squeeze-and-excitation (DRSE) block, an extended version of SE [62] (the raw SE did not achieve dimension reduction), to model channel correlation. It can suppress useless channels and highlight valuable ones meanwhile reducing channel dimension, which reduces the risk of the training oscillation due to excessive irrelevant backgrounds. Consequently, moderate contexts can be offered for mask prediction. Figure 11 shows DRSE's implementation. In the collateral branch, the global average pooling is used to achieve the global spatial information; a 1×1 conv with a sigmoid activation is used to squeeze channels to focus on important ones. The squeeze ratio p is set to 3 ($256 \times 3 \rightarrow 256$). In the main branch, the input channel's number is reduced directly using a 1×1 conv with a ReLU activation. The broadcast element-wise multiplication is used for compressed channel weighting. DRSE will model channel correlation of the input feature maps in a reduced dimension space. Then, it leverages the learned weights from the reduced dimension space to pay attention to the important features of the main branch. In this way, the potential information loss from the crude dimension reduction is avoided. The above is described by

$$F_{\mathrm{DRSE}} = \mathrm{ReLU}(conv_{1\times1}(F_{\mathrm{CS}})) \odot \sigma(conv_{1\times1}(GAP(F_{\mathrm{CS}}))) \tag{9}$$

where F_{CS} denotes the input, i.e., the output of channel shuffle, F_{DRSE} denotes the output, σ denotes the sigmoid function, and $\odot$ denotes the broadcast element-wise multiplication.

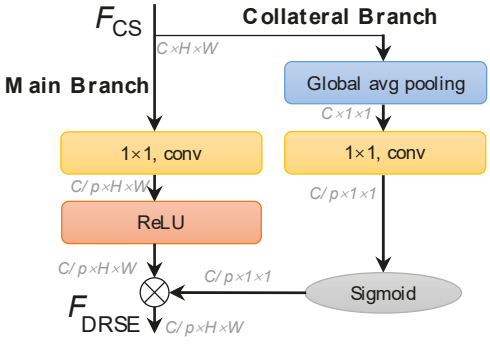

Figure 11. Implementation of DRSE.

3.5. Enhanced Mask Interaction Network (EMIN)

Existing approach. The raw HTC designed the mask interaction network (MIN) as shown in Figure 12a to establish a connection between different stages. Mask features of previous stage M_{i-1} are refined by a 1×1 conv for next stage M_i. A simple addition is used for feature fusion, i.e., $conv_{1\times1}(M_{i-1}(F)) + F$ where F is feature maps of backbone networks. We observe that a 1×1 conv offers limited feature refinement effects; a direct feature addition also offers limited fusion benefits.

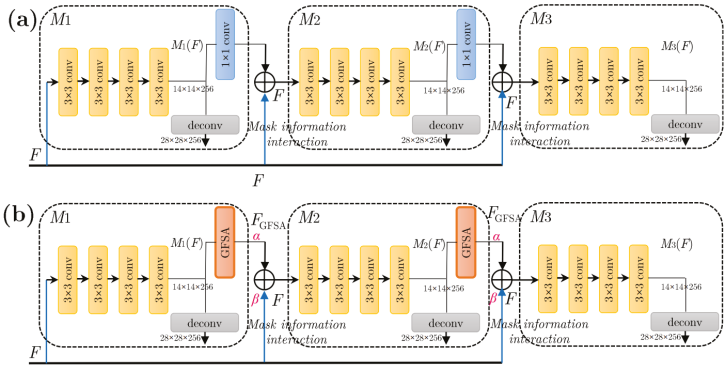

Figure 12. Mask interaction network (MIN) (**a**) Existing approach: MIN of HTC. (**b**) Proposed approach: EMIN of HTC+.

Proposed approach. Thus, we design an enhanced mask interaction network (EMIN) whose architecture is shown in Figure 12b. EMIN has two design concepts, i.e., (1) global feature self-attention (GFSA) in Section 3.5.1, and (2) adaptive mask feature fusion (AMFF) in Section 3.5.2.

3.5.1. Global Feature Self-Attention (GFSA)

We design a global feature self-attention block (GFSA) to replace the raw 1×1 conv, inspired by the advanced non-local neural networks [61]. GFSA can capture long-range dependencies of each mask pixel in the whole space, to enable a global receptive field, which is conducive to the efficient flow of information and context modeling. Figure 13a shows its implementation. In Figure 13a, features at the i-position are denoted by ϕ using a 1×1 conv W_ϕ. Features at the j-position are denoted by θ using a 1×1 conv W_θ. f is obtained from adaptive learning between ϕ and θ where the normalization process is equivalent to a *softmax* calculation function. The representation of the input at the j-position g is learned using another one 1×1 conv W_g. The response at the i-position y_i is obtained by a matrix multiplication. Note that we embed all features into $C/4$ channel space to reduce computational burdens. To apply response to the input readily, we use another one 1×1 conv W_z to transform dimension for the adding operation ($\oplus$). Finally, we achieve the global feature self-attention output F_{GFSA} that will be transmitted to the next stage.

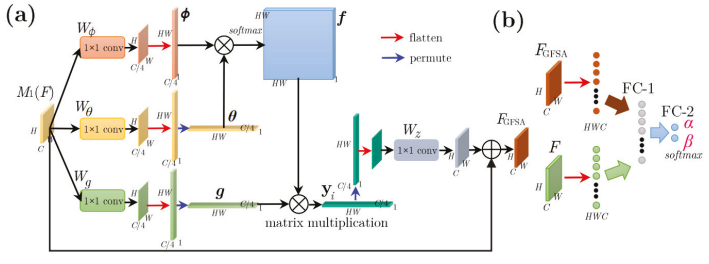

Figure 13. (**a**) Implementation of the global feature self-attention (GFSA). (**b**) Implementation of the adaptive mask feature fusion.

3.5.2. Adaptive Mask Feature Fusion (AMFF)

We arrange an adaptive mask feature fusion (AMFF) scheme for reasonably allocating contributions, instead of the direct feature adding. AMFF is depicted in Figure 13b. Firstly,

the previous mask feature F_{GFSA} and the backbone network feature F are flattened into 1D column vectors respectively, i.e., from $H \times W \times C$ to $HWC \times 1$.

Then, they are concatenated directly to be inputted into a fully-connected (FC-1) layer. Finally, the terminal 2-element FC-2 layer with a *softmax* activation is used to achieve two adaptive weight parameters α and β. Here, due to the use of the *softmax* activation, α plus β equals 1. The above is described by

$$W = softmax\{FC_2(FC_1([flatten(F_{\mathrm{GFSA}}), flatten(F)]))\} \tag{10}$$

where $W = [\alpha, \beta]^T$ denotes the weight vector. Finally, the mask interaction is implemented by

$$M_i(F) = \alpha \cdot F_{\mathrm{GFSA}} + \beta \cdot F \tag{11}$$

where $F_{\mathrm{GFSA}} = \mathrm{GFSA}(M_{i-1}(F))$. In summary, Equation (11) will be used to replace the original expression $M_i(F)$=$conv_{1\times1}(M_{i-1}(F)) + F$ in Figure 12a to form the final Figure 12b.

3.6. Post-Processing Technique (PPT)

Existing approach. The raw HTC offers NMS [27] and Soft-NMS [28] to remove duplicate detections, but the two both did not consider the prior knowledge of ships, that is, in most cases, only those ships with similar aspect ratios just dock together side by side, as shown in Figure 14. Not considering this prior knowledge will cause that the boxes which should be retained are removed when NMS is used; the boxes which should be deleted are retained when Soft-NMS is used. We think that when the ship aspect ratios are similar, one should better use Soft-NMS to avoid missed detections; however, when the ship aspect ratios have a huge difference, one should better use NMS to delete redundant boxes.

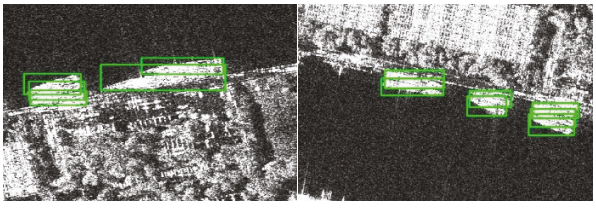

Figure 14. Densely moored ships. There are some hull overlaps between ships. In most cases, only ships with similar aspect ratios dock together. Green boxes denote the ground truths.

Proposed approach. Thus, we propose a post-process technique (PPT) guided by the prior of ship aspect ratios to adaptively select NMS and Soft-NMS. Algorithm 1 shows the implementation of PPT. We set a similarity threshold of ship aspect ratios ϵ_r to judge two cases, i.e., (i) a huge aspect ratio difference $|r_i - r_m| > \epsilon_r$ where r_m denotes the aspect ratio with the highest score s_m and r_i denotes the remaining boxes needed to traverse; (ii) a small aspect ratio difference $|r_i - r_m| \leq \epsilon_r$. Here, ϵ_r is set to 0.20 empirically, (see Section 6.5). For the former, NMS is executed to remove boxes safely (i.e., $\mathcal{B} \leftarrow \mathcal{B} - b_i$, $\mathcal{S} \leftarrow \mathcal{S} - s_i$). For the latter, Soft-NMS is executed to retain boxes (i.e., $\mathcal{B} \leftarrow \mathcal{B}$, $\mathcal{S} \leftarrow \mathcal{S}$) but the current box is given with a penalty score $s_i \leftarrow s_i \exp\left(\frac{IOU(\mathcal{M},b_i)^2}{\sigma}\right)$ for the densely moored ship detections in Figure 14.

Algorithm 1: PPT guided by the prior of ship aspect ratios.

Input: $\mathcal{B} = \{b_1, b_2, \cdots, b_N\}$, $\mathcal{R} = \{r_1, r_2, \cdots, r_N\}$, $\mathcal{S} = \{s_1, s_2, \cdots, s_N\}$, N_t, ϵ_r
$\mathcal{B}$ denotes the list of initial detection boxes. $\mathcal{R}$ denotes the list of initial detection aspect ratios. $\mathcal{S}$ denotes the list of initial detection scores. N_t denotes the IOU threshold. ϵ_r denotes the similarity threshold of aspect ratios.

Begin
$\mathcal{D} \leftarrow \{\}$
while $\mathcal{B} \neq \varnothing$ **do**
  $m \leftarrow \text{argmax}\, \mathcal{S}$
  $\mathcal{M} \leftarrow b_m$
  $\mathcal{P} \leftarrow r_m$
  $\mathcal{D} \leftarrow \mathcal{D} \cup \mathcal{M}$; $\mathcal{B} \leftarrow \mathcal{B} - \mathcal{M}$; $\mathcal{R} \leftarrow \mathcal{R} - \mathcal{P}$
  for (b_i, r_i) in ***zip*** $(\mathcal{B}, \mathcal{R})$ **do**
    if $IOU(\mathcal{M}, b_i) \geq N_t$ **then**
      Case 1: $|r_i - r_m| > \epsilon_r$
        $\mathcal{B} \leftarrow \mathcal{B} - b_i$; $\mathcal{R} \leftarrow \mathcal{R} - r_i$; $\mathcal{S} \leftarrow \mathcal{S} - s_i$ # NMS
      Case 2: $|r_i - r_m| \leq \epsilon_r$
        $\mathcal{B} \leftarrow \mathcal{B}$; $\mathcal{R} \leftarrow \mathcal{R}$; $\mathcal{S} \leftarrow \mathcal{S}$
        $s_i \leftarrow s_i e^{\frac{IOU(\mathcal{M}, b_i)^2}{\sigma}}, \forall b_i \notin \mathcal{D}$ # Soft-NMS
  Existing approach: consider one of Case 1 and Case 2. Proposed approach: consider both Case 1 and Case 2.
  end
  end
return $\mathcal{D}$, $\mathcal{S}$
end

Output: $\mathcal{D}$, $\mathcal{S}$

3.7. Hard Sample Mining Training Strategy (HSMTS)

Existing approach. The raw HTC did not offer useful training strategies to boost learning benefits as shown in Figure 15a, so we propose a hard sample mining training strategy (HSMTS) to supplement this blank for better accuracy. HSMTS is inspired by the extreme imbalance between positive and negative samples in SAR images, i.e., ships exhibit a sparse distribution in the whole SAR image, but backgrounds occupy more pixels. This causes the number of negative samples being much larger than the number of positive samples, so one should select more typical ones among a large number of negative samples to train the network so as to ensure the background discrimination ability of models. Otherwise, the network will fall into the over fitting of a large number of simple negative samples with low values. More typical negative samples should be those which are difficult to distinguish (close to positive). Only by emphasizing learning on them can the network improve its discrimination ability; repeated and mechanical learning on simple samples is worthless.

Proposed approach. HSMTS is in fact motivated by [66], but we add the extra supervision of the mask prediction loss. Figure 15b shows its implementation. From Figure 15b, we monitor the terminal training loss of EMIN where $Loss = Loss_{CLS} + Loss_{REG} + Loss_{MASK}$. Here, $Loss_{CLS}$ denotes the box classification loss. $Loss_{REG}$ denotes the box regression loss. $Loss_{MASK}$ denotes the mask prediction loss. The total training loss is first ranked. In training, the K negative samples with top K losses are collected to a hard negative sample pool. When the number of samples in the pool reaches a batch size, these hard negative samples are mapped into the feature maps of the backbone network via CROIE to extract feature subsets again for the next box and mask prediction. The above process repeated until the end of the training does not destroy the end-to-end training. The total number of the required samples is 512. The positive negative ratio is 1:3, in line with the raw report, so the number of positive samples is 128; as a result, K is equal to 384.

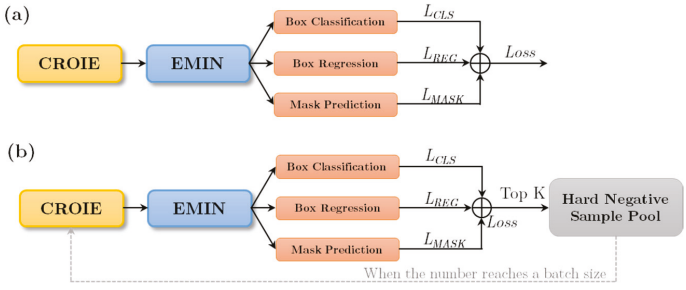

Figure 15. Different training strategies. (**a**) Existing approach: There are no hard negative sample mining mechanism of HTC. (**b**) Proposed approach: Hard sample mining training strategy (HSMTS) of HTC+.

4. Experiments

4.1. Dataset

SSDD [13] offers 1160 image samples with 512 × 512 size from RadarSat-2, TerraSAR-X and Sentinel-1. The training-test ratio is 4:1 [13]. There are 2551 ships in SSDD. The smallest ship is 28 pixel^2 and the largest one is 62,878 pixel^2 (pixel^2 denotes the product of width pixel and height one). SAR ships in SSDD are provided with various resolutions from 1m to 10m, and HH, HV, VV, and VH polarizations. In SSDD, images with suffix 1 and 9 (232 samples) are selected as the test set, and the others as the training set (928 samples).

HRSID [15] offers 5604 image samples with 800 × 800 average size from TerraSAR-X and Sentinel-1. The training set has 3643 samples and the rest serves as the test set, same as [15]. There are 16,965 ships in HRSID. SAR ships in HRSID are provided with resolutions from 0.1 m to 3 m, and HH, HV, and VV polarizations. The smallest one is 3 pixel^2, and the largest one is 522,400 pixel^2. HRSID is divided into a training and test set by the ratio of 13:7, same as [15].

4.2. Training Details

The backbone sub-network MRFEN of HTC+ and other backbone networks for performance comparison are pretrained on ImageNet [67]. Following Faster R-CNN [31], we first train the backbone network, the EFPN sub-network, and the region generation sub-network SGAAL jointly. Then, we fix them to train the CROIE sub-network and the EMIN sub-network. Moreover, the same as for HTC, we end-to-end to train and test HTC+. We train all networks (HTC+ and the other 9 models) by 12 epochs on the SAR ship datasets using SGD [68]. The learning rate is set to 0.008 that will be reduced 10 times at 8- and 11-epoch. The batch size is set to 4. Other training details are consistent with HTC. Experiments were run on a personal computer with RTX 3090 GPU, i9-9900 CPU, and 32G memory based on mmdet [69] and Pytorch. In the test, the trained weights are loaded to evaluate performance.

4.3. Evaluation Criteria

Similar to COCO [53], AP is the mean of different IOU thresholds with 0.50:0.05:0.95. AP_{50} is the accuracy with a 0.50 IOU threshold. AP_{75} is that with a 0.75 IOU threshold. AP_S is that of small ships (<32^2 pixels). AP_M is that of medium ships (>32^2 pixels and <96^2 pixels). AP_L is that of large ships (>96^2 pixels). In this paper, AP serves as the core index for accuracy comparison.

5. Results

To reveal the state-of-the-art performance of our HTC+, nine competitive models are reproduced for comparison of accuracy. The comparative experiments are conducted on SSDD and HRSID datasets.

5.1. Quantitative Results

Tables 2 and 3 show the quantitative comparison results on SSDD and HRSID. HTC is the experimental baseline reproduced basically in line with the raw report. Its box and mask AP are comparable to reports [17,18].

From Tables 2 and 3, the following conclusions can be drawn:

1. Compared with HTC, HTC+ offers 6.7% box AP and 5.0% mask AP increments on SSDD; they are 4.9% and 3.9% on HRSID. Seven novelties enable such excellent accuracy. Accuracy increments of different novelties are different, but the resulting accuracy always presents an upward trend, showing the effectiveness of each novelty. AP_L has some fluctuations because the proportion of large ships in datasets is relatively small as in Figure 3a. Sensitivity analysis of different novelties on the total performance will be introduced in Section 6. Certainly, the speed indeed becomes lower and lower as expected. The trade-off between accuracy and speed is an eternal topic which will be further considered in the future.
2. Compared with the second-class model, HTC+ offers 6.7% box AP and 4.7% mask AP increments on SSDD; they are 4.8% and 3.7% on HRSID. This shows the state-of-the-art performance of HTC+. The increment of the box AP is lower than that of the mask AP, which is in line with common sense, because the pixel-level mask segmentation is more challenging.
3. Compared with the other methods, HTC+ offers the modest operation speed (i.e., 3.36 FPS on SSDD and 2.18 FPS on HRSID) due to its heavier network. This disadvantage needs to be resolved in the future. Moreover, although YOLACT [36] indeed offers the optimal speed, its accuracy is too poor to meet applications.

Table 2. Quantitative results on SSDD. The suboptimal method is marked by underline "—". FPS: frames per second.

MRFEN	EFPN	SGAALN	CROIE	EMIN	PPT	HEMTS	Box (%)						Mask (%)						FPS
							AP	AP_{50}	AP_{75}	AP_S	AP_M	AP_L	AP	AP_{50}	AP_{75}	AP_S	AP_M	AP_L	
–	–	–	–	–	–	–	65.6	93.6	76.3	65.2	68.4	27.5	59.3	91.7	73.1	58.7	61.6	34.8	11.60
√							67.0	90.9	81.3	67.8	65.8	34.6	61.6	90.9	78.8	61.5	61.8	37.6	8.26
√	√						67.9	93.5	81.5	68.0	68.1	43.4	62.0	92.7	77.1	62.0	62.3	50.2	7.25
√	√	√					68.3	94.3	81.5	68.4	68.1	43.3	62.4	93.5	77.1	62.4	62.3	50.2	6.27
√	√	√	√				69.0	95.4	82.8	69.4	68.7	34.6	62.8	93.6	79.6	62.9	62.5	37.6	3.93
√	√	√	√	√			69.8	96.3	83.8	69.6	71.4	34.2	63.2	93.5	80.0	63.3	63.6	32.6	3.63
√	√	√	√	√	√		71.6	96.8	86.8	71.5	72.7	42.3	63.7	94.5	80.9	63.6	64.4	51.2	3.36
√	√	√	√	√	√	√	72.3	96.8	87.2	72.0	74.0	51.0	64.3	94.7	82.3	64.1	64.9	65.0	3.36
							+6.7	+3.2	+10.9	+6.8	+5.6	+23.5	+5.0	+3.0	+9.2	+5.4	+3.3	+30.2	

Method	Backbone	Box (%)						Mask (%)						FPS
		AP	AP_{50}	AP_{75}	AP_S	AP_M	AP_L	AP	AP_{50}	AP_{75}	AP_S	AP_M	AP_L	
Mask R-CNN [30]	ResNet-101	62.0	91.5	75.4	62.0	64.4	19.7	57.8	88.5	72.1	57.2	60.8	27.4	11.05
Mask Scoring R-CNN [32]	ResNet-101	62.4	91.0	75.1	61.9	66.0	15.7	58.6	89.4	73.2	58.0	61.4	22.6	12.88
Cascade Mask R-CNN [33]	ResNet-101	63.0	89.6	75.2	62.4	66.0	12.0	56.6	87.5	70.5	56.3	58.8	22.6	10.55
PANet [34]	ResNet-101	63.3	93.4	75.4	63.4	65.5	40.8	59.6	91.1	74.0	59.3	61.0	52.1	13.65
YOLACT [36]	ResNet-101	54.0	90.6	61.2	56.9	48.2	12.6	48.4	88.0	52.1	47.3	53.5	40.2	15.47
GRoIE [35]	ResNet-101	61.2	91.5	71.6	62.2	59.8	8.7	58.3	89.8	72.7	58.6	58.7	21.8	9.67
HQ-ISNet [16]	HRNetV2-W18	64.9	91.0	76.3	64.7	66.6	26.0	58.6	89.3	73.6	58.2	60.4	37.2	8.59
HQ-ISNet [16]	HRNetV2-W32	65.5	90.7	77.3	65.6	66.9	23.2	59.3	90.4	75.5	58.9	61.1	37.3	8.00
HQ-ISNet [16]	HRNetV2-W40	63.6	87.8	75.3	62.6	67.8	27.9	57.6	86.0	72.6	56.7	61.3	50.2	7.73
SA R-CNN [17]	ResNet-50-GCB	63.2	92.1	75.2	63.8	64.0	7.0	59.4	90.4	73.3	59.6	60.3	20.2	13.65
FL-CSE-ROIE [21]	ResNet-101	68.0	95.9	81.1	67.6	70.1	56.2	62.6	93.7	78.3	63.3	61.2	75.0	8.92
GCBANet [22]	ResNet-101	68.4	95.4	82.2	68.9	68.0	45.6	63.1	93.5	78.8	63.2	63.0	55.1	6.11
HTC [24]	ResNet-101	65.6	93.6	76.3	65.2	68.4	27.5	59.3	91.7	73.1	58.7	61.6	34.8	11.60
HTC+ (Ours)	MRFEN	72.3	96.8	87.2	72.0	74.0	51.0	64.3	94.7	82.3	64.1	64.9	65.0	3.36
		+6.7	+3.2	+9.9	+6.4	+7.4	+10.2	+4.7	+3.0	+6.8	+4.5	+3.3	+12.9	

Table 3. Quantitative results on HRSID. FPS: frames per second.

MRFEN	EFPN	SGAALN	CROIE	EMIN	PPT	HEMTS	Box (%)						Mask (%)						FPS
							AP	AP_{50}	AP_{75}	AP_S	AP_M	AP_L	AP	AP_{50}	AP_{75}	AP_S	AP_M	AP_L	
–	–	–	–	–	–	–	66.6	86.0	77.1	67.6	69.0	28.1	55.2	84.9	66.5	54.7	63.8	19.2	7.42
√							67.3	85.8	77.8	68.2	68.6	21.7	55.6	84.7	67.8	55.3	63.5	22.7	5.30
√	√						68.1	87.9	78.4	69.0	69.5	24.8	56.3	86.1	68.4	55.8	64.0	24.2	4.75
√	√	√					68.5	88.2	78.5	69.4	69.5	29.0	56.7	86.3	68.7	56.3	63.8	25.7	4.01
√	√	√	√				68.7	88.3	78.7	69.6	70.0	31.3	56.9	86.4	68.7	56.4	64.6	27.5	2.55
√	√	√	√	√			69.2	88.9	79.3	70.1	70.6	31.7	57.2	87.1	69.3	56.8	64.9	27.7	2.30
√	√	√	√	√	√		70.5	91.3	81.3	71.5	70.6	36.7	58.1	89.2	69.4	57.8	64.6	26.5	2.18
√	√	√	√	√	√	√	71.5	92.3	82.5	72.6	71.4	38.2	59.1	90.3	71.0	58.7	65.7	26.8	2.18
							+4.9	+6.3	+5.4	+5.0	+2.4	+10.1	+3.9	+5.4	+4.5	+4.0	+1.9	+7.6	

Method	Backbone	Box (%)						Mask (%)						FPS
		AP	AP_{50}	AP_{75}	AP_S	AP_M	AP_L	AP	AP_{50}	AP_{75}	AP_S	AP_M	AP_L	
Mask R-CNN [30]	ResNet-101	65.1	87.7	75.5	66.1	68.4	14.1	54.8	85.7	65.2	54.3	62.5	13.3	7.07
Mask Scoring R-CNN [32]	ResNet-101	65.2	87.6	75.4	66.5	67.4	13.4	54.9	85.1	65.9	54.5	61.5	12.9	8.24
Cascade Mask R-CNN [33]	ResNet-101	65.1	85.4	74.4	66.0	69.0	17.1	52.8	83.4	62.9	52.2	62.2	17.0	6.75
PANet [34]	ResNet-101	65.4	88.0	75.7	66.5	68.2	22.1	55.1	86.0	66.2	54.7	62.8	17.8	8.74
YOLACT [36]	ResNet-101	47.9	74.4	53.3	51.7	34.9	3.3	39.6	71.1	41.9	39.5	46.1	7.3	10.02
GRoIE [35]	ResNet-101	65.4	87.8	75.5	66.5	67.2	21.8	55.4	85.8	66.9	54.9	63.5	19.7	6.19
HQ-ISNet [16]	HRNetV2-W18	66.0	86.1	75.6	67.1	66.3	8.9	53.4	84.2	64.3	53.2	59.7	10.7	5.50
HQ-ISNet [16]	HRNetV2-W32	66.7	86.9	76.3	67.8	68.3	16.8	54.6	85.0	65.8	54.2	61.7	13.4	5.12
HQ-ISNet [16]	HRNetV2-W40	66.7	86.2	76.3	67.9	68.6	11.7	54.2	84.3	64.9	53.9	61.9	12.8	4.95
SA R-CNN [17]	ResNet-50-GCB	65.2	88.3	75.2	66.4	65.4	10.2	55.2	86.2	66.7	54.9	60.9	12.3	8.74
FL-CSE-ROIE [21]	ResNet-101	69.0	90.2	79.5	69.9	71.1	32.3	57.9	88.6	69.5	57.3	65.7	26.1	5.24
GCBANet [22]	ResNet-101	69.4	89.8	79.2	70.4	71.3	32.2	57.3	88.6	68.9	57.0	64.3	25.9	4.06
HTC [24]	ResNet-101	66.6	86.0	77.1	67.6	69.0	28.1	55.2	84.9	66.5	54.7	63.8	19.2	7.42
HTC+ (Ours)	MRFEN	71.5	92.3	82.5	72.6	71.4	38.2	59.1	90.3	71.0	58.7	65.7	26.8	2.18
		+4.8	+4.3	+5.4	+4.7	+2.4	+10.1	+3.7	+4.1	+4.1	+3.8	+1.9	+7.6	

Table 4 shows the computational complexity calculations of different methods. Here, we adopt the floating point of operations (FLOPs) to measure calculations whose unit is the giga multiply add calculations (GMACs) [70]. From Table 4, the calculation amount of GCBANet is more than other models, so the future model computational complexity optimization is needed.

Table 4. Computational complexity calculations of different methods. Here, we adopt the floating point of operations (FLOPs) to measure calculations whose unit is the giga multiply add calculations (GMACs) [70].

Method	Backbone	FLOPs (GMACs)
Mask R-CNN [30]	ResNet-101	121.32
Mask Scoring R-CNN [32]	ResNet-101	121.32
Cascade Mask R-CNN [33]	ResNet-101	226.31
PANet [34]	ResNet-101	127.66
YOLACT [36]	ResNet-101	67.14
GRoIE [35]	ResNet-101	581.28
HQ-ISNet [16]	HRNetV2-W18	201.84
HQ-ISNet [16]	HRNetV2-W32	226.90
HQ-ISNet [16]	HRNetV2-W40	247.49
SA R-CNN [17]	ResNet-50-GCB	101.87
GCBANet [22]	ResNet-101	947.96
HTC [24]	ResNet-101	228.90
HTC+ (Ours)	ResNet-101	1289.45

5.2. Qualitative Results

Figures 16 and 17 show the qualitative results on SSDD and HRSID. Due to limited pages, we only show the comparison results with HTC. From Figures 16 and 17, HTC+ can detect more real ships than HTC (e.g., the #5 sample in Figure 16). It can suppress false alarms (e.g., the #2 sample in Figure 16). It also offers better positioning performance (e.g., the #1 sample in Figure 16) and higher confidence scores (e.g., the #6 sample in Figure 16). These reveal the state-of-the-art performance of HTC+.

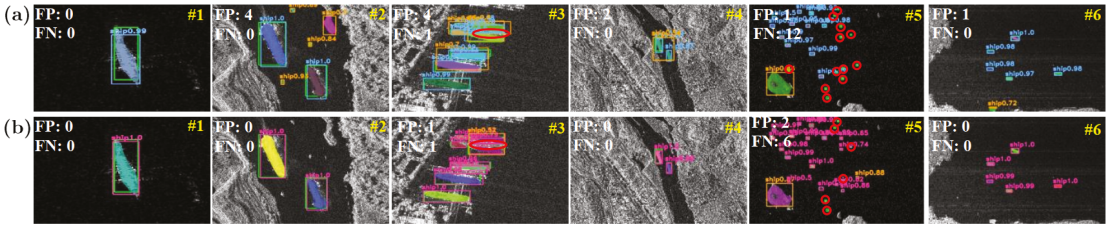

Figure 16. Qualitative results on SSDD. (**a**) The vanilla HTC. (**b**) Our HTC+. Green boxes denote the ground truths. Orange boxes denote the false alarms (i.e., false positives, FP). Red circles denote the missed detections (i.e., false negatives, FN).

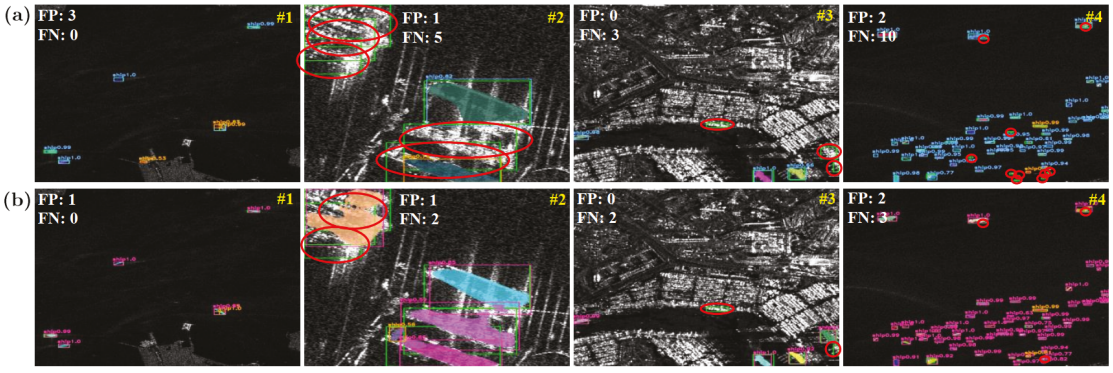

Figure 17. Qualitative results on HRSID. (**a**) The vanilla HTC. (**b**) Our HTC+. Green boxes denote the ground truths. Orange boxes denote the false alarms (i.e., false positives, FP). Red circles denote the missed detections (i.e., false negatives, FN).

6. Ablation Study

In this section, we will conduct ablation studies for sensitivity analysis of each technique. All the following experiments are conducted on SSDD. These ablation studies can also confirm the effectiveness of each technique. For rigorous comparison, we install and remove the particular technique while freezing the other six.

6.1. Ablation Study on MRFEN

6.1.1. Effectiveness of MRFEN

Table 5 shows the quantitative results with and without MRFEN. MRFEN offers a better accuracy than the common plain structure, because it expands the range of network spatial search to achieve multi-resolution analysis, enabling better multi-scale ship feature representation.

Table 5. Quantitative results on with and without MRFEN.

MRFEN	Box AP (%)	Mask AP (%)	FPS
× [1]	70.9	63.7	6.52
√ [2]	72.3	64.3	3.36

[1] ResNet-101 in Figure 2a. [2] Our MRFEN in Figure 2b.

6.1.2. Component Analysis in MRFEN

Table 6 shows the results of component analysis in MRFEN. All components are conducive to improving accuracy, showing their effectiveness. Three components enhance the multi-scale feature description of the network, enabling better performance. MRFE reduces the speed greatly because it makes the network heavier. Although MRFE offers an only 0.2% box AP gain, its mask AP gain is more significant than others, so it is still effective. One can also find that after the feature fusion is established, the box AP is further improved by 0.4%. Therefore, it is essential to exchange information in multi-resolution parallel branches. Moreover, CBAM can improve accuracy further because it can focus on more important features.

Table 6. Quantitative results of component analysis in MRFEN.

MRFE [1]	FF in MSAFF [2]	CBAM in MSAFF [3]	ASPP [4]	Box AP (%)	Mask AP (%)	FPS
–	–		–	70.9	63.7	6.52
√				71.1	64.0	3.84
√	√			71.5	64.1	3.72
√	√	√		71.7	64.2	3.53
√	√	√	√	72.3	64.3	3.36

[1] MRFE denotes the multi-resolution feature extraction. Feature fusion and CBAM are deleted. [2] FF denotes the feature fusion in the multi-scale attention-based feature fusion (MSAFF). [3] CBAM denotes the convolutional block attention module in the MSAFF. [4] ASPP denotes the atrous spatial pyramid pooling.

6.1.3. Compared with Other Backbones

We compare performance of other backbones in Table 7. MRFEN offers the optimum accuracy. HRNetV2-W40 [16] offers a comparable 72.2% box AP, but its mask AP is lower than MRFEN (63.5% < 64.3%). Furthermore, in our MRFEN, MRFE+MSAFF can be regarded as an improved version of HRNet [41], because CBAM is added during feature fusion. We also study the advantage of HRNet compared with other backbones under the condition that ASPP is used. The results are shown in Table 8. From Table 8, HRNet achieves the best box AP and mask AP, thus the multi-resolution parallel structure is better than the plain structure.

Table 7. Quantitative results of different backbones. ASPP is not used in other backbones.

Backbone	Box AP (%)	Mask AP (%)	FPS
ResNet-101 [39]	70.9	63.7	6.52
ResNeXt-101-32x4d [40]	71.0	63.5	5.15
ResNeXt-101-32x8d [40]	71.3	63.8	4.93
ResNeXt-101-64x4d [40]	71.2	64.1	3.85
HRNetV2-W18 [16]	71.0	63.2	3.85
HRNetV2-W32 [16]	70.6	64.0	3.76
HRNetV2-W40 [16]	72.2	63.5	3.40
Res2Net-101 [38]	71.9	64.0	4.62
MRFEN (Ours)	72.3	64.3	3.36

Table 8. Quantitative results on with and without MRFEN. ASPP is used in other backbones.

	Backbone [1]	Box AP (%)	Mask AP (%)	FPS
MRFEN	ResNet-101 [39]	71.1	63.7	6.50
	ResNeXt-101-32x4d [40]	71.3	63.6	5.10
	ResNeXt-101-32x8d [40]	71.6	64.0	4.86
	ResNeXt-101-64x4d [40]	71.9	64.1	3.81
	Res2Net-101 [38]	72.0	64.1	4.58
	HRNet (Ours) [2]	72.3	64.3	3.36

[1] The backbone (MRFE+MSAFF) inside MRFEN is replaced. [2] In MRFEN, MRFE+MSAFF can be regarded as an improved version of HRNet because CBAM is added during feature fusion.

6.2. Ablation Study on EFPN

6.2.1. Effectiveness of EFPN

Table 9 shows the results with or without EFPN. EFPN offers a ~3% box AP gain; a ~2% mask AP gain. The speed is sacrificed, but it offers better multi-scale performance, considering large and small ships simultaneously.

Table 9. Quantitative results on with and without EFPN.

EFPN	Box AP (%)	Mask AP (%)	FPS
× [1]	69.4	62.2	6.89
√ [2]	72.3	64.3	3.36

[1] FPN in Figure 5a. [2] Our EFPN in Figure 5b.

6.2.2. Component Analysis in EFPN

Table 10 shows the results of component analysis in EFPN. Each component is conducive to improving accuracy more or less, showing their effectiveness. CARAFE reduces the speed more obviously, because it adds FPN levels with increased calculation costs.

Table 10. Quantitative Results of Component Analysis in EFPN.

CARAFE [1]	FB [2]	FR [3]	FE [4]	Box AP (%)	Mask AP (%)	FPS
–	–	–	–	69.4	62.2	6.89
√				70.1	63.4	3.96
√	√			70.7	64.0	3.53
√	√	√		71.5	64.2	3.40
√	√	√	√	72.3	64.3	3.36

[1] CARAFE denotes the content-aware reassembly of features. [2] FB denotes the feature balance. [3] FR denotes the feature refinement. [4] FE denotes the feature enhancement.

6.2.3. Compared with Other FPNs

We compare performance of other FPNs in Table 11. MFPN offers the best accuracy except for the mask AP of Quad-FPN [58]. Still, MFPN is better than Quad-FPN, because its box AP is higher (72.3% > 71.8%).

Table 11. Quantitative results of different FPNs.

Type	Box AP (%)	Mask AP (%)	FPS
FPN [51]	69.4	62.2	6.89
B-FPN [59]	69.8	62.9	5.45
CARAFE-FPN [55]	71.3	63.5	5.62
Quad-FPN [58]	71.8	64.3	3.48
MFPN (Ours)	72.3	64.3	3.36

6.3. Ablation Study on SGAALN

6.3.1. Effectiveness of SGAALN

Table 12 shows the results with and without SGAALN. SGAALN boosts the box AP and the mask AP by ~1%. It can generate more optimized location- and shape-adaptive anchors to better match SAR ships. This can ease background interferences for better performance.

Table 12. Quantitative results on with and without SGAALN.

SGAALN	Box AP (%)	Mask AP (%)	FPS
× [1]	71.2	63.5	3.63
√ [2]	72.3	64.3	3.36

[1] Fixed anchors and aspect ratios used in the vanilla HTC. [2] Our SGAALN in Figure 8.

6.3.2. Component Analysis in SGAALN

Table 13 shows the results of component analysis in SGAALN. ALP boosts accuracy in any case, but ASP must be equipped with FA to give full play to its advantages, because FA aligns the raw feature maps to width-height of anchors to eliminate feature differences.

Table 13. Quantitative results of component analysis in SGAALN.

ALP [1]	ASP [2]	FA [3]	Box AP (%)	Mask AP (%)	FPS
–	–	–	71.2	63.5	3.63
√			72.0	64.0	3.58
√	√		71.9	64.0	3.54
√	√	√	72.3	64.3	3.36

[1] ALP denotes the anchor location prediction. [2] ASP denotes the anchor shape prediction. [3] FA denotes the feature adaption.

6.3.3. Different Probability Thresholds

We adjust probability thresholds to determine their optimal value in Table 14. One finds that when $\epsilon_t = 0.10$, the accuracy reaches the peak, so it is selected, as also suggested by [29], because it can remove many false positives meanwhile maintaining an unaffected recall rate.

Table 14. Quantitative results of component analysis in SGAALN.

ϵ_t	Box AP (%)	Mask AP (%)	FPS
0.00	71.5	63.9	3.35
0.05	71.8	64.0	3.36
0.10	72.3	64.3	3.36
0.15	72.0	64.1	3.34
0.20	70.8	63.7	3.26

6.4. Ablation Study on CROIE

6.4.1. Effectiveness of CROIE

Table 15 shows the results with/without CROIE. CROIE improves the accuracy by ~0.5%, because it offers more context information to the network, conducive to enhancing the background discrimination ability.

Table 15. Quantitative results on with and without CROIE.

CROIE	Box AP (%)	Mask AP (%)	FPS
× [1]	71.2	63.5	3.63
√ [2]	72.3	64.3	3.36

[1] ROI is used as shown in Figure 9a. [2] ROI, ROI-C1 and ROI-C2 are used as shown in Figure 9b.

6.4.2. Different Range Contexts

We survey the influences of different range contexts on performance as shown in Table 16. We observe that moderate contexts are beneficial, but excessive ones will lead to negative effects. When using CROIE, a special parameter adjustment is required to be in line with actual applications. For the best accuracy, we set the two amplification factors c_1 and c_2 to 1.5 and 2.0 respectively.

Table 16. Quantitative results of different range contexts.

c_1	c_2	Box AP (%)	Mask AP (%)	FPS
1.5	2.0	72.3	64.3	3.36
1.5	2.5	72.0	64.1	3.20
2.0	2.5	71.5	63.7	3.19
2.5	3.0	70.7	62.5	2.96

6.5. Ablation Study on EMIN

6.5.1. Effectiveness of EMIN

Table 17 shows the results with and without EMIN. EMIN offers better accuracy than the raw MIN. It transmits more important mask features to the next stage. It further balances the contributions between the backbone network's features and the previous stage's features. Consequently, the efficiency of information flow is improved, bringing better learning benefits.

Table 17. Quantitative results with and without EMIN.

EMIN	Box AP (%)	Mask AP (%)	FPS
× [1]	71.7	63.9	3.87
√ [2]	72.3	64.3	3.36

[1] The raw MIN in Figure 12a. [2] Our EMIN in Figure 12b.

6.5.2. Component Analysis in EMIN

Table 18 shows the results of component analysis in EMIN. Each component offers an observable accuracy gain, showing their effectiveness. They do not impose great impacts on speed, so they are cost-effective.

Table 18. Quantitative results of component analysis in EMIN.

GFSA [1]	AMFF [2]	Box AP (%)	Mask AP (%)	FPS
–	–	71.7	63.9	3.87
√		72.1	64.1	3.58
√	√	72.3	64.3	3.36

[1] GFSA denotes the global feature self-attention. [2] AMFF denotes the adaptive mask feature fusion.

6.6. Ablation Study on PPT

6.6.1. Effectiveness of PPT

Table 19 shows the results with or without PPT. PPT has a slightly better accuracy than NMS and Soft-NMS with little sacrifice of speed. It considers the ship aspect ratio prior to determine whether to suppress boxes, with the advantages of NMS and Soft-NMS, enabling better performance.

Table 19. Quantitative results on with and without PPT.

PPT	NMS	Soft-NMS	Box AP (%)	Mask AP (%)	FPS
	√		71.5	63.7	3.40
		√	72.0	64.1	3.38
√	√	√	72.3	64.3	3.36

6.6.2. Different Similarity Thresholds of Aspect Ratios

We survey the influences of different similarity thresholds of aspect ratios on the performance as in Table 20. Due to SAR imaging error and annotation deviation, it is impossible to be sure that ships moored in parallel have absolutely-equal aspect ratios. Therefore, setting this threshold reasonably is needed. In our work, we set ϵ_r to 0.20 because it offers the best accuracy.

Table 20. Quantitative results of different similarity thresholds of aspect ratios.

ϵ_r	Box AP (%)	Mask AP (%)	FPS
0.10	71.8	63.9	3.34
0.15	72.1	63.9	3.36
0.20	72.3	64.3	3.36
0.25	72.2	64.1	3.36
0.30	72.0	64.0	3.35

6.7. Ablation Study on HSMTS

6.7.1. Effectiveness of HSMTS

Table 21 shows the results with and without HEMTS. HEMTS further improves the accuracy; the network boosts learning benefits by focusing on difficult samples to boost foreground-background recognition ability. HEMTS is only used in training, so the speed is not affected.

Table 21. Quantitative results on with and without HSMTS.

HSMTS	Mask Loss	Box AP (%)	Mask AP (%)	FPS
× [1]		71.6	63.7	3.36
√ [2]		72.0	63.9	3.36
√ [3]	√ [3]	72.3	64.3	3.36

[1] The raw random sampling. [2] OMEM. Here, the mask prediction loss is not monitored. [3] Our HSMTS in Figure 15. Here, the mask prediction loss is monitored.

6.7.2. Compared with OHEM

In Table 21, HEMTS (the second row) performs better than OHEM (the third row) because HEMTS adds the extra supervision of the mask prediction loss. This is conducive to mining more representative difficult negative samples.

7. Discussions

7.1. Multi-Scale Training and Test

We also discuss the multi-scale training and test on SSDD in Table 22. The single-scale input is [512 × 512]; the multi-scale input is [416 × 416, 512 × 512, 608 × 608] inspired by YOLOv3 [25]. Multi-scale training and test can further improve the accuracy but the speed becomes lower for all models. Our single-scale HTC+ surpasses all other multi-scale models. This advantage comes from the multi-resolution feature extraction. Our multi-scale HTC+ enables the better performance from 72.3% to 72.9% box AP and from 64.3% to 65.1% mask AP. It is always far superior to all other competition models, which shows its better performance.

7.2. Extension to Mask R-CNN

To confirm the universal effectiveness of the proposed techniques on other instance segmentation models, we extend them to the mainstream Mask R-CNN [30]. Here, EMIN is not applicable, because Mask R-CNN does not have mask information interaction branches, whose mask head is not cascaded. The results are shown in Table 23. From Table 23, six novelties all offer continuous accuracy growth, from the initial 62.0% to the final 70.8% box AP, i.e., a huge 8.8% incremental improvement, and from the initial 57.8% to the final 62.5% mask AP, i.e., a huge 4.7% incremental improvement. The above reveals the universal validity of our proposed techniques.

Table 22. Quantitative results of multi-scale training and test on SSDD. The suboptimal method is marked by underline "—".

Method	Backbone	Box AP (%)	Mask AP (%)	FPS
Mask R-CNN-Multi	ResNet-101	64.1	60.6	7.48
Mask Scoring R-CNN-Multi	ResNet-101	65.8	60.4	7.25
Cascade Mask R-CNN-Multi	ResNet-101	65.4	60.0	5.80
HTC-Multi	ResNet-101	66.8	60.7	5.52
PANet-Multi	ResNet-101	65.4	60.4	7.48
YOLACT-Multi	ResNet-101	55.2	51.4	10.78
GRoIE-Multi	ResNet-101	63.5	60.4	4.64
HQ-ISNet-Multi	HRNetV2-W18	65.6	59.4	4.07
HQ-ISNet-Multi	HRNetV2-W32	66.0	59.5	3.87
HQ-ISNet-Multi	HRNetV2-W40	63.8	59.5	3.57
SA R-CNN-Multi	ResNet-50-GCB	64.1	60.3	8.00
HTC+-Single [1]	MRFEN	72.3	64.3	3.36
HTC+-Multi [2]	MRFEN	72.9	65.1	2.02

[1] Single denotes the input size [512 × 512]. [2] Multi denotes the input size [416 × 416, 512 × 512, 608 × 608] inspired by YOLOv3 [25].

Table 23. Quantitative results of extension to Mask R-CNN on SSDD.

	MRFEN	EFPN	SGAALN	CROIE	PPT	HSMTS	Box AP (%)	Mask AP (%)	FPS
Mask R-CNN [30] *	–	–	–	–	–	–	62.0	57.8	11.05
	√						63.6	59.0	9.34
	√	√					65.2	60.6	8.02
	√	√	√				65.9	61.0	7.85
	√	√	√	√			68.5	61.2	3.96
	√	√	√	√	√		69.6	62.0	3.55
	√	√	√	√	√	√	70.8	62.5	3.55

* Mask R-CNN does not have mask information interaction branches, because its mask head is not cascaded. Thus, EMIN is not applicable to Mask R-CNN.

7.3. Extension to Faster R-CNN

We also extend the proposed techniques (except EMIN only used in segmentation models) to the pure detection model. We take the mainstream two-stage model Faster R-CNN [31] as an example. The results are shown in Table 24. From Table 24, six novelties all offer continuous accuracy growth, from the initial 62.1% to the final 69.1% box AP, i.e., a huge 7% incremental improvement, which shows their universal validity. Certainly, these benefits are achieved at a certain sacrifice of speed, which will be considered in the future.

Table 24. Quantitative results of extension to Faster R-CNN on SSDD.

	MRFEN	EFPN	SGAALN	CROIE	PPT	HSMTS	Box AP (%)	FPS
Faster R-CNN [31] *	–	–	–	–	–	–	62.1	13.65
	√						64.5	10.56
	√	√					66.8	8.74
	√	√	√				67.2	8.38
	√	√	√	√			68.0	7.69
	√	√	√	√	√		68.5	6.72
	√	√	√	√	√	√	69.1	6.72

* EMIN is only used in segmentation models, but Faster R-CNN is a detection model. Therefore, EMIN cannot be applied to Faster R-CNN.

8. Conclusions

We propose HTC+ to boost SAR ship instance segmentation. Seven techniques (MR-FEN, EFPN, SGAALN, CROIE, EMIN, PPT, and HSMTS) are used ensure the state-of-the-art accuracy of HTC+. HTC+ is elaborately designed for SAR ship tasks in consideration of the targeted SAR characteristics. HTC+ is superior to the vanilla HTC by 6.7% box AP and 5.0% mask AP and by 4.9% and 3.9% on HRSID. It outperforms the other nine advanced models. Moreover, we also extend the proposed techniques to Faster R-CNN to confirm their effectiveness for pure detection tasks; results reveal that they can offer continuous accuracy growth.

In the future, the speed optimization [71,72] will be considered; other tricks [73] will also be considered for better accuracy.

Author Contributions: Conceptualization, T.Z.; methodology, T.Z.; software, T.Z.; validation, T.Z.; formal analysis, T.Z.; investigation, T.Z.; resources, T.Z.; data curation, T.Z.; writing—original draft preparation, T.Z.; writing—review and editing, X.Z.; visualization, T.Z.; supervision, T.Z.; project administration, X.Z.; funding acquisition, X.Z. All authors have read and agreed to the published version of the manuscript.

Funding: This work was supported by the National Natural Science Foundation of China (61571099).

Data Availability Statement: Not applicable. No new data were created or analyzed in this study. Data sharing is not applicable to this article.

Conflicts of Interest: The authors declare no conflict of interest.

References

1. Shao, Z.; Wang, L.; Wang, Z.; Du, W.; Wu, W. Saliency-Aware Convolution Neural Network for Ship Detection in Surveillance Video. *IEEE Trans. Circuits Syst. Video Technol.* **2020**, *30*, 781–794. [CrossRef]
2. Shan, Y.; Zhou, X.; Liu, S.; Zhang, Y.; Huang, K. Siamfpn: A Deep Learning Method for Accurate and Real-Time Maritime Ship Tracking. *IEEE Trans. Circuits Syst. Video Technol.* **2021**, *31*, 315–325. [CrossRef]
3. Ribeiro, R.; Cruz, G.; Matos, J.; Bernardino, A. A Data Set for Airborne Maritime Surveillance Environments. *IEEE Trans. Circuits Syst. Video Technol.* **2017**, *29*, 2720–2732. [CrossRef]
4. Shao, Z.; Wu, W.; Wang, Z.; Du, W.; Li, C. SeaShips: A Large-Scale Precisely Annotated Dataset for Ship Detection. *IEEE Trans. Multimedia* **2018**, *20*, 2593–2604. [CrossRef]
5. Zhang, T.; Zhang, X. A Polarization Fusion Network with Geometric Feature Embedding for SAR Ship Classification. *Pattern Recognit.* **2021**, *123*, 108365. [CrossRef]
6. Zhang, T.; Zhang, X.; Ke, X.; Liu, C.; Xu, X.; Zhan, X.; Wang, C.; Ahmad, I.; Zhou, Y.; Pan, D.; et al. HOG-ShipCLSNet: A Novel Deep Learning Network with HOG Feature Fusion for SAR Ship Classification. *IEEE Trans. Geosci. Remote. Sens.* **2021**, *60*, 5210322. [CrossRef]
7. Zhang, T.; Zhang, X. Squeeze-and-Excitation Laplacian Pyramid Network with Dual-Polarization Feature Fusion for Ship Classification in SAR Images. *IEEE Geosci. Remote Sens. Lett.* **2021**, *19*, 4019905. [CrossRef]
8. Oh, J.; Youm, G.Y.; Kim, M. Spam-Net: A CNN-Based SAR Target Recognition Network with Pose Angle Marginalization Learning. *IEEE Trans. Circuits Syst. Video Technol.* **2020**, *31*, 701–714. [CrossRef]
9. Ma, F.; Gao, F.; Wang, J.; Hussain, A.; Zhou, H. A Novel Biologically-Inspired Target Detection Method Based on Saliency Analysis for Synthetic Aperture Radar (SAR) Imagery. *Neurocomputing.* **2020**, *402*, 66–79. [CrossRef]
10. Tao, D.; Anfinsen, S.N.; Brekke, C. Robust CFAR Detector Based on Truncated Statistics in Multiple-Target Situations. *IEEE Trans. Geosci. Remote. Sens.* **2015**, *54*, 117–134. [CrossRef]
11. Zhang, T.; Zhang, X.; Liu, C.; Shi, J.; Wei, S.; Ahmad, I.; Zhan, X.; Zhou, Y.; Pan, D.; Li, J.; et al. Balance Learning for Ship Detection from Synthetic Aperture Radar Remote Sensing Imagery. *ISPRS J. Photogramm. Remote Sens.* **2021**, *182*, 190–207. [CrossRef]
12. Zhang, T.; Zhang, X.; Shi, J.; Wei, S.; Wang, J.; Li, J.; Su, H.; Zhou, Y. Balance Scene Learning Mechanism for Offshore and Inshore Ship Detection in SAR Images. *IEEE Geosci. Remote Sens. Lett.* **2020**, *19*, 4004905. [CrossRef]
13. Zhang, T.; Zhang, X.; Li, J.; Xu, X.; Wang, B.; Zhan, X.; Xu, Y.; Ke, X.; Zeng, T.; Su, H.; et al. SAR Ship Detection Dataset (SSDD): Official Release and Comprehensive Data Analysis. *Remote Sens.* **2021**, *13*, 3690. [CrossRef]
14. Xu, Z.; Zhang, H.; Wang, Y.; Wang, X.; Xue, S.; Liu, W. Dynamic Detection of Offshore Wind Turbines by Spatial Machine Learning from Spaceborne Synthetic Aperture Radar Imagery. *J. King Saud Univ. Com. Inf. Sci.* **2022**, *34*, 1674–1686. [CrossRef]
15. Wei, S.; Zeng, X.; Qu, Q.; Wang, M.; Su, H.; Shi, J. HRSID: A High-Resolution SAR Images Dataset for Ship Detection and Instance Segmentation. *IEEE Access.* **2020**, *8*, 120234–120254. [CrossRef]
16. Su, H.; Wei, S.; Liu, S.; Liang, J.; Wang, C.; Shi, J.; Zhang, X. HQ-ISNet: High-Quality Instance Segmentation for Remote Sensing Imagery. *Remote Sens.* **2020**, *12*, 989. [CrossRef]

17. Zhao, D.; Zhu, C.; Qi, J.; Qi, X.; Su, Z.; Shi, Z. Synergistic Attention for Ship Instance Segmentation in SAR Images. *Remote Sens.* **2021**, *13*, 4384. [CrossRef]
18. Gao, F.; Huo, Y.; Wang, J.; Hussain, A.; Zhou, H. Anchor-Free SAR Ship Instance Segmentation with Centroid-Distance Based Loss. *IEEE J. Sel. Top. Appl. Earth Obs. Remote Sens.* **2021**, *14*, 11352–11371. [CrossRef]
19. Tianwen, Z.; Xiaowo, X.; Xiaoling, Z. SAR Ship Instance Segmentation Based on Hybrid Task Cascade. In Proceedings of the International Computer Conference on Wavelet Active Media Technology and Information Processing (ICCWAMTIP), Chengdu, China, 17–19 December 2021; pp. 530–533.
20. Fan, F.; Zeng, X.; Wei, S.; Zhang, H.; Tang, D.; Shi, J.; Zhang, X. Efficient Instance Segmentation Paradigm for Interpreting SAR and Optical Images. *Remote Sens.* **2022**, *14*, 531. [CrossRef]
21. Zhang, T.; Zhang, X. A Full-Level Context Squeeze-and-Excitation ROI Extractor for SAR Ship Instance Segmentation. *IEEE Geosci. Remote Sens. Lett.* **2022**, *19*, 4506705. [CrossRef]
22. Ke, X.; Zhang, X.; Zhang, T. GCBANet: A Global Context Boundary-Aware Network for SAR Ship Instance Segmentation. *Remote Sens.* **2022**, *14*, 2165. [CrossRef]
23. Zhang, T.; Zhang, X.; Li, J.; Shi, J. Contextual Squeeze-and-Excitation Mask R-CNN for SAR Ship Instance Segmentation. In Proceedings of the IEEE Radar Conference (RadarConf), New York City, NY, USA, 21–25 March 2022; pp. 1–6.
24. Chen, K.; Pang, J.; Wang, J.; Xiong, Y.; Li, X.; Sun, S.; Feng, W.; Liu, Z.; Shi, J.; Ouyang, W.; et al. Hybrid Task Cascade for Instance Segmentation. In Proceedings of the IEEE/CVF Conference on Computer Vision and Pattern Recognition (CVPR), Long Beach, CA, USA, 15–20 June 2019; pp. 4969–4978.
25. Redmon, J.; Farhadi, A. YOLOv3: An Incremental Improvement. *arXiv* **2018**, arXiv:1804.02767.
26. Bochkovskiy, A.; Wang, C.-Y.; Liao, H.-Y.M. YOLOv4: Optimal Speed and Accuracy of Object Detection. *arXiv* **2020**, arXiv:2004.10934.
27. Hosang, J.; Benenson, R.; Schiele, B. Learning Non-Maximum Suppression. In Proceedings of the IEEE Conference on Computer Vision and Pattern Recognition (CVPR), Honolulu, HI, USA, 21–26 July 2017; pp. 6469–6477.
28. Bodla, N.; Singh, B.; Chellappa, R.; Davis, L.S. Soft-Nms—Improving Object Detection with One Line of Code. In Proceedings of the IEEE International Conference on Computer Vision (ICCV), Venice, Italy, 22–29 October 2017; pp. 5562–5570.
29. Wang, J.; Chen, K.; Yang, S.; Loy, C.C.; Lin, D. Region Proposal by Guided Anchoring. In Proceedings of the IEEE Conference on Computer Vision and Pattern Recognition (CVPR), Long Beach, CA, USA, 15–20 June 2019; pp. 2960–2969.
30. He, K.; Gkioxari, G.; Dollar, P.; Girshick, R. Mask R-CNN. In Proceedings of the IEEE International Conference on Computer Vision (ICCV), Venice, Italy, 22–29 October 2017; pp. 2980–2988.
31. Ren, S.; He, K.; Girshick, R.; Sun, J. Faster R-CNN: Towards Real-Time Object Detection with Region Proposal Networks. *IEEE Trans. Pattern Anal. Mach. Intell.* **2017**, *39*, 1137–1149. [CrossRef] [PubMed]
32. Huang, Z.; Huang, L.; Gong, Y.; Huang, C.; Wang, X. Mask Scoring R-CNN. In Proceedings of the IEEE/CVF Conference on Computer Vision and Pattern Recognition (CVPR), Long Beach, CA, USA, 15–20 June 2019; pp. 6402–6411.
33. Cai, Z.; Vasconcelos, N. Cascade R-CNN: High Quality Object Detection and Instance Segmentation. *IEEE Trans. Pattern Anal. Mach. Intell.* **2021**, *43*, 1483–1498. [CrossRef]
34. Liu, S.; Qi, L.; Qin, H.; Shi, J.; Jia, J. Path Aggregation Network for Instance Segmentation. In Proceedings of the IEEE Conference on Computer Vision and Pattern Recognition (CVPR), Salt Lake City, UT, USA, 18–23 June 2018; pp. 8759–8768.
35. Rossi, L.; Karimi, A.; Prati, A. A Novel Region of Interest Extraction Layer for Instance Segmentation. In Proceedings of the International Conference on Pattern Recognition (ICPR), Milan, Italy, 10–15 January 2021; pp. 2203–2209.
36. Bolya, D.; Zhou, C.; Xiao, F.; Lee, Y.J. YOLACT: Real-Time Instance Segmentation. In Proceedings of the IEEE/CVF International Conference on Computer Vision (ICCV), Seoul, Korea, 27 October–2 November 2019; pp. 9156–9165.
37. Sun, K.; Xiao, B.; Liu, D.; Wang, J. Deep High-Resolution Representation Learning for Human Pose Estimation. In Proceedings of the IEEE/CVF Conference on Computer Vision and Pattern Recognition (CVPR), Long Beach, CA, USA, 15–20 June 2019; pp. 5686–5696.
38. Gao, S.-H.; Cheng, M.-M.; Zhao, K.; Zhang, X.-Y.; Yang, M.-H.; Torr, P.H. Res2net: A New Multi-Scale Backbone Architecture. *IEEE Trans. Pattern Anal. Mach. Intell.* **2019**, *43*, 652–662. [CrossRef]
39. He, K.; Zhang, X.; Ren, S.; Sun, J. Deep Residual Learning for Image Recognition. In Proceedings of the IEEE Conference on Computer Vision and Pattern Recognition (CVPR), Las Vegas, NV, USA, 27–30 June 2016; pp. 770–778.
40. Xie, S.; Girshick, R.; Dollar, P.; Tu, Z.; He, K. Aggregated Residual Transformations for Deep Neural Networks. In Proceedings of the IEEE Conference on Computer Vision and Pattern Recognition (CVPR), Honolulu, HI, USA, 21–26 July 2017; pp. 5987–5995.
41. Wang, J.; Sun, K.; Cheng, T.; Jiang, B.; Deng, C.; Zhao, Y.; Liu, D.; Mu, Y.; Tan, M.; Wang, X.; et al. Deep High-Resolution Representation Learning for Visual Recognition. *IEEE Trans. Pattern Anal. Mach. Intell.* **2020**, *43*, 3349–3364. [CrossRef]
42. Newell, A.; Yang, K.; Deng, J. Stacked Hourglass Networks for Human Pose Estimation. In Proceedings of the European Conference on Computer Vision, Cham, Switzerland, 8–16 October 2016; pp. 483–499.
43. MacLean, J.; Tsotsos, J. Fast Pattern Recognition Using Gradient-Descent Search in an Image Pyramid. In Proceedings of the International Conference on Pattern Recognition (ICPR), Barcelona, Spain, 3–7 September 2000; pp. 873–877.
44. Zhang, T.; Zhang, X. ShipDeNet-20: An Only 20 Convolution Layers and <1-Mb Lightweight SAR Ship Detector. *IEEE Geosci. Remote Sens. Lett.* **2021**, *18*, 1234–1238. [CrossRef]

45. Zhang, T.; Zhang, X.; Shi, J.; Wei, S. HyperLi-Net: A hyper-light deep learning network for high-accurate and high-speed ship detection from synthetic aperture radar imagery. *ISPRS J. Photogramm. Remote Sens.* **2020**, *167*, 123–153. [CrossRef]
46. Woo, S.; Park, J.; Lee, J.-Y.; Kweon, I.S. CBAM: Convolutional Block Attention Module. In Proceedings of the European Conference on Computer Vision (ECCV), Munich, Germany, 8–14 September 2018; pp. 3–19.
47. Niu, Z.; Zhong, G.; Yu, H. A Review on the Attention Mechanism of Deep Learning. *Neurocomputing* **2021**, *452*, 48–62. [CrossRef]
48. Chen, L.C.; Papandreou, G.; Kokkinos, I.; Murphy, K.; Yuille, A.L. DeepLab: Semantic Image Segmentation with Deep Convolutional Nets, Atrous Convolution, and Fully Connected Crfs. *IEEE Trans. Pattern Anal. Mach. Intell.* **2018**, *40*, 834–848. [CrossRef] [PubMed]
49. Yu, F.; Koltun, V. Multi-Scale Context Aggregation by Dilated Convolutions. In Proceedings of the 4th International Conference on Learning Representations (ICLR), San Juan, Puerto Rico, 2–4 May 2016; pp. 1–13.
50. Chen, L.-C.; Zhu, Y.; Papandreou, G.; Schroff, F.; Adam, H. Encoder-Decoder with Atrous Separable Convolution for Semantic Image Segmentation. In Proceedings of the European Conference on Computer Vision, Cham, Switzerland, 8–14 September 2018; pp. 833–851.
51. Lin, T.-Y.; Dollar, P.; Girshick, R.; He, K.; Hariharan, B.; Belongie, S. Feature Pyramid Networks for Object Detection. In Proceedings of the IEEE Conference on Computer Vision and Pattern Recognition (CVPR), Honolulu, HI, USA, 21–26 July 2017; pp. 936–944.
52. Zhou, Z.; Guan, R.; Cui, Z.; Cao, Z.; Pi, Y.; Yang, J. Scale Expansion Pyramid Network for Cross-Scale Object Detection in SAR Images. In Proceedings of the IEEE International Geoscience and Remote Sensing Symposium (IGARSS), Brussels, Belgium, 11–16 July 2021; pp. 5291–5294.
53. Lin, T.-Y.; Maire, M.; Belongie, S.; Hays, J.; Perona, P.; Ramanan, D.; Dollár, P.; Zitnick, C.L. Microsoft Coco: Common Objects in Context. In Proceedings of the 13th European Conference on Computer Vision (ECCV), Zurich, Switzerland, 6–12 September 2014; pp. 740–755.
54. Everingham, M.; Eslami, S.M.A.; Gool, L.V.; Williams, C.K.I.; Winn, J.; Zisserman, A. The Pascal Visual Object Classes Challenge: A Retrospective. *Int. J. Comput. Vis.* **2015**, *111*, 98–136. [CrossRef]
55. Wang, J.; Chen, K.; Xu, R.; Liu, Z.; Loy, C.C.; Lin, D. Carafe: Content-Aware Reassembly of Features. In Proceedings of the IEEE/CVF International Conference on Computer Vision (ICCV), Seoul, Korea, 27 October–2 November 2019; pp. 3007–3016.
56. Zeiler, M.D.; Krishnan, D.; Taylor, G.W.; Fergus, R. Deconvolutional Networks. In Proceedings of the IEEE Conference on Computer Vision and Pattern Recognition (CVPR), San Francisco, CA, USA, 13–18 June 2010; pp. 2528–2535.
57. Shelhamer, E.; Long, J.; Darrell, T. Fully Convolutional Networks for Semantic Segmentation. *IEEE Trans. Pattern Anal. Mach. Intell.* **2017**, *39*, 640–651. [CrossRef] [PubMed]
58. Zhang, T.; Zhang, X.; Ke, X. Quad-FPN: A Novel Quad Feature Pyramid Network for SAR Ship Detection. *Remote Sens.* **2021**, *13*, 2771. [CrossRef]
59. Pang, J.; Chen, K.; Shi, J.; Feng, H.; Ouyang, W.; Lin, D. Libra R-CNN: Towards Balanced Learning for Object Detection. In Proceedings of the IEEE/CVF Conference on Computer Vision and Pattern Recognition (CVPR), Long Beach, CA, USA, 15–20 June 2019; pp. 821–830.
60. Cao, Y.; Xu, J.; Lin, S.; Wei, F.; Hu, H. GCNet: Non-Local Networks Meet Squeeze-Excitation Networks and Beyond. In Proceedings of the IEEE/CVF International Conference on Computer Vision Workshop (ICCVW), Seoul, Korea, 27–28 October 2019; pp. 1971–1980.
61. Wang, X.; Girshick, R.; Gupta, A.; He, K. Non-Local Neural Networks. In Proceedings of the IEEE/CVF Conference on Computer Vision and Pattern Recognition (CVPR), Salt Lake City, UT, USA, 18–23 June 2018; pp. 7794–7803.
62. Hu, J.; Shen, L.; Albanie, S.; Sun, G.; Wu, E. Squeeze-and-Excitation Networks. *IEEE Trans. Pattern Anal. Mach. Intell.* **2020**, *42*, 2011–2023. [CrossRef]
63. Ioffe, S.; Szegedy, C. Batch normalization: Accelerating deep network training by reducing internal covariate shift. In Proceedings of the 32 nd International Conference on Machine Learning (ICML), Lile, France, 6–11 July 2015; pp. 448–456.
64. Dai, J.; Qi, H.; Xiong, Y.; Li, Y.; Zhang, G.; Hu, H.; Wei, Y. Deformable Convolutional Networks. In Proceedings of the IEEE International Conference on Computer Vision (ICCV), Venice, Italy, 22–29 October 2017; pp. 764–773.
65. Kang, M.; Ji, K.; Leng, X.; Lin, Z. Contextual Region-Based Convolutional Neural Network with Multilayer Fusion for SAR Ship Detection. *Remote Sens.* **2017**, *9*, 860. [CrossRef]
66. Shrivastava, A.; Gupta, A.; Girshick, R. Training Region-Based Object Detectors with Online Hard Example Mining. In Proceedings of the IEEE Conference on Computer Vision and Pattern Recognition (CVPR), Las Vegas, NV, USA, 27–30 June 2016; pp. 761–769.
67. He, K.; Girshick, R.; Doll´ar, P. Rethinking ImageNet Pre-Training. In Proceedings of the IEEE International Conference on Computer Vision (ICCV), Seoul, Korea, 27 October–2 November 2019; pp. 4917–4926.
68. Goyal, P.; Dollár, P.; Girshick, R.; Noordhuis, P.; Wesolowski, L.; Kyrola, A.; Tulloch, A.; Jia, Y.; He, K. Accurate, Large Minibatch SGD: Training ImageNet in 1 Hour. *arXiv* **2017**, arXiv:1706.02677.
69. Chen, K.; Wang, J.; Pang, J.; Cao, Y.; Xiong, Y.; Li, X.; Sun, S.; Feng, W.; Liu, Z.; Xu, J.; et al. MMDetection: Open MMLab Detection Toolbox and Benchmark. *arXiv* **2019**, arXiv:1906.07155.
70. Eric, Q. Floating-Point Fused Multiply–Add Architectures. Ph.D. Thesis, The University of Texas at Austin, Austin, TX, USA, 2007.
71. Zhang, T.; Zhang, X.; Shi, J.; Wei, S. Depthwise Separable Convolution Neural Network for High-Speed SAR Ship Detection. *Remote Sens.* **2019**, *11*, 2483. [CrossRef]

72. Zhang, T.; Zhang, X. High-Speed Ship Detection in SAR Images Based on a Grid Convolutional Neural Network. *Remote Sens.* **2019**, *11*, 1206. [CrossRef]
73. Zhang, T.; Zhang, X. Injection of Traditional Hand-Crafted Features into Modern CNN-Based Models for SAR Ship Classification: What, Why, Where, and How. *Remote Sens.* **2021**, *13*, 2091. [CrossRef]

remote sensing

MDPI

Communication

Low Sidelobe Series-Fed Patch Planar Array with AMC Structure to Suppress Parasitic Radiation

Qingquan Tan [1], Kuikui Fan [1,*], Wenwen Yang [2] and Guoqing Luo [1]

[1] School of Electronics and Information, Hangzhou Dianzi University, Hangzhou 310018, China; tanqingquan@hdu.edu.cn (Q.T.); luoguoqing@hdu.edu.cn (G.L.)
[2] School of Information Science and Technology, Nantong University, Nantong 226019, China; wwyang@ntu.edu.cn
* Correspondence: kkfan@hdu.edu.cn

Abstract: For automobile radar systems, the antenna array requires a low sidelobe level (SLL) to reduce interference. A low-SLL and low-cost planar antenna array are proposed in this article for millimeter-wave automotive radar applications. The proposed array consists of six linear series-fed patch arrays, a series distribution network using a grounded co-planar waveguide (GCPW), and a bed of nails. First, a hybrid HFSS-MATLAB optimization platform is set up to easily obtain good impedance matching and low SLL of the linear series-fed patch array. Then, a six-way GCPW power divider is designed to combine the optimized linear sub-array to achieve a planar array. However, since CCPW is a semi-open structure, like a microstrip line, the parasitic radiation generated by the GCPW feeding network will lead to the deterioration of the SLL. To solve this problem, a bed of nails—as an artificial magnetic conductor (AMC)—is designed and placed above the feeding networking to create an electromagnetic stopband in the working band. Its working mechanism has been explained in detail. The feeding network cannot effectively radiate electromagnetic waves into free space. Thus, the parasitic radiation can be suppressed. A low-SLL planar array prototype working at 79 GHz is designed, manufactured, and measured. The measured results confirm that the proposed low-SLL planar array has a −10 dB impedance bandwidth of 3 GHz from 77 to 80 GHz and a maximum peak gain of 21 dBi. The measured SLL is −24 dB and −23 dB in the E-plane and H-plane at 79 GHz, respectively. The proposed low SLL array can be used for adaptive cruise control (ACC) system applications.

Keywords: 79-GHz automotive radar; low sidelobe level (SLL); series-fed array; AMC

Citation: Tan, Q.; Fan, K.; Yang, W.; Luo, G. Low Sidelobe Series-Fed Patch Planar Array with AMC Structure to Suppress Parasitic Radiation. *Remote Sens.* **2022**, *14*, 3597. https://doi.org/10.3390/rs14153597

Academic Editors: Zhihuo Xu, Jianping Wang and Yongwei Zhang

Received: 21 June 2022
Accepted: 22 July 2022
Published: 27 July 2022

1. Introduction

The rise of driverless vehicles has raised higher demands and challenges for millimeter-wave (mmW) automotive radars [1–6]. At present, automotive radars have moved the working frequency to 76–81 GHz. According to the detection distance, an automotive radar can be classified into three main categories: long-range radar (LRR), medium-range radar (MRR), and short-range radar (SRR) [7]. The frequency band from 77 to 81 GHz is mainly used for MMR and SSR. Compared to 24 GH automotive radars, the 77/79 GHz automotive radars have a higher resolution and smaller volume. This will extend promising applications for intelligent transportation, such as adaptive cruise control (ACC), blind-spot detection (BSD), cross-traffic alerts (CTA), etc. Antennas, as a key component in automotive radar systems, have also been one of the subjects of research. To compensate for high path loss in the mmW band and to increase the detection range, the radar antennas usually need to be designed as high-gain antenna arrays. Furthermore, regardless of the application scenario, a low sidelobe level (SLL) is desirable to reduce the interference from clutter. Hence, for automotive radar systems, antenna arrays with low SLL, high gain, and low cost are the preferred choice.

Over the past decade, a lot of efforts have been devoted to designing antennas for automotive radars [8–26]. Some linear arrays are investigated in [8–20]. In consideration of the cost and compactness, the series-fed array is a good way to implement a linear array, such as a series-fed patch array [8–11], grid antenna array [12–16], comb-line array [17], etc. The SLL of the array is an important index in automotive radar systems, which reflects its anti-interference ability. The reported grid arrays and comb-line array have relatively high SLL due to the difficulty in suppressing sidelobe. Comparatively, the series-fed patch antenna array can more easily achieve a low SLL through a tapered patch width. In [8], a series-fed microstrip patch array of unequal interelement spacing and non-uniform amplitude is designed in the microwave band and achieves an SLL of −25 dB by using the differential evolution algorithm (DEA). Yet, the mutual coupling between elements is neglected for the simplicity of calculation, which is not desirable for a 79-GHz band with serious coupling. In [10], the series-fed linear and planar binomial patch arrays are designed by tapering the width of the radiation element. Both linear and planar binomial arrays provide an SLL of less than −28 dB. The reported low series-fed patch arrays [8,10,11] are designed in the microwave band. It is more difficult to design a low SLL series-fed patch array in the W-band due to the smaller wavelength. In [9], by adopting the design method of controlling the radiated-to-available power ratio (RAPA), three types of patch antennas are introduced to design a low SLL series-fed linear array. The SLLs below −17 dB are constructed over the operating band. A drawback of the reported methods for designing a low SLL is that they only consider the SLL, while they cannot optimize both S_{11} and SLL simultaneously.

To meet the detection of medium and long distances, high-gain planar arrays are required as transmitting antennas. Several different types of planar arrays have been designed for automotive radar applications [21–26]. Traditional microstrip-based feeding networks suffer from an increasing loss with the frequency increase in the mmW band. In particular, it will produce undesirable radiation (parasitic radiation), which has a bad effect on the radiation pattern and radar system. Given this concern, other transmission line technologies with closed structures, such as substrate-integrated wave and ridge waveguides, have been used to design a planar array. In [21], a planar array with a flat-shoulder shaped radiation pattern is achieved by adopting linear series-fed patch arrays and an SIW feeding network with a phase shift. The downside is that the SIW feeding network usually suffers from a large size due to the cut-off frequency. A high-gain slotted waveguide array with low SLL is proposed in [25] for vehicular applications in the 71–81 GHz band. A full-corporate single-ridge waveguide network with a Taylor amplitude distribution is used to design a low-SLL planar array. The SLLs below −19 dB and −24 dB are achieved in the E- and H-planes, respectively. Nevertheless, the full metal structure is very bulky and difficult to integrate with the front-end circuit. Several 77 GHz automotive radar systems are exhibited in [1,4,5]. It can be found that although the microstrip structure has some inherent shortcomings, the microstrip-based planar arrays are still the mainstream choice for automotive radar systems due to the compact structure, low cost, and ease of integration. Thus, it is very promising to design a simple and low-cost packaging to suppress the parasitic radiation from microstrip-based feeding networks. This will greatly improve the performance and reliability of automotive radar systems.

In this work, a compact and low-cost microstrip antenna planar array with low SLL is designed for LRR and MRR applications. The major contributions of this letter are shown as follows:

1. The reported methods for achieving the low SLL of a series-fed array cannot take into account the reflection coefficient. In this work, we built a Matlab-HFSS joint optimizing platform to easily optimize the SLL and S_{11} of the series-fed patch array.
2. Aimed at the problem of parasitic radiation from a microstrip-based feeding network, we propose an efficient method of loading an artificial magnetic conductor (AMC) to solve this problem. A bed-of-nails structure is used as an AMC and is arranged above the feeding network to suppress the unwanted radiation, which enables the

radiation performance of the linear array to be unaffected. The proposed method has the advantage of a simple design and low cost. Meanwhile, there is no perfect electrical contact between the AMC structure and feeding network, which greatly facilitates assembly and enhances its practicality.

3. A prototype of the designed low-SLL microstrip antenna planar array is fabricated and measured for verification. The SLLs of −24 dB and −23 dB in the E- and H-planes at 79 GHz are realized, respectively. The measured results verify the correctness of the design.

2. Planar Array Design

2.1. The Design of a Low-SLL, Series-Fed Patch Antenna Sub-Array

Based on antenna array theory, the linear array can achieve a low SLL by tuning the amplitude and phase of each element. For a series-fed patch antenna array, the amplitude and phase are related to the patch width and element spacing, respectively. Therefore, its low SLL can be achieved by tapering the patch width and unequal element spacing. Figure 1 shows the geometry of the proposed low SLL series-fed microstrip patch antenna linear array. It will act as the sub-array of the proposed low-SLL planar array. The sub-array is designed on a single-layer Rogers RO3003 substrate (ε_r = 3, tan δ = 0.0013) with a thickness of $h_s = 0.127$ mm, and it consists of 10 patch elements, an impedance transformer, and a feeding line with 50 ohms. The 10 patch elements with the same length l_p are arranged symmetrically, and they are connected by a narrow microstrip line with width w_t. The impedance transformer is utilized to achieve good impedance matching between the array and 50-Ω feeding line. As mentioned above, the sub-array is set to the unequal element spacing and tapered width to achieve low SLL. Since the patch elements of the series-fed sub-array have progressive phases, the element spacing between the adjacent patches needs to be kept at around one λ_g to maintain the radiation pattern in the broadside direction. (Here, λ_g is the guided wavelength in the substrate at 79 GHz). According to (1), the λ_g is 2.19 mm. The final sizes of the sub-array are given in Table 1:

$$\lambda_g = \frac{c}{f\sqrt{\varepsilon_r}} \tag{1}$$

where c and ε_r are the speed of light and relative permittivity, respectively. For a series-fed patch antenna array, it is very laborious to achieve low SLL directly by parameter optimization or Taylor synthesis. To easily optimize SLL and S_{11}, we construct a HFSS-MATLAB joint optimizing platform. Previously, a preliminary result has been reported in [27], but it does not have a detailed illustration and experimental results. Hence, the details of HFSS-Matlab joint optimization will be discussed here. The flowchart of the optimization method combining HFSS with Matlab is shown in Figure 2. First, a genetic algorithm (GA) is selected as the optimization algorithm because it has outstanding stochastic search capacity based on the mechanism of evolutionary biology. The GA starts with an initial set of random solutions, a population. Each individual in the population is coded as a chromosome, representing a solution of the target problem. Next, based on the MATLAB platform, HFSS-Matlab-API (HMA) is created as the interface between MATLAB and HFSS. The HMA provides a series of functions of HFSS operation commands. By using HMA, antenna models can be automatically created and simulated in HFSS. Thus, the precise results of each individual can be obtained. Then, the evaluation function is used to analyze and deal with these results provided by HFSS. Finally, according to the data from the evaluation function, good individuals will be selected by GA to enter the next iteration. The whole process will continue until the optimal result can be obtained.

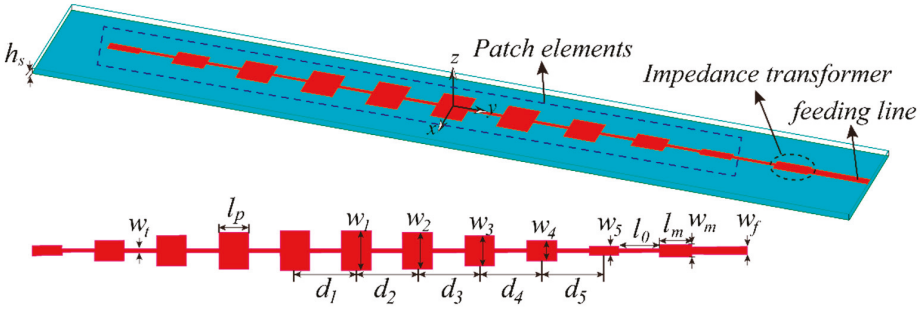

Figure 1. The geometry of the low SLL, linear series-fed patches sub-array.

Table 1. The dimensions of the optimized series-fed patch antenna array. (Unit: mm).

w_1	w_2	w_3	w_4	w_5	w_m	w_f	d_1
0.32	0.72	1.08	1.3	1.41	0.44	0.3	2.19
d_2	d_3	d_4	d_5	l_p	l_0	l_m	w_t
2.19	2.23	2.22	2.23	1.06	1.49	1.15	0.12

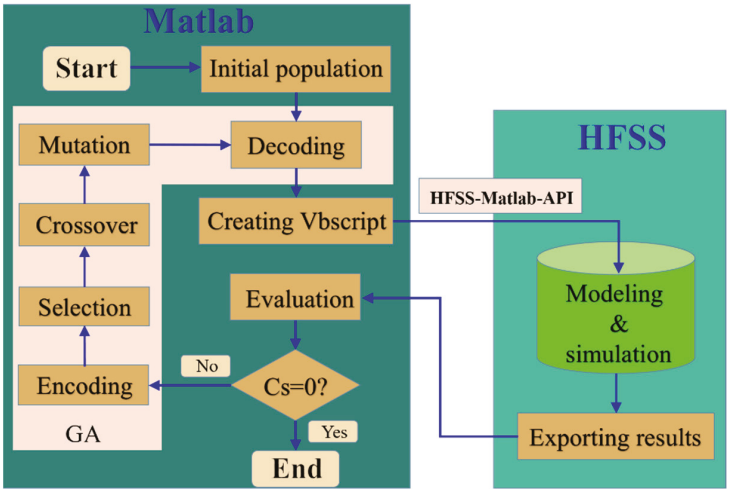

Figure 2. The framework of HFSS-MATLAB joint optimizing platform.

Here, our goal is to achieve an SLL of −25 dB at 79 GHz and a working bandwidth covering 78 to 80 GHz. Accordingly, the objective function can be expressed as:

$$\begin{aligned} e_1 &= \begin{cases} 25-|E_S| & |E_S| < 25 \\ 0 & |E_S| \geq 25 \end{cases} \\ e_2 &= \begin{cases} 30 & |S_{11}| > -10 \text{ dB } form \text{ 78 } to \text{ 80 GHz} \\ 2-\omega & the\ others \end{cases} \\ C_S &= e_1 + e_2 \end{aligned} \tag{2}$$

where E_S is the SLL at 79 GH in the E-plane. The ω represents the value of the bandwidth ($|S_{11}| \leq -10$ dB) in the specified frequency range of 78 to 80 GHz. The width of the patches (w_1–w_5), the element spacing (d_1–d_5), and the size of the impedance transformer (w_m, l_m) will be selected for optimization. Considering the actual patch size at 79 GHz,

proper constraints may be added to the main function to make the whole optimizing process more efficient. For the main function, the patch width w_i and spacing d_i are set at a range of [0.3 mm, 1.5 mm] and [0.95λ_g, 1.05λ_g], respectively. In this design, the configuration of GA is summarized as population = 20, crossover probability = 0.7, and mutation probability = 0.1.

By using hybrid HFSS-MATLAB optimization, a low-SLL, series-fed patch sub-array that satisfies our goals has been realized. The optimized dimensions are given in Table 1. The simulated reflection coefficient and gain are depicted in Figure 3a. The series-fed patch sub-array achieves good impedance matching in the range of 78 to 80 GHz and has stable gains at the working frequency band. Figure 3b–d show the simulated normalized radiation patterns at 78, 79, and 80 GHz. The series-fed patch sub-array exhibits good radiation characteristics in the operating band. It can be seen that the simulated SLL is −21 dB, −25 dB, and −24 dB at 78, 79, and 80 GHz in the E-plane, respectively.

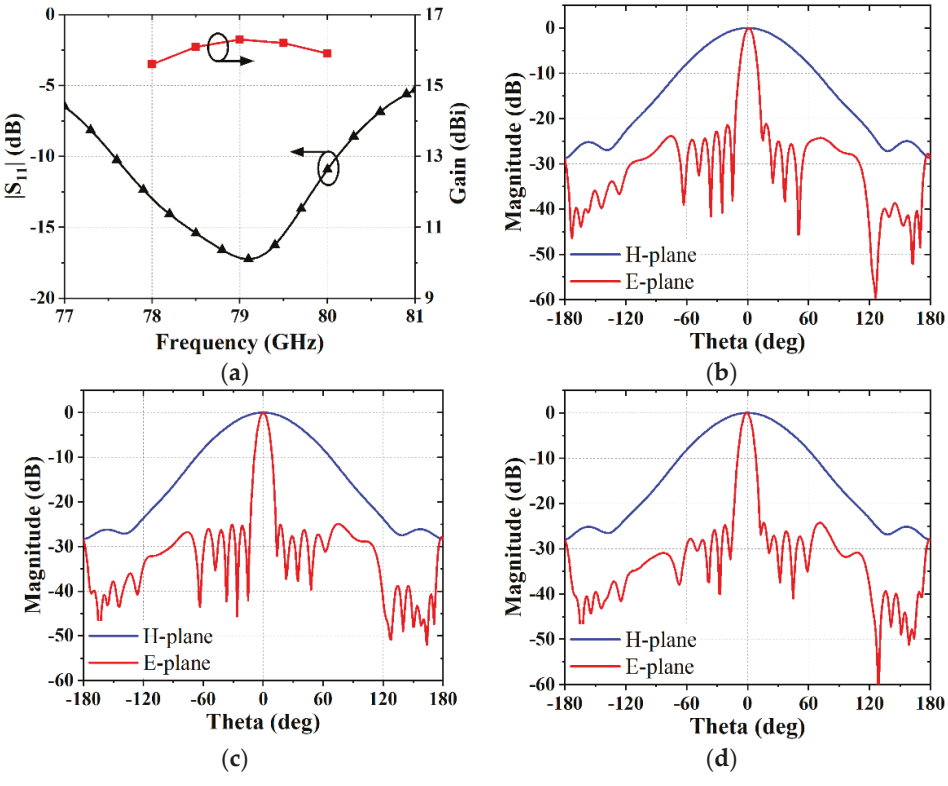

Figure 3. Simulated results of the series−fed patch array. (**a**) Reflection coefficient and gain. (**b**) Pattern at 78 GHz. (**c**) Pattern at 79 GHz. (**d**) Pattern at 80 GHz.

2.2. The Design of the Feeding Network

To implement a planar array, a full-corporate feeding network needs to be designed. We chose a series feeding way because it has a more compact structure compared to the parallel feeding way. Figure 4 shows the geometry of the designed series feeding network. The GCPW is used instead of the microstrip line, given the fact that its ground vias can effectively suppress surface waves. The designed feeding network consists of T-junction equal power dividers and an impedance transformer. As shown in Figure 5, three types of structures are used to design the series feeding network. To decrease the low SLL in the H-plane, unequal power distribution needs to be employed in the feeding network.

Here, through a cascading equal power divider, the power ratio of 0.25:0.5:1:1:0.5:0.25 can be achieved, which is enough to ensure the SLL below −20 dB at 79 GHz. Similar to a series-fed sub-array, the series feeding network also has a progressive phase. Given this, the output ports should be spaced about one λ_g to remain in-phase. To achieve a good impedance matching of the feeding network, the key is to calculate the characteristic impedance (Z_{t1} and Z_{t2}) of the impedance transformer. Structure 1 is based on a quarter wavelength impedance transformer for impedance matching. According to transmission line theory, the Z_{in} can be derived as:

$$\begin{aligned} l &= \lambda/4 \\ \theta_t &= \beta l = \pi/2 \\ Z_{in} &= Z_{t1}\frac{Z_2 + jZ_{t1}\tan(\theta_t)}{Z_{t1} + jZ_2\tan(\theta_t)} = \frac{{Z_{t1}}^2}{Z_2} \end{aligned} \tag{3}$$

where Z_2, Z_{t1}, and θ_t denote the characteristic impedance and electrical length of the transmission line, respectively. To achieve a perfect matching, i.e., the reflection coefficient $\Gamma = 0$, $Z_{in} = Z_1$ will be satisfied. Thus, the Z_{t1} can be obtained:

$$Z_{t1} = \sqrt{Z_1 Z_2} \tag{4}$$

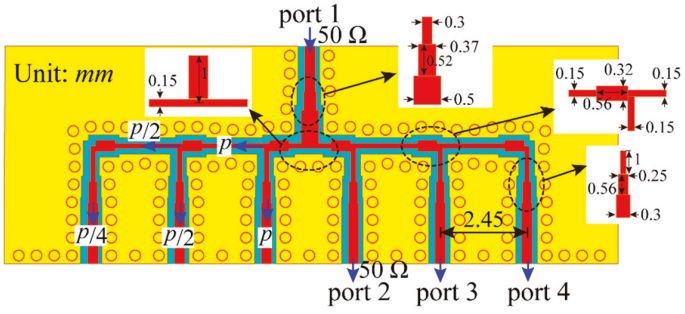

Figure 4. The geometry of the designed series feeding network. (The impedance of the input and outputs are 50 Ω. The p denotes power.).

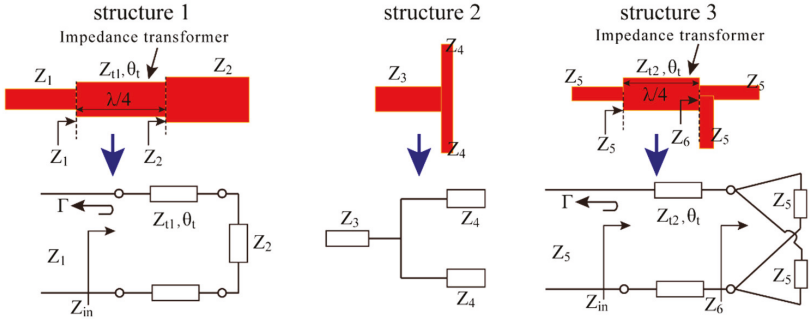

Figure 5. Three types of structures required to design the series feeding network and their corresponding equivalent circuit models.

Structure 2 is a typical T-junction equal power divider. It can be regarded as a parallel circuit. Thus, the relationship of the characteristic impedances can be expressed as:

$$\frac{1}{Z_3} = \frac{1}{Z_4} + \frac{1}{Z_4} \tag{5}$$

Structure 3 can be considered as the combination of structure 1 and structure 2. According to (3)–(5), the characteristic impedance Z_{t2} can be derived as:

$$\begin{aligned} Z_6 &= Z_5/2 \\ Z_{t2} &= \sqrt{Z_5 Z_6} = \frac{Z_5}{\sqrt{2}} \end{aligned} \tag{6}$$

In this design, according to (3)–(6), the initial design of the series feeding network can be completed by setting a characteristic impedance Z_6 of structure 3. Then, the feeding network is further optimized in HFSS to obtain the desired results. Figure 4 gives the final design dimensions. Figure 6 presents the simulated results of the designed feeding network. It achieves a good impedance matching with $|S_{11}| < -15$ dB covering 76 to 85 GHz. From Figure 6b, good agreement of the output phases can be observed from 77 to 81 GHz.

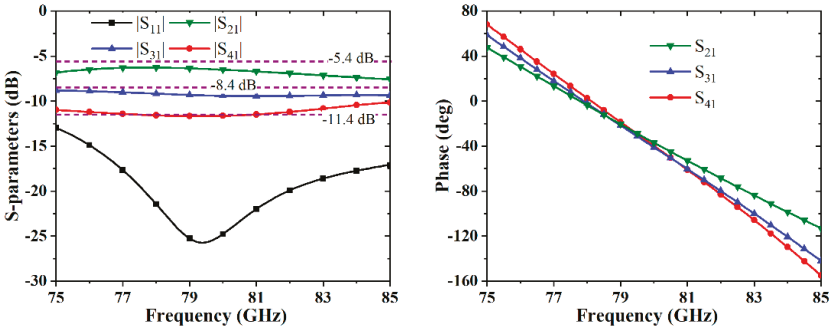

Figure 6. The simulated results of the feeding network. (**a**) S−parameters. (**b**) Output phases.

2.3. The Design and Analysis of AMC Structure

As mentioned in the introduction, the microstrip-based feeding network inevitably generates undesirable radiation due to its semi-open structure. In this sub-section, the principle and design process of using AMC to suppress the undesirable radiation will be elaborated upon. A new type of high-impedance electromagnetic (EM) surface is developed in [28]. The typical geometry is mushroom-like structures arranged in a two-dimensional lattice. In this design, we use a bed of nails formed by pins distributed in a two-dimensional lattice to achieve a high-impedance EM surface. Figure 7a shows the geometry of the bed of nails. Since the size and periodicity of the unit cell are much smaller than the operating wavelength, a simplified lumped circuit model can be used to describe the EM properties of the bed of nails. Figure 7b shows the equivalent lumped circuit model. It can be seen as a parallel resonant circuit, consisting of capacitance and inductance. The surface impedance can be expressed as:

$$Z = \frac{j\omega L}{1 - \omega^2 LC} \tag{7}$$

The impedance is infinite near the resonant frequency ω_0. In the frequency range where the surface impedance is very high, the tangential magnetic field is small and the image currents are in-phase [28]. Based on these properties, the high-impedance surface can be regarded as a kind of AMC:

$$\omega_0 = \frac{1}{\sqrt{LC}} \tag{8}$$

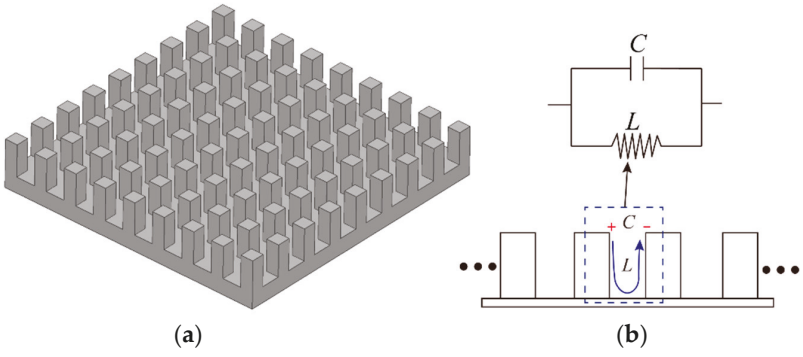

Figure 7. The high surface impedance can be formed by square metal pins in two−dimensional, a bed of nails. (**a**) The geometry of the bed of nails. (**b**) Equivalent lumped circuit model.

Based on the theory of soft and hard surfaces [29], and some related research [30–32], a new metamaterial-based ridge gap waveguide technology is proposed in [33]. Figure 8 plotted the evolution process of the ridge gap waveguide. A TEM wave cannot propagate between a perfect electric conductor (PEC) and perfect magnetic conductor (PMC) due to the limitation of boundary conditions. When the distance between the PEC and PMC is smaller than a quarter wavelength, no waves can propagate in the gap (i.e., all modes are below cut-off [34]). This is similar to the cut-off characteristic of a rectangular waveguide. Thus, a frequency stopband can be created. As we all know, the PMC does not exist in nature. The bed of nails with a high surface impedance (regarded as AMC) is used to constitute an approximate PMC surface. If a metal ridge or metal strip is embedded in the PMC, the EM wave is bound to follow the ridge, and the electric fields are located between the top of the ridge and PEC, like a microstrip line located over a metal ground. As a result, in a frequency stopband, a local quasi-TEM mode electromagnetic wave can propagate between the ridge and PEC, while wave propagation at the sides of the ridge is prohibited.

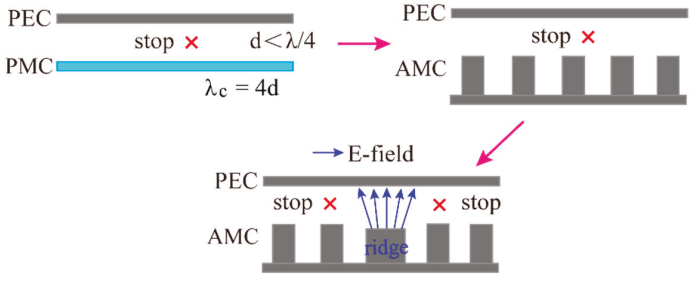

Figure 8. The evolution process of the ridge gap waveguide.

Inspired by the concept of a gap waveguide (GW), we utilize the stopband features on both sides of the metal ridge to shield the parasitic radiation from a microstrip-based feeding network. To do this, a unit cell of GW needs to be designed. The EM stopband can be observed by the dispersion curves of the modes. Figure 9 shows the dispersion diagram of the unit cell. The dispersion curve is calculated by the Eigenmode solver of the CST studio. A stopband from 65 to 152 GHz is obtained by tuning the dimensions of the pin and the gap. To further understand the characteristics of the unit cell, the effect of several parameters on the stopband was studied. The influence of the pin height on the stopband is given in Figure 10a. As the high d increases, the stopband moves towards the lower frequency band. The effect of gap g is then studied. As shown in Figure 10b, the working frequency band of mode 1 moves towards a higher frequency with

the increase of g, while mode 2 exhibits the opposite variation. Accordingly, the stopband bandwidth is significantly reduced as g increases. Figure 10c shows the effect of different intervals between pins on the stopband. The interval p has a significant effect on mode 2. As p increases, the stopband moves slightly towards the lower band and the stopband bandwidth decreases. Figure 10d shows the influence of the pin width a on the stopband. It can be found that the stopband is only slightly affected.

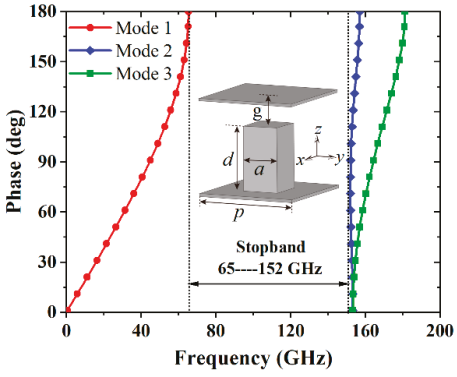

Figure 9. The geometry of the unit cell and its dispersion diagram (g = 0.2 mm, d = 0.7 mm, a = 0.4 mm, p = 1.1 mm).

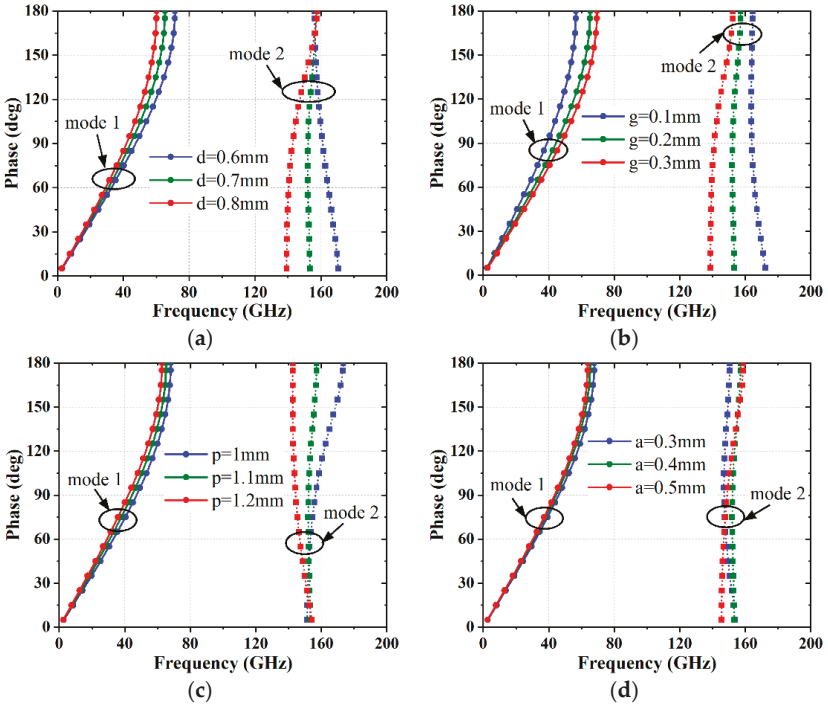

Figure 10. The effect of the unit cell dimensions on the stopband. (**a**) high d. (**b**) gap g. (**c**) interval p. (**d**) pin width a.

2.4. The Design and Analysis of the Proposed Low-SLL Planar Array

Figure 11 shows the overall configuration of the proposed low-SLL planar array. The planar array consists of the optimized series-fed sub-array and a 1-to-6 series feeding network. Due to the semi-open structure of GCPW, the parasitic radiation from the feeding networking will deteriorate the SLL of the radiation pattern. It is necessary to suppress parasitic radiation to keep a good radiation performance of the planar array. A bed of nails as an AMC is designed and placed above the feeding networking. As illustrated by the above theory, a stopband will be created in the gap between the bed of nails and the top ground of the feeding network, while the quasi-TEM wave can still propagate between the signal line of GCPW and the ground on bottom. This is similar to an inverted microstrip gap waveguide (IMGP) structure [35]. Meanwhile, the parallel plate modes do not appear due to the EM stopband, which enables the array to maintain its original performance. The feeding network will not be able to radiate EM waves into outer space. Therefore, the parasitic radiation of the feeding network can be suppressed in the operating frequency band.

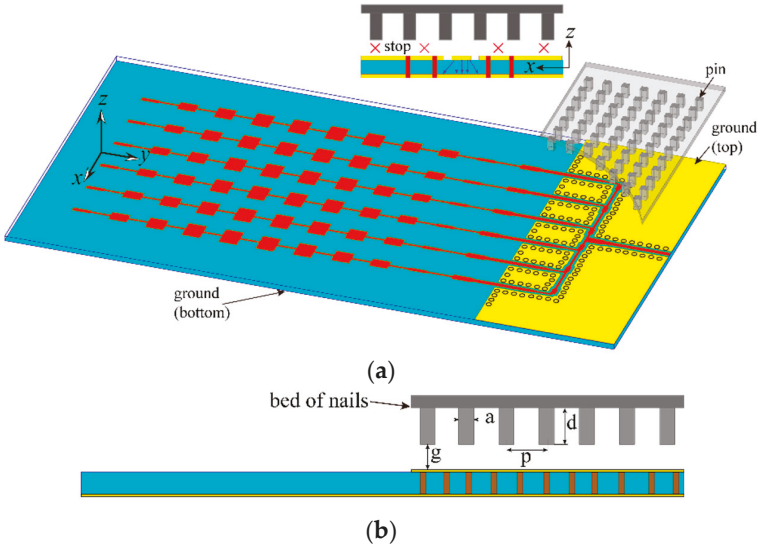

Figure 11. The configuration of the proposed low-SLL planar array. (**a**) 3-D view. (**b**) Side view.

To further understand this design, the magnitude of the electric field with and without the bed of nails in the plane above the feeding network was plotted in Figure 12. When there is no bed of nails, the electric field above the feeding network is more cluttered and has many speckles with strong energy. Although the radiated energy is much weaker than the main beam of the array, it is comparable to the energy of the sidelobes. It is foreseeable that they will interfere with the radiation performance of the array, especially the sidelobes. It can be seen from Figure 12b that when the bed of nails is loaded, the strong electric field only appears above the signal line, while the amplitude of the electric field in other regions is almost zero due to the existence of the electromagnetic stopband. Thus, the feeding network will not produce any EM leakage. In addition, any parallel plate modes that interfere with the array performance do not exist in the gap. Figure 13 shows the simulated radiation patterns of the proposed low-SLL array with and without the bed of nails at 79 GHz. The array without a bed of nails has an SLL of −20 and −21 dB in the E-plane and H-plane, respectively. By loading a bed of nails as an AMC, the SLLs of the array are reduced by 5 dB and 2 dB in the E-plane and H-plane, respectively. This verifies the correctness of the design. Figure 14 shows the comparison of the radiation pattern between

the proposed SLL array and the array with the common package of a metal box. It can be found that the radiation pattern of the array with the metal-shielded box has a relatively high SLL (−20 dB) at a negative E-plane angle due to the influence of the high-order cavity resonance mode and metallic sidewall.

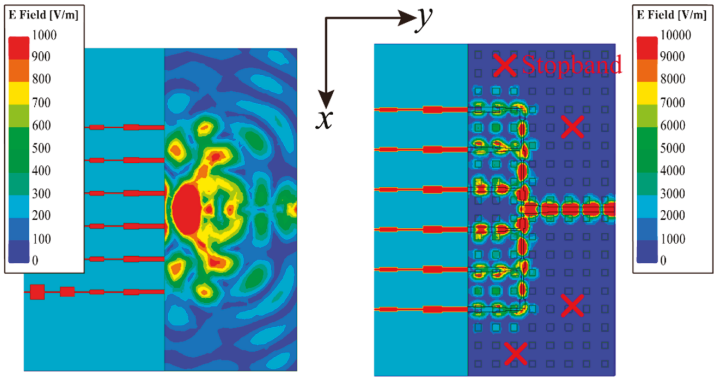

Figure 12. The full-wave extracted magnitude of the electric field in a plane above the GCPW feeding network. (**a**) Without the bed of nails. (**b**) With the bed of nails.

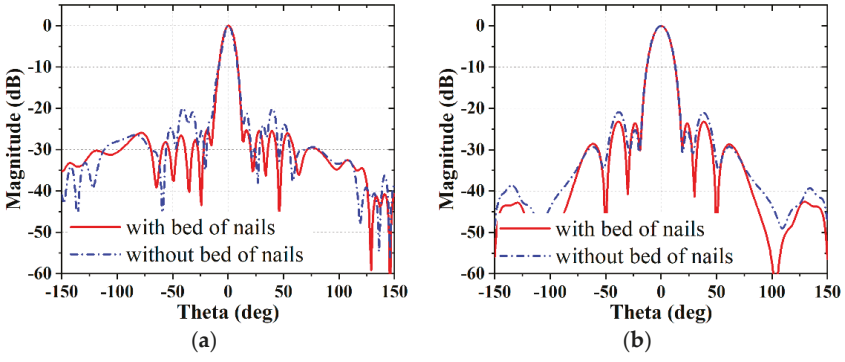

Figure 13. The radiation pattern with and without the bed of nails. (**a**) E−plane. (**b**) H−plane.

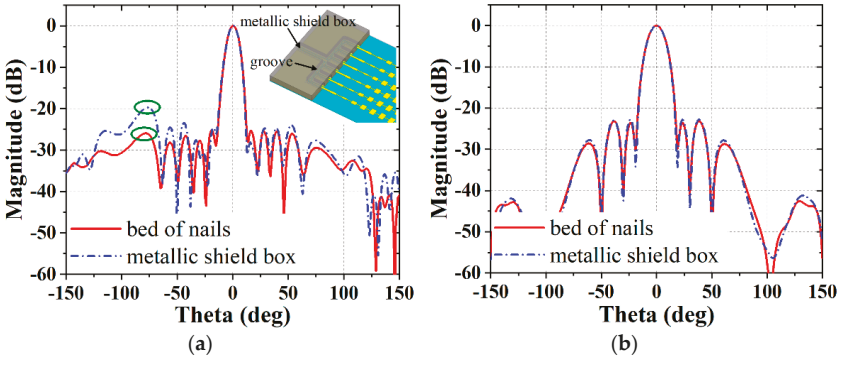

Figure 14. The radiation pattern of the proposed array and the radiation pattern of the planar array with the common package of a metal box. (**a**) E−plane. (**b**) H−plane.

3. Results and Discussion

To measure the designed planar array, a microstrip line to WR-10 waveguide transition is designed and achieves good performance in the frequency band of interest. Then, a prototype of the proposed SLL patch array was fabricated. Figure 15 shows the photograph of a fabricated array prototype. Agilent Vector Network analyzer N5245A and WR-10 mm-wave extenders are employed to measure the reflection coefficient. The measured and simulated reflection coefficients are plotted in Figure 16a. The measured result shows that the frequency range of $|S_{11}| < -10$ dB is 77 to 80.2 GHz. There is a slight discrepancy between the measured and simulated reflection coefficients. The reason can be attributed to manufacturing and assembly tolerances of the transition structure. Given the existence of a quarter-wavelength back-short, small manufacturing errors in the transition will result in a discernible difference in terms of the reflection coefficient.

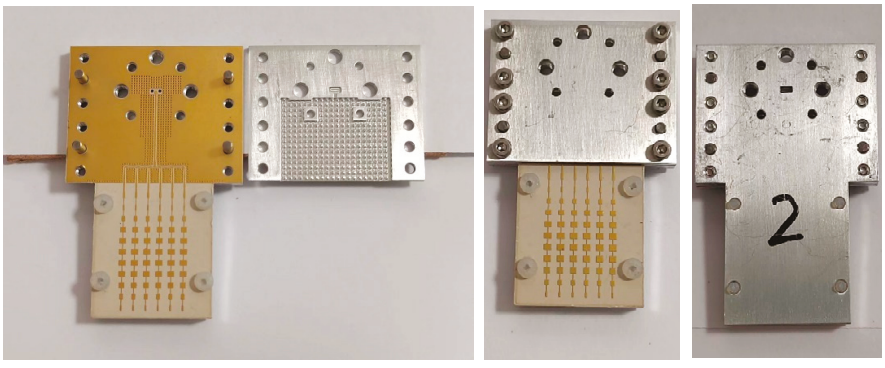

Figure 15. A fabricated prototype of the proposed low-SLL planar array.

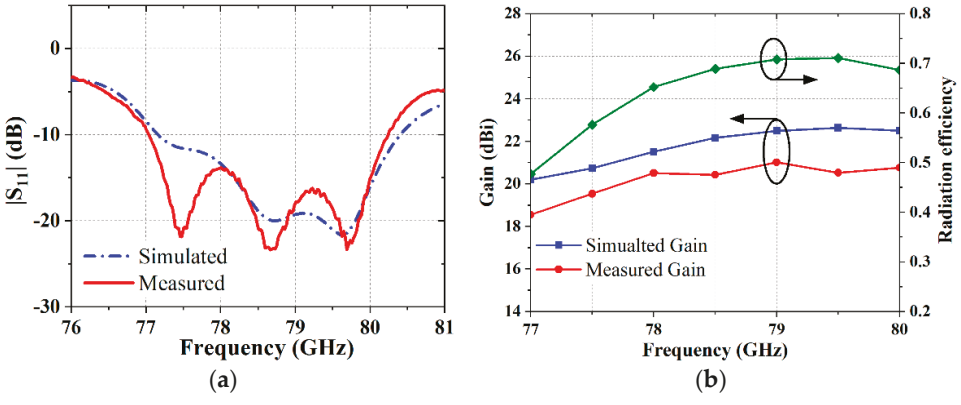

Figure 16. Experimental and simulated data. (**a**) $|S_{11}|$ (**b**) Gain and radiation efficiency.

Moreover, the gains and radiation patterns are measured in an anechoic chamber with a far-field test system. Figure 16b shows the measured and simulated gain in the operating band. The measured peak gains are 20.5 dBi at 78 GHz, 21 dBi at 79 GHz, and 20.76 dBi at 80 GHz, respectively. The measured gains are, on average, 1.5 dB lower than the simulated ones. One reason for this comes from the uncertain dielectric loss tangent. This is because the nominal loss tangent of RO3003 is 0.0013 at 10 GHz, but the design experience shows that the loss tangent of the substrate increases with the operating frequency. Therefore, the actual dielectric loss is higher than the nominal value. Another reason may come from the insertion loss of the microstrip line to the waveguide transition. Usually, the

experimental insertion loss of the transition is higher than the simulated insertion loss due to the material loss (including dielectric loss, conductor loss, and connection loss). Since the directivity cannot be measured in our far-field chamber, only the simulated radiation efficiency is given in Figure 16b. It can be seen that the radiation efficiency is higher than 70% at 79 GHz. Figure 17 shows the simulated and measured radiation in the E-plane and H-plane at 78 GHz, 79 GHz, and 80 GHz, which indicates a good agreement between these two results. The measured SLLs of the E-plane are −20 dB, −24 dB, and −22 dB at 78, 79, and 80 GHz, respectively. The measured SLLs of the H-plane are −21 dB, −23 dB, −22 dB at 78, 79, and 80 GHz, respectively. All of these values are slightly higher than the simulated ones, which are mainly caused by the multipath reflection from the metallic bracket in the anechoic chamber.

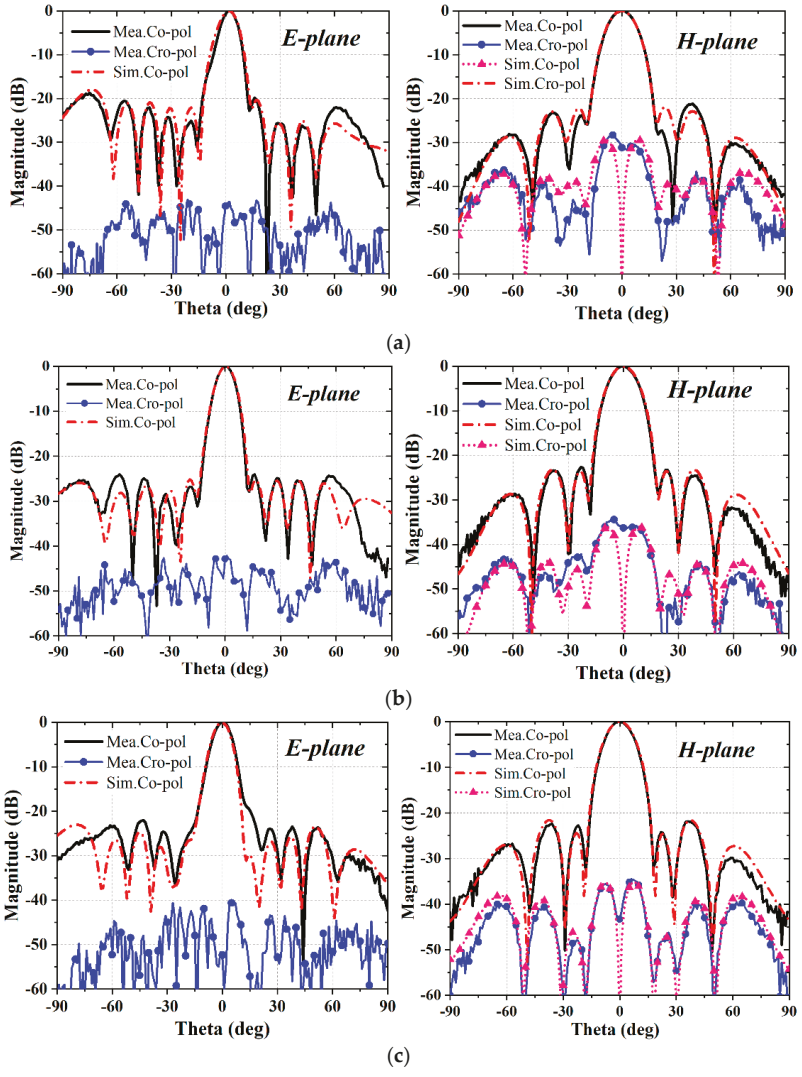

Figure 17. The simulated radiation patterns of the proposed low SLL planar array at (**a**) 78 GHz, (**b**) 79 GHz, and (**c**) 80 GHz.

4. Conclusions

A low-SLL planar array based on linear series-fed patch sub-arrays has been presented in this work. The technical contributions of this work are twofold. On the one hand, a hybrid HFSS-Matlab optimization method is constructed to easily optimize a series-fed sub-array in terms of impedance matching and SLL. The complete design framework of the HFSS-Matlab joint optimizing platform is given. Owing to the accurate results provided by HFSS, the series-fed patch sub-array achieves an SLL of −25 dB in the E-plane at 79 GHz and obtains a good impedance matching from 78 to 80 GHz. Combining a 1-to-6 GCPW distribution network and the optimized series-fed patch array, a high-gain planar array is designed. On the other hand, we propose a simple and effective method for loading the AMC to suppress unwanted radiation from the microstrip-based feeding network. A bed of nails is designed and acts as an AMC. It has the advantages of being low cost and easily fabricated. There is no perfect electrical contact between the AMC structure and feeding network, which greatly facilitates assembly and enhances its practicality. Meanwhile, owing to the EM stopband between the bed of nails and metal ground, the parallel plate modes that might exist in the package of a common metal box do not appear. For verification, the proposed low-SLL planar array is designed, fabricated, and measured. The measured results show that the array has good impedance matching in the designed band from 78 to 80 GHz and a stable radiation performance. Meanwhile, the measured SLLs at 79 GHz are −24 dB and −23 dB in the E-plane and H-plane, which is in good agreement with the simulated results. With the metrics of low cost, low SLL, stable radiation, and ease of integration, the proposed low-SLL planar array is promising for 79-GHz automobile radar applications.

Author Contributions: Conceptualization, Q.T. and K.F.; data curation, Q.T.; formal analysis, Q.T.; methodology, Q.T.; software, Q.T.; validation, K.F., W.Y. and G.L.; investigation, Q.T.; resources, K.F. and G.L.; writing—original draft preparation, Q.T.; writing—review and editing, K.F., W.Y. and G.L.; visualization, Q.T.; supervision, K.F. and G.L.; project administration, K.F.; funding acquisition, K.F. and G.L. All authors have read and agreed to the published version of the manuscript.

Funding: This research was funded by the National Natural Science Foundation of China under Grant 61801156, and Grant 62125105.

Data Availability Statement: Not applicable.

Acknowledgments: The authors would like to thank W. Sun for their assistance in the measurement.

Conflicts of Interest: The authors declare that they have no conflict of interest in the publication of this manuscript.

References

1. Ku, B.H.; Schmalenberg, P.; Inac, O.; Gurbuz, O.D.; Lee, J.S.; Shiozaki, K.J.; Rebeiz, G.M. A 77–81-GHz 16-Element Phased-Array Receiver With ±50° Beam Scanning for Advance Automotive Radars. *IEEE Trans. Microw. Theory Tech.* **2014**, *62*, 2823–2832. [CrossRef]
2. Ahmad, W.A.; Kucharski, M.; Ergintav, A.; Ng, H.J.; Kissinger, D.A. Planar Differential Wide Fan-Beam Antenna Array Architecture: Modular high-gain array for 79-GHz multiple-input, multiple-output radar applications. *IEEE Antennas Propag. Mag.* **2021**, *63*, 21–23. [CrossRef]
3. Engels, F.; Heidenreich, P.; Zoubir, A.M.; Jondral, F.K.; Wintermantel, M. Advances in Automotive Radar: A framework on computationally efficient high-resolution frequency estimation. *IEEE Signal Process. Mag.* **2017**, *34*, 36–46. [CrossRef]
4. Menzel, M.; Moebius, A. Antenna Concepts for Millimeter-Wave Automotive Radar Sensors. *Proc. IEEE* **2012**, *100*, 2372–2379. [CrossRef]
5. Hasch, J.; Topak, E.; Schnabel, R.; Zwick, T.; Weigel, R.; Waldschmidt, C. Millimeter-Wave Technology for Automotive Radar Sensors in the 77 GHz Frequency Band. *IEEE Trans. Microw. Theory Tech.* **2012**, *60*, 845–860. [CrossRef]
6. Harter, M.; Hildebrandt, J.; Ziroff, A.; Zwick, T. Self-Calibration of a 3-D-Digital Beamforming Radar System for Automotive Applications with Installation Behind Automotive Covers. *IEEE Trans. Microw. Theory Tech.* **2016**, *64*, 2994–3000. [CrossRef]
7. Pimentel, J.R. Data heterogeneity, characterization, and integration in the context of autonomous vehicles. In Proceedings of the IECON 2017—43rd Annual Conference of the IEEE Industrial Electronics Society, Beijing, China, 29 October–1 November 2017; pp. 4571–4576.

8. Yin, J.; Wu, Q.; Yu, C.; Wang, H.; Hong, W. Low-Sidelobe-Level Series-Fed Microstrip Antenna Array of Unequal Interelement Spacing. *IEEE Antennas Wirel. Propag. Lett.* **2017**, *16*, 1695–1698. [CrossRef]
9. Kang, Y.; Noh, E.; Kim, K. Design of Traveling-Wave Series-Fed Microstrip Array with a Low Sidelobe Level. *IEEE Antennas Wirel. Propag. Lett.* **2020**, *19*, 1395–1399. [CrossRef]
10. Chopra, R.; Kumar, G. Series-Fed Binomial Microstrip Arrays for Extremely Low Sidelobe Level. *IEEE Trans. Antennas Propag.* **2019**, *67*, 4275–4279. [CrossRef]
11. Khalili, H.; Mohammadpour-Aghdam, K.; Alamdar, S.; Mohammad-Taheri, M. Low-Cost Series-Fed Microstrip Antenna Arrays with Extremely Low Sidelobe Levels. *IEEE Trans. Antennas Propag.* **2018**, *66*, 4606–4612. [CrossRef]
12. Arnieri, A.; Greco, F.; Boccia, L.; Amendola, G. A Reduced Size Planar Grid Array Antenna for Automotive Radar Sensors. *IEEE Antennas Wirel. Propag. Lett.* **2018**, *17*, 2389–2393. [CrossRef]
13. Alsath, M.G.N.; Lawrance, L.; Kanagasabai, M. Bandwidth-Enhanced Grid Array Antenna for UWB Automotive Radar Sensors. *IEEE Trans. Antennas Propag.* **2015**, *63*, 5215–5219. [CrossRef]
14. Khan, O.; Meyer, J.; Baur, K.; Waldschmidt, C. Hybrid Thin Film Antenna for Automotive Radar at 79 GHz. *IEEE Trans. Antennas Propag.* **2017**, *65*, 5076–5085. [CrossRef]
15. Zhang, L.; Zhang, W.; Zhang, Y.P. Microstrip Grid and Comb Array Antennas. *IEEE Trans. Antennas Propag.* **2011**, *59*, 4077–4084. [CrossRef]
16. Mosalanejad, M.; Ocket, I.; Soens, C.; Vandenbosch, G.A.E. Multilayer Compact Grid Antenna Array for 79 GHz Automotive Radar Applications. *IEEE Antennas Wirel. Propag. Lett.* **2018**, *17*, 1677–1681. [CrossRef]
17. Mosalanejad, M.; Ocket, I.; Soens, C.; Vandenbosch, G.A.E. Wideband Compact Comb-Line Antenna Array for 79 GHz Automotive Radar Applications. *IEEE Antennas Wirel. Propag. Lett.* **2018**, *17*, 1580–1583. [CrossRef]
18. Yoo, S.; Milyakh, Y.; Kim, H.; Hong, C.; Choo, H. Patch Array Antenna Using a Dual Coupled Feeding Structure for 79 GHz Automotive Radar Applications. *IEEE Antennas Wirel. Propag. Lett.* **2020**, *19*, 676–679. [CrossRef]
19. Yu, C.A.; Jin, H.Y.; Cao, Y.; Su, G.R.; Che, W.Q.; Chin, K.S. 24 GHz Horizontally Polarized Automotive Antenna Arrays With Wide Fan Beam and High Gain. *IEEE Trans. Antennas Propag.* **2019**, *67*, 892–904. [CrossRef]
20. Yang, X.Y.; Liu, X.F. Design of a Wide-Beam Microstrip Array Antenna for Automotive Radar Application. *IEEE Access* **2021**, *9*, 142340–142347. [CrossRef]
21. Xu, J.; Hong, W.; Zhang, H.; Wang, G.L.; Yu, Y.R.; Jiang, Z.H. An Array Antenna for Both Long- and Medium-Range 77 GHz Automotive Radar Applications. *IEEE Trans. Antennas Propag.* **2017**, *65*, 7207–7216. [CrossRef]
22. Xu, J.F.; Chen, Z.N.; Qing, X.M. CPW Center-Fed Single-Layer SIW Slot Antenna Array for Automotive Radars. *IEEE Trans. Antennas Propag.* **2014**, *62*, 4528–4536. [CrossRef]
23. Shin, D.H.; Kim, K.B.; Kim, J.G.; Park, S.O. Design of Null-Filling Antenna for Automotive Radar Using the Genetic Algorithm. *IEEE Antennas Wirel. Propag. Lett.* **2014**, *13*, 738–741. [CrossRef]
24. Chen, R.S.; Zhu, L.; Wong, S.W.; Yu, X.Z.; Li, Y.; Zhang, L.; He, Y.J. Low-Sidelobe Cavity-Backed Slot Antenna Array With Simplified Feeding Structure for Vehicular Communications. *IEEE Trans. Veh. Technol.* **2021**, *70*, 3652–3660. [CrossRef]
25. Qin, L.T.; Lu, Y.L.; You, Q.C.; Wang, Y.; Huang, J.F.; Gardner, P. Millimeter-Wave Slotted Waveguide Array With Unequal Beamwidths and Low Sidelobe Levels for Vehicle Radars and Communications. *IEEE Trans. Veh. Technol.* **2018**, *70*, 10574–10582. [CrossRef]
26. Yu, Y.R.; Hong, W.; Zhang, H.; Xu, J.; Jiang, Z.H. Optimization and Implementation of SIW Slot Array for Both Medium- and Long-Range 77 GHz Automotive Radar Application. *IEEE Trans. Antennas Propag.* **2018**, *66*, 3769–3774. [CrossRef]
27. Tan, Q.Q.; Chen, K.; Fan, K.K.; Luo, G.Q. A Low-sidelobe Series-fed Microstrip Patch Antenna Array for 77 GHz Automotive Radar Applications. In Proceedings of the 2020 Cross Strait Radio Science & Wireless Technology Conference (CSRSWTC), Fuzhou, China, 3–16 December 2020; pp. 1–3.
28. Sievenpiper, D.; Zhang, L.J.; Broas, R.F.J.; Alexopolous, N.G.; Yablonovitch, E. High-impedance electromagnetic surfaces with a forbidden frequency band. *IEEE Trans. Microw. Theory Tech.* **1999**, *47*, 2059–2074. [CrossRef]
29. Kildal, P.S. Artificially soft and hard surfaces in electromagnetics. *IEEE Trans. Antennas Propag.* **1990**, *38*, 1537–1544. [CrossRef]
30. Valero-Nogueira, A.; Alfonso, E.; Herranz, J.I.; Baquero, M. Planar slot-array antenna fed by an oversized quasi-TEM waveguide. *Microw. Opt. Technol. Lett.* **2007**, *49*, 1875–1877. [CrossRef]
31. Alfonso, E.; Kildal, P.S.; Valero, A.; Herranz, J.H. Study of local quasi-TEM wave in oversize waveguide with one hard wall for killing higher order global modes. In Proceedings of the 2008 IEEE Antennas and Propagation Society International Symposium, San Diego, CA, USA, 5–11 July 2008; pp. 1–4.
32. Padilla de la Torre, P.; Fernández, J.M.; Sierra-Castañer, M. Characterization of artificial magnetic conductor strips for parallel plate planar antennas. *Microw. Opt. Technol. Lett.* **2008**, *50*, 498–504. [CrossRef]
33. Kildal, P.S.; Alfonso, E.; Valero-Nogueira, A.; Raji-Iglesias, E. Local metamaterial-based waveguides in gaps between parallel metal plates. *IEEE Antennas Wirel. Propag. Lett.* **2009**, *8*, 84–87. [CrossRef]
34. Alfonso, E.; Kildal, P.S.P.; Valero-Nogueira, A.; Herranz, J.I. Numerical analysis of a metamaterial-based ridge gap waveguide with a bed of nails as parallel-plate mode killer. In Proceedings of the 2009 3rd European Conference on Antennas and Propagation, Berlin, Germany, 23–27 March 2009; pp. 23–27.
35. Liu, J.L.; Yang, J.; Zaman, A.U. Analytical Solutions to Characteristic Impedance and Losses of Inverted Microstrip Gap Waveguide Based on Variational Method. *IEEE Trans. Antennas Propag.* **2018**, *66*, 7049–7057. [CrossRef]

remote sensing

MDPI

Article

Cramér-Rao Bound of Joint DOA-Range Estimation for Coprime Frequency Diverse Arrays

Zihuan Mao [1,2], Shengheng Liu [1,2,*], Si Qin [3] and Yongming Huang [1,2]

[1] School of Information Science and Engineering, Southeast University, Nanjing 210096, China; mzh@seu.edu.cn (Z.M.); huangym@seu.edu.cn (Y.H.)
[2] Purple Mountain Laboratories, Nanjing 211111, China
[3] Microsoft Research Asia, Beijing 100080, China; si.qin@microsoft.com
* Correspondence: s.liu@seu.edu.cn

Abstract: Frequency diverse array (FDA) produces a beampattern with controllable direction and range by slightly shifting the carrier frequencies across the elements, which is attractive in many applications. By further incorporating coprime array structure and coprime frequency offsets, improved degrees-of-freedom and spatial/range resolutions have been achieved. For such a relatively new array configuration, theoretical performance analyses are essential to explore the potentials and to facilitate practical implementation. In this work, we consider coprime-FDA-based joint/separate angle-range estimation of far-field targets that exhibit two different types of Swerling fluctuation behavior, which are respectively modelled as deterministic and stochastic sources. Analytical expressions of the Cramér–Rao bounds (CRB) and numerical simulations for both cases are provided. The results reveal that the relationship between CRB and coprime FDA parameters is not simply monotonic. As shown in the numerical simulations, the CRB of coprime FDA outperforms that of uniform FDA-MIMO for more than 60% under commonly-adopted coprime patterns. The presented results can be used as a guideline for optimal design of coprime FDA.

Keywords: Cramér–Rao bound (CRB); direction of arrival (DOA); parameter estimation; coprime array; frequency diverse array (FDA)

Citation: Mao, Z.; Liu, S.; Qin, S.; Haung, Y. Cramér-Rao Bound of Joint DOA-Range Estimation for Coprime Frequency Diverse Arrays. *Remote Sens.* **2022**, *14*, 583. https://doi.org/10.3390/rs14030583

Academic Editors: Zhihuo Xu, Jianping Wang and Yongwei Zhang

Received: 8 December 2021
Accepted: 25 January 2022
Published: 26 January 2022

1. Introduction

The concept of frequency diverse array (FDA) was first proposed by Antonik et al. in 2006 [1,2]. In the pioneer work, a small and progressive frequency offset upon the carrier frequency is applied across the radiating elements. The use of element-to-element frequency offset generates a time-range-angle-dependent beampattern. Such a pattern is highly attractive for numerous applications including radar target localization [3–5], synthetic aperture radar (SAR) imaging [6,7], and wireless communications [8], since it enhances the flexibility of beam scanning and offers the potential to resist interference in a specific spatial region [9]. Nevertheless, the FDA beampattern generally exhibits periodicity in angle, range, and time [10,11]. Additionally, a standard FDA, i.e., a uniform linear FDA employing linearly increasing frequency offsets, yields coupling angle and range responses in the far-field beampattern. These unfavorable characteristics conspire to a spatiotemporal periodic S-shaped energy distribution in the angle-range plane, which further leads to ambiguity in target localization.

Owing to the fact that the FDA beampattern distribution can be controlled by tuning the frequency offsets, various solutions, such as time-dependent [12], logarithmic [13,14], and random [15] offsets, have been suggested to achieve a spatial-focusing and also preferably a time-invariant beampattern. Some sophisticated selection mechanisms have also been designed, which includes a transmit subarray strategy [16], adaptive selection scheme [17], and a multi-carrier transmission scheme [18,19], to name but a few. Additionally, by imposing certain evaluation metrics and penalty functions, the problem of frequency

offset selection can be recast as an optimization problem [19]; different algorithms [20–22] have been employed to determine the optimal frequency offset.

The FDA angle-range estimation can also be decoupled from an array structure perspective. For example, many efforts have been made to incorporate the multiple-input multiple-output (MIMO) concept into FDA [4,23,24] to form a range-dependent-only beampattern. For MIMO enjoys the merits of increased degrees-of-freedom (DoF) and spatial diversity gain [25], it has attracted considerable interests. On the other hand, several types of sparse arrays have emerged to provide an enlarged array aperture and to overcome the DoF limitation for a given number of physical sensors. Among these sparse arrays, nested and co-prime configurations are compelling because they are more flexible and permit systematical design guided by explicit close-form expression [26,27]. But the latter is usually preferred, primarily due to the reduced mutual coupling [28,29]. FDA-MIMO radars exploit the DoF in the angle-range domain to jointly estimate the direction and range parameters of the targets [23]. In order to further achieve an improved DoF and spatial/range resolutions, a coprime FDA is proposed [30]. On the one hand, by incorporating the idea of coprime sampling to circumvent the limitation of physical sampling and using the virtual difference coarray concept, coprime FDA shows prominent advantages in terms of DOA-range resolution, localization accuracy, and the number of resolvable targets. Under the space-frequency difference equivalence of a coprime FDA, the unqiue non-negative lags of coarray produce extensive DoFs compared to the physical array [31]. On the other hand, the robustness of the coprime configuration in spatially filtering the interference [32] shows huge potential of adaptive beamforming using coprime FDA.

Objective performance analysis and optimal subarray design strategy are of paramount importance for arrays in practice, and they are often interconnected. In general, the Cramér–Rao bound (CRB) serves as a statistical benchmark to evaluate the degree of suboptimality that a certain unbiased parameter estimator exhibits. CRB also provides insights into the optimization of the array structure (cf., e.g., [20,33–35]). In the field of array signal processing, conventional research with respect to CRB mostly focuses on DOA estimation [36–38]. Motivated by the potentials of coprime FDAs and given the fact that their CRBs with respect to joint DOA-range estimation and the dependence between joint and separate estimations remain as yet uninvestigated, the technical contributions of this work are threefold, which are summarized as follows.

- In an attempt to capture the amplitude fluctuation of a target signal return due to the temporal variations of radar cross-section (RCS), Swerling models were established. Swerling 0 model [39,40] is associated with non-fluctuating RCS, and the radar return of such a target type shows deterministic characteristics. For complex targets that have many small surfaces and joints with different orientations, a Swerling I target-type model [41] is used, and the corresponding receive signal is subject to a stochastic model. In this work, we investigate far-field target detection, and both deterministic and stochastic signal models are considered.
- CRB identifies the potential performance of a signal model with the variance lower bound of unbiased estimation. For DOA-range estimation, the prior information of the radar target makes an impact on the CRB result. In this work, this issue is described as separate parameter estimation, i.e., CRB of DOA (range) estimation while range (DOA) is known. The relation between CRB of separate parameter estimation and CRB of joint estimation is studied via Fisher information with respect to angle and range.
- Analytical form expressions are derived for the input signal-to-noise ratio (SNR) and CRBs of DOA and range. Accordingly, numerical simulations are presented to compare CRBs for deterministic and stochastic source cases, and separate parameter estimation and joint estimation models. According to the analyses of CRB results, an intuitive method for coprime FDA design is proposed based on CRB minimization.

This paper is organized as follows. In Section 2, the configuration of coprime FDA and the transmit-receive steering vectors in deterministic case and stochastic cases are formulated. Based on the steering vectors, the array signal model is given. In Section 3,

the explicit analytical form CRBs of joint estimation and separate estimation in deterministic signal cases are derived in terms of Gaussian distribution probability density function (PDF). When it comes to the stochastic signal case, the CRB is derived on the basis of the matrix form solution [42] in Section 4. Moreover, Section 5 presents some numerical simulations of CRBs in deterministic and stochastic source cases for different uniform FDA structures and coprime FDA structures. The comparisons of CRBs in different scenarios, i.e., two kinds of statistical characteristics and joint/separate estimation are analyzed. Ultimately, we make our conclusion in Section 6.

Notations: Lower (upper)-case bold characters are used to denote vectors (matrices). Vectors are by default in column orientation. $(\cdot)^{\mathrm{T}}$ and $(\cdot)^{\mathrm{H}}$ respectively represent the transpose and Hermitian operators of a matrix. $\mathrm{tr}(\cdot)$ returns the trace of a matrix. Symbol $\odot$ stands for the Hardmard-product. $\mathbb{E}[\cdot]$ returns the expected value of a discrete random variable. ∇ is the Nabla symbol. $\Re$ returns the real part of a complex value. Operators $(\cdot)^{\perp}$ represents the ortho-complement of a projector matrix.

2. Signal Model

In this work we consider a coprime FDA that consists of two collocated uniform linear subarrays. The transmit and receive subarrays respectively have N and M elements, where N and M are coprime integers. The array configuration of the coprime FDA is illustrated in Figure 1.

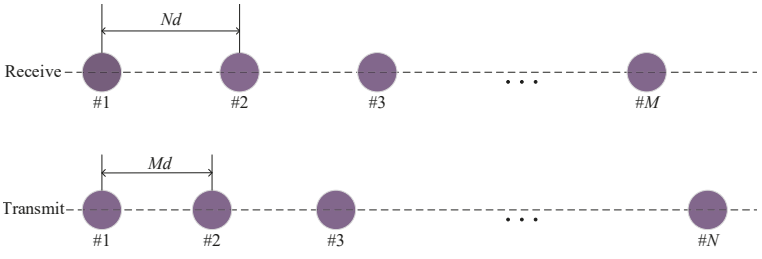

Figure 1. Configuration of the coprime FDA under investigation.

We assume that the unit inter-element spacing d is $\lambda/2$, where λ denotes the wavelength. For a coprime FDA, a frequency increment as a multiple of Δf is applied across the array element. As such, the carrier frequency of the nth transmit element can be expressed as

$$f_n = f_0 + (n-1) \cdot M \cdot \Delta f,\ n = 1, 2, \cdots, N, \tag{1}$$

where f_0 represents the FDA carrier frequency.

In array signal processing, the modelling of signal sources commonly falls into two categories [43], i.e., the deterministic and stochastic models. The former model category is adopted to describe the Swerling 0 type radar targets [39,40] and also in wireless communications [44]. The latter is related to Swerling I type targets and generic interferences [45] in radar applications as well as acoustic signals [46], where the signals are assumed to be driven by a Gaussian random process. In the following, we investigate radar detection performance for Swerling 0 and I targets, where the receive signals are respectively represented by deterministic and stochastic models.

2.1. Deterministic Signal Model

We first establish a deterministic signal model in this subsection. As stated above, we assume that a *priori* knowledge on the scattered waveform from the target is accessible to the radar operators. Consider a far-field Swerling 0 target at position (θ, r), where $r \in [0, c/2\Delta f]$ denotes the range from the far-field target to the first element and $\theta \in$

$[-\pi/2, \pi/2]$ denotes the angle between arrival direction and array normal. Then, in the transmit stage, the phase of the signal radiated from the first element is

$$\varphi_1 = \frac{2\pi f_1}{\mathrm{c}} r. \tag{2}$$

Likewise, we can express the phase of the signal transmitted from the second element as

$$\varphi_2 = \frac{2\pi f_2}{\mathrm{c}}(r - Md\sin\theta) = \frac{2\pi(f_0 + M\Delta f)}{\mathrm{c}}(r - Md\sin\theta). \tag{3}$$

The phase difference between the first and the second elements caused by the path length difference is

$$\Delta\varphi_2 = \varphi_2 - \varphi_1 = \frac{2\pi}{\mathrm{c}}(-f_0 Md \cdot \sin\theta + M\Delta f \cdot r - M^2\Delta f d \cdot \sin\theta). \tag{4}$$

Similarly, the phase of the signal transmitted from the nth transmit element is

$$\varphi_n = \frac{2\pi f_n}{\mathrm{c}}(r - (n-1)Md\sin\theta) = \frac{2\pi(f_0 + M(n-1)\Delta f)}{\mathrm{c}}(r - (n-1)Md\sin\theta). \tag{5}$$

The phase difference $\Delta\varphi_n$ between the first and the nth transmit element is

$$\Delta\varphi_n = \varphi_n - \varphi_1 = \frac{2\pi}{\mathrm{c}}\Big[- f_0(n-1)Md \cdot \sin\theta + (n-1)M\Delta f \cdot r - M^2(n-1)^2\Delta f d \cdot \sin\theta\Big]. \tag{6}$$

By taking the first transmit element as the reference, the transmit steering vector $\mathbf{a}_t(\theta, r)$ is given by

$$\mathbf{a}_t(\theta, r) = [\ a_{t1}(\theta, r),\ a_{t2}(\theta, r),\ \cdots,\ a_{tN}(\theta, r)\ ]^{\mathrm{T}}, \tag{7}$$

where $a_{tn}(\theta, r) = e^{\jmath\Delta\varphi_n}, n = 1, \cdots, N$, and $\jmath = \sqrt{-1}$.

In the receive stage, the receive steering vector corresponding to the carrier frequency $f_n = f_0 + (n-1)M\Delta f$ can be derived as

$$\begin{aligned}\mathbf{a}_{rn}(\theta, r) = &\exp\Big(\tfrac{\jmath 2\pi\cdot(n-1)M\Delta f\cdot r}{\mathrm{c}}\Big)\cdot\\ &\big[\ 1,\quad \exp\big(-\jmath\tfrac{2\pi}{\mathrm{c}}(f_0 + (n-1)M\Delta f)Nd\sin\theta\big), \cdots,\\ &\quad \exp\big(-\jmath\tfrac{2\pi}{\mathrm{c}}(f_0 + (n-1)M\Delta f)(M-1)Nd\sin\theta\big)\ \big]^{\mathrm{T}}.\end{aligned} \tag{8}$$

The first term denotes the phase shift caused by carrier frequency f_n, and the vector in the steering vector corresponds to the sparse receive array. To concentrate on the impact of coprime FDA structure, we consider an ideal case without mutual coupling and other hardware impairments in this work. Therefore, the overall transmit-receive steering vector $\mathbf{a}(\theta, r) \in \mathbb{C}^{MN\times 1}$ which captures the phase difference generated in the transmit-receive stages can be written as

$$\mathbf{a}(\theta, r) = \Big[\ a_{t1}(\theta, r)\cdot\mathbf{a}_{r1}^{\mathrm{T}}, \cdots, a_{tN}(\theta, r)\cdot\mathbf{a}_{rN}^{\mathrm{T}}\ \Big]^{\mathrm{T}}. \tag{9}$$

More concretely, the entry in $\mathbf{a}(\theta, r)$ that corresponds to the nth transmit element and the mth receive element is

$$\begin{aligned}a_{n,m}(\theta, r) = &\exp\Big(-\jmath\frac{2\pi}{\mathrm{c}}\big(f_0 M(n-1)d\sin\theta - 2\Delta f M(n-1)r + \Delta f M^2(n-1)^2 d\sin\theta\big)\Big)\\ &\cdot\exp\Big(-\jmath\frac{2\pi}{\mathrm{c}}\big(f_0 + M(n-1)\Delta f\big)\big(m-1\big)Nd\sin\theta\Big).\end{aligned} \tag{10}$$

Overall, the output of matched filter corresponding to the nth transmit element and the mth receive element can be expressed as

$$y_{n,m}(k) = a_{n,m}(\theta, r)s_{\text{det}}(k) + n_{n,m}(k), \quad k = 1, \cdots, K, \tag{11}$$

where $s_{\text{det}}(k), k = 1, \cdots, K$ denotes a signal with non-zero mean and zero variance [45]. Furthermore, $n_{n,m}(k)$ is the additive white Gaussian noise. Stacking $y_{n,m}(k)$ for all $n = 1, \cdots, N$ and $m = 1, \cdots, M$ yields an $MN \times 1$ vector and we have the deterministic receive signal vector

$$\mathbf{y}_{\text{det}}(k) = \mathbf{a}(\theta, r)s_{\text{det}}(k) + \mathbf{n}(k), \quad k = 1, \cdots, K. \tag{12}$$

2.2. Stochastic Signal Model

In this subsection we discuss the stochastic signal model that is used in Swerling I type target detection. Concretely, the statistics are governed by a chi-squared probability density function with two DoFs, and the echoed signal is modelled as a complex Gaussian process with zero mean and known variance. Suppose that we have a target at (ψ, l). By following a similar derivation to (12), we obtain the stochastic receive signal vector below:

$$\mathbf{y}_{\text{sto}}(k) = \mathbf{a}(\psi, l)s_{\text{sto}}(k) + \mathbf{n}(k), \quad k = 1, \cdots, K, \tag{13}$$

where $s_{\text{sto}}(k), k = 1, \cdots, K$ denotes a stochastic signal driven by a complex Gaussian process $\mathcal{N}(0, \delta_s^2)$. We so far have established two different signal models for coprime FDA, which serve as the foundation for the following analyses of CRBs for joint DOA-range estimation in the following sections.

3. CRB of Deterministic Signal for Coprime FDA

3.1. Deterministic Signal Model and CRB Derivation

The deterministic CRB is the lower bound of the square error for target parameter estimation, which precisely defines the performance boundary of a specific array system, and is commonly used as the benchmark for the evaluation of estimation algorithms [43]. In this section, we derive the CRB of deterministic signal model.

Recall that the far-field target is located at (θ, r). The matched filter at output of the receive antenna array can be expressed as (12). The covariance matrix of the zero-mean complex Gaussian white noise vector $\mathbf{n}(k)$ is

$$\mathbf{R}_{\mathbf{n}} = \mathbb{E}\left[\mathbf{n}(k)\mathbf{n}^{\text{H}}(k)\right] = \sigma_n^2 \mathbf{I}_{MN}, \tag{14}$$

where σ_n^2 is the noise power, and $\mathbf{I}_{MN}$ denotes the $MN \times MN$ identity matrix.

For simplicity of derivation, the subscript of $\mathbf{y}_{\text{det}}(k)$ is omitted and the estimation parameters (θ, r) are denoted as $\boldsymbol{\alpha}$. We first consider the single-snapshot case, in which the observed vector follows a Gaussian distribution, i.e., $\mathbf{y} \sim \mathcal{N}(\mathbf{m}_{\mathbf{y}}(\boldsymbol{\alpha}), \sigma_n^2 \mathbf{I}_{MN})$, where $\mathbf{m}_{\mathbf{y}}(\boldsymbol{\alpha})$ represents the mean value of the observed vector $\mathbf{y}$. As such, the PDF of $\mathbf{y}$ is

$$P_{\mathbf{y}|\boldsymbol{\alpha}}(\mathbf{y}) = \frac{1}{\det(\pi \mathbf{R}_{\mathbf{n}})} \cdot \exp\left\{-(\mathbf{y} - \mathbf{m}_{\mathbf{y}}(\boldsymbol{\alpha}))\mathbf{R}_{\mathbf{n}}^{-1}(\mathbf{y} - \mathbf{m}_{\mathbf{y}}(\boldsymbol{\alpha}))^{\text{H}}\right\}, \tag{15}$$

where $\det(\cdot)$ denotes the matrix determinant. Then, the log-likelihood function of $\mathbf{y}$ is expressed as

$$\mathcal{L}_{\mathbf{y}}(\boldsymbol{\alpha}) \triangleq \ln P_{\mathbf{y}|\boldsymbol{\alpha}}(\mathbf{y}) = -\ln\det(\pi \mathbf{R}_{\mathbf{n}}) - \{(\mathbf{y} - \mathbf{m}_{\mathbf{y}}(\boldsymbol{\alpha}))\mathbf{R}_{\mathbf{n}}^{-1}(\mathbf{y} - \mathbf{m}_{\mathbf{y}}(\boldsymbol{\alpha}))^{\text{H}}\}. \tag{16}$$

The CRB gives the lower bound of the variance of unbiased estimation for parameter set $\boldsymbol{\alpha}$, which is denoted as $\hat{\mathbf{a}}$. That is to say, the covariance matrix $\mathbf{C}(\boldsymbol{\alpha}) \triangleq \mathbb{E}[(\hat{\boldsymbol{\alpha}} - \boldsymbol{\alpha})(\hat{\boldsymbol{\alpha}} - \boldsymbol{\alpha})^{\mathrm{T}}]$ satisfies the following inequality:

$$\mathbf{C}(\boldsymbol{\alpha}) \succeq \mathbf{C}_{\mathrm{CR}}(\boldsymbol{\alpha}) \triangleq \mathbf{J}^{-1}, \tag{17}$$

where $\mathbf{J}$ is the Fisher information matrix (FIM) giving by

$$\mathbf{J} = -\mathbb{E}\Big[\nabla_{\boldsymbol{\alpha}} \nabla_{\boldsymbol{\alpha}}{}^{\mathrm{T}} \mathcal{L}_{\mathbf{y}}(\boldsymbol{\alpha})\Big], \tag{18}$$

and $\nabla_{\boldsymbol{\alpha}} = \left[\frac{\partial}{\partial \theta} \;\; \frac{\partial}{\partial r}\right]^{\mathrm{T}}$. Furthermore, for deterministic signals,

$$J_{i,j} = \frac{\partial^2}{\partial \alpha_i \partial \alpha_j}[\mathcal{L}_{\mathbf{y}}(\boldsymbol{\alpha})] = 2 \cdot \Re\left\{\frac{\partial \mathbf{m}_{\mathbf{y}}^{\mathrm{H}}(\boldsymbol{\alpha})}{\partial \alpha_i} \cdot \mathbf{R}_{\mathbf{n}}^{-1} \cdot \frac{\partial \mathbf{m}_{\mathbf{y}}(\boldsymbol{\alpha})}{\partial \alpha_j}\right\}, \tag{19}$$

where $J_{i,j}$ represents the element of the ith row and the jth column, α_i represents the ith parameter in $\boldsymbol{\alpha}$. The detailed proof of (19) can be found in Appendix A. Therefore, the CRBs for parameter estimation are obtained as follows

$$\mathrm{CRB}(\boldsymbol{\alpha}) = \begin{bmatrix} \mathrm{CRB}(\theta) & \\ & \mathrm{CRB}(r) \end{bmatrix} = \mathrm{diag}(\mathbf{J}^{-1} \odot \mathbf{I}), \tag{20}$$

where $\mathrm{diag}(\cdot)$ returns the diagonal elements of the matrix as a vector.

3.2. CRB of Joint DOA-Range Estimation

As mentioned above, the steering vector of coprime FDA is a function of both range and angle which leads to the capacity of joint DOA-range estimation. For the situation where the DOA and the range of the far-field target are both unknown and need to be estimated jointly, the corresponding FIM is expressed as

$$\mathbf{J} = \begin{bmatrix} J_{\theta\theta} & J_{\theta r} \\ J_{r\theta} & J_{rr} \end{bmatrix}. \tag{21}$$

Based on the deterministic signal model established in Section 2.1, we first derive the analytical expression of Fisher information with respect to θ. Formula (19) is first rewritten as

$$J_{1,1} = \frac{\partial^2}{\partial \theta^2}[\mathcal{L}_{\mathbf{y}}(\boldsymbol{\alpha})] = 2 \cdot \frac{\partial \mathbf{m}_{\mathbf{y}}^{\mathrm{H}}(\boldsymbol{\alpha})}{\partial \theta} \cdot \mathbf{R}_{\mathbf{n}}^{-1} \cdot \frac{\partial \mathbf{m}_{\mathbf{y}}(\boldsymbol{\alpha})}{\partial \theta} = 2 \cdot \frac{A_{\mathbf{y}}^2}{\sigma_n^2} \cdot \frac{\partial \mathbf{a}^{\mathrm{H}}(\theta, r)}{\partial \theta} \cdot \frac{\partial \mathbf{a}(\theta, r)}{\partial \theta}, \tag{22}$$

where $A_{\mathbf{y}}^2 = |\mathbf{m}_{\mathbf{y}}(\boldsymbol{\alpha})|^2$ represents the power of the deterministic signal. For each element $a_{n,m}(\theta, r)$ in the steering vector $\mathbf{a}(\theta, r)$, we readily obtain

$$\begin{aligned} \frac{\partial a_{n,m}(\theta, r)}{\partial \theta} = a_{n,m}(\theta, r) \cdot (-\jmath\eta) \cdot \Big\{ & f_0 \cdot [M(n-1) + N(m-1)] \\ & + \Delta f \cdot [M^2(n-1)^2 + MN(m-1)(n-1)] \Big\}, \end{aligned} \tag{23}$$

where $\eta = 2\pi d \cos\theta / \mathrm{c}$. Substituting (23) into (22) and considering the property $\Delta f^2 \ll f_0^2$, we have the following approximation

$$\frac{\partial \mathbf{a}^{\mathrm{H}}(\theta,r)}{\partial \theta}\cdot\frac{\partial \mathbf{a}(\theta,r)}{\partial \theta}=\eta^2 f_0^2\sum_{m=0}^{M-1}\sum_{n=0}^{N-1}(Mn+Nm)^2$$
$$+\eta^2\Delta f^2\sum_{m=0}^{M-1}\sum_{n=0}^{N-1}(M^2n^2+MNmn)^2+2\eta^2\Delta f f_0\sum_{m=0}^{M-1}\sum_{n=0}^{N-1}(M^3n^3+2M^2Nmn^2+MN^2m^2n)$$
$$\approx\eta^2 f_0^2\left(M^3\sum_{n=0}^{N-1}n^2+N^3\sum_{m=0}^{M-1}m^2+2MN\sum_{m=0}^{M-1}m\sum_{n=0}^{N-1}n\right)$$
$$+2\eta^2\Delta f f_0\left(M^4\sum_{n=0}^{N-1}n^3+2M^2N\sum_{m=0}^{M-1}m\sum_{n=0}^{N-1}n^2+MN^2\sum_{m=0}^{M-1}m^2\sum_{n=0}^{N-1}n\right). \tag{24}$$

Accordingly, the Fisher information with respect to θ for the coprime FDA can be expressed as (25),

$$J_{\theta\theta}=J_{1,1}$$
$$=2\cdot\mathrm{SNR}\cdot\frac{4\pi^2d^2\cos^2\theta}{\mathrm{c}^2}\cdot\left\{f_0^2\cdot\left(M^3\sum_{n=0}^{N-1}n^2+N^3\sum_{m=0}^{M-1}m^2+2MN\sum_{m=0}^{M-1}m\sum_{n=0}^{N-1}n\right)\right.$$
$$\left.+2\cdot\Delta f f_0\cdot\left(M^4\sum_{n=0}^{N-1}n^3+2M^2N\sum_{m=0}^{M-1}m\sum_{n=0}^{N-1}n^2+MN^2\sum_{m=0}^{M-1}m^2\sum_{n=0}^{N-1}n\right)\right\}$$
$$=2\cdot\mathrm{SNR}\cdot\frac{4\pi^2d^2\cos^2\theta f_0}{\mathrm{c}^2}\cdot\left\{f_0\cdot\frac{(7M^3-6M^2+M)N^3+(-6M^3+3M^2)N^2+M^3N}{6}\right.$$
$$\left.+\Delta f\cdot\frac{(9M^4-7M^3+M^2)N^4+(-14M^4+9M^3-M^2)N^3+(5M^4-2M^3)N^2}{6}\right\}. \tag{25}$$

We next consider the Fisher information with respect to r. Similar to the derivation of (22), we obtain the Fisher information with respect to r as follows:

$$J_{2,2}=\frac{\partial^2}{\partial r^2}[\mathcal{L}_{\mathbf{y}}(\boldsymbol{\alpha})]=2\cdot\frac{A_{\mathbf{y}}^2}{\sigma_n^2}\cdot\frac{\partial \mathbf{a}^{\mathrm{H}}(\theta,r)}{\partial r}\cdot\frac{\partial \mathbf{a}(\theta,r)}{\partial r}. \tag{26}$$

We also get

$$\frac{\partial a_{n,m}(\theta,r)}{\partial r}=a_{n,m}(\theta,r)\cdot\frac{\jmath 2\pi\Delta f}{\mathrm{c}}\cdot(n-1)2M, \tag{27}$$

and

$$\frac{\partial \mathbf{a}^{\mathrm{H}}(\theta,r)}{\partial r}\cdot\frac{\partial \mathbf{a}(\theta,r)}{\partial r}=\left(\frac{2\pi\Delta f}{\mathrm{c}}\right)^2\cdot4M^3\cdot\sum_{n=0}^{N-1}n^2. \tag{28}$$

Thus, the Fisher information with respect to r is expressed as

$$J_{rr}=J_{2,2}=2\mathrm{SNR}\cdot\frac{4\pi^2\Delta f^2}{\mathrm{c}^2}\cdot4M^3\cdot\sum_{n=0}^{N-1}n^2$$
$$=2\cdot\mathrm{SNR}\cdot\frac{4\pi^2\Delta f^2}{\mathrm{c}^2}\cdot\left(\frac{8M^3N^3-12M^3N^2+4M^3N}{6}\right). \tag{29}$$

Thus far, $J_{\theta\theta}$ and J_{rr} have been derived. In addition, we know that $J_{\theta r}=J_{r\theta}$ and we have

$$J_{1,2}=2\cdot\Re\left\{\frac{\partial \mathbf{m}_{\mathbf{y}}^{\mathrm{H}}(\boldsymbol{\alpha})}{\partial\theta}\cdot\mathbf{R}_{\mathbf{n}}^{-1}\cdot\frac{\partial \mathbf{m}_{\mathbf{y}}(\boldsymbol{\alpha})}{\partial r}\right\}=2\cdot\frac{A_{\mathbf{y}}^2}{\sigma_n^2}\cdot\Re\left\{\frac{\partial \mathbf{a}^{\mathrm{H}}(\theta,r)}{\partial\theta}\cdot\frac{\partial \mathbf{a}(\theta,r)}{\partial r}\right\}. \tag{30}$$

We further obtain

$$\frac{\partial \mathbf{a}^{\mathrm{H}}(\theta,r)}{\partial \theta}\cdot\frac{\partial \mathbf{a}(\theta,r)}{\partial r}=\frac{8\pi^2 d\cos\theta\Delta f}{\mathrm{c}^2}\cdot \left\{f_0\big(M^3\sum_{n=0}^{N-1}n^2+MN\sum_{m=0}^{M-1}m\sum_{n=0}^{N-1}n\big)+\Delta f\big(M^4\sum_{n-0}^{N-1}n^3+M^2N\sum_{m=0}^{M-1}m\sum_{n=0}^{N-1}n^2\big)\right\}. \tag{31}$$

Hence, Fisher information with respect to θ and r is computed as (32),

$$\begin{aligned} J_{\theta r}=J_{1,2}&=2\cdot\mathrm{SNR}\cdot\frac{8\pi^2 d\cos\theta\Delta f}{\mathrm{c}^2}\cdot \left\{f_0\left(M^3\sum_{n=0}^{N-1}n^2+MN\sum_{m=0}^{M-1}m\sum_{n=0}^{N-1}n\right)+\Delta f\left(M^4\sum_{n-0}^{N-1}n^3+M^2N\sum_{m=0}^{M-1}m\sum_{n=0}^{N-1}n^2\right)\right\}\\ &=2\cdot\mathrm{SNR}\cdot\frac{8\pi^2 d\cos\theta\Delta f}{c^2}\cdot\left\{f_0\cdot\frac{(7M^3-3M^2)N^3+(-9M^3+3M^2)N^2+2M^3N}{12}\right.\\ &\left.+\Delta f\cdot\frac{(5M^4-2M^3)N^4+(-9M^4+3M^3)N^3+(4M^4-M^3)N^2}{12}\right\}. \end{aligned} \tag{32}$$

Substituting (25), (29) and (32) into (20) yields the analytical expression of the CRB for the joint DOA-range estimation, given as

$$\mathrm{CRB}_\theta=\left[\mathbf{J}^{-1}\right]_{1,1}=\frac{1}{J_{\theta\theta}-\frac{J_{\theta r}J_{r\theta}}{J_{rr}}}, \tag{33}$$

$$\mathrm{CRB}_r=\left[\mathbf{J}^{-1}\right]_{2,2}=\frac{1}{J_{rr}-\frac{J_{\theta r}J_{r\theta}}{J_{\theta\theta}}}, \tag{34}$$

where $\left[\cdot\right]_{i,j}$ denotes the element of the ith row and the jth column. For the K-snapshot case, the Fisher information are scaled up by a factor of K on the basis of (25), (29) and (32). As a result, the CRBs are scaled down by a factor of K on the basis of (33) and (34).

According to above results, we notice that all Fisher information increase with the coprime FDA parameters, i.e., coprime integers M, N and the carrier increment Δf. Clearly, the Fisher information $J_{\theta\theta}$ of an FDA is generally greater than or equal to that of a phased array and, in particular, the equality holds when $\Delta f=0$. Nevertheless, this does not lead to the conclusion that CRB_θ decreases with the increase of Δf. The reason is that the CRB of joint DOA-range estimation is also influenced by the fisher information $J_{\theta r}$, which increases with Δf. As a result, the mutual dependence of the DOA and the range estimations are stronger in the joint estimation case. As will be shown in the numerical results of Section 5, the relationship between CRB_θ and Δf is nonmonotonic.

3.3. CRB of Separate Estimation

If either parameter of $\boldsymbol{\alpha}=(\theta,r)$ is known, the problem of joint parameter estimation degrades to a separate parameter estimation problem. In this subsection, we assume a certain one of the target parameters is known from a previous detection [47,48]. Based on the Fisher information with respect to θ and r established in Section 2.2, we derive the analytical expression of CRB of DOA (range) estimation with coprime FDA parameters while the range (DOA) is known. The CRBs of separate estimation, which are denoted as SCRB, are given by

$$\mathrm{SCRB}_\theta=\frac{1}{J_{\theta\theta}}\quad\text{and}\quad\mathrm{SCRB}_r=\frac{1}{J_{rr}}. \tag{35}$$

We readily observe from (35) that, SCRB_θ decreases with the increase of the coprime FDA parameters, but the impact of Δf to SCRB_θ is very limited, for coprime FDA is narrowband in nature. This result agrees with our common sense that the performance of DOA

estimation is fundamentally determined by the array aperture. Likewise, SCRB_r decreases with the increase of the coprime FDA parameters.

4. CRB of Stochastic Signal for Coprime FDA

4.1. Stochastic Signal Model and CRB Derivation

In the following, we examine the stochastic signal case and derive the CRB for parameter estimation in coprime FDA. For notational convenience, we also simplify $s_{\mathrm{sto}}(k)$ and the estimation parameters (ψ, l) as $s(k)$ and $\boldsymbol{\xi}$, respectively. The mean and variance of the observed vectors $\mathbf{y}_{\mathrm{sto}}(k)$ are respectively assumed to be

$$\mathbf{m}_{\mathbf{y}}(\boldsymbol{\xi}) = 0, \tag{36}$$

$$\mathbf{R}_{\mathbf{y}}(\boldsymbol{\xi}) = \mathbf{a}\sigma_s^2\mathbf{a}^{\mathrm{H}} + \sigma_n^2\mathbf{I}_{MN}. \tag{37}$$

The log-likelihood function of $\mathbf{y}$ is expressed as

$$\mathcal{L}_{\mathbf{y}}(\boldsymbol{\xi}) \triangleq \ln P_{\mathbf{y}|\boldsymbol{\xi}}(\mathbf{y}) = -\ln\det(\pi\mathbf{R}_{\mathbf{y}}) - \mathbf{y}\mathbf{R}_{\mathbf{y}}^{-1}\mathbf{y}^{\mathrm{H}}, \tag{38}$$

where $\det(\cdot)$ represents the matrix determinant. Similar to the deterministic signal case, according to the matrix form solution [42], the FIM of stochastic signal can be written as

$$\mathbf{J} = -\mathbb{E}\left[\nabla_{\boldsymbol{\xi}}\nabla_{\boldsymbol{\xi}}{}^{\mathrm{T}}L_{\mathbf{y}}(\boldsymbol{\xi})\right] = \frac{2}{\sigma_n^2}\Re\{(\sigma_s{}^2\mathbf{a}\mathbf{R}_{\mathbf{y}}^{-1}\mathbf{a}\sigma_s{}^2)\cdot(\nabla_{\boldsymbol{\xi}}\mathbf{a}^{\mathrm{H}}\mathbf{P}_{\mathbf{a}}^{\perp}\nabla_{\boldsymbol{\xi}}\mathbf{a})\}, \tag{39}$$

where $\nabla_{\boldsymbol{\xi}} = \left[\frac{\partial}{\partial\psi} \quad \frac{\partial}{\partial l}\right]^{\mathrm{T}}$ and $\mathbf{P}_{\mathbf{a}}^{\perp} = \mathbf{I} - \mathbf{a}(\mathbf{a}^{\mathrm{H}}\mathbf{a})^{-1}\mathbf{a}^{\mathrm{H}}$. In order to facilitate the numerical computing, the former factor in (39) is expressed as

$$\sigma_s{}^2\mathbf{a}^{\mathrm{H}}\mathbf{R}_{\mathbf{y}}^{-1}\mathbf{a}\sigma_s{}^2 = [\mathbf{I} - \mathbf{a}^{\mathrm{H}}\mathbf{a}\Sigma(\mathbf{a}^{\mathrm{H}}\mathbf{a}\Sigma + \mathbf{I})^{-1}]\mathbf{a}^{\mathrm{H}}\mathbf{a}\Sigma = \frac{MN\cdot\mathrm{SNR}}{1+MN\cdot\mathrm{SNR}}\cdot\sigma_s^2, \tag{40}$$

where $\Sigma = \sigma_s^2/\sigma_n^2 = \mathrm{SNR}$. The readers are referred to the proof given in Appendix B for more details. The latter factor in (39) can be reformulated as

$$\nabla_{\boldsymbol{\xi}}\mathbf{a}^{\mathrm{H}}\mathbf{P}_{\mathbf{a}}{}^{\perp}\nabla_{\boldsymbol{\xi}}\mathbf{a} = \nabla_{\boldsymbol{\xi}}\mathbf{a}^{\mathrm{H}}[\mathbf{I} - \mathbf{a}(\mathbf{a}^{\mathrm{H}}\mathbf{a})^{-1}\mathbf{a}^{\mathrm{H}}]\nabla_{\boldsymbol{\xi}}\mathbf{a} = \nabla_{\boldsymbol{\xi}}\mathbf{a}^{\mathrm{H}}\cdot\nabla_{\boldsymbol{\xi}}\mathbf{a} - \frac{1}{MN}\cdot\nabla_{\boldsymbol{\xi}}\mathbf{a}^{\mathrm{H}}\cdot\mathbf{a}\mathbf{a}^{\mathrm{H}}\cdot\nabla_{\boldsymbol{\xi}}\mathbf{a}. \tag{41}$$

Hence, the FIM of stochastic signal can be derived as

$$\mathbf{J} = 2\cdot\frac{MN\cdot\mathrm{SNR}^2}{1+MN\cdot\mathrm{SNR}}\cdot\left(\nabla_{\boldsymbol{\xi}}\mathbf{a}^{\mathrm{H}}\cdot\nabla_{\boldsymbol{\xi}}\mathbf{a} - \frac{1}{MN}\cdot\nabla_{\boldsymbol{\xi}}\mathbf{a}^{\mathrm{H}}\cdot\mathbf{a}\mathbf{a}^{\mathrm{H}}\cdot\nabla_{\boldsymbol{\xi}}\mathbf{a}\right). \tag{42}$$

4.2. CRB of Joint DOA-Range Estimation

Similar to the analysis of the deterministic signals, in deriving the analytical form CRB of joint DOA-range estimation, the corresponding joint FIM is expressed as

$$\mathbf{J} = \begin{bmatrix} J_{\psi\psi} & J_{\psi l} \\ J_{l\psi} & J_{ll} \end{bmatrix}. \tag{43}$$

According to Formula (42), the Fisher information with respect to ψ is

$$J_{1,1} = 2\cdot\frac{MN\cdot\mathrm{SNR}^2}{1+MN\cdot\mathrm{SNR}}\cdot\left(\frac{\partial\mathbf{a}^{\mathrm{H}}(\psi,l)}{\partial\psi}\cdot\frac{\partial\mathbf{a}(\psi,l)}{\partial\psi} - \frac{1}{MN}\cdot\frac{\partial\mathbf{a}^{\mathrm{H}}(\psi,l)}{\partial\psi}\cdot\mathbf{a}\mathbf{a}^{\mathrm{H}}\cdot\frac{\partial\mathbf{a}(\psi,l)}{\partial\psi}\right). \tag{44}$$

For arbitrary element $a_{n,m}(\psi,l)$ in the steering vector $\mathbf{a}(\psi,l)$, which corresponds to the nth transmit element and the mth receive element, we have

$$\frac{\partial a_{n,m}(\psi,l)}{\partial \psi}=\frac{\partial a_{n,m}(\theta,r)}{\partial \theta}\Big|_{\theta=\psi,r=l}. \tag{45}$$

Since $\Delta f^2 \ll f_0^2$, we further have

$$\frac{\partial \mathbf{a}^{\mathrm{H}}(\psi,l)}{\partial \psi}\cdot\frac{\partial \mathbf{a}(\psi,l)}{\partial \psi}=\frac{\partial \mathbf{a}^{\mathrm{H}}(\theta,r)}{\partial \theta}\cdot\frac{\partial \mathbf{a}(\theta,r)}{\partial \theta}\Big|_{\theta=\psi,r=l}, \tag{46}$$

and

$$\begin{aligned}&\frac{\partial \mathbf{a}^{\mathrm{H}}(\psi,l)}{\partial \psi}\cdot\mathbf{a}\mathbf{a}^{\mathrm{H}}\cdot\frac{\partial \mathbf{a}(\psi,l)}{\partial \psi}=\left\|\frac{\partial \mathbf{a}^{\mathrm{H}}(\psi,l)}{\partial \psi}\cdot\mathbf{a}\right\|^2\\&=\vartheta^2\left\{f_0\left(M^2\sum_{n=0}^{N-1}n+N^2\sum_{m=0}^{M-1}m\right)+\Delta f\left(M^3\sum_{n=0}^{N-1}n^2+MN\sum_{m=0}^{M-1}m\sum_{n=0}^{N-1}n\right)\right\}^2,\end{aligned} \tag{47}$$

where $\vartheta=2\pi d\cos\psi/\mathrm{c}$. Substituting (47) into (44), the Fisher information with respect to ψ is derived as (48),

$$\begin{aligned}J_{\psi\psi}&=2\cdot\frac{MN\cdot\mathrm{SNR}^2}{1+MN\cdot\mathrm{SNR}}\cdot\frac{4\pi^2d^2\cos^2\psi f_0}{\mathrm{c}^2}\cdot\left\{f_0\cdot\left(M^3\sum_{n=0}^{N-1}n^2+N^3\sum_{m=0}^{M-1}M^2+2MN\sum_{m=0}^{M-1}M\sum_{n=0}^{N-1}N\right)\right.\\&+2\cdot\Delta f\cdot\left(M^4\sum_{n=0}^{N-1}n^3+2M^2N\sum_{m=0}^{M-1}m\sum_{n=0}^{N-1}n^2+MN^2\sum_{m=0}^{M-1}m^2\sum_{n=0}^{N-1}n\right)-\frac{f_0}{MN}\cdot\left(M^2\sum_{n=0}^{N-1}n+N^2\sum_{m=0}^{M-1}m\right)^2\\&\left.-2\cdot\frac{\Delta f}{MN}\cdot\left(M^2\sum_{n=0}^{N-1}n+N^2\sum_{m=0}^{M-1}m\right)\left(M^3\sum_{n=0}^{N-1}n^2+MN\sum_{m=0}^{M-1}m\sum_{n=0}^{N-1}n\right)\right\}\\&=2\cdot\frac{MN\cdot\mathrm{SNR}^2}{1+MN\cdot\mathrm{SNR}}\cdot\frac{4\pi^2d^2\cos^2\psi f_0}{\mathrm{c}^2}\cdot\left\{f_0\cdot\frac{(2M^3-M)N^3-M^3N}{12}\right.\\&\left.+\Delta f\cdot\frac{(4M^4-M^3-M^2)N^4+(-3M^4+M^2)N^3+(-3M^4+M^3)N^2+2M^4N}{12}\right\}.\end{aligned} \tag{48}$$

In the same way, the Fisher information with respect to l is

$$J_{2,2}=2\cdot\frac{MN\cdot\mathrm{SNR}^2}{1+MN\cdot\mathrm{SNR}}\cdot\left(\frac{\partial \mathbf{a}^{\mathrm{H}}(\psi,l)}{\partial l}\cdot\frac{\partial \mathbf{a}(\psi,l)}{\partial l}-\frac{1}{MN}\cdot\frac{\partial \mathbf{a}^{\mathrm{H}}(\psi,l)}{\partial l}\cdot\mathbf{a}\mathbf{a}^{\mathrm{H}}\cdot\frac{\partial \mathbf{a}(\psi,l)}{\partial l}\right). \tag{49}$$

For arbitrary element $a_{n,m}(\psi,l)$, we can get

$$\frac{\partial a_{n,m}(\psi,l)}{\partial l}=\frac{\partial a_{n,m}(\theta,r)}{\partial r}\Big|_{\theta=\psi,r=l}. \tag{50}$$

Likewise, the first term in between the parentheses in (49) can be reformulated as

$$\frac{\partial \mathbf{a}^{\mathrm{H}}(\psi,l)}{\partial l}\cdot\frac{\partial \mathbf{a}(\psi,l)}{\partial l}=\frac{\partial \mathbf{a}^{\mathrm{H}}(\theta,r)}{\partial r}\cdot\frac{\partial \mathbf{a}(\theta,r)}{\partial r}\Big|_{\theta=\psi,r=l}, \tag{51}$$

and the latter term can be derived as

$$\frac{\partial \mathbf{a}^{\mathrm{H}}(\psi,l)}{\partial l}\cdot\mathbf{a}\mathbf{a}^{\mathrm{H}}\cdot\frac{\partial \mathbf{a}(\psi,l)}{\partial l}=\left\|\frac{\partial \mathbf{a}^{\mathrm{H}}(\psi,l)}{\partial l}\cdot\mathbf{a}\right\|^2=\frac{4\pi^2\Delta f^2}{\mathrm{c}^2}\left\{2M^2\sum_{n=0}^{N-1}n\right\}^2. \tag{52}$$

Then, the Fisher information with respect to l is expressed as

$$\begin{aligned} J_{ll} &= 2 \cdot \frac{MN \cdot \mathrm{SNR}^2}{1 + MN \cdot \mathrm{SNR}} \cdot \frac{4\pi^2 \Delta f^2}{\mathrm{c}^2} \cdot 4M^3 \cdot \left\{ \sum_{n=0}^{N-1} n^2 - \frac{1}{N} \left(\sum_{n=0}^{N-1} n \right)^2 \right\} \\ &= 2 \cdot \frac{MN \cdot \mathrm{SNR}^2}{1 + MN \cdot \mathrm{SNR}} \cdot \frac{4\pi^2 \Delta f^2}{\mathrm{c}^2} \cdot \frac{M^3 N^3 - M^3 N}{3}. \end{aligned} \tag{53}$$

In the scenarios where the DOA and the range of the stochastic signal source are both unknown and need to be estimated jointly, the Fisher information with respect to ψ and l is expressed as

$$J_{\psi l} = J_{1,2} = 2 \cdot \frac{MN \cdot \mathrm{SNR}^2}{1 + MN \cdot \mathrm{SNR}} \cdot \left(\frac{\partial \mathbf{a}^{\mathrm{H}}(\psi, l)}{\partial \psi} \cdot \frac{\partial \mathbf{a}(\psi, l)}{\partial l} - \frac{1}{MN} \cdot \frac{\partial \mathbf{a}^{\mathrm{H}}(\psi, l)}{\partial \psi} \cdot \mathbf{a}\mathbf{a}^{\mathrm{H}} \cdot \frac{\partial \mathbf{a}(\psi, l)}{\partial l} \right). \tag{54}$$

The two terms in between the parentheses in (54) are respectively further developed as

$$\frac{\partial \mathbf{a}^{\mathrm{H}}(\psi, l)}{\partial \psi} \cdot \frac{\partial \mathbf{a}(\psi, l)}{\partial l} = \frac{\partial \mathbf{a}^{\mathrm{H}}(\theta, r)}{\partial \theta} \cdot \frac{\partial \mathbf{a}(\theta, r)}{\partial r} |_{\theta=\psi, r=l}, \tag{55}$$

and

$$\begin{aligned} &\frac{\partial \mathbf{a}^{\mathrm{H}}(\psi, l)}{\partial \psi} \cdot \mathbf{a}\mathbf{a}^{\mathrm{H}} \cdot \frac{\partial \mathbf{a}(\psi, l)}{\partial l} = \frac{8\pi^2 d \cos\psi \Delta f}{\mathrm{c}^2} \cdot \left\{ f_0 \left(M^2 \sum_{n=0}^{N-1} n + N^2 \sum_{m=0}^{M-1} m \right) \right. \\ &\left. + \Delta f \left(M^3 \sum_{n=0}^{N-1} n^2 + MN \sum_{m=0}^{M-1} m \sum_{n=0}^{N-1} n \right) \right\} \cdot M^2 \sum_{n=0}^{N-1} n. \end{aligned} \tag{56}$$

As such, the Fisher information with respect to ψ and l is derived as (57),

$$\begin{aligned} J_{\psi l} &= 2 \cdot \frac{MN \cdot \mathrm{SNR}^2}{1 + MN \cdot \mathrm{SNR}} \cdot \frac{8\pi^2 d \cos\theta \Delta f}{\mathrm{c}^2} \cdot \\ &\left\{ f_0 \cdot \left(M^3 \sum_{n=0}^{N-1} n^2 + MN \sum_{m=0}^{M-1} m \sum_{n=0}^{N-1} n \right) + \Delta f \cdot \left(M^4 \sum_{n=0}^{N-1} n^3 + M^2 N \sum_{m=0}^{M-1} m \sum_{n=0}^{N-1} n^2 \right) \right. \\ &\left. - \frac{1}{MN} \left[f_0 \cdot \left(M^2 \sum_{n=0}^{N-1} n + N^2 \sum_{m=0}^{M-1} m \right) - \Delta f \cdot \left(M^3 \sum_{n=0}^{N-1} n^2 + MN \sum_{m=0}^{M-1} m \sum_{n=0}^{N-1} n \right) \right] \cdot \left(M^2 \sum_{n=0}^{N-1} n \right) \right\} \\ &= 2 \cdot \frac{MN \cdot \mathrm{SNR}^2}{1 + MN \cdot \mathrm{SNR}} \cdot \frac{8\pi^2 d \cos\theta \Delta f}{\mathrm{c}^2} \cdot \left\{ f_0 \cdot \frac{M^3 N^3 - M^3 N}{12} + \Delta f \cdot \frac{\left(3M^4 - M^3\right) N^4 - 5M^4 N^3 + M^3 N^2 + 2M^4 N}{24} \right\}. \end{aligned} \tag{57}$$

Substituting (48), (53) and (57) into (43) yields the analytical expression of the CRB for the joint DOA-range estimation in stochastic signal case, i.e.,

$$\mathrm{CRB}_{\psi} = \left[\mathbf{J}^{-1} \right]_{1,1} = \frac{1}{J_{\psi\psi} - \frac{J_{\psi l} J_{l\psi}}{J_{ll}}}, \tag{58}$$

$$\mathrm{CRB}_{l} = \left[\mathbf{J}^{-1} \right]_{2,2} = \frac{1}{J_{ll} - \frac{J_{\psi l} J_{l\psi}}{J_{\psi\psi}}}. \tag{59}$$

Note that, the K-snapshot PDF $P_{\mathbf{y}_1, \mathbf{y}_2, \cdots, \mathbf{y}_K | \boldsymbol{\alpha}}(\mathbf{y})$ is the product of K single-snapshot PDFs and the result resembles the aforementioned situation of the deterministic signal.

4.3. CRB of Separate Estimation

Similar to the deduction in the deterministic signal case, the analytical expression of CRB of DOA (range) estimation while range (DOA) is known can be expressed as

$$\mathrm{SCRB}_{\psi} = \frac{1}{J_{\psi\psi}} \quad \text{and} \quad \mathrm{SCRB}_{l} = \frac{1}{J_{ll}}. \tag{60}$$

We can see from (58), (59) and (60) that, the dependence of CRB_{ψ} (SCRB_{ψ}) and the coprime FDA parameters M, N, and Δf is quite similar to that in the deterministic signal case. On the other hand, CRB_{l} (SCRB_{l}) decreases with the increase of the coprime FDA parameters. The detailed analyses will be provided in Section 5.

5. Numerical Simulations and Analyses

In this section, numerical simulations are presented to exemplify the CRBs in different scenarios. We assume that the coprime FDA under investigation operates at the X-band with a carrier frequency of $f_0 = 10$ GHz. Both deterministic and stochastic signal cases are investigated in the simulations. The location of the deterministic and stochastic signal sources are set as $\boldsymbol{\alpha} = \boldsymbol{\xi}$, and the azimuth angle is 30° while the range is 2.8 km. To observe and analyze the CRB of coprime FDA, the following commonly-used coprime designs are simulated as examples: (a) $M = 5, N = 3, \Delta f = 15$ kHz; (b) $M = 7, N = 3, \Delta f = 15$ kHz; (c) $M = 5, N = 4, \Delta f = 15$ kHz; (d) $M = 5, N = 3, \Delta f = 30$ kHz; (e) $M = 7, N = 3, \Delta f = 30$ kHz; (f) $M = 5, N = 4, \Delta f = 30$ kHz. Note that the CRB results can be easily extended to other parameter settings using the closed-form solutions. We also include the CRBs of uniform FDA-MIMO [49] with the same number of array sensors in the numerical analyses to demonstrate the benefits of coprime configuration. The markers on the curves are used to distinguish between the CRBs of coprime and uniform FDAs.

Figure 2 shows the results of deterministic CRB_{θ} and stochastic CRB_{ψ} for joint estimation versus SNR. The zoomed-in view in Figure 2a,b indicates that the impact of the frequency increment values on the CRBs of DOA estimation is trivial. Figure 3 presents the curves of the deterministic CRB_{r} and stochastic CRB_{l} versus SNR. We can see from Figure 3 that, in both deterministic and stochastic cases, the CRBs of range estimation decrease with the increase of the coprime FDA parameters M, N, and Δf. Furthermore, in contrast to the DOA estimation, the range estimation performance is significantly influenced by the unit frequency increment Δf. As for the comparison between the coprime FDA and the uniform FDA-MIMO, we infer from the numerical results that the CRB of coprime FDA is more than 60% which is lower than that of uniform FDA-MIMO owing to the coprime configuration. The CRB performance for the detection of signals with different statistical characteristics is evaluated in Figure 4. Three groups of array design are simulated for deterministic and stochastic signal models. The simulation results suggest that the deterministic CRB outperforms the stochastic one, which tallies with the common knowledge in array signal processing.

In the following, we investigate the variation of angle CRB with the increase of frequency increment Δf. A variable ∂_{CRB} is used to quantify the magnitude of the CRB variation, which is defined as

$$\partial_{\mathrm{CRB}} \triangleq \frac{\mathrm{CRB}_{B} - \mathrm{CRB}_{0}}{\mathrm{CRB}_{0}}, \tag{61}$$

where CRB_0 and CRB_B denote the CRB of DOA when bandwidth is 0 and B, respectively. We let B and $\kappa = B/f_0$ respectively denote the overall and relative bandwidth of the coprime FDA. To ensure that the narrow-band assumption of coprime FDA is met, we assume that κ is confined to $\leq$0.1. As depicted in Figure 5a, CRBs of DOA estimation in stochastic signal case decline with the increase of Δf. The curves in Figure 5a also implies a non-monotonic dependence of the deterministic CRB_{θ} on the bandwidth. From (32) we notice that $J_{\theta r}$ increases with the increase of Δf. Hence, the dependence between

parameters in the joint estimation cases is stronger. As a result, deterministic CRB_θ first decreases and then increases when the bandwidth reaches a certain level. Nevertheless, in the case of joint estimation of stochastic signals as shown in Figure 5b, this phenomenon is inconspicuous.

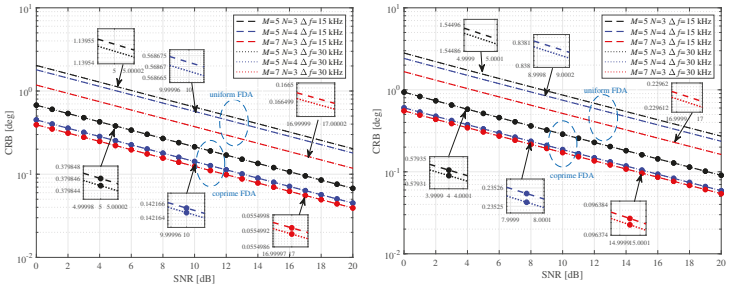

(**a**) (**b**)

Figure 2. CRB of DOA in joint DOA-range estimation. (**a**) Deterministic signal case. (**b**) Stochastic signal case.

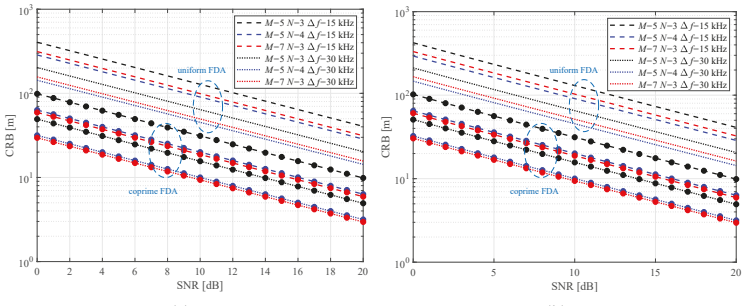

(**a**) (**b**)

Figure 3. CRB of range in joint DOA-range estimation. (**a**) Deterministic signal case. (**b**) Stochastic signal case.

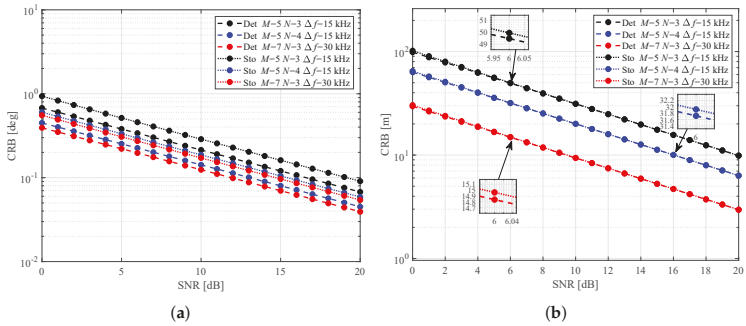

(**a**) (**b**)

Figure 4. Comparison between two types of CRB. (**a**) CRB of DOA estimation in deterministic case and stochastic case. (**b**) CRB of range estimation in deterministic case and stochastic case.

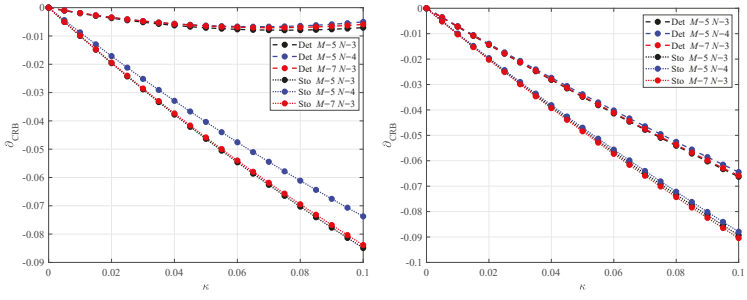

(**a**) (**b**)

Figure 5. Influence of Δf on the DOA estimation performance. (**a**) $\partial_{\mathrm{CRB}_\theta}$ and $\partial_{\mathrm{CRB}_\psi}$ versus κ. (**b**) $\partial_{\mathrm{SCRB}_\theta}$ and $\partial_{\mathrm{SCRB}_\psi}$ versus κ.

We compare the CRBs of separate and joint estimations under both deterministic and stochastic signal models, which are respectively given in Figures 6 and 7. In addition, we examine the root mean square errors (RMSEs) of the classical spatial spectrum estimation algorithms including the two-dimensional MUltiple SIgnal Classification (2-D MUSIC) [50] and two-dimensional minimum variance distortionless response (2-D MVDR) [51], and compare them with the CRBs. We observe from Figure 8 that both the RMSEs of 2-D MUSIC and 2-D MVDR can approach the CRB gradually as SNR increases.

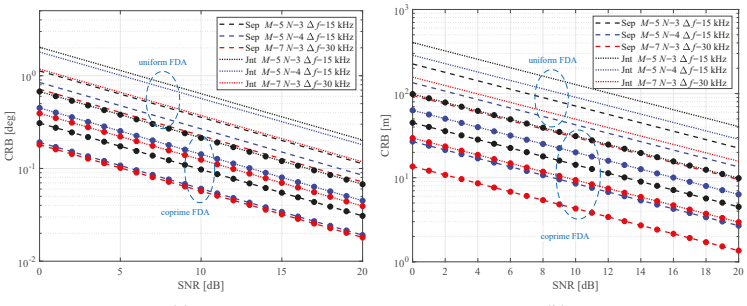

(**a**) (**b**)

Figure 6. CRBs of joint/separate DOA-range estimations in deterministic signal case. (**a**) CRB of DOA estimation. (**b**) CRB of range estimation.

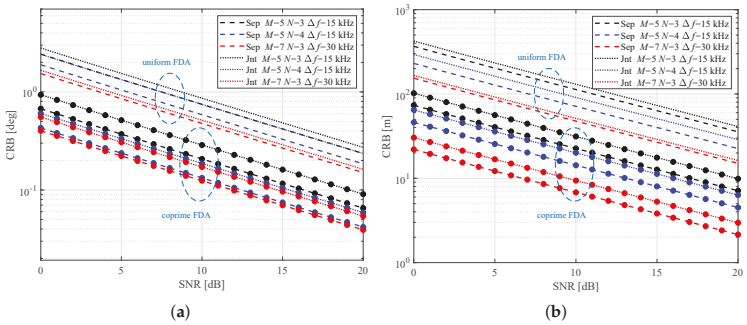

(**a**) (**b**)

Figure 7. CRBs of joint/separate DOA-range estimations in stochastic signal case. (**a**) CRB of DOA estimation. (**b**) CRB of range estimation.

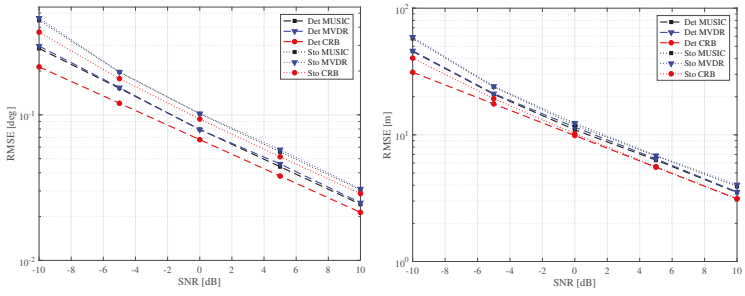

(**a**) (**b**)

Figure 8. RMSEs of 2-D MUSIC and 2-D MVDR algorithm. The coprime FDA parameters are set as $M = 5, N = 3$ and $\Delta f = 15$ kHz. The number of snapshots is set as 100 and the result is obtained through 500 Monte Carlo trials. (**a**) RMSE of DOA estimation. (**b**) RMSE of range estimation.

In addition to the analyses of the numerical results, from the analytical form expressions given in (33)–(35) and (58)–(60), we arrive at the following remarks.

- Deterministic CRB_r (SCRB_r) and stochastic CRB_l (SCRB_l) are independent of the range, meaning that the range of signal source has no influence on the CRB of range estimation from the premise that the path loss is not considered.
- Since a coprime FDA is narrow-band in nature, the frequency-increment-induced phase difference with respect to angle is much smaller than the array-spacing-induced one. As such, deterministic CRB_θ and stochastic CRB_ψ are weakly dependent on the frequency increment Δf (see Figure 2). This is, however, not the case for deterministic CRB_r (SCRB_r) and stochastic CRB_l (SCRB_l). Furthermore, the range estimation performance improves with the increase of the frequency increment (see Figure 3).
- Connecting to frequency increment Δf has limited impact on the DOA estimation, and the dependence is not consistent in deterministic and stochastic CRBs for DOA estimation (see Figure 5). Connecting this phenomenon to the previous remark, the impact of Δf on CRB for DOA estimation defies generalisations.
- For a sufficient number of sensors, deterministic CRB_θ, stochastic CRB_ψ, deterministic CRB_r and stochastic CRB_l of coprime FDA are $\mathcal{O}(1/M^3N^3)$.
- The CRB of joint estimation is slightly worse than the SCRB. This implies that the prior knowledge on the range/DOA of target is conducive to improve measurement accuracy for deterministic and stochastic signal case (see Figures 6 and 7).

Furthermore, we observe from Figure 2 that the CRBs of both DOA and range estimations decrease with the increase of coprime integers M, N, which leads to the expansion of array aperture and bandwidth. This result tallies with our common sense. Accordingly, we can use the largest M, N possible to design a theoretically best-performance coprime FDA. Nevertheless, in reality, array designs are often subject to resource constraints such as the total number of antenna elements and/or bandwidth. Therefore, a rational design with limited resources is important in practice. From the analytical CRB results given in the above sections, we notice that a larger total number of antenna elements $M + N$ is not equivalent to superior CRB. The above conclusion is drawn in Figure 3a. More concretely, the CRB of range estimation for the coprime FDA choosing $M = 5, N = 4, \Delta f = 15$ kHz, which uses a smaller number of elements, performs better than the coprime FDA choosing $M = 7, N = 3, \Delta f = 15$ kHz. Based on this conclusion, we propose to use the CRB of coprime FDA to choose the optimal solution of coprime integers M and N to assist the array design.

Consider a practical scenario where the total number of antennas is L and the upper limit of bandwidth is $\tilde{B}$. By further denoting the coprime integers set as $\mathbb{S}_c$, we formulate the coprime FDA array design as the following optimization problem:

$$\begin{aligned} \min_{M,N} \quad & \mathrm{CRB}_\theta + \gamma \cdot \mathrm{CRB}_r, \\ \text{s.t.} \quad & M + N \leq L, (M-1)N \cdot \Delta f \leq \tilde{B}, \\ & \{M, N\} \in \mathbb{S}_c, \end{aligned} \tag{62}$$

where γ represents the trade-off coefficient that controls the compromise between the CRB of DOA (range) estimation. This problem can be readily solved via exhaustive search. In doing so, we are able to design a theoretically optimal coprime FDA configuration with constrained physical resources.

6. Conclusions

In this work, the analytical expressions of the CRBs in deterministic/stochastic signal cases for joint DOA-range estimation using coprime FDA are derived. Extensive numerical simulations are also provided and analyzed. We are able to arrive at the following conclusions from the simulation results: (i) The CRB of DOA estimation is weakly related with the frequency increment; (ii) The difference between the deterministic and stochastic CRBs is distinct; (iii) The relation between frequency increment and the CRB of DOA for joint estimation is nonmonotonic in the deterministic signal case; (iv) The CRB of joint DOA-range estimation is slightly worse than the separate parameter estimation in both the deterministic and stochastic signal cases; and (v) The CRB of coprime FDA outperforms that of uniform FDA-MIMO for more than 60% under commonly-adopted coprime patterns. The difference between the CRBs of joint and separate DOA-range estimation methods is analyzed and we also propose an intuitive method for coprime FDA design based on CRB minimization.

Author Contributions: Conceptualization, Z.M. and S.L.; Data curation, Z.M.; Formal analysis, Z.M.; Funding acquisition, S.L. and Y.H.; Investigation, Z.M.; Methodology, Z.M.; Project administration, S.L.; Resources, S.L. and Y.H.; Software, Z.M.; Supervision, S.L. and Y.H.; Validation, S.L. and S.Q.; Visualization, Z.M.; Writing—original draft, Z.M. and S.L.; Writing—review & editing, S.L., S.Q. and Y.H. All authors have read and agreed to the published version of the manuscript.

Funding: This research was supported in part by the National Natural Science Foundationof China under Grant Nos. 62001103, U1936201 and the Basic Research Program of Jiangsu Province under Grant No. BK20190338.

Institutional Review Board Statement: Not applicable.

Informed Consent Statement: Not applicable.

Data Availability Statement: The data and code used in this study are available upon request to the corresponding author.

Conflicts of Interest: The authors declare that they have no conflict of interest regarding the publication of this manuscript.

Appendix A

The log-likelihood function $\mathcal{L}_{\mathbf{y}}(\boldsymbol{\alpha})$ can be written as

$$
\begin{aligned}
-J_{i,j} = \frac{\partial^2}{\partial\boldsymbol{\alpha}_i\partial\boldsymbol{\alpha}_j}[\mathcal{L}_{\mathbf{y}}(\boldsymbol{\alpha})] &= \mathrm{tr}\left(-\mathbf{R}_{\mathbf{y}}^{-1}(\boldsymbol{\alpha})\frac{\partial\mathbf{R}_{\mathbf{y}}(\boldsymbol{\alpha})}{\partial\boldsymbol{\alpha}_j}\mathbf{R}_{\mathbf{y}}^{-1}(\boldsymbol{\alpha})\frac{\partial\mathbf{R}_{\mathbf{y}}(\boldsymbol{\alpha})}{\partial\boldsymbol{\alpha}_i} + \mathbf{R}_{\mathbf{y}}^{-1}(\boldsymbol{\alpha})\frac{\partial^2\mathbf{R}_{\mathbf{y}}(\boldsymbol{\alpha})}{\boldsymbol{\alpha}_i\boldsymbol{\alpha}_j}\right)\\
&- \left[\left(\mathbf{y}^{\mathrm{H}} - \mathbf{m}_{\mathbf{y}}^{\mathrm{H}}(\boldsymbol{\alpha})\right)\Big(- \mathbf{R}_{\mathbf{y}}^{-1}(\boldsymbol{\alpha})\frac{\partial\mathbf{R}_{\mathbf{y}}(\boldsymbol{\alpha})}{\partial\boldsymbol{\alpha}_j}\mathbf{R}_{\mathbf{y}}^{-1}(\boldsymbol{\alpha})\frac{\partial\mathbf{R}_{\mathbf{y}}(\boldsymbol{\alpha})}{\partial\boldsymbol{\alpha}_i}\mathbf{R}_{\mathbf{y}}^{-1}(\boldsymbol{\alpha})\right.\\
&+ \mathbf{R}_{\mathbf{y}}^{-1}(\boldsymbol{\alpha})\frac{\partial^2\mathbf{R}_{\mathbf{y}}(\boldsymbol{\alpha})}{\boldsymbol{\alpha}_i\boldsymbol{\alpha}_j}\mathbf{R}_{\mathbf{y}}^{-1}(\boldsymbol{\alpha}) + \mathbf{R}_{\mathbf{y}}{}^{-1}(\boldsymbol{\alpha})\frac{\partial\mathbf{R}_{\mathbf{y}}(\boldsymbol{\alpha})}{\partial\boldsymbol{\alpha}_j}\mathbf{R}_{\mathbf{y}}^{-1}(\boldsymbol{\alpha})\frac{\partial\mathbf{R}_{\mathbf{y}}(\boldsymbol{\alpha})}{\partial\boldsymbol{\alpha}_i}\mathbf{R}_{\mathbf{y}}^{-1}(\boldsymbol{\alpha})\Big)\left(\mathbf{y} - \mathbf{m}_{\mathbf{y}}(\boldsymbol{\alpha})\right)\Big]\\
&- 2\Re\Big\{ - \frac{\partial^2\mathbf{m}_{\mathbf{y}}^{\mathrm{H}}(\boldsymbol{\alpha})}{\boldsymbol{\alpha}_i\boldsymbol{\alpha}_j}\mathbf{R}_{\mathbf{y}}^{-1}(\boldsymbol{\alpha})\left(\mathbf{y} - \mathbf{m}_{\mathbf{y}}(\boldsymbol{\alpha})\right) + \frac{\partial\mathbf{m}_{\mathbf{y}}^{\mathrm{H}}(\boldsymbol{\alpha})}{\partial\boldsymbol{\alpha}_i}\mathbf{R}_{\mathbf{y}}^{-1}(\boldsymbol{\alpha})\frac{\partial\mathbf{R}_{\mathbf{y}}(\boldsymbol{\alpha})}{\partial\boldsymbol{\alpha}_j}\mathbf{R}_{\mathbf{y}}^{-1}(\boldsymbol{\alpha})\left(\mathbf{y} - \mathbf{m}_{\mathbf{y}}(\boldsymbol{\alpha})\right)\\
&+ \frac{\partial\mathbf{m}_{\mathbf{y}}^{\mathrm{H}}(\boldsymbol{\alpha})}{\partial\boldsymbol{\alpha}_j}\mathbf{R}_{\mathbf{y}}^{-1}(\boldsymbol{\alpha})\frac{\partial\mathbf{R}_{\mathbf{y}}(\boldsymbol{\alpha})}{\partial\boldsymbol{\alpha}_i}\mathbf{R}_{\mathbf{y}}^{-1}(\boldsymbol{\alpha})\left(\mathbf{y} - \mathbf{m}_{\mathbf{y}}(\boldsymbol{\alpha})\right) + \frac{\partial\mathbf{m}_{\mathbf{y}}^{\mathrm{H}}(\boldsymbol{\alpha})}{\partial\boldsymbol{\alpha}_i}\mathbf{R}_{\mathbf{y}}^{-1}(\boldsymbol{\alpha})\frac{\partial\mathbf{m}_{\mathbf{y}}(\boldsymbol{\alpha})}{\partial\boldsymbol{\alpha}_j}\Big\}.
\end{aligned}
\tag{A1}
$$

where $\mathrm{tr}(\cdot)$ returns the trace of the matrix. We notice that the first three terms in between the curly brackets are zero, and (60) can be simplified as

$$
\begin{aligned}
J_{i,j} &= -\mathrm{tr}\Big\{\Big[- \mathbf{R}_{\mathbf{y}}^{-1}(\boldsymbol{\alpha})\frac{\partial\mathbf{R}_{\mathbf{y}}(\boldsymbol{\alpha})}{\partial\boldsymbol{\alpha}_j}\mathbf{R}_{\mathbf{y}}^{-1}(\boldsymbol{\alpha})\frac{\partial\mathbf{R}_{\mathbf{y}}(\boldsymbol{\alpha})}{\partial\boldsymbol{\alpha}_i}\\
&+ \mathbf{R}_{\mathbf{y}}^{-1}(\boldsymbol{\alpha})\frac{\partial^2\mathbf{R}_{\mathbf{y}}(\boldsymbol{\alpha})}{\boldsymbol{\alpha}_i\boldsymbol{\alpha}_j}\Big] + \Big[\mathbf{R}_{\mathbf{y}}^{-1}(\boldsymbol{\alpha})\frac{\partial\mathbf{R}_{\mathbf{y}}(\boldsymbol{\alpha})}{\partial\boldsymbol{\alpha}_j}\mathbf{R}_{\mathbf{y}}^{-1}(\boldsymbol{\alpha})\frac{\partial\mathbf{R}_{\mathbf{y}}(\boldsymbol{\alpha})}{\partial\boldsymbol{\alpha}_i}\\
&- \mathbf{R}_{\mathbf{y}}^{-1}(\boldsymbol{\alpha})\frac{\partial^2\mathbf{R}_{\mathbf{y}}(\boldsymbol{\alpha})}{\boldsymbol{\alpha}_i\boldsymbol{\alpha}_j}\Big] - \mathbf{R}_{\mathbf{y}}^{-1}(\boldsymbol{\alpha})\frac{\partial\mathbf{R}_{\mathbf{y}}(\boldsymbol{\alpha})}{\partial\boldsymbol{\alpha}_i}\mathbf{R}_{\mathbf{y}}^{-1}(\boldsymbol{\alpha})\frac{\partial\mathbf{R}_{\mathbf{y}}(\boldsymbol{\alpha})}{\partial\boldsymbol{\alpha}_j}\Big\} + 2\Re\Big\{\frac{\partial\mathbf{m}_{\mathbf{y}}^{\mathrm{H}}(\boldsymbol{\alpha})}{\partial\boldsymbol{\alpha}_i}\mathbf{R}_{\mathbf{y}}^{-1}(\boldsymbol{\alpha})\frac{\partial\mathbf{m}_{\mathbf{y}}(\boldsymbol{\alpha})}{\partial\boldsymbol{\alpha}_j}\Big\}\\
&= \mathrm{tr}\Big[\mathbf{R}_{\mathbf{y}}^{-1}(\boldsymbol{\alpha})\frac{\partial\mathbf{R}_{\mathbf{y}}(\boldsymbol{\alpha})}{\partial\boldsymbol{\alpha}_i}\mathbf{R}_{\mathbf{y}}^{-1}(\boldsymbol{\alpha})\frac{\partial\mathbf{R}_{\mathbf{y}}(\boldsymbol{\alpha})}{\partial\boldsymbol{\alpha}_j}\Big] + 2\Re\Big\{\frac{\partial\mathbf{m}_{\mathbf{y}}^{\mathrm{H}}(\boldsymbol{\alpha})}{\partial\boldsymbol{\alpha}_i}\mathbf{R}_{\mathbf{y}}^{-1}(\boldsymbol{\alpha})\frac{\partial\mathbf{m}_{\mathbf{y}}(\boldsymbol{\alpha})}{\partial\boldsymbol{\alpha}_j}\Big\}.
\end{aligned}
\tag{A2}
$$

In the deterministic signal case, we have $\frac{\partial\mathbf{R}_{\mathbf{y}}(\boldsymbol{\alpha})}{\partial\boldsymbol{\alpha}_i} = \frac{\partial\mathbf{R}_{\mathbf{y}}(\boldsymbol{\alpha})}{\partial\boldsymbol{\alpha}_j} = 0$. As a result, (19) is obtained.

Appendix B

For the stochastic signal case, according to the theorem of Woodbury matrix identity $\mathbf{R}_{\mathbf{y}}^{-1} = \frac{1}{\sigma_n^2}[\mathbf{I} - \frac{\sigma_s^2}{\sigma_n^2}\mathbf{a}(\frac{\sigma_s^2}{\sigma_n^2}\mathbf{a}^{\mathrm{H}}\mathbf{a} + \mathbf{I})^{-1}\mathbf{a}^{\mathrm{H}}]$ and denoting σ_s^2/σ_n^2 (SNR) as Σ, we have

$$
\begin{aligned}
\mathbf{a}^{\mathrm{H}}\mathbf{R}_{\mathbf{y}}^{-1}\mathbf{a}\sigma_s^2 &= \mathbf{a}^{\mathrm{H}}[\mathbf{I} - \mathbf{a}\Sigma(\mathbf{a}^{\mathrm{H}}\mathbf{a}\Sigma + \mathbf{I})^{-1}\mathbf{a}^{\mathrm{H}}]\mathbf{a}\Sigma\\
&= \mathbf{a}^{\mathrm{H}}\mathbf{a}\Sigma - \mathbf{a}^{\mathrm{H}}\mathbf{a}\Sigma(\mathbf{a}\mathbf{a}^{\mathrm{H}}\Sigma + \mathbf{I})^{-1}\mathbf{a}^{\mathrm{H}}\mathbf{a}\Sigma\\
&= [\mathbf{I} - \mathbf{a}^{\mathrm{H}}\mathbf{a}\Sigma(\mathbf{a}^{\mathrm{H}}\mathbf{a}\Sigma + \mathbf{I})^{-1}]\mathbf{a}^{\mathrm{H}}\mathbf{a}\Sigma\\
&= [(\mathbf{a}^{\mathrm{H}}\mathbf{a}\Sigma + \mathbf{I})(\mathbf{a}^{\mathrm{H}}\mathbf{a}\Sigma + \mathbf{I})^{-1} - \mathbf{a}^{\mathrm{H}}\mathbf{a}\Sigma(\mathbf{a}^{\mathrm{H}}\mathbf{a}\Sigma + \mathbf{I})^{-1}]\mathbf{a}^{\mathrm{H}}\mathbf{a}\Sigma\\
&= (\mathbf{a}^{\mathrm{H}}\mathbf{a}\Sigma + \mathbf{I})^{-1}\mathbf{a}^{\mathrm{H}}\mathbf{a}\Sigma = \frac{MN\cdot\mathrm{SNR}}{1 + MN\cdot\mathrm{SNR}}.
\end{aligned}
\tag{A3}
$$

Thus, Formula (40) is obtained.

References

1. Antonik, P.; Wicks, M.C.; Griffiths, H.D.; Baker, C.J. Range-dependent beamforming using element level waveform diversity. In Proceedings of the 2006 International Waveform Diversity & Design Conference, Las Vegas, NV, USA, 22–26 Janurary 2006; pp. 140–144.
2. Antonik, P.; Wicks, M.C.; Griffiths, H.D.; Baker, C.J. Frequency diverse array radars. In Proceedings of the 2006 IEEE Conference on Radar, Verona, NY, USA, 24–27 April 2006; pp. 215–217.
3. Wang, W.-Q. Phased-MIMO radar with frequency diversity for range-dependent beamforming. *IEEE Sens. J.* **2013**, *13*, 1320–1328. [CrossRef]
4. Sammartino, P.F.; Baker, C.J.; Griffiths, H.D. Frequency diverse MIMO techniques for radar. *IEEE Trans. Aerosp. Electron. Syst.* **2013**, *49*, 1320–1328. [CrossRef]
5. Liao, Y.; Wang, W.; Zheng, Z. Frequency diverse array beampattern synthesis using symmetrical logarithmic frequency offsets for target indication. *IEEE Trans. Antennas Propag.* **2019**, *67*, 3505–3509. [CrossRef]

6. Wang, C.; Xu, J.; Liao, G.; Xu, X.; Zhang, Y. A range ambiguity resolution approach for high-resolution and wide-swath SAR imaging using frequency diverse array. *IEEE J. Sel. Top. Signal Process.* **2017**, *11*, 336–346. [CrossRef]
7. Lan, L.; Liao, G.; Xu, J.; Zhang, Y.; Liao, B. Transceive beamforming with accurate nulling in FDA-MIMO radar for imaging. *IEEE Trans. Geosci. Remote Sens.* **2020**, *58*, 4145–4159. [CrossRef]
8. Nusenu, S.Y.; Wang, W.-Q. Range-dependent spatial modulation using frequency diverse array for OFDM wireless communications. *IEEE Trans. Veh. Technol.* **2018**, *67*, 10886–10895. [CrossRef]
9. Wang, W.-Q. Range-angle dependent transmit beampattern synthesis for linear frequency diverse arrays. *IEEE Trans. Antennas Propag.* **2013**, *61*, 4073–4081. [CrossRef]
10. Secmen, M.; Demir, S.; Hizal, A.; Eker, T. Frequency diverse array antenna with periodic time modulated pattern in range and angle. In Proceedings of the 2007 IEEE Radar Conference, Boston, MA, USA, 17–20 April 2007; pp. 427–430.
11. Huang, S.; Tong, K.F.; Baker, C.J. Frequency diverse array: Simulation and design. In Proceedings of the 2009 Loughborough Antennas & Propagation Conference, Loughborough, UK, 16–17 November 2009; pp. 253–256.
12. Khan, W.; Qureshi, I.M. Frequency diverse array radar with time-dependent frequency offset. *IEEE Antennas Wirel. Propag. Lett.* **2014**, *13*, 758–761. [CrossRef]
13. Khan, W.; Qureshi, I.M.; Saeed, S. Frequency diverse array radar with logarithmically increasing frequency offset. *IEEE Antennas Wirel. Propag. Lett.* **2015**, *14*, 499–502. [CrossRef]
14. Mahmood, M.; Mir, H. Frequency diverse array beamforming using nonuniform logarithmic frequency increments. *IEEE Antennas Wirel. Propag. Lett.* **2018**, *17*, 1817–1821. [CrossRef]
15. Liu, Y.; Ruan, H.; Wang, L.; Nehorai, A. The random frequency diverse array: A new antenna structure for uncoupled direction-range indication in active sensing. *IEEE J. Sel. Top. Signal Process.* **2017**, *11*, 295–308. [CrossRef]
16. Wang, W.-Q.; So, H.C.; Shao, H. Nonuniform frequency diverse array for range-angle imaging of targets. *IEEE Sens. J.* **2014**, *14*, 2469–2476. [CrossRef]
17. Shao, H.; Li, J.; Chen, H.; Wang, W.-Q. Adaptive frequency offset selection in frequency diverse array radar. *IEEE Antennas Wirel. Propag. Lett.* **2014**, *13*, 1405–1408. [CrossRef]
18. Gao, K.; Wang, W.; Chen, H.; Cai, J. Transmit beamspace design for multi-carrier frequency diverse array sensor. *IEEE Sens. J.* **2016**, *16*, 5709–5714. [CrossRef]
19. Shao, H.; Dai, J.; Xiong, J.; Chen, H.; Wang, W.-Q. Dot-shaped range-angle beampattern synthesis for frequency diverse array. *IEEE Antennas Wirel. Propag. Lett.* **2016**, *15*, 1703–1706. [CrossRef]
20. Wang, Y.; Wang, W.-Q.; Chen, H.; Shao, H. Optimal frequency diverse subarray design with Cramér-Rao lower bound minimization. *IEEE Antennas Wirel. Propag. Lett.* **2015**, *14*, 1188–1191. [CrossRef]
21. Xiong, J.; Wang, W.-Q.; Shao, H.; Chen, H. Frequency diverse array transmit beampattern optimization with genetic algorithm. *IEEE Antennas Wirel. Propag. Lett.* **2017**, *16*, 469–472. [CrossRef]
22. Yang, Y.-Q.; Wang, H.-Q.; Wang, H.; Gu, S.-Q.; Xu, D.-L.; Quan, S.-L. Optimization of sparse frequency diverse array with time-invariant spatial-focusing beampattern. *IEEE Antennas Wirel. Propag. Lett.* **2018**, *17*, 351–354. [CrossRef]
23. Xu, J.; Liao, G.; Zhu, S.; Huang, L.; So, H.C. Joint range and angle estimation using MIMO radar with frequency diverse array. *IEEE Trans. Signal Process.* **2015**, *63*, 3396–3410. [CrossRef]
24. Wang, Y.; Huang, G.; Li, W. Transmit beampattern design in range and angle domains for MIMO frequency diverse array radar. *IEEE Antennas Wirel. Propag. Lett.* **2016**, *16*, 1003–1006. [CrossRef]
25. Li, J.; Stoica, P. MIMO radar with colocated antennas. *IEEE Signal Process. Mag.* **2007**, *24*, 106–114. [CrossRef]
26. BouDaher, E.; Jia, Y.; Ahmad, F.; Amin, M.G. Multi-frequency co-prime arrays for high-resolution direction-of-arrival estimation. *IEEE Trans. Signal Process.* **2015**, *63*, 3797–3808. [CrossRef]
27. Zheng, H.; Shi, Z.; Zhou, C.; Haardt, M.; Chen, J. Coupled coarray tensor CPD for DOA estimation with coprime L-shaped array. *IEEE Signal Process. Lett.* **2021**, *28*, 1545–1549. [CrossRef]
28. Qin, S.; Zhang, Y.D.; Amin, M.G. Generalized coprime array configurations for direction-of-arrival estimation. *IEEE Trans. Signal Process.* **2015**, *63*, 1377–1390. [CrossRef]
29. Vaidyanathan, P.P.; Pal, P. Sparse sensing with co-prime samplers and arrays. *IEEE Trans. Signal Process.* **2011**, *59*, 573–586. [CrossRef]
30. Qin, S.; Zhang, Y.D.; Amin, M.G.; Gini, F. Frequency diverse coprime arrays with coprime frequency offsets for multitarget localization. *IEEE J. Sel. Top. Signal Process.* **2017**, *11*, 321–335. [CrossRef]
31. Ahmed, A.; Zhang, Y.D. Generalized non-redundant sparse array designs. *IEEE Trans. Signal Process.* **2021**, *69*, 4580–4594. [CrossRef]
32. Zhou, C.; Gu, Y.; He, S.; Shi, Z. A robust and efficient algorithm for coprime array adaptive beamforming. *IEEE Trans. Veh. Technol.* **2018**, *67*, 1099–1122. [CrossRef]
33. Wang, W.-Q. Information geometry resolution optimization for frequency diverse array in DOA estimation. *Digit. Signal Process.* **2019**, *44*, 58–67. [CrossRef]
34. Liu, C.; Vaidyanathan, P.P. Cramér-Rao bounds for coprime and other sparse arrays, which find more sources than sensors. *Digit. Signal Process.* **2017**, *61*, 43–61. [CrossRef]
35. Xiong, J.; Wang, W.-Q.; Wang, Z. Optimization of frequency increments via CRLB minimization for frequency diverse array. In Proceedings of the 2017 IEEE Radar Conference, Seattle, WA, USA, 8–12 May 2017; pp. 645–650.

36. Stoica, P.; Nehorai, A. MUSIC, maximum likelihood and Cramer-Rao bound. In Proceedings of the International Conference on Acoustics, Speech, and Signal Processing, New York, NY, USA, 11–14 April 1988; pp. 2296–2299.
37. Zhou, C.; Gu, Y.; Fan, X.; Shi, Z.; Mao, G.; Zhang, Y.D. Direction-of-arrival estimation for coprime array via virtual array interpolation. *IEEE Trans. Signal Process.* **2018**, *66*, 5956–5971. [CrossRef]
38. Zhou, C.; Gu, Y.; Shi, Z.; Zhang, Y.D. Off-grid direction-of-arrival estimation using coprime array interpolation. *IEEE Signal Process. Lett.* **2018**, *25*, 1710–1714. [CrossRef]
39. Bekkerman, I.; Tabrikian, J. Target detection and localization using MIMO radars and sonars. *IEEE Trans. Signal Process.* **2006**, *54*, 3873–3883. [CrossRef]
40. Jiang, H.; Yi, W.; Kirubarajan, T.; Kong, L.; Yang, X. Multiframe radar detection of fluctuating targets using phase information. *IEEE Trans. Aerosp. Electron. Syst.* **2017**, *53*, 736–749. [CrossRef]
41. Kay, S. Waveform design for multistatic radar detection. *IEEE Trans. Aerosp. Electron. Syst.* **2009**, *45*, 1153–1166. [CrossRef]
42. Stoica, P.; Larsson, E.G.; Gershman, A.B. The stochastic CRB for array processing: A textbook derivation. *IEEE Signal Process. Lett.* **2001**, *8*, 148–150. [CrossRef]
43. Korso, M.N.E.; Boyer, R.; Renaux, A.; Marcos, S. Conditional and unconditional Cramér-Rao bounds for near-field source localization. *IEEE Trans. Signal Process.* **2010**, *58*, 2901–2907. [CrossRef]
44. Lebrun, J.; Comon, P. An algebraic approach to blind identification of communication channels. In Proceedings of the International Symposium on Signal Processing and Its Applications, Paris, France, 26 July 2003; pp. 665–668.
45. Trees, H.V. *Detection, Estimation, and Modulation Theory, Optimum Array Processing*; Wiley: Hoboken, NJ, USA, 2004.
46. Kumar, L.; Hegde, R.M. Stochastic Cramér-Rao bound analysis for DOA estimation in spherical harmonics domain. *IEEE Signal Process. Lett.* **2015**, *22*, 1030–1034. [CrossRef]
47. He, Q.; Blum, R.S.; Haimovich, A.M. Noncoherent MIMO radar for location and velocity estimation: More antennas means better performance. *IEEE Trans. Signal Process.* **2010**, *58*, 3661–3680. [CrossRef]
48. He, Q.; Blum, R.S. The significant gains from optimally processed multiple signals of opportunity and multiple receive stations in passive radar. *IEEE Signal Process. Lett.* **2014**, *21*, 180–184. [CrossRef]
49. Cong, J.; Wang, X.; Huang, M.; Bi, G. Feasible sparse spectrum fitting of DOA and range estimation for collocated FDA-MIMO radars. In Proceedings of the 2020 IEEE 11th Sensor Array and Multichannel Signal Processing Workshop (SAM), Hangzhou, China, 8–11 June 2020; pp. 1–5.
50. Xie, R.; Hu, D.; Luo, K.; Jiang, T. Performance analysis of joint range-velocity estimator with 2D-MUSIC in OFDM radar. *IEEE Trans. Signal Process.* **2021**, *69*, 4787–4800. [CrossRef]
51. Gu, Y.; Zhang, Y.D.; Goodman, N.A. Optimized compressive sensing-based direction-of-arrival estimation in massive MIMO. In Proceedings of the 2016 IEEE International Conference on Acoustics, Speech and Signal Processing (ICASSP), New Orleans, LA, USA, 20–25 March 2016; pp. 3181–3185.

MDPI
St. Alban-Anlage 66
4052 Basel
Switzerland
Tel. +41 61 683 77 34
Fax +41 61 302 89 18
www.mdpi.com

Remote Sensing Editorial Office
E-mail: remotesensing@mdpi.com
www.mdpi.com/journal/remotesensing

Academic Open
Access Publishing

www.mdpi.com

ISBN 978-3-0365-7955-9